UNIVERSIDAD DE GRANADA

Climate-change Projections in the Iberian Peninsula: a Study on the Hydrological Impacts

MEMORIA PRESENTADA PARA OPTAR AL GRADO DE DOCTORA EN FÍSICA Y CIENCIAS DEL ESPACIO POR:

Matilde María del Valle García-Valdecasas Ojeda

Directoras: Dra. Yolanda Castro Díez
Dra. María Jesús Esteban Parra

Granada 2018

Editor: Universidad de Granada. Tesis Doctorales
Autor: Matilde María del Valle García Valdecasas Ojeda
ISBN: 978-84-9163-891-9
URI: http://hdl.handle.net/10481/51890

UNIVERSIDAD
DE GRANADA

La doctoranda *the doctoral candidate*: Matilde García-Valdecasas Ojeda y las directoras de la tesis *and the thesis supervisor/s*: Yolanda Castro Díez y María Jesús Esteban Parra,

Garantizamos, al firmar esta tesis doctoral, que el trabajo ha sido realizado por el doctorando bajo la dirección de los directores de la tesis y hasta donde nuestro conocimiento alcanza, en la realización del trabajo, se han respetado los derechos de otros autores a ser citados, cuando se han utilizado sus resultados o publicaciones. *Guarantee, by signing this doctoral thesis, that the work has been done by the doctoral candidate under the direction of the thesis supervisor/s and, as far as our knowledge reaches, in the performance of the work, the rights of other authors to be cited (when their results or publications have been used) have been respected*

Granada, a 30 de abril de 2018

Yolanda Castro Díez
Catedrática
Universidad de Granada

María Jesús Esteban Parra
Profesora Titular
Universidad de Granada

Matilde María del Valle García-Valdecasas Ojeda
Doctoranda

Agradecimientos

Hace casi cuatro años que comenzó esta andadura y casi desde ese instante siempre vi este día, este momento, con gran esperanza, pues indicaría que un largo camino ha sido recorrido. Hoy, al fin, podemos decir que lo hemos conseguido.

En primer lugar quiero dar las gracias a mis directoras de tesis, María Jesús y Yolanda. Me habéis dado la gran oportunidad de poder dedicarme a investigar algo que tanto me apasiona. No tengo palabras para agradeceros vuestra gran ayuda, guía y consejos a lo largo de todos estos años. Y en este agradecimiento no quiero olvidarme de Sonia, que aunque no es mi directora, es como si lo fuera, pues tu apoyo ha sido fundamental para que este trabajo haya llegado a buen puerto. Mil gracias a las tres.

Agradezco a la Junta de Andalucía su financiación a través del Proyecto de Excelencia LICUA P11-RCM-7941 que ha permitido la realización de esta Tesis y al Ministerio de Economía, Industria y Competitividad por la financiación en mis labores de investigación (CGL2013-48539-R).

A lo largo del sendero que he ido recorriendo desde que llegué a Granada he tenido la oportunidad de conocer a gente estupenda con la que he podido llegar a entablar una bonita amistad. Ana, no olvidaré las salidas contigo y Gonzalo, y por supuesto esas charlas de política. Gracias por ser como sois, no cambiéis nunca. Sonia, fuiste una gran compañera de despacho y una buena amiga, recuerdo los paseos por Granada con una bonita sonrisa, sinceramente me llevo muy buenos recuerdos y consejos de tu parte.

De gran ayuda en todo este mundo del modelado ha sido Dani. Si no fuera

por tu ayuda, primeros consejos y scripts, estaría corriendo aún las simulaciones con WRF. No sabes lo mucho que me ayudaste y por eso nunca podré agradecértelo del todo.

Gracias a todos los compañeros del despacho que han hecho de él mi segundo hogar en Granada. Jose, con quién compartí unos cuantos cafés al principio de mi andadura, gracias por tus consejos. Samir y Reiner, fue una gran alegría conoceros, nunca olvidaré esas charlas tan interesantes sobre un sin fin de temas y cultura colombiana. Vuestra ayuda con Matlab fue indispensable para mí. Y por supuesto, Enrique, un gran compañero de despacho y prácticas, contigo las cosas parecen más sencillas y eso me parece una gran virtud. Sebastiano, fuiste un buen compañero aunque siempre recordaré ese viaje Málaga Granada con tu coche, madre mía, pensé que no llegaba. Gracias César por tu apoyo y compañía, a Trino por su ayuda con las simulaciones del modelo. A Patricio, gracias por aguantar mis "neuras" en estos últimos momentos de tesis y gracias por tu ayuda con ArcGIS. Me llevo un buen recuerdo del Congreso en Nueva Orleans, y no olvido que te debo un concierto de jazz. Emilio, que hace poquito que te incorporaste, pero que seguro te va a ir muy bien, estoy segura. Y a todos aquellos que habéis estado de paso, unos más tiempo y otros un poquito menos, Ala'a, Fharid, Clemente, también gracias por todo lo que me habeís aportado. No quiero olvidarme de Andy, Juanlu, Penélope y Ana Meijide. Siempre con una palabra de ánimo, una palmadita de apoyo, una frase. Gracias a los cuatro.

A lo largo de estos años se me ha brindado la oportunidad de conocer nuevos lugares así como a gente realmente interesante durante Congresos y mi estancia en Boulder. Thanks to Jimy Dudhia, and all the NCAR staff for all your support during my stay in Boulder. Special thanks to Cindy Bruyère. It was a real pleasure to know you. Thanks for all your help, I have learned a lot from you and your group. De dicha ciudad, me llevo un grato recuerdo de Jon y Raquel. Jon por su gran ayuda en los modelos, charlas, paseos, apoyo, por su tortilla de patatas y guacamole y por esas rutas de senderismos en esos parajes inigualables. Y Raquel, por su alegría, gran acogida y salidas por Boulder. Siempre recordaré la aventura en la que nos embarcamos para comprar su nuevo coche junto a Domingo. A Marta, Álvaro, Pedro, Jordi, Gonzalo y en general a todo el grupo Not a science chat, gracias por todo.

A todos los compañeros de prácticas, Jorge, Jesús, Artur, Silvia, Leonor, Kiko, Javier y Elisa. Ha sido una auténtica maravilla compartir clases con vosotros. Gracias por brindarme la posibilidad de aprender a vuestro lado en esa bonita escuela de arquitectura. Gracias a todos los compañeros del Departamento de Física Aplicada, ha sido un honor pertenecer a esta gran familia.

No quiero olvidarme tampoco de Santiago y, en general, de todo el equipo que administra el servicio de supercomputación ALHAMBRA. Vuestra ayuda y consejos han hecho que la realización de las simulaciones no haya sido una tarea tan ardua. A Juanjo, Chus y Sixto que me guiaron en ciertos momentos de duda. A Conrado y Belén, por su amabilidad y ayuda en esas tareas administrativas, sin ellos todo hubiera sido más complejo. Como digo, han sido casi cuatro años a pleno rendimiento, y sois muchos más de los aquí citados los que habéis pasado a mi vera. Cada uno, cada una, en distintos tiempos y distintos lugares, habéis aportado, como mínimo, vuestro pequeño granito de arena. A todos, mil gracias.

Y por supuesto gracias a mi madre, mi padre y mis hermanas, que aunque estemos separados en la distancia y nos veamos menos de lo que deberíamos, siempre me ha apoyado y ayudado a lo largo de toda mi vida. A mi prima Cori, que si no fuera por ella no hubiera descubierto lo que me apasiona la meteorología, muchas gracias prima. A mi familia en general, tanto la familia que conozco desde que nací, como la que me adoptó como una más hace ya… ¿Cuánto? Más de dieciséis años y medio!!! Un millón de gracias a todos, y especialmente a Maricarmen. Mil gracias a mi otra familia de Torremolinos, que desde hace tantos años están conmigo, y especialmente a Rosa que siempre ha estado apoyándome, confiando en mí y valorándome tanto, ¡ah! y por supuesto a Alejandra siempre siempre tan bonita. En fin, espero no haberme olvidado de nadie, en todo caso no me lo toméis en cuenta.

Y por último y más importante a Tí, mi amigo, mi familia, mi hogar, mi todo. Gracias por tu infinita paciencia y comprensión, por ser mi mayor apoyo, por hacerme el cafelito todas las mañanas, por ayudarme, preocuparte por mí como el que más y facilitarme tanto las cosas. Son muchas las experiencias a lo largo de tantos años que nunca olvidaré ... Siempre me has hecho la vida más bonita y por eso te quiero.

Summary

The global-climate projections indicate an acceleration of the hydrological cycle as a consequence of global warming. However, substantial uncertainties about its magnitude persist, especially at the regional scale. If the predictions hold true, substantial impact on society is expected. Therefore, it is essential to gain a fuller understanding of the role of the different hydrological variables in a warming-world context at an adequate spatial scale in order to mitigate the potential effects of the climate change.

In this thesis, the dynamical-downscaling approach was selected to perform high-resolution climate-change projections of hydrological variables over a region particularly vulnerable to climate change, i.e. the Iberian Peninsula (IP), using the Weather Research and Forecasting (WRF) model. The different simulations were performed at a spatial resolution of 0.088° (10 km approximately) in order to capture the effect of the topography in the different climate variables analyzed. This regional climate model (RCM) was driven by two different global climate models (GCMs), the CCSM4 and the MPI- ESM-LR, which adequately represent the climate over the study region. However, the GCMs are not free of systematic errors, so that for a reduction of inherited errors in the WRF simulations, a previous bias-correction approach was applied to the different GCM outputs.

For an appropriate characterization of the climate over the IP, an analysis of the different configurations was made. For this, a set of 7 runs of 2 years (1995-1996) were performed by combining different physics schemes, which were compared with observational gridded products. Thus, we selected the combination that best captured the main characteristics of the Iberian climate. No

configuration performs better than all others for all variables over the entire IP, so the combination that presented the best broad agreement with respect to observations was selected.

An adequate study of the impact that climate change will exert on hydrological variables in the future requires a clarification of the model's ability to represent the current climate. The model evaluation consisted of comparing the WRF outputs in terms of primary climate variables, i.e. precipitation, maximum (T_{max}) and minimum (T_{min}) temperature, but also in other hydrological variables closely related to drought events, i.e. surface evapotranspiration and soil-moisture content. For this, a set of 3 different runs were completed. On the one hand, a 35-year simulation (1980-2014) was performed, driven by ERA-Interim reanalysis in order to detect uncertainties associated with the RCM. On the other hand, two simulations from the aforementioned bias-corrected data from CCSM4 and the MPI-LSM-LR were undertaken to characterize inaccuracies inherited by the GCMs. The results of the model evaluation evidenced that, although the WRF model has certain difficulties, it is able to represent the main characteristics of the Iberian climate in both long-term means and extreme events. Therefore, it can be used to perform regional climate projections over the IP.

Additionally, the model's capability to detect drought events in Spain was also evaluated. In this context, drought characterization was examined with two widely used drought indices, i.e. the Standardized Precipitation Index (SPI), which is based solely on precipitation data, and the Standardized Precipitation Evapotranspiration Index (SPEI) that takes into account the effect of the temperature. Because both indices are based on the same calculation procedure, the direct comparison between the two in space and time will elucidate the effect of temperature on drought severity. For this purpose, the WRF outputs from the simulation conducted by ERA-Interim were used to compute the indices and they were compared with those provided from observational data. The analysis was also focused on determining the added value by using downscaled climate data to detect drought events, so the drought indices computed from WRF fields were also compared with those from the WRF-driving data (the ERA-Interim fields). In this analysis, the results suggest that the WRF model characterizes reasonably well the spatio-temporal drought variability in a topographically complex region such as Spain, providing an added value with respect to its driving data.

Finally, future climate projections in terms of hydrological variables were achieved. For this purpose, 8 different runs were generated by using the bias-corrected outputs from the two aforementioned GCMs. To analyze the effects of different greenhouse gas (GHG) concentrations, the model was driven along two different representative concentration pathways (RCPs), i.e. an intermediate-emissions scenario (the RCP4.5) and the highest-emissions scenario (the RCP8.5), and for two different periods, i.e. the so-called near future (2021-2050) and the far future (2071-2100) period. Thus, by comparing the results for each period, we can elucidate short-term and long-term climate trends. The analysis of future changes was based on comparing the different WRF outputs for the future climate with those achieved from the present, using the so-called Delta-change approach. The projected changes were analyzed in terms of primary climate variables, i.e. precipitation and extreme temperatures, as well as surface evapotranspiration and soil-moisture content, which provided additional information about the future trend towards dryness or wetness conditions.

In general, the results of the high-resolution projections suggest that the IP will likely undergo substantial changes in terms of primary climate variables as well as related drought variables, leading to a potential increase of drought phenomenon, more marked for the far future and under the RCP8.5. That is, significant reductions of the precipitation are expected by the end of this century, at least in long-term mean values as well as with a substantial rise in temperatures, especially during the warm seasons and over the southern half of the IP. Such a trend is accompanied by a sharp reduction in surface evapotranspiration and in the soil-moisture content, which will very likely exacerbate the dryness conditions over the IP. In this context, the IP will also undergo greater risks of megadrought events.

The findings presented in this work constitute a valuable contribution to the understanding of the effects of the climate change on the hydrological cycle over an especially vulnerable region such as the IP. This work also provides significant results in relation to the GHG-induced climate-change signal in terms of hydrological variables and their effects in the increasing drought-condition in the IP, which is particularly relevant for drought-related decision making in a context of changing climate.

Resumen

Las proyecciones globales de cambio climático indican una aceleración del ciclo hidrológico como consecuencia del calentamiento global. Sin embargo, aún existen importantes incertidumbres sobre la magnitud de dicho cambio. Si estas predicciones son ciertas, importantes impactos se producirán en la sociedad. Por tanto, es esencial un mayor entendimiento del comportamiento de las distintas variables relacionadas con el ciclo del agua ante un aumento de la temperatura a una escala espacial adecuada con el fin de mitigar los efectos del cambio climático.

En esta Tesis se usó un *downscaling dinámico* con el objetivo de realizar proyecciones de cambio climático de variables hidrológicas en una región especialmente vulnerable, la Península Ibérica (IP), utilizando el modelo Weather Research and Forecasting (WRF). Para ello, se realizaron diferentes simulaciones usando una resolución espacial de 0.088° (aproximadamente 10 km) con el propósito de capturar los efectos de la topografía en las diferentes variables analizadas. Este modelo climático regional (RCM), fue conducido por dos modelos climáticos globales (GCMs), el CCSM4 y el MPI-ESM-LR, que representan adecuadamente el clima en esta región a una mayor escala. Sin embargo, todo GCM posee ciertos errores sistemáticos. Por esta razón, con el objetivo de evitar errores heredados de los modelos globales, se aplicó una técnica de corrección de sesgo sobre las salidas de los modelos globales.

Con el objetivo de caracterizar adecuadamente el clima de la IP, se analizó diferentes configuraciones del modelo. Con tal propósito, se realizaron 7 simulaciones de 2 años de duración (1995-1996), resultado de combinar diferentes esquemas de parametrizaciones. Tales simulaciones se compararon con datos

observacionales con el objetivo de seleccionar aquella combinación de parametrizaciones que capturaba mejor las características del clima de la península. Como resultado de dicho análisis se obtuvo que ninguna configuración representaba mejor las características climáticas para toda la península, por lo que se seleccionó aquella configuración que tuvo un comportamiento general más parecido a las observaciones.

Para el estudio adecuado del impacto del cambio climático en variables hidrológicas en el futuro, es necesario analizar la habilidad del modelo para representar el clima actual. La evaluación del modelo consistió en comparar las salidas del modelo WRF en términos de variables climáticas primarias, es decir, precipitación y temperaturas máxima y mínima, y también para otras variables hidrológicas íntimamente relacionadas con eventos de sequía (evapotranspiración superficial y contenido de humedad del suelo). Para esto, se realizaron un conjunto de tres simulaciones. Por un lado, se completó una simulación de 35 años (1980-2014) utilizando los datos de ERA-Interim para conducir el modelo, pudiendo evaluar así incertidumbres propias del modelo regional. Por otro lado, también se realizaron 2 simulaciones usando las salidas corregidas en sesgo de los GCMs. De esta forma se pueden dilucidar incertidumbres heredadas de los modelos globales. Los resultados de la dicha evaluación evidenciaron que WRF, aunque muestra ciertas dificultades, es capaz de capturar adecuadamente el clima de la IP, tanto en valores medios como en valores extremos. Por tanto, puede considerarse que WRF es adecuado para realizar proyecciones climáticas en la IP.

Adicionalmente se evaluó la capacidad del modelo para detectar eventos de sequía. En este contexto, la caracterización de la sequía se realizó mediante el uso de dos índices ampliamente conocidos: el índice estandarizado de precipitación (SPI), el cual está basado únicamente en valores de precipitación, y el índice estandarizado de precipitación evapotranspiración (SPEI) que también tiene en cuenta el efecto de la temperatura. Debido a que ambos índices se basan en el mismo procedimiento de cálculo, la comparación directa de los resultados obtenidos para ambos índices es útil para el análisis de los efectos de la temperatura en la severidad de las sequías. Para tal análisis las salidas del modelo WRF de la simulación conducida por ERA-Interim fuerom usadas en el cálculo de los índices y estos se compararon con los índices calculados con valores observacionales. Además, dicho análisis se enfocó también en determinar si WRF proporcionaba un valor añadido con respecto a sus datos de entrada. En este análisis, los resultados sugirieron que el modelo WRF captura razonablemente bien la variabilidad espacio-temporal de las sequías en España, una región topográficamente compleja, proporcionando un valor añadido con respecto a sus condiciones iniciales y de contorno.

Finalmente, se realizaron diferentes proyecciones climáticas de distintas variables hidrológicas. Para ello, se obtuvieron 8 simulaciones mediante el uso de las salidas de los GCMs corregidas en sesgo. Para analizar los efectos en el sistema climático de diferentes concentraciones de gases de efecto invernadero (GHGs) las simulaciones se realizaron usando diferentes escenarios de emisión (RCP), el RCP4.5 que corresponde a un escenario intermedio de emisiones de GHGs, y el RCP8.5 el cual contempla las mayores concentraciones de GHGs y para dos periodos distintos, el llamado futuro cercano (2021-2050) y para el futuro lejano (2071-2100). De esta forma, mediante la comparación entre los diferentes periodos se puede examinar tendencias en el siglo XXI a corto y largo plazo. El análisis de los cambios en el futuro se basó en la comparación de las salidas del modelo en el futuro con respecto a las del presente mediante la aproximación Delta-Change. Los cambios proyectados se analizaron en términos de variables climáticas primarias (precipitación y temperaturas) y otras variables asociadas con el ciclo hidrológico (evapotranspiración superficial y contenido de humedad del suelo), las cuales proporcionan información adicional sobre la tendencia hacia unas condiciones de sequedad o humedad.

Los resultados de las proyecciones de cambio climático sugieren que es muy probable que la IP sufra fuertes cambios en términos de las variables climáticas primarias así como en aquellas relacionadas con los eventos de sequía, lo cual puede generar un aumento de los fenómenos de sequía. Es decir, se esperan importantes reducciones de precipitación para finales de este siglo, al menos en los valores medios, así como un incremento importante de las temperaturas. Tal tendencia climática probablemente esté acompañada por una reducción de la evapotranspiración así como del contenido de la humedad del suelo. En dicho contexto, la IP sufrirá un aumento en el riesgo de megasequías.

Los resultados de este estudio representan una valiosa contribución para un mejor entendimiento de los efectos del cambio climático sobre el ciclo hidrológico en un área especialmente vulnerable como es la IP. Este trabajo también aporta resultados significativos en relación a la señal de cambio climático en términos de variables hidrológicas y sus efectos en el incremento de condiciones de sequía en la IP, lo cual es particularmente relevante para la toma de decisiones relacionadas con la sequía en un contexto de clima cambiante.

Contents

List of Figures

List of Tables

Acronyms

ACM2 Asymmetric convective model.

AEMET Spanish National Meteorological Agency.

AHC agglomerative hierarchical clustering.

AR5 Fifth Assessment Report.

ARW Advanced Research WRF.

BMJ Betts-Miller-Janjic.

CAM3.0 NCARs Community Atmosphere Model.

CAM5.1 CAM5.1 2-moment-5-class scheme.

CAPE convective available potential energy.

CCSM4 Fourth Version of the Community Climate System Model.

CLWRF CLimate WRF.

CMIP5 Coupled Model Intercomparison Project's Fifth Phase.

CORDEX COordinated Regional Downscaling Experiment.

CSI Critical Success Index.

EA East Atlantic.

ECMWF European Centre for Medium-Range Weather Forecasts.

ESM Earth system model.

ETCCDI Expert Team on Climate Change Detection and Indices.

GCM global climate model.

GF Grell-Freitas.

GHG greenhouse gas.

GLEAM Global Evaporation Amsterdam Model.

HG-PP Modified Hargreaves equation.

IP Iberian Peninsula.

IPCC Intergovernmental Panel on Climate Change.

KF Kain-Fritsh.

LAM limited area model.

LBC lateral boundary condition.

LSM Land-Surface Model.

MAE mean absolute error.

MOPREDAS Monthly Precipitation Database of Spain.

MOTEDAS Monthly Temperature Database of Spain.

MPI-ESM-LR Max Plank Earth System Model at Low Resolution.

NAO North Atlantic Oscillation.

NCAR National Center for Atmospheric Research.

PBL planetary boundary layer.

PCA principal component analysis.

PDF probability density function.

PSS Perkins skill score.

RCM regional climate model.

RCP representative concentration pathway.

RMSE root mean squared error.

S/N signal to noise.

SF surface layer.

SLP sea level pressure.

SN Spectral Nudging.

SPEI Standardized Precipitation Evapotranspiration Index.

SPI Standardized Precipitation Index.

SST sea-surface temperature.

SWC soil-water content.

TKE turbulent kinetic energy.

ToE Time of Emergence.

UW Bretherton and Park scheme.

WMO World Meteorological Organization.

WRF Weather Research & Forecasting Model.

WSM3 WRF Single-Moment 3-class.

YSU Yonsei University.

Chapter 1

Introduction

1.1. Assessing Uncertainties on the Hydrological Cycle under Climate Change

Climate change has already been considered one of the major threats for the Earth for the 21^{st} century (Mishra and Singh, 2010). In fact, the Intergovernmental Panel on Climate Change (IPCC) Fifth Assessment Report (AR5) pointed out that warming of the climate system is unequivocal and almost certainly caused by the human activities. The recent anthropogenic emissions of greenhouse gases (GHGs) are the highest in history, leading a further warming, which will worsen if these emissions continue, with the subsequent impact on ecosystems and ultimately on humans (IPCC, 2014).

Although substantial uncertainty persists concerning the magnitude of global warming, increasing trends in temperature are already noticeable worldwide, not only in long-term mean values, but also in the greater frequency and intensity of extreme events. For example, Perkins et al. (2012) revealed that intensity, frequency, and duration of summertime heatwaves and warm spells have increased since the early 1950s in many parts of the world. In this context, this warming trend is expected to exert a powerful impact on water cycle on the global scale, altering the water-holding capacity of atmosphere, precipitation patterns, evapotranspiration, infiltration, and surface runoff. In fact, a general consensus among the scientific community holds that a warmer world will intensify the hydrologic cycle (Milly et al., 2002, Huntington, 2006, Held and Soden, 2006, Sheffield and Wood, 2008, Sherwood and Fu, 2014).

To mitigate the effects of the climate change, a fuller understanding of the global water balance and its role in a warmer world is essential. However, our current capacity to directly monitor the time course of certain hydrological variables is unfortunately weak. In this sense, Dolman and de Jeu (2010) emphasized that so long as trends in surface evapotranspiration remain uncertain, our understanding of water-cycle behavior will remain limited. Moreover, different studies (eg., Seneviratne et al., 2006a) have pointed out the importance of the soil-moisture content in the characterization of the atmosphere processes, since this parameter strongly influences climate variability. This is important in regions where interseasonal and interannual changes in soil-water availability fluctuates between dry and wet conditions (i.e. transitional climate zones). Consequently, current global drying and wetting trends over land are unclear and the results reported are sometimes even contradictory (Dai, 2011, Seneviratne et al., 2012, Sheffield et al., 2012), making it also uncertain as to whether the climate-change signal, in terms of hydrological variables, has emerged.

For instance, Greve et al. (2014) examined global dryness trends over land through the analysis of changes in precipitation, potential evapotranspiration and actual evapotranspiration during the period 1949-2005. In this study, the authors indicate that changes in dryness conditions remain mostly inconclusive over land, and only 10.8% of the global land area revealed significant changes toward drier conditions. In another recent study, Orlowsky and Seneviratne (2013) indicated that there is no robust signal of change in the magnitude of droughts in recent years. This study was performed in terms of drought trends by using the Standardized Precipitation Index (SPI) from observations-based data and the Coupled Model Intercomparison Project's Fifth Phase (CMIP5) simulations. It is important, however, to take into account that the internal variability that affects the different hydrological variables could be masking trends toward dryness conditions (New et al., 2000).

On the contrary, Feng and Fu (2013) suggested an expansion of dryland areas around the world in the last 60 years. Jung et al. (2010) also pointed out that the global aridity has grown. These researchers found, by combining in situ measurements and remote sensing of surface evapotranspiration, that a global negative trend has been occurring for the last few years, which is likely associated with soil-moisture limitation. Additional works (Trenberth, 2010, Lin et al., 2015, Burke et al., 2006, Dai, 2013) indicate that the global aridity has risen in step with the warming trend, which has been accompanied by a greater frequency and severity of drought events.

In any case, the possibility of an intensification of the hydrological cycle and its consequences make it essential to investigate their effects under different plausible scenarios of anthropogenic GHG emissions in the future, in order to mitigate as much as possible the expected impact. For instance, drought is already recognized as one of the most devastating natural disasters, causing damages of many billions of dollars while affecting millions of people in the world each year (Heathcote, 1983, Wilhite, 2000). If due to warming, the climate-system response actually accelerates the hydrological cycle, the frequency and intensity of such drought events are expected to increase (Touma et al., 2015, Seneviratne et al., 2012).

For studying the effect of the warming in a future predicted to undergo greater GHG concentrations, global climate models (GCMs) constitute the first source of information about the possible future climate response. These represent the global climate system through the use of different components that describe the atmosphere, ocean, and land-surface processes. Thus, by testing GCM outputs under different radiative scenarios, we may be able to detect the influence of climate change by identifying the behavior in the hydrological cycle, offering a powerful tool to elucidate the climate shift by the end of the 21^{st} century (Giorgi et al., 2011).

In recent years, many works have addressed the study of future changes in hydrological conditions (Burke et al., 2006, Zhao and Dai, 2015). For instance, Cook et al. (2014) examined the 21^{st} century drying trends at the global scale by using different GCM projections and they found that the potential evapotranspiration is key in the greater drying. Thus, regions expected to have greater precipitation are likely to shift towards drier conditions due to the increase in evaporative demand. Furthermore, drought will be intensified by this process in regions where the precipitation is projected to diminish as well. In this latter case, the land surface-atmosphere coupling is expected to intensify the aridity due to different feedback mechanisms (Seneviratne et al., 2013). Ault et al. (2016) suggested that under future scenarios with major rises in temperature, the risk of megadrought events increases substantially. Thus, in the predictions of future changes in the water availability multiple factors should be taken into account, which are even more uncertain at the regional scale (Burke and Brown, 2008).

In this context, the great efforts in recent years from the climate-model groups have enabled the new generation of GCMs to resolve processes at a rather fine scale of resolution. However, due to the complexity of the climate system, enormous computational resource is required to compile climate information at the regional scale. Thus, the horizontal grid spacing of the atmospheric components of the GCMs that participate in CMIP5 is from 0.5° to 4° (Taylor et al., 2012). Therefore, these remain unable to adequately capture climate information with fine detail at a reasonable computational cost.

1.2. Regional Climate Models (RCMs)

The dynamical downscaling approach has been commonly used to overcome the spatial resolution limitations of GCMs. One of the main rationales for developing the dynamical downscaling is the need of compiling trustworthy climate information at different spatiotemporal scales in order to mitigate the effect of human activities on the future climate change (Di Luca et al., 2015).

This approach is based on using a regional climate model (RCM) or limited area model (LAM) nested in either observational reanalysis or GCM outputs in order to generate small-scale features in response to the interactions between large-scale flow from the lateral boundary conditions (LBCs), local forcings (e.g. topography, coastlines or soil forcings) and non-linear dynamical interactions. Therefore, the model is focused on a limited region, and consequently the computational cost substantially decreases. Note that the nested model is not developed with the purpose of correcting the large-scale circulation provided by the driving data (Giorgi, 2006) but rather to gather high-resolution details as accurately as possible over a region of interest. One of the main advantages of using dynamical downscaling is that RCM are physically consistent and not are based on empirical relationships that occur in the present, but do not have to occur in the future as in the statistical downscaling (Bruyère et al., 2014).

However, important issues should be taken into account in order to configure the model adequately for dynamical downscaling. It has been widely demonstrated that for short time ranges, RCMs offer better results than do the GCMs in which they are nested, due to their great ability to represent regional-scale characteristics. However, the added value provided by regional modelling for long-term simulations is not so clear. In fact, the regional model accuracy decreases very quickly because the boundary conditions for the nested domain are mathematically not well established (Staniforth, 1997, Miguez-Macho et al., 2004). That is, it is not possible to determine the exact boundary conditions because there is no single solution. Moreover, the LBCs in which the RCM is embedded should be continuous in order to accurately solve the model equations. This, together with the discretization of the model formulations, can cause numerical instability to emerge, providing meaningless simulations. Therefore, although the RCMs constitute a powerful tool to generate regional climate information, the correct configuration of the model is required as well as further evaluation concerning the current characterization of the climate.

Dynamical downscaling is a relatively new technique, but due to its great capacity to generate climate information at a suitable spatial and temporal resolution with a reasonable computational cost, it has been widely used. In the last decade, different regional climate-change projections have been offered within the framework of different international and national initiatives. For example, NARCAPP[1] (North American Regional Climate Change Assessment Program, Mearns et al., 2012) is an international project intended to satisfy the need of decision makers and of impact, vulnerability, and adaptation research communities for high-resolution climate-change projections over United States, Canada, and northern Mexico. NARCLIM[2] (NSW and ACT Regional Climate Modelling, Evans et al., 2014) was developed with the same purpose for the southeastern Australia domain. The PRUDENCE[3] (Prediction of Regional scenarios and Uncertainties for Defining European Climate changes risk and Ef-

[1]http://www.narccap.ucar.edu/
[2]http://climatechange.environment.nsw.gov.au/Climate-projections-for-NSW/About-NARCliM
[3]http://prudence.dmi.dk/

fects, Christensen et al., 2007a) Project and, more recently, the ENSEMBLES[4] (Ensemble-based Predictions of Climate Changes and their Impacts, van der Linden and Mitchell, 2009) Project were developed to provide regional climate information in the European region, which has produced valuable results.

The COordinated Regional Downscaling Experiment (CORDEX)[5] (COordinated Downscaling Experiment, Giorgi et al., 2009) project is currently underway and provides regional climate data for different regions worldwide. Within this framework, the EURO-CORDEX (Jacob et al., 2014) domain encompasses the European Union in a rotated grid by using three different spatial resolutions: 0.44° (~50 km), 0.22° (~25 km), and 0.11° (~12.5 km). Currently, EURO-CORDEX provides projections at the regional scale driven by different CMIP5 global models under two scenarios of the AR5 (RCP4.5 and RCP8.5). The high-resolution RCM simulations were completed for historical (1971-2000) and future in three different periods (2011-2040, 2041-2070 and 2071-2100). In a similar way, Med-CORDEX (Ruti et al., 2016) has been proposed by the Mediterranean region also covering the Iberian Peninsula (IP).

In Spain, the ESCENA[6] project was created within the framework of the Spanish Strategic action on energy and climate change in order to provide the scientific basis for assessing regional climate-change impact over Spain. ESCENA was focused on the near future (2021-2050) for a domain that covers the whole of Spain. PNACC (Escenarios-PNACC, 2012) is a recent initiative undertaken by Spanish researchers within the framework of Spanish R+D 2008-2011 Program. In its first version, PNACC (Plan Nacional de Adaptación al Cambio Climático) was based on CMIP3 global model outputs and provides high-resolution temperature and precipitation information. More recently, ESCENARIOS PNACC 2017 was created using the EURO-CORDEX domain by downscaling CMIP5 global models. Under this initiative, more variables have been made available for the scientific community (Fernández et al., 2017).

Due to the different sources of RCM uncertainty, one of the most important steps when applying dynamical downscaling is to ascertain the model's ability

[4]http://ensembles-eu.metoffice.com/
[5]http://www.cordex.org/
[6]http://proyectoescena.uclm.es/

to represent the real climate (Christensen et al., 2007b, Evans and McCabe, 2010, Montávez et al., 2017). In this context, different studies have been performed analyzing the ability of different RCMs to characterize current climate conditions over the IP, which are focused mainly on analyzing precipitation and temperature (Herrera, 2011, Argüeso et al., 2011, 2012a, Gómez-Navarro et al., 2013, Cardoso et al., 2013, Jerez et al., 2013, López-Franca et al., 2013, Pérez et al., 2014, Fernández et al., 2007, Soares et al., 2012a, 2016). Other studies examine variables such as the wind, snow, radiation or land surface-atmosphere fluxes (Lorente-Plazas et al., 2015a, Jiménez et al., 2010, Lorente-Plazas et al., 2015b, Gómez et al., 2016, Pons et al., 2016, Ruiz-Arias et al., 2013, Knist et al., 2017). All these works draw the general conclusion that the climate of the IP is better represented by RCMs mainly because they are able to represent local effects and surface features produced by a complex orography than the GCMs enable to represent.

In terms of climate projections, different studies have also been performed in order to examine future trends over the IP. Thus, several works examine changes in temperature (Turco et al., 2015, Gómez-Navarro et al., 2010, Jerez et al., 2018), precipitation (Argüeso et al., 2012b, López-Franca et al., 2015, Jerez et al., 2012), wind (Gómez et al., 2016) and other variables (Pons et al., 2016) by using results from different RCMs.

1.3. Objective and Structure of the Thesis

This work aims to generate climate-change projections at high resolution over the IP, for a near and far future, by using the Weather Research & Forecasting (WRF, Skamarock et al., 2008) as RCM in order to elucidate the effects of the climate change in different variables involved in the hydrological cycle under different GHG emissions scenarios. To this end, the outputs of GCMs of CMIP5 have been downscaled with the purpose of collecting climate information at an adequate scale resolution.

The IP is an excellent region to study the effects of increased GHG concentrations under dryness conditions and how the hydrological cycle could be altered. Indeed, Diffenbaugh and Giorgi (2012) determined that the IP, as part of the Mediterranean region, is a hotspot in a context of global warming, and therefore is especially vulnerable to human inducement of global warming.

Moreover, the IP (Figure ***1.1***) is characterized by a high spatio-temporal variability in precipitation due to its high altitudinal gradient, extensive coasts, and it is influenced by factors such as its localization between two climate regions (the subtropical and the mid-latitude areas) as well as between two completely different water masses (the Mediterranean Sea and the Atlantic Ocean). These facts indicate that, for the gathering of trustworthy climate information for this region, it is particularly important to use high-resolution techniques to adequately characterize the future climate in this region.

This Thesis is structured as follows: Chapter ***2*** describes the data from observations as well as GCMs used to drive the WRF model together with the methodology applied to correct systematic errors in those models. Chapter ***3*** details the configuration selected to simulate both the current and future climate over the IP as well as a detailed sensitivity study performed to select an

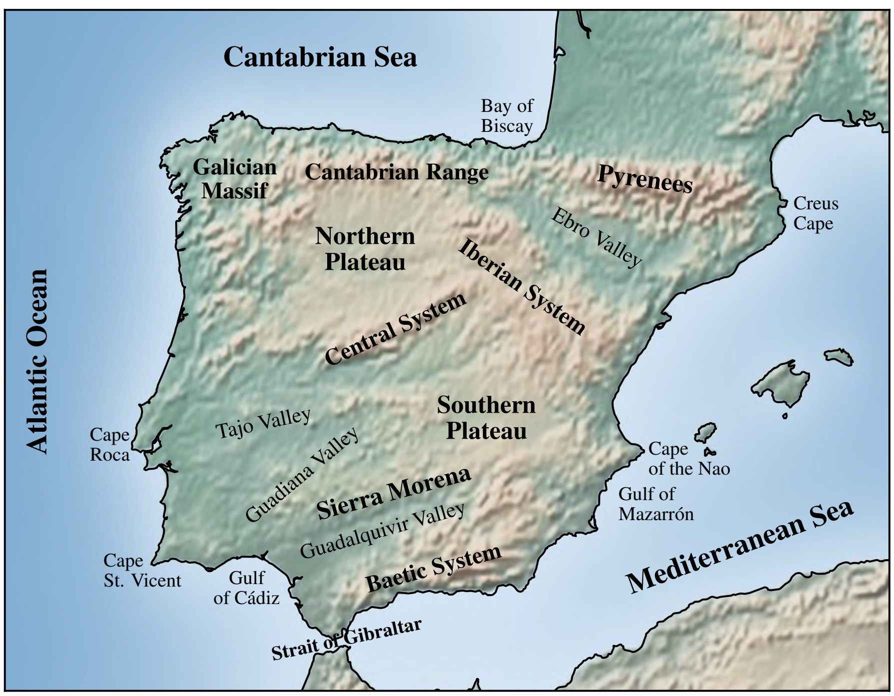

Figure 1.1: *Main geographical features of the Iberian Peninsula.*

adequate combination of parameterizations. The assessment of the model capability to capture the main current climate characteristics (model evaluation) in terms of different hydrological variables is addressed in Chapter ***4***. Chapter ***5*** studies the ability of the model to characterize drought events by using drought indices, with an analysis also of the added value provided by WRF in the detection of droughts regarding its driving data. Chapter ***6*** examines possible future changes in terms of primary climate variables that are the main precursors of drought events. Chapter ***7*** analyzes projected changes in drought events as well as in other variables related with such phenomenon (i.e. surface evapotranspiration and soil moisture). Finally, Chapter ***8*** summarizes the most noteworthy results and the conclusions of the study as well as potential future works.

Chapter 2

Data: Observations and Lateral Boundary Conditions

This chapter presents the data both from observations and from GCMs used in this thesis. On the one hand, different gridded products have been used to validate the WRF capability to characterize current climate conditions. On the other hand, data from different sources have been selected in order to drive the WRF model (which are known as the lateral boundary conditions of the model). The results of the dynamical downscaling approach depend strongly on the LBCs, which usually are not free of systematic errors. Therefore, a bias-correction approach was followed to create more adequate LBCs, as detailed also in this chapter.

2.1. Observational Gridded Datasets

A gridded database is a two-dimensional array, regular in both space and time, created to represent an atmospheric variable such as temperature or precipitation. Such products are the results of applying different quality controls and interpolation techniques using the observational networks of different meteorological variables. In recent years, several gridded datasets have been created at different scales in time and space (CRU, New et al., 2002, GHCN-daily, Caesar et al., 2006, E-OBS, Haylock et al., 2008).

In the context of RCMs, an adequate analysis of the changing climate strongly relies on the good skill of the model to capture the main climate characteristics throughout the study region. A standard approach to evaluate the model performance is through the analysis of the simulations of current climate by direct comparisons with observations. For this, assessments by using of gridded products may be more appropriate than those based on the measurements of specific meteorological stations. That is true because the in-situ stations represent a meteorological value in a particular place, and the model outputs consist of spatially averaged values for each grid, which are calculated by the mean features in the same grid as well. Therefore, the model outputs and gridded observations are more comparable, this being especially important for hydrological variables such as precipitation (Osborn and Hulme, 1997), which are characterized by a high spatial and temporal variability. Furthermore, due to the similarity between observational gridded datasets and the WRF outputs, the spatial differences should not be significant, and then, a simple projection of the model outputs onto the observational grid is possible for comparing them.

However, gridded data are not free of errors, and occasionally these can be large. The inherent uncertainties in gridded products arise from several factors such as measurement errors (instrumental malfunctions and reallocation of climate station among many others), but also due to statistical procedures applied to build them. In fact, observational uncertainties can be of similar magnitude as the inherent RCM biases (Prein and Gobiet, 2017), even in areas where the gridded products are based on dense networks (Gómez-Navarro et al., 2012). Such uncertainties are unavoidable, so it is essential to take them into account since they could lead a misinterpretation of the model's ability to capture the climate behaviors, especially in regions such as the IP. It should be noted that the IP is characterized by a strong spatio-temporal climate variability, mainly because of the interaction of the large-scale flow and its complex topography.

As a result, different sets of gridded products were used in this thesis to address different aspects related to the ability of the WRF model to represent the current climate characteristics in terms of different hydrological variables. The use of the most suitable observational gridded product according to the analysis performed at each point in time might reduce the uncertainty associated with the observational gridded product in the study.

2.1.1. Daily Gridded Observations

Precipitation

For an appropriate evaluation of the capacity of the WRF model to capture the high spatio-temporal precipitation of the IP, it is desirable to use a high-resolution gridded product in both space and time. Therefore, we can reduce misinterpretations due to observational uncertainties. In this context, Spain02 (Herrera et al., 2012, 2016) is a high-resolution daily gridded dataset developed for peninsular Spain and the Balearic islands.

For precipitation, Spain02 has been widely used by many authors (Argüeso et al., 2011, 2012a, Prein and Gobiet, 2017, Turco et al., 2017, San-Martín et al., 2017, Quintana-Seguí et al., 2017), proving to be notably apt for climate studies, for determining not only long-term means but also extreme values. These data are based on a dense network prepared by using 2576 time series of daily precipitation stored at 07 UTC from the Spanish National Meteorological Agency (AEMET). Details of its development can be found in Herrera et al. (2012) and Herrera et al. (2016).

Among different versions and products provided by the MetGroup Data Server[1], the Spain02 Versions 4.0 and 5.0 in their area-averaged monthly trivariate thin-plate splines and ordinary kriging (AA-3D) approach were selected in this thesis. Beyond details, it was constructed following the methodology of the E-OBS datasets, which takes into account the orography in the interpolation approach in order to reduce uncertainties associated to networks with few stations, These gridded products, which are available at different spatial resolutions, are based on a rotated coordinated grid corresponding to those used in the EURO-CORDEX and ENSEMBLE projects for the periods of 1971 to 2010 and 1971 to 2015 in Version 4.0 and 5.0, respectively. Here, the spatial resolution of 0.11° (~12 km) was selected (hereafter called SPAIN011) because this is the grid most similar to that from the WRF outputs and thus more comparable.

Although the Spain02 Version 4.0 showed an appropriate climate charac-

[1]http://meteo.unican.es/datasets/spain02

terization for the period used in a preliminary analysis[2], the data displayed some problems when long-term mean values were calculated for the entire period of study (1980-2014). Therefore, the grid of SPAIN011 Version 4.0 was changed to its new version, SPAIN011 Version 5.0, which is an updated version covering a longer period and solving the aforementioned problem.

To compare the model outputs against an accurately observational dataset over mainland Portugal, we used the PT02 database Belo-Pereira et al. (2011). This is a high-resolution 0.2° regular grid product of daily precipitation data stored at 09 UTC that covers the period from 1950 to 2003. PT02 has been demonstrated to be adequate to validate precipitation patterns over Portugal, as shown by Soares et al. (2016) and Cardoso et al. (2013), among others. This gridded dataset consists of about 400 precipitation gauges from the Portuguese Meteorological Service and National Water Institute covering the period from 1950 to 2003. The stations used for its creation have adequate altitudinal distribution, so that the PT02 gridded data is able to capture the effects of the orography in the precipitation patterns over this region. The PT02 data are freely distributed as requested by the Portuguese Instituto de Meteorologia[3].

Maximum and Minimum Temperature

The Spain02 Version 4.0 with the grid at 0.11° of spatial resolution was also used for maximum and minimum temperature. For these variables, the gridded products from Spain02 were constructed using the same procedure as for precipitation, but they are based on approximately 250 stations of the AEMET network. As for precipitation, the AA-3D approach was selected as recommended by the authors Herrera et al. (2016).

These data were also used in preliminary studies for the period 1995-1996 showing adequate climate behavior. However, a simple assessment of the data was performed for the entire study period and several anomalous values were identified for both maximum and minimum gridded dataset. Such problems, which are also found in Version 5.0, did not allow us to perform several analyses to evaluate the model outputs and, consequently, the SPAIN011 datasets

[2]SPAIN011 Version 4 was used in a sensitivity test that was performed to adequately select the WRF configuration, which will be detailed in Chapter **3**.

[3]http://www.ipma.pt/pt/produtoseservicos/index.jsp?page=dataset.pt02.xml

for maximum and minimum temperature was not used to evaluate the model outputs. Furthermore, as opposed to precipitation, no gridded dataset such as PT02 was available to compare the WRF temperature outputs over Portugal, and consequently, the E-OBS database was selected with this purpose. Although E-OBS is based on a sparser station network than Spain02 and PT02, it has proved suitable in comparisons against model outputs (Jerez et al., 2010, Warrach-Sagi et al., 2013) mainly due to their interpolation approach.

The E-OBS database (Haylock et al., 2008) is a set of daily gridded products, which was developed as part of the ENSEMBLES project. This database has been one of the most widely database used for regional climate studies over many different regions of Europe. E-OBS products version 16.0 span the entire European land surface for the period of 1950 to 2016 and they based on the observations from European Climate Assessment and Dataset (ECA&D) and additional data from different research projects. The data are available upon registration in the ECA&D Website[4] previously requested in regular and rotated grids, and for different spatial resolutions. Among the different configurations, 0.22° (~25 km) was selected here because this grid is the most similar to the native resolutions of the WRF outputs, and thus more comparable.

Land-Surface Variables

To compare the model outputs in terms of land surface variables, we also used the daily Global Evaporation Amsterdam Model (GLEAM, Martens et al., 2017, Miralles et al., 2011) dataset. The surface evapotranspiration and soil moisture from GLEAM have been used in hydrological studies of spatial variability and trends (Miralles et al., 2014, Greve et al., 2014). Additionally, these data are beginning to be of interest to climate-model community to compare them with outputs from the models (Jaeger and Seneviratne, 2011, González-Rojí et al., 2018, Knist et al., 2017) due to the sparseness of observational networks in terms of these variables. Such data are the result to applying a set of algorithms created to estimate the different components of the surface evapotranspiration. The GLEAM database Version 3 is composed of 3 different data sets, the difference between them being the source data to calculate the land-surface variables. Here, we use Version 3a, which covers the longest period

[4]http://www.ecad.eu/download/ensembles/ensembles.php

(1980-2015), thus being more appropriate to compare against the WRF outputs in terms of climate. The different GLEAM products are freely available upon request from the Website of GLEAM[5].

The algorithm used to develop the 0.2° global regular grid of GLEAM 3a is based on satellite data of soil moisture, vegetation optical depth, and snow water equivalent. Additionally, it uses the reanalysis of air temperature, radiation, and multi-source precipitation products. The detailed description of the algorithm used as well as different aspects related to the construction of these datasets can be found in Miralles et al. (2014), and the description of the last version (Version 3) in Martens et al. (2017). GLEAM outputs used here are composed of three gridded products: surface evapotranspiration, surface soil moisture and root-zone soil moisture.

In this context, for the use of GLEAM data to analyze WRF outputs, it is important note the different uncertainties associated with the algorithm approach of construction, since these data, at the end are the product of applying a model, and thus the different approximations are subject to inherited errors of the model. Martens et al. (2017) validated the GLEAM data against different measures from eddy-covariance towers and soil-moisture sensors across a broad number of ecosystems. They found that the average correlation values of soil moisture were around 0.64 with respect to soil-moisture sensors, and the mean value of the correlation for surface evapotranspiration was in a range between 0.78 and 0.81 with respect to eddy-covariance towers values. Additionally, soil moisture strongly depends on soil properties, so these data should be compared with those from WRF outputs while bearing in mind that differences could be due to the different definitions of the soil parameters such as the depth of the layers, the land use, or the soil category.

Finally, remarkable effort has been made to create a global gridded product such as GLEAM in terms of land-surface variables. The availability of these database can be extremely useful to elucidate land-surface processes and to improve the simulation results.

[5]https://www.gleam.eu/

2.1.2. Monthly Gridded Observations

Additionally, for monthly comparisons, precipitation as well as maximum and minimum temperatures from Monthly Temperature Database of Spain (MOTEDAS) and Monthly Precipitation Database of Spain (MOPREDAS) have been used. Both MOTEDAS and MOPREDAS are high-resolution gridded datasets based on a dense network for temperature (1358 stations) and precipitation (2670 stations) over peninsular Spain. Such data consist of a regular grid of 0.1° of spatial resolution, which was created using the records stored by the AEMET. The period covered by MOPREDAS and MOTEDAS was 1951 to 2010. Further details on the methodology applied to prepare these products are provided in González-Hidalgo et al. (2011) and Gonzalez-Hidalgo et al. (2015) for MOPREDAS and MOTEDAS databases, respectively. These databases are highly appropriate for studies requiring high spatial resolution but do not need the daily time scale.

2.2. Lateral Boundary Conditions (LBCs)

A suitable selection of the initial and LBCs is crucial in the dynamical downscaling approach because they are the main data source of the climate information. LBCs are divided into two main groups: reanalysis and the GCM. The first ones are widely known as the "Perfect Boundary Conditions" since they offer the best performance of the atmospheric state. They enable us to analyze the present-day climate characteristics, and then, to analyze the added value to perform regional climate simulations using a RCM. On the other hand, the GCMs provide the needed information for future climate studies.

2.2.1. Reanalysis Datasets

A global climate historical analysis (reanalysis) is a numerical description of the state of the atmosphere, a result of combining observations and models. The estimations made by reanalysis offer a better representation of the current climate. Reanalysis data are generated by the assimilation of a widespread network of measurement (millions of observations) around the earth, which come from different sources such as radiosondes, satellites, ocean-buoys, and aircraft as well as ship reports. These observational measurements are treated to estimate different atmospheric variables on the surface as well as at different altitudes.

Currently, several global climate reanalysis databases are available to the scientific community, for example, the NCEP–DOE Atmospheric Model Intercomparison Project Reanalysis (AMIP-II, Kanamitsu et al., 2002) or the JRA55 Reanalysis (Kobayashi et al., 2015). However, reanalysis products are not perfect, being susceptible to having major biases with respect to observations over certain regions (Brands et al., 2012). Studies such as Yang et al. (2012) or Brands et al. (2012) have also shown that no single reanalysis data set outperforms the others for all regions and periods of study. Therefore, it is important to select the most suitable reanalysis data, such as LBC (Jacob and Podzun, 1997), in order to ensure regional climate simulations over a specific study region.

In this thesis, the ERA-Interim Reanalysis (Berrisford et al., 2011, Dee et al., 2011) from the European Centre for Medium-Range Weather Forecasts (ECMWF) has been used. This reanalysis database has been widely proved to be suitable in the Northern Hemisphere, the reanalysis also being applied within the CORDEX initiative (Brands et al., 2013) for its suitability in representing current climate conditions (Cardoso et al., 2013). The ERA-Interim project (hereafter referred to as ERA) was prepared by the ECMWF in 2006 as a next-generation reanalysis from previous ERA-40 (Uppala et al., 2005) reanalysis product. The ERA data are available from January 1979 to the present, covering the global atmosphere in a T255 spherical harmonic representation that corresponds to a latitude-longitude transform grid (a reduced N128 Gaussian grid) with a spatial resolution about 79 km on 60 vertical levels (from the surface up to 0.1 hPa). Further information about ERA-Interim configuration can be found in the ECMWF Website[6].

The ERA data used here to create the WRF LBCs were gathered from the ECMWF Data Server[7], which provides a widespread number of parameters at different spatial resolution freely available upon registration. The ERA climate fields are divided into three main groups: time-invariant, surface and vertical-

[6]http://www.ecmwf.int/en/research/climate-reanalysis/era-interim
[7]http://apps.ecmwf.int/datasets

level. As time-invariant fields, WRF requires different data that are fixed in the time and that are surface geopotential and land-sea mask. The surface fields used to adequately run WRF were 2-meter temperature and dewpoint temperature, 10-meter U and V wind components, skin temperature, sea ice, mean sea-level pressure. Additionally, soil variables (soil volumetric water content and temperature) are determined at different levels (1-7, 7-28, 28-100, and 100-289 cm). Furthermore, in the vertical, U and V wind components, relative humidity, geopotential, and temperature at the 46 pressure levels (from 1000 to 1 hPa) were also selected. All these variables were downloaded at the regular grid at 0.75° spatial resolution.

2.2.2. Global Climate Models (GCMs)

GCMs are the primary source of climate data to simulate, understand and predict climate variability and change. Such models consist of complex systems that integrate different components to simulate atmosphere, ocean, land-surface processes, and sea ice, as well as other aspects related to the climate at different time scales (Di Luca et al., 2015). In recent years, a new generation of GCMs has been developed as part of the CMIP5. These models, known as Earth system models (ESMs), take into account additional aspects such as the atmospheric chemistry, aerosols, and the carbon cycle (Taylor et al., 2012) and are available for current climate and future representative concentration pathway (RCP) scenarios.

Unfortunately, the ESMs are not perfect and may have shortcomings to resolve certain climate processes. In this context, the model's skill to reproduce the current conditions as well as to project the future climate depends heavily on the methods to solve the equations that describe the atmospheric and oceanic dynamic processes. Therefore, it is important to appropriately select the GCMs driving the RCM in order to avoid those with serious deficiencies, thus reducing the presence of possible model errors.

In this thesis, among the ESMs from the CMIP5, the Fourth Version of the Community Climate System Model (CCSM4) and the Max Plank Earth System Model at Low Resolution (MPI-ESM-LR) models were used to drive the WRF model. These were selected GCM because of their appropriate performance over the EURO-CORDEX region (McSweeney et al., 2015) together with the availability of the data required to generate the LBC.

The Representative Concentration Pathways (RCPs)

The CMIP5 GCMs run under different representative concentration pathways (RCPs, Moss et al., 2010). The RCPs are a new generation of future scenarios developed by the scientific community as a baseline for long-term modeling experiments, which are included in the IPCC Fifth Assessment Report (IPCC-AR5, 2013). As a novelty with respect to their predecessors (e.g. the scenarios from the Special Report on Emission Scenarios, SRES), they are not a complete set of emission, climate, and socio-economic scenarios, but rather a package of projections based on the components of radiative forcing.

There are four different pathways, which lead to to radiative forcing levels of 2.6, 4.5, 6.0 and 8.5 W/m^2 for 2100 with respect to the pre-industrial era (Figure ***2.1***). Such forcings are due mainly to GHGs, but also different land use/land cover are considered in the RCP definition since changes in the land use can affect the climate in many different ways (e.g. through direct emissions, biogeophysical and hydrological impact, and changes in the vegetation stock altering the carbon cycle). For instance, under the RCP8.5, croplands and grasslands expand due mainly to the increasing population. However, for RCP4.5, there is a worldwide change in land use as part of global climate policy in which land uses for croplands and grasslands diminish (van Vuuren et al., 2011). In short, these pathways include one scenario of mitigation (RCP2.6), two of stabilization (RCP4.5 and RCP6.0), and a final scenario that involves very high emissions (RCP8.5).

In this thesis, the outputs from the two different RCPs (4.5 and 8.5) were used to perform regional climate simulations. The selection of such scenarios was based on data availability and because these are two widely used scenarios to consider the influence of the human activity on future climate, using a moderate conservative perspective (RCP4.5) and with a more pessimistic viewpoint (RCP8.5). These scenarios assume a CO_2 concentration of about 650 and 1370 ppm by the end of the century, corresponding to a rise in global temperature of approximately 1.8 and 4.0°C compared with the recent past (Moss et al., 2010) for the RCP4.5 and the RCP8.5, respectively.

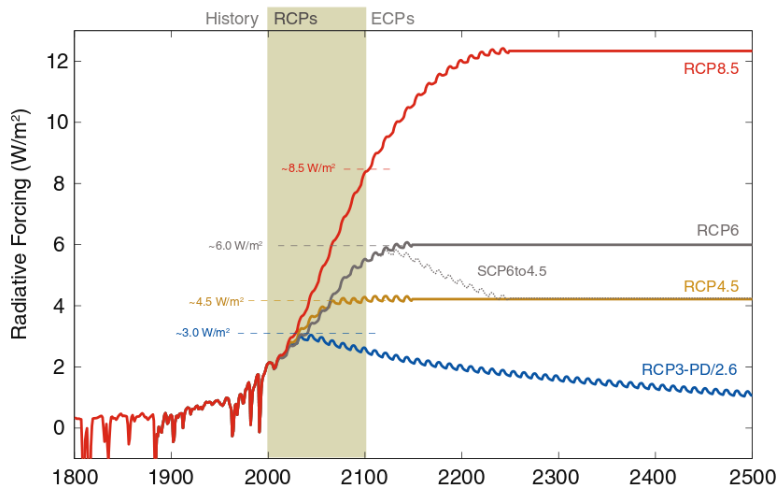

Figure 2.1: *Total radiative forcing (anthropogenic and and natural) for the set of pathways: RCP2.6 (called here RCP3-PD), RCP4.5, RCP6.0 and RCP8.5. Taken from Meinshausen et al. (2011, pp. 230).*

2.2.3. The Bias-Correction Method

The dynamical downscaling approach has been traditionally based on using a RCM directly nested within a GCM. Nevertheless, the GCMs are affected by systematic errors which may be acceptable on a global scale, but can be problematic when used to generate local or regional climate characteristics (Done et al., 2015).

Wu and Lynch (2000), Sato et al. (2007) and Cook and Vizy (2008) carried out similar studies through a dynamical downscaling approach using a simple bias correction in the driving data, and found that the correction of the LBCs provided results closer to observational ones than achieved from simulations driven directly by GCMs. For that reason, to simulate the regional climate through a RCM, the GCMs selected were previously bias corrected in an effort to improve the LBCs in term of systematic errors. It bears noting the difference between unsystematic errors that generate random variations in the model and the model biases, as these can be defined as systematic differences between models simulations and observations. These latter are generally the main source of uncertainty for long-term scales (Hawkins and Sutton, 2011).

Different ways can be followed to correct systematic errors of the GCMs, for example, approaches based on correcting bias in the mean and variance (Xu and Yang, 2012) or by using quantile-quantile mapping (Colette et al., 2012). Among them, the method developed by Holland et al. (2010), has been applied in the bias-corrected CMIP5 CESM Data (Bruyère et al., 2015), which was used here to drive WRF. This approach has proven suitable to bias correct GCMs outputs because it can represent the diurnal and synoptic effects as well as the internal variability (Bruyère et al., 2014, Done et al., 2015).

This approach consists of correcting inherent errors of the GCMs by using reanalysis data. Thus, the bias in mean states is removed whereas the synoptic-scale and climate-scale variability originated by the GCM is retained. This latter assumption allows its use for the analysis of different model performance both for interannual variability as well as for climate extremes (Xu and Yang, 2012). For this, 6-hourly fields from GCMs and from reanalysis were broken down into two components: the climate mean annual cycle ($\overline{GCM}$ and $\overline{Rea}$) and a term of perturbation (GCM' and Rea'), expressed as:

$$GCM = \overline{GCM} + GCM' \tag{2.1}$$

$$Rea = \overline{Rea} + Rea' \tag{2.2}$$

Thus, the GCM climate mean is replaced by those from the reanalysis data, the final formal expression being for each variable:

$$GCM = \overline{Rea} + GCM' \tag{2.3}$$

Therefore, the bias-corrected fields are the result of combining a monthly varying climate from reanalysis data ($\overline{Rea}$) with 6-hourly weather from the GCM (GCM'). The bias-corrected CMIP5 CESM Data, which are freely available, upon registration from NCAR's CISL Research Data Archive[8], are composed of current (1951-2005) and future (2006-2100) climate fields developed in an adequate format (intermediate format files) to directly use them as WRF

[8]http://rda.ucar.edu/datasets/ds 316.1

LBCs. Together with these data, the software *CESM_to_Intermediate.tar.gz* is also available in order to provide the scientific community with a tool to generate bias-corrected fields.

The next section describes the technical procedure used to establish the bias corrected fields through the application of this software as well as the description of the data required. In addition, this procedure was also applied to generate the corresponding bias corrected fields from the MPI-ESM-LR. Note that due to the differences between the two models, different modifications became necessary in the code, which will be also described.

The Fourth Version of the Community Climate System Model (CCSM4) Bias Corrected

The fourth version of the Community Climate System Model (CCSM4, Gent et al., 2011), which is a part of the Community Earth System Model Version 1 (CESM, Hurrell et al., 2013), was created by the National Center for Atmospheric Research (NCAR). CCSM4 simultaneously models the earth's climate system by using of four different coupled components: atmosphere (CAM 5 model), ocean (POP2 model), land surface (CLM model) and sea ice (CICE component). These are coupled by the use of an additional module (CPL). The horizontal resolution is based on a Gaussian latitude-longitude grid, with 288 x 200 points with a spatial resolution of 1.25° x 0.9°, and the vertical is defined in 26 hybrid levels. The detailed information on this ESM can be found in Hurrell et al. (2013).

Among the different runs of the CCSM4 model, the outputs from the ensemble member 6# was used for historical data, because this is the only member that has all variables needed[9]. For future, the data for three different RCPs (RCP4.5, RCP6.0 and RCP8.5) are available, which are developed by using an ensemble of CESM simulations in order to characterize the model's uncertainty. Also, to compute the mean climate, the ERA was selected as reanalysis data for a 25-year period (1981-2005) thus avoiding possible significant climate trends in the data.

The variables used were both 3-dimensional and 2-dimensional fields, which

[9]Additional details at http://www.cesm.ucar.edu/experiments/cesm1.0/

were provided at different time intervals. In the vertical, the 6-hourly variables on the 26 hybrid levels available used were: zonal and meridional wind (UU and VV, respectively), geopotential height (GHT), temperature (TT), and specific humidity (SPECHUM). Regarding the surface fields, the variables collected on a monthly time scale were: skin temperature (SKINTEMP), snow-water equivalent (SNOW) and soil parameters (moisture and temperature, SM and ST, respectively) at different soil depths. Sea surface temperature (SST) and sea ice (SEAICE) were collected daily, and finally, surface pressure (PSFC) was used on a 6-hourly temporal resolution. In addition, the fixed field were terrain elevation (SOILHGT) and land-sea mask (LANDSEA)[10].

The software *CESM_to_Intermediate.tar.gz* is composed of three different modules: (1) CESM TO INT, (2) ERA TO INT and (3) BIAS CORRECTION. The work-flow to execute the software is depicted in Figure ***2.2***.

GCM TO INT[11] is the first module and its main purpose is to determine all variables to run the WRF and to write them in intermediate format. Note that all the variables will not be bias corrected, but are necessary to run such models. In this context, the variables that were not corrected by systematic errors were skin temperature, snow, and soil variables (moisture and temperature), since these were considered to be less relevant variables. One of the most important steps in this module is the conversion of the original 3-dimensional fields from the GCM, which is based on 26 hybrid levels. For this, the script *convert_gcm_hybrid_nc_to_pressure_int.ncl*, performs a vertical interpolation from vertical coordinates to the final pressure levels of 1000, 975, 950, 925, 900, 850, 800, 750, 700, 650, 600, 550, 500, 450, 400, 350, 300, 250, 200, 150, 100, 70, 50 , 30, 20, and 10 hPa. This code also provides other approximations to determine all the variables required. For instance, different superficial variables are calculated by using the corresponding vertical level such as the 2 m temperature or the 2 m relative humidity. In addition, to establish the surface wind components, it is assumed that meridional and zonal wind components at 10

[10]Most of these original variables are provided from the NCAR's CISL Research Data Archive (http://rda.ucar.edu/datasets/ds316.0) and from the Earth System Grid Program for Climate model Diagnosis and Intercomparison (ESG-PCMDI) Gateway at Lawrence Livermore National Laboratory (http://pcmdi.llnl.gov/projects/esgf-llnl).

[11]In the original software package, all scripts as referred as CESM rather than GCM. Here the name has been modified for to include the process for MPI-ESM-LR model.

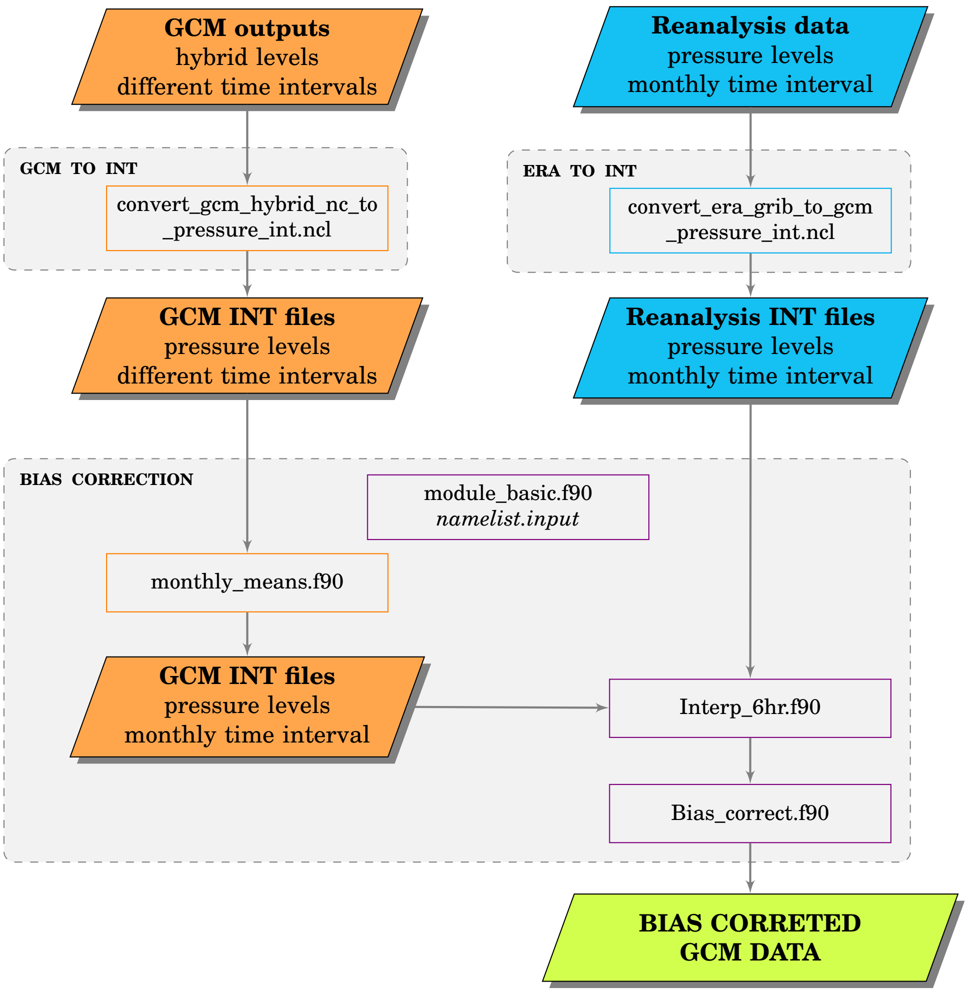

Figure 2.2: *Bias-correction approach flow chart.*

m high follow a power law for a neutrally stable atmosphere (Hsu et al., 1994), and then, the lowest hybrid level is extrapolated. Finally, the script generates the intermediate files from the GCM fields, which is the compatible format to use them as LBC for the WRF model. The cylindrical equidistant (Lat/Lon) projection was selected to create the intermediate files.

ERA TO INT is the second module and creates the intermediate files format from reanalysis data. Among the different modifications, it transforms the reanalysis data by reformatting them onto the same horizontal grid from the GCM data, in order to make both datasets comparable. Thus, the reanalysis data is regridded from Gaussian to a regular grid using the spatial resolution of the GCM fields through spherical-harmonics approach. In this step, the NCL script *convert_era_grib_to_gcm_ pressure_int.ncl* is the main code to generate the reanalysis climate fields. All ERA-Interim monthly data required to run it are stored at the NCAR RDA web site[12], and are also available free of charge.

Finally, the BIAS CORRECTION module performs this approach (Bruyère et al., 2014) by using both the ERA and GCM intermediate files previously created in the modules described above. This module is a set of scripts, written in Fortran code, its first step being the computation of monthly values using the *monthly_means.f90*. For this, mean climate fields are computed for the aforementioned 25-year period. Then, both reanalysis and GCM monthly fields are interpolated into 6-hourly means by using an interpolation approach, which is performed by the *interp_6hr.f90* routine. Finally, the bias correction of the GCM data by replacing annual climate cycles from the GCM with those from reanalysis data was carried out through the *bias_correct.f90*. The set of all Fortran routines depends on an additional code, the *module_basic.f90*, which is a common program across the entire process. All the steps are performed throughout the namelist.input file.

Results from the bias-correction approach applied to the CCSM4 outputs of mean seasonal sea level pressure (SLP) for the entire period of study (1980-2014) were compared with those determined from the original output field, in order to elucidate the effects of the bias-correction approach. The SLP was chosen for this comparison because this is an important variable that defines the circulation patterns. Figure ***2.3*** shows the CCSM4 outputs of SLP without bias correction (CCSM4 NBC) as well as those calculated by its application (CCSM4 BC). Both data sets accurately describe the different phases of the SLP over the year. As shown, the surface circulation over the IP is controlled by the presence of the Azores High, being a determinant factor in the precipitation regime in this region (Esteban-Parra et al., 1998). In winter, this high pressure is usually centred at lower latitudes, and hence the entire IP is affected by a zonal circulation from the west. Conversely, in summer, the subtropical high pressure shifts towards higher latitudes, thereby blocking the western circulation except in

[12]http://rda.ucar.edu/datasets/ds627.1

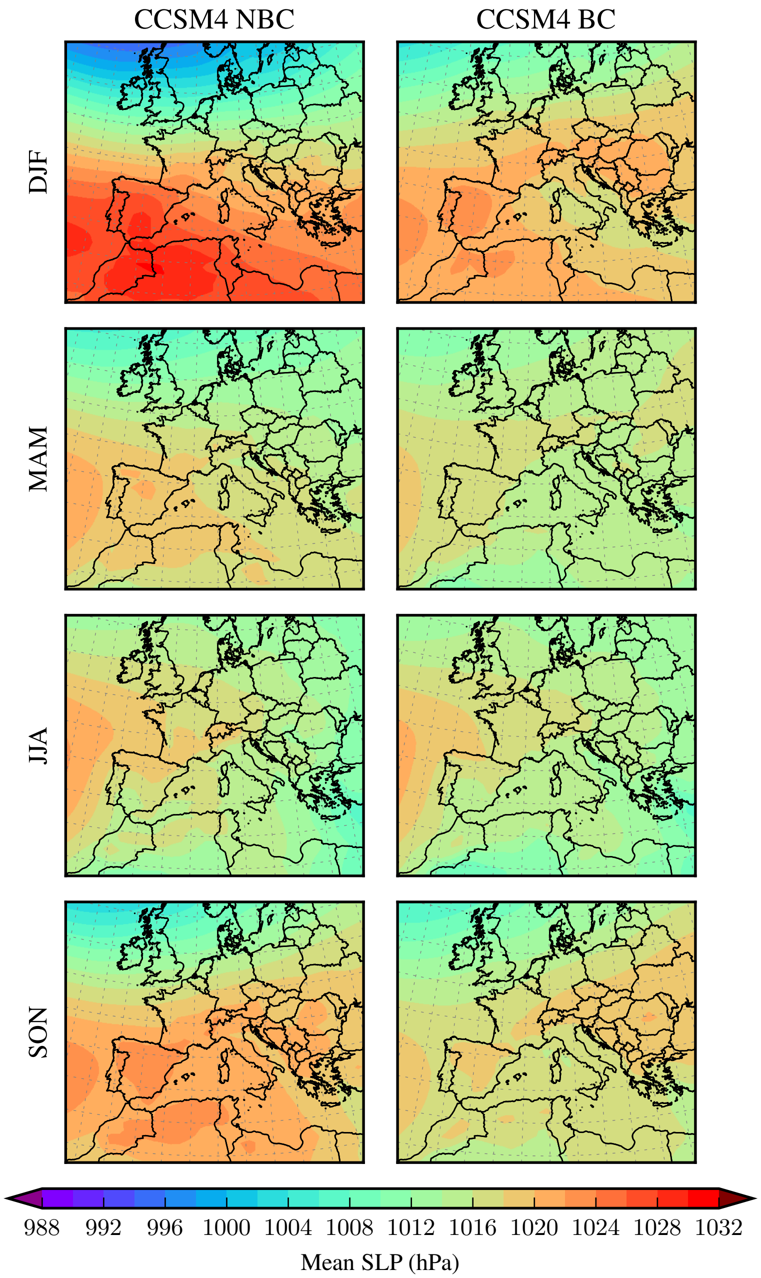

Figure 2.3: *SLP seasonal means from CCSM4 calculated over the period 1980-2014. In rows, the seasons, winter (DJF), spring (MAM), summer (JJA) and autumn (SON) mean values for the entire period. In columns, the original (CCSM4 NBC) and the bias-corrected (CCSM4 BC) outputs from the GCM.*

the northern region. This behavior appears in both corrected and non-corrected fields, but the results from the original SLP show a strongly zonal gradient for winter, spring and summer, being especially strong in winter, which is fixed through the bias-correction approach. Otherwise, the summer mean SLP is normally lower than the winter ones, this behavior being represented for both the CCSM4 BC and CCSM4 NBC.

The results found here could be compared partly with the study performed by Argüeso et al. (2012a) in which a set of WRF climate simulation was validated over the IP. These researchers found a substantial underestimation in mean winter precipitations using outputs from the CCSM3-driven simulation, which could be associated with strong zonal gradients in the mean SLP. In fact, such values of SLP are prescribed largely by the LBCs and are similar to the winter non-bias corrected mean SLP displayed here. Therefore, the results suggest that the noteworthy changes provided by the bias correction could improve the mean precipitation results, at least for winter.

The results of the bias-corrected SLP, therefore, suggest a possible improvement in the WRF simulations, at least in terms of precipitation patterns, which make the use of this technique appropriate for the CCSM4-driven WRF simulations.

The Max Plank Institute Earth System Model at Low Resolution (MPI-ESM-LR) Bias Corrected

The Max Planck-Institute Earth System Model (MPI-ESM, Giorgeta et al., 2013) is a set of coupled models composed mainly of 5 components: ECHAM6, MPIOM, JSBACH, HAMOCC, and OASIS3. ECHAM6, the atmospheric general circulation model, is coupled directly to the land-surface model (JSBACH), which describes aspects related to the soil and vegetation. MPIOM is the general circulation model, which includes ocean biochemistry by using the HAMOCC model. Finally, OASIS3 is the linkage program, computing the exchange fluxes of water, energy, momentum, and CO_2 between the atmosphere, land surface, and ocean.

Among the different configurations developed in the MPI-ESM, the low-resolution T63L47/GR15L40 configuration (MPI-ESM-LR), is used for ECHAM5 at T63[13] horizontal resolution, corresponding to a horizontal grid of about 1.9° (~200 km). In the vertical, the model is composed by 47 hybrid sigma pressure levels, which are extended to 0.01 hPa. A further description about the modeling can be found in Stevens et al. (2013).

To apply the bias-correction approach for the MPI-ESM-LR model, the different variables required were collected from CERA WWW-Gateway[14], which provides different runs from the ESM-LR experiments upon registration. For MPI-ESM-LR, CERA contains a set of runs that cover the period 1949-2005, as well as future projections (2006-2100) under different RCP scenarios (RCP2.6, RCP4.5 and RCP8.5). Here, the run selected corresponded to r1i1p1 for both historical and future projections (under two scenarios: RCP4.5 and RCP8.5)[15].

The 6-hourly 3-dimensional variables used were air temperature (ta), relative atmosphere vorticity (svo), wind divergence (sd), and specific humidity (hus), which were recorded for all vertical levels. The surface fields were liquid-water content of the snow layer where land (lwsnl), sea-ice area fraction (sic), sea surface temperature (tos), surface temperature where land or land ice (tsl), and surface air pressure (ps), while the fixed parameter of sea-land mask (slm) and surface geopotential (geosp) were used to create the lateral and boundary conditions of WRF. As for vertical variables, the surface fields were stored at 6-hourly interval. Note that several variables such as the surface temperature or the skin temperature were provided by CERA at a higher temporal resolution than those used for applying the bias correction to CCSM4 model. This could slightly improve the results of the correction for MPI-ESM-LR outputs.

To create the LBCs from MPI-ESM-LR, a procedure analogous to that described for CCSM4 was performed, but with some differences due to aspects related to the characteristics of the source data. Firstly, prior to the use of the GCM TO INT module, the 3-dimensional data provided are svo and sd rather than wind components, so a transformation of this data into component winds was required. For the vertical, the 47 hybrid levels were interpolated onto pressure levels, these being the same as the ones used for the CCSM4 model. Also,

[13]T63 is a triangular truncation at wave number 63.

[14]https://cera-www.dkrz.de

[15]The variables required are available in three different datasets for each run (rcm_c5, rcm_c5_133 and rcm_etc) plus a dataset with the fixed variables (rcm_fx).

for MPI-ESM-LR datasets the soil moisture was in a format different from that required for running WRF-Noah[16], so that soil variables were not added in the intermediate format files from MPI-ESM-LR. In this context, it is important to remember that in the original bias-corrected method the soil components were not corrected because they were considered to be less variable.

Some modifications were also made in the *convert_gcm_hybrid_nc_to_pressure_int.ncl* code. For instance, the snow variable provided by this model, SNOW, was transformed into the variable required by WRF (SNOWEC), following the procedure that the UNGRIB module uses. In addition, skin temperature was calculated by combining the sea surface temperature and the variable called "surface temperature where land". In this case, the intermediate files were generated to a Gaussian projection rather than the cylindrical equidistant (Lat/Lon) projection. The modifications made in the ERA TO INT module were related to the transformation of the monthly data from ERA-Interim onto the MPI-ESM-LR grid. For this, the interpolation was performed from a Gaussian grid to another Gaussian grid. The bias-correction approach for MPI-ESM-LR was carried out entirely in the Yellowstone supercomputer at NCAR.

The SLP seasonal mean were also computed for the entire period of study (1980-2014) in order to compare the outputs from MPI-ESM-LR with and without bias correction. Figure ***2.4*** depicts a generally lower effect of the bias correction in the MPI-ESM-LR model than in the CCSM4. This suggests that this model is less affected by systematic errors, at least for the SLP field. For instance, although the zonal-gradient in winter is slightly slower in MPI-ESM-LR BC than in the original SLP field (MPI-ESM-LR NBC), this is not as zonal as is shown by CCSM4. Moreover, for all seasons, high values appear to be extended further towards the north in the corrected field, but the effect of this configuration over the precipitation is not clear and further analysis of the bias-corrected results is necessary to gain information about the underlying mechanism.

[16]The soil-moisture content provided for the MPI-ESM model is the total soil moisture content in the column layer (mrso). For an adequate run of the WRF, the model needs the volumetric soil moisture at different layers.

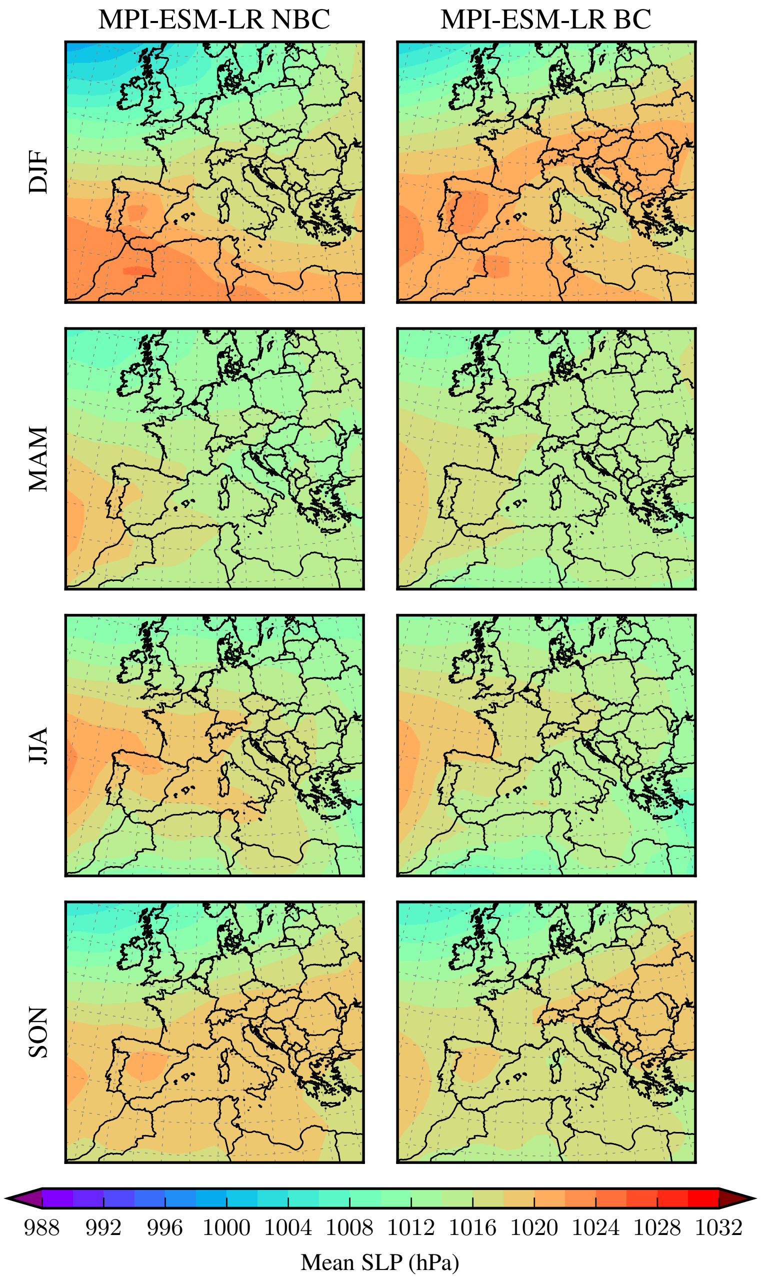

Figure 2.4: *The same as Figure* ***2.3*** *but for the model MPI-ESM-LR.MPI-ESM-LR NBC are the results from the original data and MPI-ESM-LR BC the results of applying the bias-correction approach.*

Chapter 3

The WRF Configuration

As mentioned in Chapter ***1***, the dynamical downscaling approach using RCMs raises conceptual issues which must be taken into account in the configuration of the model. This chapter describes the configuration of the model used to carry out both current and future regional climate simulations. The different parameters were selected in order to minimize the inherent uncertainties in the RCM itself. Among the different aspects to consider, the domain design, the time periods, the static fields, and the spectral nudging applied are detailed here. Finally, a key factor for the model setup is related to the selection of an optimal set of parameterizations. For this reason, a previous sensitivity test was performed to elucidate the most suitable of parameterizations, which is also described here.

3.1. The WRF Setup

The WRF model with the Advanced Research WRF (ARW) dynamical core, WRF-ARW version 3.6.1, was chosen to carry out the different simulations in the climate mode. The diverse aspects of the model setup detailed here were selected with the purpose of evaluating the impact of climate change over the IP in terms of hydrological variables, so that the final model configuration was selected for this goal.

3.1.1. Domain Design

Defining the domain consists of determining the study area. For this, certain considerations had to be taken into account to delimit the optimal domain. Here, the domain was designed with the purpose of establishing climate fields at an adequate spatial resolution to perform impact studies in terms of hydrological variables. In this context, Heikkilä et al. (2011) pointed out that simulations with a spatial resolution of about 10 km are able to capture the processes involved at the regional scale, and hence, its application to perform impact studies is adequate.

The climate in a region is influenced by the rest of globe, and therefore in order to simulate regional features, the domain must be large enough to characterize the large-scale dynamical patterns that affect the region of interest. However, it is also important to bear in mind that domains that are too large could show major departures from driving data (Leduc and Laprise, 2009). Moreover, the domain must be positioned to avoid as much as possible orographic irregularities along the borders, since these may generate spurious numerical features, affecting the quality of the regional outputs. Additionally, Seth and Giorgi (1998) showed that as a means of avoiding unworkable responses to internal forcings the LBCs must be well located outside of the region of interest.

Moreover, in limited-area modeling, the resolution *jump* between the LBCs used to drive the model and the final desired resolution must be consistent. Indeed, great differences in spatial resolution could generate inconsistencies in the borders. Thus, when the difference is greater than 10 grid-distances an alternative *multi-nesting* approach must be performed. This latter is carried out by a consensus between the number of nested domains and the grid-distance ratio. Grid ratios that are too high could generate non-desired artefacts, but also, the higher number of nested domains, the greater uncertainties associated with the problem of boundary values.

Also, nested grid simulations can be carried out using either *1-way* or *2-way* strategies. The difference between them is related to how the outer (also known as the parent domain) and inner domains (also referred to as the child domain) interact between them. For *1-way* nest, the information exchanges are only from the parent domain to the child domain, so no feedbacks between domains are performed. Conversely, in a *2-way* strategy the information exchange is produced in both directions at each time step, and thus both domains run simultaneously.

With all these considerations taken into account, a two-nested domain (Figure 3.1) was selected with the following characteristics: The parent domain (d01) covers the area corresponding to 72°N-27°N of latitude and 22°W - 45°E of longitude, in a rotated latitude-longitude map projection at 0.44° (c. 50 km) of spatial resolution and 126 longitude x 123 latitude grid points (6300 km x 6150 km). This domain contains most of the Atlantic storm track and a large part of the western Mediterranean Sea, which are major sources of the IP climate variability. The latitude-longitude grid is rotated by placing the coordinate of the pole at 39.25°N and 162°W. Thus, the distortion of the map projection is avoided and a quasi-uniform resolution is achieved (Jones et al., 1995). The domain so defined corresponds to the EURO-CORDEX domain, which has been widely proved to be an adequate domain to perform regional climate simulations over the European region. Also, using this domain, we can compare our results with those found under the CORDEX initiative. The nested domain (d02) was centred over the IP through a rotated grid with 221 x 221 points (2210 km (W-E) x 2210 km (S-N), with a 0.088° of spatial resolution (c. 10 km). Therefore, the grid ratio applied was of 1:5, which has been used by other autors (eg., Evans et al., 2014, Di Luca et al., 2016a, Ulazia et al., 2016, Di Luca et al., 2016b).

The *1-way* strategy was selected due to its extensive use for regional climate simulations, and because a *2-way* nest might to show instability for climate simulations (Argüeso et al., 2011). Therefore, the runs were performed conventionally with two grids integrating concurrently, but with the feedback option switch off.

In the vertical, both domains were defined using 41 levels with the top set to 10 hPa. Soil variables were defined for 4 different layers as required by the coupled land-surface model (LSM).

3.1.2. Time-Period Configuration and Boundary Conditions

Different climate data were used in this thesis to drive the WRF model, which are updated every 6 hours. Thus, with the purpose of analyzing the downscaling biases, a 35-year simulation was carried out for current conditions (1979-2014) using the reanalysis ERA data. For this to be run, the simulation was broken down in three different runs in order to optimize the computational resources. Therefore, the period between December 1979 and November 2014 was divided into three sub-periods (December-1979/November-1991, December-1991/November-2003 and December-2003/November-2014).

On the other hand, two different GCMs were also used, the CCSM4 and the MPI-ESM-LR. The outputs from these GCMs were previously bias corrected, and then, used to force WRF. Current simulations using the same period as for ERA (1979-2014) were performed for both GCMs, with two different purposes: (1) Analyzing the biases inherited from the GCMs and (2) quantifying the projected changes in the future. However, the historical runs of the GCMs end

(b)

(a)

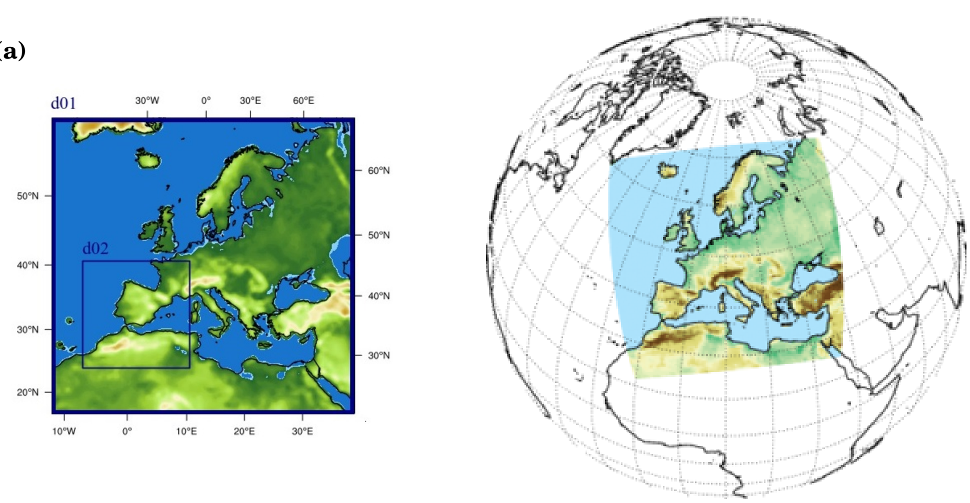

Figure 3.1: *(a) EURO-CORDEX domain. Taken from www.euro – cordex.net. (b) two 1-way nested domains used (d01: Outer domain configured following the 0.44 EURO-CORDEX specifications, and d02: nested domain centered over the IP at 0.088° spatial resolution).*

in 2005, so the period between 2006 and 2014 of the current simulations were completed by using the data from the corresponding GCM for the RCP 8.5, In fact, the use of the RCP8.5 outputs to extend current simulations appeared to be reasonable according to the current GHG emissions (Granier et al., 2011) Additionally, future projections from both GCMs were also used for two different periods, i.e. a near future (December 2020-November 2050) and a far future (December 2071-November 2100) as well as for the two RCPs selected. For these periods, the simulations were divided into decadal runs.

For MPI-ESM-LR model, the soil-moisture content was not available for different soil layers as was required to perform the soil LBCs, and therefore a different strategy was used for those simulations embedded in this GCM. Using an initial state of the soil, the model can generate its own boundary conditions through the coupled Land-Surface Model (LSM). Thus, the soil variables (soil moisture content and temperature) from ERA were used to create the initial state of the soil, the variables selected here being the ones corresponding to January 1^{st} 1979 at 00 UTC.

The spin-up time is the period needed to achieve a balance between external forcing and internal dynamics. Intrinsic difficulties due either to inconsistencies in the LBCs or the formulation result in unreliable solutions at the beginning of the simulation, and therefore, the model needs a period to adjust itself. After this time period, the model becomes more stable and the results can be trusted.

Each component of the model reaches equilibrium at different times. For instance, the atmosphere has a short memory, so a relatively short spin-up is required. However, for soil variables (i.e. deep soil temperature and moisture content) and surface hydrology, the model requires longer periods to reach such stable conditions, with spin-up time of the order of months to years (Denis et al., 2002, Yang et al., 2011). For this reason, to ensure that the model reaches its own internal equilibrium, we selected a spin-up of 11-months, and thus, we started all simulations with an additional 11-month period, i.e. all runs actually started on January 1^{st} of the corresponding year.

3.1.3. Time-invariant Fields and SST Update

For WRF to be run in the real mode[1] requires some time-invariant fields related to the topography and the geology of the domain, such as the soil texture, the land-use categories, or the terrain height. For this, the MODIS Land Cover from the International Geosphere-Biosphere Programme was used at a resolution of 30 arc seconds, which corresponds to approximately 1 km of spatial resolution. This is composed by 20 land-use categories plus an additional category for water bodies corresponding to lakes when the Alternative Initialization of Lake sea-surface temperature (SST) option is switched on (Mallard et al., 2015). Each category is associated with a set of properties such as monthly surface albedo, roughness length or leaf-area index, which are determinate in the approximation of land-surface processes. Moreover, a time-varying SST was used instead of the default time invariant, typically used for short-term simulations. Thus, the SST was determined from the driving data and updated with a 6-hour frequency, as the boundary conditions.

3.1.4. Sponge Zone and Spectral Nudging

Different strategies have been developed to avoid contaminated simulations by the inward propagation due to the boundary-values problem in long-term simulations. Davies (1976) proposed the lateral boundary relaxation, in which the model solutions are relaxed towards the driving data along the boundaries through the *sponge zone*. In this way, the possible inconsistencies created by spurious numerical features between the RCM and its LBCs are dumped. This method successfully solves the problem associated with small-scale characteristics. Here, the lateral boundary relaxation was addressed by using the 10 outer grid points of the coarser domain as a *sponge zone*.

However, although this approach prevents inconsistencies of small-scale features in the borders, it does not correctly handle large-scales features, and thus the internal circulation can be altered by large-scale long waves. Thus, to keep the large scale consistent with the driving data, we also applied Spectral

[1]WRF can be run in two different modes, i.e. the idealized mode and real mode. The idealized mode is usually selected to study very specific conditions (e.g. large eddy simulations or convection or sea breeze) which do not require detailed information of the geographical characteristics of the domain, so here the real-model is required.

Nudging (SN). Through the SN technique, the inconsistencies associated with the design of the domain are avoided (Miguez-Macho et al., 2004), ensuring greater reliability of the outputs from those simulations with either excessively large domain sizes or inadequate domain positions.

The SN technique was firstly introduced for a regional model by Waldron et al. (1996), and adapted for regional climate simulations in von Storch et al. (2000). It consists of adding a nudging term to certain model equations in order to relax part of the spectrum to the corresponding waves from the driving data. Therefore, the large-scale forcings are imposed not only at the lateral boundaries but also in the interior domain. Such new term provides maximum efficiency for large scales, avoiding effects in the small-scale features (Alexandru et al., 2009).

For all these reasons, the WRF simulations were nudged using wave numbers of 11 and 10 in the x and y directions, respectively. This means that we adjust only waves above 600 km (Messmer et al., 2017). The nudging coefficient was set to be 0.0003 seconds for all nudged variables and, during the simulation, nudging was conducted every 6 h, consistently with the frequency of the reanalysis data. SN was used only in the coarser domain and above the planetary boundary layer (PBL) in order to allow the RCM to create small-scale characteristics in the finer-resolution domain and near the surface. The SN was applied for wind, temperature, and geopotential height. However, it was not applied for humidity, avoiding errors associated to the competition with the convective scheme (Argüeso et al., 2012a).

3.1.5. Additional Configuration Aspects

Additionally, other parameters were selected to simulate the regional climate over the IP:

- The atmosphere equations were discretized in space and time, the time step being the parameter that controls the time discretization. The time step selected here was 240 sec, following the scheme used in the CORDEX-Australasia project[2] for simulations with the same spatial resolution do-

[2]The model configuration of those simulations can be found in cordex-australasia.wikidot.com

mains[3].

- All WRF simulations were conducted in parallel, configured to use 128 cores in the Fujitsu Primergy CX250/RX350/RX500 cluster ALHAMBRA[4]
- Model outputs were established for different time slices, most of them being stored at a 3-hour frequency (00, 06, 09, 12, 15, 18, and 21 h). Additionally, accumulated precipitation was stored at hourly frequency in order to compare the daily amount of precipitation with the observations[5]. The maximum and minimum temperatures were also recorded daily through the wrfxtrm file generated from the CLimate WRF (CLWRF) module (Fita et al., 2010).

3.2. The Physics Schemes Configuration

The WRF model, through the Euler equations based on the basic principles of conservation of energy, mass, and momentum simulates the climate at the discrete grid scale chosen. However, there are different physical phenomena in the climate system that occur at a sub-grid scale in time and space, and therefore, they are unresolved by the fundamental equations. Such processes may be as essential as those explicitly defined by the model equation to achieve realistic simulations, so that they must also be accurately represented. For this reason, the subgrid processes are included by using several semi-empirical assumptions, which are determined through the so-called parameterizations (also known as physics schemes or physics). The adequate selection of the physics schemes is one of the greatest challenges of the procedure of mode-set configuration to adequately simulate the climate in a region. For that reason, a preliminary study was performed in order to select the physics schemes to run the WRF in the climate mode. This section describes in detail the sensitivity analysis performed, in order to finally select an adequate combination of parameterizations.

[3]A good practice to run WRF is through the use of recommended values of time step, which should be between 5- and 6-fold the spatial resolution in km.

[4]The ALHAMBRA supercomputer system is part of the University of Granada (Spain) and is composed by 1808 cores.

[5]The observational data are stored at 7 UTC and 9 UTC in Spain and Portugal, respectively.

3.2.1. Choosing the Adequate Combination of Parameterizations

To run WRF, different parameterizations can be used. In fact, WRF in its version 3.6.1 has numerous possibilities with a total of 13 options for PBL schemes, 21 for microphysics, 11 for convection, 7 for radiation, and 4 LSMs, which differ in their level of complexity. Such schemes were usually developed in order to resolve sub-grid processes under specific conditions, so that an incorrect selection of the parameterization can generate large impacts in the final simulations (Argüeso et al., 2011).

The selection of the schemes depends heavily on the domain (i.e. region of study, size of the domain and resolution), and also on the issue to be addressed. Thus, for climate purposes, the principal aim is to determine the main climate characteristics or trends rather than specific values of a given variable, and then, very complex schemes may not be necessary. Moreover, the complexity is linked to a greater computational cost, which is not adequate in long-term simulations. With the purpose attempting to minimize systematic errors associated with an inadequate selection of the parameterizations for climate simulations on the IP, a set of parameterizations was examined. In this sense, the schemes were selected in relation to previous studies (Argüeso et al., 2011, Jerez et al., 2013, Pérez et al., 2014), together with the examination of new schemes included in the updated versions of the WRF model. Below, the selected schemes are summarized.

Radiation

This set of parameterizations deals with the atmospheric heating due to both radiative flux divergence and the surface downward radiation for interchange for the ground-heat budget. Here, the processes involved are absorption, reflection and the scattering in the atmosphere and at the surface, the only external source of energy being the sun. In the WRF, the long-wave and short-wave radiations are approximated separately, so that different options can be used for each type of radiation.

The NCARs Community Atmosphere Model (CAM3.0, Collins et al., 2004) scheme was selected here for both long-wave and short-wave radiation, mainly because this scheme allows the use of variable atmospheric concentrations of

GHGs through the application of CLWRF. CLWRF is a code modification developed by the Santander MetGroup that provides a more flexible approach by modifying concentrations of CO_2, N_2O, CH_4, CFC-11 and CFC-12 for the different RCPs scenarios. This fact, together with the monthly-varying distribution of ozone provided by this radiation parameterization makes the CAM3.0 a reliable approximation scheme for climate regional simulations.

Land Surface Model

The LSM coupled to WRF deals the interchange of fluxes of heat and moisture over the land and sea-ice points, using different sources of information such as the approximations of other physics schemes together with the land-surface properties. The LSM captures the main hydrological features and is related to the atmosphere through the surface-energy balance, the surface-layer stability, and the water-balance equation (Greve et al., 2013), needed to adequately model the climate in order to reduce large uncertainties.

Here, the NOAH LSM was selected because it is a widely used scheme which has proved to be accurate for climate purposes. This approximates surface processes by using a multi-layer approach, composed by four layers with different thicknesses (10, 30, 60, and 100 cm). This module computes the soil thermal state and soil moisture through a water and energy balance, taking into account the evapotranspiration, water intercepted by the canopy, root absorption, surface runoff, and subsurface drainage processes. A detailed description of the approach applied can be found in Chen and Dudhia (2001).

Microphysics

Microphysics schemes are responsible of computing the cloud microphysics processes, namely processes related to atmospheric water vapour, cloud, liquid water, and cloud ice as well as the different types of precipitation. Notable among their effects in the climate system is the capacity to alter the radiative properties of the atmosphere as well as the water and energy budget.

Two different microphysics schemes have been explored, the widely used WRF single-moment[6] 3-class (WSM3, Hong et al., 2004) and the CAM5.1 2-

[6]Single-moment schemes calculate only the mass concentrations of hydrometeors.

moment-5-class schemes (CAM5.1, Neale et al., 2012). The purpose here was to examine schemes with different degrees of complexity, and also analyze the benefit of using more complex microphysics approximations vs. their computational costs.

WSM3 is a simple microphysics approximation that takes into account only three types of hydrometers (vapour, cloud, and rain) in a bulk[7] single-moment scheme. Its simplicity ensures a relative low computational cost of the simulations in terms of microphysical processes. On the other hand, CAM5.1 is a more complex scheme, which is applied as a microphysics parameterization in CESM. This is a two-moment[8] formulation for cloud droplet and cloud ice that includes five liquid and ice species (cloud water, rain, cloud ice, snow, and graupel).

Convection

Cumulus schemes are focused on resolving the convective processes produced by convective and shallow clouds at sub-grid scale, and therefore, not explicitly resolved by the model equations. An adequate characterization of convective scheme is important because processes such as heavy rainfall are modulated by it, and thus the capability of representing extreme precipitation depends strongly on the convection scheme. Among the different possibilities available in WRF to approximate sub-grid convection, three different schemes were considered. The difference between such parameterizations lies mainly in the trigger function[9], closure assumption[10] and the cloud models used.

Kain-Fritsh (KF, Kain, 2004) scheme has been widely used for regional climate simulation at different sites of the world. This parameterization is an update of the conventional mass-flux scheme from Kain and Fritsch (1990, 1993). As is defined in Stensrud (2007), the KF is a low-level control scheme which determines the cloud base mass flux by the amount of convective available potential energy (CAPE) in the environment that needs to be removed using a

[7]The size distribution of the different hydrometers consists of an empirical function which is non-varying for the entire simulation. This simplification is computationally efficient and conceptually simple.

[8]Double-moment schemes prognostically calculate both the mass and number concentrations of hydrometeors.

[9]The trigger function is the set of criteria that define the onset of deep convection.

[10]The closure assumption determines the intensity and amplitude of the convection.

complex trigger function.

For a second convection scheme, we used the Betts-Miller-Janjic (BMJ, Janjić, 1994), which is a modification of the Betts-Miller scheme (Betts, 1986, Betts and Miller, 1986). This is based on achieving stability through the adjustment of the vertical profile of temperature and humidity.

Finally, the Grell-Freitas (GF, Grell and Freitas, 2014) scheme is an improved version of the parameterization proposed by Grell and Dévényi (2002), which attempts to smooth the transition to cloud-resolving scales using the Arakawa (2004) approach. To calculate the precipitation amount, GF uses the averaged value resulting from the application of an ensemble (144 members) of cumulus mass-flux schemes, which are run under different controls of statics and dynamics. Each member of the ensemble has different triggering requirements based on the amount of CAPE.

Planetary Boundary Layer

The PBL schemes are used to parameterize the sub-grid scale turbulent fluxes. These processes are related to the vertical transport of heat, moisture and momentum created in the turbulent layer, which is developed due to surface heating, wind shear, and friction. Therefore, this is highly relevant for forecasting surface variables. The main issue of the PBL scheme is related to the turbulence-closure problem (Stull, 1988), the approach applied to deal with this aspect being the main difference between the options available. Regarding the planetary boundary layer and convection processes, the WRF features were analyzed by using the scheme of Yonsei University (YSU, Hong et al., 2006), that of Bretherton and Park (UW, Bretherton and Park, 2009), and the Asymmetric convective model (ACM2, Pleim, 2007).

The first one (YSU) is a non-local[11] first-order[12] closure approximation that uses diffusivity coefficients to compute turbulent fluxes. The second one (UW) is a scheme derived from Grenier and Bretherton (2001), which was modified to improve its numerical stability and performance for long-time steps normally

[11]These schemes are based on parameters that depend on non-consecutive levels or on the whole vertical profile.

[12]The PBL processes are determined through equations for state variables the covariance terms being parameterized.

used in climate models. It is a local[13] 1.5-order[14] turbulent closure model with an entrainment closure at the top of the boundary layer using the turbulent kinetic energy (TKE) as a diagnostic variable. Finally, the ACM2 is a first-order closure scheme that represents the fluxes of the PBL combining a local and non-local hybrid scheme to approximate the upward fluxes for unstable conditions, meanwhile the scheme only uses local parameters for stable conditions.

Also, the PBL parameterization works paired with the surface layer (SF) physic scheme. The SF schemes calculate friction velocities and exchange coefficients that enable the calculation of surface heat and moisture fluxes by the land-surface models. These fluxes provide a lower boundary condition for the vertical transport done in the PBL schemes. Here, the MM5-similarity scheme[15] was used to parameterize the surface layer.

3.2.2. Sensitivity Study of the WRF Parameterizations

Description of the Simulations

The physics schemes are intimately related, providing multiple feedbacks. Therefore, to carry out accurate high-resolution climate simulations the sensitivity test must take into account not only the effect of the each scheme separately, but also the effects of the combination of them. To ensure the best combination of parameterizations the most suitable strategy would be to examine all possible combinations of the parameterizations, but that would involve a great computational cost. As a result, just one set of combinations was examined.

Thus, seven runs were carried out by combining different physics schemes (Table ***3.1***). These experiments were performed using the same model setup except for parameterizations, as detailed in section ***3.1***. The sensitivity test to parameterizations was based on comparing the results from the different runs with observed values. Because the best representation of the current climate data is required, the simulations were driven by the ERA data.

[13]The PBL processes are approximated by using variables and parameters that are defined at each model layer or its neighbours.

[14]TKE is predicted by diagnosis second order moments for some variables.

[15]The MM5-similaraty theory corresponds with the SF scheme based on the fifth-generation Pennsylvania State University-National Center for Atmospheric Research Mesoscale model (MM5) parameterization.

Table 3.1: *Experiments performed by combining different physics schemes in the WRF simulations.*

Experiment	Convection	Microphysics	PBL
KA3	KF	ACM2	WSM3
GY3	GF	YSU	WSM3
GA3	GF	ACM2	WSM3
BAC	BMJ	ACM2	CAM5.1
BY3	BMJ	YSU	WSM3
BU3	BMJ	UV	WSM3
BA3	BMJ	ACM2	WSM3

A means of ensuring adequate behavior from a set of physics schemes for running the model with climate purposes, at least one entire year must be simulated. In fact, the capability of the model may vary for different seasonal situations, and thus it is necessary to test the good performance of the approach over the entire year. On the other hand, long simulations are not necessary to test the appropriate configuration in terms of physics packages, which are also very expensive computationally. Therefore, a period that covers two entire years (1995-1996) was used for this sensitivity test. The years were selected for sharp contrast in their precipitation regimes (dry and wet), and hence the impact of the combination of the parameterizations used in different climate conditions was analyzed. In this context, the first year (1995) was characterized by a lower amount of precipitation than the annual average. By contrast, the second one (1996) was affected by a high amount of precipitation. The spin-up period used here was one year, so the run actually started on January 1^{st} 1994.

Description of the Analysis

The sensitivity was evaluated over Spain by comparing the WRF outputs against gridded observational products from SPAIN011 version 4.0 in terms of maximum and minimum temperature (T_{max} and T_{min}) as well as precipitation values. Although this analysis covers only the Spanish region, this can be considered a good approximation of the model's capacity to serve for the entire IP, since this is a large part of the peninsula encompassing remarkably different climate regimes.

Because the observational data and the WRF outputs have different spatial resolutions, the first step is the regridding of the WRF output fields onto the SPAIN011 grid by using a bilinear interpolation. Thus, simulations and observation can be directly compared. Here, two different temporal aggregation intervals were used. Firstly, the monthly values were computed for all simulations and observations, formulating monthly time series for each grid point. The purpose of using this time scale is to compare the WRF's capability to simulate different climate characteristics along the year. Additionally, a daily time interval was used to assess the performance in terms of high-order statistics. In addition, different spatial viewpoints were examined. Firstly, an overall analysis was made for the whole of Spain with the purpose of drawing a global conclusion. In this context, the values of root mean squared error (RMSE), mean absolute error (MAE), bias and temporal correlation[16], for each grid point, were used to calculate a spatially averaged value. However, in this analysis, different error compensation could mask the actual spatial behavior of some configurations, so that the conclusions drawn in the global analysis must be contrasted with a further analysis by directly comparing grid-points. This latter was performed by computing the same skill scores.

Moreover, in order to facilitate the assessment in terms of parameters such as the annual monthly cycles and high-order statistics, an approach consisting of comparing such parameters region by region was also applied. Taking this into account, since the final purpose is to evaluate impacts in terms of hydrological variables, we considered six main watersheds in Spain: the northwest (composed by the Miño-Sil, Galicia Costa, Cantábrico Oriental, and Cantábrico Occidental), interior (Duero and Tajo), northeast (Ebro, and Internas Catalanas), southeast (Júcar and Segura), south (Guadiana, Guadalquivir, Tinto, Odiel and Piedras, Guadalete and Barbate, and Internas Andaluzas), and Balearic Islands (Baleares Islands watersheds) . Thus, the time series of a given variable for each watershed is established as the average of all grid-points that belong in such basin.

[16]The formulation of these skill scores is detailed in Appendix ***A***.

Table 3.2: *Mean values for the entire Spanish region of RMSE, MAE, bias and correlation coefficients calculated from the experiments using different parameterizations schemes with respect to observations, on a monthly time scale in terms of precipitation. Note that here the RMSE, MAE, and bias are expressed in relative terms with respect to observations, so the units appear as percentages.*

	Precipitation (dry year)				**precipitation (wet year)**			
	RMSE	MAE	Bias	r	RMSE	MAE	Bias	r
KA3	67.726	47.946	14.386	0.814	83.434	60.411	4.656	0.832
GY3	70.107	48.376	-2.501	0.769	96.108	67.049	-19.153	0.779
GA3	62.589	42.876	-3.518	0.824	83.292	58.666	-19.218	0.846
BAC	56.932	38.615	-13.517	0.867	83.191	57.977	-20.222	0.860
BY3	59.407	41.284	-6.048	0.850	78.578	55.337	-18.485	0.857
BU3	57.641	40.434	-3.884	0.865	76.892	54.433	-14.397	0.868
BA3	54.802	38.435	-5.195	0.860	73.870	53.078	-12.536	0.870

Results at Monthly Time Scale

Table ***3.2*** shows the results of the sensitivity test from the global viewpoint, for the precipitation. The lowest values of relative RMSE and MAE for precipitation appeared with the BA3 combination for both dry and wet year (RMSE and MAE of about 54.8% and 38.4% for the dry year, and 73.9% and 53.1% for the wet year, respectively). In term of biases, KA3 was the only parameterizations combination that performed an overall overestimation. Conversely, the rest of parameterizations tended to underestimate the monthly amount of precipitation, in general, reaching the lowest values for GY3 under dry conditions and for KA3 under wet conditions. For correlation values, all WRF configurations gave high values (above 0.7), the worst performance being for GY3 for both dry and wet years.

In general, results reveal good agreement regarding observations for the combinations configured using the BMJ convection scheme. Conversely, the microphysics schemes did not appear to provide great differences. Thus, the most complex scheme (CAM5.1), which was computationally more expensive, did not appear to be adequate for regional climate simulations over the IP, at least in terms of overall precipitation values. The results also show that WRF had more difficulties to simulate the wet year, as reflected by the different skill scores calculated.

Table 3.3: *The same as Table **3.2**, but in terms of temperature. RMSE, MAE, and bias are expressed in Celsius.*

	Maximum Temperature				**Minimum Temperature**			
	RMSE	MAE	Bias	r	RMSE	MAE	Bias	r
KA3	2.995	2.735	-2.633	0.983	1.997	1.783	-1.216	0.973
GY3	3.235	3.018	-2.948	0.984	1.953	1.736	-1.187	0.973
GA3	2.964	2.715	-2.615	0.983	2.009	1.794	-1.250	0.973
BAC	3.060	2.800	-2.706	0.982	1.857	1.633	-0.987	0.973
BY3	3.007	2.791	-2.707	0.984	1.954	1.736	-1.151	0.973
BU3	2.822	2.569	-2.461	0.983	1.999	1.787	-1.217	0.973
BA3	2.779	2.530	-2.410	0.983	1.958	1.743	-1.150	0.973

When we compared the performance of these combinations in terms of temperature over the entire region of Spain, different results appeared for T_{max} and T_{min} (Table ***3.3***). For maximum temperature, the best agreement with observations was found for the BA3 configuration (values of about 2.78°C, 2.53°C, and -2.41°C for RMSE, MAE, and bias, respectively), whereas GY3 showed the worst. In terms of minimum temperature, however, BAC appeared to outperform the others (values around of 1.86°C, 1.63°C, and -0.99°C for RMSE, MAE, and bias, respectively) while GA3 presented the worst agreement with SPAIN011. In general, all the simulations depicted underestimated values for both maximum and minimum monthly temperature, especially marked for T_{max}. Regarding temporal correlations, all configurations reached high values (above 0.97). These results suggest that the GF scheme was not adequate in terms of temperature, given that it presented the worst performance for both T_{max} and T_{min}. Conversely, results also suggest that the BMJ scheme appeared to outperform the others analyzed.

To draw further conclusions from the combined parameterization performance, we analyzed the same skill scores by using a direct grid-point comparison. However, the conclusions from all parameters were the same, and thus only the results for the bias are shown here.

Figure ***3.2*** depicts the relative bias respect to SPAIN011 for each grid point, in terms of precipitation. The first conclusion drawn is that the model has more difficulty representing the amount of precipitation for a wet year, when the presence of negative biases is greater than for a dry year. This behavior is especially notable for southern Spain. In general, the results also indicate that the runs configured using BMJ appeared to outperform the others, in agreement with the global results. By contrast, the KF scheme appeared to show more difficulties in representing the precipitation amount over Spain in general. Moreover, between the different results found on applying the BMJ scheme, the BA3 combination appeared to reflect slightly better agreement with SPAIN011 in general terms, at least for dry conditions.

Regarding temperature, Figure ***3.3*** shows the bias with respect to the observations from SPAIN011 in terms of both maximum and minimum temperatures. In general, all configurations portray a good agreement with observations, showing an overall underestimation, which is especially marked for T_{max} T_{max} (Figure ***3.3a***), as was indicated in the global analysis. The results reveal that the benefit of using one or another configuration is not so clear as for precipitation, because there was no configuration that outperformed all the others over the entire Spanish region, and the performance proved to be very similar between them. These similar spatial patterns may have resulted because the temperature depends mainly on the SST, the model elevation, and the radiation schemes, and these were the same for all configurations evaluated here.

Again, the global results appeared to be corroborated by the grid-point analysis for both T_{max} and T_{min}. In terms of T_{max}, BA3 proved slightly better agreement with the observational features, which are found in certain areas of the Ebro Valley, most of *Girona* and *Barcelona* and areas of *Huelva* and *Cádiz*. On the contrary, GY3 showed slightly worse agreement with SPAIN011. For T_{min} (Figure ***3.3b***), the results suggest that BAC outperformed the other combinations in general terms, but the difference was very slight in this context while involving a greater computational cost. Therefore, simulations run with the BMJ together with ACM2 appeared to be accurate to simulate the climate over the IP.

Results for Annual Cycles of Monthly Values

Through the analysis of annual cycles of monthly values, the performance over the year can be examined, identifying months when the model presented

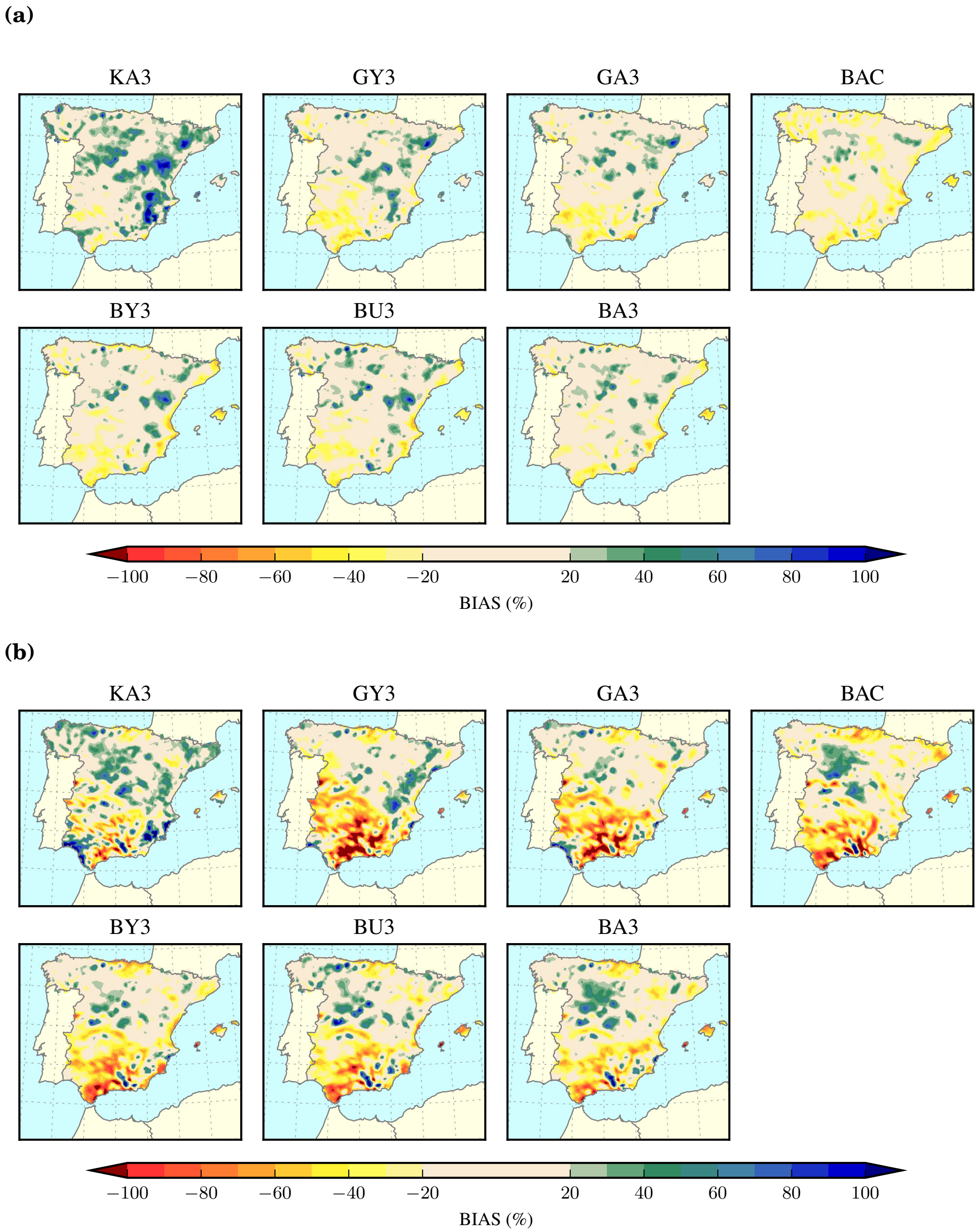

Figure 3.2: *Spatial distribution of the relative bias (%) for precipitation regarding observations from SPAIN011 for each WRF configuration for (a) dry conditions and (b) wet conditions.*

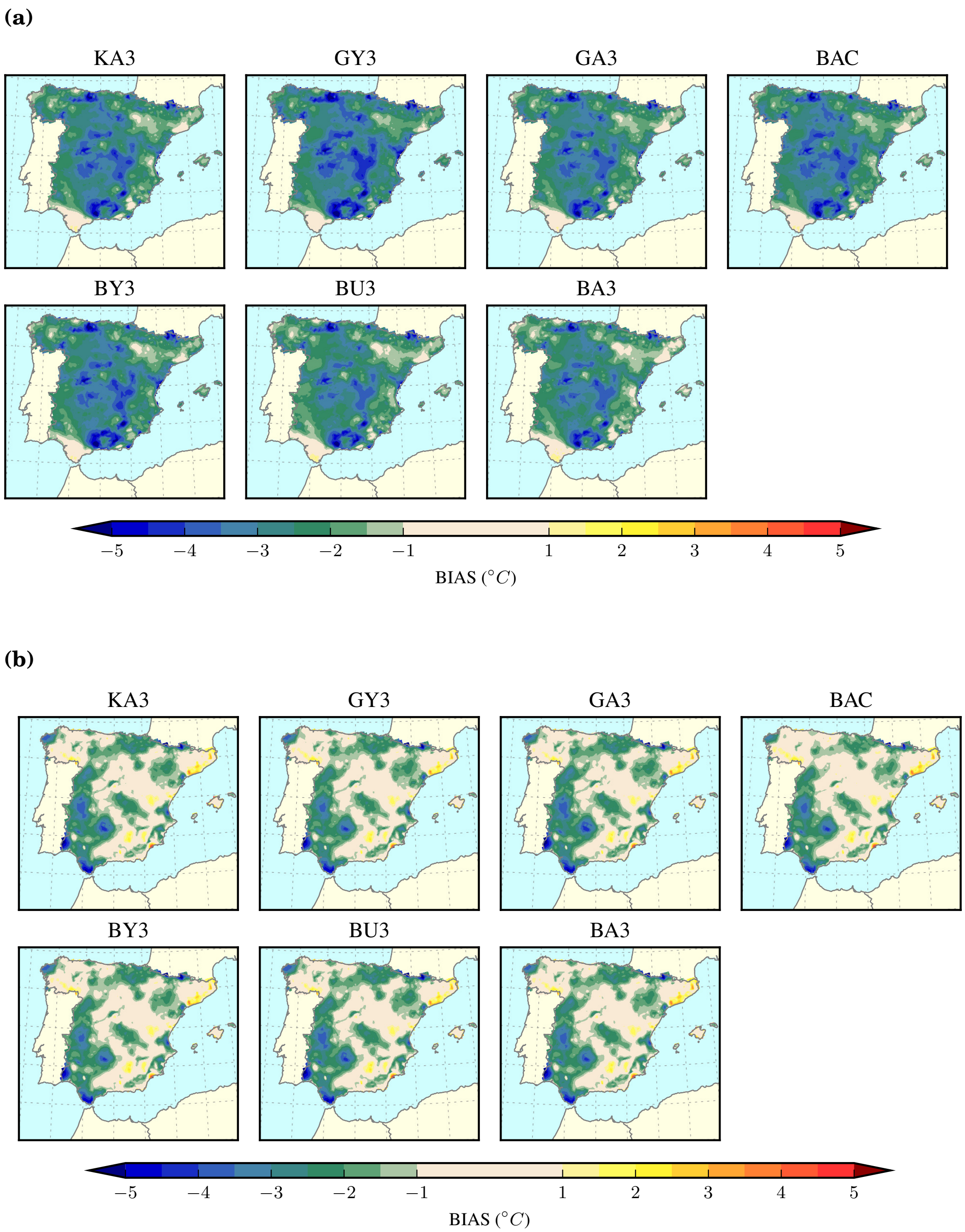

Figure 3.3: *Spatial distribution of the bias (°C) regarding observations from SPAIN011, for each combination of parameterizations for (a)* T_{max} *and (b)* T_{max}*.*

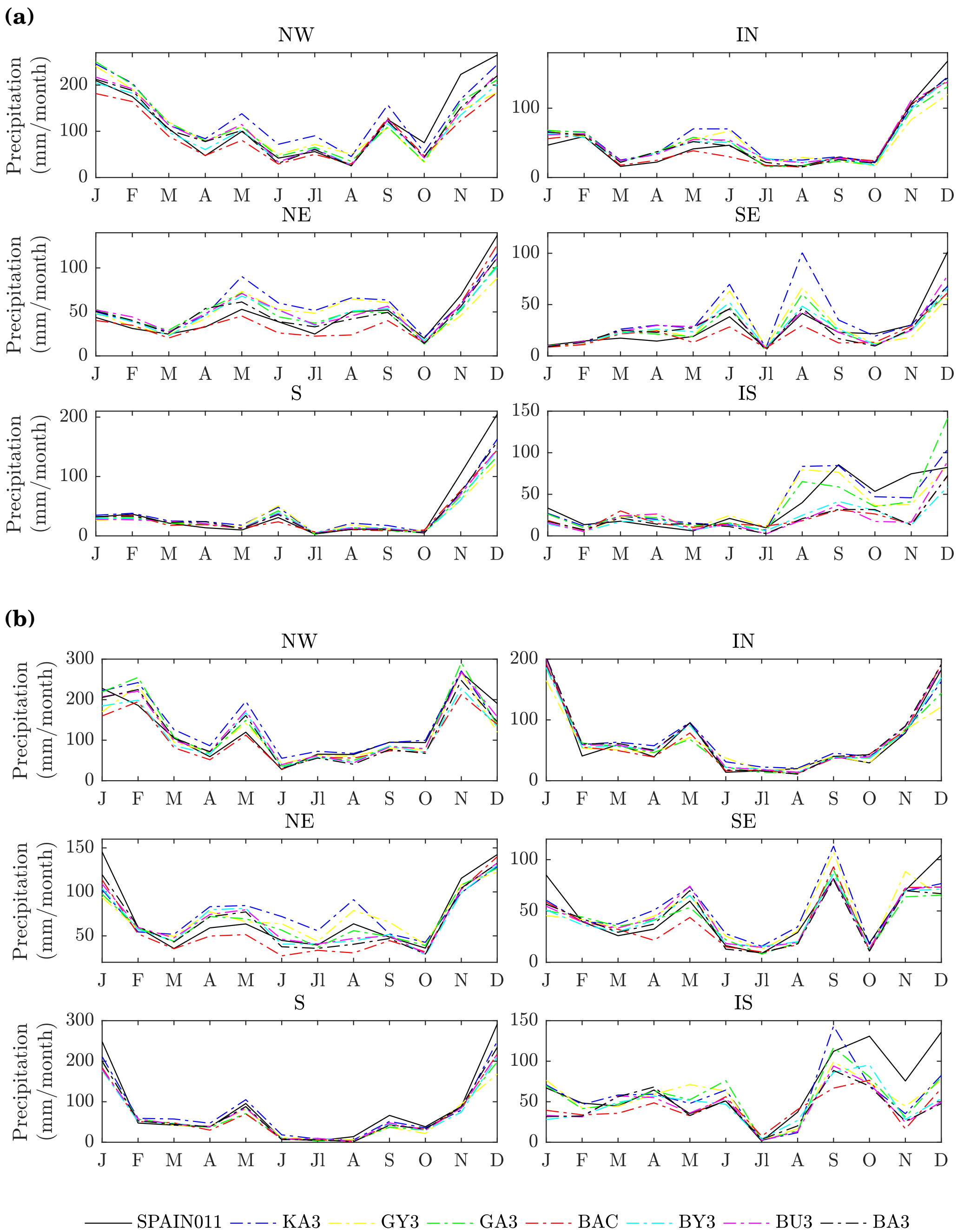

Figure 3.4: *Annual cycle of monthly accumulated precipitation for a (a) dry year, and (b) wet year, over the six main watersheds of Spain: northwest (NW), interior (IN), northeast (NE), southeast (SE), south (S), and Balearic Islands (IS).*

the most problems. Figure ***3.4*** shows the annual cycle of monthly accumulated precipitation for the six selected main watersheds of Spain. In general, the model represented reasonably well the annual cycle for both dry and wet conditions. However, it tended to overestimate the precipitation for spring and summer months, while underestimating autumn months. The results also reveal that some physics schemes outperformed others. For instance, the runs configured using the KF and GF appeared to accumulate larger amounts of precipitation, and thus the combinations in which they were present tended to overestimate the monthly precipitation in most cases. On the other hand, the configurations with BMJ appeared to generate less precipitation than the other, being thus more consistent with the observed values. BA3 and BAC configurations showed better agreement for both the dry and wet year.

In terms of temperature, the annual cycles of monthly values were also computed and the results are shown in Figure ***3.5***. We can see the noteworthy ability of WRF to capture the annual cycle of the temperature regardless of the combination of parameterizations used. However, in general the model tended to underestimate both extreme temperatures. Again, the results from all configurations were very similar, although some configurations slightly outperformed the others. For T_{max}, for example, GY3 generated a greater underestimation, especially for IS, SE, and NE, while BA3 showed slightly better agreement regarding to SPAIN011,as can be seen in NW, NE, and IS. For Tmin, all the combinations performed similarly, although the BY3 combination slightly outperformed the others in the IN, NE, and S watersheds.

High-Order Statistics

Finally, the high-order statistics were examined using the percentiles in a region-by-region analysis. The percentiles were calculated using all the daily values of all the grid points within a region.

Figure ***3.6*** shows the percentiles (50^{th}, 75^{th}, 90^{th}, 95^{th} and 99^{th}) of daily precipitation for all WRF configurations vs. the observed ones, through a Q-Q representation. Although the model performed well for the different percentiles for all watersheds, some differences were found. For instance, the WRF tended to underestimate extreme values for SE, S, and especially IS in most of the

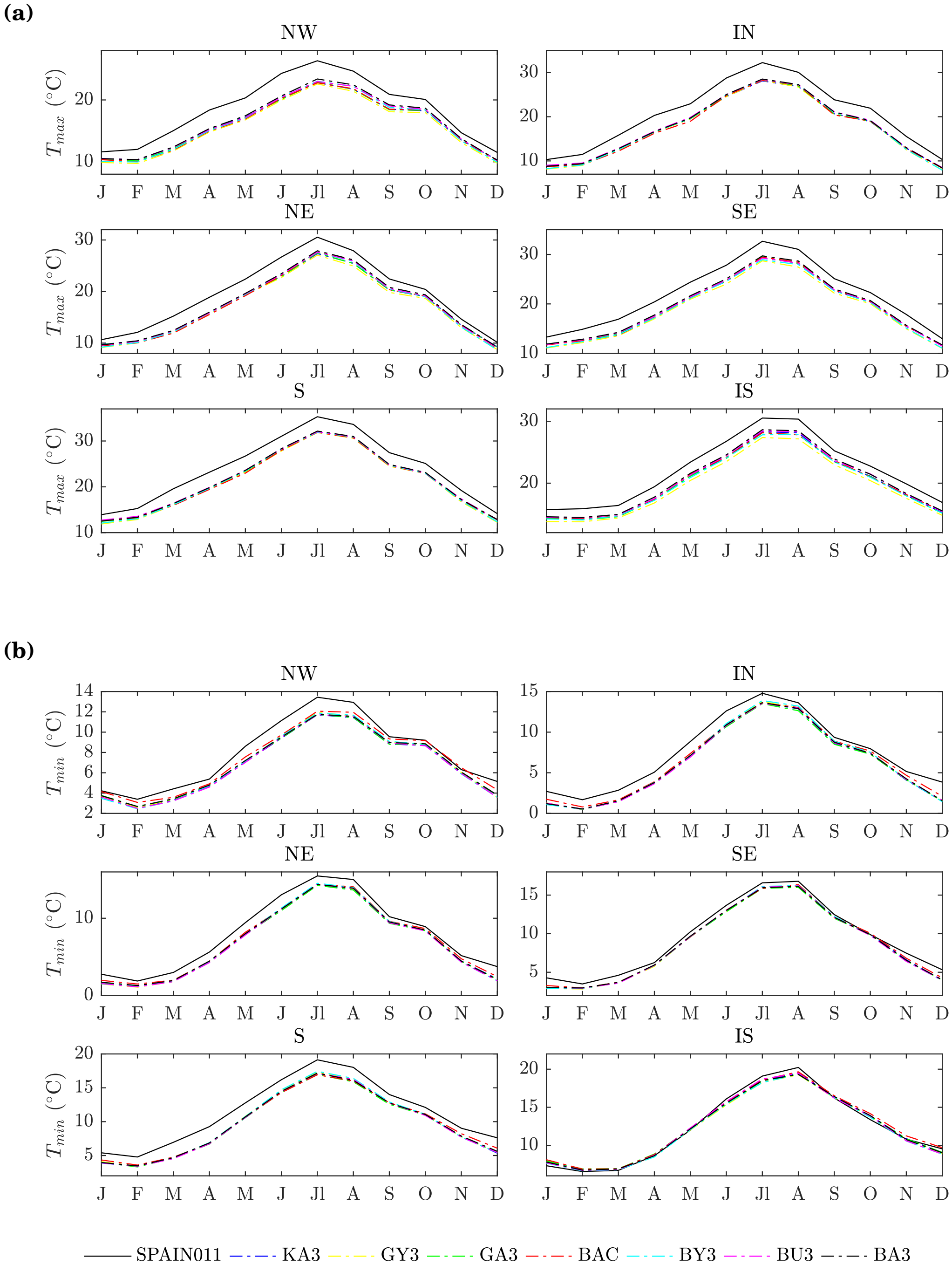

Figure 3.5: *Annual cycle of monthly (a) maximum temperature (T_{max}) and (b) minimum temperature (T_{min}), over the six main watersheds of Spain: northwest (NW), interior (IN), northeast (NE), southeast (SE), south (S) and Balearic Islands (IS).*

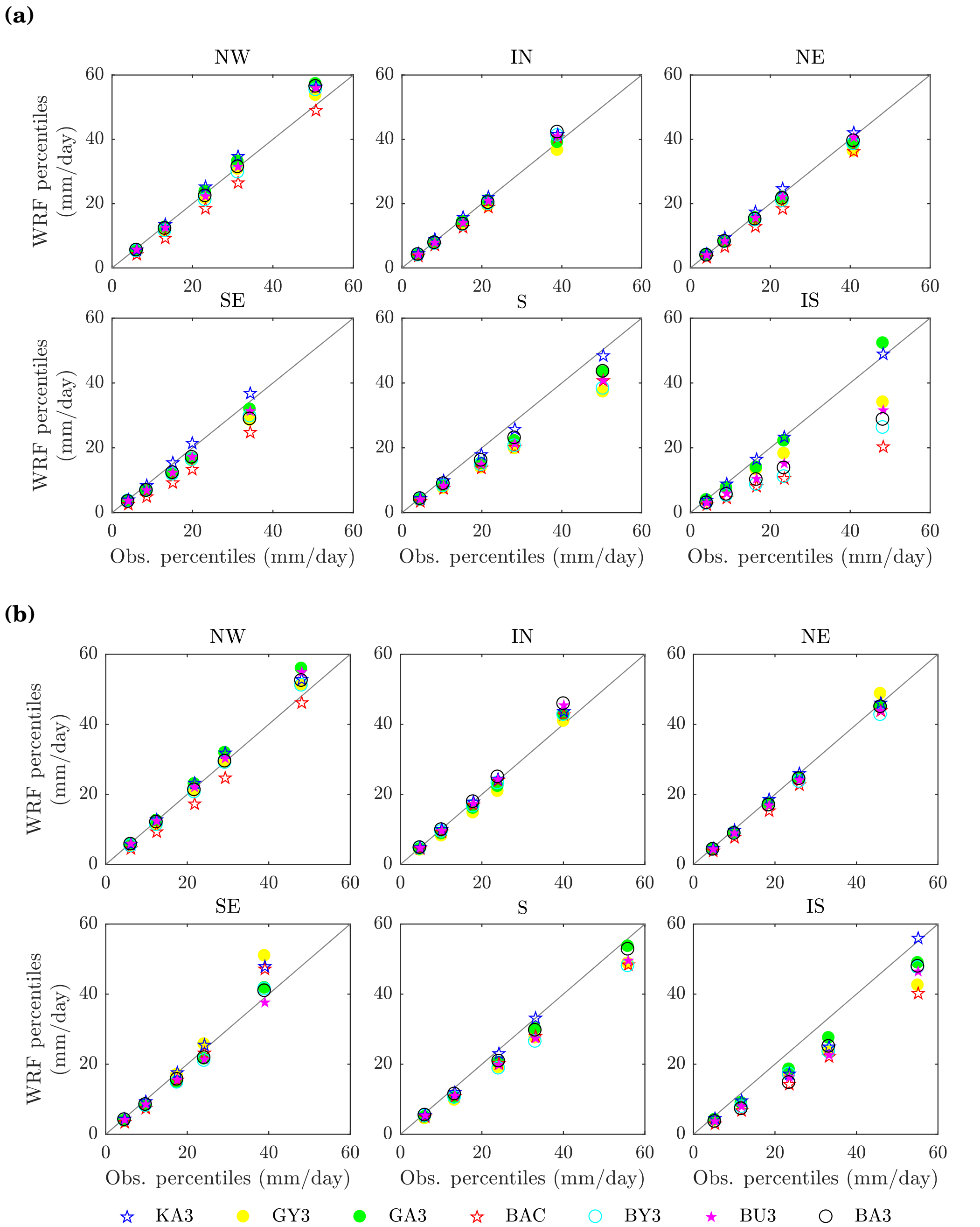

Figure 3.6: *Daily precipitation percentiles (50^{th}, 75^{th}, 90^{th}, 95^{th} and 99^{th}) for a (a) dry, and (b) wet year, over the six main watersheds of Spain: northwest (NW), interior (IN), northeast (NE), southeast (SE), south (S) and Balearic Islands (IS). The grey line indicates a perfect fit.*

configurations, under dry conditions; meanwhile such values were accurately represented or even slightly overestimated for NW, IN, and NE watersheds in most of the configurations as well. Similar behavior was found for the wet year, but with greater overestimations in the NW watershed in terms of extreme precipitation. In general, all configurations performed similarly for the different climate conditions, but KA3 tended to outperform the other configurations, except for the SE under wet conditions where the BA3 seemed to offer the best agreement with SPAIN011 observations.

Figure ***3.7*** depicts the Q-Q plots for T_{max} (Figure ***3.7a***) using the 25^{th}, 50^{th}, 75^{th}, 90^{th}, 95^{th}, and 99^{th} percentiles, and for T_{min} (Figure ***3.7b***) using the 1^{th}, 5^{th}, 10^{th}, 25^{th}, 50^{th}, and 75^{th} percentiles. In general, the model showed a noteworthy capacity to capture the different percentiles of both T_{max} and T_{min}, with a slight underestimation, which was clearer for smaller percentiles for T_{min}. Here, BA3 appeared to be the configuration with a slightly better capability to represent extreme temperatures in all watersheds although all configurations presented very similar features. Here, no configuration appeared to outperform the others in general.

Selection of the Parameterizations Set

Throughout different combinations of parameterizations, the sensitivity test has displayed the capacity of the model to capture the climate characteristics, in terms of precipitation and temperature, over the year throughout Spain and under different precipitation regimes. This cannot ensure the best combination of parameterizations due to computational limitations, but enables the selection of an optimal set of these parameters in order to minimize uncertainties related to them. This selection is based on the main conclusions drawn from the sensitivity test, which are:

- The model showed a noteworthy capacity to simulate the climate behavior over the year in terms of precipitation and extreme temperatures, although some configurations showed more difficulties than did others.
- The model presented more difficulty simulating precipitation than temperature, and also showed more ability to simulate a year with scarcer

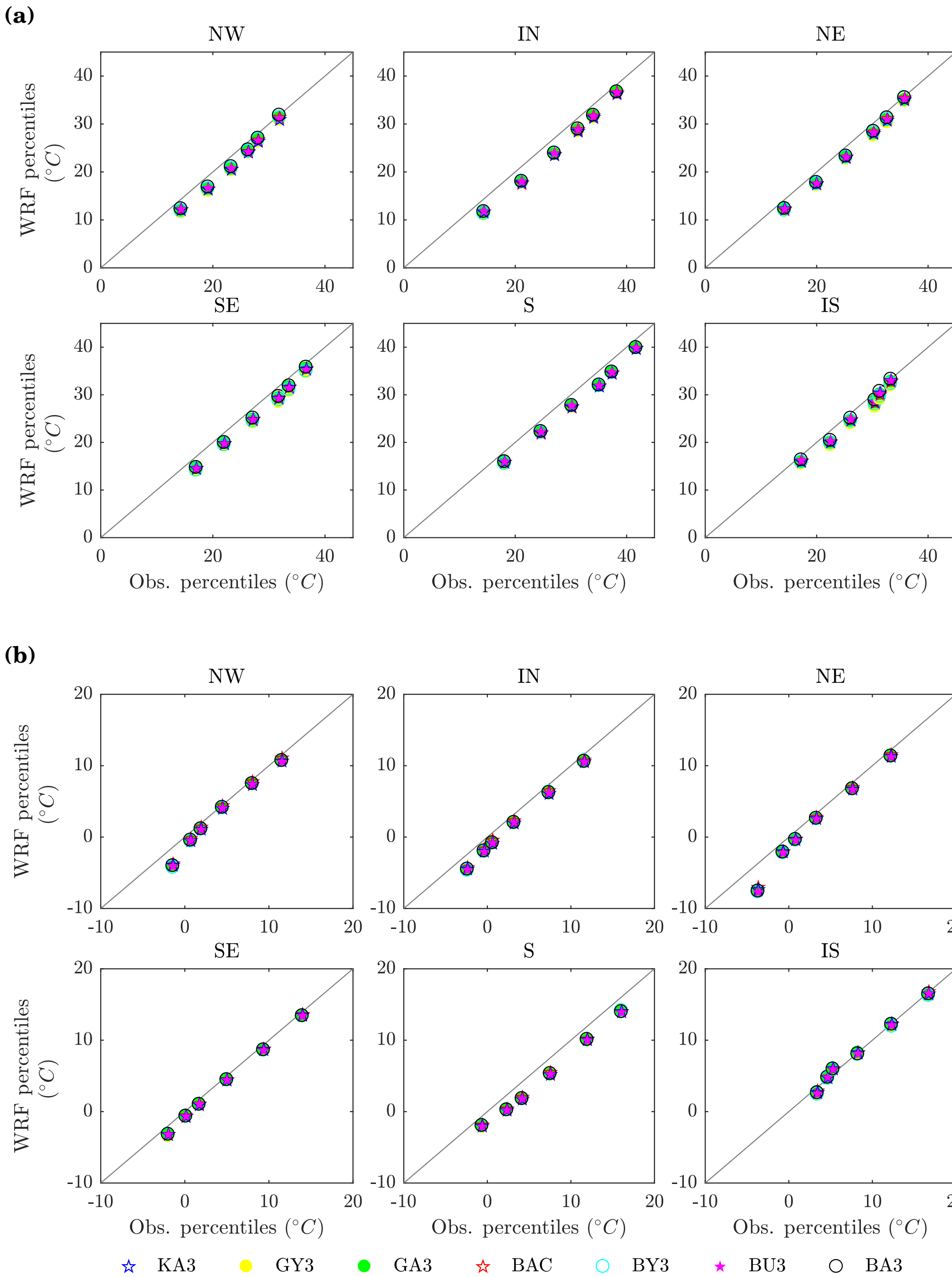

Figure 3.7: *Daily percentiles for (a) T_{max} (25^{th}, 50^{th}, 75^{th} , 90^{th}, 95^{th} and 99^{th}) and (b) T_{min} (1^{th}, 5^{th}, 10^{th} , 25^{th}, 50^{th} and 75^{th} over the six main watersheds of Spain: northwest (NW), interior (IN), northeast (NE), southeast (SE), south (S) and Balearic Islands (IS). The grey line indicates a perfect fit.*

precipitation, so that the selection of an appropriate combination of these parameters should focus on its ability to capture the amount of precipitation in a wet year.

- No configuration performed better than all others for all variables and for all regions, but those that contain both the BMJ cumulus scheme and the ACM2 planetary boundary layer scheme showed broadly better agreement with the observations.

- Concerning to microphysics, although in some cases the most complex scheme outperformed the simpler one, the improvements were small with a greater computational cost. Therefore, the WSM3 seems to be more adequate for long-term simulations.

All these considerations lead us to affirm with certain confidence that the **BA3** is an appropriate configuration to simulate current conditions and, therefore, has also been used for future simulations. Although BA3 is not always the best configuration, it showed its statistical robustness throughout the analyses for the different variables and time scales. Moreover, the results of this analysis agree with those found by Argüeso et al. (2011), who conducted a WRF sensitivity analysis over southern Spain using different combinations of parameterizations in a set of 10-year WRF simulations. Later, Argüeso et al. (2012b) confirmed that it was adequate to perform high-resolution projections on mean values and extremes of precipitation over the IP.

Chapter 4

Current Climate: The Model Evaluation

In this chapter, we evaluate the ability of the WRF Model to adequately reproduce the current characteristics of the climate over the IP. Such analysis helps to establish whether the WRF model, with the configuration selected here, is suitable to carry out simulations of the present climate, and therefore, make future high-resolution projections for the IP.

Here not only is the capability of WRF to simulate primary climate variables (i.e. precipitation and temperature) explored, but also the variables related to land-surface processes are evaluated (i.e. surface evapotranspiration and soil-moisture content). Indeed, land-surface processes have strong influence when projecting future changes in precipitation and temperature over a complex area such as the IP.

4.1. Configuration of Present-Day Simulations

Three historical runs were made using WRF in order to perform the model evaluation. All WRF simulations were performed by applying the same model configuration, and differ only in the LBCs used to drive the WRF model. On the one hand, the first simulation was forced by the Era-Interim data (denoted here by the WRFERA simulation). When the outputs from the WRFERA are compared against observational gridded data the uncertainties associated with the dynamical downscaling approach using the WRF as the RCM can be identified, because this simulation is driven by the more realistic boundary conditions, widely known as the "Perfect Boundary Conditions". By contrast, the other two runs were driven by the bias-corrected outputs of two different GCMs, i.e. the CCSM4 and the MPI-ESM-LR, which will hereafter be referred to as the WRFCCSM and the WRFMPI, respectively. These latter with observations were compared in an attempt to elucidate errors associated with the uncertainties inherited from the GCM used. Although the WRF setup was detailed in Chapter ***3***, Table ***4.1*** lists the most relevant parameters of the model configuration as a summary.

Table 4.1: *Main model setup.*

Parameters	**Description**
LBC	Reanalysis: ERA (WRFERA). GCMs: CCSM4 (WRFCCSM) and MPI-ESM-LR (WRFMPI).
Domain	Two one-way nested domains: the coarser domain (d01) corresponds to the EURO-CORDEX region at 0.44° (~ 50 km) of spatial resolution. The finer domain (d02) spanned the IP at a spatial resolution of 0.088° (~10 km).
Period	December-1979 to November-2014 split into three continuous runs with a spin-up of 11 months.
Vertical Layer	41 vertical levels with the top of the atmosphere located at 10 hPa.
Nudging	Spectral nudging for waves above 600 kms (11 and 10 for x and y wavenumber, respectively) over the coarser domain and above the PBL for winds, temperature and geopotential height.
Physics schemes	Microphysic: WSM3 Cumulus: BMJ Planetary Boundary Layer: ACM2 Land Surface: Noah LSM Radiation (long-wave and short-wave): CAM3

4.2. Comparison Methods

In recent years, different authors have pointed out the importance of evaluating the dynamical downscaling outputs (Argüeso et al., 2012a, Soares et al., 2012a, Jerez et al., 2013), the results of such an evaluation strongly depending on the observational datasets selected to perform it (Gómez-Navarro et al., 2012, Prein and Gobiet, 2017).

Thus, the model capability to detect current climatic variability in the IP was evaluated in terms of different hydrological variables, which were divided into primary climate variables and land surface variables. In this context, primary climate variables include the precipitation and the maximum (T_{max}) and minimum (T_{min}) temperature. The land-surface variables, determined by using the LSM coupled to the WRF, are the surface evapotranspiration and the soil-moisture content.

The evaluation was focused on a direct grid-point comparison between the outputs from current WRF simulations against different gridded datasets. For this, the data have to be comparable, so that the WRF outputs were firstly regridded onto the observational grid. Thus, precipitation, surface evapotranspiration, and soil moisture were interpolated using a nearest-neighbor approach whereas for temperatures a bilinear interpolation was performed. Because the assessment was based on high-resolution observational climate data, the comparison was performed using only the outputs of the finer domain and only for land points.

Primary climate variables were compared against observational gridded products[1] at different time-aggregation intervals (from annual to daily). The annual and seasonal time scales enable us to examine the model's ability to capture the main spatial and temporal patterns as well as the interannual variability. However, several authors (Herrera et al., 2010, IPCC, 2007, Leung et al., 2003) have pointed out that a suitable model evaluation requires a multi-temporal approach based not only on long-term mean climate, but also on the distribution of daily values. In fact, by evaluating daily values, we can check the model's capability in terms of high-order statistics, and thus in terms of extreme values. This latter capacity is crucial in a climate-change context, since extreme events are expected to exert greater impact on society and natural systems than would those due to changes in long-term mean values. In

[1]The Precipitation evaluation was performed by comparing the WRF outputs against two different gridded products, the SPAIN011 and the PT02, which are at 0.11 and 0.2° of spatial resolution. As observational gridded temperatures were used the T_{max} and T_{min} from E-OBS at 0.22° of spatial resolution. Details of these products can be found in Chapter ***2***.

addition, the study of daily values enables us to avoid the compensation error that could occur for long-term mean (Argüeso et al., 2012a).

In terms of land-surface variables, the lack of a suitable observational database caused the evaluation of these variables to be based fundamentally on annual and seasonal values. Such an evaluation was made regarding the GLEAM database, and therefore the nature of the data and the possible sources of errors associated with them should be borne in mind. In fact, the surface evapotranspiration and soil moisture from GLEAM is the result of applying a model, so that such data are subject to potential sources of uncertainty derived from a model. Therefore this variable was assessed only by using long-term values. Until now, the evaluation has been performed for the period from December 1979 to November 2014. Hence, to use a similar period because the GLEAM data began in January 1980, we chose the period between December 1980 and November 2014. Thus, a 34-year period was used, which has an adequate length to perform the current climate evaluation.

The soil-moisture content is provided daily by GLEAM in two different datasets, i.e. the so-called surface soil moisture content (smois), and the root-zone soil moisture. In this context, smois is the water contained in the upper 10 cm of the soil while moisture in the root zone is accessible for plants. Thus, the water availability depends on the root depth, which is determined by the land cover. In this context, GLEAM involves three layers (0-10, 10-100, and 100-250 cm), two (0-10 and 10-100 cm) or only one (0-10 cm) for tall vegetation canopy, low vegetation cover, and bare soil, respectively. However, the WRF model through the NOAH LSM, simulates the water content based on a multilayer approximation, which is composed of four layers (0-10, 10-40, 40-100, 100-200), corresponding the three upper layers in the root zone (Chen and Dudhia, 2001). Therefore, the different characterization of the soil does not allow a direct comparison in terms of total available soil moisture content. Thus, two different analyses were selected to perform this evaluation.

Firstly, only the surface soil moisture content was evaluated using the same procedure used in the other variables for long-term means. Secondly, a comparison was made for the time course between the root soil-moisture content provided by GLEAM and the total soil-moisture content from WRF. Finally, to gain a clearer understanding of the performance of the WRF simulation, as well as to check how this parameterization distributes the moisture throughout the soil column, we computed the mean annual cycles in each layer for the different soil types presented in the IP.

4.3. Primary Climate Variables

4.3.1. Long-term Mean Precipitation: from Annual to Seasonal Values

The time series of annual and seasonal accumulated precipitation corresponding to each grid point were computed as the sum of the daily precipitation for each year and season, respectively. For that, each year corresponds to the period between December of the previous year to November of the given year. For instance, the accumulated precipitation for 1980 is the rainfall accumulated from December 1979 to November 1980. In the same way, for defining the corresponding seasons, winter was designated as the months December, January, and February (DJF); spring as March, April, and May (MAM); summer as June, July, and August (JJA); and finally, autumn as September, October, and November (SON). This procedure was applied to observations (SPAIN011 and PT02) as well as for the three WRF simulations (WRFERA, WRFCCSM, and WRFMPI) in order to compare them. Then, different statistical metrics were calculated for the 35-year period from December 1979 to November 2014. Note that the observation depicted here comes from two different gridded datasets, but to summarize the climate information, we represented both analyses on the same maps, and for simplicity, the two observational data are referred to as SPAIN02-PT02.

The ability of the model to provide the main spatial distribution was evaluated through the annual precipitation climatology, i.e. mean of the series of accumulated annual precipitation. This first assessment enabled to identify the regions where WRF provided larger deviations with respect to the observations. As shown in Figure ***4.1***, SPAIN011-PT02 depicts a significant northwest to southeast precipitation gradient across the IP, which is well reflected by WRFERA As several authors have pointed out (Esteban-Parra et al., 1998, Rodriguez-Puebla et al., 1998), the northwestern IP is characterized by a large

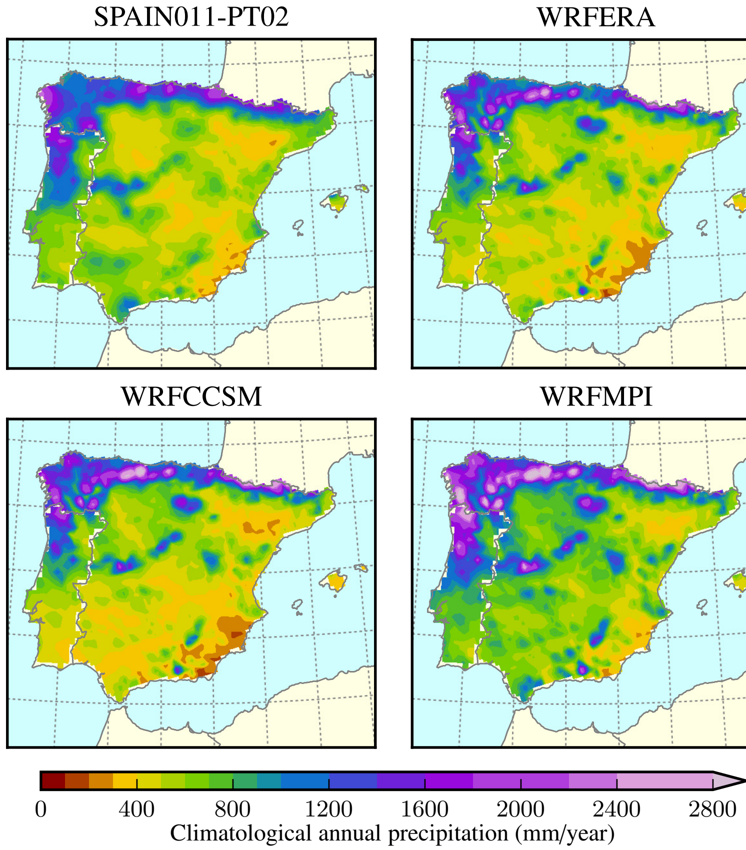

Figure 4.1: *Annual climatology of precipitation (mm / year) from the observational data set (SPAIN011-PT02) and from the WRF outputs, driven by ERA (WRFERA), CCSM4 (WRFCCSM) and MPI-ESM-LR (WRFMPI).*

amount of annual accumulated precipitation (from 900 to 2500 mm/year) which is associated with the continuous arrival of Atlantic frontal systems (Herrera, 2011). This characteristic is adequately represented by the WRF, showing, however, an overestimation, linked mainly to the orography. Note that this overestimation is particularly notable in the complex mountainous regions with elevations higher than 2000 m a.s.l., such as the Picos de Europa (in the Cantabrian Range), and the Sierra de Gredos, Sierra de Guadarrama, and the Serra da Estrela (in what is known as the Central System). Here, the reanalysis-driven simulation reaches values higher than 2000 mm/year whereas observed gridded data display precipitations of about 1200 mm. Note, however that in areas with high mountainous ranges, gridded observational datasets are affected by a scarcity of observation stations, and therefore, they might be not able to adequately record the annual precipitation (Caldwell et al., 2009, Soares et al., 2012b).

Conversely, areas such as southern Portugal and mainly the southeastern coast of the IP were generally underestimated by the WRF. This latter was characterized by registering amounts of annual precipitation corresponding to desert regions (200 mm/year or less). As for the northwestern region, the great overestimation associated with the orography appears in most of the high mountains in the central and southern areas of the IP such as the Picos de Urbión and the Sierra de la Demanda (both located in the Iberian System) and Sierra Nevada (in the Baetic System). Finally, it is important to note the differences found in some areas close to the border between Spain and Portugal (e.g. the northwestern and southern borders). This is probably because the comparison was made using two different observational gridded data instead of a single grid.

Regarding the results from WRF driven by the GCMs, the WRFMPI substantially overestimated the annual precipitation, while the WRFCCSM failed to depict a clear pattern. In fact, this latter offered underestimates in some regions (e.g. most of the southern region), and overestimates in other ones (e.g. the northwestern region). Again, for both the WRFCCSM and the WRFMPI, a large overestimation occurred for the high mountains. Otherwise, the WRFMPI agreed well with SPAIN011-PT02 in the southern IP, as can be clearly seen in the Sierra de Grazalema as well as over the eastern coast.

As a further analysis of the WRF performance in terms of mean fields, the relative bias was also computed[2] as an accurate measure of the average error and its sign. Therefore, relative biases were calculated for annual and seasonal time aggregation intervals. In this context, the seasonal analysis enabled us to identify biases associated with possible compensation errors in the annual scale. Additionally, a two-sided Student's t test was performed to identify the areas with non-significant differences between observations and simulations at

[2]The relative bias consists of the mean difference between modeled and observed total precipitation with respect to the observed data, expressed as a percentage. The equation is given in Appendix ***A***.

the 95% confidence level.

Figure ***4.2*** shows that the WRF provided adequate results when driven by ERA for the annual scale. Here, the deviation with respect to the corresponding observations was not significant or below 20% in many regions. Furthermore, only for a few regions did the WRF depict biases of more than 40%, such differences being both positive and negative. The largest negative biases were found over certain areas in the southern third of the IP, as well as in the eastern region, the Cantabrian coast and the Balearic Islands. Conversely, the positive biases appeared mainly around the region between the Northern Plateau, the Cantabrian Range, and the Baetic System, with the highest values located in the Picos de Europa and Sierra de la Demanda, the latter presenting values of more than 100%.

In the results from GCMs-driven simulations, the WRFCCSM showed results very similar to those of the WRFERA, although presenting larger significant biases both positive and negative. The dry biases were larger in both magnitude and surface area, appearing fundamentally over the south-central regions as well as around the entire east coast of the IP. The wet biases appear in high mountains, around the Northern Plateau, Cantabrian Range, Pyrenees, and certain areas of Galicia. The WRFMPI, however, gave a generalized overestimation, particularly over the northwestern quarter of the IP, the positive biases being less than 60% in many regions.

In a seasonal context, the WRFERA provided remarkable results in most of the IP, with the dry and wet biases of less than 60%. However, several exceptions were found in high mountains with large biases in all seasons. The best agreement with SPAIN011-PT02 appeared in summer and the worst in autumn. The wet deviations occurred fundamentally in winter and spring, reaching the maximum values over the northern high-mountain regions (values around 100%). Conversely, dry biases were found in summer and especially in autumn. This latter covered a significant area over the southern IP with deviations of around 20-60%. The results over the entire region of Portugal are notable, where no significant differences between observations and simulations were found, except in autumn. For this season the dry biases were about 40% in many regions throughout Portugal.

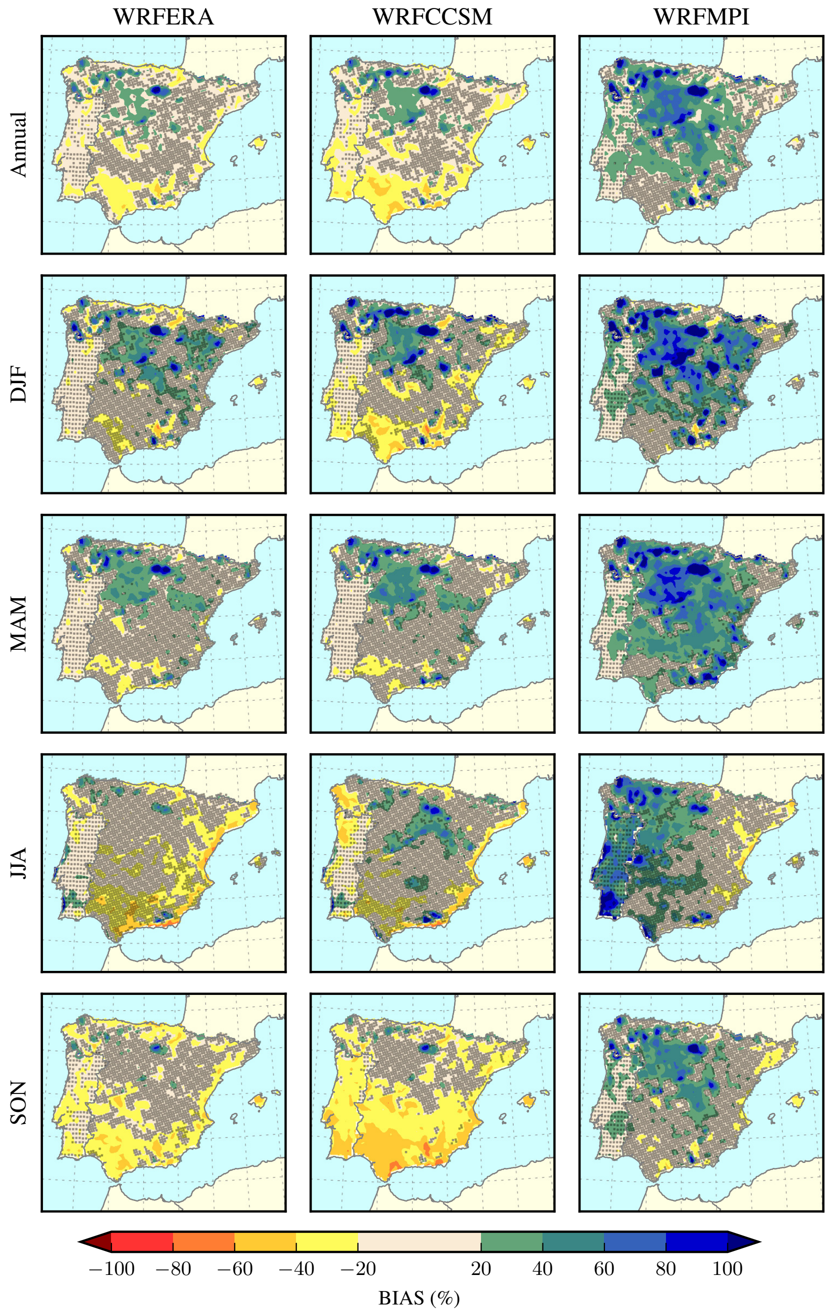

Figure 4.2: *Relative bias of the annual and seasonal precipitation from WRF outputs (WRFERA, WRFCCSM and WRFMPI) in relation to observations (SPAIN011-PT02) expressed as a percentage. In rows the annual and seasonal biases. No significant differences between the mean from observed and simulated distributions according to Student's t test at the 95% confidence level are shown as black dots.*

In general, the results from the WRFCCSM and WRFMPI simulations agreed reasonably well with the observations, with great differences between them. These different results suggest that the major errors were associated with the LBCs. On the one hand, the WRFCCSM provided results similar to those of the WRFERA in both sign and spatial pattern. However, this latter showed more significant biases in all seasons. The largest deviation in relation to WRFERA seems to occur during the autumn, being generally negative and especially strong over the southern third of the IP. On the other hand, for the WRFMPI deviation, we conclude that this run systematically tended to generate wet deviations in all seasons.

Furthermore, to determine the spatial agreement between the simulated and observed mean data, the pattern correlation (r) was also calculated. It is important to remark that this pattern correlation, which is the standard Pearson correlation over space, displays the spatial similarity between maps not being a measurement of the model bias. As illustrated in Table ***4.2***, the spatial agreement between mean values from the WRFERA and SPAIN011-PT02 was quite satisfactory, with an r value of around 0.820 to 0.929. The best agreement appeared in summer and the worst in winter. For GCM-nested simulations, pattern correlations again proved reliable and similar to those of the WRFERA. These results imply that the WRF accurately represented the spatial distribution throughout the IP and distributed well the main features of the both annual and seasonal precipitation.

Table 4.2: *Annual and seasonal pattern correlations (r) from WRF outputs driven by ERA (WRFERA), CCSM4 (WRFCCSM), and MPI-ESM-LR (WRFMPI) against observations from SPAIN011-PT02.*

	WRFERA	**WRFCCSM**	**WRFMPI**
Annual	0.855	0.848	0.854
DJF	0.824	0.820	0.830
MAM	0.849	0.850	0.846
JJA	0.929	0.886	0.903
SON	0.853	0.836	0.841

The standard deviation of the annual and seasonal total precipitation has also been computed. Using this measure, we attempt to elucidate the performance of the model in terms of interannual variability of precipitation, thus compiling additional information concerning the statistical distribution. In this context, Figure ***4.3*** displays the normalized standard deviation[3] for the WRF simulations regarding SPAIN011-PT02. A value of normalized standard deviation equal to 1 means a perfect agreement between simulations and observations. Conversely, a value over 1 indicates a model standard deviation overestimation, while a value below 1 reveals underestimations.

In relation to annual values, the WRFERA run provides acceptable results in terms of interannual variability, reaching normalized standard deviation values close to 1 in many places. However, the results also show slight weaknesses such as the overestimations located in high-mountain regions. WRFCCSM features were similar to those of the WRFERA, but this reveals larger overestimation over the Northern Plateau and in the Cantabrian Range. The underestimation was also larger in regions such as the south of the IP. For WRFMPI, however, a widespread overestimation of the interannual variability was found throughout the IP.

With respect to seasonal values, in winter and spring, the WRFERA offered an overall overestimation in northern IP while the underestimation appeared to be widespread in the south. However, the spatial patterns of the normalized standard deviation for summer and less for autumn resulted in an underestimation in most of the IP. As for relative biases, the WRFCCSM presented similar characteristics to those of the WRFERA, but with larger differences in both magnitude and area with respect to the observations. For the WRFMPI, large standard deviation overestimations were found in all seasons, covering most of the area for spring and autumn.

The results also suggest that the spatial patterns of both, interannual variability (Figure ***4.3***) and biases (Figure ***4.2***) were quite similar. Indeed, mean values and interannual variability were closely related, as can be seen from the results, since the amount of precipitation was underestimated where the variability was also underestimated. Similarly, an overestimation in the interannual variability involved the overestimation of the amount of precipitation.

[3]The normalized standard deviation is the ratio between modelled and observed standard deviation of the total amount of precipitation. Further details can be found in Appendix ***A***.

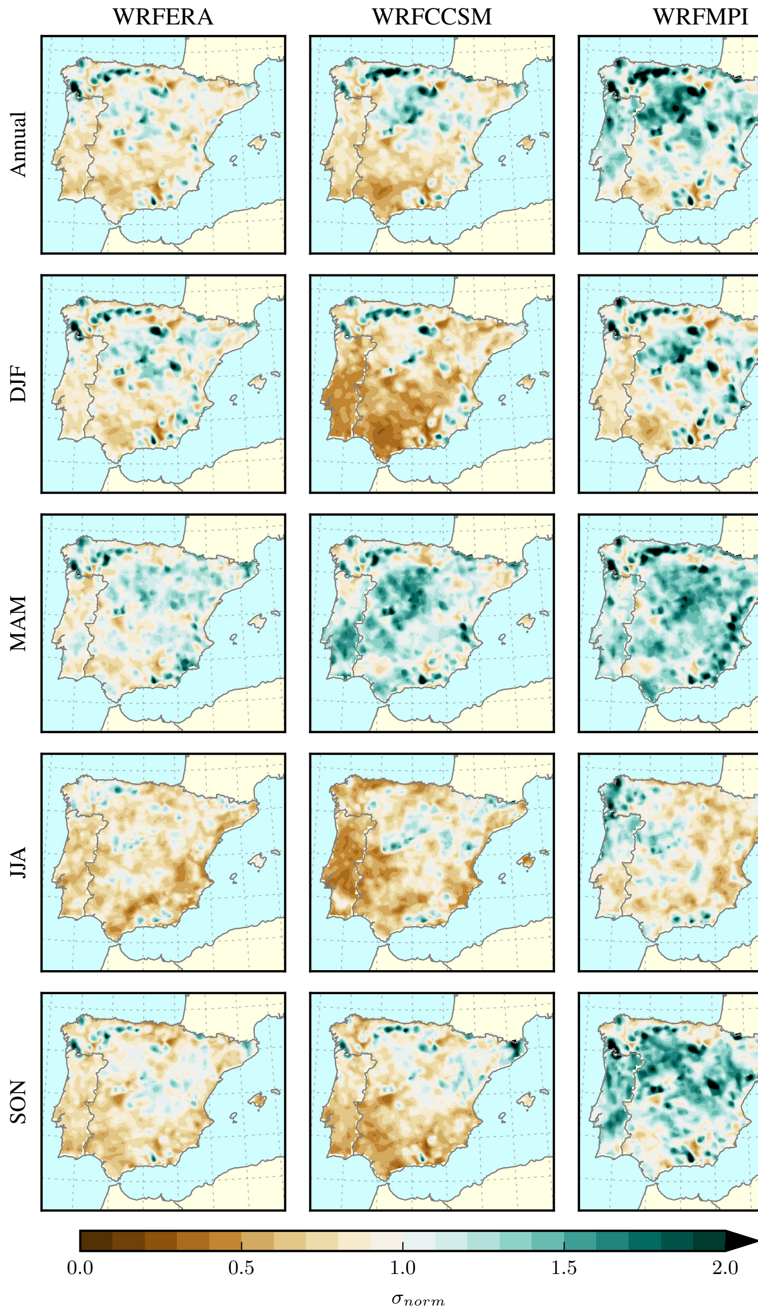

Figure 4.3: *Normalized standard deviation of accumulated annual and seasonal precipitation from WRF outputs (WRFERA, WRFCCSM, and WRFMPI) with respect to observations (SPAIN011-PT02).*

4.3.2. Daily Distribution of Precipitation: High-order Statistics and Extreme Values

To evaluate the model's capacity to reproduce the daily distribution of precipitation, we used the Perkins skill score (PSS) developed by Perkins et al. (2007). This skill score has been used by other authors (e.g., Boberg et al., 2010, Kjellström et al., 2010, Evans and McCabe, 2010, Ji et al., 2016). This parameter measures the similarity between the simulated and observed distributions of daily precipitation through the quantification of the common area of their probability density functions (PDFs). Therefore, a PSS of 1 means a perfect fit, and a value of 0 indicates that the simulated PDF is completely different from the observed one[4].

The shape of the PDF depends on the intervals selected to perform it, so that to generate such PDFs, bins of 1 mm/day ranging from 0 to the maximum observed daily precipitation were considered. The bin of 1 mm was selected because it has already been demonstrated to be a suitable interval for representing the precipitation PDF (Perkins et al., 2007, Argüeso et al., 2012a). Furthermore, a statistical test was considered in order to interpret the quality of the model performance in terms of PSS. Therefore, the null hypothesis was that there is no difference between modeled and observed PDF. Thus, the empirical distribution of the PSS was established by applying a Monte Carlo approach with 1000 random samples generated by using the observed PDFs. Hence, if the value of the simulated PSS was below the 5^{th} percentile of this empirical distribution, it was considered significantly different from the observed PDFs. A more detail description of the procedure appears in Keellings (2016).

Figure ***4.4*** depicts the spatial distribution of the PSS from the three simulations across the IP. Black points indicate that the PSS do not reach a satisfactory value in that grid point, and thus we considered that the observed PDF was not well represented by the model.

The results show that the common shape between the PDFs from simulations and observations are strongly satisfactory, with values exceeding 85% in the entire IP for the three WRF simulations. The lowest PSS values appear

[4]See Appendix ***A*** for a further description of the PSS.

in the northwestern IP, reaching the lowest ones in the north of the Iberian System. Here, the PDFs from all of the WRF simulations significantly differed with respect to the observed ones, indicating difficulty in representing the distributions of daily precipitations in these regions. Again, the performance of the WRFCCSM proved similar to that of the WRFERA except in Portugal, where the PSS values were lower. The WRFMPI, however, had more serious shortcomings, especially in the Cantabrian region and in the Northern Plateau where several grid points with no significant PSS were found.

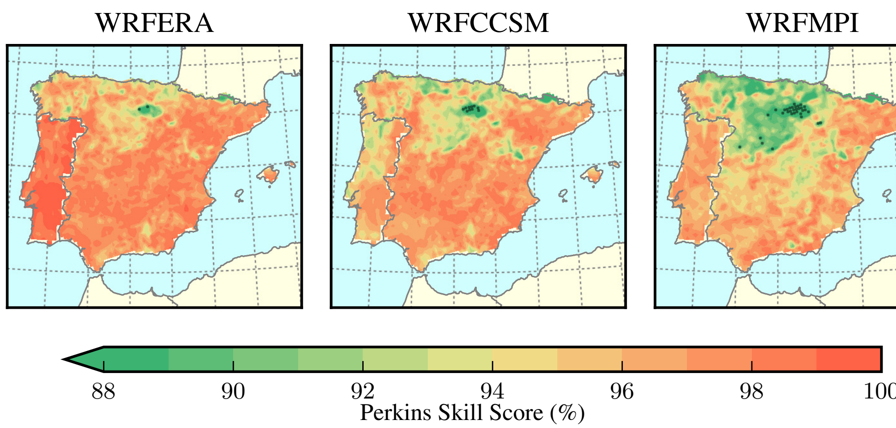

Figure 4.4: *Perkins Skill Score values in terms of the daily precipitation for the WRFERA, WRFCCSM, and WRFMPI simulations with respect to observations from SPAIN011-PT02, expressed in percentages. Black dots indicate significant differences with observational data PDF PSS values.*

In terms of weather extremes, the widely known extreme indices, developed by the ETCCDI, were applied to evaluate the model's capacity to provide realistic values from the tail of the probability distributions. Such indices were defined in order to provide the scientific community with a tool to address aspects related to extreme events of precipitation and temperature[5]. As detailed in Sillmann et al. (2013), the indices can be divided into four broad categories: (i) absolute indices or indices that describe climate characteristics such as the maximum and minimum values within a period; (ii) indices based on the duration of events that exceed a given threshold (denominated as threshold indices); (iii) duration indices or indices that depict the persistence of certain

[5]For a further description of the definition of these indices see Tank et al. (2009).

extreme events; and (iv) the percentile-based threshold indices, which consist of the analysis of the values above or below a threshold. These latter define their threshold by using the percentiles of the daily distributions for a given reference period (e.g. the 10^{th} or the 90^{th} percentile).

Among the different measures defined by the ETCCDI, a set of eight indices has been selected to analyze the WRF capacity to simulate extreme events, which are summarized in Table ***4.3***. To compute percentile-based threshold indices, the ETCCDI defined the years 1961 to 1999 as the base period. In this study, however, this reference period was selected as the entire period of the current simulation (1980-2014). Thus, the indices were calculated for each year, and, for each index, an annual average value was calculated for each grid point.

Table 4.3: *ETCCDI extreme precipitation indices selected.*

Index	Definition	Units	Type
RX5day	Maximum 5-days consecutive precipitation	mm	**I**
SDII	Average precipitation on days with accumulated values above 1 mm	mm	**I**
R10	Number of days with precipitation above 10 mm	days/year	**II**
R20	Number of days with precipitation above 20 mm	days/year	**II**
CWD	Annual mean maximum number of consecutive days with precipitation $\geq$ 1 mm	days/year	**III**
CDD	Annual mean maximum number of consecutive days with precipitation < 1	days/year	**III**
R95pTOT	Annual sum where daily precipitation exceeds the 95^{th} percentile of daily precipitation in the reference period	%	**IV**
R99pTOT	Annual sum where daily precipitation exceeds the 99^{th} percentile of daily precipitation in the reference period	%	**IV**

Figure ***4.5*** portrays the absolute (RX5day and SDII) and the threshold (R10 and R20) indices for the observations from SPAIN011-PT02 and from the three WRF simulations for the entire period simulated (1980-2014). In general, the three WRF outputs suitably capture the spatial patterns of the absolute indices, although the WRFMPI appears to give overestimations in most of these indices.

The observational maximum of 5 days of consecutive precipitation (RX5day) was characterized by low values over the Interior Plateaus and over the Ebro Valley, with mean annual RX5day of approximately 40-60 mm. On the contrary,

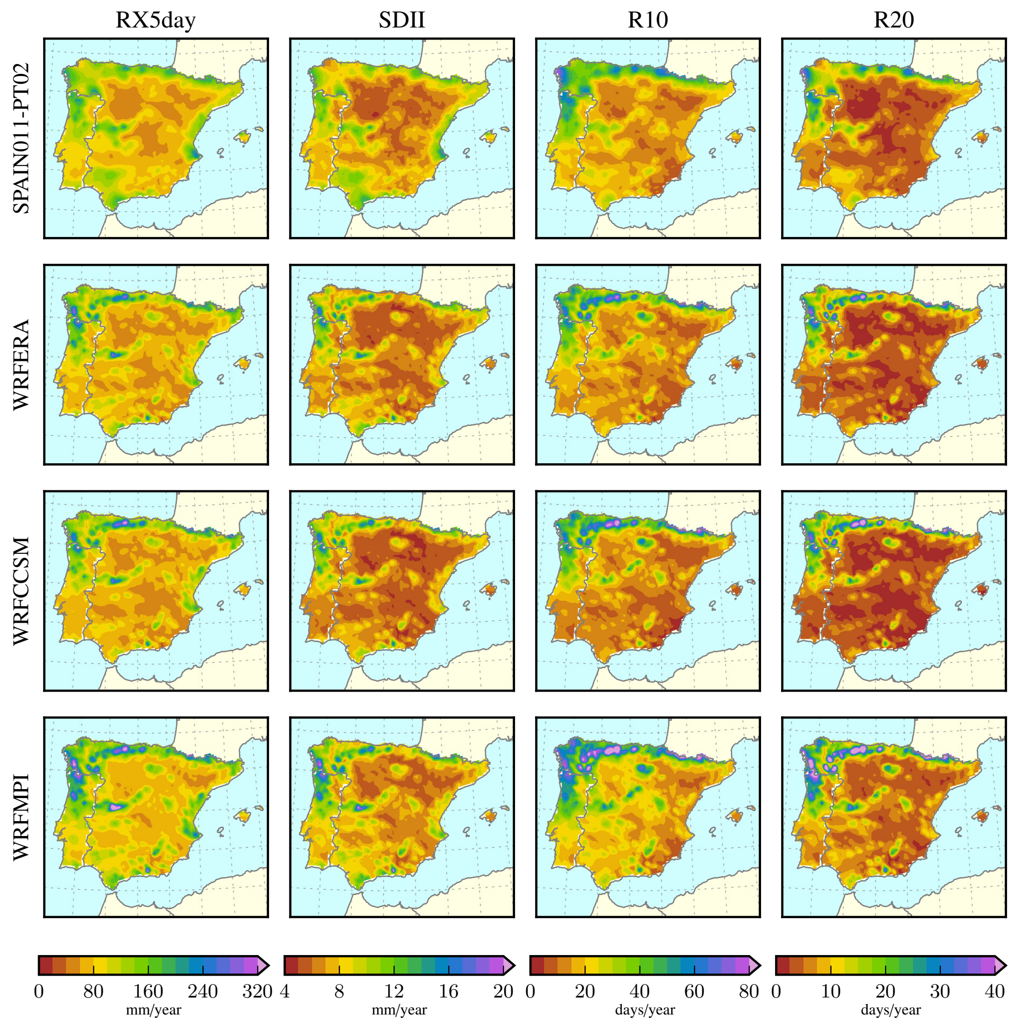

Figure 4.5: *Annual mean of ETCCDI precipitation indices based on absolute values (RX5day and SDII) and those above a given threshold (R10 and R20) for observations (SPAIN011-PT02) and simulations (WRFERA, WRFCCSM, and WRFMPI).*

the highest ones were achieved especially in areas located in coast regions (e.g. Cape of the Nao, Coast of Cádiz, Cantabrian Coast, west of Galicia and northwest of Portugal) and over high mountains (Pyrenees, Cantabrian Range and Central System) where the annual value of this index is over 160 mm. Regarding the model's ability to represent the RX5day, although the agreement between observations and simulations was remarkable, the WRF shows an overall overestimation related to the orography, as shown across the high-mountain regions such as the Cantabrian Range or the Central System. Here, observational values are around 120-160 mm whereas the WRFERA provides values of around 240-280 mm/year and even more for GCM-driven simulations. Similar conclusions may be drawn when the intensity of precipitation in days above 1 mm (SDII) was analyzed, the highest values again arising in the coast and over high mountains (values above 10 mm/year). In general, the WRFERA properly represented the SDII spatial distribution. Nonetheless, both the WRFERA and the WRFCCSM revealed a slight underestimation in the central IP, which was not so evident in the WRFMPI.

Concerning heavy-precipitation days (R10), a northwest to southeast gradient was shown, the range of the mean values being around 10-70 days. Although the spatial distributions were well represented by the three WRF simulations, both the WRFERA and WRFCCSM showed a small underestimation in general, whereas the WRFMPI appeared to overestimate the R10. Again a widespread overestimation associated with the orography was shown. This latter trend was clear in the Cantabrian Range for the WRFCCSM and WRFMPI, reaching values above 80 days/year, while the observations indicate R10 about 40 to 60 days/year. For days of very heavy precipitation (R20), i.e. days with accumulated precipitation exceeding 20 mm, the conclusion was similar to those recorded for heavy-precipitation days. However, for this latter, the WRFERA and WRFCCSM overestimated only in some regions such as the Strait of Gibraltar or the western of Sierra Morena.

Figure ***4.6*** depicts the so-called duration indices as well as the percentile-based threshold indices. On the one hand, the consecutive dry days (CDD) and the consecutive wet days (CWD), represent the longest duration of dry and wet periods, respectively. High persistence of these may be harmful to different ecosystems, so their accurate characterization is necessary, especially in regions such as the IP. For the CDD, the three model simulations performed similarly, giving underestimations throughout the IP except in its southern third, where the opposite occurred, with the driest spatial distribution corresponding to the WRFERA and WRFCCSM. The WRFMPI, nonetheless, appeared to give wetter results for the southern half of the IP, so that the results were better in the southeast for this simulation. Regarding CWD, despite an overall underestimation for the WRFERA and WRFCCSM, and a widespread overestimation for

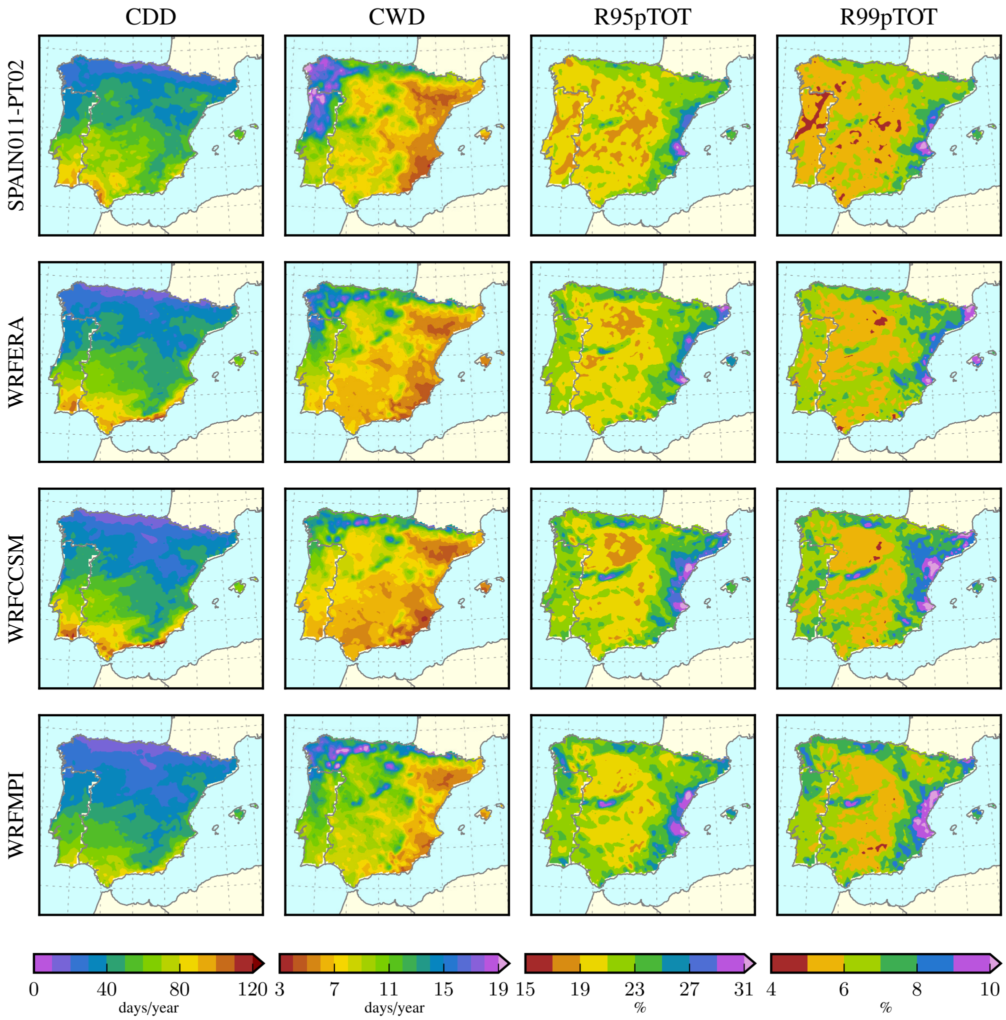

Figure 4.6: *Annual mean of ETCCDI precipitation indices of duration (CDD and CWD) and those based on a percentile threshold (R95pTOT and R99pTOT) for observation (SPAIN011-PT02), and simulations (WRFERA, WRFCCSM, and WRFMPI).*

the WRFMPI, the results again indicate that WRF was able to represent the performance of this extreme index. On the other hand, in the IP, heavy rainfall constitutes a major contribution to its precipitation regime, making it important to address the WRF capability to simulate precipitation events above the 95^{th} and the 99^{th} percentiles (R95pTOT and R99pTOT, respectively). Results from these indices suggest a generalized overestimation, especially for Portugal. Note that, as reflected by the observations, the maximum percentage of annual rainfall above the two percentiles was reached in the eastern IP, denoting the torrential character of the precipitation in this area. This aspect was adequately captured by the three simulations.

4.3.3. Long-term Mean Temperatures: from Annual to Seasonal Values

The evaluation in terms of temperatures begins with the analysis of the annual climatology of T_{max} and T_{min}. For this, the annual mean time series of both variables were calculated for each grid point, and then the means of the annual temperatures for the entire period were calculated (Figures ***4.7*** and ***4.8***).

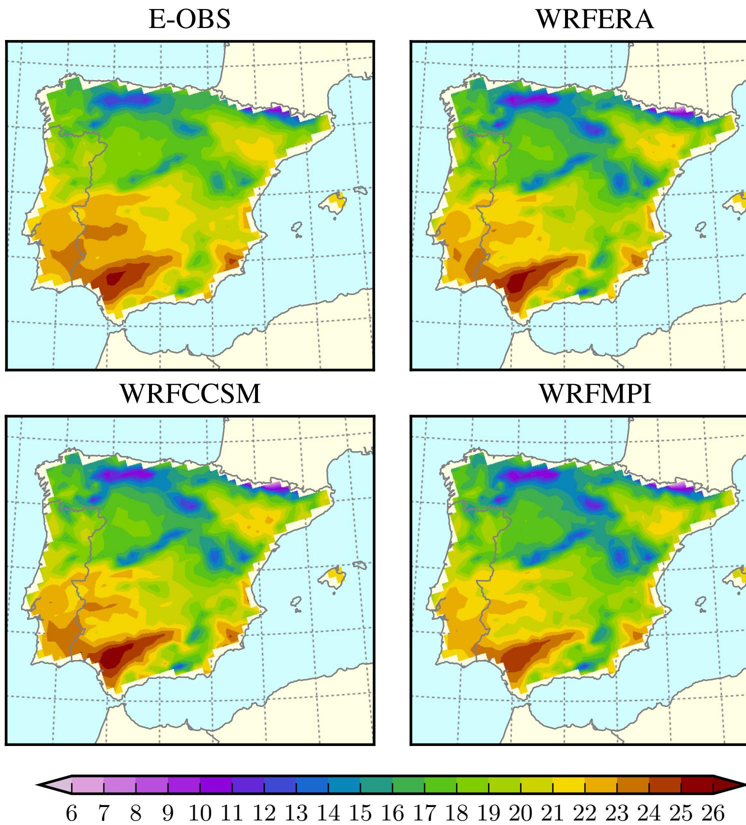

Figure 4.7: *Annual climatology of mean T_{max} from observational datasets (E-OBS) and from the WRF outputs driven by ERA (WRFERA), CCSM4 (WRFCCSM), and MPI-ESM-LR (WRFMPI).*

Broadly speaking, the temperature regime over the IP is determined for three main factors: the latitude, the elevation, and the distance to the sea. Thus, the spatial temperature distribution presents gradients from north to south and from inland to coastal regions. In general, all WRF simulations can accurately reproduce the spatial distribution of the T_{max} and T_{min}, with overall good agreement regarding the different factors that affect to such temperature regimes. For instance, for both T_{max} and T_{min} all WRF simulations locate the hottest temperatures in coastal regions and river valleys, and the coldest ones over high mountains. Nevertheless, despite the main spatial pattern being well reproduced, the WRF generally underestimates the temperature, especially when is driven by for the MPI-ESM-LR model.

Additionally, the correlations between patterns were also computed in or-

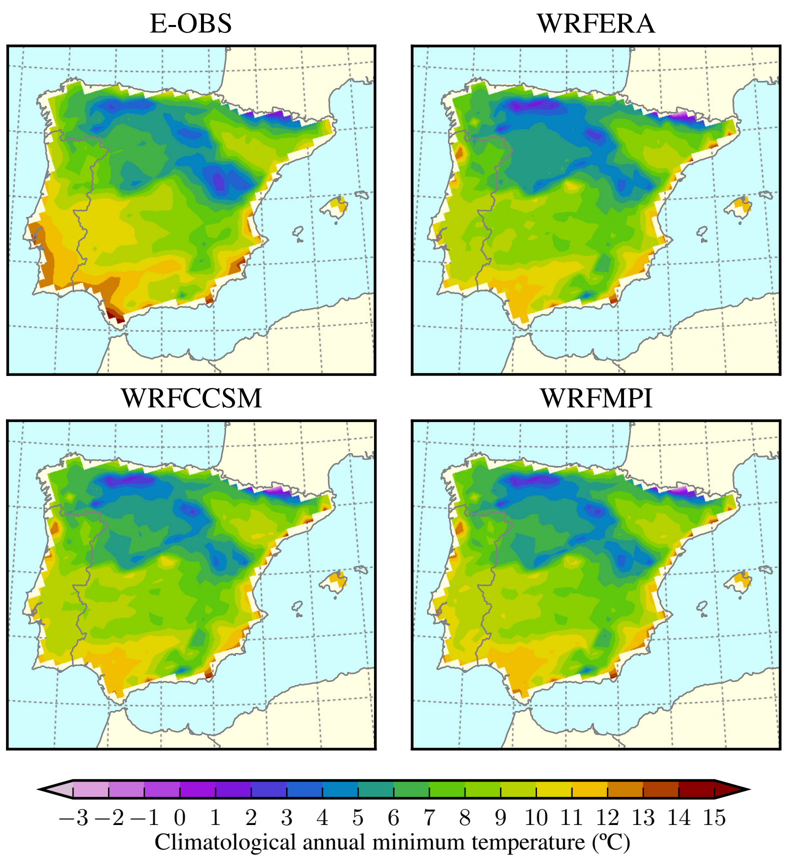

Figure 4.8: *The same as Figure **4.7** but for minimum temperature (T_{min}).*

der to determine the spatial agreement between WRF and E-OBS (Table ***4.4***). Although the spatial correlations are similar for both temperatures in all simulations (values ranging between 0.941 and 0.973 for T_{max} and between 0.913 and 0.947 for T_{min}), the lowest spatial pattern correlations for T_{max} are provided by WRFMPI, both annually and seasonally. By contrast, these latter reach the best agreement with respect to E-OBS for T_{min}.

To analyze the long-term mean errors from the WRF simulations, the bias between simulations and observations was also found for temperatures. Unlike precipitation, this measure is expressed in absolute values and thus is expressed in °C. The significance of the differences between simulations and observations in terms of long-term means was also evaluated using Student's t test at the 95 % confidence level.

Table 4.4: *Annual and seasonal pattern correlation (r) from WRF outputs driven by ERA (WRFERA), CCSM4 (WRFCCSM), and MPI-ESM-LR (WRFMPI) against observations from E-OBS.*

	WRFERA	**WRFCCSM**	**WRFMPI**
	Maximum Temperature		
Annual	0.973	0.970	0.963
DJF	0.970	0.967	0.965
MAM	0.972	0.970	0.964
JJA	0.958	0.956	0.941
SON	0.970	0.970	0.962
	Minimum Temperature		
Annual	0.930	0.930	0.942
DJF	0.914	0.913	0.923
MAM	0.922	0.926	0.930
JJA	0.926	0.923	0.941
SON	0.936	0.936	0.947

Figure ***4.9*** illustrates the annual and seasonal bias of T_{max} for the WRFERA, WRFCCSM, and WRFMPI with respect to the E-OBS. In general, the WRFERA provides a small underestimation of the annual values (errors between -1 to 2°C) for most of the interior IP. Nonetheless, for some areas located in the northeast and in the south of the IP, the WRF simulation forced by ERA-Interim showed an overestimation of about 1°C.

Beyond details, the WRFCCSM showed results similar to those of the WRF-

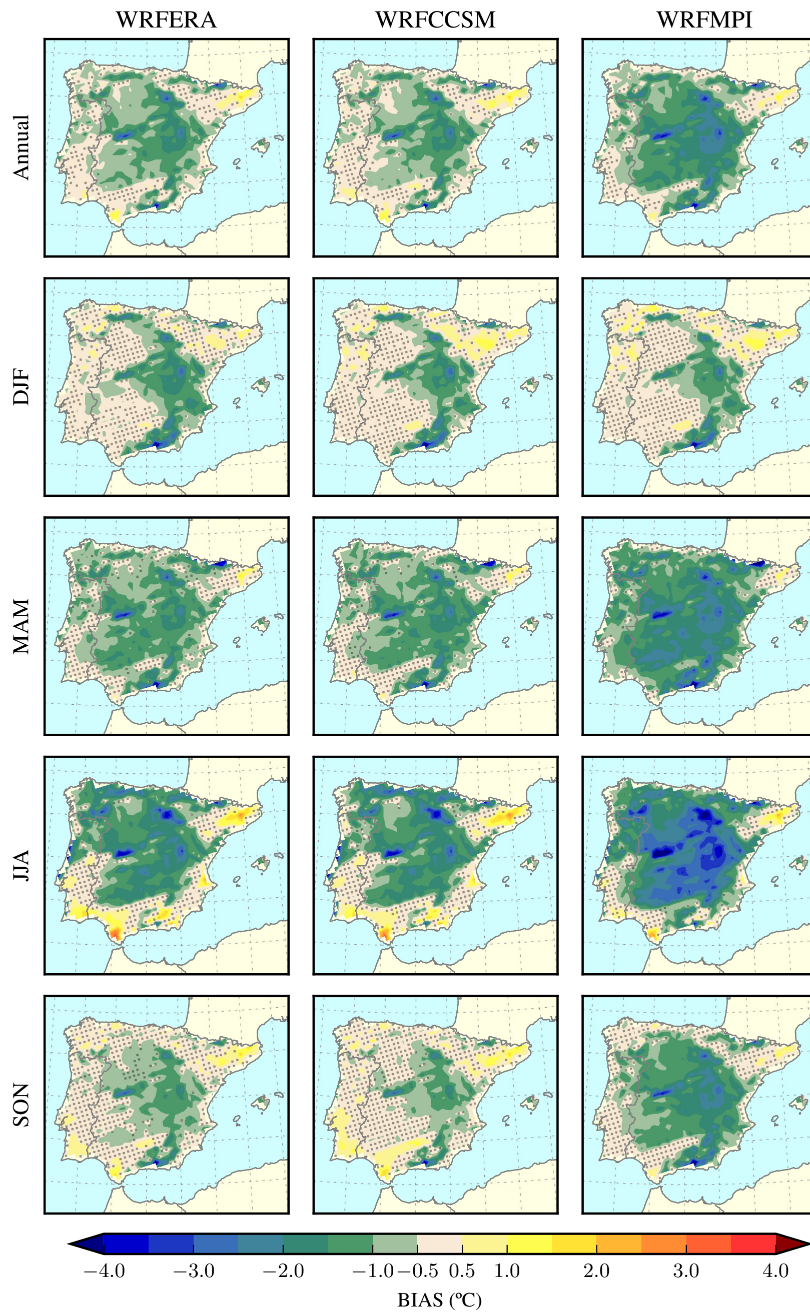

Figure 4.9: *Annual and seasonal T_{max} bias regarding E-OBS. Black dots indicate no significant differences between the mean of the distribution of T_{max} according to Student's t test at the 95% confidence level.*

ERA. The reproduction of the temperature climatology of T_{max} by the WRFMPI was worse than in the other simulations, presenting more significant negative biases. Here, the overestimations were limited to small areas in the northeast and in the south of the IP.

For seasonal differences, the best performance was shown in autumn and winter. Here, fewer significant biases occurred than in the other seasons, these being negative in general. In those seasons the greatest underestimations were depicted in certain areas in high-mountain regions such as Sierra de la Demanda (in the Iberian System), Sierra de Gredos (in the Central System), and Sierra Nevada (in the Baetic System), reaching negative values of around 2 to 3°C. However, the worst features were shown for spring and summer, where a widespread underestimation appeared throughout the IP (with negative values of c. 1 to 4°C), again with the highest biases in high mountains. On the contrary, certain areas were also depict overestimations, such as the southwest, the coast of Alicante, and the northeastern region in summer, with significant biases of some 1 to 3°C. With respect to the simulations driven by GCMs, the results again indicate that the WRFCCSM biases were quite similar to those of the WRFERA. In general, the WRFMPI performed similarly to the other ones, although showing slightly worse representations, with more significant underestimations in both intensity and surface area in spring, summer, and autumn. The similarity between simulations suggests that the major errors could associate with the regional model characterization, instead of the LBCs.

Seasonal pattern correlations showed remarkable results for all seasons and the three simulations (Table ***4.4***), suggesting that the model was able to capture the main spatial distribution of the T_{max}. The values were similar between the different simulations for all seasons (c. 0.941 to 0.973), with the lowest values in summer. This latter suggests that in summer the model was less accurate representing the spatial distributions of this extreme temperature. Also, it should be borne in mind that the results of the pattern correlation are not a measure of the model biases. For instance, as reflected in Figure ***4.9***, spring showed an overall bias throughout the IP, while its pattern correlation illustrates a result as reliable as that in autumn or winter.

Figure ***4.10*** depicts the annual and seasonal biases between the model and

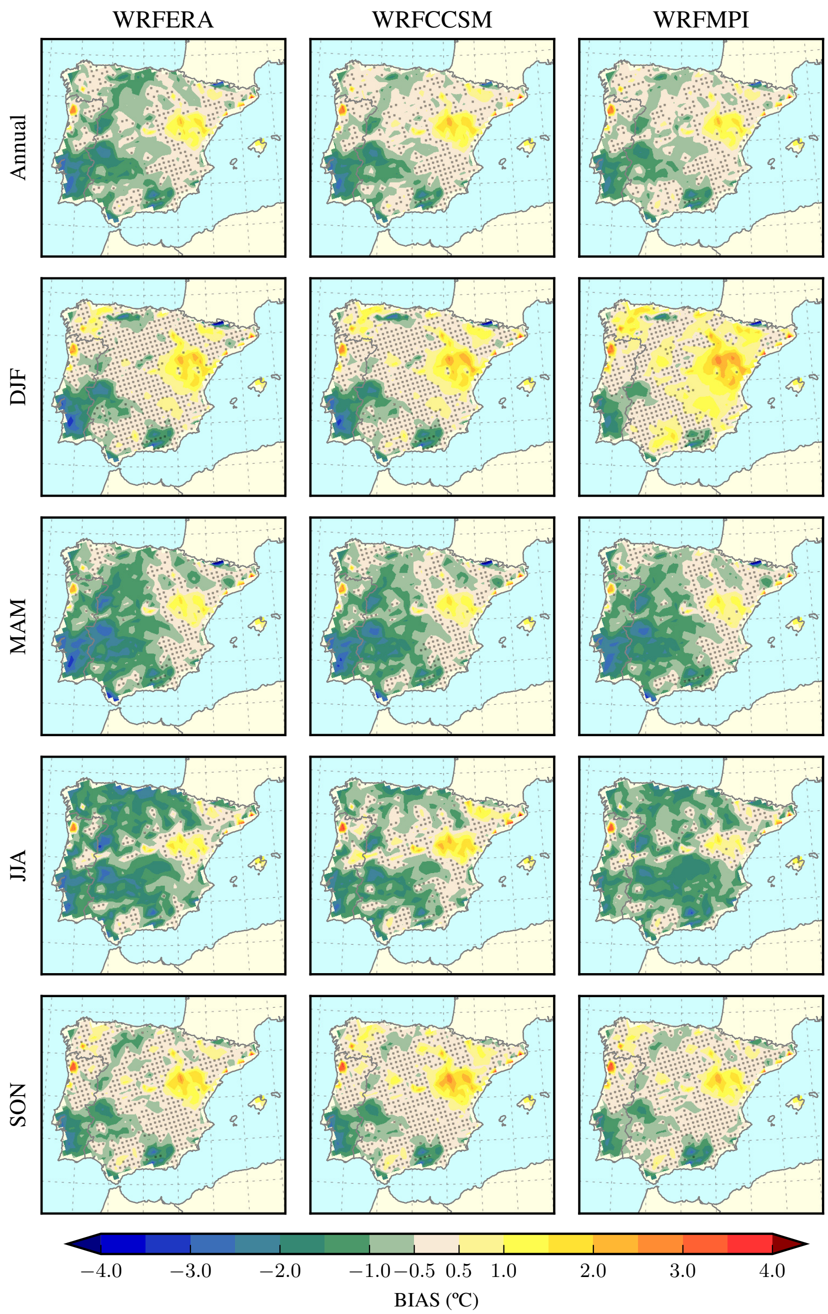

Figure 4.10: *The same as Figure **4.9** but for mean* T_{min}.

the corresponding observations in terms of T_{min}. Although the results show a close agreement between the WRF and observations, the errors found in terms of this variable were slightly higher than those for T_{max} in general. In terms of annual values, the WRFERA had a remarkable capability to simulate the T_{min}, although it showed both positive and negative biases between -3°C and 3°C. The largest area with negative biases was found mainly in the southern quarter of the IP, with differences of about -2.5°C with respect to observations. Conversely, with respect to the results from T_{max}, a major presence of positive differences appeared in relation to the observations, with the greatest positive biases being found in a limited area in northwestern Portugal. In comparison to the simulations performed using the GCMs as LBCs, the results showed a similar spatial distribution in the annual mean biases for both the WRFCCSM and the WRFMPI.

In reference to seasonal biases the three simulations performed well and again with similar ability, except for winter. In this latter season, the overestimation was larger in area and more intense for the WRFMPI. As for T_{max}, the best performance appeared in winter and particularly in autumn, with more non-significant biases for IP. Here, both positive and negative biases were found. Nonetheless, in spring and summer the model appeared to provide underestimations in general.

Despite the spatial agreement between observations and simulations, it bears noting that the seasonal pattern correlations in terms of T_{min} were generally lower than those for T_{max}. Such measures of spatial agreement reached values of some 0.913 to 0.947 (Table ***4.4***), and again the differences between simulations and seasons proved minor. However, the lowest values corresponded to winter and the greatest to autumn. Moreover, the WRFMPI appeared to slightly outperform the other ones in terms of spatial patterns.

To evaluate the capability of the WRF to represent the interannual variability, the standard deviation of annual and seasonal temperatures were also computed. Figures ***4.11*** and ***4.12*** show the normalized standard deviation in terms of T_{max} and T_{min}, respectively.

The annual normalized standard deviation analysis in terms of T_{max} (Figure ***4.11***) revealed that the model driven by the ERA-Interim generated a slight

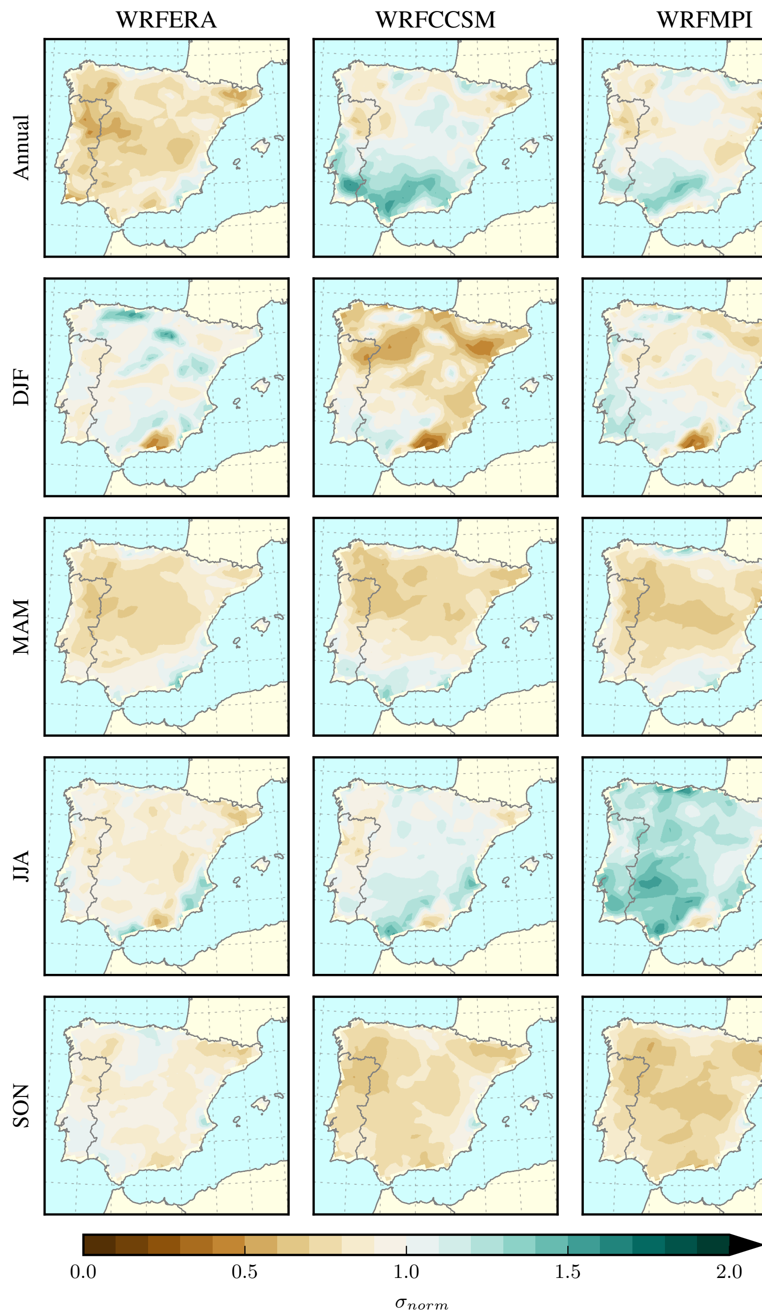

Figure 4.11: *Normalized standard deviation of T_{max} respect to E-OBS. In rows the annual and seasonal values. In columns results from the different WRF simulations (WRFERA, WRFCCSM and WRFMPI).*

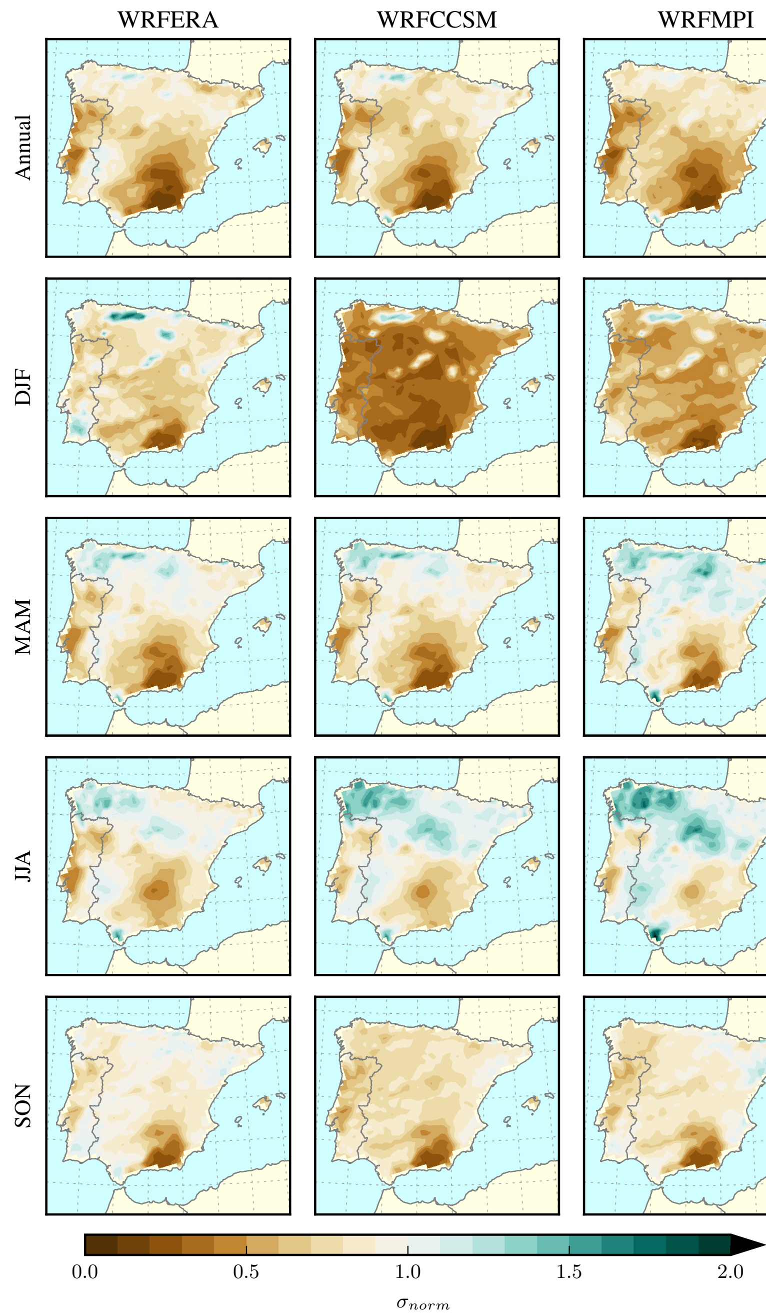

Figure 4.12: *The same as Figure **4.11** but for* T_{min}.

underestimation, extending throughout the IP. Only in the southeast did the WRFERA provide small overestimations. Regarding the simulations driven by GCMs, the results show different features with a generalized overestimation in the south for both the WRFCCSM and the WRFMPI. The results also reveal that the interannual variability was better represented by the WRFMPI, except in the Guadalquivir Valley.

Concerning the seasonal values, the results reveal that the WRFERA accurately simulated the interannual variability in summer and autumn, when the normalized standard deviations were generally close to 1. In spring, however, the model provided a generalized underestimation in terms of interannual variability, except for the southern to the southeastern coast, the Ebro Valley, the Balearic Islands, and the Cantabrian Coast. For winter, although the widespread spatial pattern was well represented, the WRFERA appeared to have faltered in simulating the interannual variability associated with the orography. Also, the results from simulations driven by GCMs reveal similar patterns with respect to the WRFERA in spring and autumn. However, winter was characterized by a markedly different spatial distribution, with a major presence of underestimations in the WRFCCSM simulation, and conversely an overall overestimation was displayed in summer by the WRFMPI.

The results of the normalized standard deviations of T_{min} (Figure ***4.12***) suggest that the three WRF simulations represented the interannual variability similarly, as shown by the annual and the most seasonal values. The general underestimation in the southeast was remarkable, and with less intensity over Portugal, for all the seasons and simulations. High overestimations were found in the northern half of the IP, mainly in summer and for the WRFMPI. The major discrepancies appeared in winter, when the WRFCCSM gave the greatest underestimations throughout the IP.

4.3.4. Daily Distribution of Temperatures: High-Order Statistics and Extreme Values

In terms of daily values, the PDFs of the T_{max} and T_{min} were also established. For this, bins of 1°C were used to perform the PSSs of both extreme temperatures. As for precipitation, a test of the significance of this skill score was made based on a Monte Carlo approach to determine the threshold value from which a PSS could be considered adequate. This value was the 5^{th} percentile of the 1000 replications made by using the Monte Carlo technique over the observations from E-OBS.

Figure ***4.13*** shows the PSS for daily T_{max} distribution from the three WRF simulations with respect to E-OBS observations. As can be seen, the WRF had a remarkable ability to simulate the T_{max} daily distribution with values of PSS roughly between 80 and 100%. The worst performance was related to the orography, as reflected by certain areas in the Pyrenees, Cantabrian Range, Central System, and especially near Sierra Nevada. Meanwhile, the WRF appeared to have greater difficulty to simulate the daily distribution of temperature in coastal regions such as the southeastern Spanish coast. The WRFCCSM results proved similar to those of the WRFERA, and again the WRFMPI appeared to perform worse than the others, although the differences were minor. For this variable, all grid points presented significant PSSs.

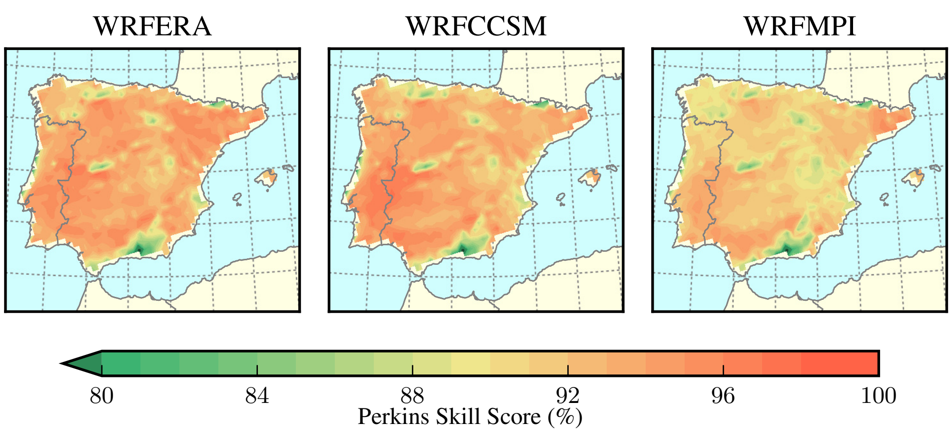

Figure 4.13: *Perkins Skill Score (%) values in terms of the daily T_{max} for the WRFERA, WRFCCSM, and WRFMPI simulations with respect to observations from E-OBS. Black dots indicate no significant PSS values.*

Regarding the ability to perform the daily PDFs of T_{min}, Figure ***4.14*** reveals that, although the result was still highly satisfactory, it was worse than the results for T_{max}, but in any case always with non-significant differences in relation to observations. Furthermore, for this variable, the influence of orography shown in T_{max} was not so obvious. As for T_{max}, all PSS values were significant for the three WRF simulations. Comparing simulations, we conclude that the performance of the WRFERA, WRFCCSM, and WRFMPI were similar, with only the ability of the WRFMPI to perform the daily PDF of T_{min} being slightly worse.

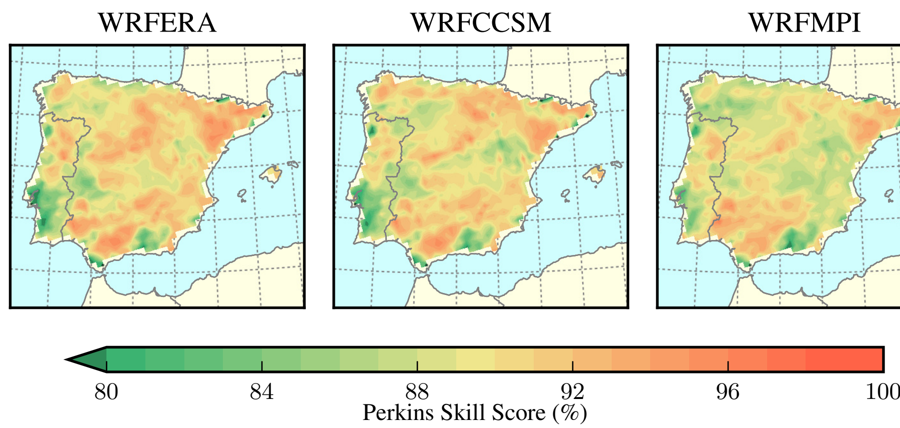

Figure 4.14: *The same as **4.13** but for daily T_{min} distributions.*

A set of extreme indices proposed by the ETCCDI was selected (Table ***4.5***) in order to examine the WRF ability to simulate extreme temperature events. Because the analyses of extreme values were strongly affected by systematic errors (Argüeso, 2011), to adequately characterize extremes, we firstly used a bias-correction approach over the daily time series of T_{max} and T_{min}. Actually, the bias found in both extreme temperature may have masked the persistence of anomalous temperatures and thus provided an inaccurate interpretation of the model's ability to detect extreme values. This correction consisted of the aggregation of the mean annual bias regarding the observations[6] for the daily time series of both, T_{max} and T_{min}.

On the one hand, the ability of the model to detect threshold indices was evaluated. Such indices were defined as those that measure of the number of days that exceeded a given threshold of temperature. For instance, the icing days (ID) was the number of days with T_{max} below 0°C. Moreover, an additional threshold, the hot days (HD) proposed by Argüeso (2011), computed as

[6]Such biases are shown in Figure **4.9** and Figure **4.10**.

the number of days with T_{max} > 35°C, was also evaluated. The HD was chosen because it appeared to be more accurate than the summer days (SU) to evaluate extreme summer conditions in a region such as the IP, and especially under climate change. On the other hand, indices based on the persistence of a given extreme event such as the warm-spell duration (WSDI) or the cold-spell duration (CSDI) were also computed. For these indices, the reference period selected was 1980-2014 rather than the 1961-1990 period defined as the base period by the ETCCDI. Finally, the daily temperature range (DTR) was also evaluated, this consisting of the daily difference between T_{max} and T_{min}. All the indices were computed from the E-OBS and from the three WRF bias-corrected simulations, using a yearly period, and then the mean annual value was determined. The results are shown in Figures ***4.15*** and ***4.16***.

Table 4.5: *ETCCDI extreme temperature indices selected.*

Index	Definition	Units	Type
DTR	Daily temperature range	°C	**Other**
ID	Icing days, i.e. T_{max} < 0°C	days/year	**II**
SU	Summer days, i.e. T_{max} > 25°C	days/year	**II**
HD	Hot days, i.e. T_{max} > 35°C	days/year	**II**
FD	Frost days, i.e. T_{min} < 0°C	days/year	**II**
TR	Tropical nights, i.e. T_{min} > 20°C	days/year	**II**
WSDI	Warm spell duration index: Count of days with at least 6 consecutive days with T_{max} > 90^{th} percentile of the corresponding calendar day in the base period	days/year	**III**
CSDI	Cold spell duration index: Count of days with at least 6 consecutive days with T_{min} < 10^{th} percentile of the corresponding calendar day in the base period	days/year	**III**

As can be seen through the observations, the DTR index presents a range of values of about 8 to 14°C (Figure ***4.15***). The daily temperature range is strongly affected by elevation and the distance of the sea, the highest values appearing fundamentally over the continental mountain ranges and the lowest over the coastal regions. The WRF provided an excellent result concerning this index for the three simulations, presenting a similar pattern between them.

The number of icing days (ID) was low throughout most of the IP, with mean values below 0.2 days/year except over the high-mountain regions where the highest values were found in the Pyrenees, exceeding 30 days/year. Analo-

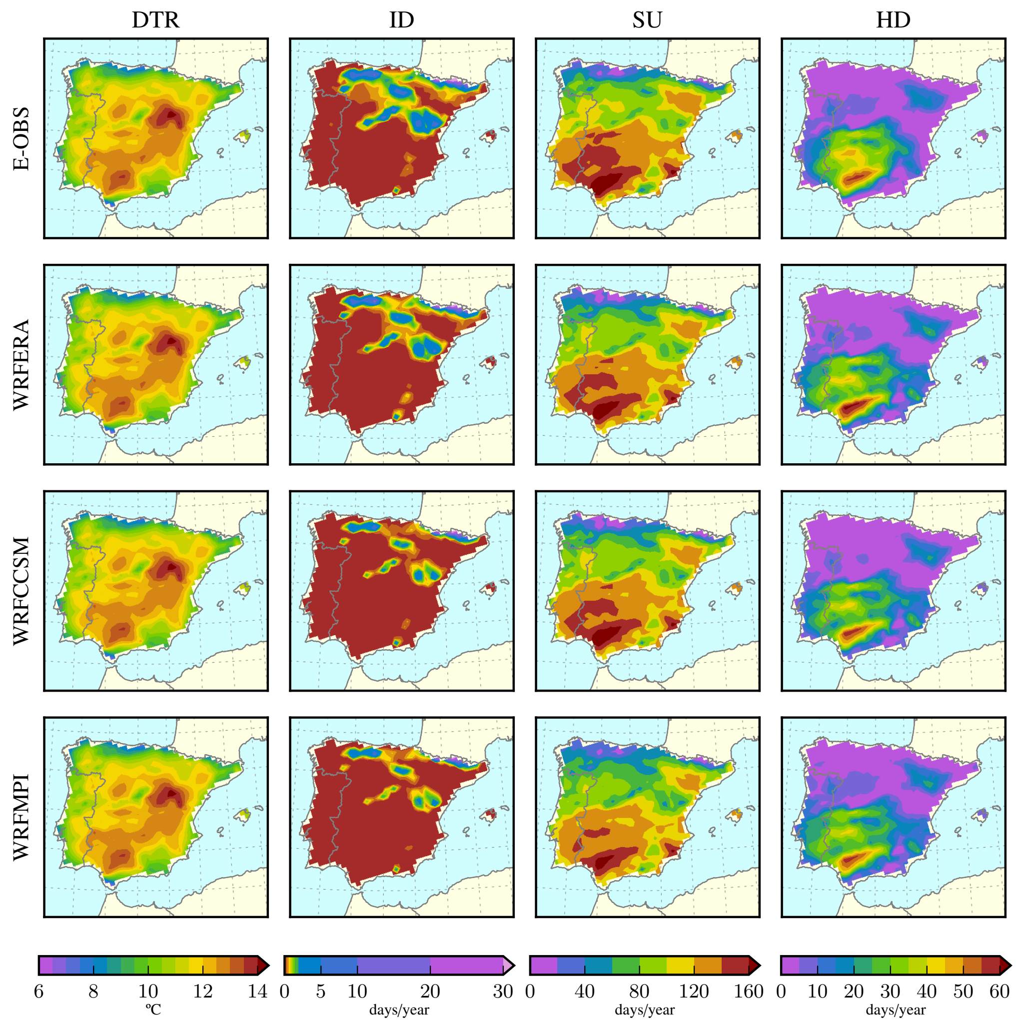

Figure 4.15: *Temperature extreme indices. In rows the observations (E-OBS) and the different WRF simulations (WRFERA, WRFCESM and WRFMPI). In columns the different ETCCDI indices (DTR, ID, SU and SU).*

gously, HD (hot days, Fig. ***4.15***) and TR (tropical nights, Fig. ***4.16*** present low values over a large extent of the IP (such values are about 5 days/year for both indices). The highest values of HD were found in the Guadalquivir Valley, while the largest TR values appeared in the south and particularly in coastal regions. Both reach values over 50 days/year.

The SU (summer days, Figure ***4.15***), however, presented a wider range of values with the lowest ones over the Cantabrian Coast and the Pyrenees (SU

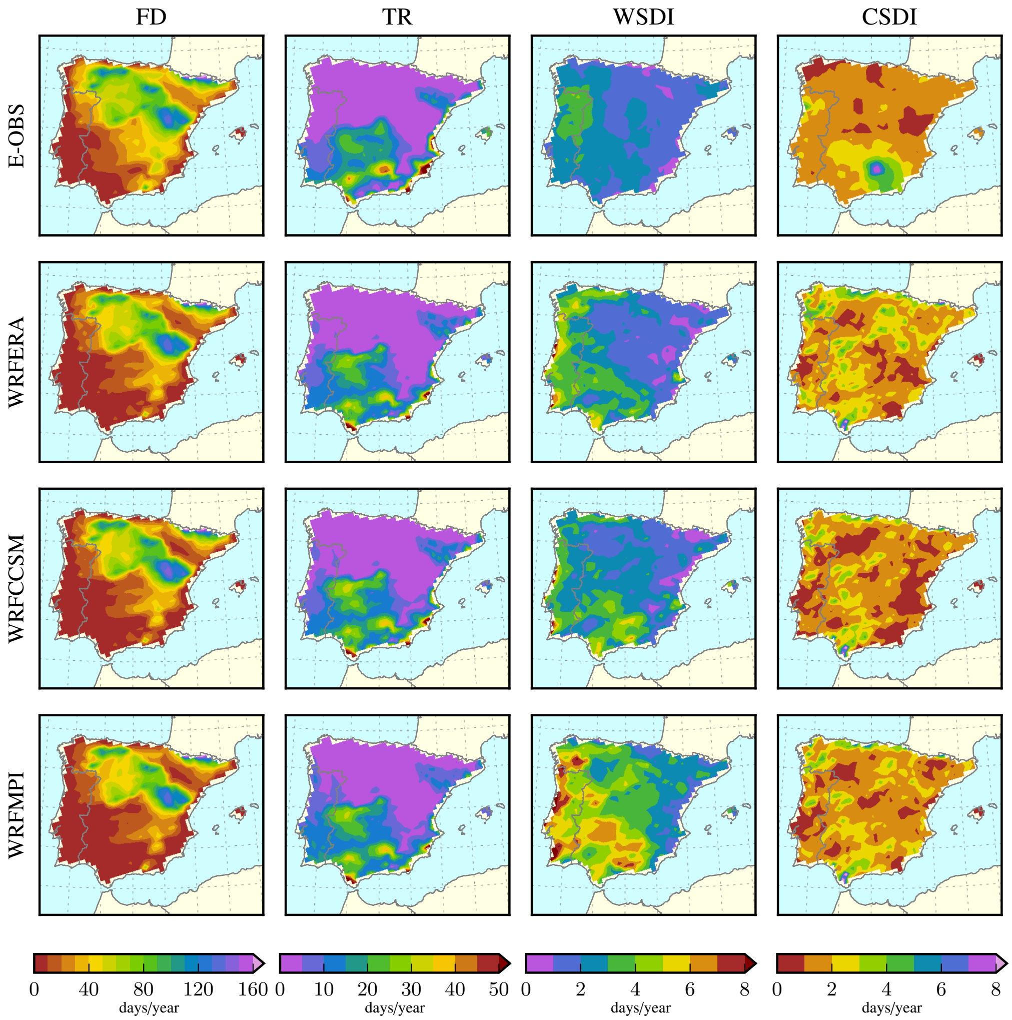

Figure 4.16: *The same as Figure **4.16** but for the ETCCDI indices FD, TR, WSDI and CSDI. The WSDI and CSDI were calculated using 1980-2014 as the base period.*

around 0-5 days/year) and the largest ones located in different areas of the southern IP (values above 160 days/year). The FD (frost days, Figure ***4.16***), also with a spatial variety of values, showed a maximum in the Pyrenees (> 160 days/year), the values being below 40 days/year in a large area of the IP. The results for all these extreme indices reveal excellent performance for the three WRF simulations.

Concerning the indices based on the persistence of a given extreme, the observational WSDI (Figure ***4.16***) presented a mean value of about 3 days/year, which covers a large area of the IP. Exceptions of this were central to northwestern Portugal, where the WSDI reached values of about 5 days/year and certain areas in the southeast and Cantabrian Coast, where the mean values were below 1 day/year. Conversely, the CSDI showed low values for most of the IP, with the highest mean scores over the northwest coast of Portugal, and especially in the south, with the highest values close to Sierra Nevada (Baetic System), which exceeded 8 days/year. The results of the WRF capacity to perform these kinds of extreme events, suggest that the model has certain shortcomings to capture the persistence of extreme events, especially in term of T_{min}. Thus, neither simulation reproduced the relative high CSDI in the southeastern IP. The WRFMPI presented a general overestimation of WSDI, while the WRFCCSM showed a marked underestimation of CSDI.

4.4. Land-Surface Variables

4.4.1. The Influence of the Land-Surface Processes in the Simulation of Climate Characteristics over the IP

Land surface has a strong influence on different processes of the climate system, inducing multiple feedbacks related to the land-atmosphere exchange of heat and water. On the one hand, although the relationship between soil forcing and precipitation remains unclear, an increase in the surface evapotranspiration could generate a subsequent surge in rainfall occurrences through near-surface transference of moisture, as pointed out by such authors such as Koster and Suarez (2004). On the other hand, the soil moisture content could have an effect in the variability of the temperature (Seneviratne et al., 2010). In the WRF model, the LSM was the module that simulated the soil forcing, and thus the coupling with the atmospheric processes occurred via the surface-energy balance, the surface-layer stability and the water balance (Greve et al., 2013). In this way, the LSM strongly influenced climate simulations.

Most of the IP can be considered a transitional zone concerning its climate/soil moisture regime (Jerez et al., 2012). That is, the soil-moisture has strong control over the surface evapotranspiration variability, and thus, over the net flux partition into sensible and latent heat fluxes (Jerez et al., 2010). Here, the effects of the land-surface processes over the temperature are stronger in summer. In fact, in this season the synoptic forcing is weaker, and therefore the local effect is more relevant. In this way, the soil-atmosphere feedbacks are stronger, leading to the constraint of the surface evapotranspiration, and consequently the temperature increase. Therefore, the suitable characterization by the WRF model of soil forcing variables such as the soil-moisture content and the surface evapotranspiration is crucial in order to accurately evaluate hydrological variables and their impacts. This latter is especially important in a climate-change context, especially in this region, where an intensification of soil forcing effects is expected, which could result in heavy impact on extreme climate events through the increase in both intensity and persistence of heat waves (Jaeger and Seneviratne, 2011) and droughts (Dai, 2013) under drier surface conditions.

4.4.2. Long-term Mean Surface Evapotranspiration: From Annual to Seasonal Values

Following the same scheme used with the primary climate variables, firstly, we computed the annual accumulated amounts of surface evapotranspiration from GLEAM for each grid point. In addition, the same procedure was also followed over the SFCEVP outputs from the three WRF simulations, in order to directly compare them.

Figure ***4.17*** depicts the annual climatology of the total amount of SFCEVP from GLEAM datasets as well as for the three WRF simulations. As for precipitation, the IP presented a marked northwest to southeast gradient, with values ranging between 800 and 100 mm/year. As a result, we conclude that precipitation is the main factor affecting the annual evapotranspiration, since the greater the precipitation, the greater the surface evapotranspiration, and vice versa. Such a spatial distribution is acceptably well resolved by the reanalysis-driven simulation but with a slight overestimation, especially over the Northern Plateau.

Conversely, a clear exception was found in the areas categorized as urban land (e.g. Madrid or Barcelona). Here, the WRF performed accumulated values for surface evapotranspiration of around 0 to 50 mm/year, while GLEAM showed no differences regarding the neighboring grid points. Indeed, as these

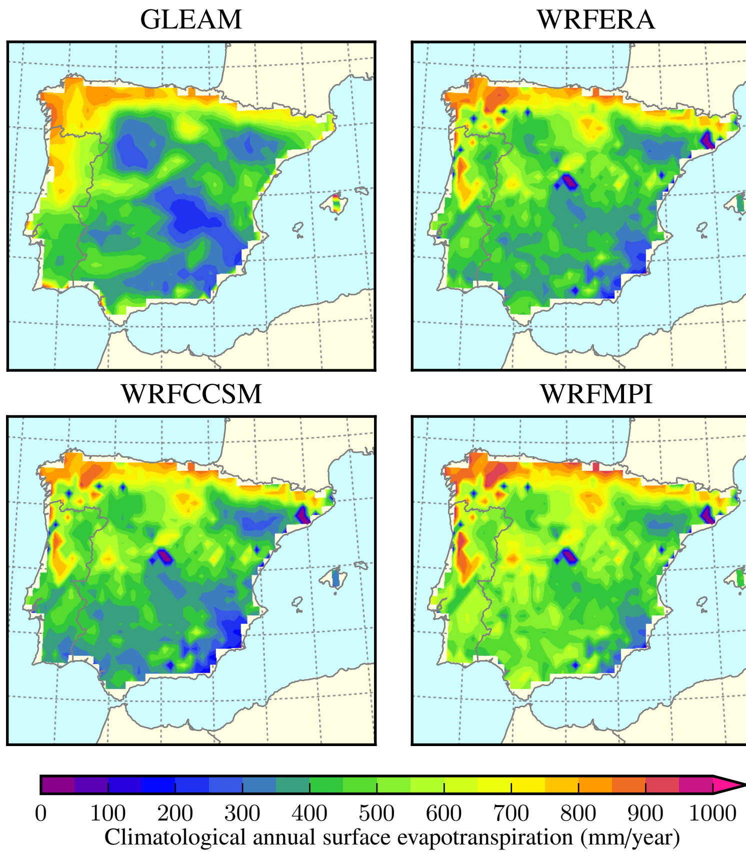

Figure 4.17: *Annual climate mean surface evapotranspiration (mm/year) from GLEAM dataset and from WRF outputs, driven by ERA (WRFERA), CCSM4 (WRF-CCSM), and MPI-ESM-LR (WRFMPI).*

results suggest, the simulated surface evapotranspiration was strongly affected by the land-use category, which was even clearer in the WRF outputs from the native resolution (results not shown). This feature was evidenced in González-Rojí et al. (2018), who pointed out that WRF does not accurately represent the SFCEVP in urban areas due to the mismatch between the real land use and the simulated one, and therefore the conclusion from this analysis must be drawn bearing this issue in mind. This feature is associated with the soil-moisture availability, which is a land-use parameter established via the pre-processing package of WRF and adapted to the Noah LSM to simulate land-surface variables. This parameter is the major factor controlling the amount of surface transpiration. With regards to the outputs from the GCM-nested-WRF, the results reveal a characterization by WRFCCSM similar to that of the WRFERA, and the WRMPI generally gives a marked overestimation.

As for previous variables, the relative biases with respect to observations were also calculated in order to perform a further analysis regarding the WRF capability to detect mean values. For that purpose, the annual and seasonal values were assessed (Figure ***4.18***). The significance of the differences between the WRF and GLEAM were also evaluated according to Student's t test[7]. The pattern correlation between observed and simulated mean long-term fields was also calculated in order to quantify the spatial agreement between the WRF and GLEAM datasets (Table ***4.6***).

Table 4.6: *Annual and seasonal pattern correlations (r) from WRF outputs driven by ERA (WRFERA), CCSM4 (WRFCCSM), and MPI-ESM-LR (WRFMPI) against observations from GLEAM.*

	WRFERA	**WRFCCSM**	**WRFMPI**
Annual	0.631	0.612	0.560
DJF	0.628	0.603	0.608
MAM	0.422	0.434	0.350
JJA	0.633	0.616	0.560
SON	0.699	0.657	0.666

The WRFERA simulation represented the mean annual values with admissible accuracy, the number of points with no significant differences respect to GLEAM being quite large. However, the model appeared to slightly overestimate the SFCEVP in the Interior Plateaus, reaching biases of over 100%. Also, some overestimations occurred in small regions associated in most cases with the aforesaid effects over urban grid points. Concerning the biases in the simulations driven by GCMs, the results show that WRFCCSM presented a pattern similar to that of the WRFERA, while WRFMPI appeared to have greater shortcomings, i.e. registering more widespread the overestimation in this case.

The values of the pattern correlations revealed that although the WRF displayed these shortcomings to represent the spatial distribution of the surface evapotranspiration (values of approx. 0.560 to 0.631), these are still acceptable.

[7]The significance was also evaluated using the Mann-Whitney-Wilcoxon U test, with the same results.

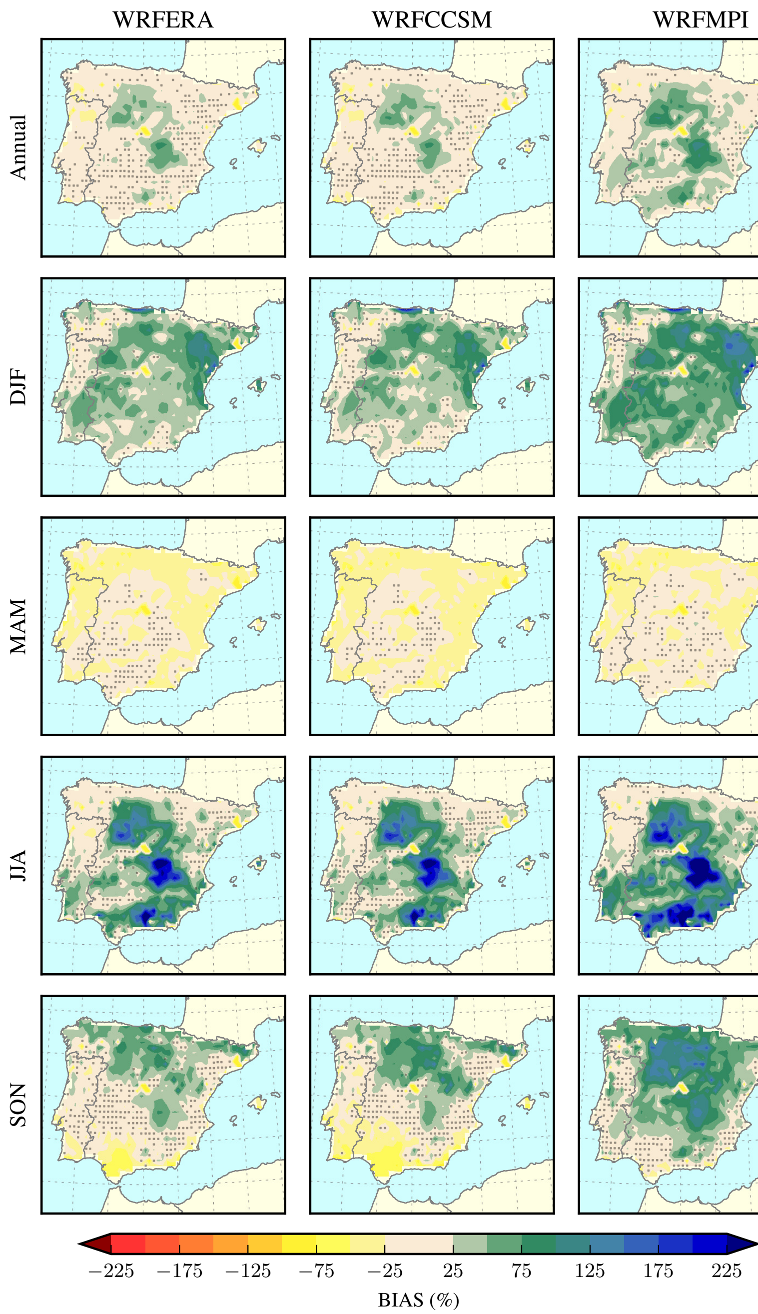

Figure 4.18: *Annual and seasonal relative bias with respect to GLEAM. Black dots indicate no significant differences between the mean of the distribution of accumulated SFCEVP according to Student's t test at a 95% confidence level.*

Moreover, it is important to bear in mind that GLEAM displayed no differences for the urban regions, and this could affect the results of correlation between the patterns.

The seasonal results from WRFERA suggest an overall overestimation in winter and summer. In this latter, such overestimation was especially pronounced, reaching values above 225% in the Interior Plateaus and in certain areas of the southern IP (Figure ***4.18***). In winter the coupling between soil moisture and temperature was weaker, the precipitation being associated mainly with large-scale forcing. In this way, the overestimation of the precipitation values could affect the soil-water availability, resulting in an overestimation of the surface evapotranspiration. Conversely, in summer a strong coupling was found between soil moisture and temperature, the land-surface processes being more important. In this context, greater soil-water availability provided by the model could have led to an overestimation in the surface evapotranspiration, and thus to an underestimation of temperature, this being consistent with the temperature values. In spring, the WRFERA simulation, however, revealed an acceptable performance with respect to the observations in general, the greatest underestimations being less than 100%, these being found mainly around the coastal areas. For autumn the representation remained admissible, the model giving overestimations in the north and underestimations in the south. The results from the WRFCCSM and WRFMPI display a similar characterization in terms of long-term mean fields, the overestimations given by the WRFMPI being larger. In any case, the best WRF spatial agreement was found in autumn and the worst in summer. Intermediate results pertain to winter and spring. Regarding the comparison between the simulations driven by GCMs, the WRFMPI appeared to fail more in reference to the spatial distribution.

As a measure of interannual variability (Figure ***4.19***), the standard deviation of annual and seasonal amount of SFCEVP was also computed, and thus the corresponding normalized values were taken as the ratio between simulated and observed ones. As shown, the WRF model offers acceptable performance in terms of annual normalized standard deviation (values between 0.5 and 2). The WRFERA and WRFCCSM showed quite similar results, the presence of both underestimation and overestimation also being similar. Nevertheless, the

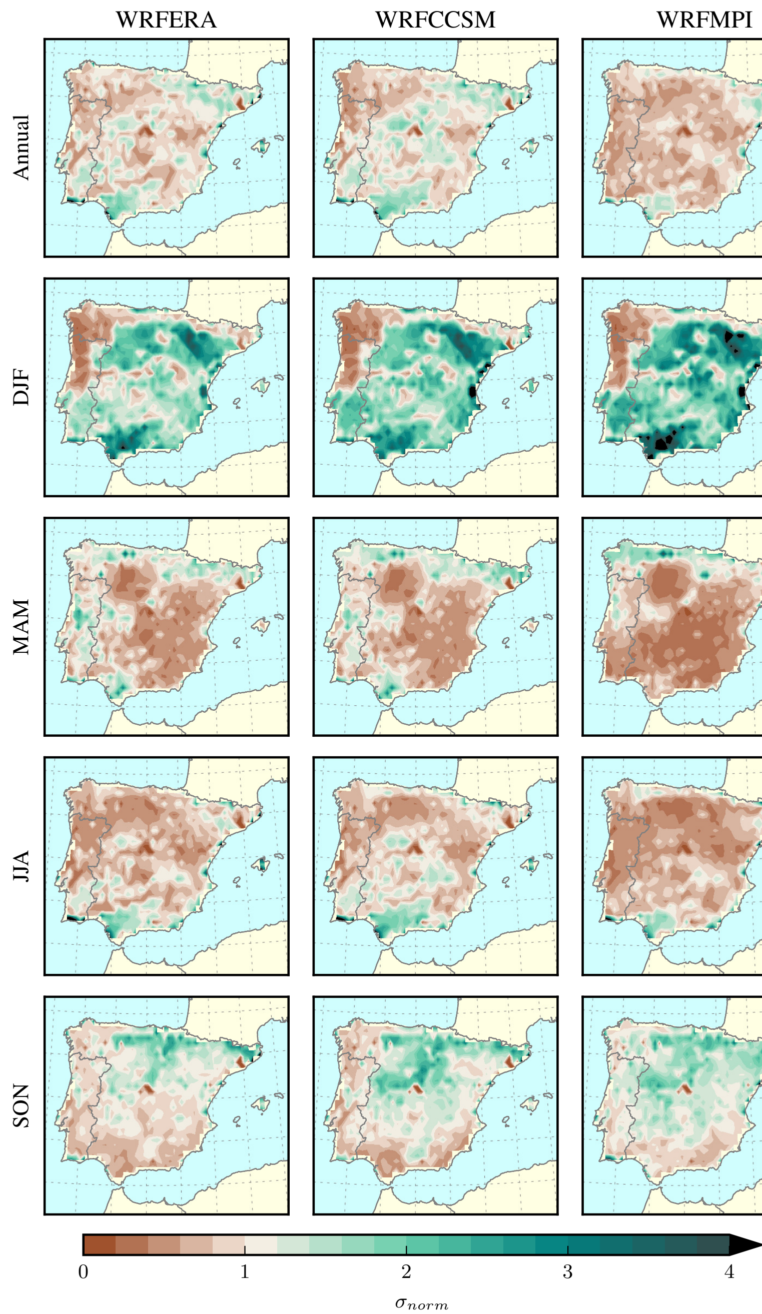

Figure 4.19: *Normalized standard deviation of the simulated SFCEVP from WRF respect to GLEAM. In rows the annual and seasonal values. In columns, results from the different WRF simulations (WRFERA, WRFCCSM, and WRFMPI).*

WRFMPI showed a more widespread underestimation. Concerning the seasonal normalized standard deviation, the results offered reasonably good agreement between WRF and observations from GLEAM, except for winter, when a highlighted overestimation appeared in most of the IP. All WRF simulations showed similar results in all seasons, but larger overestimations appeared for WRFMPI in winter, suggesting that this latter was less accurate simulating the interannual variability of the winter amount of surface evapotranspiration.

4.4.3. Long-term Mean Surface Soil-Moisture Content: from Annual to Seasonal Values

The model's ability to perform the surface-soil moisture content was analyzed by direct grid comparison. Such comparison was adequate because both the WRF outputs and GLEAM database, consider the surface-soil moisture to correspond to the soil layer spanning the upper 10 cm of the soil. Therefore, annual and seasonal means were computed expressed in volumetric surface-soil moisture[8] content from observations and from the three WRF simulations over the entire 34-year period.

Figure ***4.20*** depicts the annual climatology in terms of smois. The GLEAM annual climatology portrays the aforesaid northwest to southeast spatial pattern presented for the annual climatology of both precipitation and surface evapotranspiration. For this new variable, however, the WRFERA appeared to present greater shortcomings since its spatial distribution proved more homogeneous throughout the IP, with a generalized underestimation. Similar results were found for the WRFCCSM and WRFMPI simulations, although, the underestimation was slightly smaller for WRFMPI. Also, all WRF simulations as well as the observations showed minimum values in certain areas located close to the Northern Plateau. Such minimum values of soil-moisture content were associated with the soil texture presented in these areas (sands), as can be seen in Figure ***4.24***. This soil type is characterized by a low capacity to retain the water in its pores, and thus has high infiltration rates. However, WRF represented lower values in this soil texture, possibly for being associated with higher infiltration rates in WRF-Noah's. Indeed, the soil-moisture results

[8]The volumetric soil moisture is a relative measure that expresses the cubic meters of water in each cubic meter of soil.

were closely related to the soil texture, as clearly reflected in the native WRF resolution (results not shown).

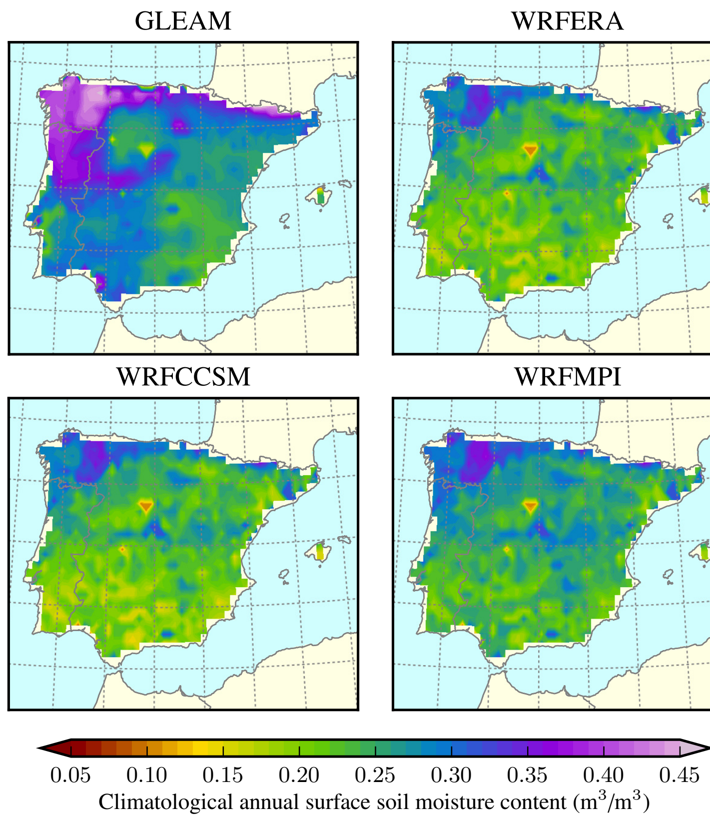

Figure 4.20: *Annual climatology of smois (m^3/m^3) from observational datasets (GLEAM) and from the WRF outputs, driven by ERA (WRFERA), CCSM4 (WRFCCSM), and MPI-ESM-LR (WRFMPI).*

Table ***4.7*** depicts the annual and seasonal spatial correlations of the smois from WRF smois with respect to GLEAM. Although the pattern correlations are weaker than for other variables analyzed (values between 0.464 and 0.614), the agreement between all WRF simulations and GLEAM are still significant. However, for this variable, no simulation outperformed the others, as reflected by the values for the different seasons. Concerning the seasonal comparison, the best agreements with respect to GLEAM appeared in summer and the worst in autumn.

Figure ***4.21*** indicates that for annual relative biases, WRF still appears

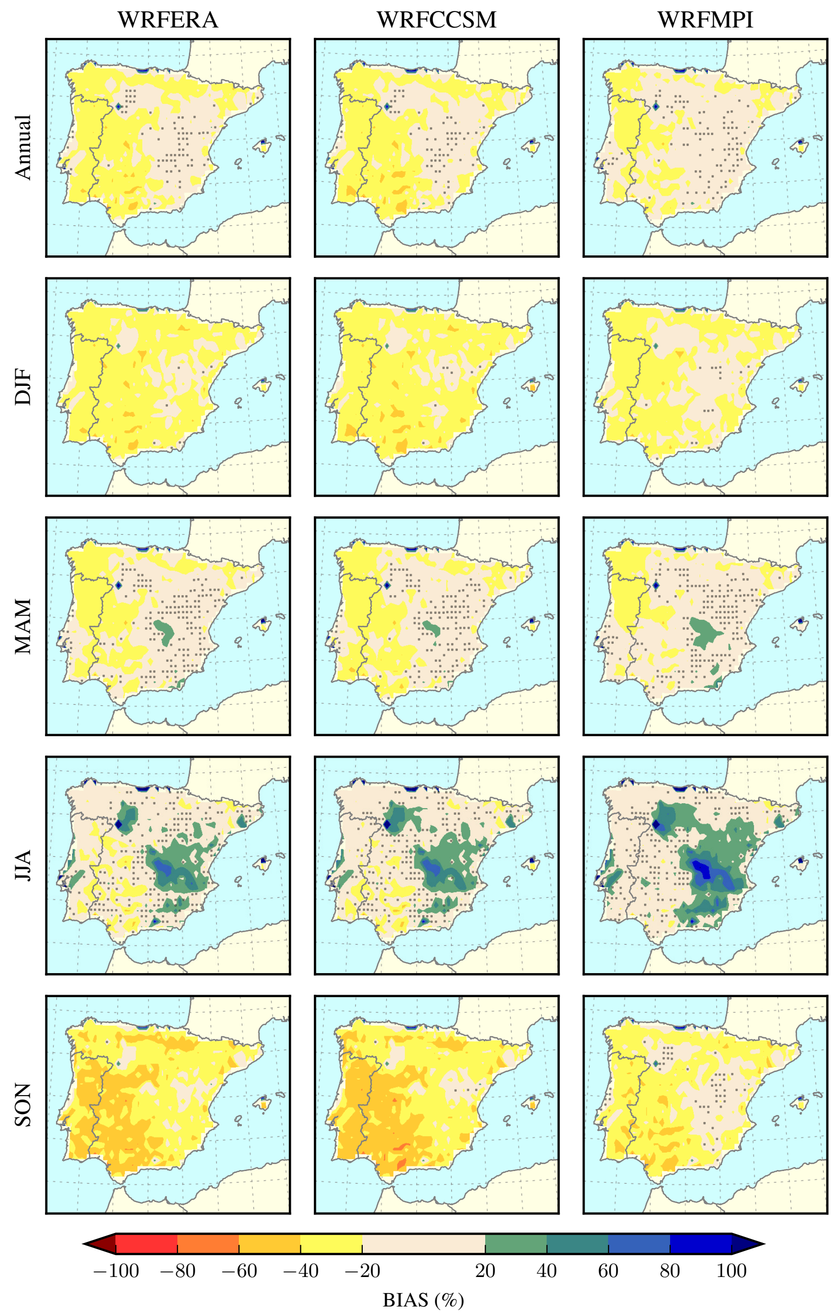

Figure 4.21: *Annual and seasonal relative bias of smois with respect to GLEAM. Black dots indicate no significant differences between the mean distribution of accumulated smois according to Student's t test at 95% confidence level.*

Table 4.7: *Annual and seasonal pattern correlations (r) from WRF outputs driven by ERA (WRFERA), CCSM4 (WRFCCSM), and MPI-ESM-LR (WRFMPI) against observations from GLEAM.*

	WRFERA	**WRFCCSM**	**WRFMPI**
Annual	0.550	0.556	0.553
DJF	0.524	0.526	0.533
MAM	0.567	0.591	0.550
JJA	0.603	0.614	0.593
SON	0.480	0.464	0.505

to be able to reasonably represent the annual mean values of smois in general for all WRF simulations. The relative biases were fundamentally negative, except for small areas located in the Cantabrian Coast, Balearic Islands, and in the Northern Plateau. Such negative biases extended over the north and throughout the west of the IP. The range of these errors was some 20 to 60%, although most were between 20% and 40%. Student's t test[9] revealed, however, that there are a quite large number of grid points with significant differences between the smois annual climatology from GLEAM and WRFERA.The two GCMs-driven WRF simulations still acceptably represented the smois, with the best representations, in terms of mean, being those provided by WRFMPI.

Regarding seasonal smois mean values, the relative biases revealed that all WRF simulations offered good agreement with mean values from observations, showing similar spatial distributions. The best WRF representation was for spring, the next best being for summer. This latter revealed an important extension with values similar in mean according to Student's t test, but also presented a overestimation, fundamentally in the Interior Plateaus, which reached some 60 to 80%, or even more for WRFMPI. It is important to note that in summer, the water limitation led a strong soil moisture-evapotranspiration coupling, so that overestimations of the soil moisture will provide the subsequent overestimations of the surface evapotranspiration. Furthermore, this positive feedback also could lead a diminution of the temperature. These results thus appear to explain the WRF performance in summer in terms of evapotranspi-

[9]As for surface evapotranspiration, the significance is also evaluated according to the Mann-Whitney-Wilcoxon U test at the 95% confidence level and that showed the same results.

ration and also temperature.

Moreover, the interannual variability was also analyzed through the normalized standard deviation of the smois, as shown in Figure ***4.22***. The results reveal similar performance for the three WRF simulations, the underestimation persisting, except for autumn. Nonetheless, results over winter and autumn WRF were underestimated, with a slightly better agreement respect to GLEAM for WRFMPI.

The results for annual values reveal a broadly satisfactory performance in terms of interannual variability. The best results were provided by WRFCCSM with values of close to 1. Nevertheless, the WRFMPI simulation showed less smois interannual variability with respect to GLEAM. For seasonal values, all WRF simulations performed more similar, showing marked overestimations with respect to GLEAM over the Pyrenees and Cantabrian region in winter and in nearly the entire southern half of the IP, across the Mediterranean Coast, and over Northern Plateau in summer. The results also display an underestimation associated with urban areas, which was not so obvious for mean values. This latter reflected the influence of the land use over the surface-soil moisture. Actually, smois is strongly influenced by the heterogeneity of topography, soil properties, and land-cover characteristics (Lin and Cheng, 2016).

4.4.4. Total Soil Moisture Content

The analysis of the surface soil moisture demonstrated that the model was able to provide a reasonable representation of the surface-water content. However, it is important to bear in mind that such conclusions are true only for the upper 10 cm of the soil. This means that such results provide only a partial view of the model's ability to represent the soil moisture content. Thus, an additional comparison between the total soil moisture[10] from the reanalysis-driven WRF simulations, in mm, and the GLEAM root-zone volumetric soil moisture was also performed by analyzing the temporal correlation patterns. In this way, we gain information concerning the WRF performance in terms of the interannual variation with respect the GLEAM database. The analysis was performed only

[10]Total soil moisture is often referred to as the absolute soil moisture expressed as the mm of water in the total soil column (mrso).

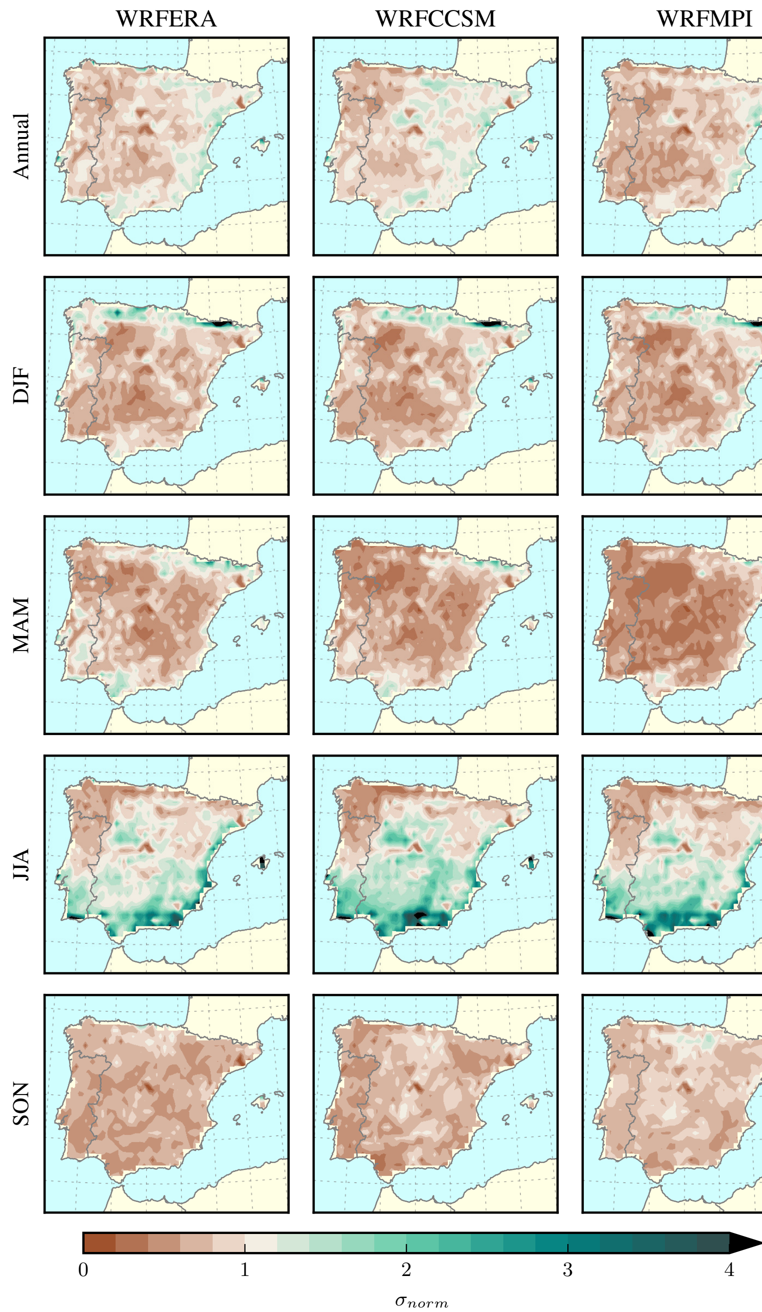

Figure 4.22: *Normalized standard deviation of smois respect to GLEAM. In rows the annual and seasonal values. In columns results from the different WRF simulations (WRFERA, WRFCCSM and WRFMPI).*

for the WRFERA simulation, because it was driven by a meteorological reanalysis and hence it represents the current natural variability, while WRFCCSM and WRFMPI were driven by GCMs, which generated their own natural variability.

Figure ***4.23*** shows the temporal correlation of the mean annual and seasonal values of the soil water between the WRFERA and GLEAM, computed for the entire 34-year period (1980-2014), for each grip point. Such correlations were considered significant above the 5% significance level.

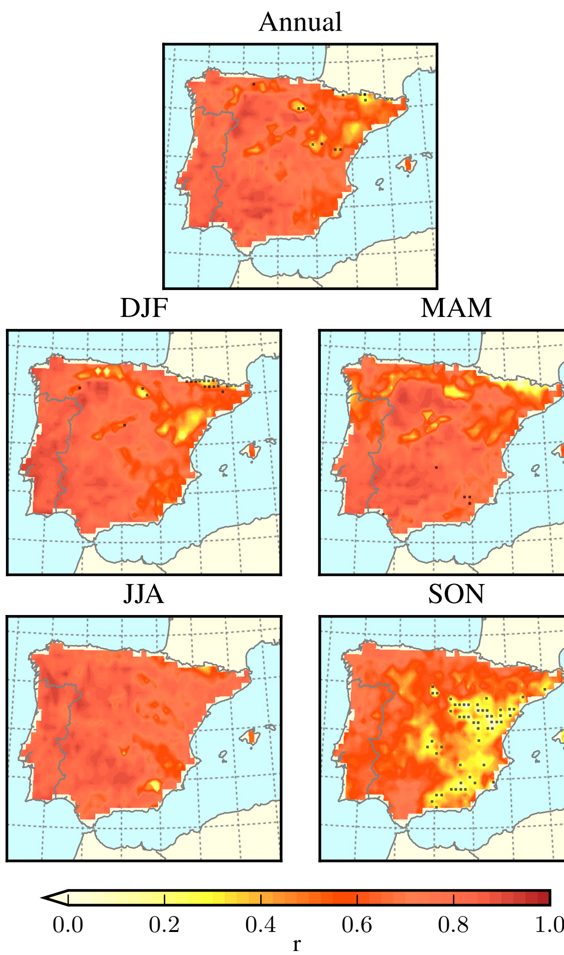

Figure 4.23: *Annual and seasonal temporal correlation of GLEAM volumetric root-zone soil moisture and the mrso from the WRF outputs driven by ERA-Interim (WRFERA). Black dots indicate no significant correlations at 95% confidence level.*

Looking at the annual values, high temporal correlations were found between WRFERA and GLEAM data in a large part of the IP (r values above 0.7). The lowest values are associated with the high altitude regions and over the northeastern IP. Only for certain points over the Pyrenees, Iberian System and Cantabrian Range the correlations were non-significant. Similarly, in winter, the results also showed high correlations over the western IP, reaching values over 0.7. However, correlations were weaker over certain high-mountain regions (e.g. the Cantabrian Range, Iberian System, and Pyrenees) and, in general, over the northeastern IP, with uncorrelated values or even negative correlations appearing here. For spring, good agreement was also found between the WRFERA and GLEAM. The worst correlations appeared in the northern IP associated with orography. For summer, the correlation was generally higher than in other seasons, in agreement with the results found in Knist et al. (2017). Conversely, the autumn results suggest that the WRFERA and GLEAM differed over time in a great region in the eastern IP. Note that the presence of low correlation values between them could be for different reasons. On the one hand, this could be related to the different parameters used in each model to characterize soil and vegetation (land use or soil parameters such as field capacity or porosity). On the other hand, the differences between WRF and GLEAM to generate the internal variability of land-surface variables could be another factor responsible. This latter could suggest shortcomings in representing the mrso from WRF outputs, but also from the GLEAM data.

Finally, the comparison of the annual monthly mean cycles for the four soil layers provided by NOAH LSM, and those from GLEAM were also computed. This analysis was carried out using the spatial averaged values for each soil type presented in the IP, using for this, the FAO 16-category soil types classification, which is applied in Noah's WRF use to simulate the soil moisture (Figure ***4.24***). Indeed, the exchange of moisture and heat between the land and the atmosphere is strongly affected by the soil texture, through related hydraulic parameters such as field capacity, wilting point, porosity, saturated matric potential , and thermal diffusivity. The maximum amount of soil water that such soil can contain is associated with porosity, so that for comparative purposes, the annual monthly cycles of soil water in each soil were expressed in m^3/m^3. In order to compare the WRF simulations with observations, the

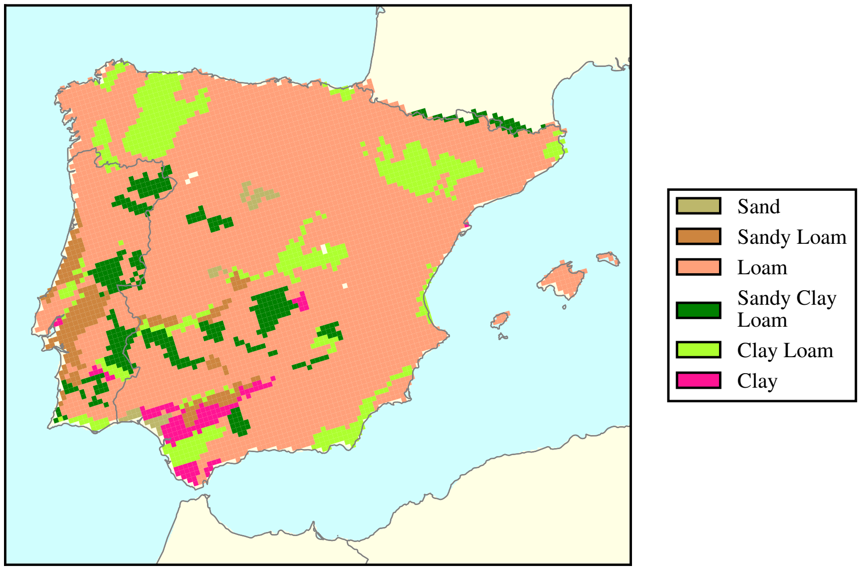

Figure 4.24: *Soil textures based on FAO 16-category soil types used by the WRF-Noah to calculate soil moisture content over the IP.*

analysis were performed using the same classification soil from WRF, and thus the WRF soil categories were firstly re-gridded onto the GLEAM grid through a nearest-neighbor approach.

Figure ***4.25*** depicts the mean annual cycles for each soil category and for each layer (WRFERA in green; WRFCCSM, in red; WRFMPI, in yellow). For GLEAM, the data were represented in black, for the two layers (surface and root zone). The main soil category present in the IP corresponds to loam, which covers the 75.37% of the total surface of the IP, followed by clay loam (11.37%), sandy clay loam (6.57%), sandy loam (3.84%), clay (2.08%), and sand (0.77%). In general, monthly annual cycles showed a similar soil-moisture evolution throughout the year for all the different soils. That is, the annual maximum values for all layers of the soil were reached in winter or at the beginning of spring, this being more evident for the 3 upper layers as well as for GLEAM data. The minimum values were reached firstly in layer 1 from WRF and in the surface-soil moisture from GLEAM at the end of summer. Layer 2, 3, and 4 from WRF as well as the root-zone from GLEAM reached this value with a lag of several months. Conversely, the deepest layer from WRF consistently had the highest amount of water, its time course being more stable throughout the year.

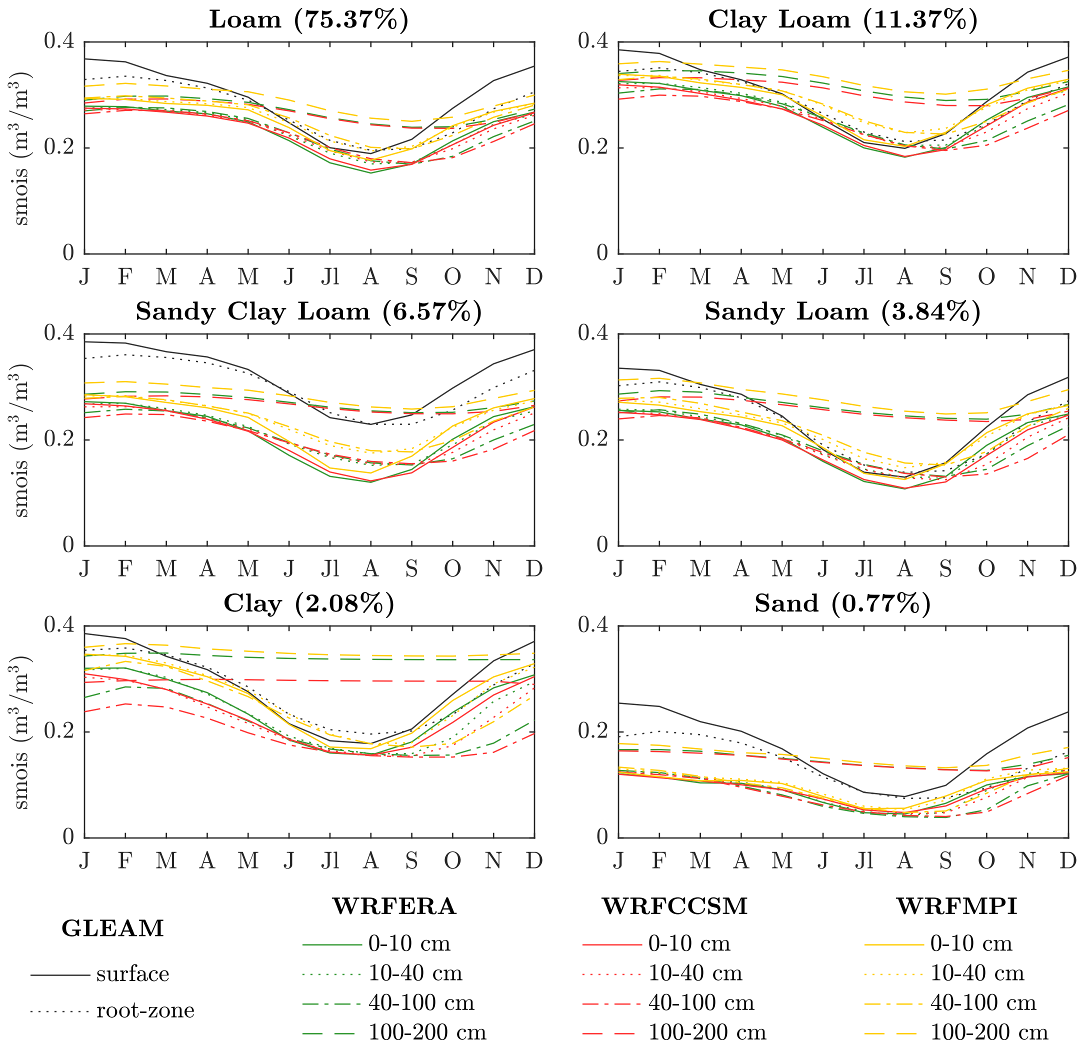

Figure 4.25: *Annual mean cycles of the volumetric soil moisture (m^3/m^3) for the soil categories presented in the IP calculated for WRFERA (green), WRFCCSM (red) and WRFMPI (yellow), at the different WRF layers (0-10, 10-40, 40-100 and 100-200 cm) and for surface-soil moisture and root-zone soil moisture from GLEAM (black). The percentage of coverage is shown in brackets for each soil category.*

Concerning the comparison between the WRF simulations and GLEAM data, the results showed larger differences for sandy clay loam and sand where

GLEAM represents a similar temporal trend along the year but the soil-water content is higher in general. Concerning differences between the simulations, the WRFERA and WRFCCSM usually showed similar soil-water contents, except for clay soils, for which the WRFCCSM invariably provided lower values. Conversely, the WRFMPI in most cases depicted higher values than did the others. These results reveal the importance of accurately simulating land-surface variables, this probably affecting the model's ability to represent the temperature and precipitation (results shown above).

The importance of the soil categories is reflected by the differences found between the annual monthly cycles for the different soils. For instance, soils with finer particles (clay, clay loam, loam, sandy clay loam, sandy loam, and sand [from the finest to the coarsest texture]) drain more slowly from the upper layers to the deepest. Thus, differences in the timing to reach minimum values of the two upper layers and the others were greater. Such soils also have higher water content. Otherwise, the hydraulic conductivity and the field capacity also influence the soil-moisture content of the soil. For example, sandy loam has a higher hydraulic conductivity and a lower field capacity than clay loam, and thus the result was a lower soil moisture content in each layer, and therefore a greater difference between layers. Such differences are especially marked under dry soil/atmosphere conditions.

4.5. Discussion and Conclusions from WRF Evaluation

Throughout this chapter the WRF capacity to accurately represent the climatology over the IP was assessed. In general, WRF showed satisfactory accuracy in representing the main characteristics of the IP climate, and therefore its application to analyze future changes through projections of the climate change, appears to be adequate in this area. Nonetheless, it is important to emphasize that the model has different shortcomings. The main results found are:

- In general, WRF satisfactorily simulated mean values and interannual variability of precipitation for a complex topographical region such as the IP, which is mainly caused by the improved representation of orography provided by high-resolution simulations as reported Prein et al. (2016). However, it tended to overestimate values in high-mountain regions and for seasons with greater precipitation. On the contrary, underestimations were found for places and seasons with lower precipitations. Our results agree with those found in Herrera et al. (2010) in which authors found a good agreement between the outputs from an ensemble of RCMs within ENSEMBLE initiative and the precipitations from the Spain02 gridded observational product to represent the spatial patterns over Spain. The results also showed major differences between simulations, suggesting that a main source of error could be due to the LBCs. These results were particularly evidenced during winter that is the season when the influence of the large-scale is the strongest (Argüeso, 2011). The good agreement of the WRF model to simulate precipitation characteristics over the IP has been also evidenced by Cardoso et al. (2013), who performed a WRF validation over the IP. They found spatial patterns of annual values similar to those found in this work. Additionally, Soares et al. (2016), studying future projections in precipitation over Portugal, revealed good agreement between current WRF simulations and observations to represent temporal and spatial precipitation patterns.

- The WRFMPI simulation showed a widespread overestimation in both mean value and interannual variability of precipitation in all assessments, which is especially strong in summer. This result appears to indicate that the overestimation could be partially associated with the larger amount of soil-water content available in the simulation. In fact, in summer the large-scale forcing was weaker, and thus the local circulation through the land-surface processes was more notable in mid-latitude regions such as the IP as indicated Jerez et al. (2012). Therefore, the greater availability of soil water could lead to more precipitation through the increase of evapotranspiration. In this context, it is important to take into account that WRFMPI was run using the ERA-Interim soil moisture as the initial condition for which the model generates its own soil moisture through the NOAH LSM.

- In general, the results also show the close relationship between mean values and interannual variability, since the model overestimated interannual variability over the areas where the amount of precipitation was also overestimated, and vice versa. This feature has been pointed out by Jerez et al. (2013), who found bias patterns similar in magnitude for mean precipitation and internal variability in a study of a multi-physic ensemble of MM5 simulations over the IP.

- The model's ability to represent the daily distribution and extreme values for precipitation was also quite good, as characterized by the PSS values and the analysis of extreme events.

- In general, these findings as well as the long-term precipitation values agree in many ways with the results reported by Argüeso et al. (2012a). In their study the authors found that WRF had strong capacity to detect current characteristics over Spain by using different WRF simulations for a 30-year period (1979-1999). That study was evaluated using the same GCMs as driving data but in their previous versions (CCSM3 and ECHAM5) so that we expected to find similarities in our study.

- For maximum and minimum temperatures, remarkable results appeared in the different time scales analyzed. Nevertheless, the mean values were systematically underestimated, this feature being more notable for T_{max}. Underestimations of temperature values in RCM simulations have also been evidenced in other studies (eg., Jerez et al., 2013, Argüeso et al., 2011, Domínguez et al., 2013).

- The similarity between results from the different WRF simulations in terms of temperature suggests that the main errors are associated to shortcomings in the regional model. In this way, winter characteristics over the IP appeared to show weaker errors, which could be associated with the strong influence exerted by the synoptic scale winds (resolved by the LBCs), and thus the local effects were partially mitigated. By contrast, summer results involved larger underestimations in both mean values and interannual variability, and especially for the WRFMPI. In fact, authors such as Jerez et al. (2012) suggested that the RCMs present certain difficulties to simulate land-surface processes lead errors in soil moisture availability, and thus inaccuracies in representing temperature values.. In fact, higher soil-moisture values could result in an overestimation of evapotranspiration and consequently an underestimation of temperature.

- As for precipitation, the results from daily values reveal again that WRF provided excellent results. Furthermore, the bias-correction applied for extreme events of temperature also showed that the systematic underestimations of temperature could be easily solved, achieving reliable results. Moreover, in the study of projected changes, such consistent deviations will be offset by using the Delta-Change approach, so that the results for this variable show that the model was remarkably suitable to perform projections in terms of temperature.

- The comparison of land-surface variables suggests that although the model still showed acceptable performance, it had greater weaknesses in capturing both their mean values and interannual variability. The acceptable characterization by WRF-Noah for simulations over Europe has been pointed out by Greve et al. (2013), who studied soil-water content (SWC) using climate hindcast simulations from 1990 to 2008. They concluded that the WRF model represents reasonably well the spatial patterns and temporal variability of the seasonal mean SWCs, although the absolute values significantly differed. In this way, the results must be interpreted bearing in mind that the GLEAM datasets were the results of applying a model, so that, although the values of the variables proved to be fairly accurate, they were subject to inherited uncertainties associated with model results.

- The results from assessing the surface evapotranspiration, in term of relative biases, suggest that the WRF model tended to overestimate annual as well as summer and winter mean values. Nonetheless, soil moisture content was broadly underestimated except in summer when all WRF simulations showed large overestimations. In this way, it should be noted that the performance in terms of soil moisture referred to the upper 10-cm layer, so that the conclusions drawn are partial, also because differences were found on assessing the correlation between the soil moisture in the root zone from GLEAM and the total soil moisture provided by WRF. The agreement in terms of temporal correlation between GLEAM and WRF found here followed the same direction as the results found in a recent study (Knist et al., 2017) that evaluated the model's capacity to represent land-atmosphere coupling by using a EURO-CORDEX ensemble of RCMs.

- The results also show that the spatial distribution of surface evapotranspiration and soil moisture was affected not only by the land-surface hydrologic processes (precipitation or surface evapotranspiration), but also by the heterogeneity of soil properties, and land-cover characteristics as reported in González-Rojí et al. (2018) in terms of surface evapotranspiration.

- These results evidence the importance of adequately representing land-surface variables because weakness to simulate soil moisture, could be affecting the capacity to simulate variables such as the temperature. This requires a better understanding of the WRF performance related to the land-surface processes, and future research in this context will be undertaken.

Chapter 5

Characterization of Current Drought Events

This chapter is devoted to analyzing the ability of the model to detect wet and dry periods by using two different drought indices. For this, primary climate variables (i.e. precipitation, T_{max} and T_{min}) from the WRF model were used. Indeed, the WRF model demonstrated noteworthy ability to reproduce the main climate characteristics discussed in Chapter ***4***, and thus this chapter addresses the benefits of using dynamical downscaled fields in current drought characterization. As a means of quantifying the added value provided by the model, the spatio-temporal comparison with respect to its driving data was also performed in terms of drought indices[1].

5.1. Characterization of Wet and Dry Events through Drought Indices

In broad terms, drought can be defined as the scarcity of precipitation over a prolonged time period. However, a more precise definition is difficult due to the great number of variables involved and the variety of sectors affected. A widely accepted approach to characterize wet and dry periods is through the so-called drought indices. By definition, they are variables that enable us to assess

[1]The results here displayed are part of a study published in Journal of Geophysical Research: Atmospheres (García-Valdecasas Ojeda et al., 2017).

the effects of a drought and defining parameters such as the duration, severity, intensity, and surface area affected by the drought, which should be able to detect droughts at different time scales (Mishra and Singh, 2010). Many indices have been formulated to characterize droughts, particularly in a context of meteorological and agricultural applications, which can be based solely on precipitation values, such as the Standardized Precipitation Index (SPI, McKee et al., 1993), but more complex indices have also been derived from hydrological models such as the Palmer Drought Severity Index (PDSI, Palmer, 1965). Because no single index outperforms the others for all regions and for all drought categories, the selection of a certain index depends mainly on its ability to reproduce the spatio-temporal characteristics of a specific drought category in a study region, but also on its main features, namely the calculation procedure and input variables required, together with its advantages and weakness (PaiMazumder and Done, 2014).

Among the indices formulated in this thesis, an index based solely on precipitation, the SPI (SPI, McKee et al., 1993) plus another that also takes into account the effect of the temperature, i.e. the Standardized Precipitation Evapotranspiration Index (SPEI, Vicente-Serrano et al., 2010), were chosen. Such indices have widely demonstrated their great capacity to detect wet and dry periods throughout the IP (Russo et al., 2017, Beguería et al., 2014, Vicente-Serrano et al., 2014b, 2011a). Additionally, because both indices are based on the same calculation procedure, the direct comparison between the two in space and time will elucidate the effect of temperature on drought severity.

5.1.1. The SPI and the SPEI

The SPI was developed as an alternative to the well-known PDSI index. In fact, although the PDSI has been widely used in the United States to detect drought as well as to analyze changes in the aridity worldwide, it is ambiguous in its calculation procedure, too complex to understand easily, spatially incomparable, and temporally invariable, i.e. it has no multiscalar properties (Guttman, 1998).

The SPI characterizes abnormal wetness and dryness by using normalized anomalies of precipitation, which can accumulate at different time scales.

Therefore, 1, 3, 6, 12, 18 or 24 months of accumulated values can be computed depending of the kind of drought to be characterized. For example, if the purpose is to characterize meteorological or agricultural drought events, the best accumulated intervals appear to be between 3 and 6 months since they are suitable to analyze short-term supplies such as the soil-moisture content available for vegetation (Sims et al., 2002, Santos et al., 2010). Furthermore, for hydrological drought characterization, longer time scales are more appropriate, which are associated with the effects in water-reservoir levels, groundwater, and river streamflow (Vicente-Serrano, 2006, Mishra and Singh, 2010).

To compute the SPI, the accumulated precipitation data are fitted to a probability density function (e.g. Gamma, Pearson III, log-normal or log-logistic, depending of the region of study), the rarity of an event being determined by the probability associated with such a distribution. Then, the cumulative probability function is transformed into a standard normal random variable Z, with mean 0 and variance of 1, thus enabling the comparison of drought values across regions with markedly different climates. Hence, Z is the corresponding drought index and indicates the number of standard deviations from the climatological mean. Positive values indicate rainfall higher than the climatological mean precipitation, while negative values show conditions drier than the normal and likely drought.

In this sense, droughts can be classified in different categories through their probability of occurrence (Table ***5.1***). For instance, a 12-month SPI with a value of -1.3 for December signifies that the conditions have been moderately dry during the period from January to December of the given year. In fact, this value indicates that the accumulated precipitation in these 12 months is 1.3 standard deviations below to the climatological mean of the January-December accumulated precipitations.

The SPI is the index recommended by the World Meteorological Organization (WMO) for analyzing droughts, due to its simplicity, easy interpretation, statistical robustness, and especially for its multi-scalar character, which enables identification of different drought categories, and consequently the analysis of the impact of drought on multiple ecosystems (Edwards and McKee, 1997, Guttman, 1998, Vicente-Serrano et al., 2010, Beguería et al., 2014). However, it

Table 5.1: *Drought Categories.*

Drought index value	**Drought Category**	**Probability (%)**
Index ≥ 2	Extremely Wet	2.3
2 ≥ Index > 1.5	Severely Wet	4.4
1.5 ≥ Index > 1	Moderately Wet	9.2
1 ≥ Index > -1	Near Normal	68.2
-1 ≥ Index > -1.5	Moderately Dry	9.2
-1.5 ≥ Index > -2	Severely Dry	4.4
Index < -2	Extremely Dry	2.3

is based solely on precipitation data considering that other factors are stationary over time (e.g. temperature). This assumption could be incorrect under a global-warming scenario.

In the same context, The SPEI is the result of applying the calculation procedure of the SPI, but using a "climatic water balance" rather than precipitation records. Therefore, the temperature effect is considered through the so-called climatic water balance, which is the difference between the accumulated values at different time scales of precipitation and the ET_0. Thus, this index combines the benefits of using the potential evapotranspiration, such as the PDSI, with the strength of the SPI, namely, simplicity, robustness, interpretation, and multi scalar properties. A critical step to determine the SPEI is to choose a suitable approach to compute the ET_0. Although this is a relatively new index, it has already been used by many authors (Yu et al., 2014, Meque and Abiodun, 2015, Kim et al., 2016) due to its main characteristics. A further description of the benefits of using this index can be found in Vicente-Serrano et al. (2014b).

5.2. Description of the Analysis

The ability of the model to simulate dry and wet periods was assessed by comparing drought indices simulated by WRF outputs with those computed using observational data. For this purpose, the outputs from the WRF simulation driven by ERA[2] were used. Here, current simulations forced by GCMs cannot be evaluated in terms of drought indices since they are characterized by creating their own natural variability, and thus, the time course is different from

[2]The description of the simulation driven by ERA is detailed in Chapter **3**.

the present one. However, the evaluation performed in Chapter ***4*** in terms of primary climate variables, together with this analysis provides a broad vision of the WRF performance with respect to drought using GCMs as driving data.

The monthly scale appears to be the most appropriate for monitoring drought in relation to agriculture resources, in river streamflow and water resources (Panu and Sharma, 2002), so that the maximum and minimum temperature as well as the amount of precipitation was aggregated monthly using the daily outputs from the WRF. As observations, in this study the monthly gridded products of the MOPREDAS and the MOTEDAS (hereafter jointly referred to as the mprmt) were selected. These gridded products are composed of observations that cover a period extending to 2010, and thus the period used here corresponds to December 1979 to November 2010. Additionally, to quantify the added value of downscaled fields concerning their LBCs, the temperature and precipitation data from ERA-Interim were also used. Because each database had a different spatial resolution, the ERA and WRFERA data sets were previously re-gridded onto the mprmt 0.1° regular grid using a bilinear interpolation. Thus, all data were then comparable.

The two indices, the SPI and SPEI, were calculated using the SPEI R Package (Beguería and Vicente-Serrano, 2013). This code allowed the formulation of both indices at different time scales, also providing an additional function to estimate the ET_0. Among the different approaches available, the Modified Hargreaves equation (HG-PP, Droogers and Allen, 2002) was used, this proving to be appropriate for estimating ET_0 values in Spain (Vicente-Serrano et al., 2014b). The HG-PP corrects the ET_0 calculated from the Hargreaves equation based on the hypothesis that the monthly accumulated precipitation value can change the moisture levels (Vicente-Serrano et al., 2014a). Thus, through the HG-PP, the results proved similar to those provided by the Penman-Monteith equation (Allen et al., 1998), which is the method adopted by the Food and Agriculture Organization to estimate this parameter, but with the advantage that only precipitation and temperature (maximum and minimum) are required to calculate it (Beguería et al., 2014).

The indices were computed at two different time scales: the 3-month time scale, which allows us the study of episodes related to meteorological droughts

(Mishra and Singh, 2010), and the 12-month time scale, wich enabled us to detect hydrological droughts and their effects on river streamflows and water resources (Vicente-Serrano, 2006, Spinoni et al., 2015). Also, for comparative purposes, both drought indices were fitted to a log-logistic probability distribution by using the maximum-likelihood method. This ensured that the differences between these two indices will be related to the temperature effects and not to the fitted probability distribution (Vicente-Serrano et al., 2011a).

Drought events were analyzed using two different approaches. On the one hand, a regional assessment was performed in order to determine the benefit of using dynamical downscaled fields at a regional scale. Thus, the time series of different regions of Spain were established as the simple average of the index values of all grid-points within a region. The criteria for making such grouping was based on a multi-step regionalization approach[3], which determined 6 main regions in terms of drought indices, that are: northwestern (NW), Cantabrian, (CA), northeastern (NE), interior (IN), southern (S), and southeastern (SE), as displayed in Figure ***5.1***.

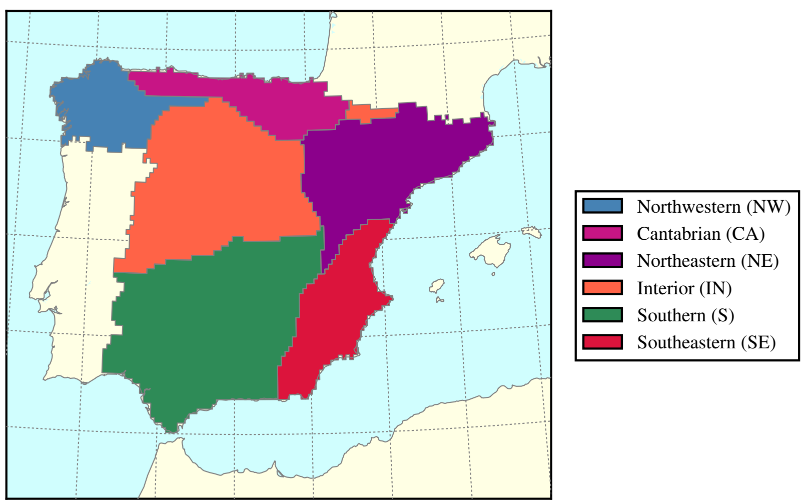

Figure 5.1: *Climate regions used for regional drought assessed*

Furthermore, to analyze the benefit gained by using downscaled fields in more detail, we used a set of different parameters for direct grid-point compar-

[3]The regionalization methodology here applied to establish homogenous climate regions is detailed in Appendix ***B***.

ison. Therefore, we can identify possible errors that occur at a local scale which could be masked by the regional average. In this way, we analyse the temporal series of both drought indices and different parameters useful for characterizing droughts, i.e. duration, magnitude, and severity.

5.3. Drought Characterization in Spain

5.3.1. Regional Analysis

To begin the assessment at a regional scale, Figure ***5.2*** shows the representation of the time course of the SPEI computed from the mprmt, ERA, and WRFERA at a 3-month time scale, for the 6 regions identified by the multi-step regionalization. The RMSEs between the WRFERA (or ERA) and the mprmt are also shown in brackets. In general, the results indicated that although there is a substantial agreement between the observational SPEI and the ones computed with ERA and WRFERA, the fits are moderately better for the downscaled SPEIs. This finding is corroborated in all regions by the lower RMSE values for the WRFERA (RMSE values of 0.21-0.36 and 0.34-0.53 for WRFERA and ERA, respectively).

The S, IN, and NW regions presented the best fit, and NE, SE, and CA the worst. Similar results are depicted in Figure ***5.3***, which represents the temporal evolution of the 12-month SPEI from the different data sources. In this case, the best fit to the observational data provided by the WRFERA was even more evident (RMSE between 0.48 in the NE region and 0.19 in the S region). Particularly, this improvement was remarkable for the NE region in the period 2002 to 2005, for the IN region in the period 2003 to 2005, and for the CA region in the period 1989 to 1996. Conversely, NE shows a poorer fit for WRFERA in the period 1999 to 2001. Similar results were found when we represented the SPI at the regional scale for both time scales and thus are not shown.

To quantify the added value provided by WRF, we made a detailed analysis of the temporal correlation between the two drought indices that resulted using simulated (ERA and WRFERA) data and the one calculated from observed (mprmt) data (Table ***5.2***).

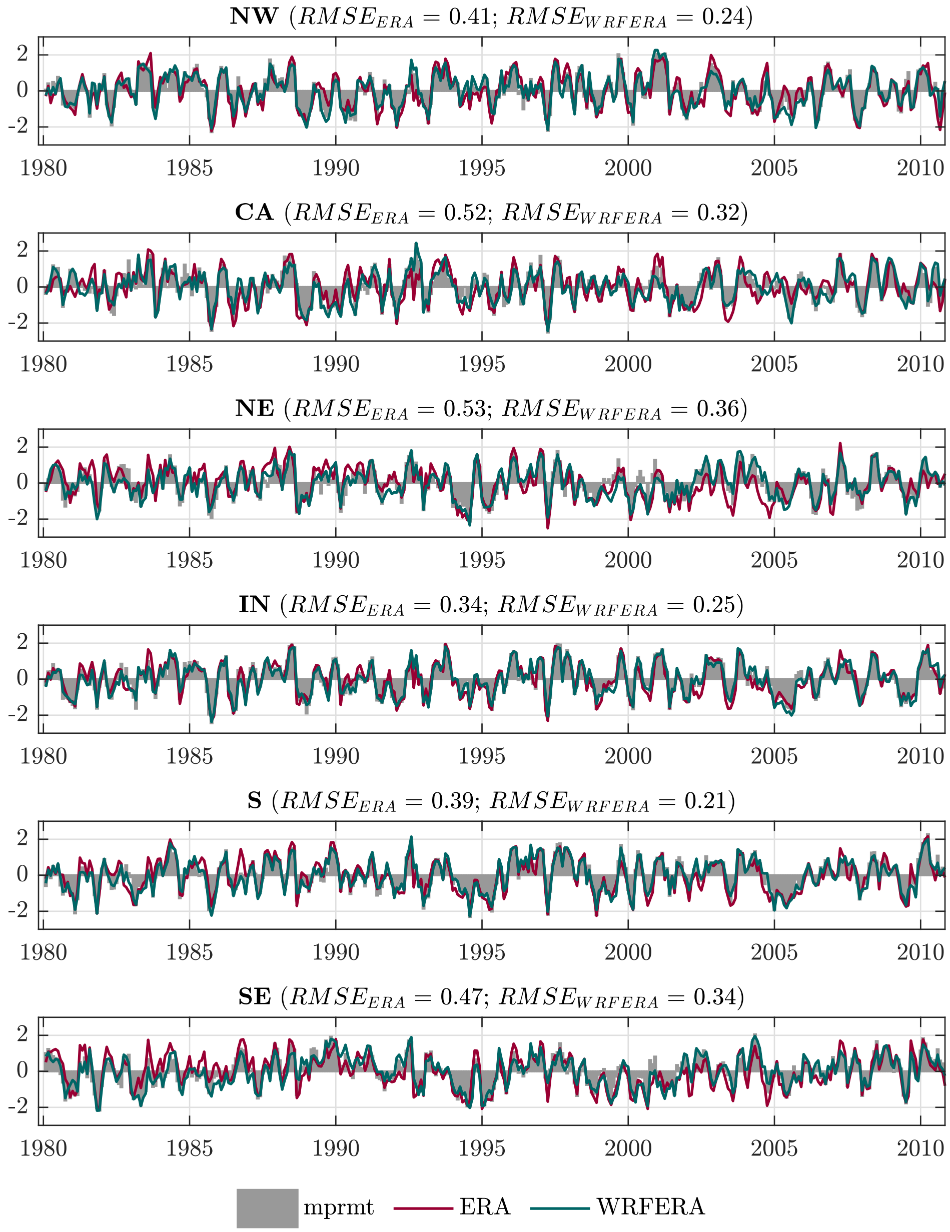

Figure 5.2: *Temporal evolution of the 3-month SPEI from the mprmt (grey columns), ERA (red lines), and the WRFERA (green lines) data sets for the 6 different regions. In brackets, the RMSEs for the ERA and the WRFERA with respect to the mprmt.*

The SPEI and SPI calculated by using WRF outputs presented higher correlation coefficients than did the indices from the ERA data, with values above

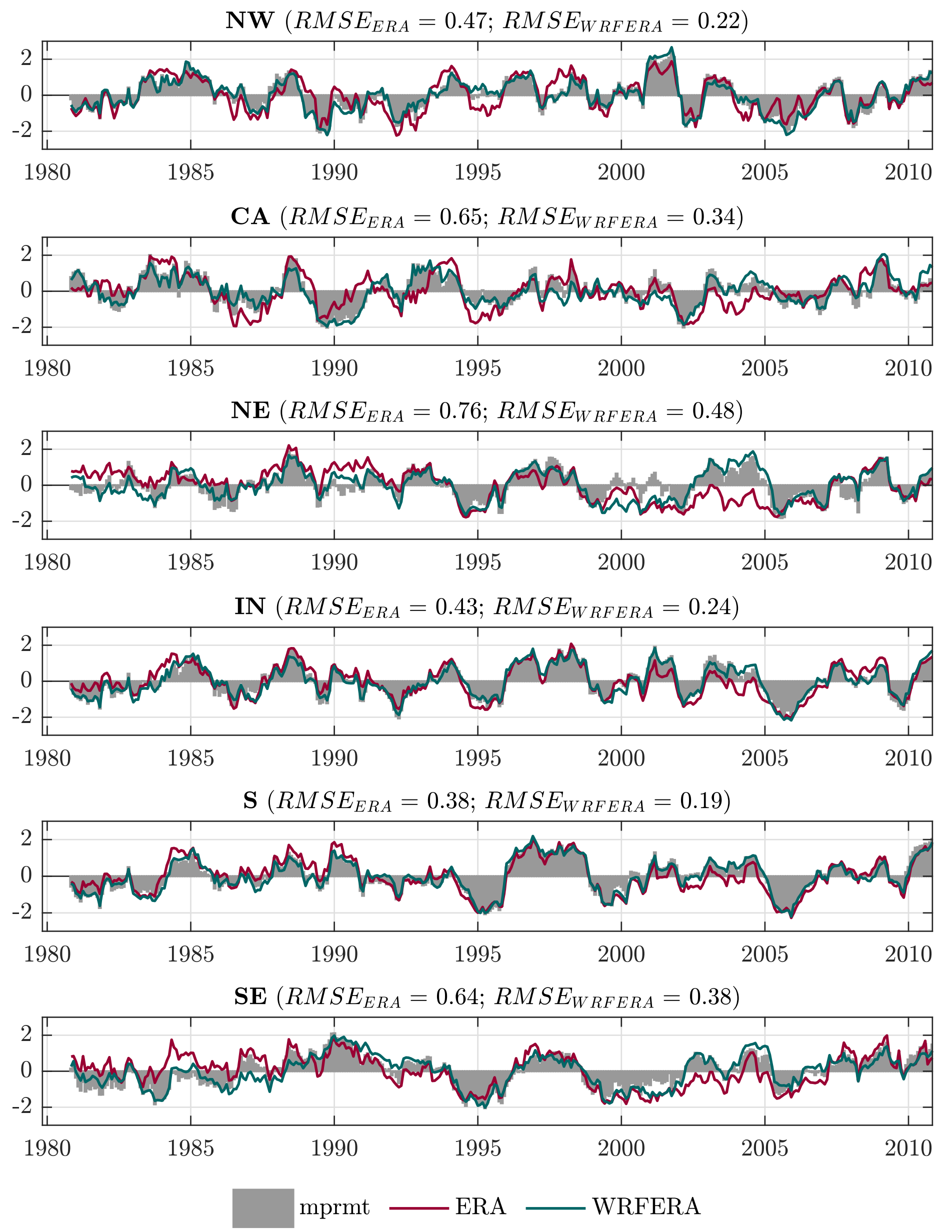

Figure 5.3: *The same as in Figure **5.2** but for the 12-month SPEI.*

0.83 in almost all regions. At a 3-month time scale, the weakest correlation corresponded to the NE region for both indices and data sources, while the S, NW, and IN regions registered the highest correlation coefficients. At a 12-month time scale, these results were repeated, with a larger difference between

Table 5.2: *Correlation coefficients between simulated (ERA and WRFERA) and observational drought indices computed at the 3-month (3-mo) and 12-month (12-mo) time scales. Such correlations were made for each region (NW, CA, NE, IN, S, and SE), and the benefit of using downscaled fields are shown in relative terms and expressed in percentages (WRFERA minus ERA / ERA). In addition, the difference of the added value found with one or the other index is also displayed (SPI minus SPEI).*

	SPI		**SPEI**		**SPI minus SPEI**	
	3-mo	12-mo	3-mo	12-mo	3-mo	12-mo
NORTHWEST (NW) REGION						
ERA	0.883	0.855	0.906	0.869	-	-
WRFERA	0.961	0.971	0.964	0.971	-	-
WRFERA minus ERA (%)	**8.800**	**13.545**	**6.499**	**11.855**	**2.30**	**1.69**
CANTABRIAN (CA) REGION						
ERA	0.797	0.660	0.830	0.716	-	-
WRFERA	0.925	0.899	0.933	0.916	-	-
WRFERA minus ERA (%)	**16.020**	**36.310**	**12.461**	**27.907**	**3.56**	**8.40**
NORTHEAST (NE) REGION						
ERA	0.750	0.521	0.809	0.589	-	-
WRFERA	0.898	0.818	0.910	0.826	-	-
WRFERA minus ERA (%)	**19.731**	**57.162**	**12.446**	**40.138**	**7.29**	**17.02**
INTERIOR (IN) REGION						
ERA	0.905	0.868	0.929	0.883	-	-
WRFERA	0.958	0.965	0.962	0.962	-	-
WRFERA minus ERA (%)	**5.782**	**11.176**	**3.551**	**9.032**	**2.23**	**2.14**
SOUTH (S) REGION						
ERA	0.901	0.935	0.908	0.916	-	-
WRFERA	0.967	0.978	0.972	0.977	-	-
WRFERA minus ERA (%)	**7.225**	**4.685**	**7.119**	**6.726**	**0.14**	**-2.04**
SOUTHEAST (SE) REGION						
ERA	0.841	0.731	0.861	0.742	-	-
WRFERA	0.913	0.898	0.922	0.905	-	-
WRFERA minus ERA (%)	**8.640**	**22.768**	**6.968**	**22.032**	**0.74**	**1.67**

the correlation coefficients for the downscaled drought indices and those found by using the driving data. The results also showed that the SPEI presented a higher correlation than did the SPI in all regions (except for the southern region). The quantification of the added value provided by WRF is reflected through the difference between the correlation coefficients from the WRFERA and the ERA (WRFERA minus ERA / ERA (%)). Such differences display that

WRF provided added value with respect to the driving data, this improvement being higher for Standardized Precipitation Index (SPI) and for the 12-month time scale. This added value was especially marked in the NE and CA regions.

The results for the comparison between the added value provided by one or the other index (sixth and seventh columns in Table ***5.2***) indicate that the greatest benefit achieved with the use of SPI rather than SPI appeared in the NE region (7.29% and 17.02% at 3 and 12 months, respectively). In the Cantabrian region, this benefit is also markedly higher for SPI downscaled (3.56% and 8.40% higher at 3 and 12 months, respectively). However, the highest added value for the SPI was not so obvious in the SE region, where the SPI improvement outperformed that found with SPEI in 1.67% and 0.74% at 3 and 12 months, respectively. Finally, the NW and IN regions showed intermediate values of improvement of SPI vs. SPEI, i.e. around 2% for both time scales.

The regional analysis indicated an added value provided by downscaled fields. However, some features may be hidden through regional aggregation, and thus a local analysis is also desirable in order to ensure the WRF ability of detecting a drought event.

5.3.2. Local Analysis

Local Evaluation of Wet and Dry Episodes Using Drought Indices

In terms of grid-points comparisons, the RMSE from the WRFERA and the ERA time series of drought indices against those from the mprmt data, were analyzed. Thus, we were able to quantify the ability of the WRF model to represent the temporal variability of drought occurrences at the local scale.

Figure ***5.4*** shows the RMSEs of the simulated drought indices with respect to the observed ones found for each grid point at the two selected time scales and for the two drought indices. Overall, the ERA RMSEs were higher than the WRFERA RMSEs. The improvement provided by the WRF was clearly reflected in areas such as the Ebro Valley, located in the NE region. The added-value of downscaled fields in this region was displayed for both time scales and indices. In reference to results of a 3-month time scale, RMSE values ranged from 0.3 to 1, approximately. Although the spatial patterns for both indices were very similar in broad terms, the simulated SPEI showed better agreement than the

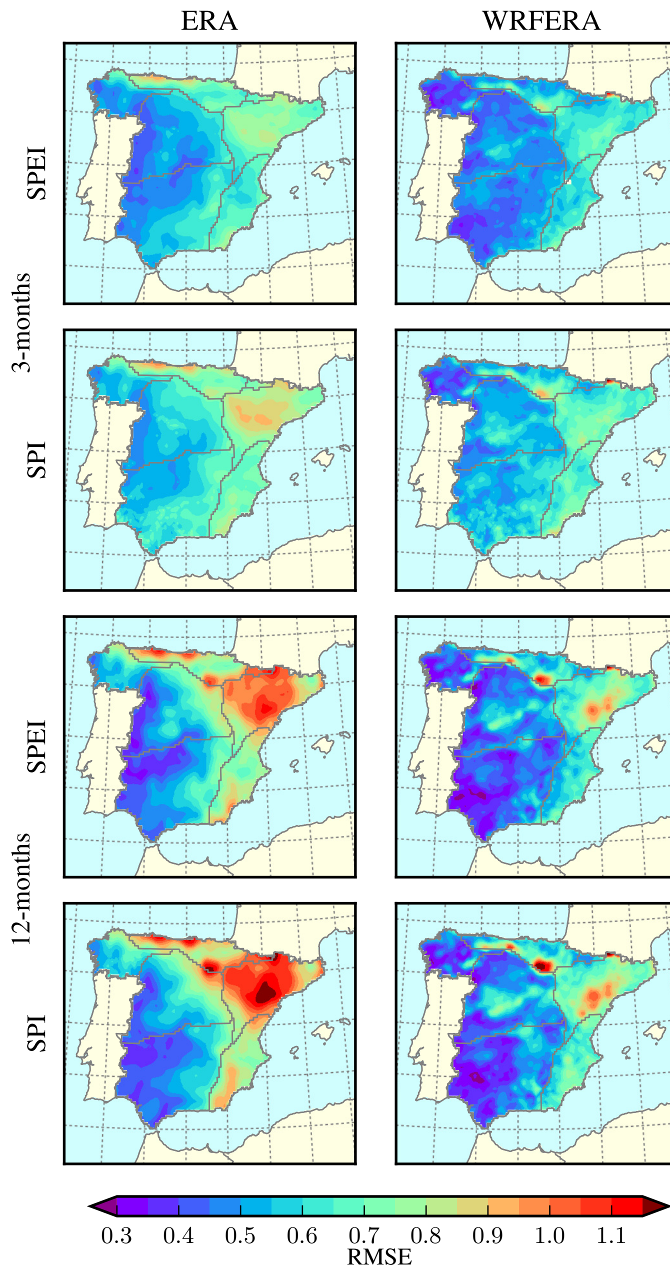

Figure 5.4: *Root mean squared errors (RMSEs) between the drought indices computed from the ERA and the WRFERA with respect to those from the mprmt. In rows, both the two indices and time scales used.*

simulated SPI with respect to the mprmt. For instance, the Ebro Valley presented RMSE values of around 0.8 and 0.95 for the SPEI and SPI, respectively, when the ERA drought indices were analyzed. The highest RMSEs, corresponding to the Cantabrian and the northeastern regions, were corrected, in general using downscaled fields. Meanwhile, the lowest RMSEs corresponded to the northwestern, southern, and interior regions of Spain.

At the 12-month time scale, the RMSE presented values of around 0.2 to 1.2, the range of values being greater than at 3-month time scale. The results indicate that the improvement for the 12-month SPEI with respect to the SPI was less evident than at 3-month time scale, with the two indices showing similar RMSEs in most regions of Spain. For both indices, the WRFERA presented the highest RMSEs (values above 1) in areas located in the Cantabrian and the northeastern regions such as the Ebro Valley, the Pyrenees, and the Cantabrian Range. However, the WRFERA simulations were generally better than the ERA ones. These results suggest that the simulated drought indices using WRF outputs were in general able to reproduce the observed indices, showing remarkable improvements with respect to the indices conducted by its LBCs. Also, these improvements were strongly influenced by the time scale analyzed. For both time scales, the RMSE values for SPEI and SPI indices found with WRFERA are similar, while the errors were greater for SPI than for SPEI when ERA data were used. Therefore, the improvement achieved by using WRF was higher for SPI than for SPEI. The results of this local analysis agreed with those depicted at the regional time scale.

The added value of the downscaling approach was also evaluated in terms of spatial variability. Spatial correlation provides information of the spatial performance of WRF, and therefore the added value of using high-resolution fields to compute drought indices over topographically complex regions. The procedure applied here is based on calculating the Pearson correlation coefficients at different spatial intervals over longitude and latitude, as is detailed in Wang et al. (2015)[4] Thereby, we calculated spatial correlations from the WRFERA, the ERA and the mprmt data by using different lags, and then the added value was assessed by directly comparing the differences between the WRFERA and

[4]For a further description see Appendix ***A***.

ERA with respect to the mprmt. In this way, a positive difference means that two points from the simulated drought indices are more similar than the same points from the observational data (ERA minus mprmt and WRFERA minus mprmt, respectively). Thus, for topographically complex regions, this implies that the simulations were unable to capture the spatial variability of drought indices. Conversely, a negative difference means that simulated fields were more sensitive to spatial variability than were the observational data. Figure ***5.5*** shows the spatial correlation between one grid and another along the south-to-north (Figure ***5.5a***) and west-to-east (Figure ***5.5b***) directions, respectively, with a lag of 0.4°. The same study was also performed with a lag of 0.2 and 0.8°, but the conclusions of the results are the same, and therefore they are not shown. The spatial correlations from observation are shown in the first rows and the differences from the ERA and the WRFERA against mprmt appear in the second and third rows, respectively.

For observations, the spatial correlation showed a noticeable decrease over the Cantabrian Range (Figure ***5.5a***), which is oriented west to east for the latitudinal lag (Figure ***5.5a***). For the longitudinal lag (Figure ***5.5b***), the main mountain ranges, oriented south to north, are adequately displayed. Also, high spatial correlations (above 0.9) were found in both plateaus (northern and southern) and also over the Guadalquivir Valley. The differences between modeled and observed spatial correlations indicate that ERA in general provided positive differences with respect to the observations, this result suggesting that ERA is unable to represent the spatial variations and the local characteristics in terms of drought indices in the main mountain ranges of Spain. However, the WRFERA fields adequately reproduced the spatial variability, even more than the observational data (the differences are negative in general), leading an added value with respect to its LBCs. For instance, it reproduced the main spatial patterns of drought in regions such as the Central Massif. These results were similar for both the SPI and the SPEI, and more evident at the 12-month time scale.

Additionally, the added value provided by downscaled fields through a categorical viewpoint was quantified. For this purpose, the critical success index (CSI, Kang et al., 2005) was analyzed. The CSI, detailed in Appendix ***A***, is a

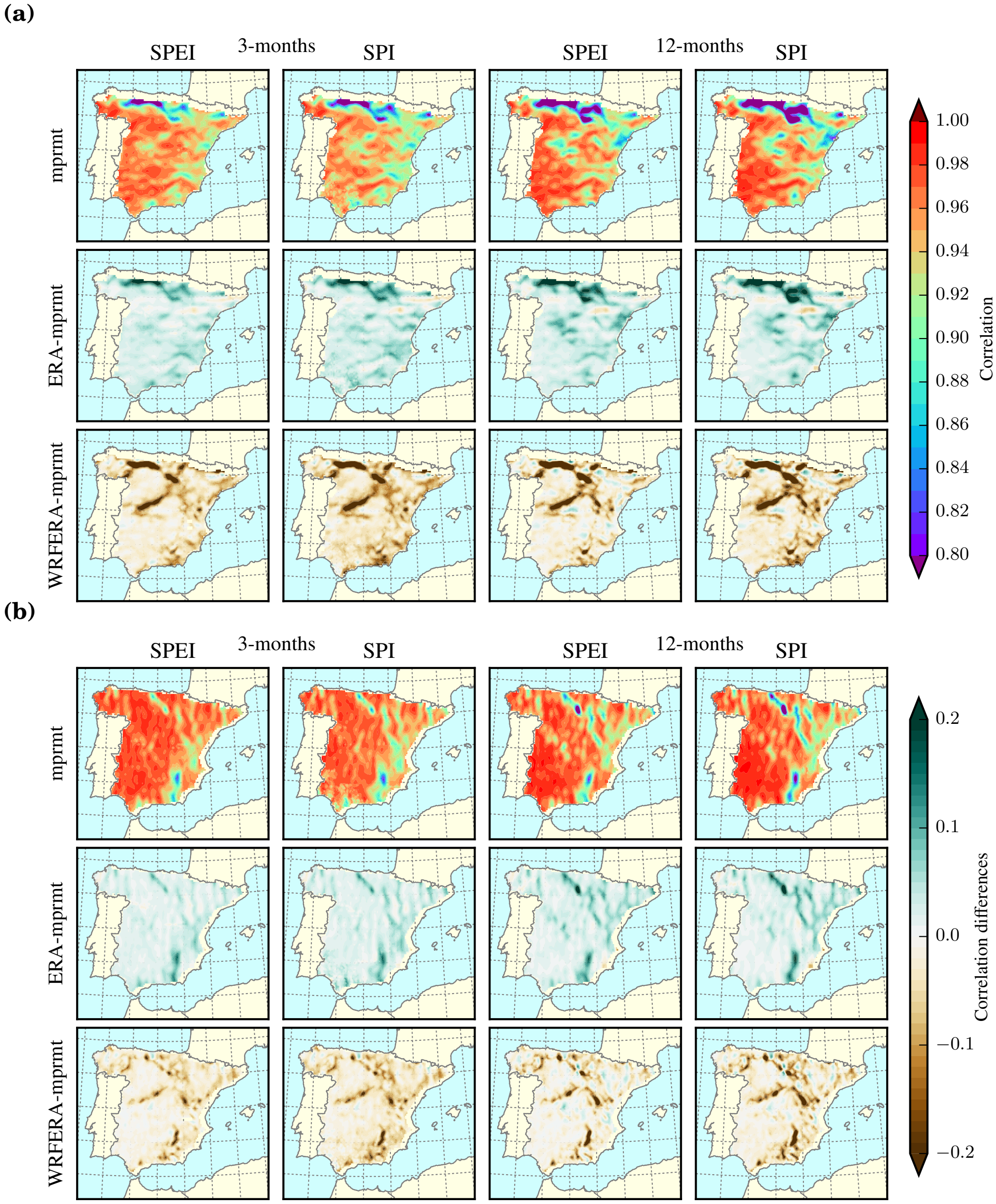

Figure 5.5: *Spatial correlation coefficients from mprmt and the differences between ERA and WRFERA with respect to mprmt, for a lag of 0.4° along the (a) south-to-north and (b) west-to-east directions. In columns, the drought indices at a time scale of 3 (first and second columns) and 12 (third and fourth columns) months.*

measure based on the ability of the model to detect drought indices values above or below a given threshold. Thus, the assessment consisted of determining whether the model offered an added value to characterize moderate-to-extreme wet and dry episodes, with analyses of events made jointly using a drought index of above 1 and below -1, following the procedure suggested by Bowden et al. (2016). Thus, the added value can be quantified as the difference of CSI values from the WRFERA and the ERA with respect to the mprmt. To determine the statistical significance of the CSI differences, we applied the two-proportion z-test (Yang et al., 2015), which consists of a significance test whose null hypothesis assumes no difference between the CSI based on modeled data and those calculated using observations. This test was used at the 95% confidence level.

Figure ***5.6*** depicts the CSI for moderate to extreme events using both the SPEI and SPI from the ERA and the WRFERA at the two time scales. The significant differences between them with respect to ERA (WRFERA minus ERA / ERA) are also shown in the third column. At the 3-month time scale, the two indices present CSI values in a range of between 20% and 80%, with the largest CSI in the northwestern, interior and south of Spain. Conversely, the lowest values correspond to the eastern region. With respect to the comparison between the two indices, the results suggest that the SPI slightly outperformed the SPEI. The comparison between WRFERA and ERA using the CSI relative differences showed that downscaled fields outperformed the driving data in areas located in the northwestern, Cantabrian, and northeastern regions, with improvements of about 60%. These improvements were more noticeable for SPI than for SPEI.

At the 12-month time scale, the two indices, which presented similar results, depicted more regions with higher CSIs, especially in the southwestern region, with values of about 80%. By contrast, the worst values were in eastern Spain, as occurred at the 3-month time scale. For this time scale, WRF again led to an improvement, of more than 100% in regions located in northern Spain (e.g. the Cantabrian Coast, Pyrenees, Galician Massif, Northern Plateau, and the Ebro Valley). When the CSI values based on the SPEI were compared with those found by using the SPI, the results showed that the greatest added value

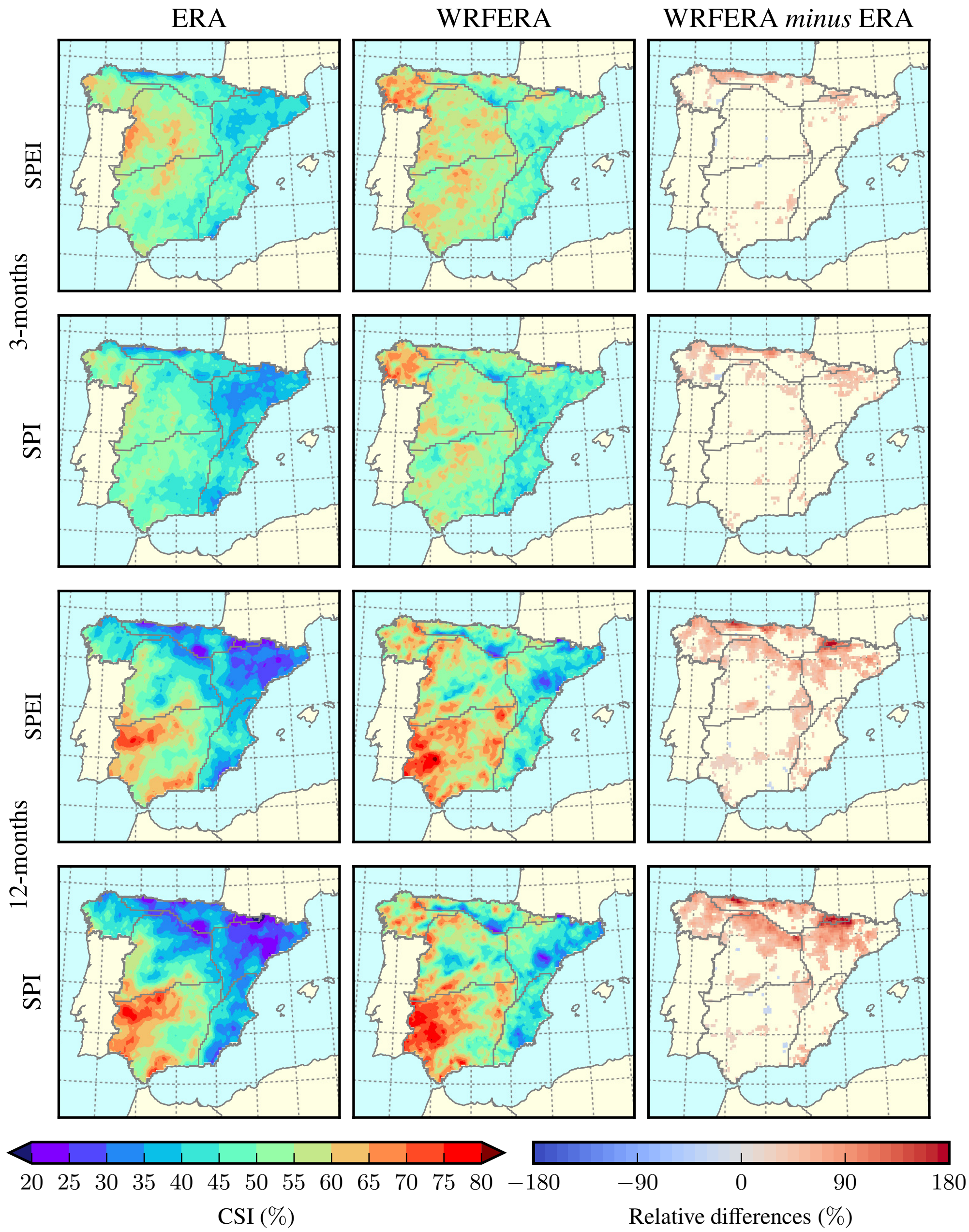

Figure 5.6: *Critical Success Index (CSI) between simulated (ERA and WRFERA) and observed (mprmt) the SPEI and the SPI at 3- and 12-month time scales (first and second columns). In the third column, the significant relative differences between them (WRF-ERA minus ERA / ERA) according to two proportional z-tests at the 95% confidence level.*

corresponds again to the SPI, in agreement with the RMSE results. Therefore, the CSI analysis suggests that the WRF led to an unambiguous added value, which depends on the time scale used (higher at12 months) and, in general, more evident for the SPI. Furthermore, for both indices and time scales, the RMSE and the CSI showed similar spatial patterns throughout Spain.

Assessing the Characteristics of Drought Events: Duration, Magnitude, and Severity

For application to drought predictions, a study of the potential capacity of the WRF model to provide suitable estimations of individual drought episodes was also performed using different characteristics such as the duration, magnitude, and severity of the individual drought events. We defined a dry episode as an event in which the SPEI and SPI values were below 0. This threshold has been used by several authors, such as Vicente-Serrano et al. (2011a), since indices below 0 correspond to those months with accumulated values (precipitation and water deficits for SPI and SPEI, respectively) below the mean of the distribution for the entire study period. Therefore, time series of duration, magnitude, and severity could be determined as well as the frequency at each grid point. For this, the duration was defined as the number of consecutive months with negative index values; the magnitude as the sum of the drought index values within that event (McKee et al., 1993, Vicente-Serrano et al., 2011a), the severity as the absolute minimum value of a given episode (PaiMazumder and Done, 2014), and the frequency as the number of events in the period. However, because the frequency was inversely related to the mean duration, providing similar information to duration time series, the results for this parameter are not displayed.

Figure ***5.7*** illustrates the magnitude averaged for the entire study period for simulated and observed drought events, for the two indices at the two time scales. The spatial RMSE in reference to the mprmt data was also calculated (shown in brackets) in order to quantify their spatial similarity with respect to observations. The average magnitude of the drought was between 2.5 and 4 at a 3-month time scale, and between 6 and 16 at a 12-month time scale. In general, at 3 months, WRF provided no clear improvement with respect to the driving data. This unclear result can also be seen in the spatial RMSE, which is

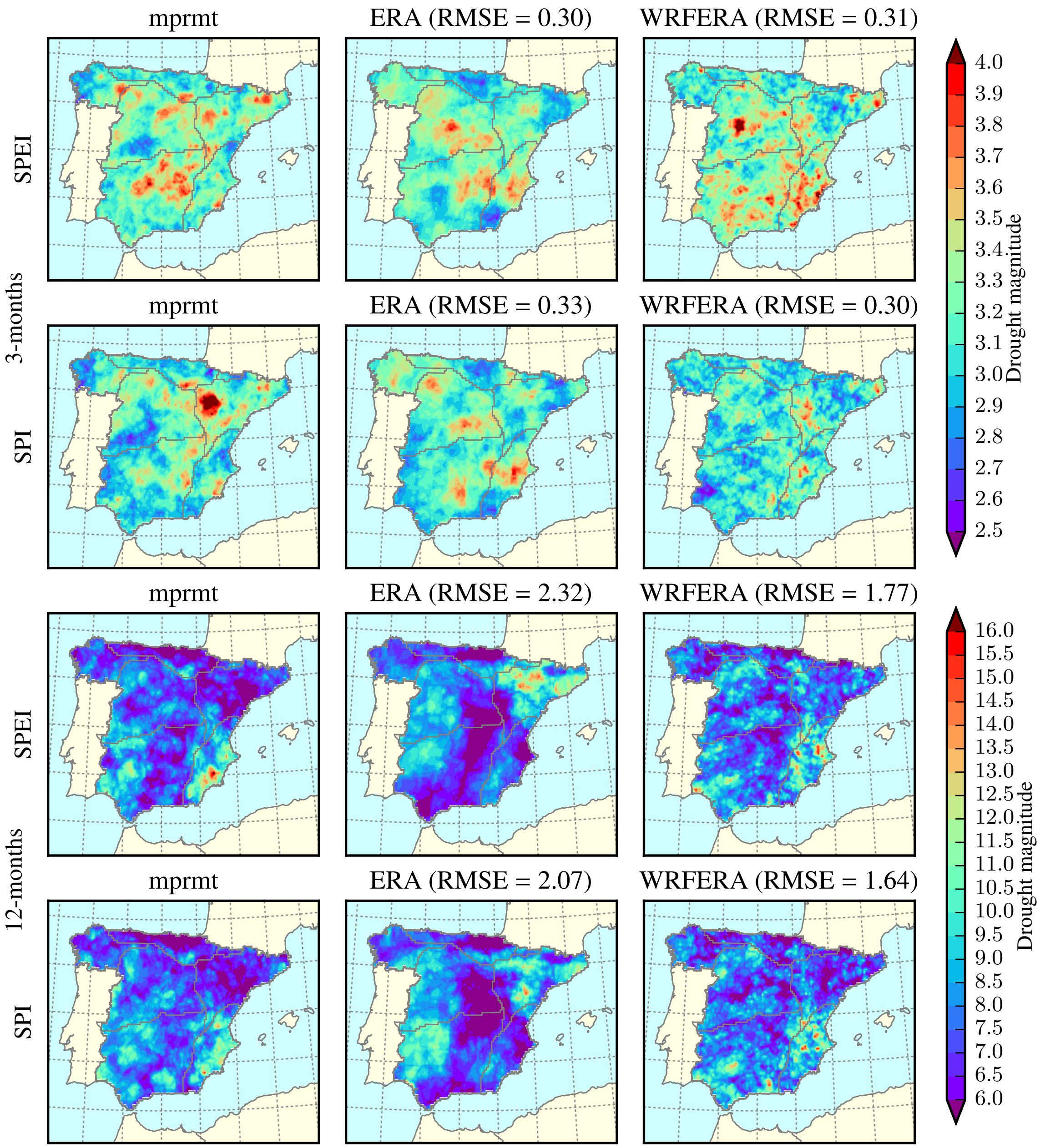

Figure 5.7: *Mean drought magnitude from the mprmt, the ERA and the WRFERA calculated for the entire period. In brackets the spatial RMSE is shown in comparison to the observations.*

even slightly worse from the WRFERA for the SPEI. However, the improvement provided by downscaled fields appeared greater when longer time scales were used, showing spatial patterns from the WRFERA at 12 months that were more similar to those from the mprmt observations, as could be seen for southern Spain for both indices.

We drew similar conclusions when the mean duration of drought events was compared (Figure ***5.8***), which presented values between 3 and 5 months and between 7 and 17 months at 3- and 12-month time scales, respectively. As for magnitude, the results from the averaged duration also suggest that although there was a moderate improvement, greater for longer time scales, the WRF did not provide clear added value with respect to its LBCs. The average drought severity (Figure ***5.9***), with values between 0.9 and 1.35 and between 0.5 and 1.5 at 3- and 12-month time scales, respectively, was overestimated from ERA simulations in most of Galicia for both indices and time scales. Nevertheless, WRF appeared to correct this inaccuracy in this area, presenting values more similar to those from the mprmt, so that the average severity in this area from the WRFERA was more similar to that found with mprmt. In general, the results suggest that the WRFERA simulations provided better results for the average drought severity, in agreement with spatial RMSE values, which was again clearer for longer time scales.

Also, the duration, magnitude and severity series at each grid point were used to compute the PSSs. Thereby, we were able to further analyze the ability of the model to represent drought characteristics through the probability distributions of duration, magnitude, and severity of drought events. In this way, authors such as Perkins et al. (2007) have pointed out that the shape of the PDF depends heavily on the interval selected, so here we used bins of 1 for duration and magnitude, and 0.5 for severity[5]. The relative differences between PSSs from the WRFERA and the ERA were also computed in order to elucidate whether the model led to an improvement with respect to its LBCs. Positive differences must be considered added value provided by the WRF model. Conversely, a negative difference means that the driving data outperformed

[5]Different bins were proved in order to elaborate the duration, magnitude and severity PDFs, providing similar results.

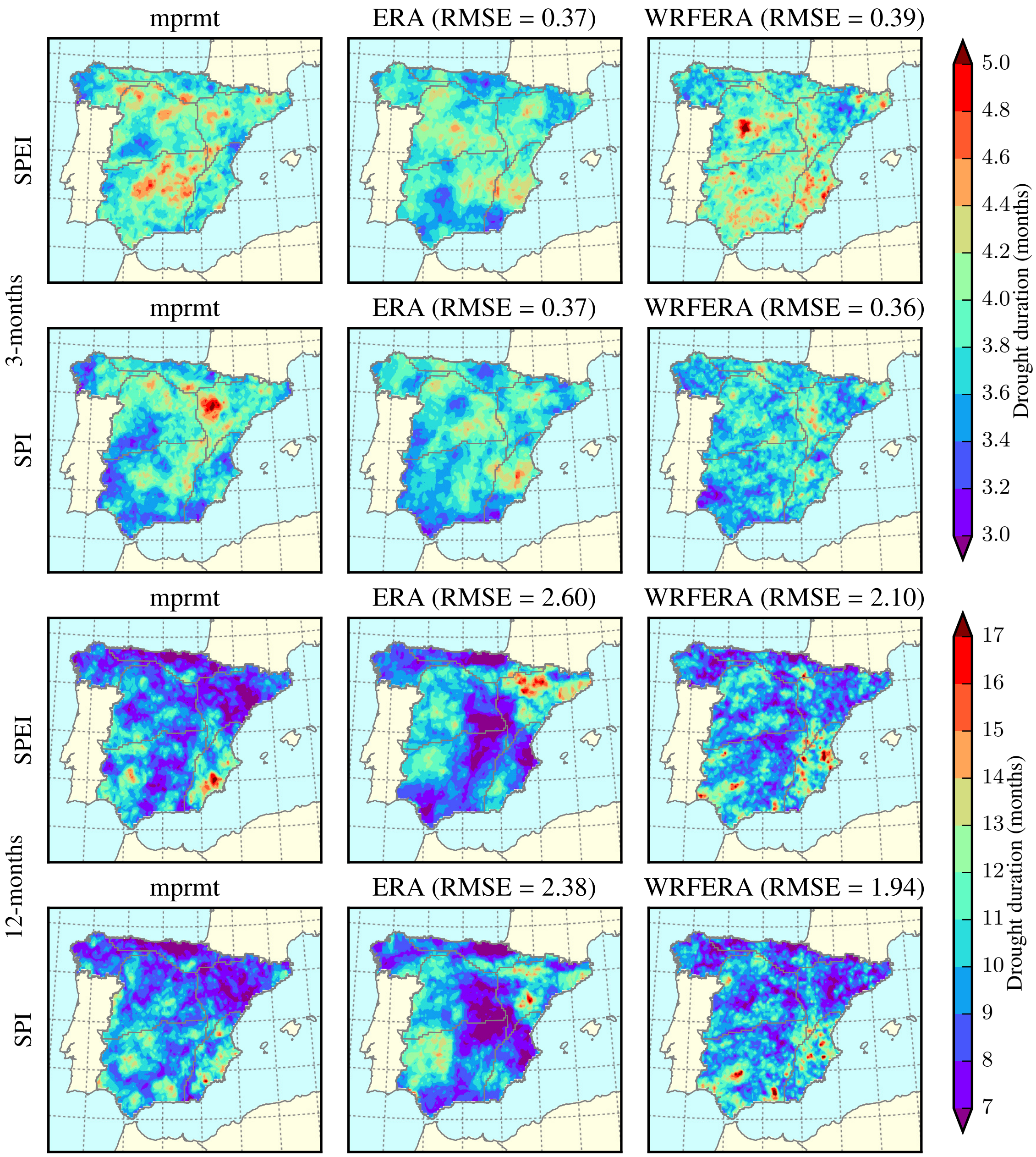

Figure 5.8: *The same as Figure **5.7** but for mean drought duration.*

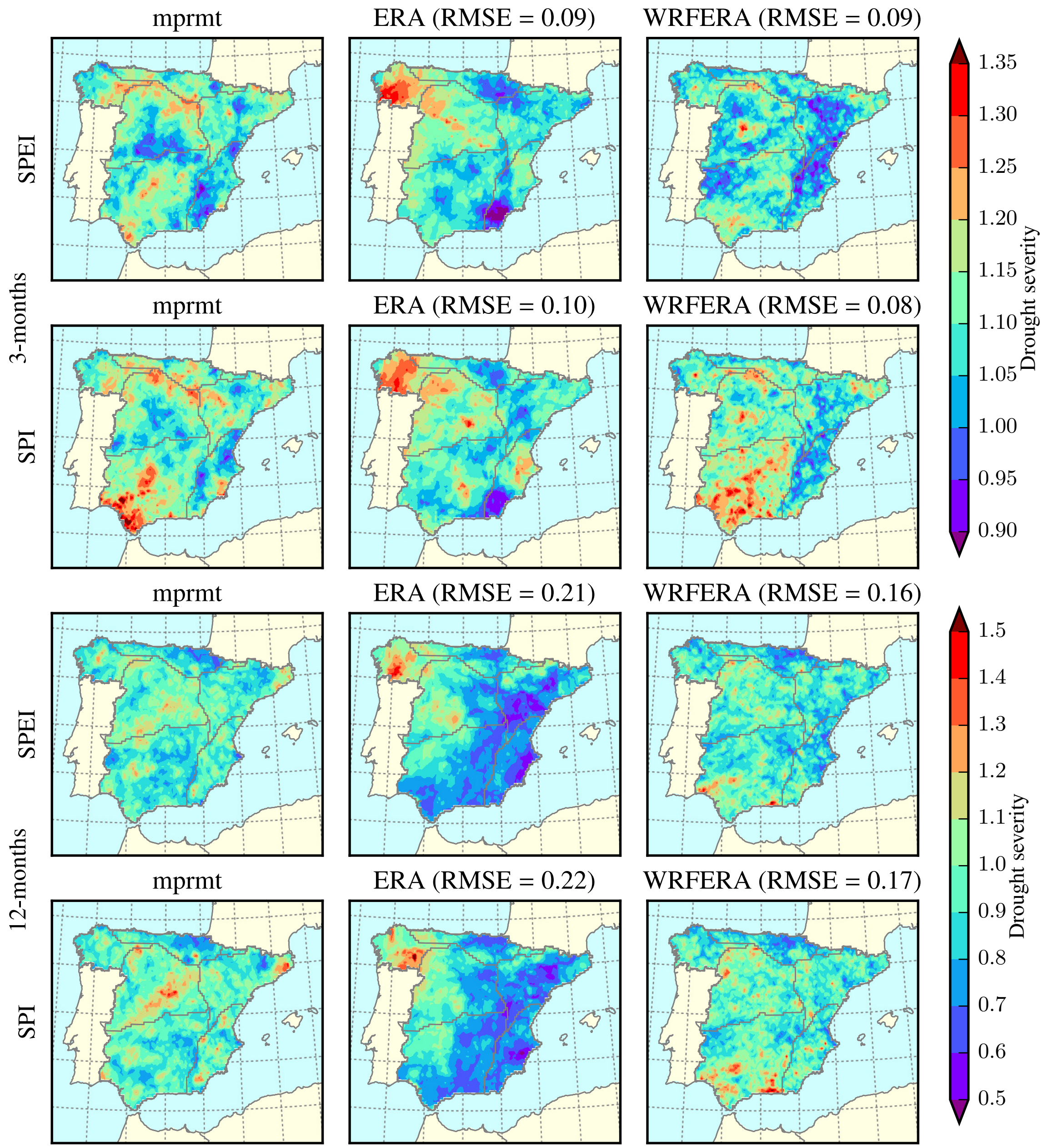

Figure 5.9: *The same as Figure **5.7** but for mean drought severity.*

downscaled fields. Furthermore, the significance of such differences at the 95% confidence level was determined using a two-proportion z-test over these PSSs differences, and thus the number of grid points with positive and negative differences as well as the average of such relative differences were computed (Table ***5.3***) in order to quantify the potential added value provided by the WRF model.

Table 5.3: *Number of grid points with significant relative differences for duration, magnitude and severity of droughts and the average of these relative differences.*

	WRFERA *minus* ERA > 0		WRFERA *minus* ERA < 0	
	No. of grid points	Average (%)	No. of grid points	Average (%)
		DURATION		
3-SPEI	229	20.54	281	17.06
3-SPI	373	21.73	236	17.25
12-SPEI	766	59.48	618	34.94
12-SPI	780	55.22	566	34.78
		MAGNITUDE		
3-SPEI	342	22.95	340	18.41
3-SPI	654	24.55	225	18.71
12-SPEI	897	60.76	803	36.85
12-SPI	842	57.13	858	36.80
		SEVERITY		
3-SPEI	612	13.09	740	11.95
3-SPI	1088	13.49	468	11.54
12-SPEI	1569	26.06	918	20.75
12-SPI	1647	24.45	930	20.86

According to the model's ability in terms of duration distribution, Figure ***5.10*** compares the PSSs for SPEI and SPI using the ERA and WRFERA with respect to mprmt (first and second columns), as well as the significant relative differences between them (third column). At the 3-month time scale, the results show that the model was reasonably successful at representing the duration distribution in many areas of Spain, the range of the values of the PSS being between 60% and 100%. However, at 12 months the ability of both the ERA and WRFERA to capture such distributions was not so evident with values of PSS of below 70%.

With respect to significant relative differences, Table ***5.3*** shows that, at the 3-month time scale, the number of grid points with positive values was greater

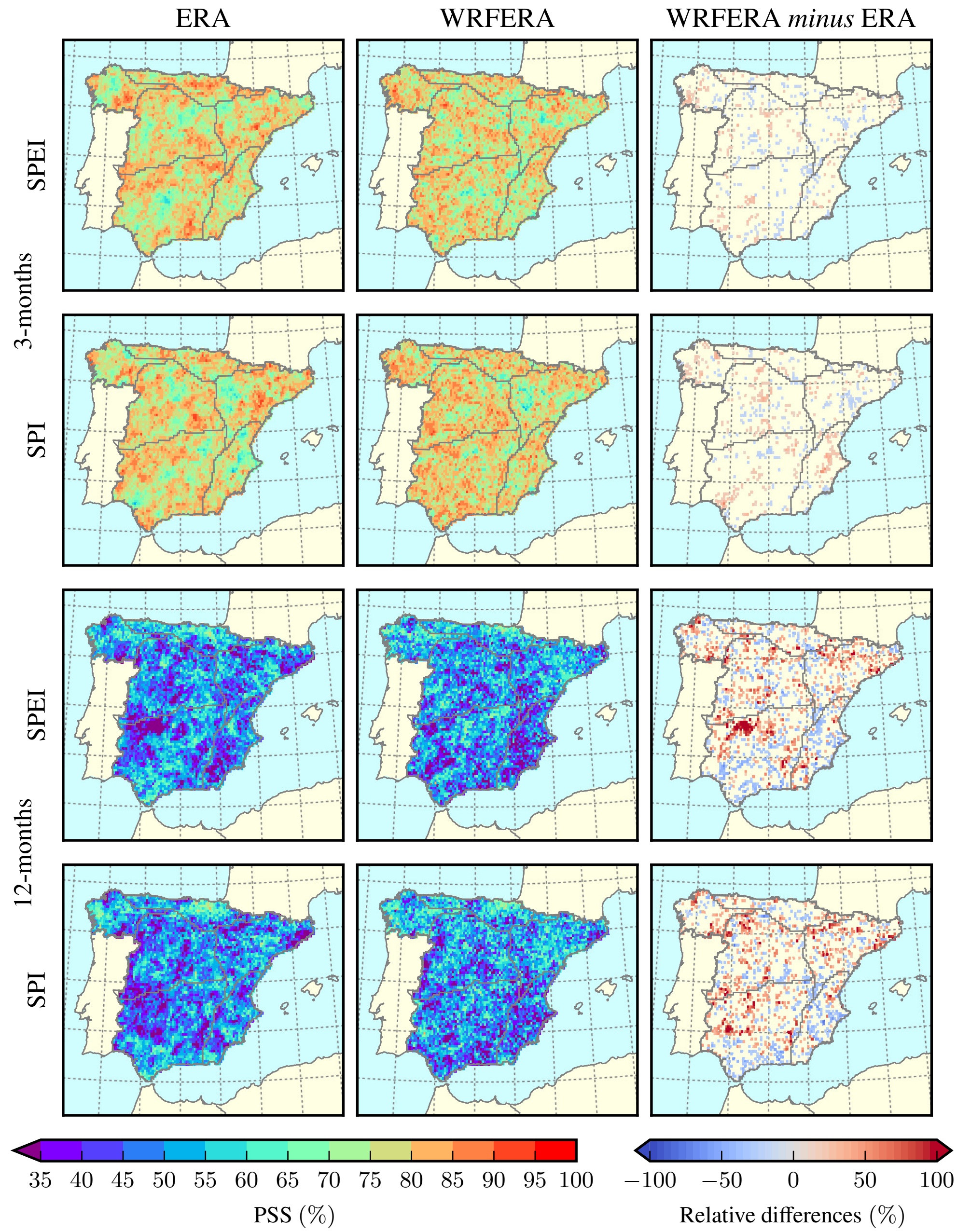

Figure 5.10: *Perkins Skill Score (PSS) in terms of the duration of drought distributions. In rows, the indices, SPEI and SPI, and the time scales analyzed (3 and 12 months). In columns, the source data (ERA and WRFERA) as well as the significant relative differences between them (WRFERA minus ERA / ERA) at the 95% confidence level according to a two-proportion z-test.*

than with negative values for SPI PSS differences. Nonetheless, for the SPEI, a contrary performance was found, and the results suggest that the duration distribution was more accurately represented by the ERA in terms of the SPEI. However, comparing the average of the relative differences, the results evidence that the added value provided by WRF was consistently higher. At the 12-month time scale, the results appear to be clearer, showing for both the number of grid points and average differences, greater added value. Therefore, these results show the benefit of using downscaled fields to detect drought-duration distribution, this being greater at longer time scales and for the SPI.

With regard to the PSS from magnitude (Figure ***5.11***), the results also display higher values at 3 months (PSSs between 60% and 100%) than at the 12-month (PSS values below 70%) time scale. Thus, the added value of downscaled fields again depends on the time scale considered. The results also show that these improvements depend on both the index and the region considered. Overall, the relative differences indicated that the added value was not obvious since the number of grid points presenting positive and negative differences were similar, except for the SPI at 3 months, which had a noticeable number of grid points with positive differences (Table ***5.3***). On the other hand, in terms of the average of the differences, the improvement was high, especially at 12-month time scales.

Figure ***5.12*** illustrates the PSSs for the distributions of the severity of drought events. Such PSSs take values of between 70% and 98% at the 3-month time scale, and between 55% and 100% at the 12-month time scale. The SPEI index showed a lower number of significant positive differences (Table ***5.3***), more evident at the 3-month time scale, whereas the SPI again gave a higher number of positive values. These differences, on average, were higher for both indices, as happened with the duration parameter, as reflected in Table ***5.3***. As for duration and magnitude, the analysis of the severity suggests that the benefit of using the WRF outputs depends on the index, time scale, and the region considered. For instance, note the high added value achieved in the northeastern region, especially remarkable at the 12-month time scale.

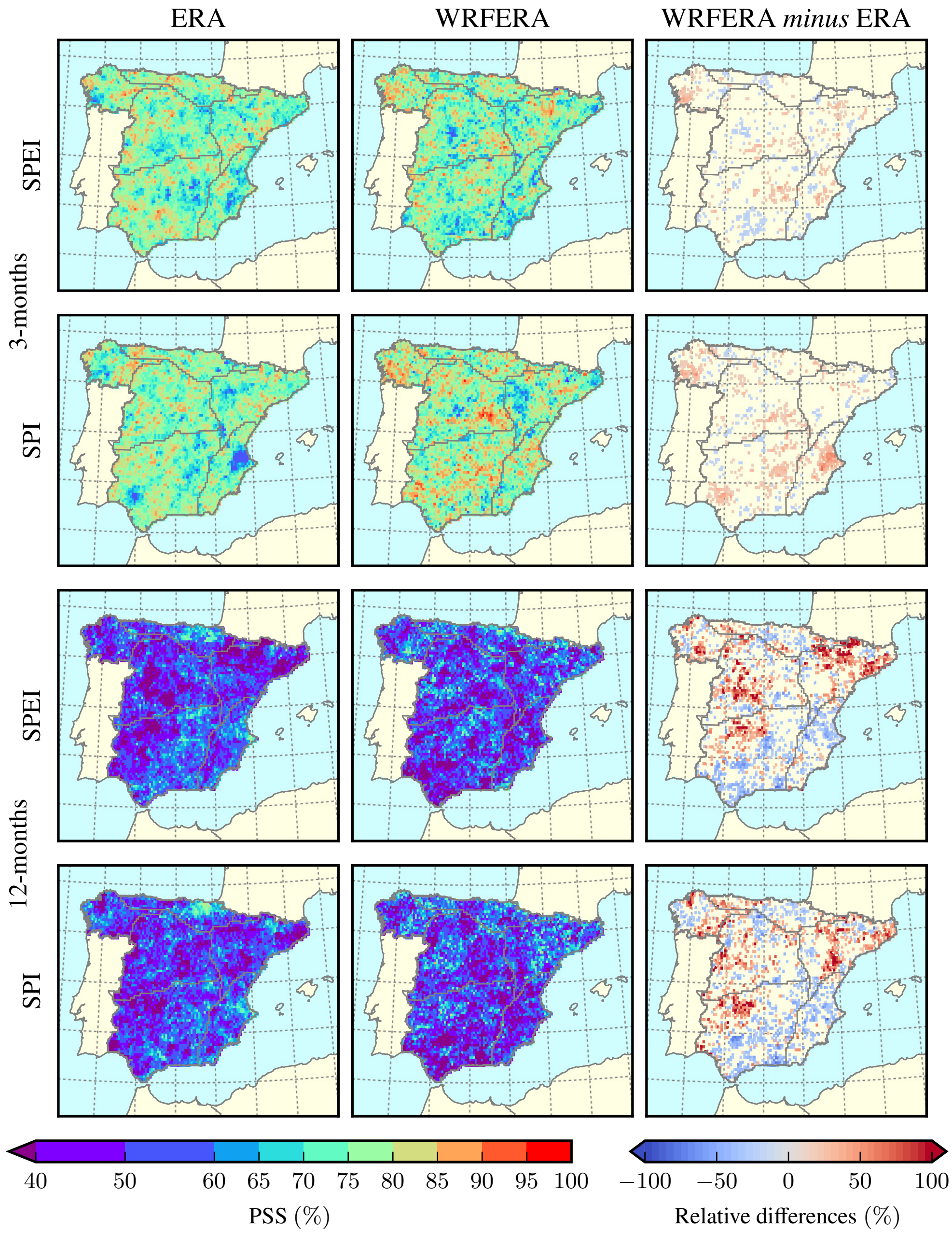

Figure 5.11: *As Figure **5.10** but for magnitude distribution.*

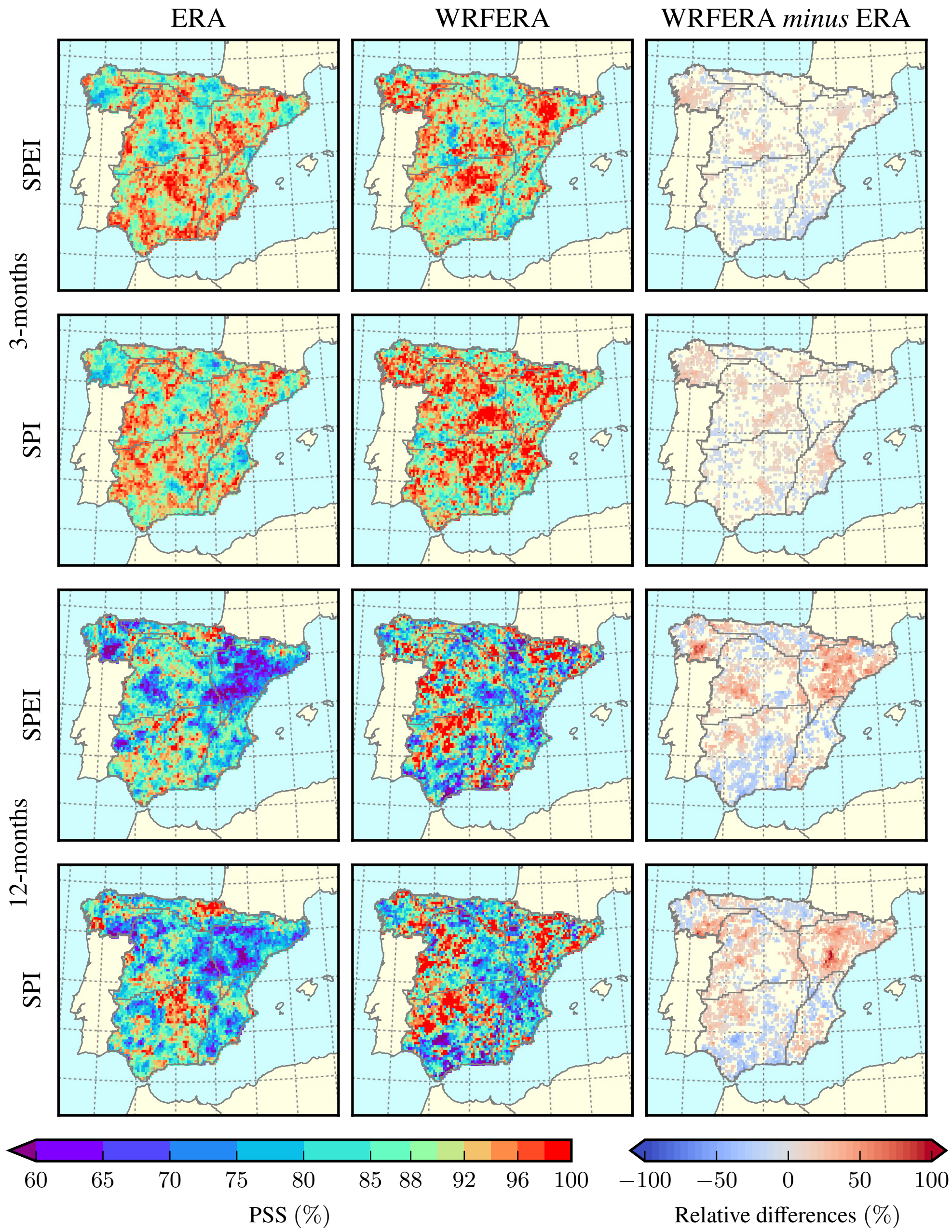

Figure 5.12: *As Figure **5.10** but for severity distribution.*

Event Evaluation Based on the SPEI and SPI

Finally, the performance of the drought indices during different extreme wet and dry periods using downscaled fields was investigated. This study is of interest because such events are associated with mechanisms in large-scale atmospheric circulation, which are already well simulated by the driving data. Thus, two different noteworthy individual wet and dry episodes were analyzed: a severe drought over the IP over 2005, and the extremely wet period in the period 2009 to 2010.

First, we focused on the severe drought episode over the IP during the year 2005. This drought episode, which began in November 2004, was considered the driest event in the last 140 years, causing historically low records for total precipitation. This intense dry event resulted from a combination of different mechanisms: a positive North Atlantic Oscillation (NAO) index between November 2004 and January 2005, followed by a negative phase of East Atlantic (EA) pattern in February, and a negative NAO phase caused by an intense and anomalous blockage displaced from its usual location from March 2005 (García-Herrera et al., 2007).

Figure ***5.13*** depicts the spatial distribution of drought indices from the mprmt, the ERA and the WRFERA corresponding to September 2005, at 3- and 12-month time scales. The correlation between patterns is displayed in brackets, showing the simple Pearson correlation coefficients with respect to those from mprmt. At the 3-month time scale (Figure ***5.13a***), although ERA reliably represented the broad pattern of drought, showing a pattern correlation of 0.44 and 0.34 for SPEI and SPI, respectively. Meanwhile WRF provided a substantial improvement, presenting higher correlations with values of 0.76 and 0.70 for the SPEI and SPI, respectively. At the 3-month time scale (Figure ***5.13a***), although ERA reliably represented the broad pattern of drought (with r of 0.44 and 0.34 for SPEI and SPI, respectively), WRF provided a substantial improvement (r values of 0.76 and 0.70 for SPEI and SPI, respectively). On the northeastern region, moderate-to-severe drought resulted from ERA drought indices (values below -1), whereas from the mprmt data normal-to-moderate wet episodes (events above 1) were found. However, the WRF correctly represented the trend of the mprmt indices values, showing that, particularly for this

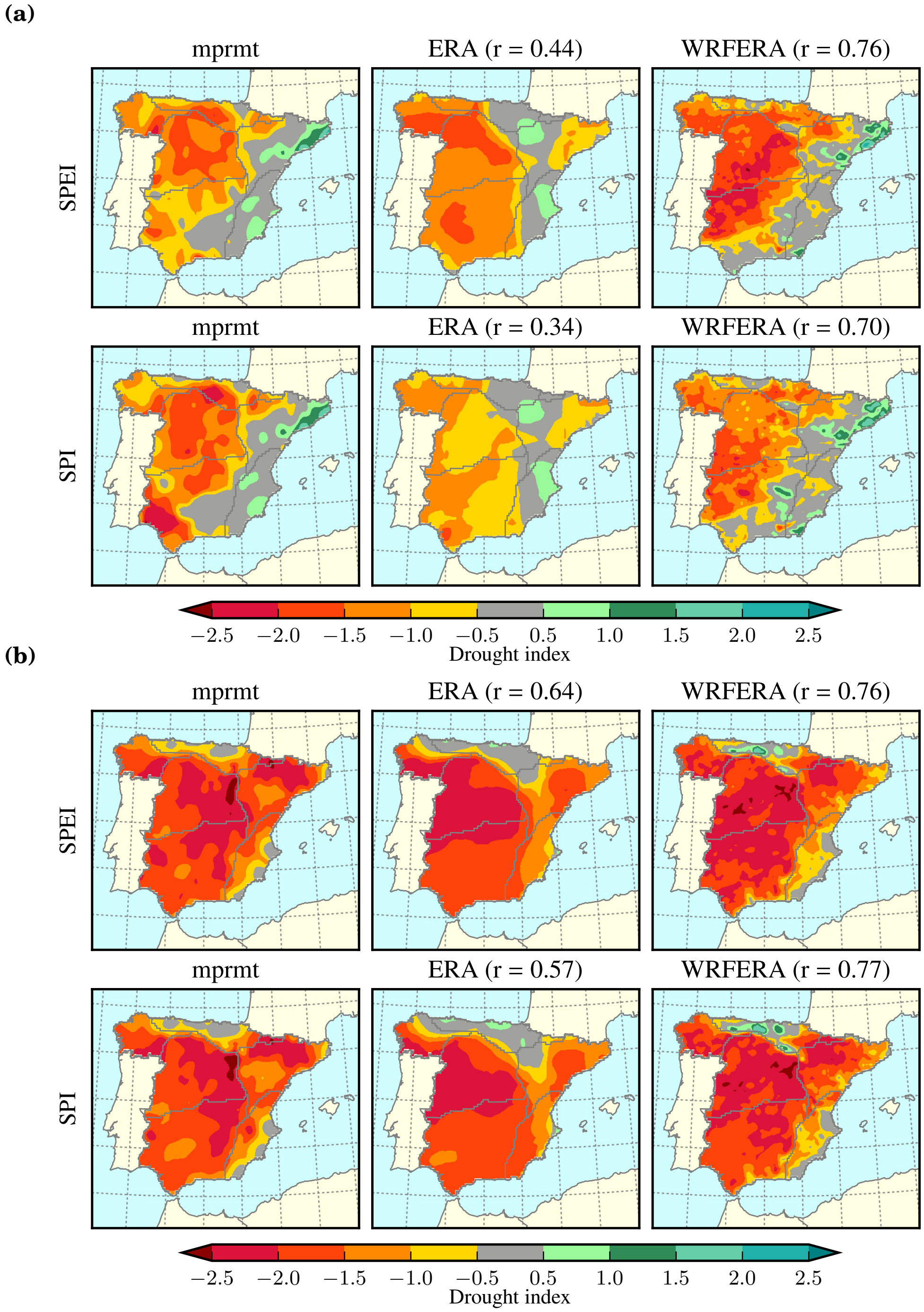

Figure 5.13: *Drought indices ending in September 2005 from the mprmt, the ERA and the WRFERA, at (a) 3-months and (b) 12-month time scales. The pattern correlations of the simulated indices values with respect to those from mprmt are shown in brackets.*

region, the model added value relative to the ERA. Furthermore, the results also show that downscaled fields properly reproduced the transition drought pattern between the Mediterranean strip and the interior Plateaus, with significant improvements with respect to the Ebro Valley. By contrast, in the southwestern region, an extreme drought was observed, which was not captured by the WRFERA at the 3-month time scale in part of the area affected.

In the comparison between the drought indices, the SPEI and the SPI showed similar drought spatial patterns, although the SPEI presents slightly higher correlation values with the observed drought event for most cases. At the 12-month time scale, both indices presented similar spatial patterns, as reflected by the Figure ***5.13b***. As expected, the ERA depicted suitable results, the pattern correlation being 0.57 and 0.64 for the SPI and SPEI, respectively. In reference to drought indices from the WRFERA, we conclude that the WRFERA offered a local improvement presenting pattern correlations of 0.76 for SPEI and 0.77 for SPI. However, on the Cantabrian region, WRF overestimated the wet conditions and represented more appropriately normal conditions over the southeastern, again showing the transition drought pattern between Mediterranean and interior. Therefore, in general, these results suggest that WRF provides an improvement with respect to its LBCs to simulate the 2005 extreme drought event at local scales.

In addition to evaluate the WRF capability of representing extremely wet periods, we also assessed the representation of the drought indices during a highly wet event. The extremely wet period selected was the winter of 2009/2010. This event was characterized by one of the most extreme negative NAO phases during the last 150 years, triggering the highest total amounts of winter precipitation in the IP, as is illustrated in Vicente-Serrano et al. (2011b).

Figure ***5.14*** shows the drought indices calculated ending in March 2010 at the 3-month time scale (Figure ***5.14a***) and those corresponding to November 2010 at the 12-month time scale (Figure ***5.14b***). At 3 months, the ERA and WRFERA agreed well with respect to general observations. Again, the WRFERA d this wet episode better than did the ERA alone, for both 3- and 12-month time scales, for most of Spain, this performance being markedly better at 3 months, with pattern correlations of 0.74 and 0.75 for SPEI and SPI,

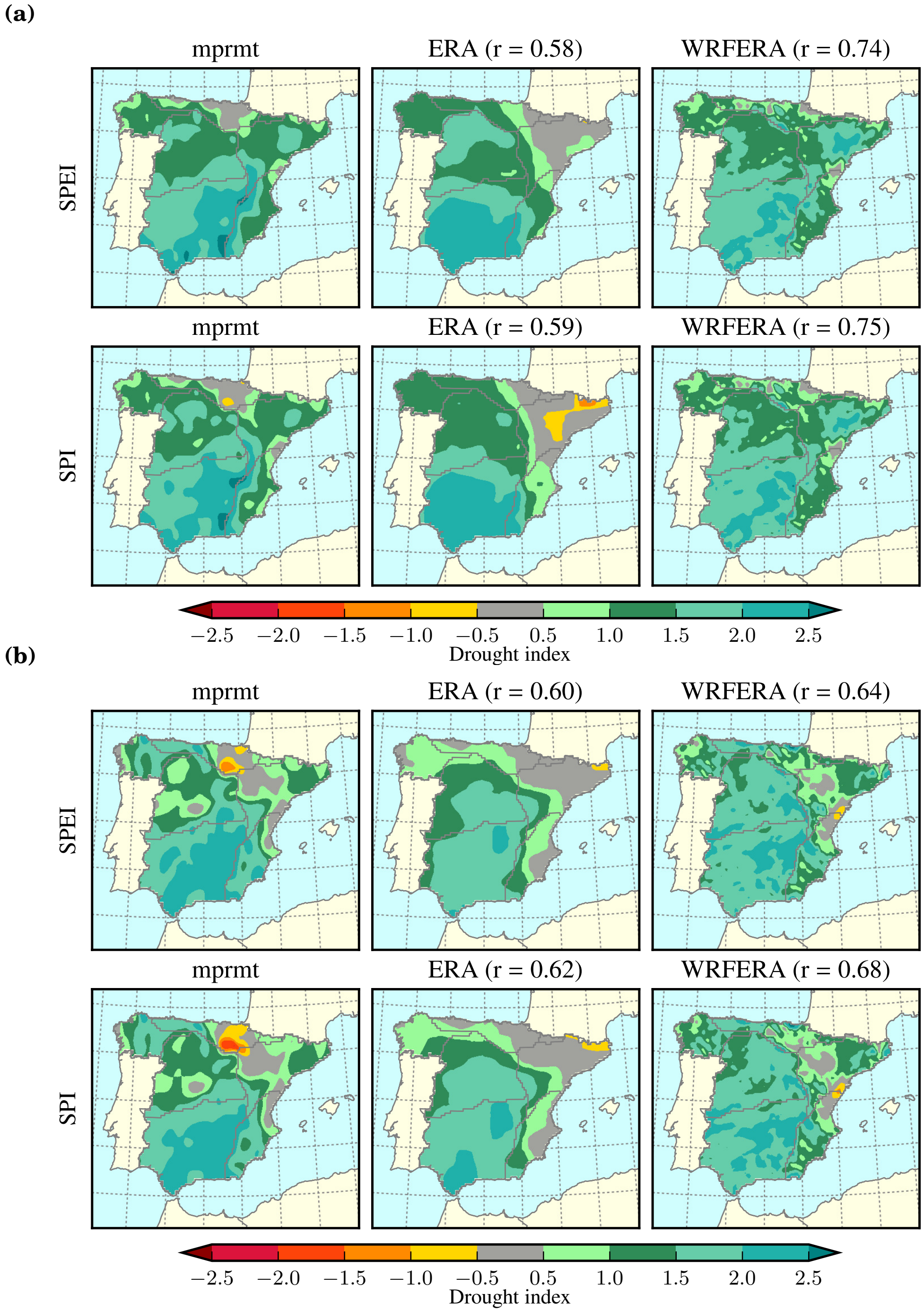

Figure 5.14: *Drought indices from the mprmt, the ERA and the WRFERA, ending in (a) March 2010 at the 3-month time scale and (b) November 2010 at 12-month time scales. The pattern correlation values of the simulated indices with respect to those from the mprmt are shown in brackets.*

respectively, vs. 0.58 and 0.59 from ERA, for SPEI and SPI, respectively. The WRFERA was able to suitably represent the wet pattern along the northwestern region, using both indices. Nevertheless, some errors persisted, such as the overestimation in the Ebro Valley and the underestimation in the south. For this wet episode in particular, the SPI appeared to moderately outperform the SPEI. As for the 3 months, the 12-month time scale showed similar performance, although shortcomings were found over the Cantabrian region for the WRF simulations. Differences between ERA and WRFERA were smaller than at the 3-month time scale, as reflected by the pattern correlations.

5.4. Discussion and Conclusions from WRF Drought Characterization

In this chapter, the primary climate variables from WRF were used to assess the model's ability to simulate wet and dry periods using two drought indices, i.e. the SPI and the SPEI. These different indices were used in order to confirm whether the model provides a suitable characterization in terms of drought events for an index that is based solely on precipitation values, but also for an index that takes into account the temperature through the calculation of the potential evapotranspiration. Additionally, this study analyzes the characterization of drought using the driven data (ERA-Interim), and thus is able to quantify the added value offered by the WRF model to detect, analyze and monitor droughts at the local scale.

Due to the multi-scalar character of the indices used, the study was performed using to different time scales, i.e. 3 and 12 months, which are useful to study meteorological and hydrological droughts, respectively. The comparison between indices, time scales, and source data was performed using two different approaches, the analysis at the regional scale and the local analysis. The main conclusions are:

- The simulations from WRF generally captured reasonably well the time evolution of droughts in Spain, showing reliable temporal correlations. These results were consistent with previous studies. Similarly, Barrera-Escoda et al. (2014) and Maule et al. (2013) found the adequate performance of different RCMs in terms of drought characteristics for different regions of Spain. Furthermore, they also found that the results from using downscaled fields outperformed those from the driving data, this improvement being greater for the SPI than for the SPEI. These results suggest that the dynamical downscaled fields could provide more reliable climate projections when assessing future drought episodes, at least in topographically complex regions such as Spain.

- At the regional scale, the added value offered by WRF was strongly influenced by the time scale used, the influence being greater at longer time scales. These results suggest that the added value provided by the WRF appeared to be highlighted particularly in a context of water resources. These results agree with the findings of Bowden et al. (2016), who have assessed the improvements provided by regional modeling to detect wet and dry periods over the United Stated using the SPI.

- Concerning the study at the local scale, the results from the analysis of the RMSE and CSI agree with the results at the regional scale. These parameters broadly show the improvements achieved by using WRF, and the influence of the time scale used, with better results at the 12-month time scale. Moreover, RMSE values reflect worse agreement of drought indices simulated with respect to the mprmt in the northeastern and southeastern regions, but better agreement was found in the southern and interior regions, which was also in accordance with the regional study. The strongest improvements provided by WRF were for the regions that presented the worst results from ERA. By contrast, the CSI analysis also showed some areas where WRF provided no added improvement, and thus this trend suggests that ERA fields already resolved well in terms of drought events in some areas of Spain.

- Drought indices computed from the ERA and the WRFERA showed difficulties representing the duration, magnitude, and severity of drought events, with worse agreement in relation to the observations at the 12-month time scale, as indicated by higher spatial RMSE values in most of these parameters and for the analysis in terms of the PSS. These results partially agree with the works of PaiMazumder and Done (2014) and PaiMazumder et al. (2013), who found that an ensemble of the Canadian RCM presented problems in representing the severity, frequency, and duration events across Canada by using different drought indices, particularly those associated with long-term events.

- This study also demonstrates that there was no substantial difference between the SPEI and the SPI in the evaluation of the ability of the WRF model to simulate droughts in Spain. Although the improvement provided by the WRF model with respect to ERA data was higher for the SPI than for the SPEI simulations, the SPEI appeared generally to provide slightly better results detecting wet and dry periods.

In summary, the results of this study show the benefit of using the WRF model to simulate downscaled fields for drought studies in peninsular Spain, emphasizing the importance of the valuable information gathered at a local spatial scale, particularly relevant for drought-related decision making. The findings presented here provide valuable information concerning the validation of using the WRF model for further studies on drought projections in a climate-change context.

Chapter 6

High-resolution Projections over the Iberian Peninsula

This chapter is devoted to examining climate changes projections over the IP by using WRF high-resolution climate fields. The WRF setup applied to carry out future simulations has been already proved to suitably perform the current climate characteristics as was shown in Chapter ***4***, so it is susceptible to be used to project the regional climate in this region. The variables here examined are the precipitation and the maximum and minimum temperature (T_{max} and T_{min}), primary climate variables that are key factors in the occurrence of drought phenomenon.

6.1. Description of the Future Climate Analysis

6.1.1. Future Climate Simulations

A set of 30-year simulations has been performed with WRF in order to elucidate possible changes in the future climate. For that purpose, two different periods have been selected, the denominated near future, which is considered as the period that covers from 2021 to 2050, and the far future, i.e. the period corresponding to 2071-2100. Thus, by comparing these two periods we can examine trends in the so-called primary climate variables. All runs were simulated using an identical configuration, except for the LBCs which was detailed in Chapter ***3***. To this end, the outputs from two different GCMs were chosen, the CCSM4 and the MPI-ESM-LR, which have been previously corrected in bias with the purpose of reducing uncertainties associated to systematic errors in the LBCs.

In order to consider the effects in the climate system of different radiative forcings, the comparison between the results from two different RCPs was also performed. Such scenarios correspond to one of intermediate emissions or scenario of stabilization, the RCP4.5, and a scenario that contemplates a future with high GHG emissions, the RCP8.5. In fact, differences between these scenarios may help to elucidate how the induced global warming would affect to these variables, which are implicated in the hydrological cycle.

6.1.2. Description of the Analysis

Future changes in precipitation and temperatures have been examined by comparing the projections from the different WRF simulations with their corresponding current runs through the Delta-change approach (Hay et al., 2000). This method assumes that to adequately analyze future values, relative changes instead of absolute values must be used. In this context, relative values are the difference between the future results (2021-2050 and 2071-2100) and those from the historical period (1980-2014). Thereby, current and future errors should be compensated through the difference between them. The projected changes thus computed were examined at different time aggregations (from annual to daily). That is, evaluating annual and seasonal values we can analyze the changes in long-term mean values, while with daily values we can characterize possible changes in terms of extremes In fact, the shift to a different mean state might lead to important damages in ecosystems that have adapted to a particular climate during hundred to thousand years (Rökstrom et al., 2009). On the other hand, changes in extreme values cause tremendous impacts on the society and the environment, which are even more relevant (Easterling et al., 2000).

Most of these analyses have been performed directly comparing grid-points, with the purpose to prevent possible compensation errors due to the smoothing effects of averaged spatial values. Thus, the projections were analyzed through the original rotated nested domain of 0.088° (~10 km) of spatial resolution, avoiding possible errors due to interpolation methods. However, there are assessments that need some spatial aggregations in order to facilitate the interpretation of the results. To this end, the different variables were spatially aggregated using the main river basins of the IP, since one of the main purposes is to analyze the impact of climate change in terms of hydrological variables.

Here, 12 different river basins have been considered. Such basins are the results of aggregating other smaller watersheds in some cases (Figure ***6.1***), which are: North Atlantic (composed by the Galician Coast, Western Cantabrian and Eastern Cantabrian watersheds), Miño-Sil (Miño-Sil, Cávado, Ave and Leça), Duero, Ebro, Northeastern Basins, Portugal Basins (Vouga, Mondego, Lis and Riveiras do Oeste), Tajo, Southeastern Basins (Júcar and Segura), Guadiana (Guadiana, Sado, Mira and Ribeiras do Algarve), Guadalquivir (Guadalquivir, Tinto, Odiel, Piedras, Guadalete and Barbate), Southern Basins and finally the Balearic Islands watersheds.

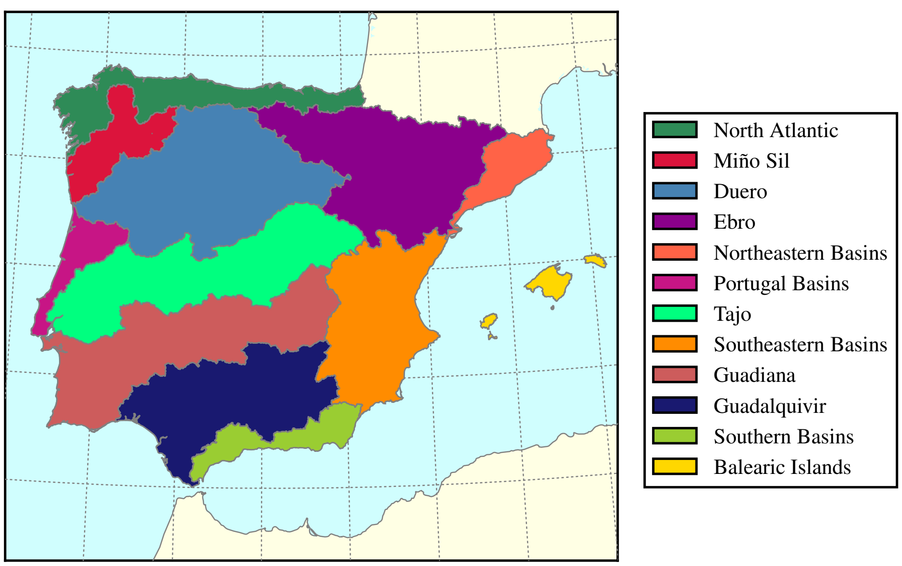

Figure 6.1: *Main river basins of the IP.*

To determine the significance of the changes, different statistical tests have been used. In the one hand, parametric statistical tests such as the two-tailed Student's t test and the Fisher-Snedecor F test were applied since in most of the grid-points the distributions of the annual and seasonal amount of precipitation, as well as the maximum and minimum temperature, are normally distributed according to a χ^2 test. The use of parametric tests has been selected because these are statistically more powerful. Additionally, a two-tailed Mann-Whitney-Wilcoxon U test was used to ensure the significance results, and also for those parameters that are not normally distributed. All these tests were evaluated at 95% confidence level.

6.2. Precipitation Projected Changes

6.2.1. Changes in Annual Values

In terms of annual mean precipitation, Figures ***6.2*** and ***6.3*** depict the projected changes for the near (2021-2050) and far (2071-2100) future, respectively, in relation to the present (1980-2014), for the simulations driven by the two GCMs and under the two RCPs. The changes are expressed in percentage, i.e. differences between the future and current amount of precipitation and divided by present values. No significant changes according to a two-tailed Student's t test[1], are marked with black dots. Figures also depict the historical (1980-2014) mean values for each GCM-driven simulation because although this is out of the Delta-change method context, can be useful to elucidate the importance of the changes.

For the near future (Figure ***6.2***), all WRF simulations fundamentally projected decreases of the mean annual precipitation, being, in any case, the significant differences only negative. In the comparison between the different driving data, the WRFCCSM simulation showed small areas with significant changes in both RCPs, meanwhile for the WRFMPI larger areas with substantial changes were found, particularly under the higher emissions pathway. Here, diminutions up to 25% are found in the southern half of the Peninsula.

Concerning the results for the far future (Figure ***6.3***), the diminution was more remarkable than for the previous period, with values of change ranging from -47% to 9%. Both the WRFCCSM and the WRFMPI revealed a similar

[1]Additionally, a two-tailed Mann-Whitney-Wilcoxon U test was used showing very similar results.

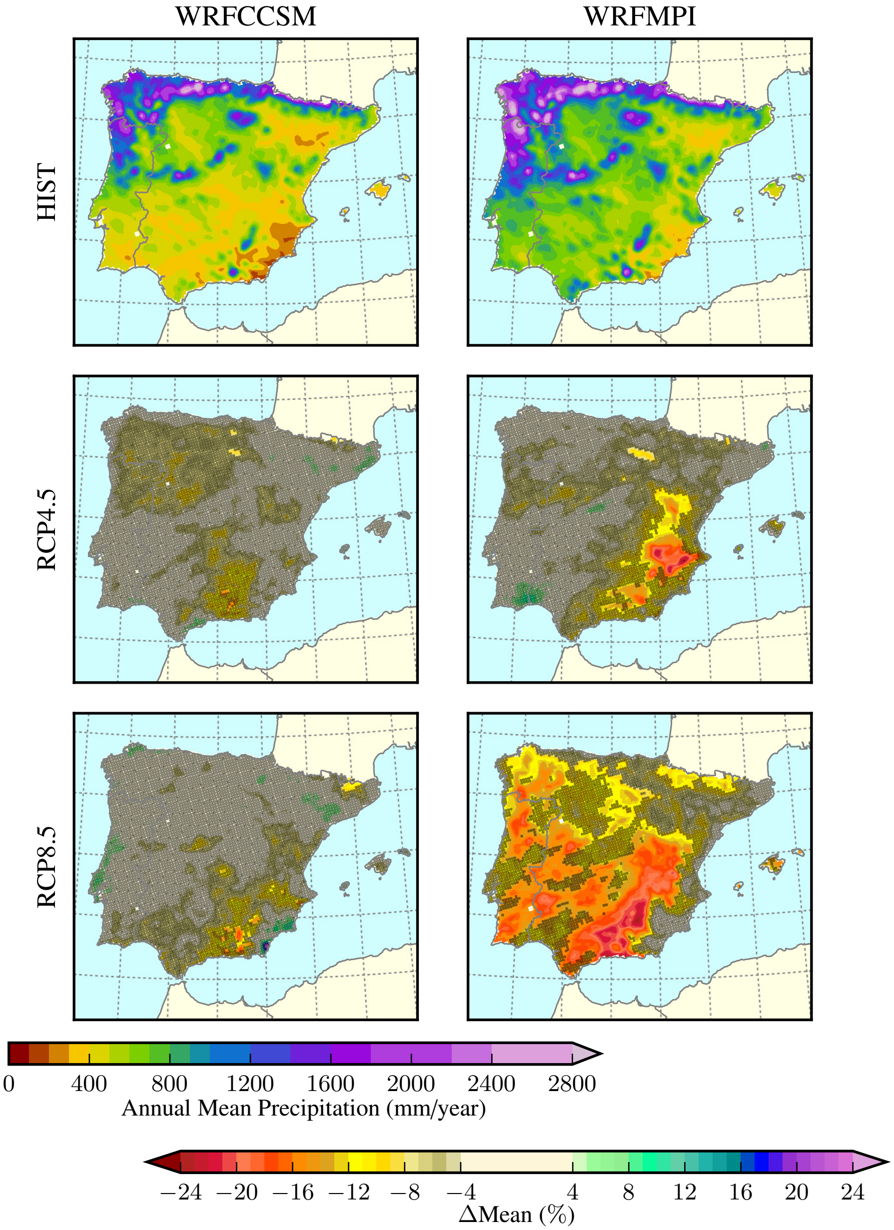

Figure 6.2: *Current (1980-2014) annual mean of the amount of precipitation (first row) and the near future (2021-2050) projected changes (second and third rows) for both RCP 4.5 and RCP 8.5 expressed in relative terms. In columns, the projections from the simulations driven by CCSM4 and MPI-ESM-LR. Black dots indicate non-significant changes according to a two-tailed Student's t test at the 95% confidence level.*

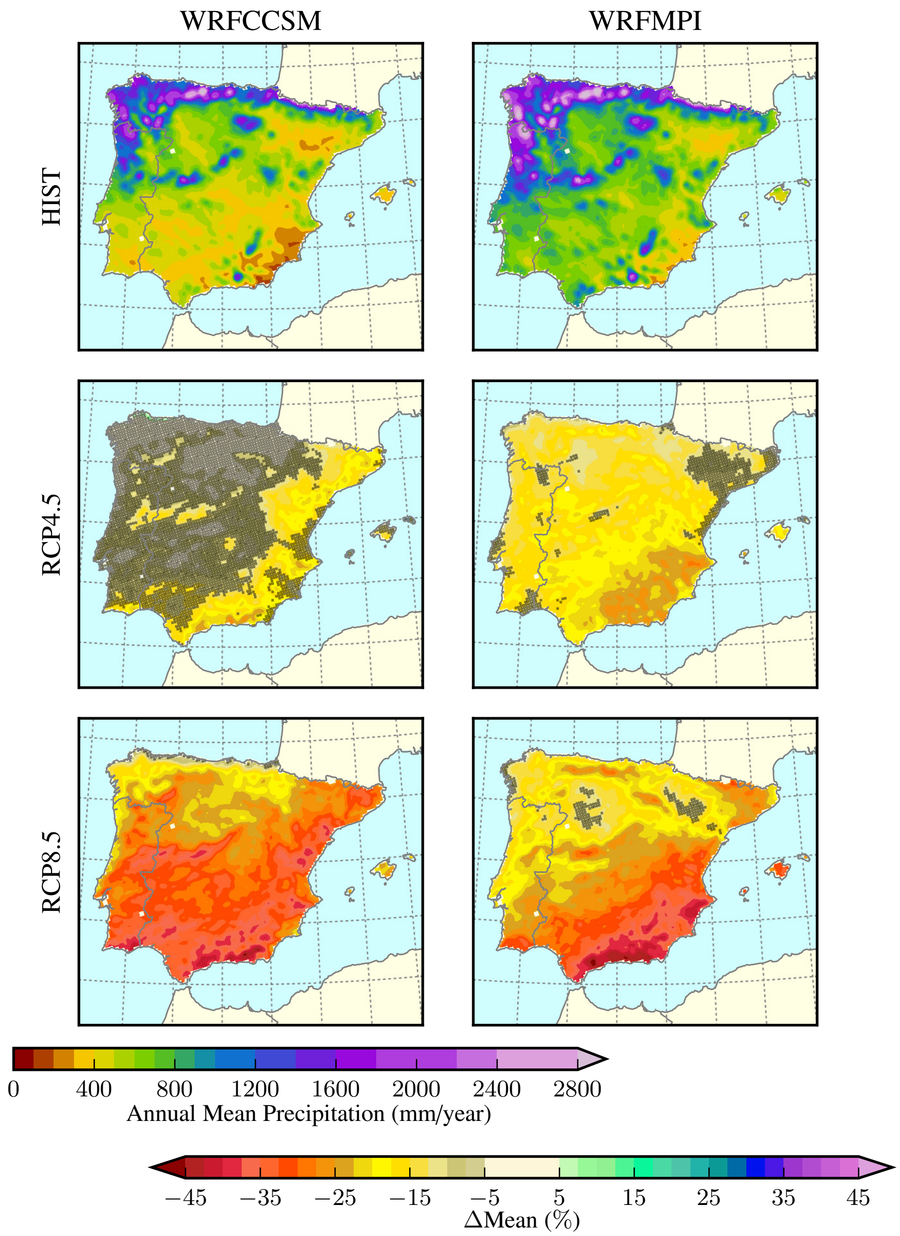

Figure 6.3: *As Figure **6.2** but for the far future (2071-2100) projected changes.*

response in reference to the GHG emissions, appearing the strongest reductions for the RCP8.5. Thus, the WRFCCSM under the RCP4.5 projected decreases up to 30% over the southeastern IP and showing an important number of grid-points with non-significant changes. However, for the RCP8.5 substantial decreases were shown appearing values below -45% over the south. On the other hand, projections from the simulations forced by the MPI-ESM-LR suggested generalized decreases of the mean annual precipitation practically over the entire IP for both RCPs, with the largest decreases in the south and especially over the southeast of the Peninsula (values below -25% and -45% for the RCP4.5 and RCP8.5, respectively).

Thus, changes in annual values have revealed important decreases in the amount of the precipitation in many areas of the IP, but such changes may be differently distributed along the year. For this reason, a further analysis was performed and the projected changes have been also examined at seasonal time scale. Thus, the amount of precipitation of both, current and future simulations, were aggregated for winter (DJF), spring (MAM), summer (JJA) and autumn (SON).

6.2.2. Changes in Seasonal Values

For the near future (2021-2050), the seasonal mean precipitation projects both increases and decreases depending on the driving data, season, scenario and region. Figure ***6.4*** and Figure ***6.5*** depict these results from the WRF simulations driven by the CCSM4 and the MPI-ESM-LR, respectively. Such changes (values range between -50% and above 70%), however, are not significant in many cases.

In winter, the WRFCCSM (Figure ***6.4***, DJF) presented an important extension with increases in precipitation although these were only significant over the northeastern peninsular. In this context, the largest enhancements appeared over Castellón and Girona (values above 70%) under the RCP4.5. The WRFMPI simulation (Figure ***6.5***, DJF) projected even fewer areas with significant changes, being the largest increases of about 45% under the RCP8.5. For this latter simulation, however, reductions were also shown but again these were mostly non-significant.

The most substantial changes for the near future were projected in spring at least for the RCP8.5. Here, WRF projected fundamentally decreases with values ranging from -10% to -50%. Under the RCP4.5, the WRFCCSM (Fig-

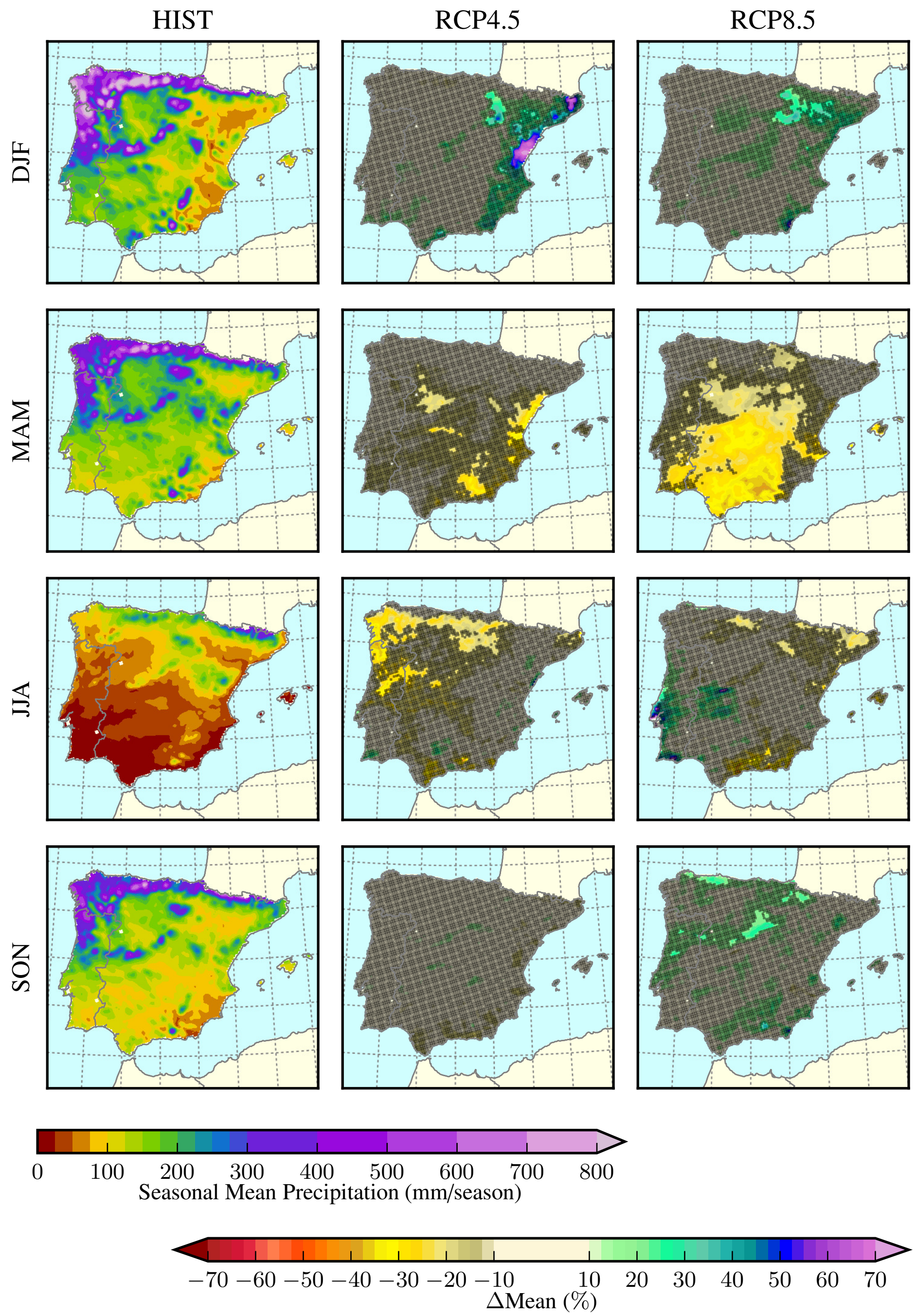

Figure 6.4: *Current (1980-2014) seasonal mean of the amount of precipitation (first column) and the near future (2021-2050) projected changes for the WRFCCSM simulations expressed in relative terms. In second and third columns, the results from the RCP4.5 and RCP8.5 are shown respectively. Black dots indicate non-significant changes according to a two-tailed Student's t test at the 95% confidence level.*

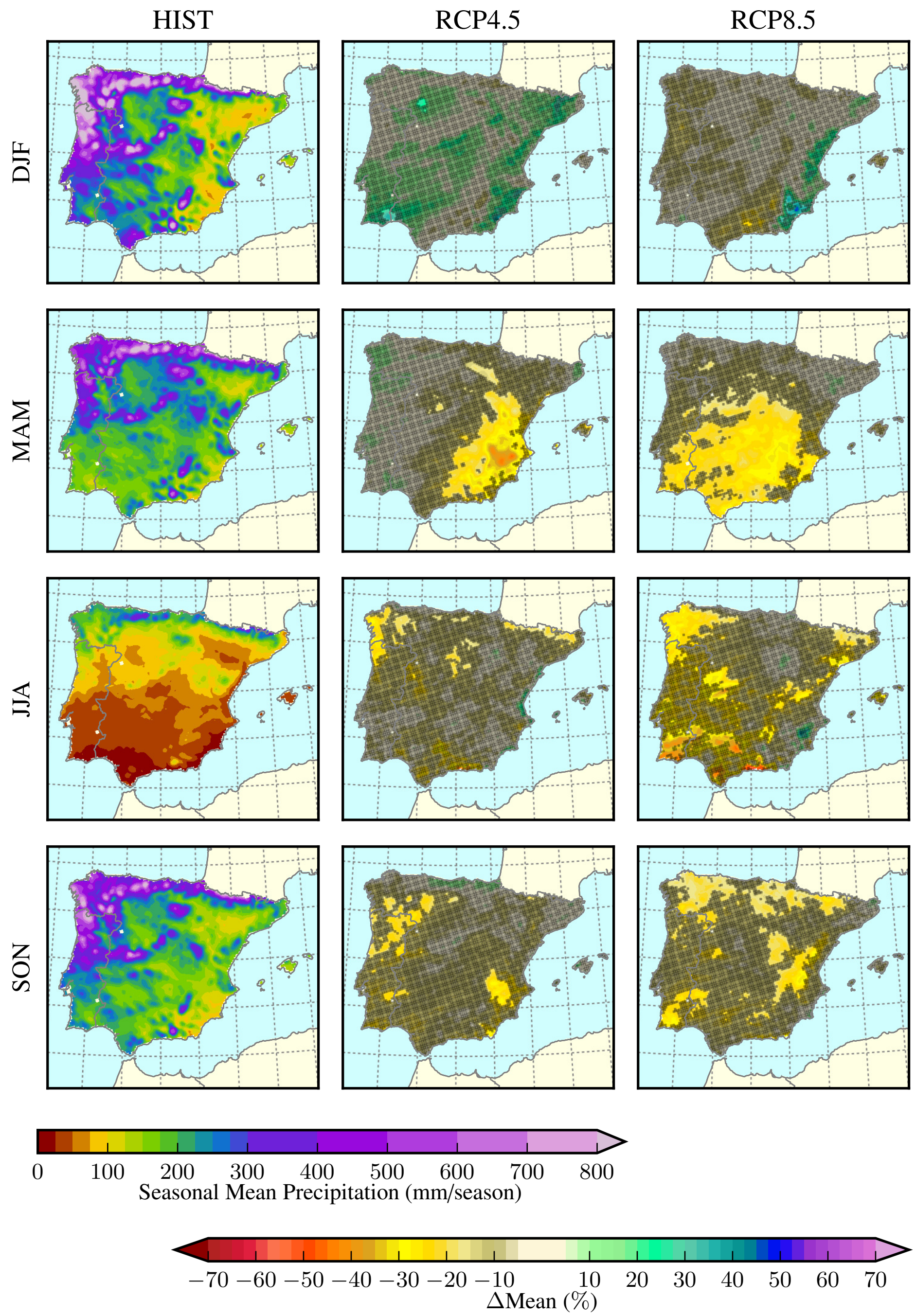

Figure 6.5: *As Figure **6.4** but for the WRFMPI simulations.*

ure ***6.4***, MAM) revealed significant decreases up to 30% throughout part of the northeast Coast, over the Baetic System and in certain areas on the Northern Plateau, whereas diminutions up to 40% were presented in most of the southern half of the Peninsula, Balearic Islands and over certain areas in the northern peninsular (Bay of Biscay) for the RCP8.5. The WRFMPI (Figure ***6.5***, MAM), however, localized the main spring changes in the eastern peninsular with values up to -50% for the intermediate emissions scenario and covering a similar broader extension to WRFCCSM for the high emissions scenario.

For summer, although both the WRFCCSM and WRFMPI projected increases and decreases, most of the significant changes being reductions (Figures ***6.4*** and ***6.5***, JJA). In this sense, although with certain differences, both the WRFCCSM and WRFMPI locate severe diminutions in the north of the Peninsula for the two RCPs, arising values between about -20% and -45%. The highest significant decreases were projected over some areas in the south of the IP in the WRFMPI and under the RCP8.5, reaching 50% of reductions regarding present values (Figure ***6.5***, JJA). Concerning the changes projected for autumn, the CCSM4-driven simulations only showed significant changes under the RCP8.5 (Figure ***6.4***, SON), when the precipitation was projected to increase in certain areas of the north of the Peninsula. The WRFMPI (Figure ***6.5***, SON), by contrast, showed very different results with reductions (values of around 10-30%) over different parts of the IP and for both RCPs.

Larger areas with significant changes were projected for the far future (Figures ***6.6*** and ***6.7*** for the WRFCCSM and the WRFMPI, respectively), with changes mainly between -70% and 46%. In general, this period showed a larger difference between scenarios with more substantial changes for the RCP8.5. In winter, as in the near future, increases and decreases appeared (Figures ***6.6*** and ***6.7***, DJF) although the significant changes still covered small areas, except for the WRFMPI simulation under the RCP8.5 (Figure ***6.7***, DJF). In this latter, only significant decreases were found, which were mainly located in southeastern and eastern (Cape of the Nao) regions, Balearic Islands and over mountain regions such as the Cantabrian Range, Central System and certain areas of the Iberian System, reaching values up to -50% in some cases. Substantial reductions were shown in spring (values between -15% and -60%), where projections

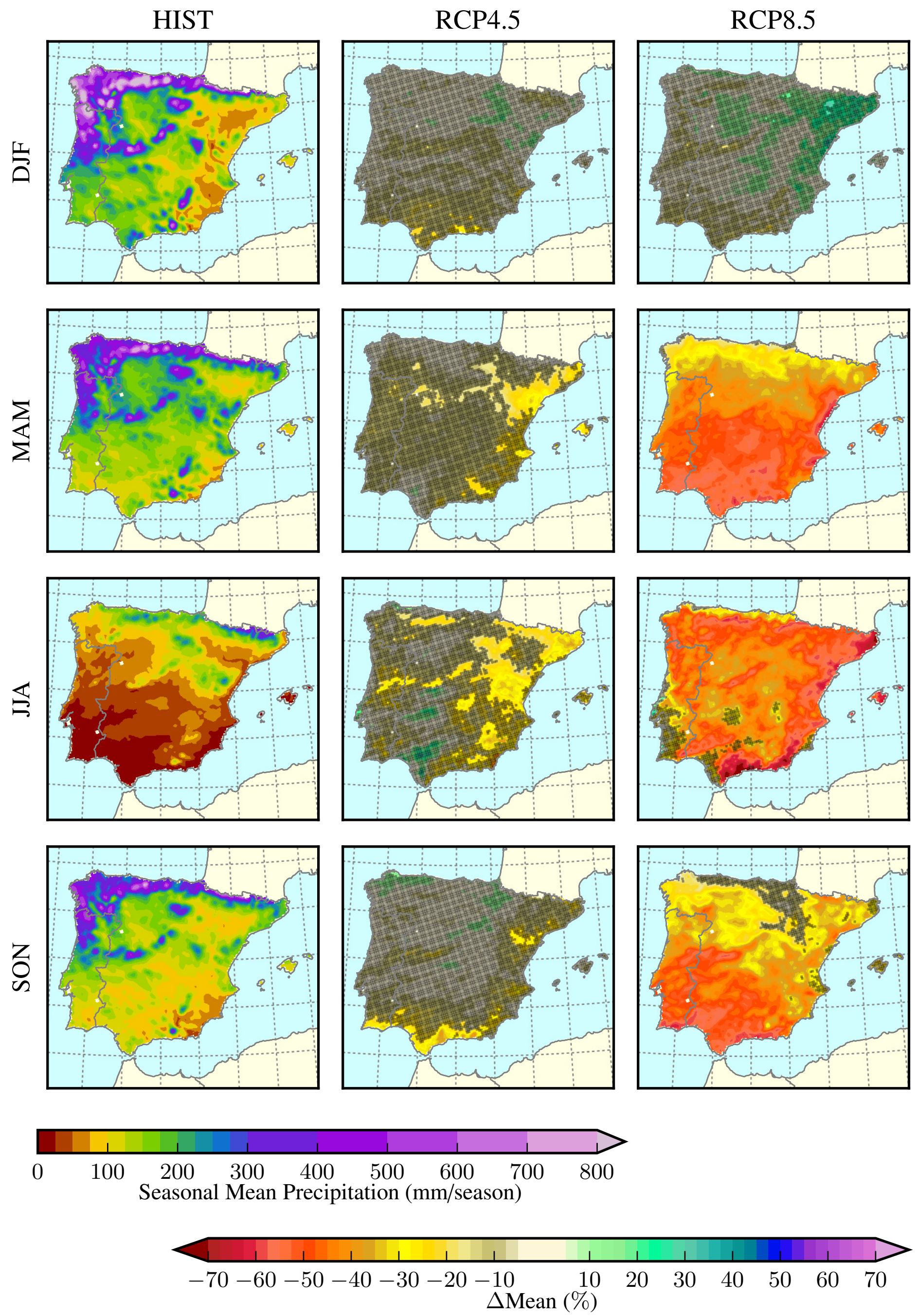

Figure 6.6: *Current (1980-2014) seasonal mean of the amount of precipitation (first column) and the far future (2071-2100) projected changes for the WRFCCSM simulations expressed in relative terms. In second and third columns, the results from the RCP4.5 and RCP8.5 are shown respectively. Black dots indicate non-significant changes according to a two-tailed Student's t test at the 95% confidence level.*

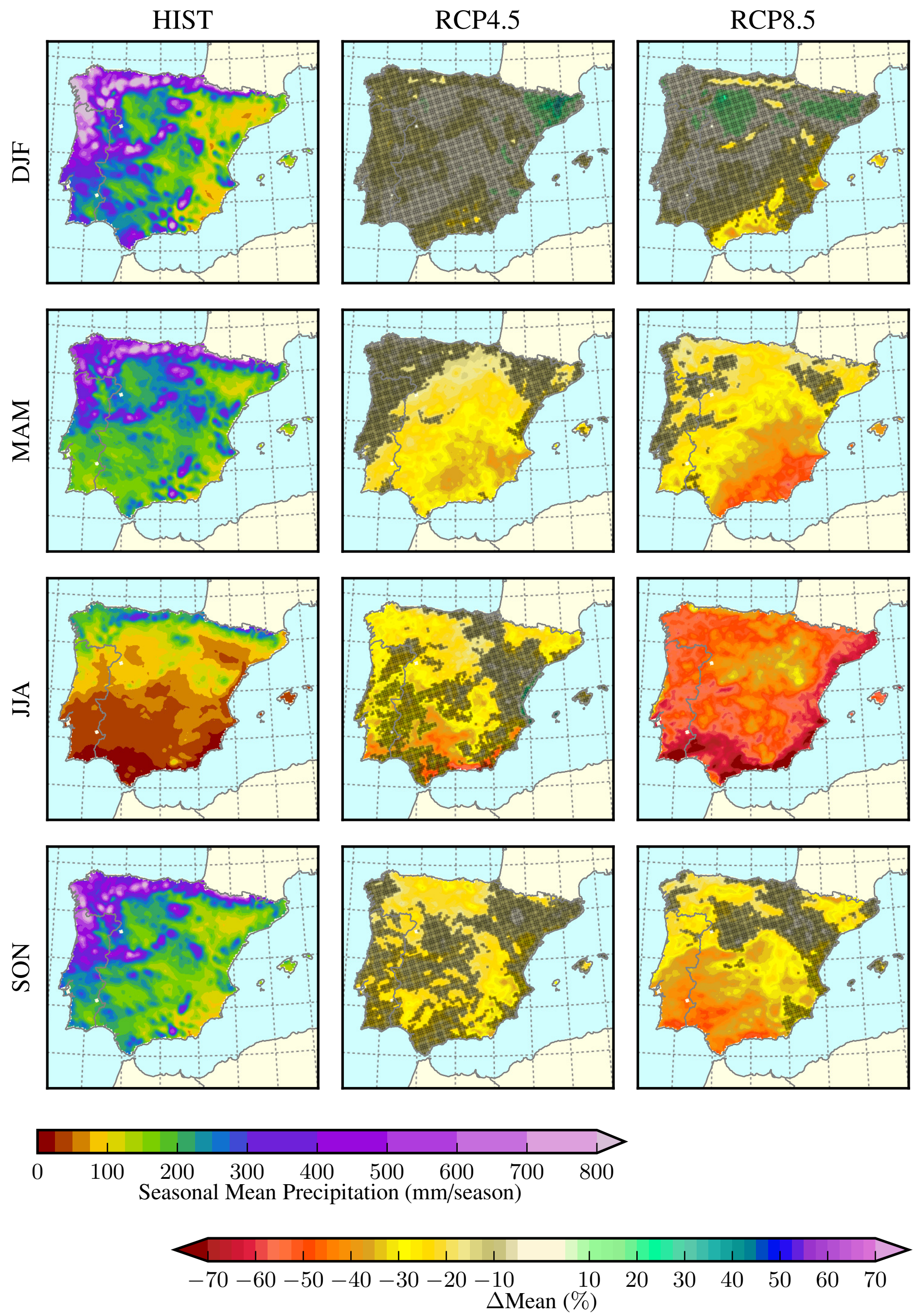

Figure 6.7: *The same as Figure **6.6** but for the WRFMPI simulations.*

from the WRFCCSM simulation under the RCP4.5 (Figure ***6.6***, MAM) revealed decreases mainly in the Ebro Valley, whilst for the higher emission scenario the reduction was generalized over the entire IP reaching values up to -60% in the south of the Peninsula. For the WRFMPI simulations (Figure ***6.7***, MAM), the area affected by decreases of precipitation was more significant than for the WRFCCSM under the RCP4.5, but this projected more moderate diminutions for the RCP8.5. In this latter the highest decreases were mainly located in the southeastern peninsular (with values of around -50%).

Many regions over the entire IP suffered the most remarkable reductions in summer, especially under the RCP8.5 (Figures ***6.6*** and ***6.7***, JJA). For the RCP4.5, the WRFCCSM projected significant decreases mainly in the east of the Peninsula and over the Cantabrian Range and Central System, where the diminution was up to 30%. Similarly, the WRFMPI simulation presented great reductions but these were more extended and larger in magnitude. For the RCP8.5, both the WRFCCSM and WRFMPI located the most affected areas across coastal regions, particularly for the Mediterranean Coast. Here changes values below -70% appeared, being stronger for the WRFMPI. As occured in spring, during autumn, the WRFCCSM (Figure ***6.6***, SON) showed a much smaller area affected by the diminution of the mean precipitation respect to the present than the WRFMPI (Figure ***6.7***, SON) for the RCP4.5 (with negative differences up to -35%). However, for the RCP8.5 the contrary behavior was found. In this latter scenario, both models located the most severe decreases in the southwest of the Peninsula, these being stronger for the WRFCCSM.

Changes in the Variability of Seasonal Precipitation

Previous results revealed substantial changes in terms of mean precipitations. However, to further analyze changes in the precipitation it is necessary to also explore changes in its variability. In fact, the study of changes in variability can provide additional information in relation to the hydrologic cycle's response to changing climate and its impacts (Pendergrass et al., 2017). Thus, changes in variability of precipitations were analyzed through the seasonal projected changes in terms of standard deviation. These were also expressed in relative terms in order to a better understanding of the magnitude of the changes. Significant changes in the interannual variability were tested according to a two-tailed Fisher-Snedecor F test at 95% confidence level.

Precipitation variability is strongly associated to mean precipitation, so variability is likely to decrease in areas where a reduction in its mean values is projected, and vice versa. Such relationship is found when one compares the projected changes through the standard deviation with those changes in terms of mean values.

For the near future, the spatial patterns in variability were substantially different depending on the season, region and simulation analyzed. For winter (Figures ***6.8*** and ***6.9***, DJF), the significant changes showed predominantly positive sign, reaching values up to 150% in different parts of the eastern peninsular façade under the RCP4.5. In spring, projections from CCSM4-driven simulations presented significant values only for certain areas (Figure ***6.8***, MAM), which were found to be either positive or negative. In this sense, the RCP8.5 projected a large area with significant changes, which were fundamentally negative. Meanwhile, WRFMPI (Figure ***6.9***, MAM) presented similar behaviors for the two RCPs with increases mainly located in the west of the Peninsula and decreases associated to the Cantabrian Range, northeast and southern peninsular.

In summer, changes in the variability seem to be more relevant than those found in mean values for simulations driven by CCSM4 (see Figure ***6.8***, JJA and Figure ***6.4***, JJA) but these were still few significant. This simulation, under the RCP4.5 projected an increase in standard deviation of about 80% over most of the Mediterranean Coast. For the RCP8.5, increases of variability mostly appeared in the western region, meanwhile the reductions were presented in southern and northeastern peninsular. For the WRFMPI (Figure ***6.8***, JJA), nonetheless, both RCPs revealed decreases fundamentally, these being significant only over certain areas in the western half. In terms of the autumn variability, a predominant increase of the variability was found in the WRFCCSM simulations (Figure ***6.8***, SON) with the highest values over the Gulf of Mazarrón (in the southeast) for the RCP8.5. However, the WRFMPI (Figure ***6.9***, SON) showed significant reductions over different areas throughout all the IP, except for the northeastern Coast where increases were found for both pathways.

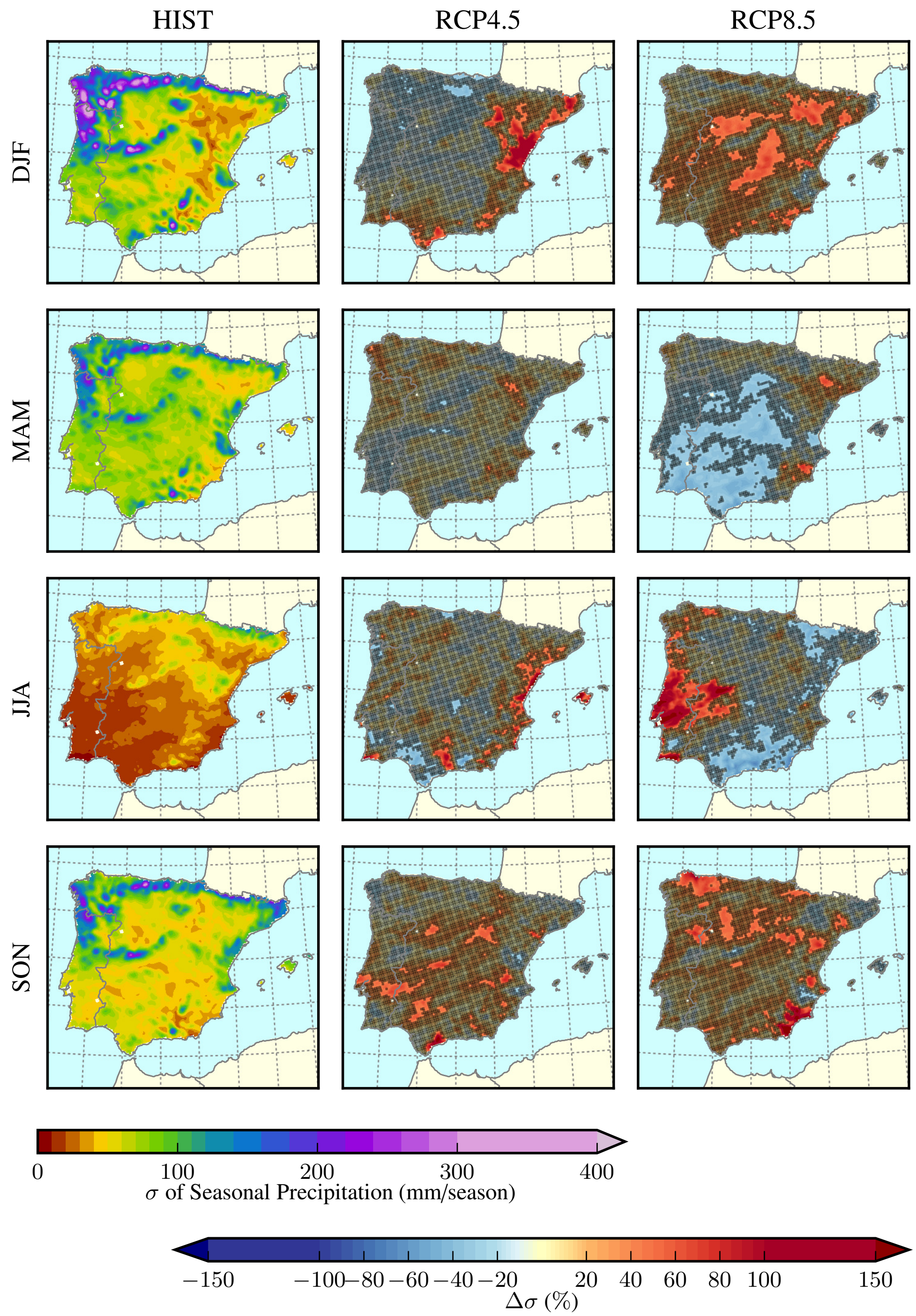

Figure 6.8: *Current (1980-2014) seasonal standard deviation of amount of the precipitation (first column) and the near future (2021-2050) relative projected changes from the WRFCCSM. In second and third columns, the results from the RCP4.5 and RCP8.5 respectively are shown. Black dots indicate non-significant changes according to a two-tailed Fisher-Snedecor F test at the 95% confidence level.*

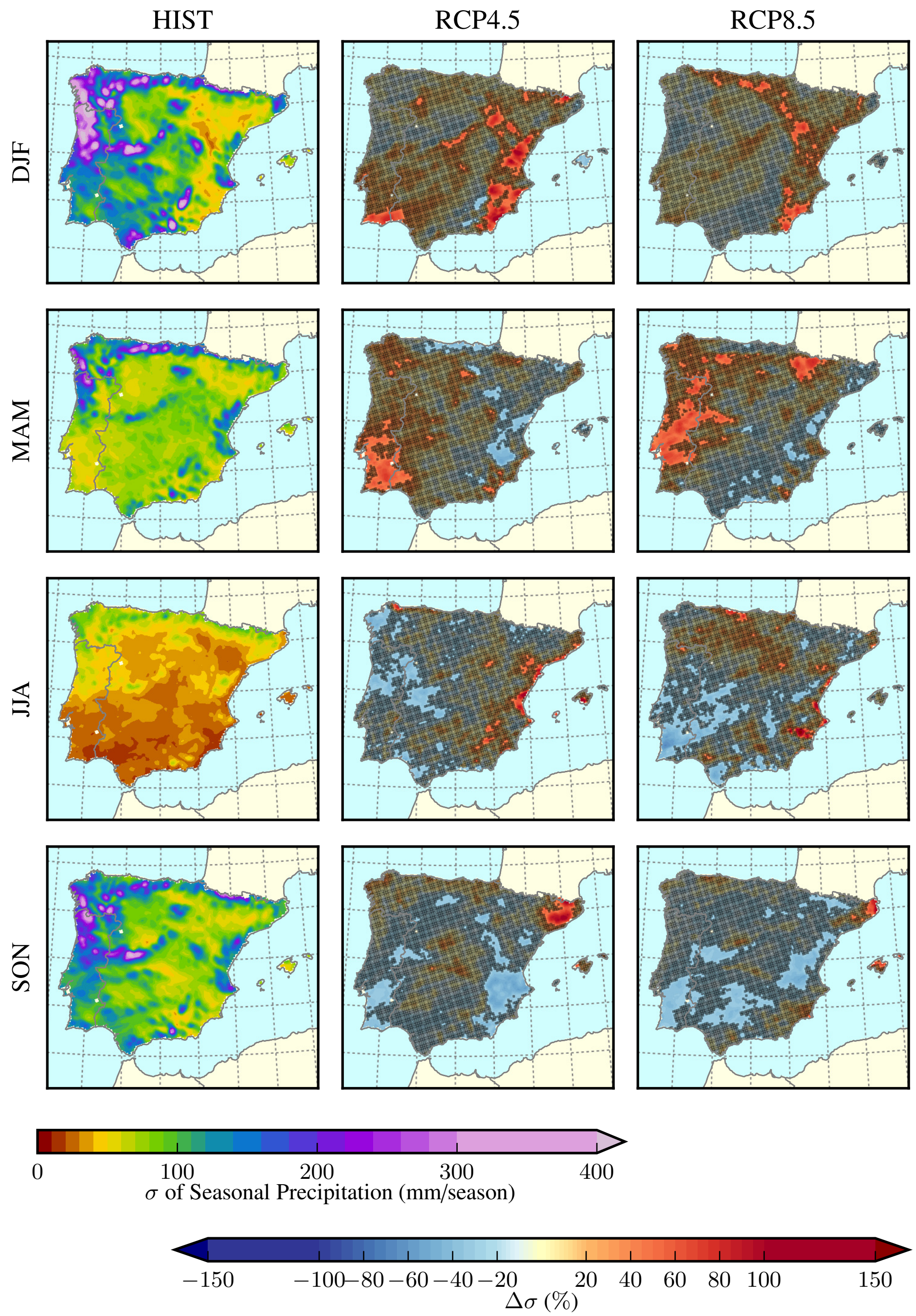

Figure 6.9: *The same as Figure **6.8** but for the WRFMPI simulations.*

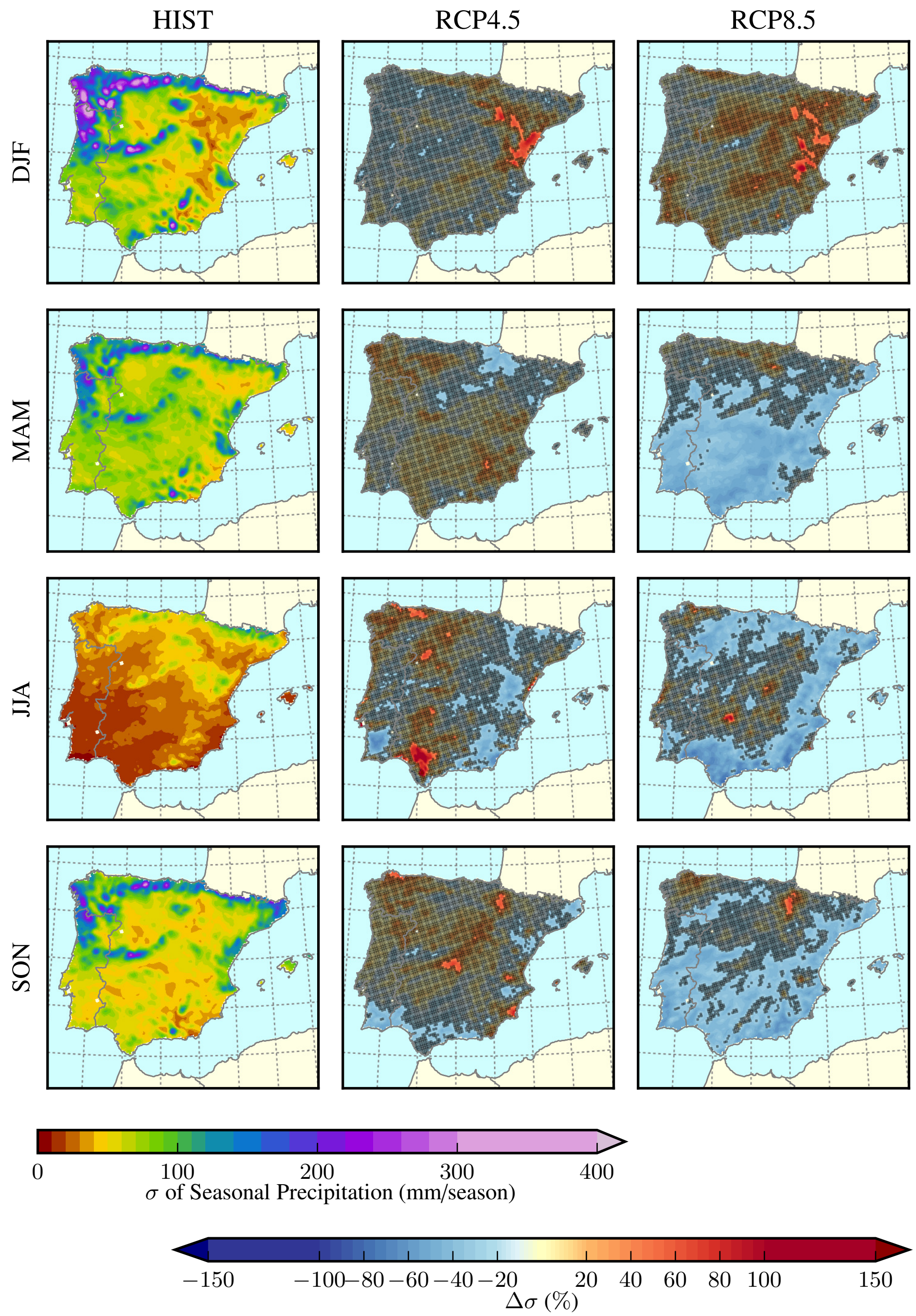

Figure 6.10: *Current (1980-2014) seasonal standard deviation of amount of the precipitation (first column) and its far future (2071-2100) relative projected changes from the WRFCCSM. In second and third columns, the results from the RCP4.5 and RCP8.5 are shown respectively. Black dots indicate non-significant changes according to a two-tailed Fisher-Snedecor F test at the 95% confidence level.*

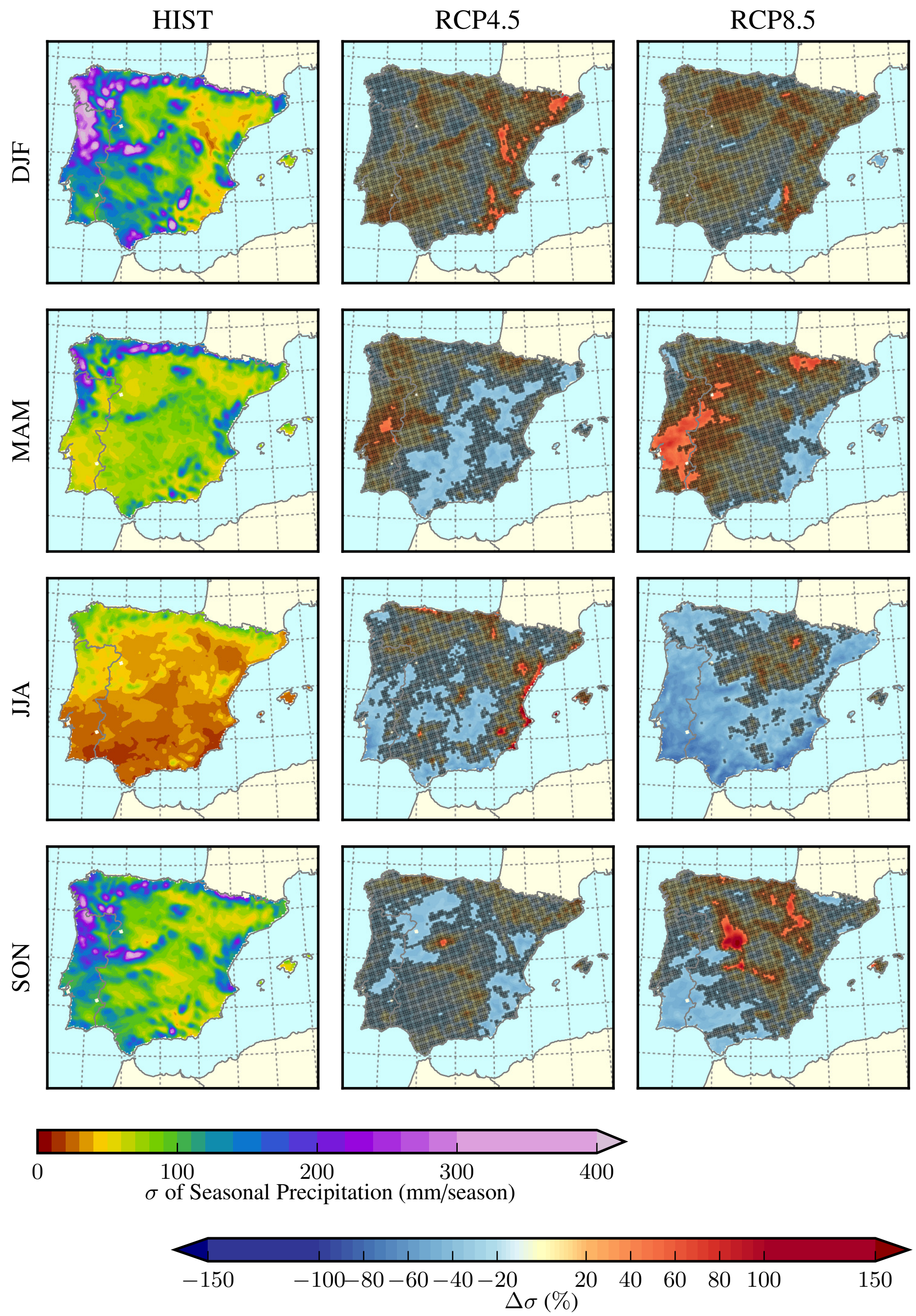

Figure 6.11: *The same as Figure* ***6.10*** *but for the WRFMPI simulations.*

The variability decreases for the far future (Figures ***6.10*** and ***6.11***) regarding the near future in general, showing less significant changes. In winter, changes in internal variability were fundamentally non-significant for both the WRFCCSM and WRFMPI and for the two RCPs, the significant changes being mostly positive and located over the eastern peninsular façade, except for WRFMPI under the RCP8.5. In spring, the WRFCCSM (Figure ***6.10***, MAM) only showed reductions up to 40% for certain areas in the north under the RCP4.5, and encompassing most of the central and southern IP for the RCP8.5. However, the WRFMPI (Figure ***6.11***, MAM) projected increases especially in western areas, more extended in the RCP8.5, and reductions over the east of the Peninsula.

In summer, prevailed the reduction of interannual variability withh respect to current values with some exceptions in both the WRFCCSM and WRFMPI (Figures ***6.10*** and ***6.11***, JJA), and under the two pathways. Note that the WRFCCSM simulation under the RCP4.5 projected strong increases in Gulf of Cádiz. In autumn (Figures ***6.10*** and ***6.11***, SON), decreases of variability were also generalized as show the results from all simulations, except for WRFMPI under the RCP8.5 where important increases (values up to 150%) were found over the Northern Plateau, Central System and certain parts of the Ebro Valley.

In general, these results suggested that the variability in precipitation presented similar spatial behaviors to the mean precipitation values, but the changes appeared to be higher in magnitude. Moreover, the differences found between the projections from the different GCMs-driven simulations suggested an considerable uncertainty, more marked for the near future.

Trends in Seasonal Precipitation

Additionally, an analysis of the long-term trends within each future period was also performed. This way, we attempted to discern the model behavior and the uncertainty (i.e., variability of the climate and scenario uncertainty) that affect at each simulation through the evolution along the years in the different run. In fact, the pronounced variability and uncertainty noise of the precipitation could lead to misrepresentation of the results in relation to the signal of global warming induced by the increase of the GHG concentrations. In order to facilitate the interpretation of the results, the study was performed by using spatial averaged values of the seasonal amount of precipitation for the different river basins of the IP (see Figure ***6.1***).

To identify if the anthropogenic climatic signal is emerging, it is required to compare the signal of change against the background of natural climate variability, or noise. Only when the signal is of sufficient magnitude, it can be detected (Hawkins and Sutton, 2012). Many studies have been performed in recent years to estimate the effects of GHG concentrations in the climate system in trying to elucidate if the recent observed changes in the climate are induced by the human activities by determining the Time of Emergence (ToE)[2]. As noted in the IPCC Fifth Assessment Report (AR5) (Kirtman et al., 2013), there is "no single metric" for estimating ToE and several authors have proposed different methods (Maraun, 2013, Hegerl et al., 2007, Mahlstein et al., 2011, Bador et al., 2016a, King et al., 2016, Bador et al., 2016b, Nguyen et al., 2018, Mora et al., 2013, Min et al., 2014). Between all the methods, the signal to noise (S/N) ratio[3] is a parameter commonly used to determine the ToE (Hawkins and Sutton, 2012, Santer et al., 2011, Hegerl et al., 2004, Sui et al., 2014), and this can be applied using different approximations of both, the signal and the noise (Christensen et al., 2007a, Hawkins and Sutton, 2009, Giorgi et al., 2009, de Elía et al., 2013). Thus, to estimate the time in which the anthropogenic climate signal becomes larger than noise different threshold has been also used, e.g., S/N > 1 (Lee et al., 2016) or S/N > 2 (Sui et al., 2014).

In this context, with the purpose of characterizing the evolution of GHG-induced climate signal, here the temporal evolution of the S/N ratio for each watershed was computed. Due to the time length of our periods, of both reference period and future ones, we only can examine the evolution of the S/N ratio instead of attempting to determine the ToE. However, thorough the temporal behavior for each river basin and for both periods, we can elucidate if the induced signal will emerged and, and if is so, approximate where and in what period. To do this, we estimated the induced signal through the temporal evolution within each future period, which was computed as the 10-year running

[2]The time of emergence (ToE) is understood as that in which anthropogenic climate change signal emerges against the natural variability, and remains along the time.

[3]The S/N ratio is a measure to ascertain the anthropogenic climate signal in relation to the noise.

mean expressed in relation to the reference period[4]. A window of 10-year was selected in order to reduce the noise associated to interannual variability, while key behaviors related to the decadal scale fluctuations are retained (Lehner et al., 2017). On the other hand, as noise, we used the interannual standard deviation (Hawkins and Sutton, 2012) in the reference period, which was previously linearly detrended (de Elía et al., 2013), reducing thus a possible linear trend in the temporal series of the reference period. In this context, it is important to keep in mind that this measure is very sensitivity to the presence of extreme values, and even with long time series must be defined bearing in mind such values.

Figure ***6.12*** shows the "portrait" diagrams of the seasonal S/N ratio for the near future at each river basin for CCSM4-driven simulations. The values centered for each running mean are represented, e.g. the 10-yr running mean for 2026 corresponds to the mean value for the period 2021-2030. Negative values indicate that the mean precipitation is below the current one and vice versa. In Figure, a negative trend is understood when the S/N values become increasingly negative over the period of time as well as a positive trend is an opposite behavior. In general, results showed that the internal natural variability was larger than the anthropogenic climate signal over the near future. That is, S/N ratios in most cases were in a range at which its absolute magnitude was less than 1. However, there were some watersheds that presented values below -1 but these did not stably remain along the time.

For this boundary condition, the winter mean precipitations were in many cases higher than current values, being the trend within the period different for the two RCPs (Figure ***6.12***, DJF). For the RCP4.5, an overall negative trend at least until 2037 was shown, except for North Atlantic, Miño-Sil, Duero and Portugal Basins, where, however, the S/N values indicated dryer condition in relation to the present, in general. By contrast, under the RCP8.5, an increase in the wetter conditions appeared at least until 2036 when some watersheds showed a change toward drying until the end of the period (e.g., Duero, Southern Basins). For spring (Figure ***6.12***, MAM), all watersheds broadly showed a

[4]That is, the difference between the 10-year running means and the mean of the entire reference period. Here, we select as reference period our entire current period.

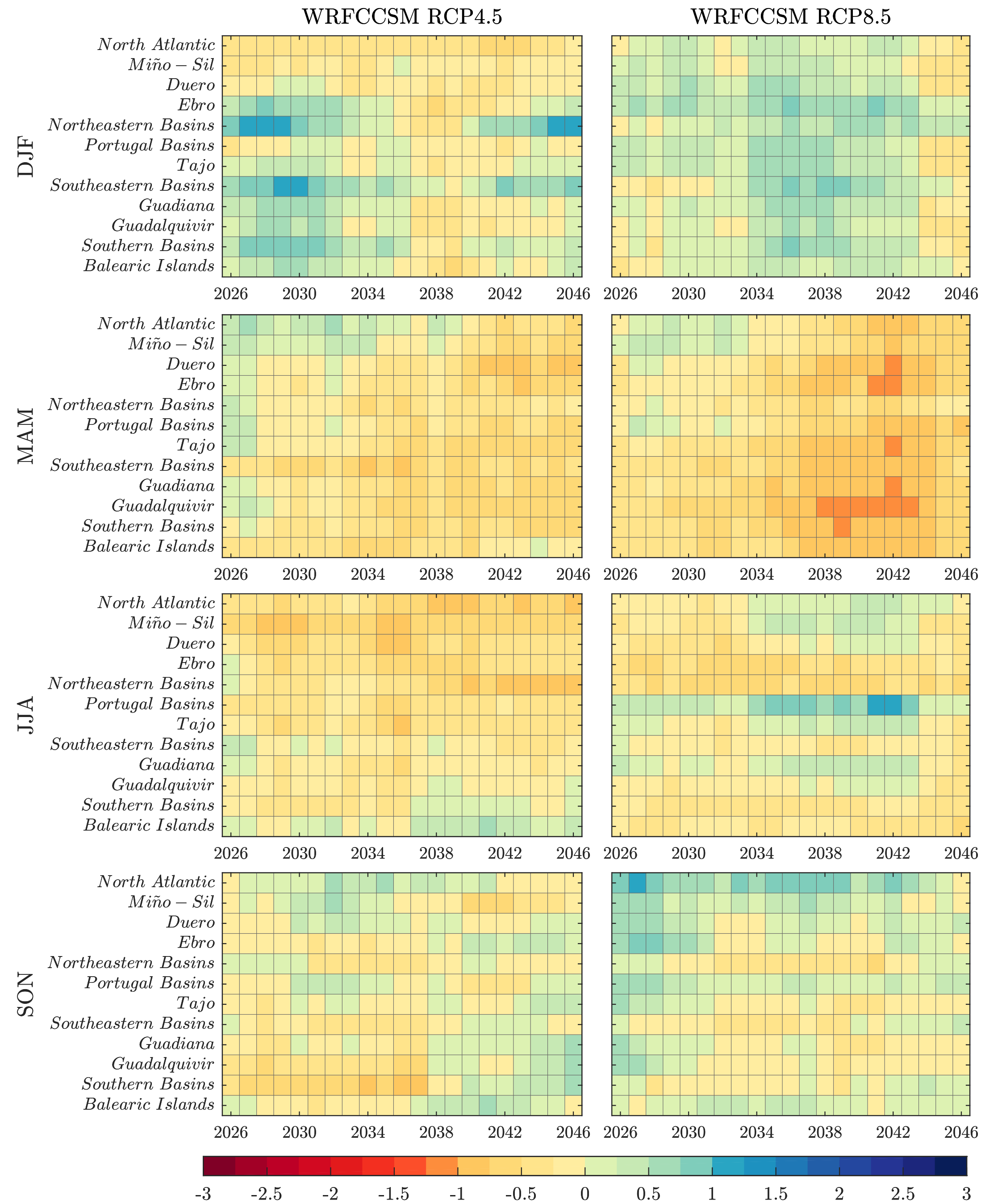

Figure 6.12: *Signal to noise (S/N) ratios of the seasonal mean precipitation for each basin within the IP. Such measure was computed for seasonal temporal series of the near future (2021-2050) total amount of precipitation in relation to the present (1980-2014) for the WRFCCSM. In rows, the portrait diagrams for the different seasons and in columns the simulations driven for the two RCPs (RCP4.5 and RCP8.5).*

common negative trend for both RCPs, and more marked under the RCP8.5. In general, the climate change signal was usually lower than the internal variability, only showing values below -1 in the Duero, Ebro, Tajo, Guadiana, Guadalquivir and Southern Basins in the RCP8.5 and for few years in most cases. Note the precipitation trends in the Guadalquivir Basin in this latter scenario, where values of S/N below -1 are reached from the decennia centered in 2038 to that centered in 2043. Thus, the results could be indicating a reduction in spring precipitation due to the increase of GHG concentrations, although the signal was still subtle.

Summer performances for the WRFCCSM (Figure ***6.12***, JJA) were characterized for a very different evolution between RCPs as showed the changes in mean values (see Figure **6.3**, JJA). Under the RCP4.5, some watersheds presented positive trends (e.g., Balearic Islands Basins from 2036 onward), others showed negative trends (e.g., Northeastern Basins), but most of them present an absence of the clear trend although their mean values were lower than the present ones. For the RCP8.5, the trends were also unclear in general. Note the results from Portugal Basins where the precipitations were higher than in the present throughout all the period and increasing trends were depicted at least for the period 2033-2042, reaching values above 1 around 2041 and 2042. In autumn (Figure ***6.12***, SON), under the RCP4.5, the results showed mean precipitation with respect to the present, both positive and negative. The Southern, Northeastern and Balearic Islands Basins presented downward trends at least until 2036. By contrast, Miño-Sil and North Atlantic Basins presented decreasing trends in the second half of the period. For the RCP8.5, both decreasing and increasing trends were shown, with important presence of values above the current ones (e.g. North Atlantic watersheds).

Regarding the results of the simulations driven by MPI-ESM-LR (Figure ***6.13***), S/N ratios also revealed a large internal variability throughout the period 2021-2050. For these simulations, however, the GHG-induced signal appeared to be slightly clearer than from the WRFCCSM simulations. Winter mean precipitation for the RCP4.5 was, in general, higher than the present ones (Figure ***6.13***, DJF), showing rising trends in many watersheds. For the RCP8.5, a generalized decreasing evolution was revealed, which was prolonged at least until

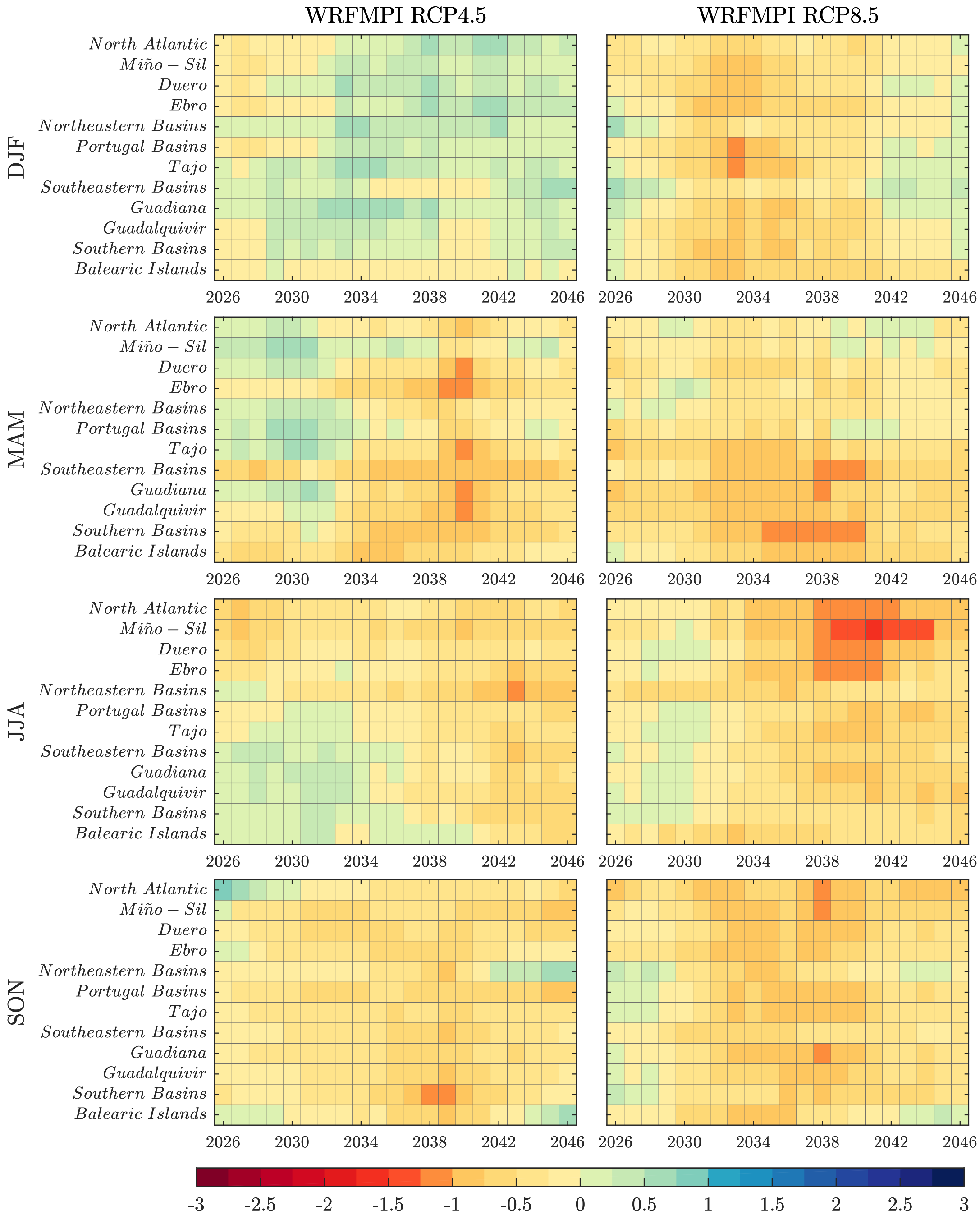

Figure 6.13: *As Figure **6.12** but for the WRFMPI simulations.*

2033. when the S/N values were below -1 in the Tajo and Portugal Basins. However, from the second half of the period to the end, nearly all watersheds tended to increase their winter mean precipitation. Negative trends appeared at least until 2039 for both RCPs, and practically in all basins, in spring (Figure ***6.13***, MAM), the mean of precipitation being lower than in the present by the end of the period for all watersheds. In the RCP4.5, at the beginning of the period, there was an important presence of positive values with respect to the present in several watersheds. Here, Duero, Ebro, Tajo, Guadiana and Guadalquivir Basins reached S/N ratios lower than -1 for 2040. Under the RCP8.5, the S/N values were fundamentally negative and only the Southeastern (around years 2038-2040), Guadiana (around 2038) and Southern Basins (around years 2035-2040) presented S/N values below -1.

In summer (Figure ***6.13***, JJA), the watersheds located in the southern half of the Peninsula and Balearic Islands showed negative trends in both RCPs. In any case, all basins presented a diminution in their mean values with respect to the present by the end of the near future, and again more highlighted for the RCP8.5. Under the RCP8.5, however, the watersheds located in the north of the Peninsula appeared to suffer larger reductions, which reached S/N ratios below -1 between 2038 and 2043. In this scenario, Balearic Islands Basins did not seem a clear trend although they remained with mean values lower than the present period. In autumn, there was also a decrease in precipitation regarding the present in nearly all basins (Figure ***6.13***, SON). Here, the RCP4.5 showed a common negative trend at least until 2039. By the end of the period, however, some watersheds were recovered, reaching values of mean precipitation even higher than the present ones (Northeastern and Balearic Islands Basins). Similar behavior is shown for the RCP8.5, although the S/N values indicated more accused dryness in general.

As for the near future, the trend of the seasonal mean precipitations was further studied in the period 2071-2100. Figure ***6.14*** portrays that in general, the simulations driven by CCSM4 presented drier conditions in this period regarding the previous one, especially for warm seasons, with differences between RCPs also notorious. Furthermore, the results also suggest a clearer climate change signal by the end of the 21^{th} century. For winter, in general the natu-

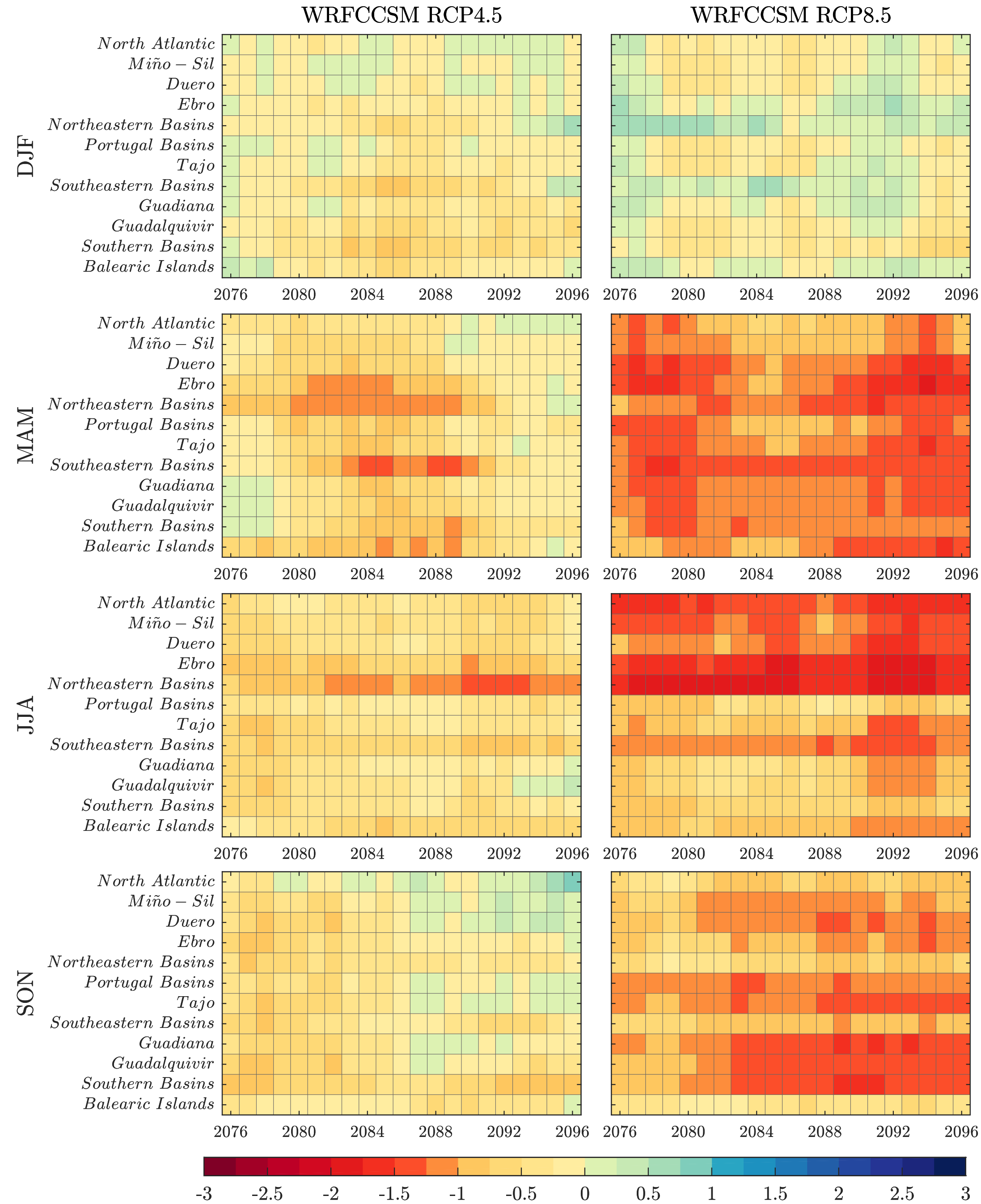

Figure 6.14: *Signal to noise (S/N) ratios of the seasonal mean precipitation for each basin within the IP. Such measure was computed for seasonal temporal series of the far future (2071-2100) total amount of precipitation in relation to the present (1980-2014) for the WRFCCSM. In rows, the portrait diagrams for the different seasons and in columns the simulations driven for the two RCPs (RCP4.5 and RCP8.5).*

ral internal variability was still large (Figure ***6.14***, DJF). For the RCP4.5, the Northeastern, Southeastern, Southern and Balearic Islands Basins showed decreasing trends at least over the period 2076-2086. Under the RC8.5, the mean precipitation was above the present one many times in most watersheds. Here, negative trends appeared in some watersheds from the second half of the period to the end of the century.

Decreasing trends were presented at least until 2089 for spring in many watersheds and under the RCP4.5 (Figure ***6.14***, MAM). Here, in different watersheds (Ebro, Northeastern and Southeastern Basins) values of S/N below -1 appeared for an important interval of time, however, these values did not remain until the end of the period. For the RCP8.5, all watersheds presented negative S/N ratios, arising values below -1 for the entire period in many of them. These results suggest a possible emergence of the climate change signal from the beginning of this period. For summer (Figure ***6.14***, JJA), the RCP4.5 showed decreasing trends at least until 2090 in many cases, arising S/N ratios lower than -1 until the end of the century in the Northeastern Basins. The RCP8.5 presented important climate change signal (values below -1) along nearly all the period, especially for Northern watersheds (North Atlantic, Miño-Sil, Duero, Ebro and Northeastern Basins) and Southeastern Basins. Note the S/N values over 2 in the Ebro and Northeastern Basins along most of the period, where the induced signal were 2 times higher than the internal variability. This latter suggests a emergence of the climate change in terms of precipitation values for the high emission scenario in such watersheds. In this regard, it is important to keep in mind that we cannot ensure that the S/N values remain for the next century.

In autumn, for the simulations driven by CCSM4 (Figure ***6.14***, SON) the signal appeared to be more moderate, at least for the RCP4.5. In this latter, the mean values were lower than in the present in the first half of the period. Here, rising trends were shown in general until 2088, although, by the end of the period different behaviors were presented. Namely, while some watersheds appeared to remain with a positive trend along the entire period (e.g., Duero Basin), others became negatives (e.g., Southern Basins). For the RCP8.5, the climate change signal was higher than the natural internal variability from

2080 (and even sooner in some watersheds) over the Miño-Sil, Duero, Tajo, Portugal Basins, Guadiana, Guadalquivir and Southern Basins, which indicate the possible emergence of the climate change signal for this season under such scenario.

In general, results from the MPI-ESM-LR-driven simulations for far future (Figure ***6.15***) also revealed mean values of precipitation lower than the present ones practically over the entire period and for all watersheds, except for winter. In this season (Figure ***6.15***, DJF), and under the RCP4.5, all watersheds appeared to end the century with drier conditions, although the internal variability was still large. For the RCP8.5, although all watersheds revealed negative trends at least until 2085, those located on the northern half presented a final period of increases, arising values higher than in the present.

Stronger values of S/N ratios were shown in spring (Figure ***6.15***, MAM), when the mean precipitations were lower than the present ones along the entire period except for Portugal Basins in the RCP4.5. In this scenario, S/N values below -1 were reached in some watersheds. Thus, the Tajo and Guadiana Basins reached such threshold around 2090, which remained until the end of the period. For the RCP8.5, many watersheds began the period with very low values, however, these increased until the middle of the period, and subsequently decreased again. Here, the Southern Basins appeared to be the most affected with a possible emergence of the climate change signal from 2089. Summer (Figure ***6.15***, JJA) was characterized for a more robust signal for the RCP8.5 in the North Atlantic, Miño-Sil, Ebro, Northeastern and Southeastern Basins, presenting S/N values below -1 (or higher) for the entire period. These results suggest the emergence of the climate change signal. By contrast, the RCP4.5 showed a moderate behavior, presenting even more internal variability than spring for this same scenario.

For autumn (Figure ***6.15***, SON), the S/N values remained negative, although the general behavior was less strong. Here, only the NorthAtlantic Basins presented S/N ratios below -1 from 2085 to 2087 in the RCP4.5. Analogously, such values were reached under the RCP8.5 in North Atlantic, Miño-Sil around 2085-2090, and for the Tajo, Southeastern, Guadiana, Guadalquivir and Southern Basins for a longer period until the end of the period.

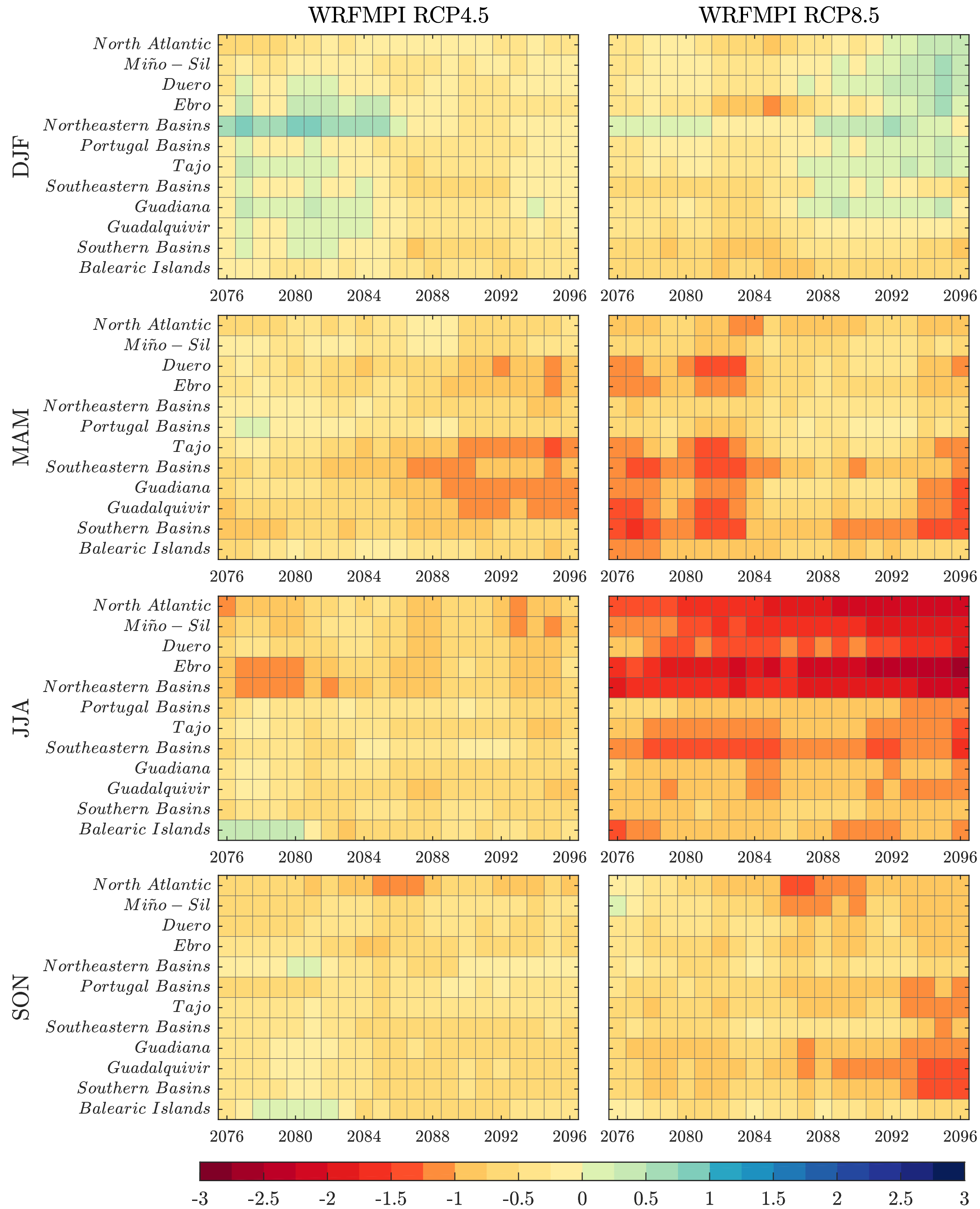

Figure 6.15: *As Figure **6.14** but for the WRFMPI simulations.*

6.2.3. Changes in Extreme Values

Results from annual and seasonal changes have evidenced substantial diminutions of precipitation throughout the 21^{th} century, which were more marked under the RCP8.5 and particularly for warm seasons. In terms of interannual variability, the results also showed a generalized reduction in the interannual standard deviation, larger in magnitude in many cases. However, such results do not provide information about extreme values which are perhaps more important because they generate even greater impacts on the society. So, it is desirable to also examine the projected changes in terms of extreme values. For this, changes in extreme precipitation were also analyzed through different ETCCDI extreme indices just as in the model evaluation (section ***4.3.2***). Such indices were the maximum 5-days consecutive precipitation (RX5day), the intensity of precipitation in wet days (SDII), the number of days with heavy and very heavy precipitation (R10 and R20, respectively), maximum number of consecutive dry and wet days (CDD and CWD, respectively), and the number of precipitation events above the 95th percentile (R95pTOT). To this end, all indices were calculated for each year, thus achieving the annual time series for each grid-point. In order to evaluate the projected changes, the future indices vs. the current ones are represented in relative terms. Additionally, the significance of the future changes has been evaluated according to a two-tailed Mann-Whitney-Wilcoxon U test at the 95% confidence level.

Figure ***6.16*** displays the changes in the maximum 5-days consecutive precipitation in relation to the present for both the near and the far future. All simulations projected both increases and decreases for the near future (Figure ***6.16a***), but these changes were significant only for some reduced areas. Thus, significant diminutions in the RX5day of about 15% were found in certain regions in the Northern Plateau and in the Ebro Valley for the WRFCCSM under the RCP4.5. By contrast, in the RCP8.5 significant increases appeared in Northern Plateau and over coastal areas, where values above 40% were reached over the northeastern and southeastern coasts. In the WRFMPI, the significant changes were predominantly negatives in both RCPs, showing reductions of about 15%. For the RCP4.5, the reductions were mainly located over the Northern Plateau, and especially in the east (values of RX5day up to -30%).

(a)

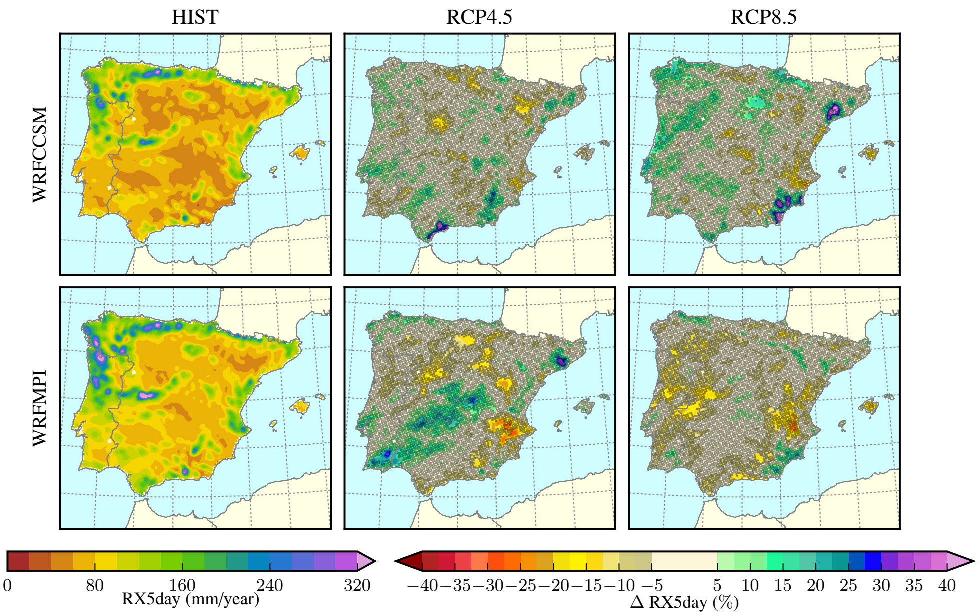

(b)

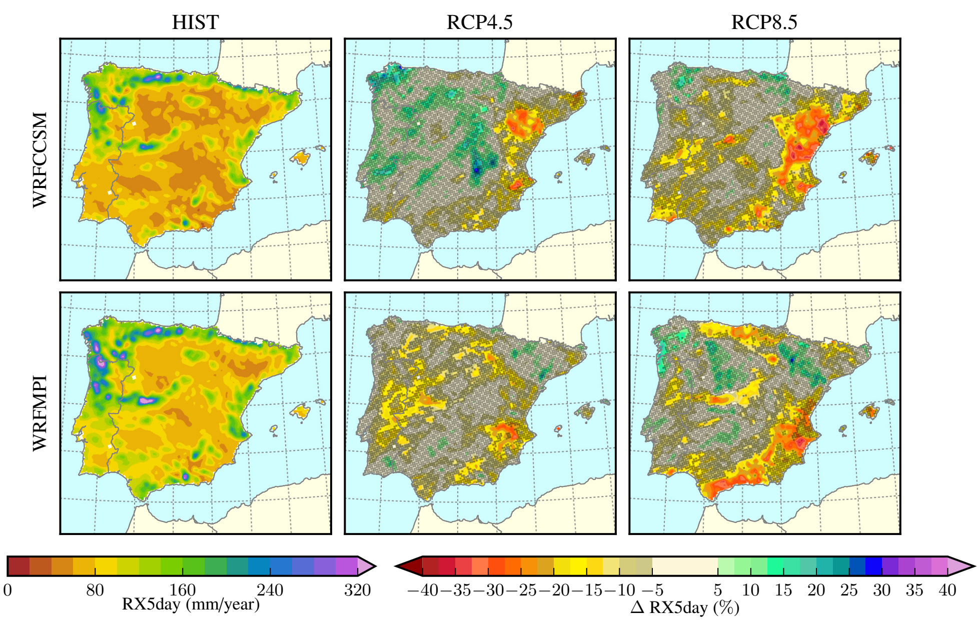

Figure 6.16: *Current (HIST) annual mean of the maximum 5-days precipitation (RX5day) and the (a) near and (b) far future projected changes for both the RCP4.5 and the RCP8.5, expressed in relative terms. Black dots indicate non-significant projected changes according to a two-tailed Mann-Whitney-Wilcoxon U test at the 95% confidence level.*

Contrariwise, important increases also appeared in disperse regions over the IP, and particularly around the southwestern coast (RX5day values up to 30%). The RCP8.5 also showed decreases, but these were less representative.

For the far future (Figure ***6.16b***), although there were certain regions where the RX5day increases (especially for WRFCCSM in the RCP4.5), it is likely to suffer a substantial decrease as all the simulations show. Under the RCP4.5, the WRFCCSM revealed reductions up to 30% mainly located over the Ebro Valley and close to Cape of the Nao, but also increases in the northwest of the Peninsula and over the Southern Interior Plateau. For the RCP8.5, the reduction was more noticeable, spanning a larger extension in the east, south of Portugal and over the Central System. For the WRFMPI simulations, the RCP4.5 only showed significant negative differences of the RX5day in relation to the present. Here, different areas are affected, reaching the highest detriments over the central west, the east and the Cantabrian Range. For the RCP8.5, the WRFMPI projected similarly to WRFCCSM, although the areas changed in location and extension. That is, the Central System, southern coast of Portugal and the eastern peninsular area (excluding the northeast) suffered strong reduction of RX5day (with values up to 35%), while in the northwest certain increases are suggested (increases of around 15%). Additionally, the WRFMPI also showed a substantial decrease in the Cantabrian Range.

In reference to the number of days with very heavy precipitation (R20), differences with respect to present values were both positive and negative in the near future (Figure ***6.17a***). WRFCCSM only showed significant increases in disperse regions over the IP, covering larger areas in Sierra Morena, and in the Southern Plateau for the RCP4.5. For the RCP8.5, Northern Plateau, Sierra Morena and Cape Roca presented increases even above 45%. By contrast, most of the significant changes for WRFMPI were predominantly negative and mainly located in the southeast and east for both RCPs, reaching values of -35%. Only an area over the south of Portugal presented a significant and marked increase (more than 45%) for this GCM under the RCP4.5.

For the far future (Figure ***6.17b***), the WRFCCSM still showed increments of R20 with respect to the present over certain areas in the Plateaus. Meanwhile, the Mediterranean Coast and the northeastern showed decreases for the

(a)

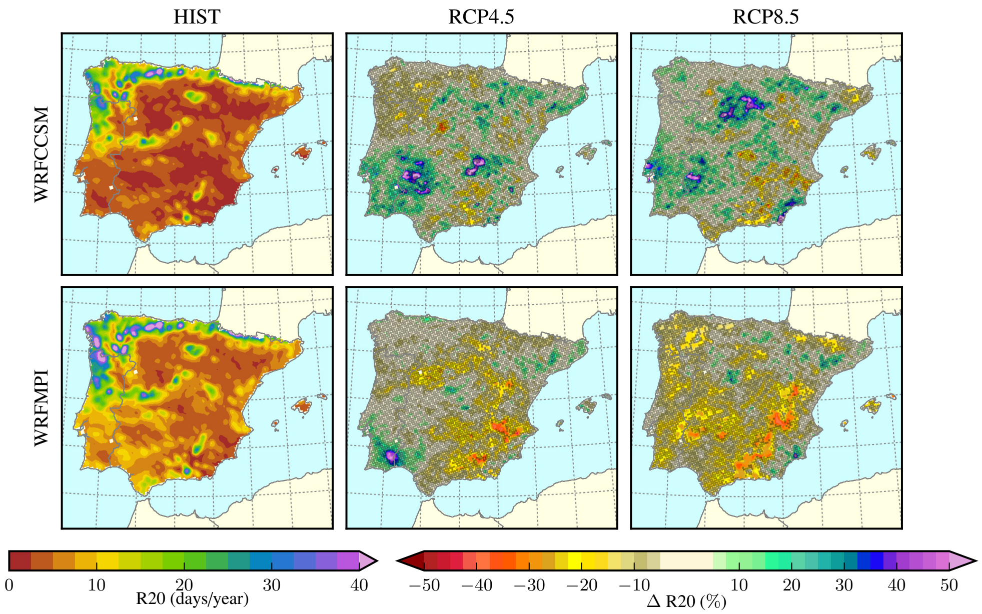

(b)

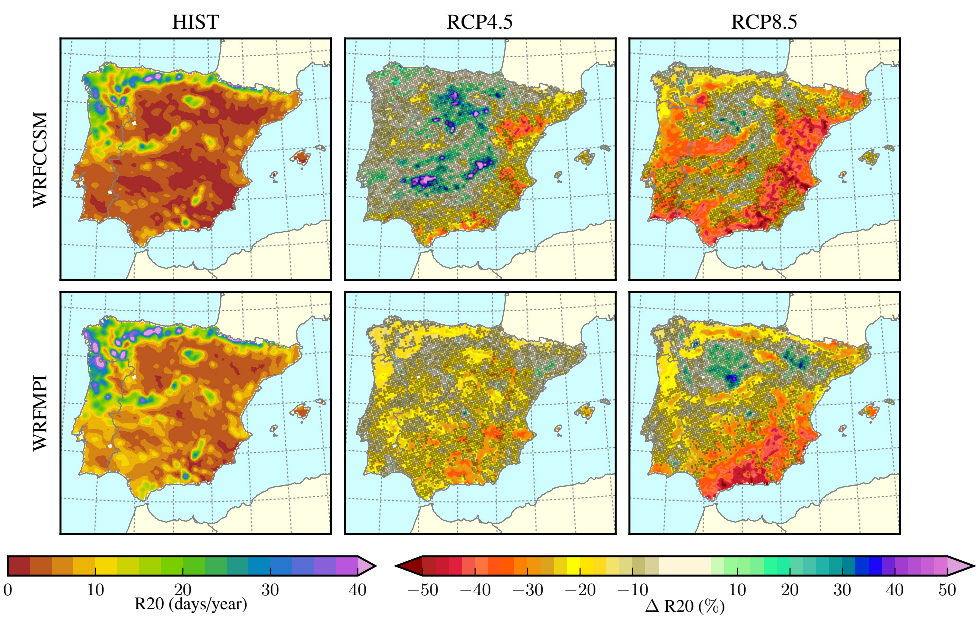

Figure 6.17: *The same as Figure* ***6.16*** *but for the number of days with precipitations above 20 mm (R20).*

RCP4.5. For the RCP8.5, notable decreases appeared in the eastern peninsular facade, reaching values of reduction with respect to the present up to 50%. Similarly, the WRFMPI only showed significant decrements, which were stronger for the RCP8.5, more intense and extended over the south and southeastern. In addition, changes in heavy rainfall were also examined (results not shown), showing all WRF simulations significant reductions in the number of R10, but with changes in extension and magnitude. Decreases of R10 were similar to R20 in magnitude and locations for all WRF simulations in the two periods. However, the area affected by changes in R10 covered larger extensions, especially for the far future.

The number of consecutive dry days (CDD) are likely to increase in the future, as revealed all WRF simulations. In the near future, nonetheless, the changes were significant only for a few regions (Figure ***6.18a***), reaching values above 30% and fundamentally located in the north and over the west (e.g., Galician Massif and in certain regions over Portugal). In general, the differences in CDD values with respect to the present ones were more extended for the RCP8.5 for both GCM-simulations. In the far future (Figure ***6.18b***), the the WRFCCSM projected significant increases for the RCP4.5 over some areas in the Northern Plateau and in the eastern peninsular façade (values up to 40%. For RCP8.5), but the increases were more substantial showing similar spatial patterns. In the same way, in the WRFMPI appeared increases in the northwest of the Peninsula and over the Mediterranean facadet, with values above 30% under the RCP4.5. For the RCP8.5, significant increases for the CDD appeared covering practically the whole IP. Here, the highest values (above 80%) were located where the RCP4.5 presented significant increases.

For the near future, the CCSM4-driven simulations showed a few regions with significant changes in the number of consecutive dry days (CWD, Figure ***6.19a***), which were negatives for both RCPs. Here, the reductions (up to 20%) appeared in disperse areas throughout the IP under the RCP4.5, and over certain areas in the south of the Peninsula under the RCP8. The WRFMPI showed decreases that covered larger extensions over the eastern half of the peninsula under the RCP4.5, but they were non-significant in many cases. Meanwhile, the RCP8.5 showed substantial reductions above 30% over many areas in the south,

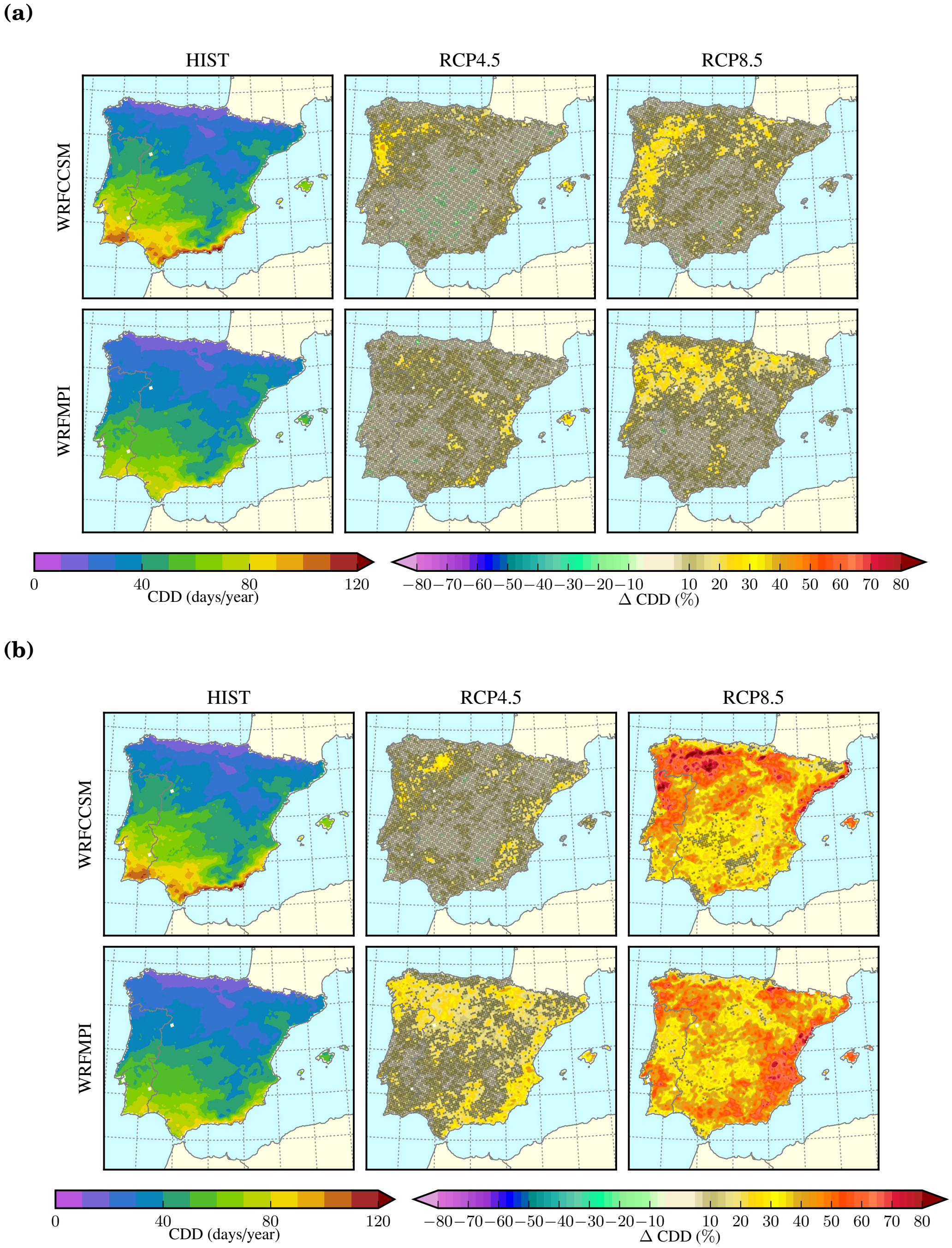

Figure 6.18: *The same as Figure **6.16** but for consecutive dry days (CDD, precipitation < 1 mm).*

north and west of the Peninsula. For the far future (Figure ***6.19b***), both the WRFCCSM and WRFMPI projected noticeable reductions (with diminutions above 30% in many places) for the higher concentration pathway, showing larger areas affected with greater magnitude for the WRFMPI. The CWD decreases for intermediate GHG emissions as well, but here a lower number of significant changes were shown. For this scenario, the effects are again stronger for the WRFMPI, and especially for the south of the Peninsula, where values below -20% were reached.

The R95pTOT (Figure ***6.20***) was used to analyze changes in the heaviest precipitations[5]. Note that the changes here were expressed as the difference between the future and present percentages of R95pTOT, and not in relative terms. For the near future (Figure ***6.20a***), all WRF simulations showed both increases and decreases over some limited areas, the most substantial changes being predominantly positive. For the WRFCCSM, the highest increases were found over Sierra Morena in the RCP4.5, and over the southeastern coast and in the Cape Roca under the RCP8.5 (percentages above 10%). Meanwhile,the WRFMPI projected significant changes in similar regions to the WRFCCSM, but with smaller extension.

For the far future (Figure ***6.20b***), the CCSM4-driven WRF simulations again presented both increases and decreases, but here the significant areas affected were larger. Both scenarios projected an increase of the heavy precipitation over different areas in the south, with values up to 10%, and reductions along the east, with values up to -10%. For WRFMPI, a few limited areas showed significant diminutions, but notable increases were displayed under the RCP8.5. In this latter, large areas were affected with values that exceed 6% and above 10% in the Ebro Valley, Northern Plateau and southern Portugal.

Projected changes in terms of the simple daily intensity index (SDII) showed results very similar to those found for the r95pTOT from the simulations driven by both GCMs under the different scenarios and for the two periods, so they do not provide additional information and then they are not shown.

[5]The R95pTOT indicates the sum of the annual precipitation in days where daily precipitation exceeds the 95^{th} percentile of the daily precipitation in the present period, expressed in percentage.

(a)

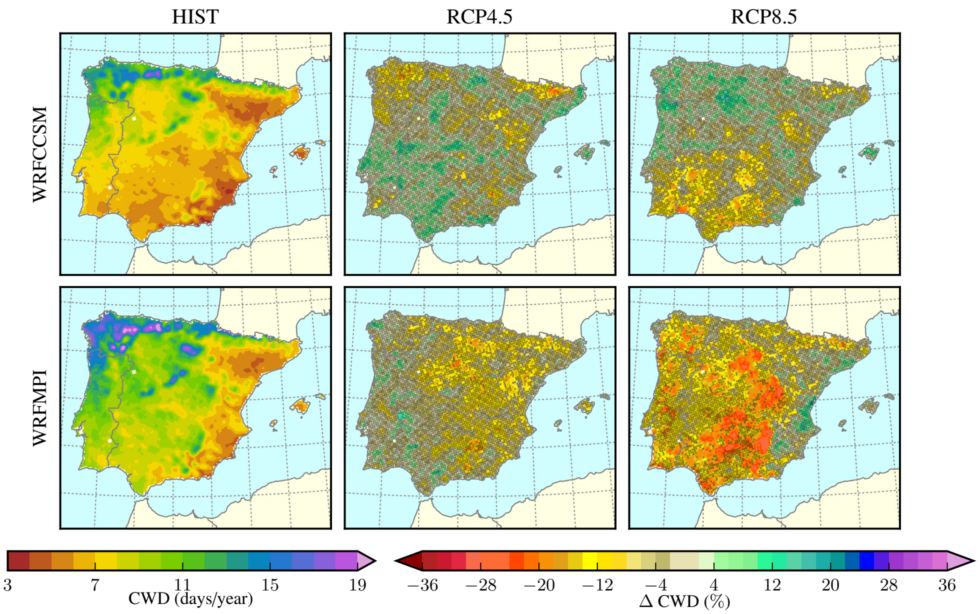

(b)

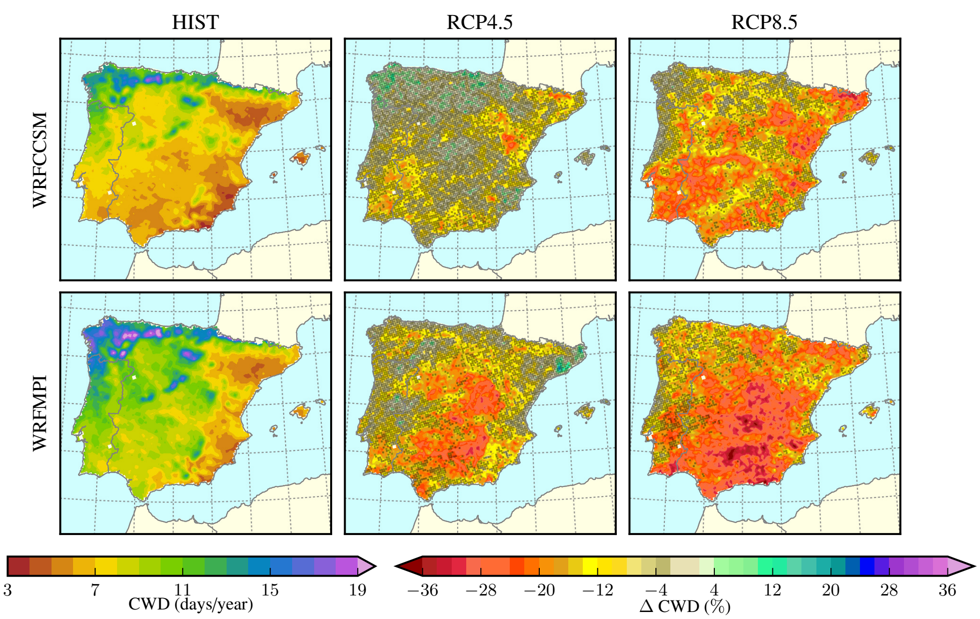

Figure 6.19: *The same as Figure* ***6.16*** *but for consecutive wet days (CWD, precipitation > 1 mm).*

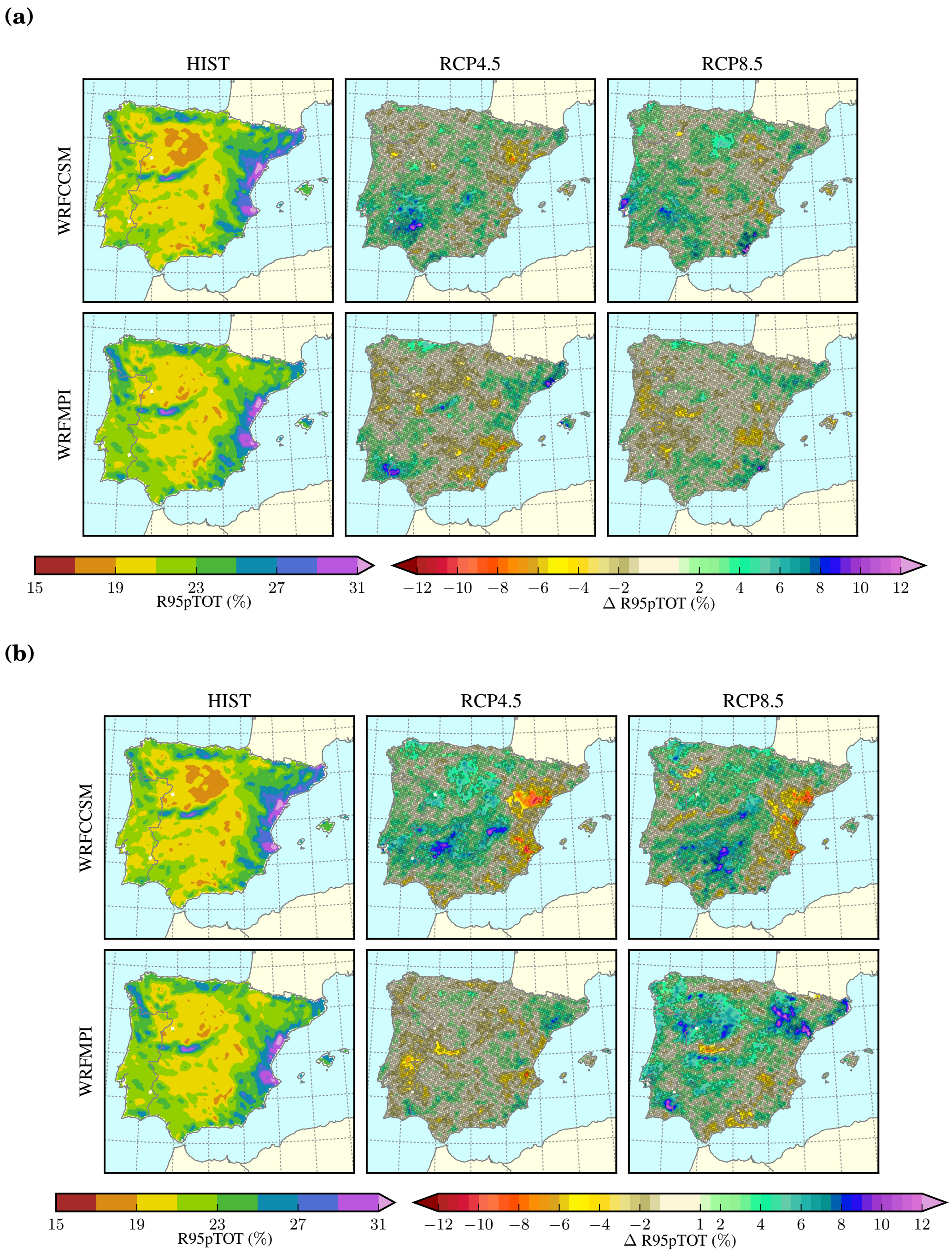

Figure 6.20: *Current (HIST) annual mean of the percentage of total precipitation above the 95th percentile and the (a) near and (b) far future projected changes, for both RCP4.5 and RCP8.5. The changes are expressed as the future vs. present values. Black dots indicate non-significant changes according to a two-tailed Mann-Whitney-Wilcoxon U test at the 95% confidence level.*

6.3. Temperature Changes

6.3.1. Changes in Annual Values

Maximum Temperature

As for precipitation, annual changes have been explored in terms of T_{max}. All runs showed a generalized significant warming for the entire IP with respect to the current climate (1980-2014). Such changes were found for both, the near and the far future (Figures ***6.21*** and ***6.22***, respectively). The increments in mean values for the near future reached values between 0.2-1.8°C. The areas less affected were located in the north-northwest of the Peninsula (e.g. coastal areas between the Bay of Biscay in the north and Cape Roca in the center of Portugal) where several points showed non-significant changes, whereas the highest rising temperatures appeared over the south-southeast. Such behavior suggests certain gradient northwest-southeast, which was particularly remarkable for the WRFMPI simulations and under the RCP4.5.

Concerning differences between simulations (Figure ***6.21***), WRFCCSM depicted similar performance between the two RCPs in the near future, and even contrary to the expected, the RCP8.5 presented lower warming than the RCP4.5, especially over western regions. The WRFMPI revealed similar changes to the WRFCCSM for the RCP4.5, although with lower values in general. However, under the RCP8.5 the most severe changes in this period were shown for WRFMPI simulations, with increases up to 1.8°C, mainly located in the southern half of IP.

For the far future (Figure ***6.22***), the entire IP were affected by highlighted significant increases. Both the WRFCCSM and WRFMPI revealed annual changes of T_{max} in a range of around 0.9-2.5°C under the RCP4.5, and between 1.7-5°C for the RCP8.5, showing similar spatial patterns to those for near future. In the comparison between scenarios, both the WRFCCSM and WRFMPI showed greater increases for the RCP8.5, being higher in magnitude for the WRFMPI. In general, the changes in T_{max} appeared to be influenced by the orography, i.e. at higher altitudes, the increases of temperatures are greater with respect to the present.

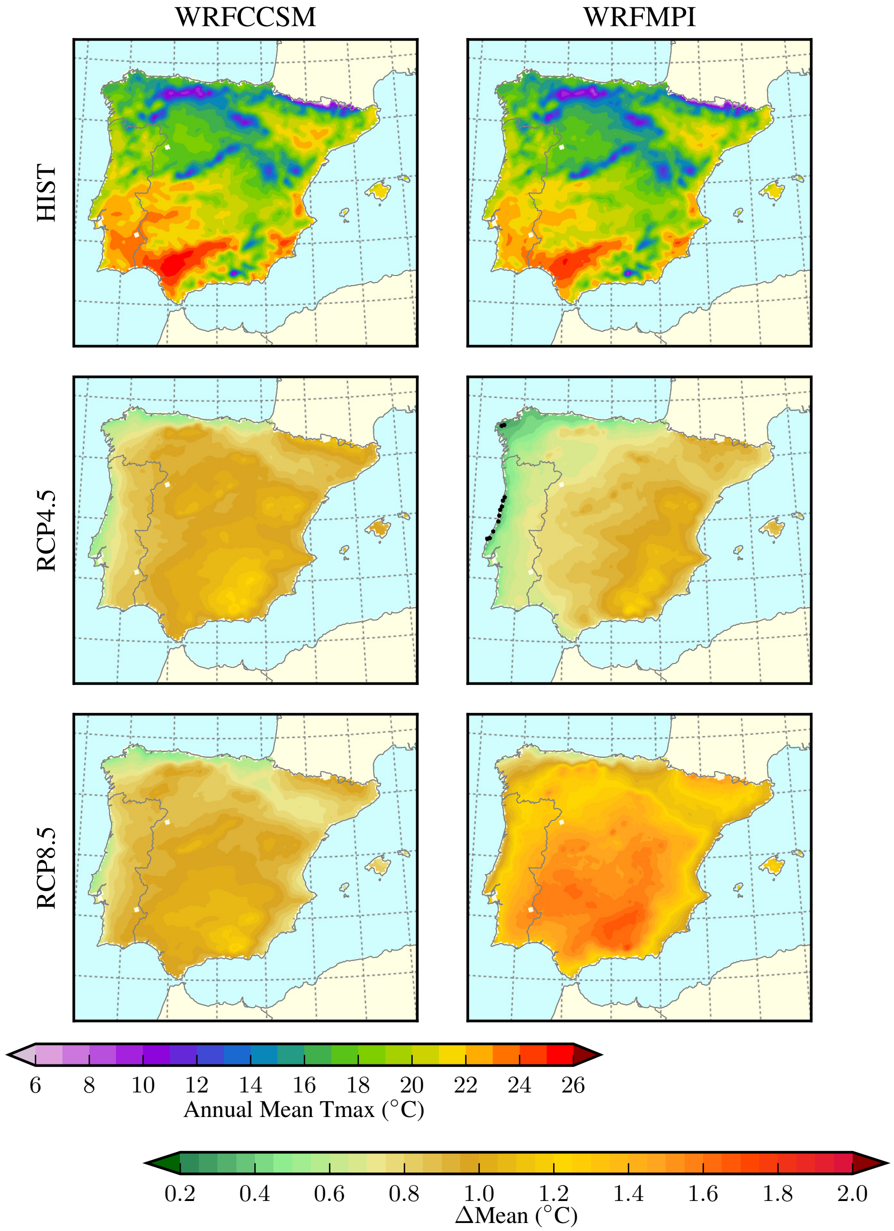

Figure 6.21: *Current (1980-2014) annual mean of T_{max} (first row) and the near future (2021-2050) projected changes (second and third rows) for both models and under the two RCPs (RCP4.5 and RCP8.5). In columns, the simulations driven by CCSM4 and MPIESM-LR are displayed. Black dots indicate non-significant changes according to a two-sided Student's test at the 95% confidence level.*

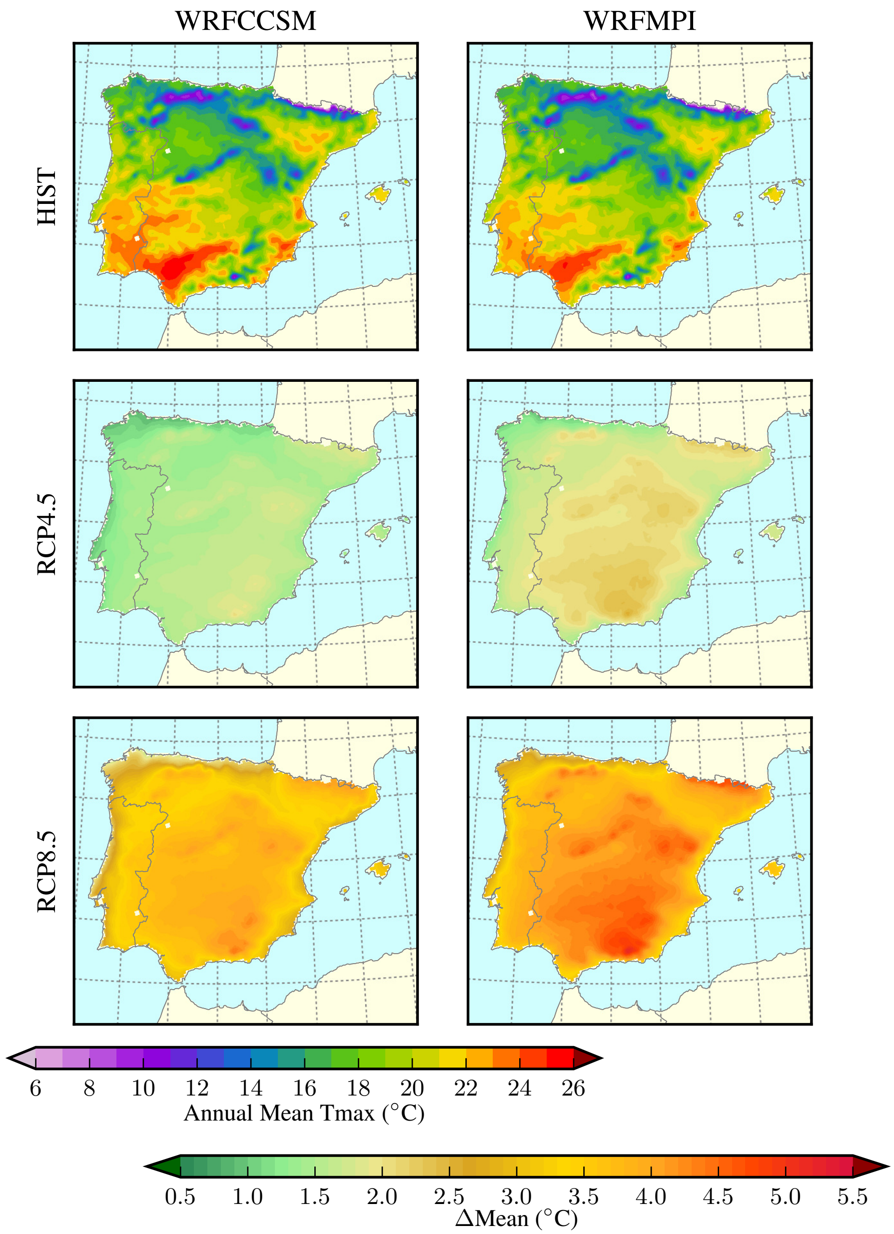

Figure 6.22: *The same as Figure **6.21** but for the far future (2071-2100).*

Minimum Temperature

Regarding changes in annual mean T_{min}, all WRF simulations revealed increments in their mean values for both the near and far future (Figures ***6.23*** and ***6.24***, respectively), being the changes significant for all grid-points and more moderate than those changes in terms of T_{max}.

Concerning the period 2021-2050 (Figure ***6.23***), the changes were between 0.4 and 1.9°C, and they appeared to be more marked in the southeast of the Peninsula, and especially for high mountain regions (e.g. the Pyrenees, the Cantabrian Range and Baetic System). Here, all WRF simulations located the greatest change in the Sierra Nevada (Baetic Sistem), where increases of temperature above 1.3°C arose. For this period, and as occurred for T_{max}, the WRFCCSM showed the strongest increments under the intermediate concentration pathway, particularly strong in the peninsular east. By contrast, the most marked changes of mean temperature were shown under the RCP8.5 for the WRFMPI simulations, with values of change above 1°C practically over the whole IP.

For the far future (Figure ***6.24***), the annual T_{min} reached values of increase in a range between 0.9 and 2.5°C for the RCP4.5, whereas such changes achieved values up to 5°C over limited areas under the RCP8.5. In this context, the WRFMPI projected the greatest changes, which were located in the interior regions and especially in high mountains again. The center and the south of Portugal, as well as the northern coast, reached the lowest increases in minimum temperature. For this period, changes between RCPs were more obvious, the difference between scenarios being of about 2°C in many areas.

In summary, results showed that the annual mean temperature is very likely to increase in the future, such increment being more marked in the far future, and under the RCP8.5. Moreover, it is possible a wider range of daily temperature in the future because the maximum temperature seems to be more affected than the minima. However, these results represent an overview of the changes, and therefore, it is desirable to further analyze the changes in both T_{max} and T_{min} through the seasonal changes. Thus, we could elucidate how will be the intra-annual distribution of the changes.

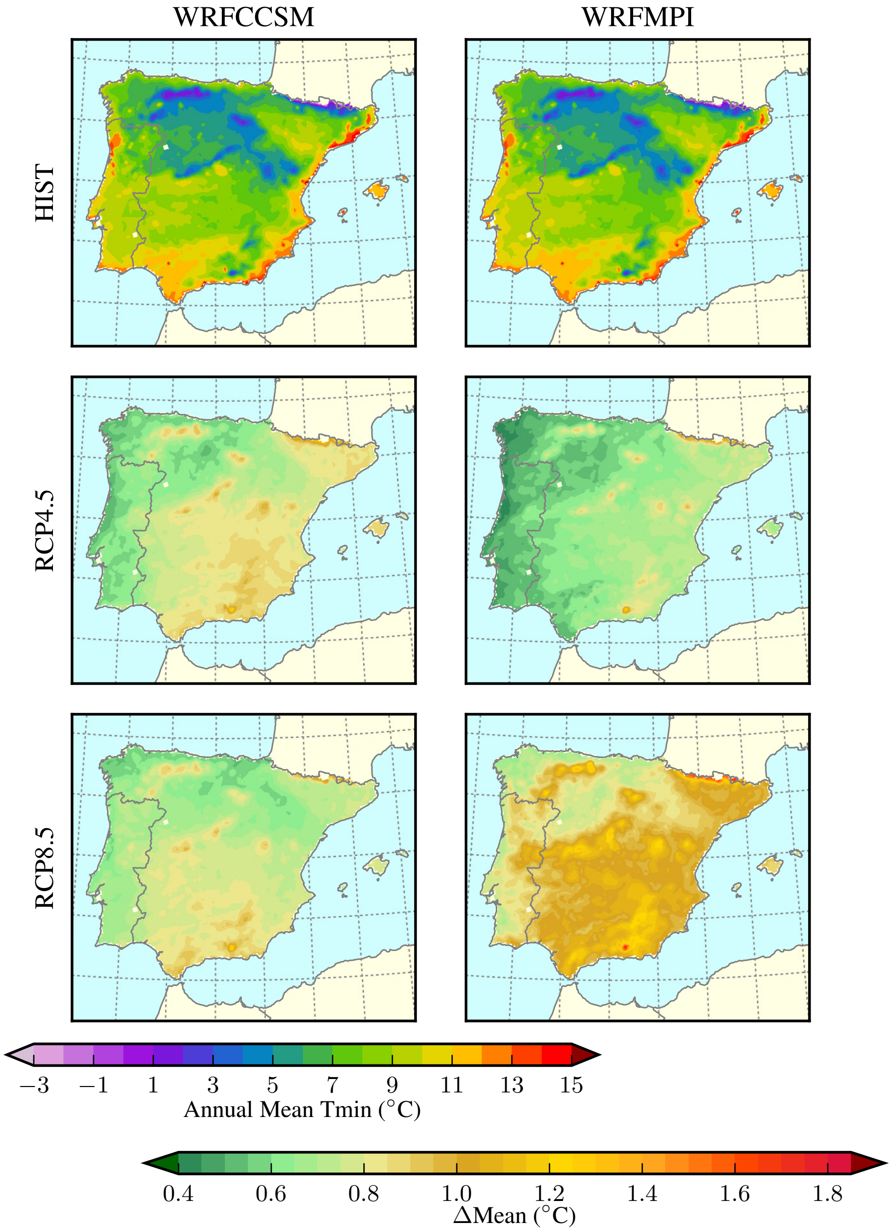

Figure 6.23: *Current (1980-2014) annual mean of T_{min} (first row) and their near future (2021-2050) projected changes (second and third rows) over the IP, for both RCP4.5 and RCP8.5. In columns, the simulations driven by CCSM4 and MPI-ESM-LR are represented. Black dots indicate non-significant changes according to a two-sided Student's t test at the 95% confidence level.*

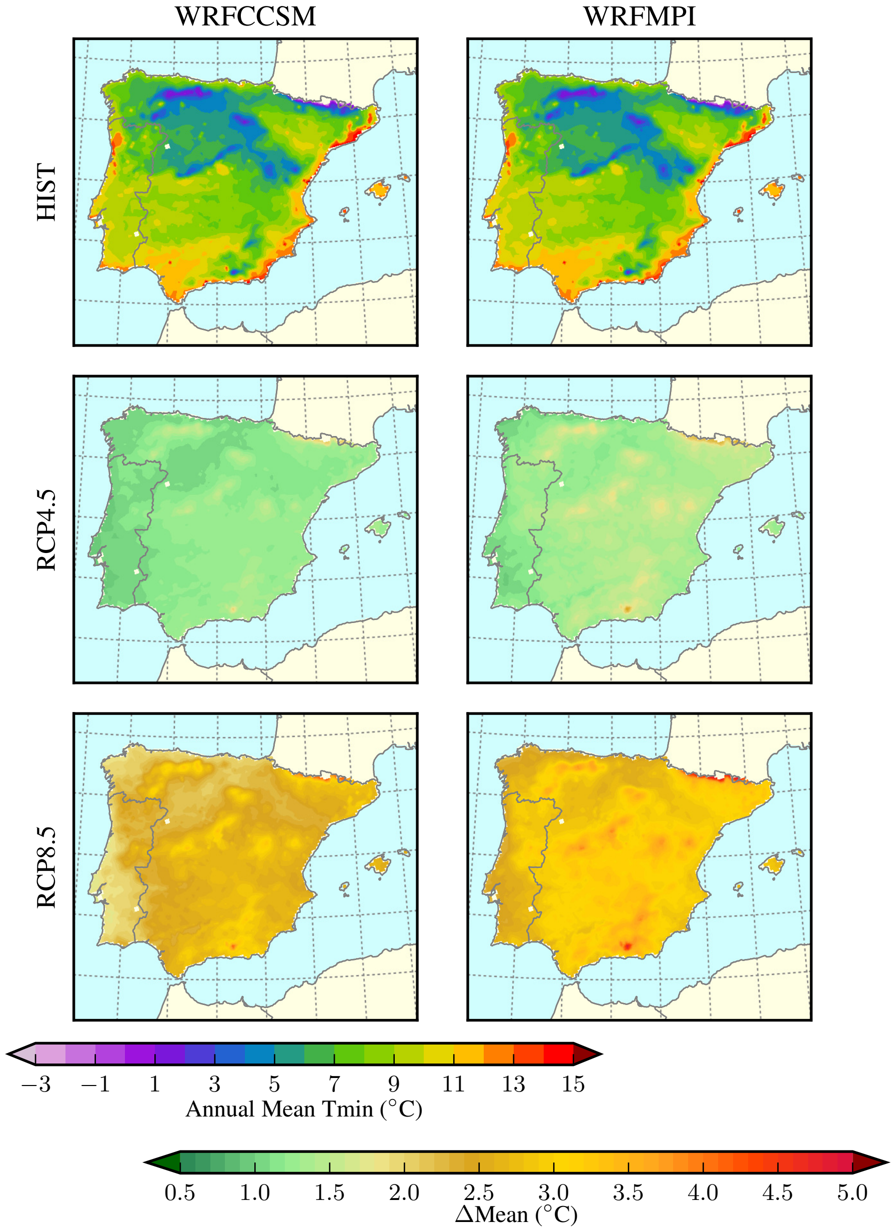

Figure 6.24: *The same as Figure* ***6.23*** *but for the far future (2071-2100).*

6.3.2. Changes in Seasonal Values

Changes in the Seasonal Mean of Maximum Temperature

Figures ***6.25*** and ***6.26*** display changes in the mean values in relation to the present, for both the WRFCCSM and WRFMPI, respectively. In the same way, Figures ***6.27*** and ***6.28*** show such changes for the period 2071-2100. In general, both the WRFCCSM and WRFMPI projected seasonal increases in T_{max} for the two periods, and under the two scenarios. The largest enhancements were found in the south, and in the east of the Peninsula, particularly over high mountains regions (the Pyrenees, Cantabrian Range, Central System, Iberian System and Baetic System). The lowest values, however, were usually located in the northwestern IP and, especially in coastal regions across the Atlantic and Cantabrian coasts, where non-significant changes appeared in some cases.

For the near future, different projected changes, in general, were shown for all seasons. Namely, although the magnitude of the changes was similar under the two RCPs, the WRFCCSM usually projected more severe changes for the RCP4.5, especially in the east of the Peninsula. By contrast, the WRFMPI revealed important differences between RCPs, more moderate under the RCP4.5, and with substantial increases under the RCP8.5, particularly for summer (up to 2°C for broad areas located in the peninsular interior) and autumn. By contrast, non-significant changes also appeared for some regions and seasons (e.g., coastal areas in the Cantabrian and Portugal during summer).

Winter was the season when the IP appeared to suffer the minor changes of T_{max}, which were even not significant in some cases. Here, the WRFCCSM (Figure ***6.25***, DJF) presented values up to 0.6°C and only a few points located in the Ebro Valley were non-significant under the RCP4.5. However, for the RCP8.5 the non-significant changes were broadly extended over the northeastern IP. By contrast, the WRFMPI (Figure ***6.26***, DJF) projected greater increases (increments of about 0.8-1°C and above 1°C for the RCP4.5 and RCP8.5, respectively), which were stronger for the RCP8.5. For this latter, the lowest increments were located over eastern regions such as the Ebro Valley and Mediterranean Coast. In spring, more substantial increases of T_{max} (values of around 0.2-1.8°C) were shown, more marked for the RCP8.5 in both GCMs. In this season, more severe

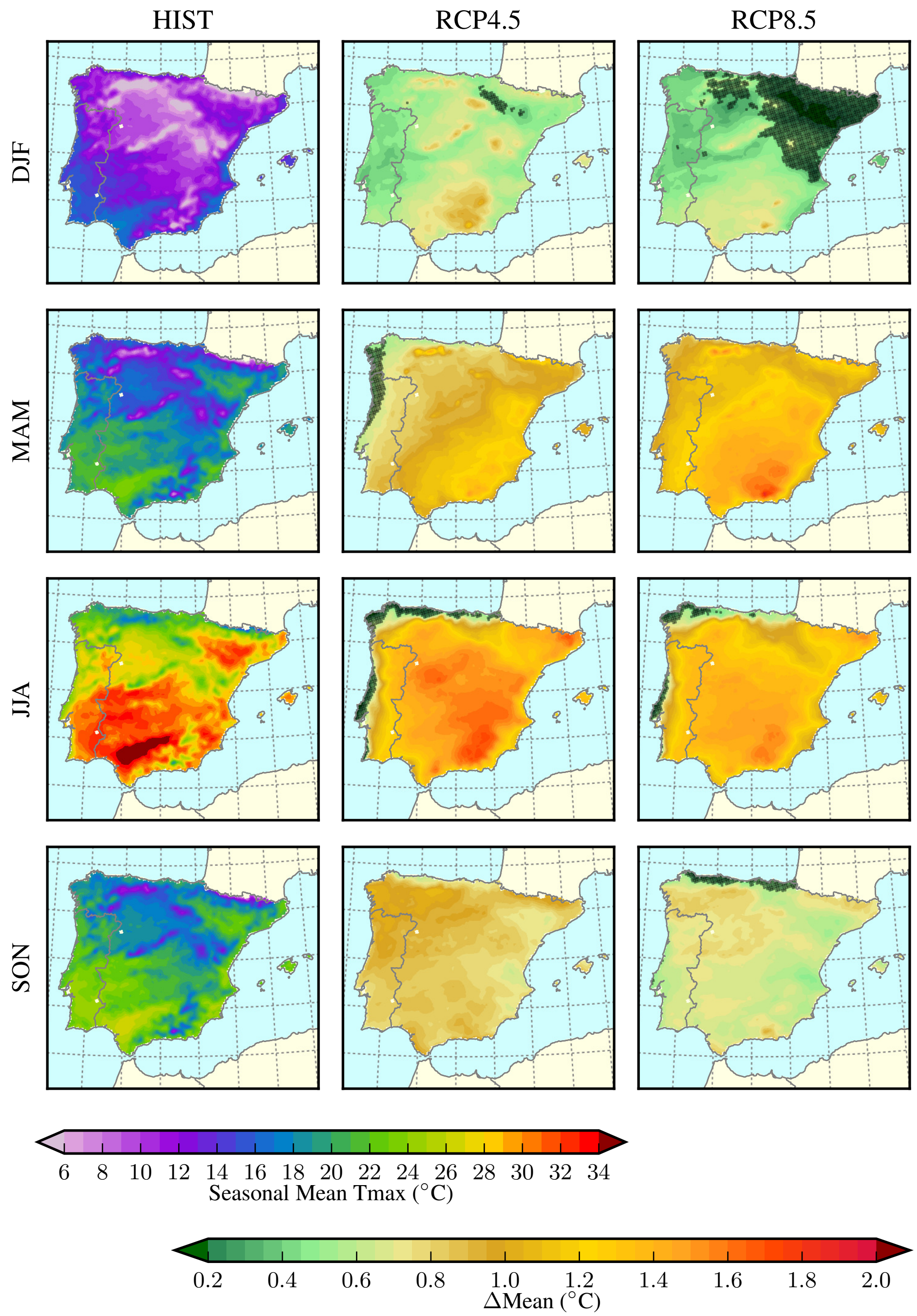

Figure 6.25: *Current (1980-2014) seasonal mean of T_{max} (first column) and its projected changes by the WRFCCSM simulations in the near future (2021-2050). In second and third columns the results from the RCP4.5 and RCP8.5 are represented, respectively. Black dots indicate non-significant changes according to a two-tailed Student's t test at the 95% confidence level.*

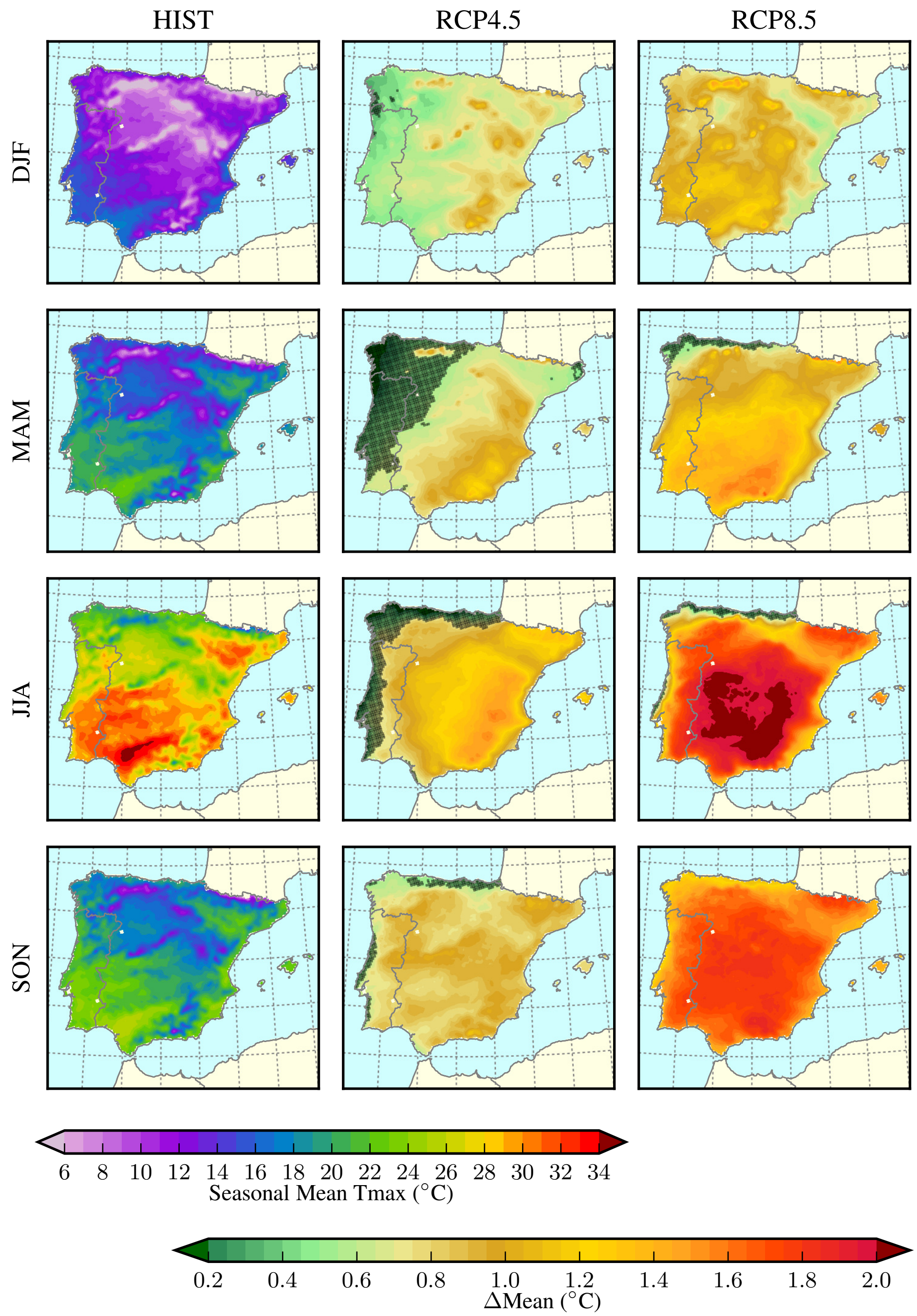

Figure 6.26: *As Figure* ***6.25*** *but for the WRFMPI simulations.*

changes appeared to be projected by WRFCCSM, at least under the RCP4.5 (Figure ***6.25***, MAM), where WRFMPI presented non-significant rises over a large region (most of Portugal, Galicia, parts of the Northern Plateau, and certain areas of the northeastern IP). However, both the WRFCCSM and WRFMPI projected over the southeast similarly, where the magnitude of the changes was the highest.

Summer was the season when the most relevant changes were projected (values of around 0.3-2°C). The WRFCCSM again showed a similar behavior for both RCPs (Figure ***6.25***, JJA), with the largest increases for the RCP4.5. Whereas WRFMPI presented higher differences (Figure ***6.26***, JJA), more marked under the RCP8.5 (values above 2°C in most of the IP). Non-significant changes were found in northern Coasts, especially extensive under the RCP4.5 and for WRFMPI. In this simulation, non-significant values were presented throughout the coastal region between the Bay of Biscay (in the north) and the Cape St. Vicent (in the south of Portugal). Regards changes in autumn, very different behaviors were found (values of about 0.4-1.8°C). The WRFCCSM simulations revealed a generalized moderate change (Figure ***6.25***, SON), whereas WRFMPI projected remarkable increases (Figure ***6.26***, SON), which were especially strong for the RCP8.5. By contrast, areas with non-significant changes appeared over the Cantabrian Coast for the RCP8.5 for the WRFCCSM, and for the RCP4.5 in WRFMPI.

For the far future (Figures ***6.27*** and ***6.28***), however, all WRF simulations revealed very similar behaviors, with significant increases everywhere. For the RCP4.5, the changes were similar to the near future, which could be suggesting a stabilization of the climate change for the intermediate GHG emissions. By contrast, important increases were found under the high emissions scenario practically over the whole IP (values above 5°C in summer). In this period, as for the previous one, the distribution of the changes along the year was the same. So, winter (Figures ***6.27*** and ***6.28***, DJF) showed the most moderate changes (increases of around 1°C and up to 4°C for the RCP4.5 and RCP8.5, respectively). Such changes were especially remarkable over mountain areas and in the southeastern IP. For this season, the WRFMPI projected more severe changes for both RCPs.

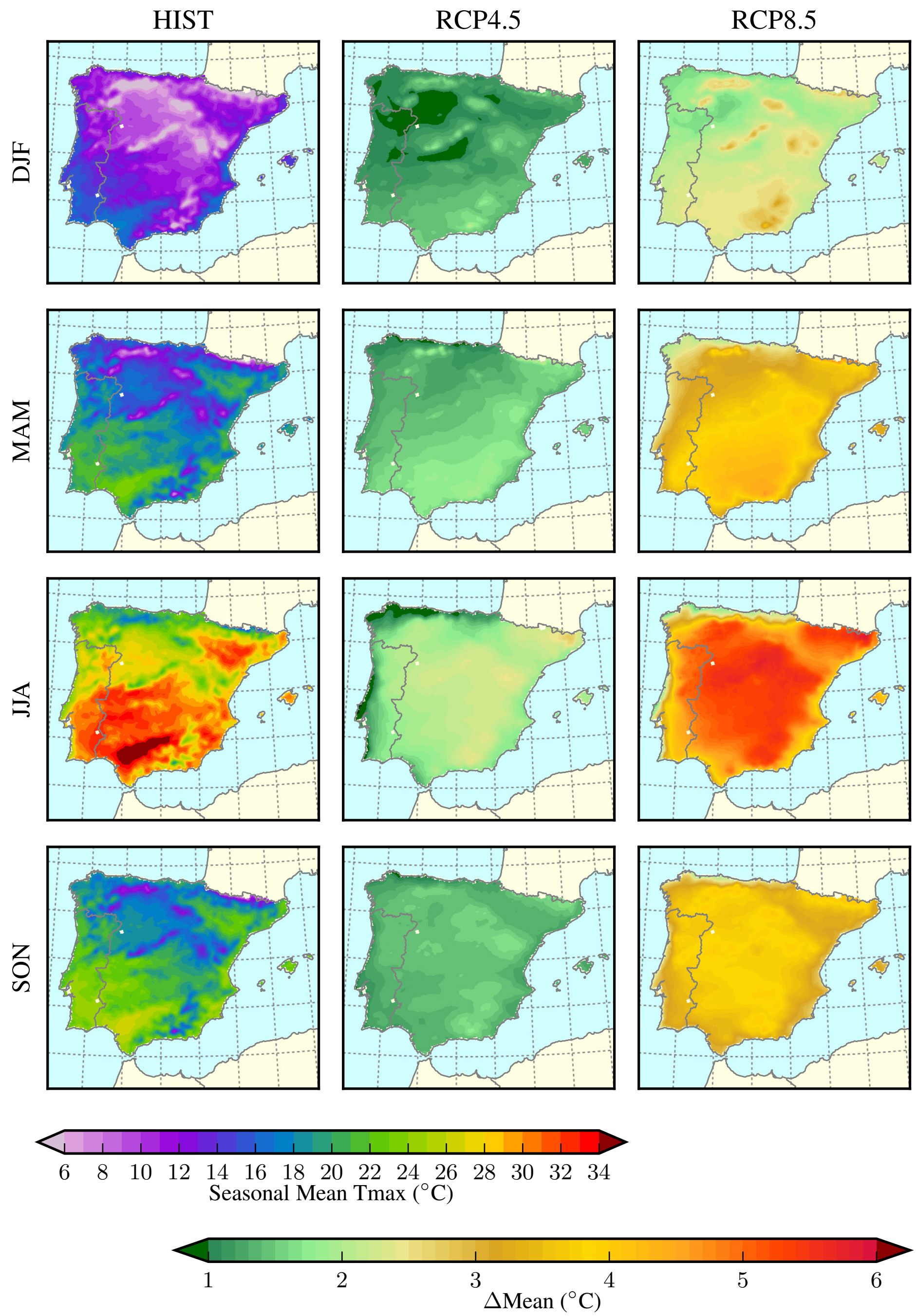

Figure 6.27: *Current (1980-2014) seasonal mean of T_{max} (first column) and its projected changes by the WRFCCSM simulations in the far future (2071-2100). In second and third columns the results from the RCP4.5 and RCP8.5 are represented, respectively. Black dots indicate non-significant changes according to a two-tailed Student's t test at the 95% confidence level.*

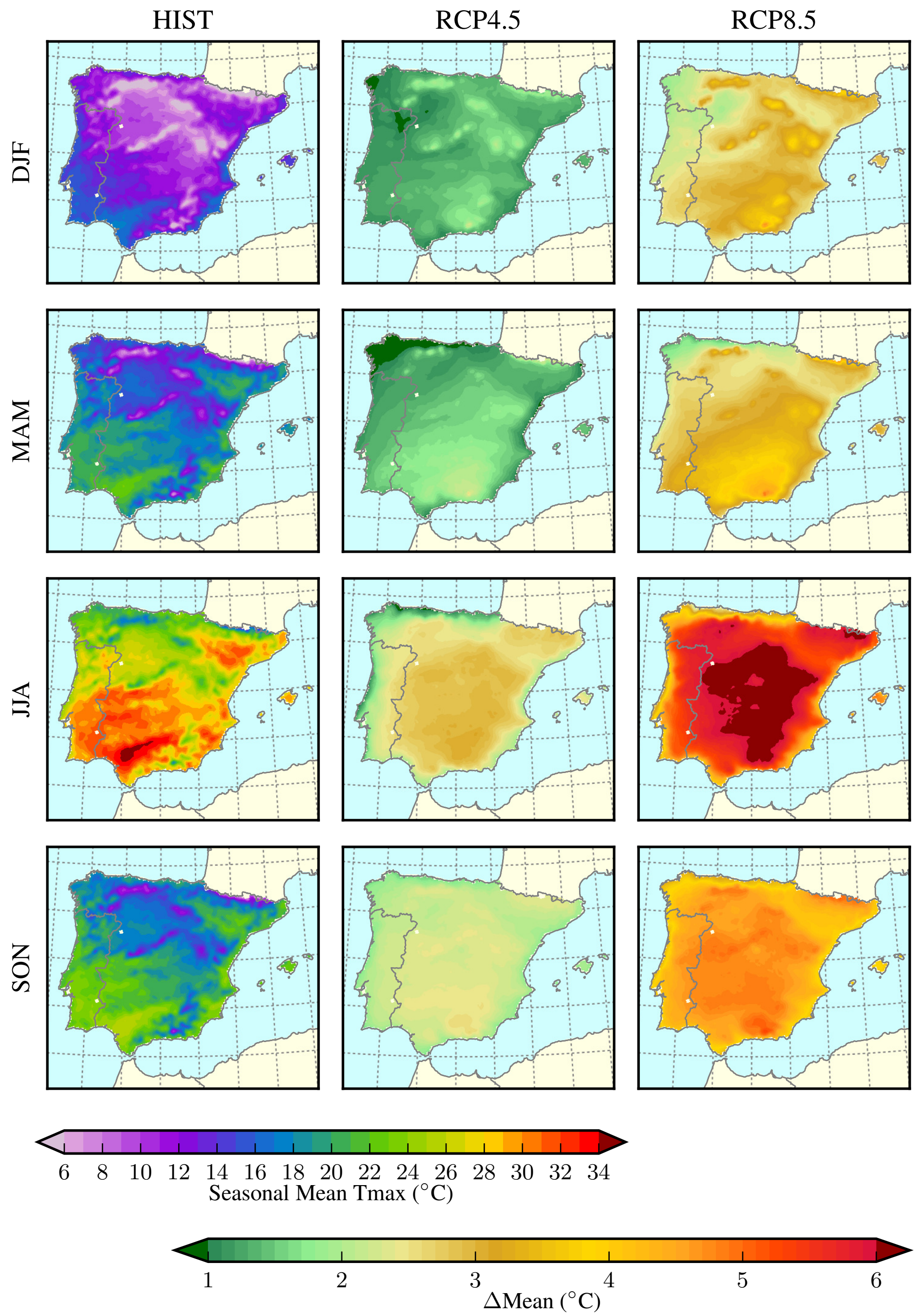

Figure 6.28: *As Figure **6.27** but for the WRFMPI simulations.*

In spring (Figures ***6.27*** and ***6.28***, MAM), all WRF simulations also showed changes with similar spatial patterns (values of around 1-5°C), the southeastern and some mountain areas being again the most affected. However, greater differences were found between RCPs in this period. Thus, under the RCP4.5 increases between 1-2°C were shown, and increments of about 2.5-3.5°C appeared for the RCP8.5. Summer again showed the most marked increments of the temperature (values between 1°C and above 6°C), particularly under the RCP8.5 (Figures ***6.27*** and ***6.28***, JJA). In this latter scenario, a larger extension showed increases above 5°C, being these increments even higher than 6°C for the WRFMPI simulations. As in the previous period, for autumn the WRFCCSM and the WRFMPI projected values of change (about 1-4.5°C) with differences in magnitude. Meanwhile, for WRFCCSM appeared moderate increases of the temperature (Figure ***6.27***, SON), substantial increases in autumn mean values were shown by WRFMPI, appearing differences between them of around 1°C (Figure ***6.28***, SON).

Changes in the Seasonal Mean of Minimum Temperature

The changes projected in terms of the seasonal T_{min} showed similar performance to the T_{max}, but with a more moderate magnitude in general. Figures ***6.29*** and ***6.30*** display the mean changes in T_{min} projected for the near future with respect to their present values, for the WRFCCSM and the WRFMPI, respectively. As showed T_{max}, the changes in this period were similar in magnitude for the two RCPs for the WRFCCSM, stronger for the RCP4.5 in all seasons except for spring. The WRFMPI simulations, however, presented important differences in magnitude between the moderate and the higher GHG emissions scenarios, more marked under the RCP8.5, in general.

Both simulations showed moderate increments of the mean T_{min} during winter with most changes ranged from 0.2 to 1°C. In WRFCCSM (Figure ***6.29***, DJF), the strongest changes appeared in the peninsular southeast under the RCP4.5, reaching values above 0.8°C. The RCP8.5, presented a large number of grid-points with non-significant changes with respect to present values over many regions in the north (e.g., the Pyrenees and the Cantabrian and Galician Coasts). Contrariwise, the WRFMPI (Figure ***6.30***, DJF) projected similarly under both RCPs, with increases above 2°C over several mountain systems. Here,

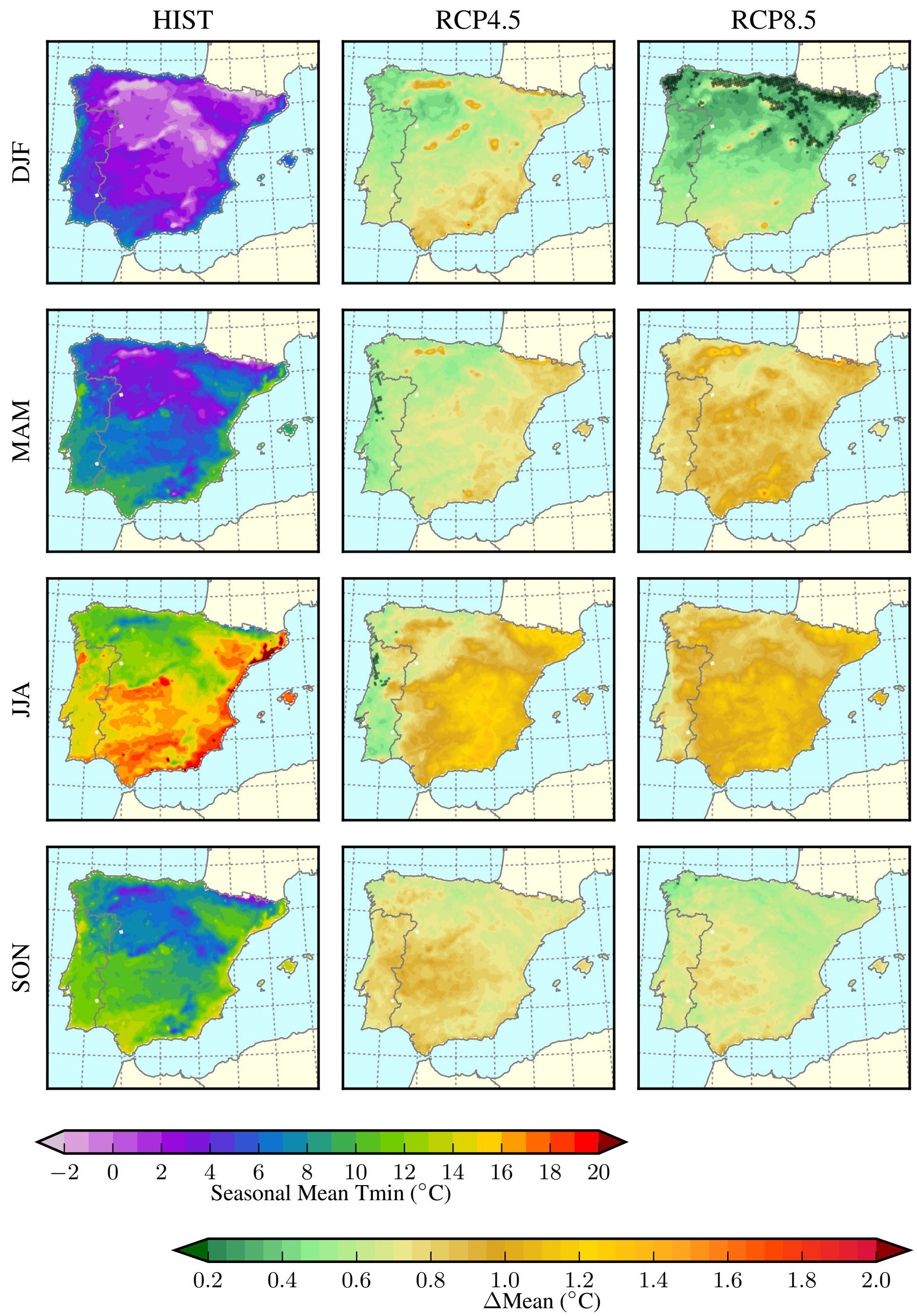

Figure 6.29: *Current (1980-2014) seasonal mean of T_{min} (first column) and its projected changes by the WRFCCSM simulations in the near future (2021-2050). In second and third columns the results from the RCP4.5 and RCP8.5 are represented, respectively. Black dots indicate non-significant changes according to a two-tailed Student's t test at the 95% confidence level.*

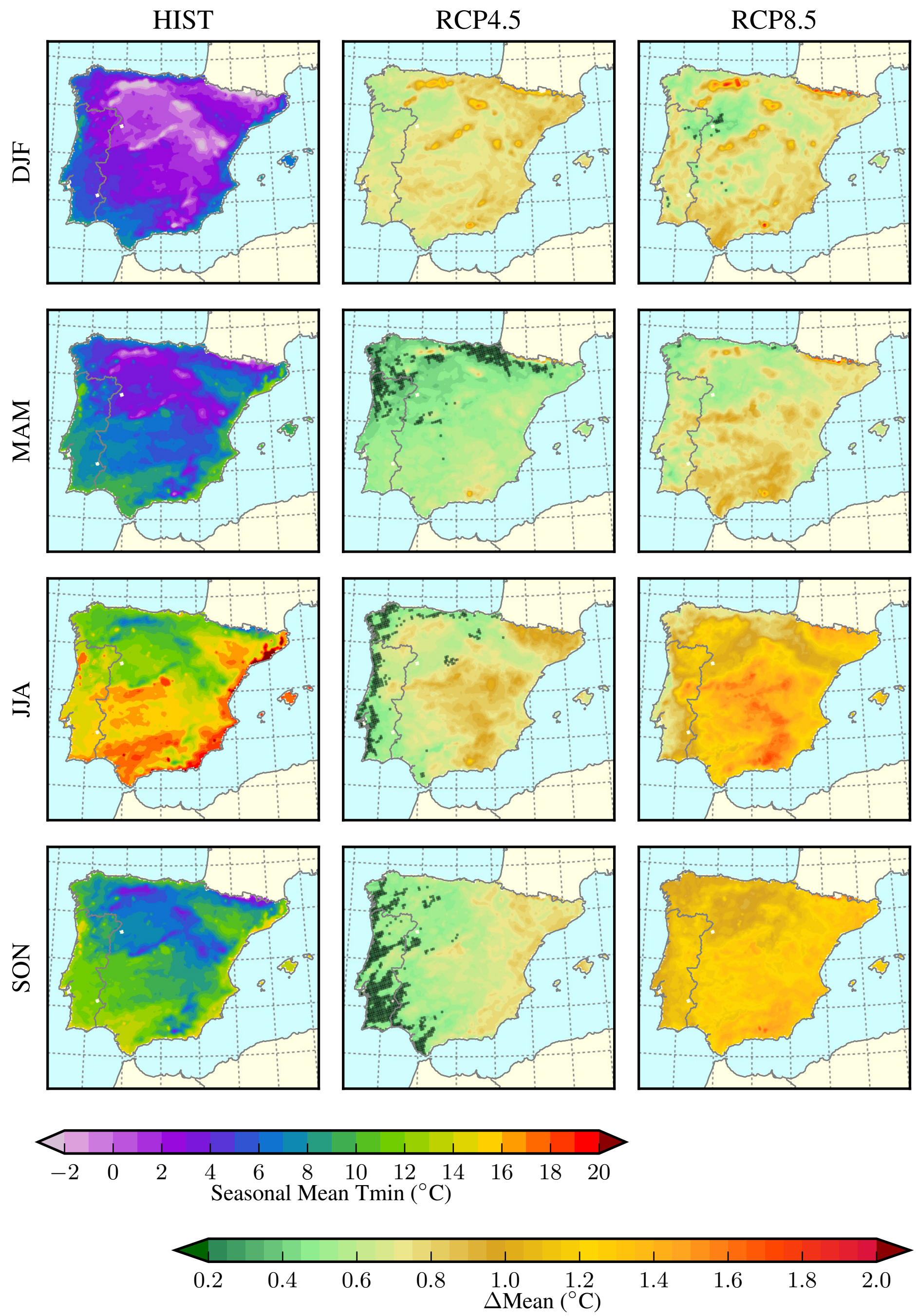

Figure 6.30: *As Figure* ***6.29*** *but for the WRFMPI simulations.*

although the magnitude was greater for the RCP8.5 in most of the IP, the increases were lower than under the RCP4.5 over the Northern Plateau and the Galician Massif. It is interesting to note that in this season changes in T_{min} are predominantly significant and higher in mountain regions than those found in T_{max}.

The spring changes appeared to be also moderate, with most of them of around 0.2-1.3°C . Under the RCP4.5, the results revealed similar changes in magnitude to winter for the WRFCCSM simulations (Figure ***6.29***, MAM), and even less pronounced for the WRFMPI simulations (Figure ***6.30***, MAM). For this latter, an important number of grid-points with non-significant changes were shown in the northern regions. However, under the RCP8.5, WRFCCSM projected more severe rises of the T_{min} in the whole IP (values above 0.8°C), with the highest values about 1.8°C. The WRFMPI, however, presented more homogenous changes with the maximum increments over the northeastern and southern half.

For summer, the most substantial changes were found (increases around 0.4-1.8°C), with the areas less affected located in the west, especially for the RCP4.5 (Figures ***6.29*** and ***6.30***, JJA). WRFMPI showed non-significant changes along the entire Atlantic Coast under the RCP4.5. Contrariwise, for the RCP8.5 severe changes were projected practically over the entire IP, with major changes over mountainous regions in the central and southeastern IP. In autumn, changes were similar to T_{max} in term of spatial patterns (changes of around 0.2-1.5°C). That is, the WRFCCSM projected moderate increments of minimum temperature similar in magnitude to those found in spring under the RCP4.5 and even lower for the RCP8.5 (values around 0.4-1°C). By contrast, the WRF-MPI suggested more pronounced changes in mean values (values of about 1.4°C in mostly IP), at least for the RCP8.5 (Figures ***6.29*** and ***6.30***, SON). Additionally, the WRFMPI simulation under the RCP4.5 revealed large differences between the east and the west of the Peninsula. Indeed, the eastern IP showed regions clearly affected by the increase of the T_{min} (increases up to 11°C), while the western IP presented a large area with non-significant changes. Under the RCP8.5, a quite homogeneous spatial pattern was shown, reaching increases about 1.2-1.41°C.

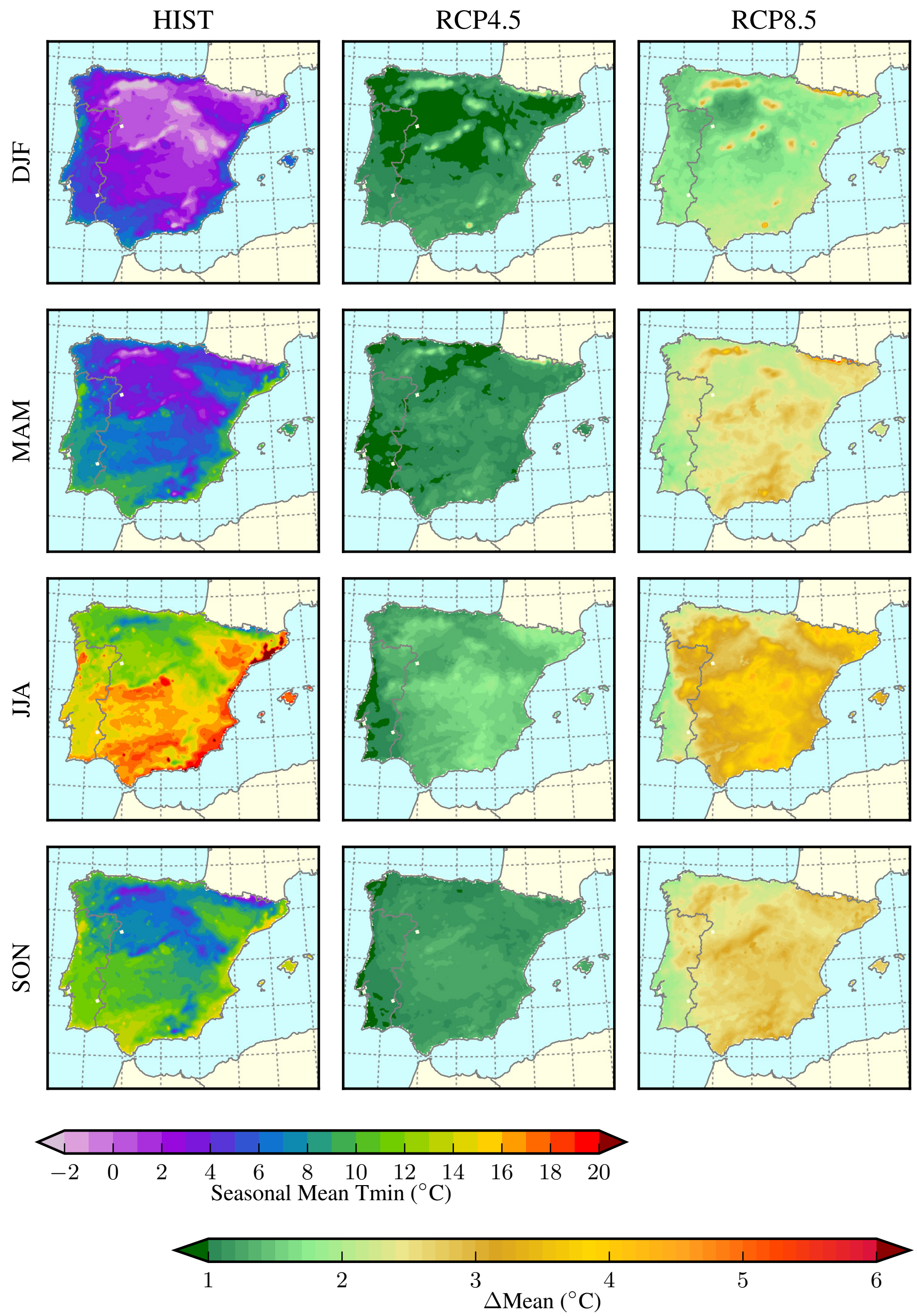

Figure 6.31: *Current (1980-2014) seasonal mean of T_{min} (first column) and its projected changes by the WRFCCSM simulations in the far future (2071-2100). In second and third columns the results from the RCP4.5 and RCP8.5 are represented, respectively. Black dots indicate non-significant changes according to a two-tailed Student's t test at the 95% confidence level.*

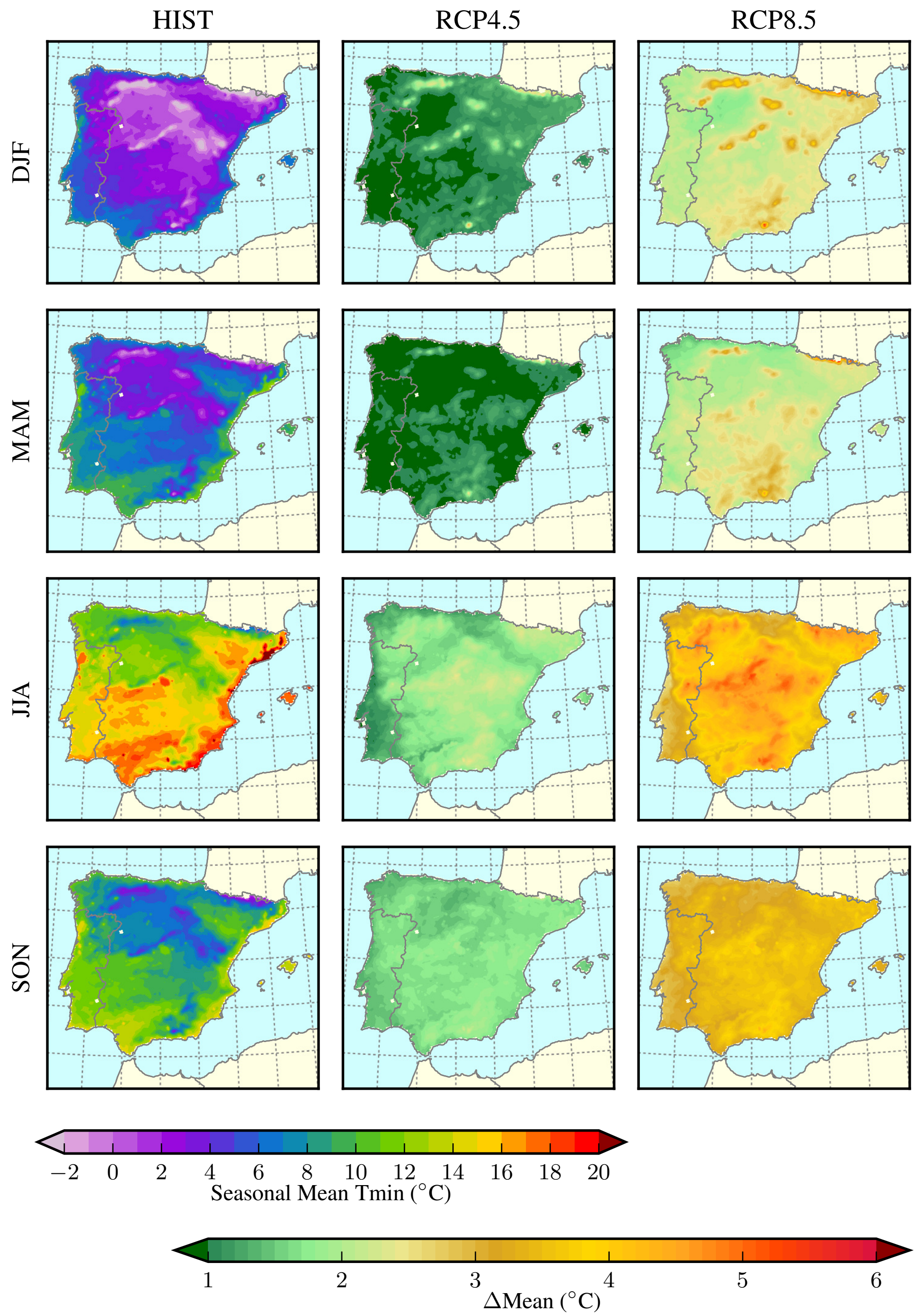

Figure 6.32: *As Figure **6.31** but for the WRFMPI simulations.*

In the same way, Figures ***6.31*** and ***6.32*** display the changes for the far future. In general, all WRF simulations presented changes with similar spatial patterns, but with larger magnitude under the RCP8.5. In winter (Figures ***6.31*** and ***6.32***, DJF), the simulations from the RCP4.5 showed changes close to those found in the near future, although with a slightly higher magnitude (up to 2.5°C). Under the RCP4.5, the WRFCCSM and the WRFMPI simulations appeared to project the highest values in mountainous regions and over the south of the Peninsula. The RCP8.5 showed the highest values for the WRFMPI (Figure ***6.32***, DJF), where the differences in the mean temperature in relation to the present were about 4°C in the Pyrenees, Cantabrian Range, Central System and, even higher in the Sierra Nevada(in the Baetic System). Here, the highest changes appeared along the eastern IP.

Values of change around 1-3.5°C were shown in spring, (Figure ***6.31*** and ***6.32***, MAM), with the most severe changes projected by the WRFCCSM. In these latter simulations, significant increases over all the IP were shown (increments of around 2-3.5°C). Again, summer is the season with the most substantial changes (increases around 1-5°C), which were similar in spatial pattern to those found in winter, but with higher magnitude (Figure ***6.31*** and ***6.32***, JJA). The WRFMPI simulations, in general, showed greater increases in minimum temperature, reaching values of 5.5°C in mountain systems. Also in autumn, substantial changes appeared for the far future (Figure ***6.31*** and ***6.32***, SON), when the changes were around 1-4°C. The greatest increases appeared under the RCP8.5 and especially for the MPI-ESM-LR-driven simulations. Here, the WRFCCSM projected more moderate increments of T_{min} for the end of the century, showing even mean values below 1°C in certain coastal areas of the peninsular western under the RCP4.5. Concerning the comparison of these extreme temperatures, note that meanwhile, T_{max} presented the highest increases (more than 6° C) over a broad area in summer at the far future and under the RCP8.5, T_{min} presented the highest increase of 5.5°C and over less extended areas.

Changes in the Variability of Maximum Temperature

To determine whether the global warming entails an increase in the climate variability as well, we also calculated changes in the standard deviation of the seasonal mean of T_{max}. These were computed in relative changes and expressed in Celsius degrees.

For winter, in the near future, the WRFCCSM projected significant increases in interannual variability (Figure ***6.33***, DJF) for both RCPs. Under the RCP4.5, such increases appeared in most of the regions where the interannual variability in the present is characterized by low values (Northern Plateau, Ebro Valley, Galician Coast, Balearic Islands and over the southeast of the Peninsula). Here, the highest changes in standard deviation arose in the Iberian System and the Northern central Plateau (values up to 0.8°C). For the RCP8.5 similar changes were also projected, although these were lower in magnitude. The WRFMPI simulations (Figure ***6.34***, DJF), however, showed significant increases only under the RCP8.5, mostly for the southern half of the Peninsula, with the maximum differences over the Baetic System (with values of around 0.5-0.7°C). For spring (Figures ***6.33*** and ***6.34***, MAM), all simulations fundamentally projected increases except for Cantabrian regions in the WRFMPI simulations, but these are non-significant in all WRF simulations.

In summer (Figures ***6.33*** and ***6.34***, JJA), the changes were predominantly negative although these were non-significant in general. Thus, only for the RCP8.5 very small areas presented significant changes. In relation to autumn values, meanwhile the WRFCCSM (Figure ***6.33***, SON) showed non-significant changes in general (with some exception of increases in interannual variability over western coasts for the RCP8.5), the WRFMPI projected remarked increases in the standard deviation (Figure ***6.34***, SON). These latter were broadly found in the western IP and with a larger surface area for the RCP4.5.

In the far future (Figures ***6.35*** and ***6.36***), the changes were more significant. During winter, the projection from the WRFCCSM simulations (Figure ***6.35***, DJF) under the RCP4.5 displayed similar performance than those for the previous period, but with slightly smaller values. Under the RCP8.5, the increases were mainly located in the west of the Peninsula. The WRFMPI simulation (Figure ***6.36***, DJF) under the RCP4.5, nevertheless, projected significant increases over the south of the Peninsula, reaching the highest values in the Baetic System (values of around 0.5°C). While, under the RCP8.5, significant changes in the interannual variability appeared to be reduced to small areas in southern IP for this GCM-driven simulations. Here, the highest values were

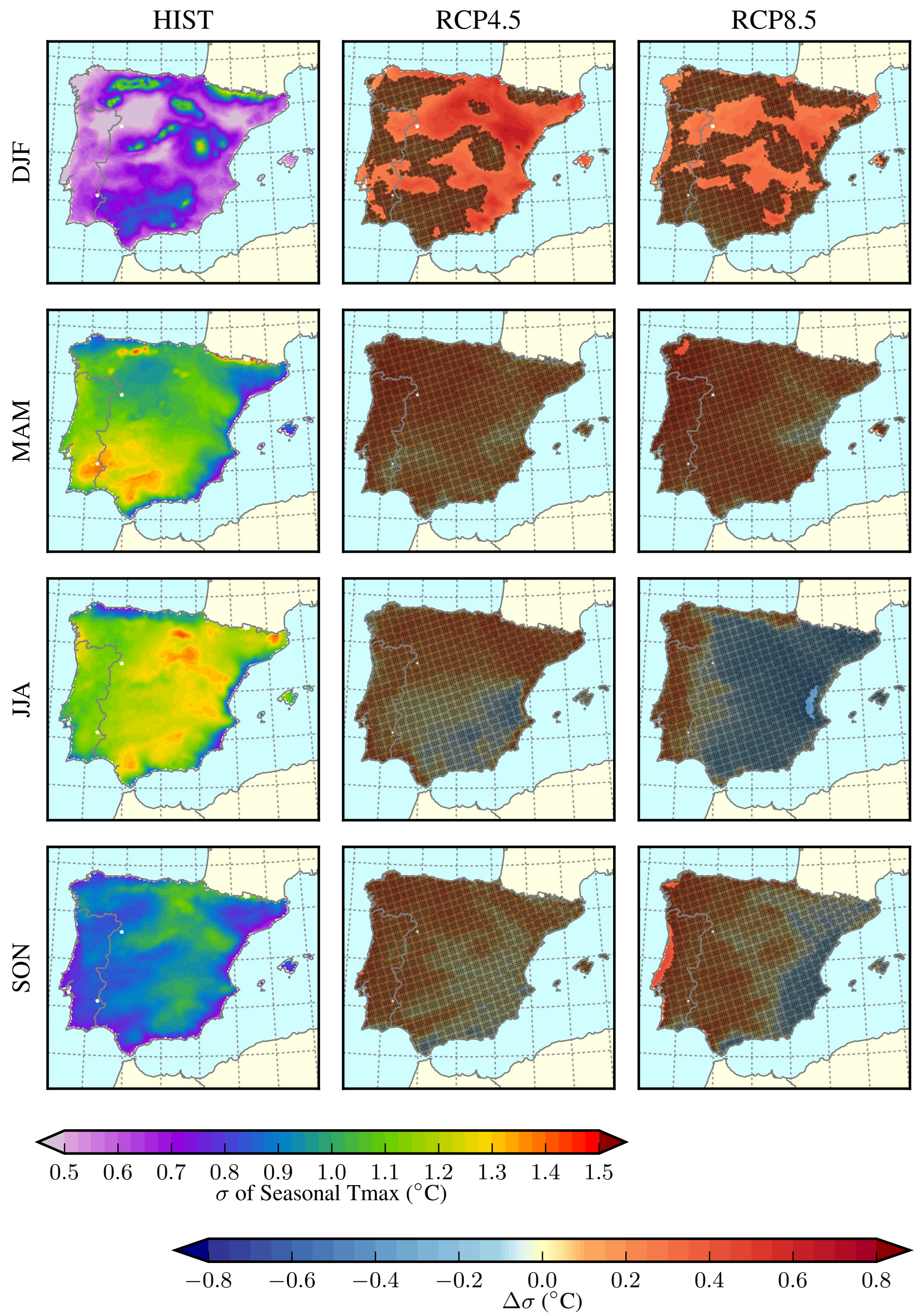

Figure 6.33: *Current (1980-2014) seasonal standard deviation of T_{max} (first column) and its near future (2021-2050) relative to projected changes from the WRFCCSM. The results from the RCP4.5 and RCP8.5 are shown in second and third columns, respectively. Black dots indicate non-significant changes according to a two-tailed Fisher-Snedecor F test at the 95% confidence level.*

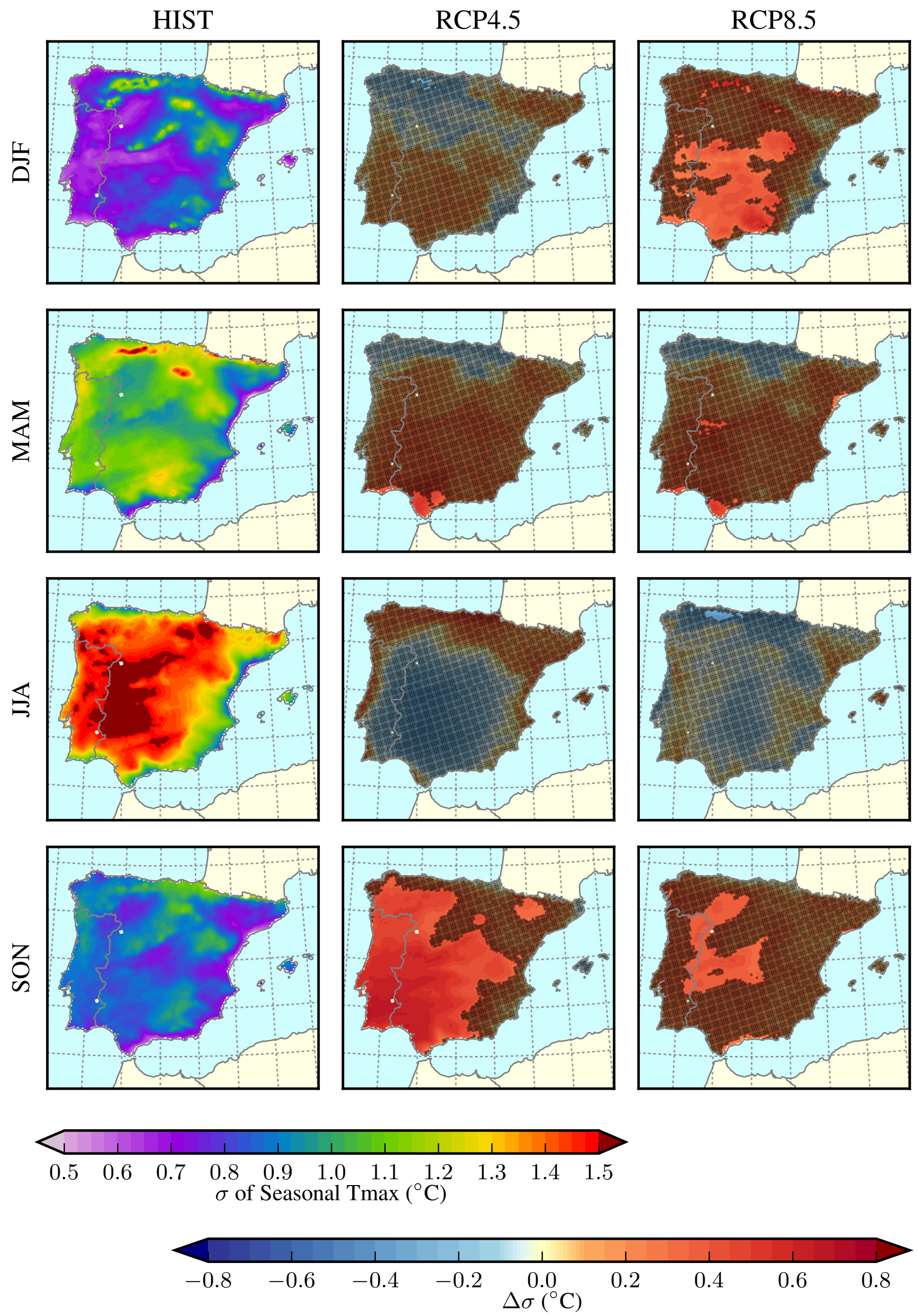

Figure 6.34: *As Figure **6.33** but for the WRFMPI simulations.*

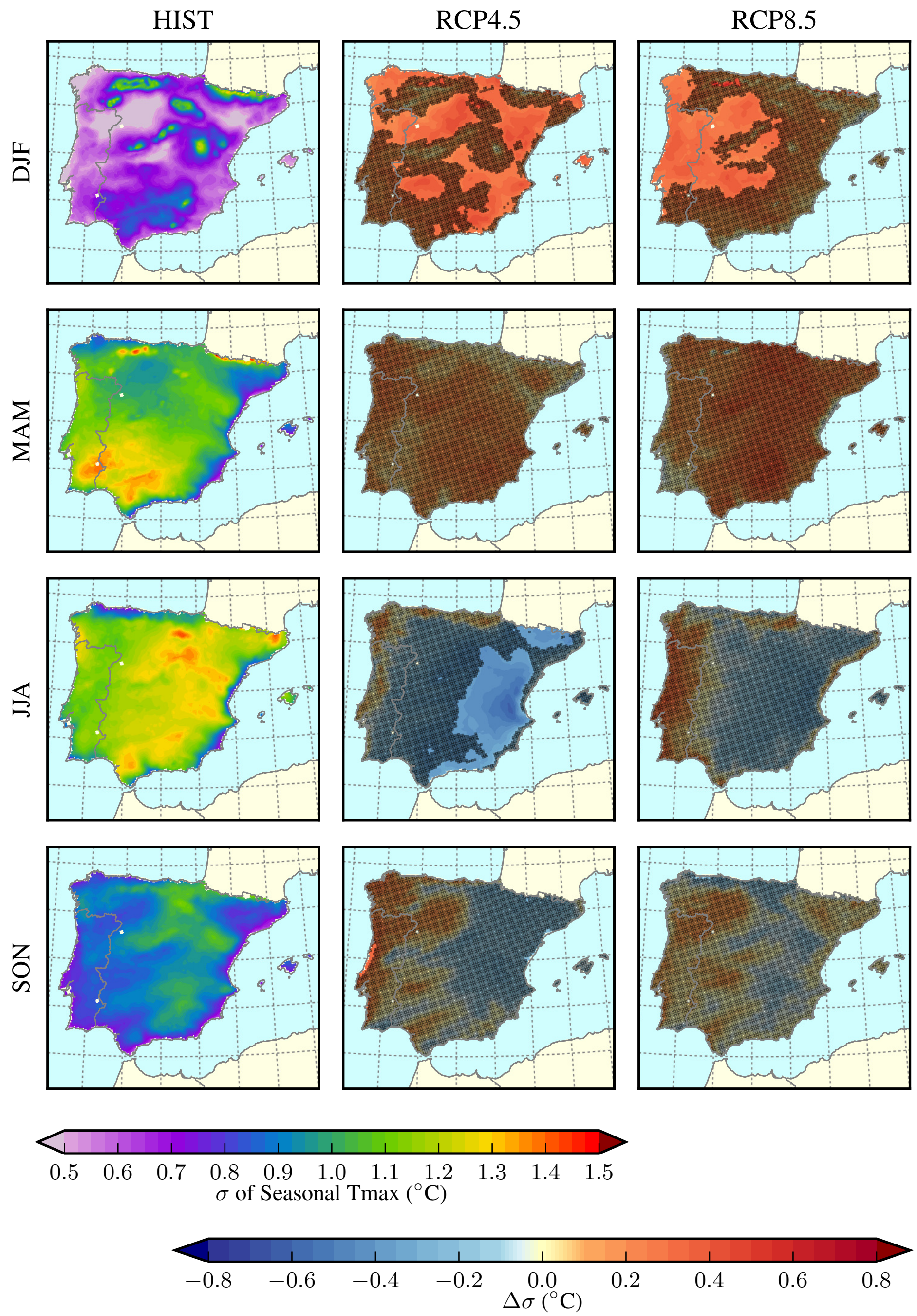

Figure 6.35: *Current (1980-2014) seasonal standard deviation of T_{max} (first column) and its far future (2071-2100) relative to projected changes from the WRFCCSM. The results from the RCP4.5 and RCP8.5 are shown in second and third columns, respectively. Black dots indicate non-significant changes according to a two-tailed Fisher-Snedecor F test at the 95% confidence level.*

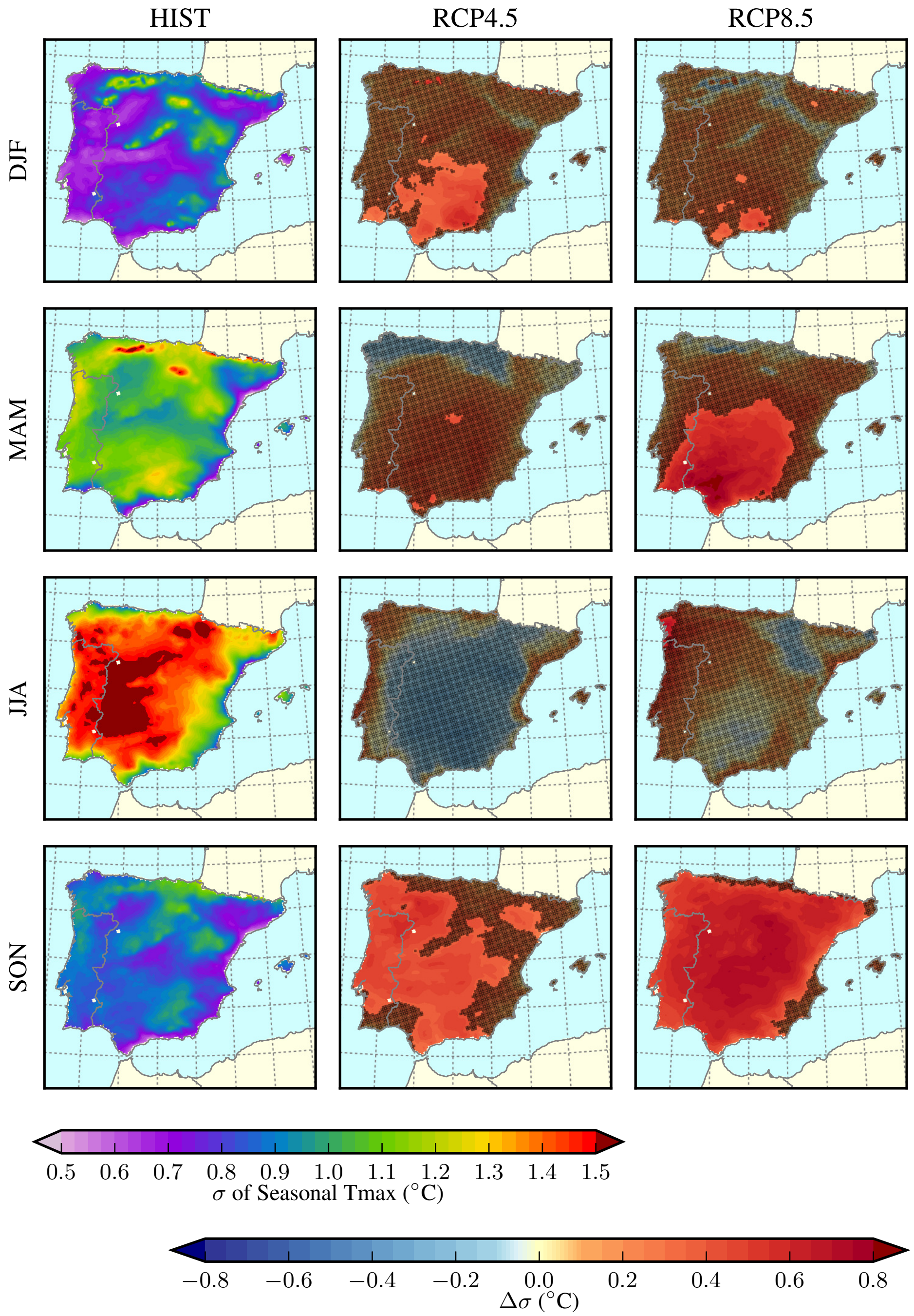

Figure 6.36: *As Figure **6.35** but for the WRFMPI simulations.*

also located in the Baetic System.

In spring, significant changes were only presented in the WRFMPI simulations, and mainly under the high emissions pathway. In this latter, large areas with significant increases were found over the southern half of the Peninsula appearing values close to 1°C (Figure ***6.36***, MAM). For summer, however, the WRFCCSM (Figure ***6.35***, JJA) revealed more extended significant reductions in the standard deviation, broadly located in the eastern IP, where the values were up to -0.6°C under intermediate emissions. For the WRFMPI (Figure ***6.36***, JJA), the changes were also predominantly negative under the RCP4.5, but these were non-significant. However, significant increases were shown in a small area located in Galician Coast for the RCP8.5. For autumn, the WRFMPI projected extended changes for both scenarios, covering practically the whole IP for the RCP8.5, with values up to 0.7°C (Figure ***6.36***, SON), while for the WRFCCSM (Figure ***6.35***, SON) non-significant changes were found.

Changes in the Variability of Minimum Temperature

Figures ***6.37*** to ***6.40*** display the results from the analysis of T_{min} variability changes for the near and far future. Significant changes in the interannual variability of T_{min} were fundamentally shown for winter and summer, being such changes more moderate in magnitude than for T_{max}.

For winter, the WRFCCSM revealed an increase in variability for the near future, reaching values up to 0.7°C (Figure ***6.37***, DJF). Such increase was more pronounced under the RCP4.5, and the non-significant changes were mainly located in high mountainous regions (e.g. Cantabrian Range, Pyrenees, Baetic System and Central System) where the present values of standard deviation showed the highest values, and over Portugal, southern half and over Mediterranean coastal regions. For the WRFMPI (Figure ***6.38***, DJF), however, only small areas around Creus Cape (increases) and in the Cantabrian Range (decreases) revealed significant differences in terms of the standard deviation. In summer, only for the WRFMPI appeared significant changes, being these mainly located in northern IP for both RCPs (Figure ***6.38***, JJA). Thus, the RCP4.5 showed positive differences in standard deviations (values of about 0.6°C) whereas under the RCP8.5 appeared decreases, which were only signifi-

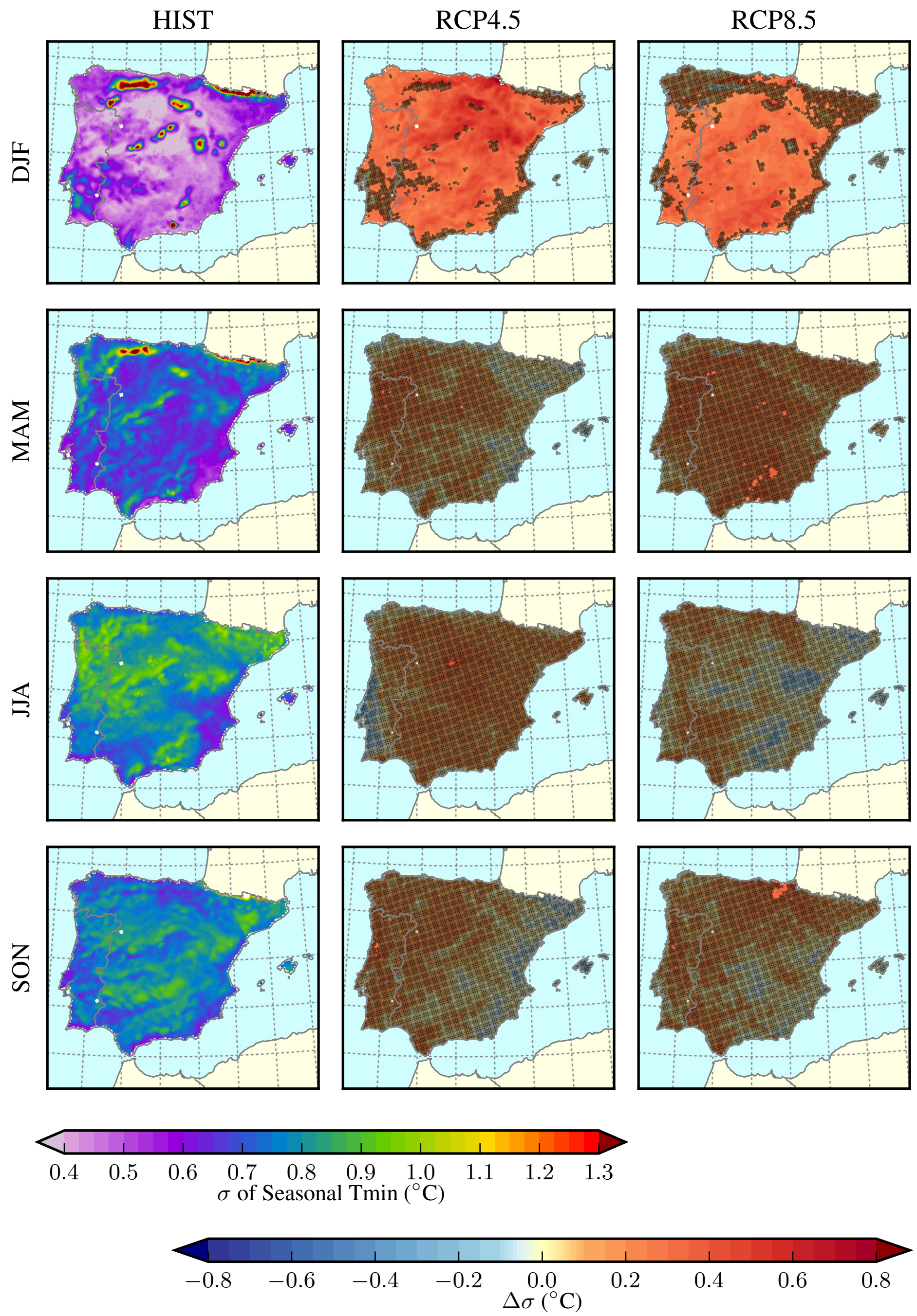

Figure 6.37: *Current (1980-2014) seasonal standard deviation of T_{min} (first column) and its near future (2021-2050) relative to projected changes from the WRFCCSM. The results from the RCP4.5 and RCP8.5 are shown in second and third columns, respectively. Black dots indicate non-significant changes according to a two-tailed Fisher-Snedecor F test at the 95% confidence level.*

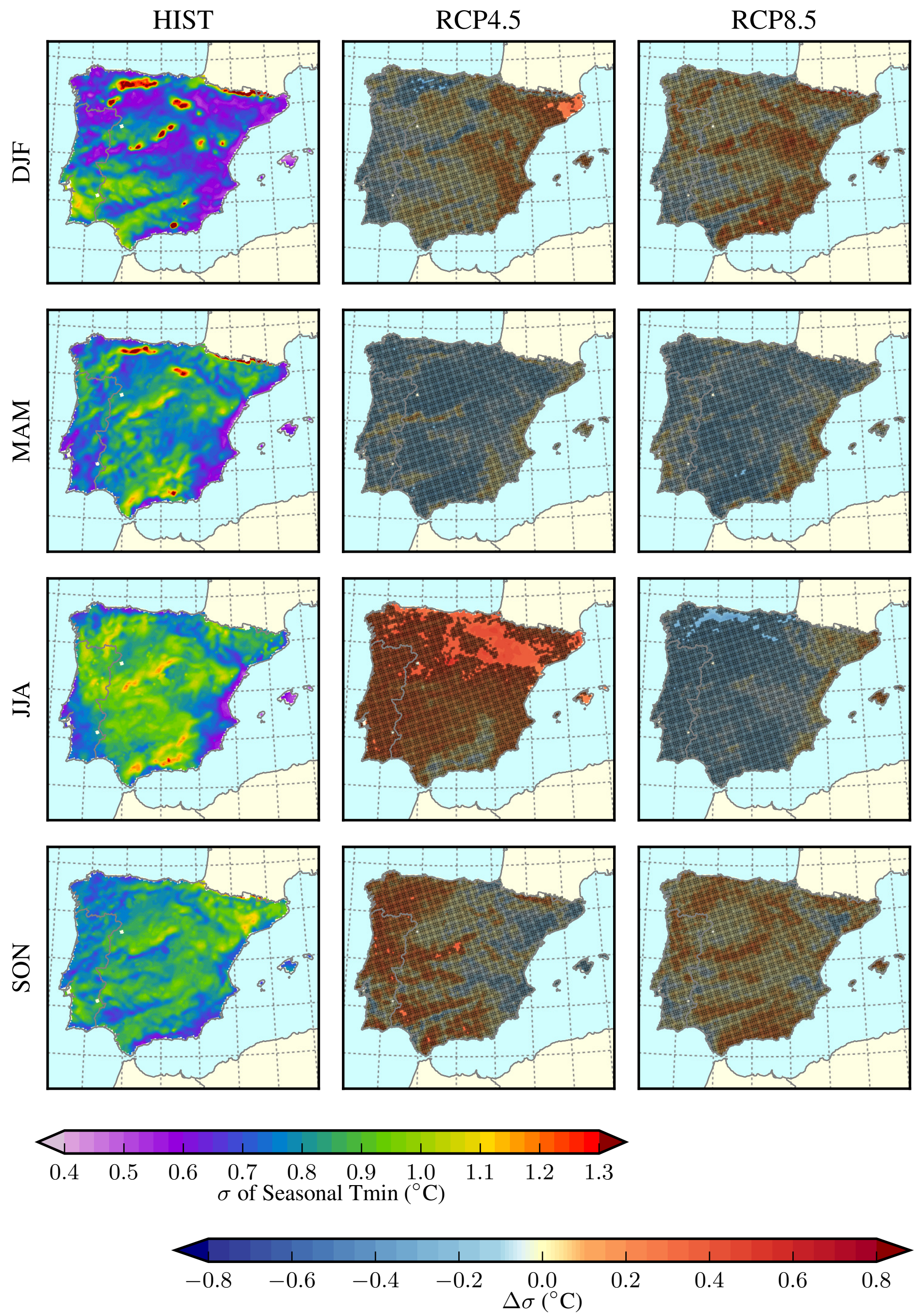

Figure 6.38: *As Figure **6.37** but for the WRFMPI simulations.*

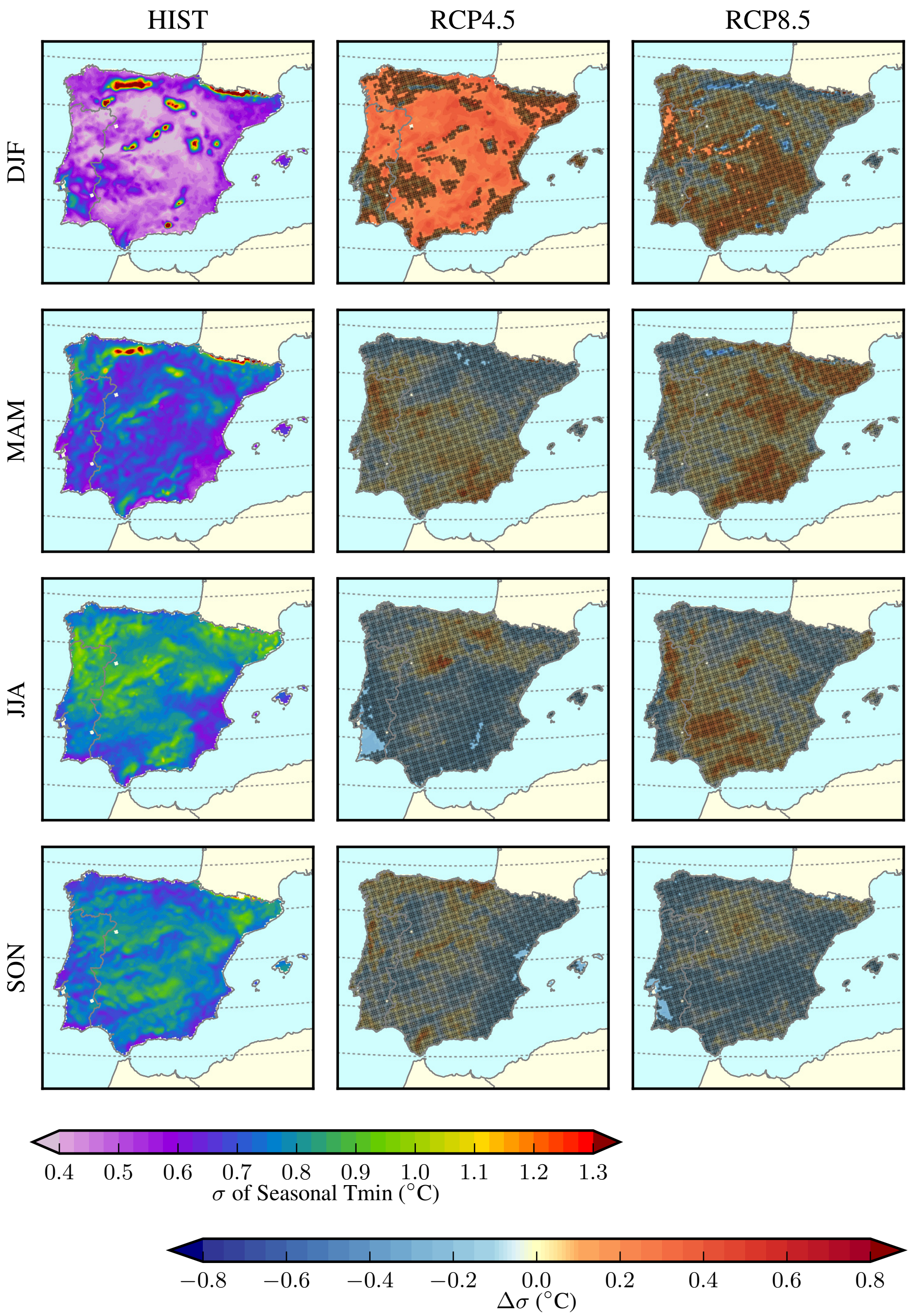

Figure 6.39: *Current (1980-2014) seasonal standard deviation of T_{min} (first column) and its far future (2071-2100) relative to projected changes from the WRFCCSM. The results from the RCP4.5 and RCP8.5 are shown in second and third columns, respectively. Black dots indicate non-significant changes according to a two-tailed Fisher-Snedecor F test at the 95% confidence level.*

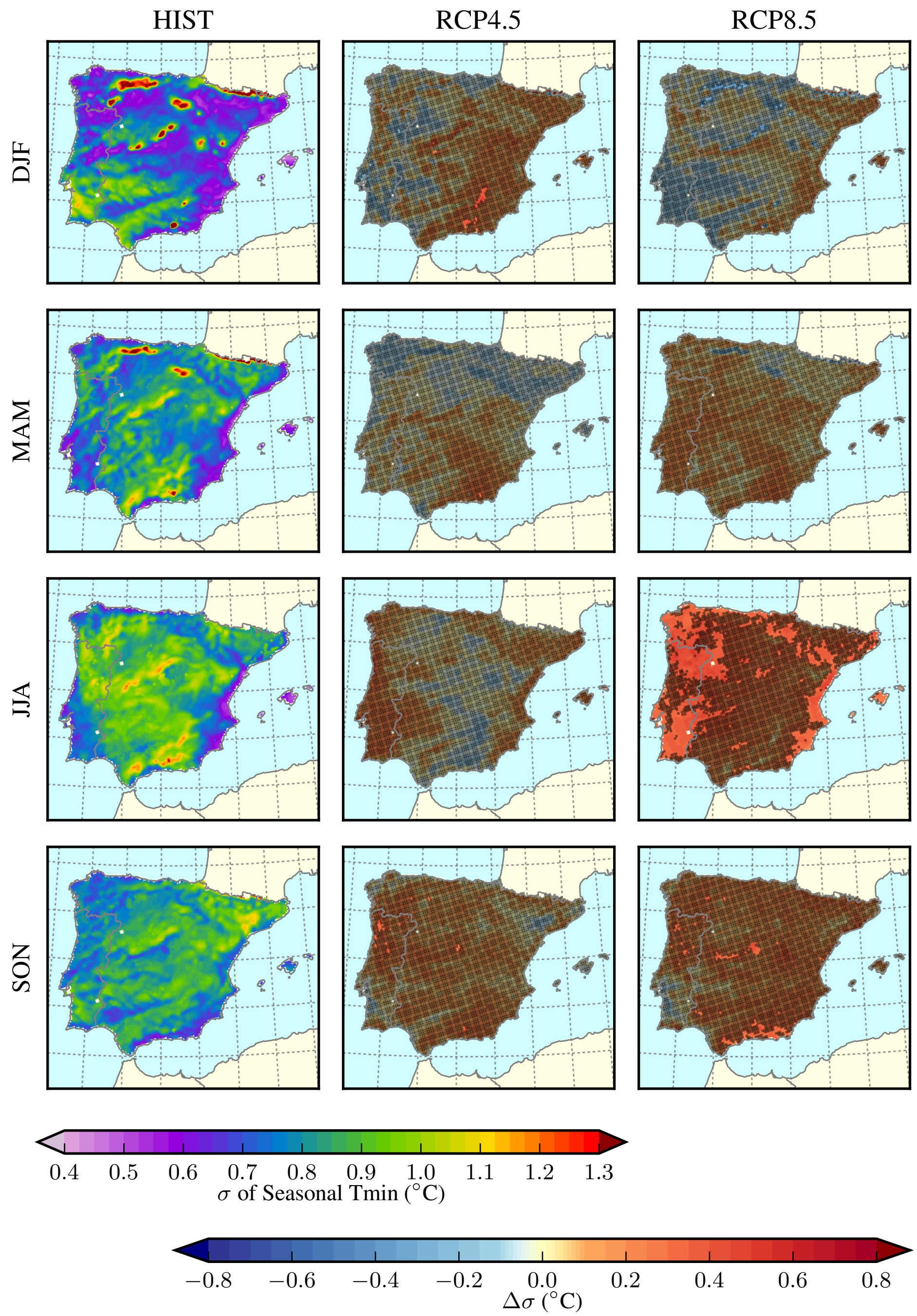

Figure 6.40: *As Figure **6.39** but for the WRFMPI simulations.*

cant in the Cantabrian region (values around -0.3°C). For spring and autumn, the changes were non-significant in almost the complete IP for this period.

For the far future in winter, the WRFCCSM simulations displayed an increase in its variability under the RCP4.5 in most of the IP, meanwhile, the RCP8.5 presented only disperse regions with significant changes, being these both positive and negative (Figure ***6.39***, DJF). However, the WRFMPI practically showed non-significant changes, with only a few points over the southwest significant (Figure ***6.40***, DJF). In summer, a small area with significant decreases in southern Portugal was projected by the WRFCCSM under the RCP4.5 (values of around -0.3°C, Figure ***6.39***, JJA). By contrast, the WRFMPI showed increases under the RCP8.5 mainly located in coastal regions over the east, north and west (values of about 0.5°C, Figure ***6.40***, JJA). Again, spring and autumn showed very a few regions with significant changes.

Trends in Seasonal Maximum Temperature

To study the temporal trend of T_{max} within each 30-year period, S/N ratios were also computed for the different river basins of the IP. Figures from ***6.41*** to ***6.44*** depict the results of this analysis for the two GCM-driven simulations, under both RCPs and for the two periods. Contrariwise to precipitation, the projected mean values of T_{max} are always higher than present values, and therefore, S/N ratios were positive. Moreover, increasing trends appeared along the entire periods in most of the watersheds, especially for the far future.

Different S/N-ratios trends were shown depending on the driving data, emissions pathway and seasons for the two periods. Figure ***6.41*** portrays the evolution of the S/N ratios for the CCSM4-driven simulations in the near future. For winter (Figure ***6.41***, DJF), the WRFCCSM broadly showed increasing trends, which were higher for the RCP4.5. In this latter, most of the watersheds presented values above 1 from 2034 onwards.

For the WRFCCSM, spring and summer (Figure ***6.41***, MAM and JJA) depicted the more substantial rising trends, showing values of GHG-induced signal higher than the natural variability in many watersheds and over long periods. For spring, values of about 2 arose by the end of the period over the Duero, Northeastern, Tajo, Guadiana, Guadalquivir, Southeastern and South-

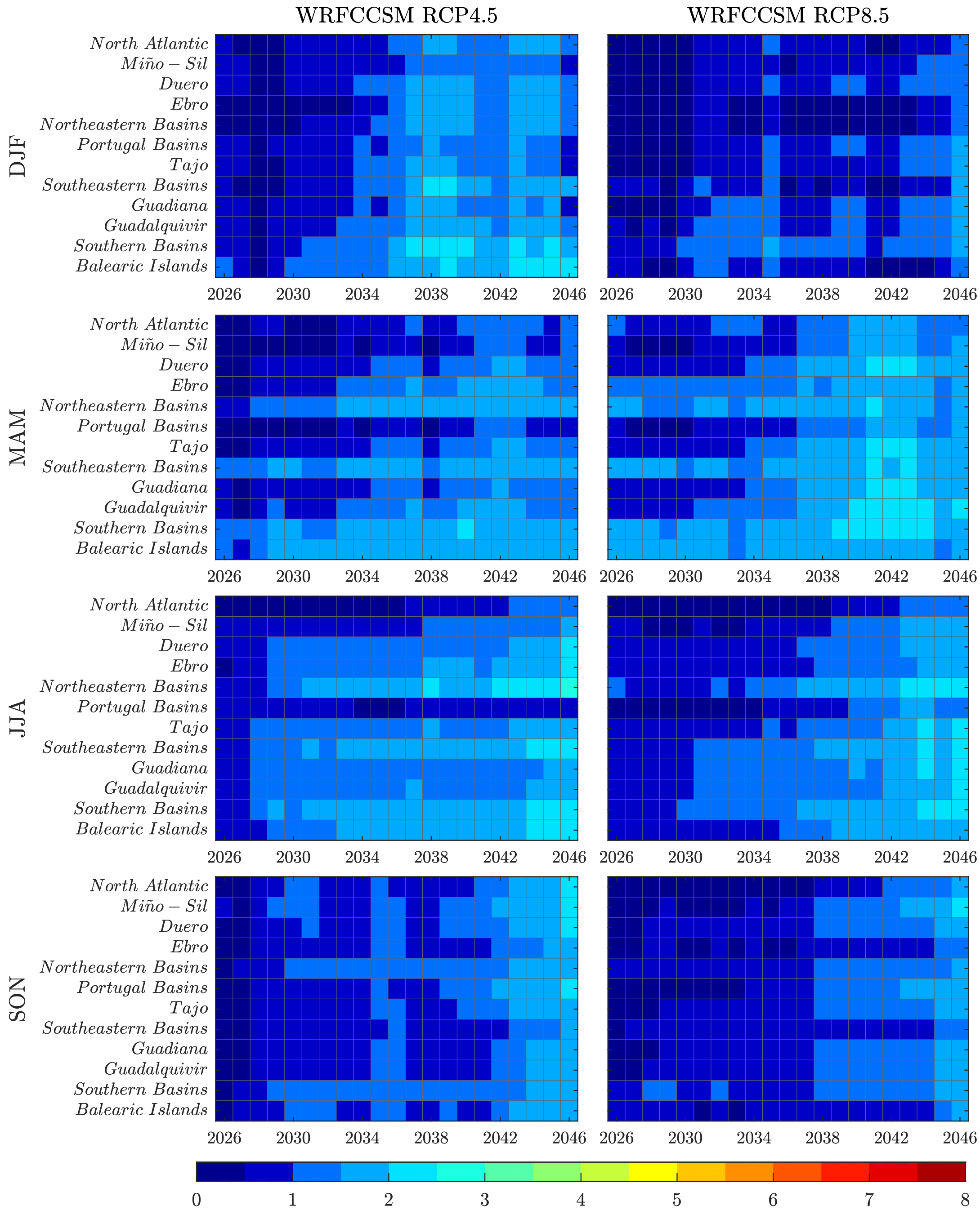

Figure 6.41: *Portrait diagrams of the seasonal S/N ratios of T_{max} for each river basin within the IP. Here, the evolution of the near future (2021-2050) in relation to the present (1980-2014) using the WRFCCSM outputs is illustrated. In rows, the different seasons are displayed and in columns the simulations driven for the different RCPs (RCP4.5 and RCP8.5).*

ern Basins for the RCP8.5. By contrast, the evolution of the S/N in summer appeared to show a clearer climate change signal for the RCP4.5, arising values above 1 from the beginning of the period. Here, the North Atlantic, Miño-Sil and Portugal Basins presented a high natural internal variability (values below 1 practically for the entire period).

Concerning autumn values, the evolution of S/N ratios suggested a moderate emergence of the climate signal, more evident for the RCP4.5 (Figure ***6.41***, SON). Here, the most substantial rising trends were found in the Northeastern and Southern Basins where values above 1 appeared from about 2030 in Northeastern, Southern and Balearic Islands Basins, remaining along the entire period. Under the RCP8.5, however, S/N values below 1 were shown at least until 2038 in general.

The simulations driven by MPI-ESM-LR displayed higher S/N ratios for the RCP8.5 along the near future (Figure ***6.42***). For winter, the RCP8.5 showed values above 1, which arose at the beginning of the period over Portugal Basins as well as the Guadiana Basin, remaining for the entire period. Other watersheds such as the Tajo and Guadalquivir Basins reached climate change signal as high as the internal variability from 2027 onwards. However, for the RCP4.5, such values were not reached until 2033 or later. A moderate emergence of the signal also appeared in spring in the WRFMPI (Figure ***6.42***, MAM). The increasing trend of the S/N ratios were lower than those found for the WRFCCSM, suggesting a higher internal variability for these simulations. Under the RCP8.5, the most marked trends were shown, being more notable over southern watersheds. In this latter, S/N ratios above 1 were found from 2030 onwards, arising maximum values of 2 over the Southeastern and Southern Basins. However, for the RCP4.5 values that remain above 1 did not appear until 2033, and only over the Southern and Southeastern Basins.

In summer (Figure ***6.42***, JJA), climate change signals were more highlighted, especially under the RCP8.5. S/N values above 1 appeared from around 2030 in some watersheds for the two RCPs, which were in many cases extended along the entire period. However, the North Atlantic, Miño-Sil and Portugal basins were less affected by rising T_{max}, particularly under the RCP4.5. Autumn presented the highest S/N ratios along the period for the WRFMPI sim-

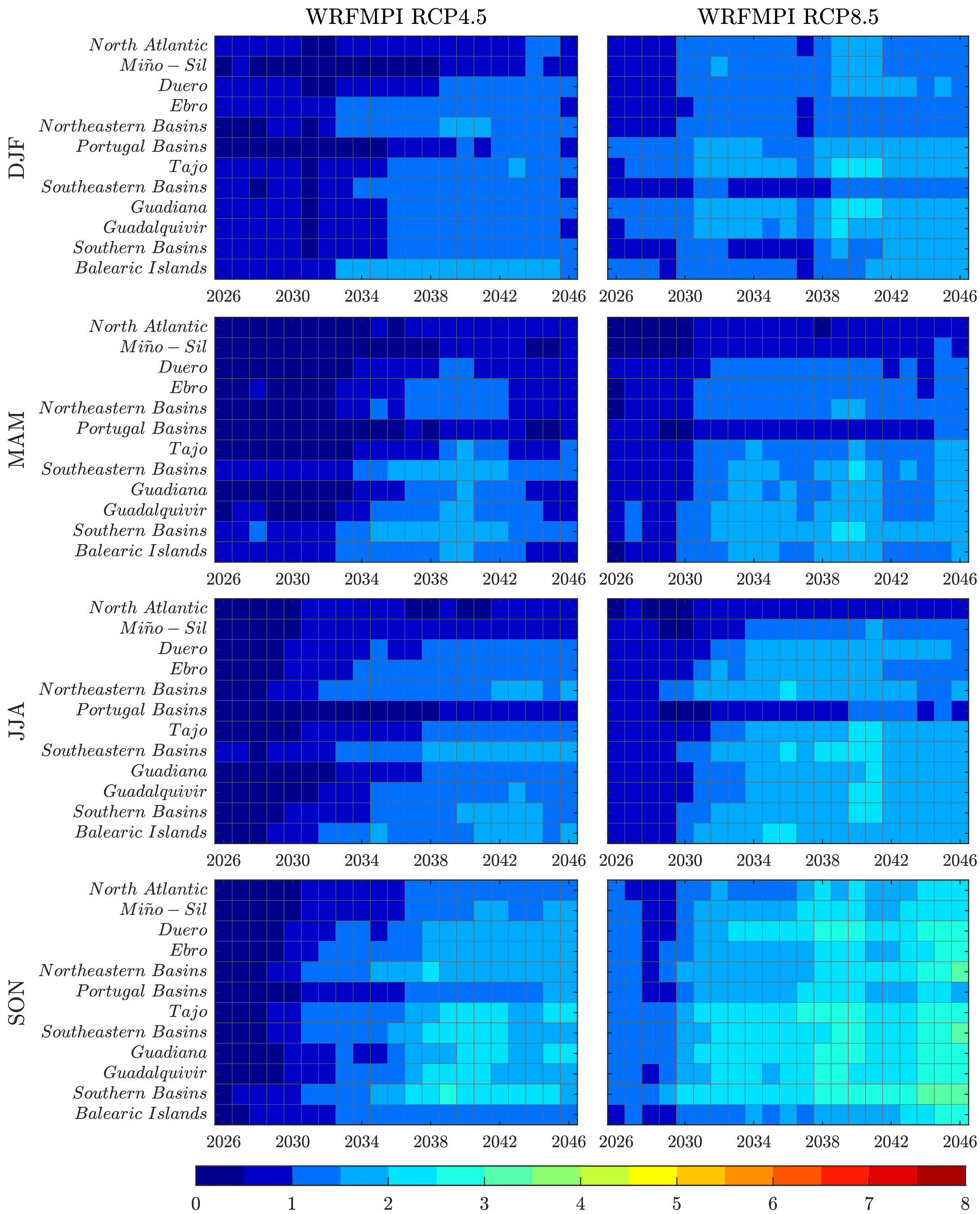

Figure 6.42: *The same as* ***6.41*** *but for the WRFMPI.*

ulations (Figure ***6.42***, SON), reaching values above 1 for long periods in both RCPs. Again, the RCP8.5 showed more severe results, where values above 2 appeared from 2030. Here, both RCPs revealed that the watersheds located in the south of the Peninsula were the most affected.

In reference to the evolution of the S/N ratios over the far future, Figure ***6.43*** reveals more marked induced climate change signal as well as a major difference between RCPs for the WRFCCSM simulations. For winter (Figure ***6.43***, DJF), the watersheds located in the north of the Peninsula appeared to present increases more moderate whereas the Southern and Balearic Islands Basins seem to suffer higher increases in the mean T_{max}. This performance was shown under the two RCPs, but with larger magnitude for the high emissions scenario, where S/N ratios above 3.5 were found over many watersheds and along the entire period.

Differences between RCPs were also noteworthy in spring (Figure ***6.43***, MAM). Under the RCP4.5, increasing trends appeared at least until 2090 in general, but subsequently, these changed in many watersheds, suggesting a possible recovery of the T_{max}. Under the RCP8.5, an overall increasing trend was also shown, appearing values of S/N above 4 in many watersheds (except for North Atlantic, Miño-Sil and Portugal Basins), so it is very likely the emergence of the climate change signal in this period and scenario. For summer (Figure ***6.43***, JJA), the S/N values were lower and even in some cases appeared to be reduced along the time under the RCP4.5, indicating a possible stabilization or even a recovery in the mean T_{max}. For the RCP8.5, however, the most substantial values of S/N were shown (values close to 6) for all watersheds except for North Atlantic and Portugal Basins, so it is virtually certain the emergence of the signal. For autumn, decreasing trends were shown along the period for the RCP4.5 in many watersheds. By contrast, under the RCP8.5, the opposite performance was shown, reaching S/N values close to 6 in some cases (Figure ***6.43***, SON). This behavior suggests a further warming due to the increase in GHG concentrations again.

Although the changes between RCPs were also notable for the simulations driven by MPI-ESM-LR during the far future period (Figure ***6.44***), the S/N evolution was more similar in magnitude between them, except for autumn. More-

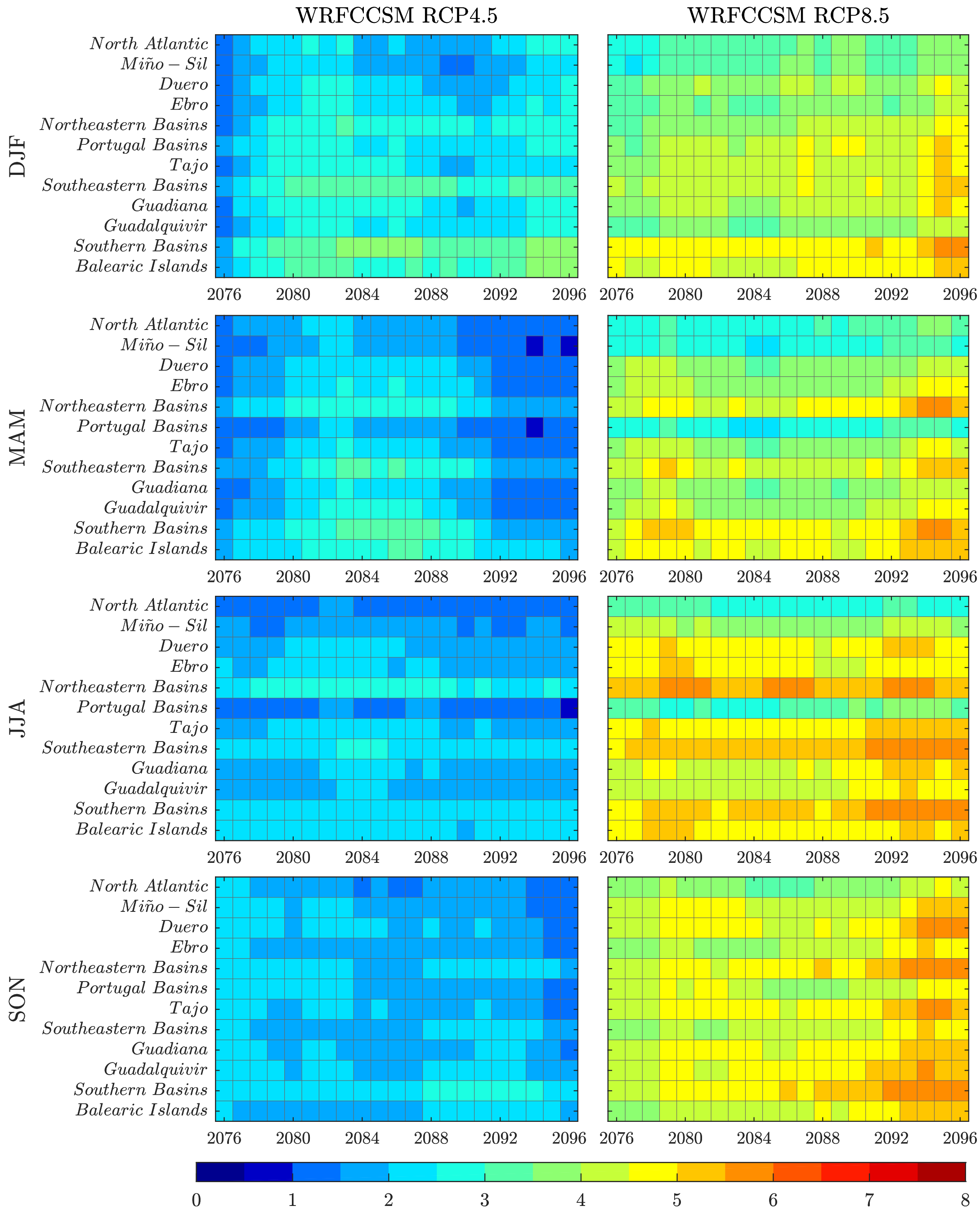

Figure 6.43: *Portrait diagrams of the seasonal S/N ratios of T_{max} for each river basin within the IP. Here, the evolution of the far future (2071-2100) in relation to the present (1980-2014) using the WRFCCSM outputs is illustrated. In rows, the different seasons are displayed and in columns the simulations driven for the different RCPs (RCP4.5 and RCP8.5).*

over, for these simulations, the less affected watersheds were again over northern IP (e.g. North Atlantic, Miño-Sil and Portugal Basins) in some cases. Concerning the annual distribution of the changes, the winter S/N ratios showed increasing trends from around 2084 to the end in many watersheds under the RCP4.5. By contrast, the RCP8.5 showed a generalized positive trend along the entire period, with S/N values between 3 and 5. This behavior suggested the possible emergence of the climate change signal in all the IP.In this context, the Balearic Islands Basins appeared to be the most affected by increasing trends of the T_{max} (Figure ***6.44***, DJF). Spring showed more moderate changes in than winter (Figure ***6.44***, MAM). Here, positive trends were shown in both RCPs, being the watersheds less affected the North Atlantic, Miño-Sil and Portugal Basins.

Similarly to spring, summer (Figure ***6.44***, JJA) results from the RCP4.5 presented S/N values up to 3, and under the RCP8.5 these were usually above 4. These results again could be indicating a possible emergence of the signal at least for the RCP8.5. In this season, Portugal Basins showed the most modest trends whereas Northeastern, Southeastern, Southern and Balearic Islands Basins appeared to be the most affected in both RCPs.As occurred in the near future, autumn presented the highest S/N values (Figure ***6.44***, SON), which remained throughout all the period. For this season, the RCP8.5 showed very high S/N ratios in nearly all the IP, growing over the entire period. The Southern, Guadiana, Guadalquivir, Tajo, Southeastern and Northeastern Basins reached S/N ratios higher than 4 over the period, and close to 8 by the end of the 21^{th} century. So a clear emergence of the signal is predicted.

Trends in Seasonal Minimum Temperature

As for T_{max}, the projected mean values were higher than the present ones along the entire 30-year periods, the S/N ratios being always positive. In general, increasing trends were shown at least at the end of the periods and particularly for the far future.

For the near future, results from WRFCCSM presented increasing trends with values ranging from 0 to 4 (Figure ***6.45***). The evolution of the T_{min} S/N values in winter revealed stronger signals of climate change than those shown for

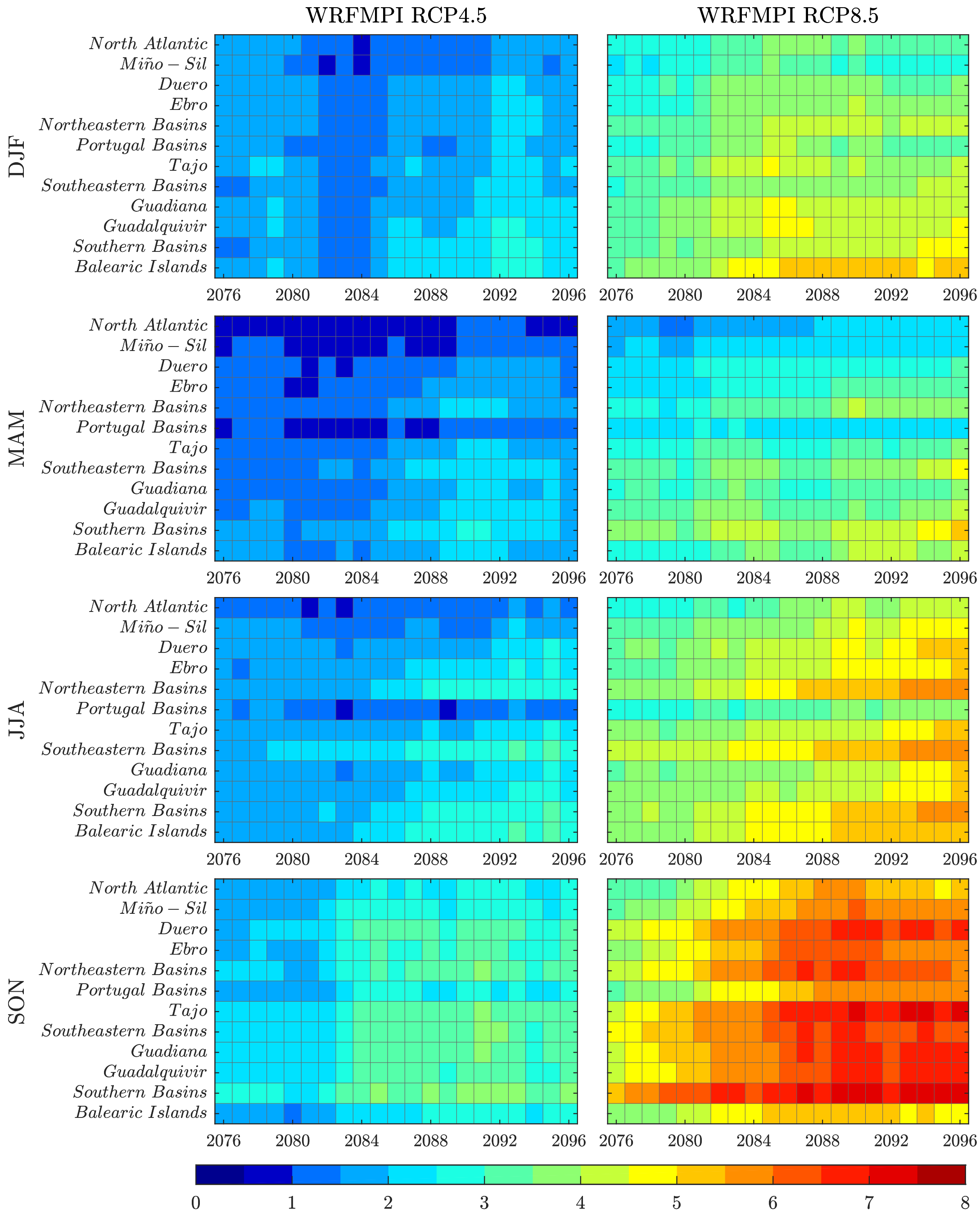

Figure 6.44: *As Figure **6.43** but for the WRFMPI simulations.*

T_{max} in both RCPs (Figure ***6.45***, DJF). Here, rising trends were more notorious under the intermediate emission scenario where they were broadly positives, appearing S/N values close to 3 in southern peninsula watersheds. Under the RCP8.5, increasing trends also were found over many watersheds at least until 2035, but they appeared to be reduced by the end of the period. For spring (Figure ***6.45***, MAM) a stronger rising trend of T_{min} in comparison with T_{max} was not so clear, although for the RCP8.5 the S/N ratios were slightly higher for T_{min}. In general, the RCP8.5 showed slightly higher values of S/N, being the Southern Basins the most affected (values above 2 practically over the entire period). By contrast, the Balearic Islands Basins revealed decreasing trends from 2037 to 2046.

For summer (Figure ***6.45***, JJA), the most substantial increasing trends were shown under the RCP4.5 appearing values close to 3 by the end of this period over the Southeastern, Southern and Balearic Islands watersheds. However, Portugal Basins remained with S/N values below 1 for the entire period. These values were also stronger than those found for T_{max} in general. Under the RCP8.5, all watersheds also presented important increasing trends, more appreciable in the southern half, with the exception of the Portugal Basins. Conversely, autumn (Figure ***6.45***, SON) appeared to show a more moderate signal of climate change, at least for the RCP8.5, although S/N values up to 2 were shown by the end of the period for some watersheds under the two RCPs. Here, all watersheds showed similar behaviors.

For the WRFMPI simulations, results revealed a higher natural internal variability than the WRFCCSM for this same period, at least for the RCP4.5 (Figure ***6.46***). For all seasons, the climate change signal was slightly more pronounced for the high emissions scenario, except for winter. In this latter season (Figure ***6.46***, DJF), the highest S/N values appeared in the RCP4.5, at least over the Ebro, Northeastern, Southeastern, Southern and Balearic Islands Basins, reaching S/N ratios higher than 2 in some cases. Under the RCP8.5, a common increasing trend appeared from 2038, less marked in the North Atlantic and Guadiana Basins. The temporal evolution in spring (Figure ***6.46***, MAM) appeared to be also moderate, showing values higher than 1.5 only for a few watersheds (Northeastern, Southeastern, Southern and Balearic Islands Basins)

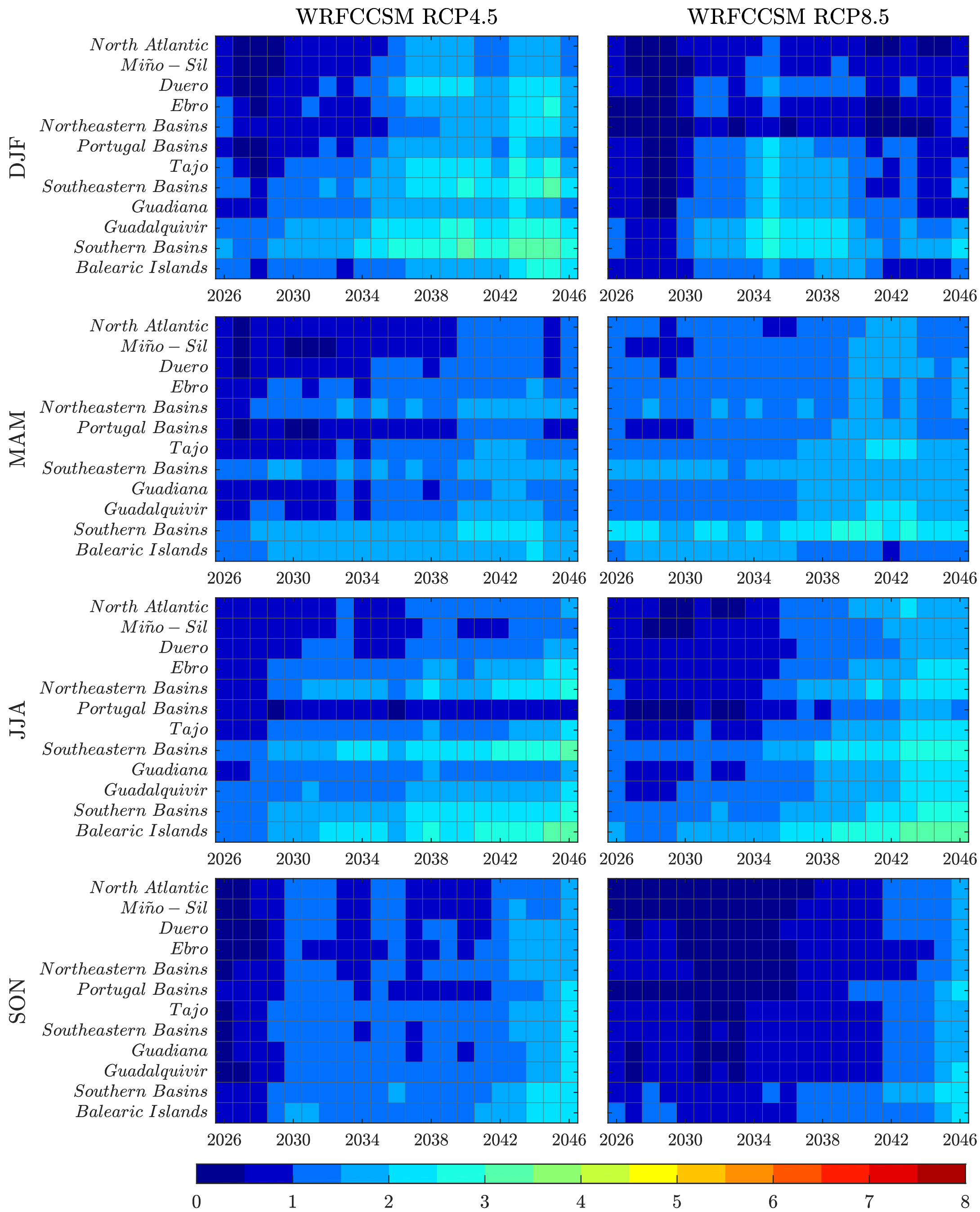

Figure 6.45: *Portrait diagrams of the seasonal S/N ratios of T_{min} for each river basin within the IP. Here, the evolution of the near future (2021-2050) in relation to the present (1980-2014) using the WRFCCSM outputs is illustrated. In rows, the different seasons are displayed and in columns the simulations driven for the different RCPs (RCP4.5 and RCP8.5).*

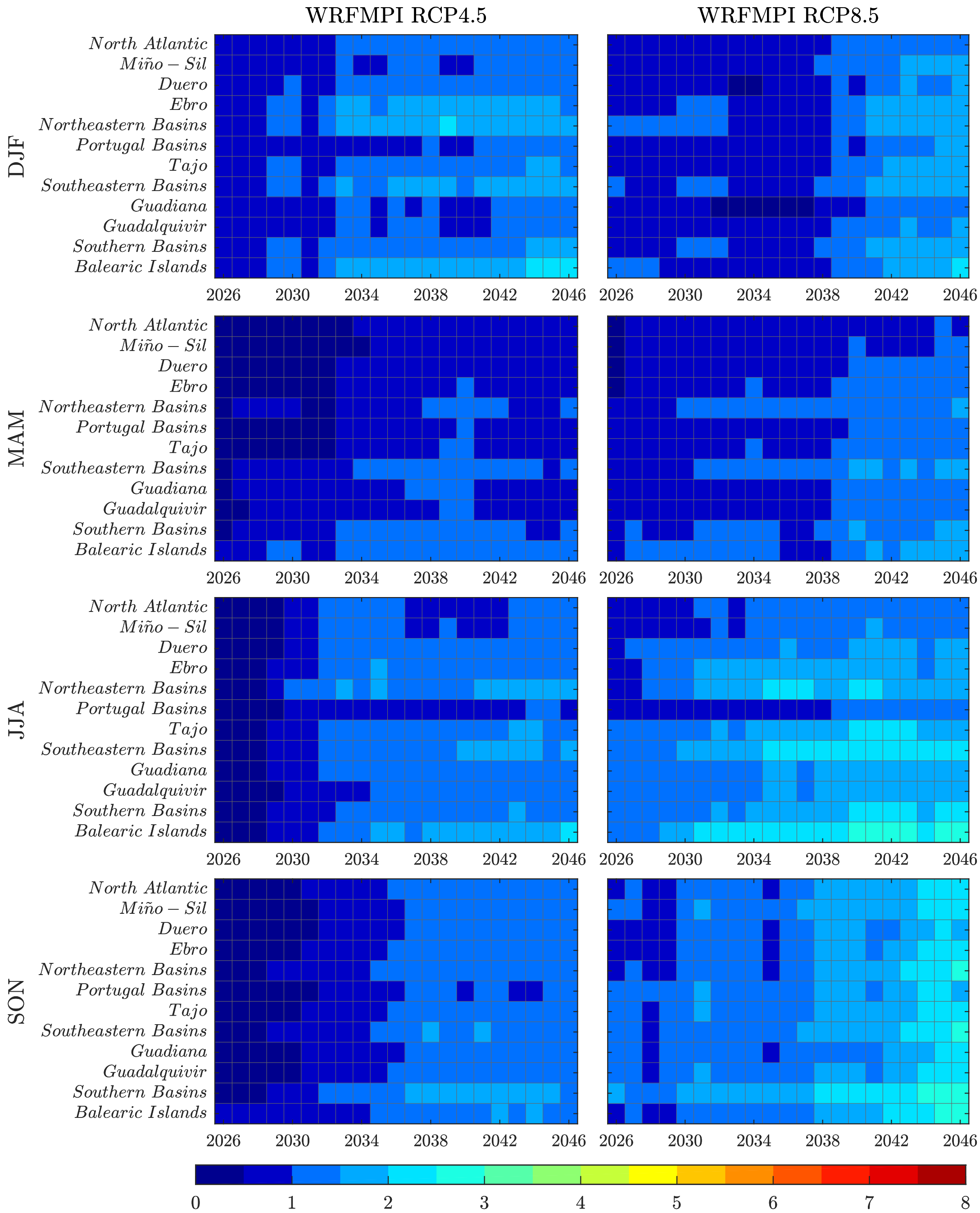

Figure 6.46: *As Figure **6.45** but for the MPI-ESM-LR-driven simulations.*

by the end of this period and under the RCP8.5. The watersheds of northern IP indeed seem not to be affected by the emergence of the climate change signal along this period. Summer and autumn (Figure ***6.46***, JJA and SON) showed the most remarkable climate change signals, and especially under the RCP8.5. Here, many watersheds ended the period with values of S/N above 2. These results indicated a possible emergence of the signal at least in those watersheds where the S/N values reached values higher than 1 and remain.

For the far future, the WRFCCSM simulations showed a generalized rising trend (values of S/N of about 1-3 and 3-8 for the RCP4.5 and RCP8.5, respectively) for all watersheds at least under the high emission scenario (Figure ***6.47***). As for the near future, the ratios from T_{min} broadly appeared to be higher than those found for T_{max}, especially in winter and summer. Here, the Southern Basins were strongly affected, where values above 3 and 5 appeared for the RCP4.5 and RCP8.5, respectively, for all seasons and throughout the entire period. These results indicated a clear emergence of the climate change signal for such watersheds. Other basins located in the south of the Peninsula also suffered high S/N ratios over the period, showing different magnitude depending on the season.

Thus, for winter (Figure ***6.47***, DJF), the Tajo, Guadalquivir, Southeastern and Balearic Islands Basins showed remarkable S/N values for the entire period, being these stronger for the RCP8.5. For summer (Figure ***6.47***, JJA), the most marked values of S/N were shown. In this season, under the RCP8.5, the most affected basins were the Southeastern, Southern and Balearic Islands Basins (values above 5.5), but also Tajo and Guadalquivir Basins (values above 4.5). By contrast, North Atlantic, Miño-Sil, Duero, and especially Portugal Basins presented the lowest values. More moderate climate signal are shown for transitional seasons (spring and autumn), being the Southern Basins the most affected. Under the RCP4.5, increasing trends appeared except for North Atlantic and Miño-Sil Basins (Figure ***6.47***, MAM and SON), but by the end of the century, these seem to become downward trends. By contrast, the evolution for the RCP8.5 in these seasons is similar to those showed for summer and winter, but with S/N values lower in magnitude.

For this far period, the projections from the simulations driven by MPI-

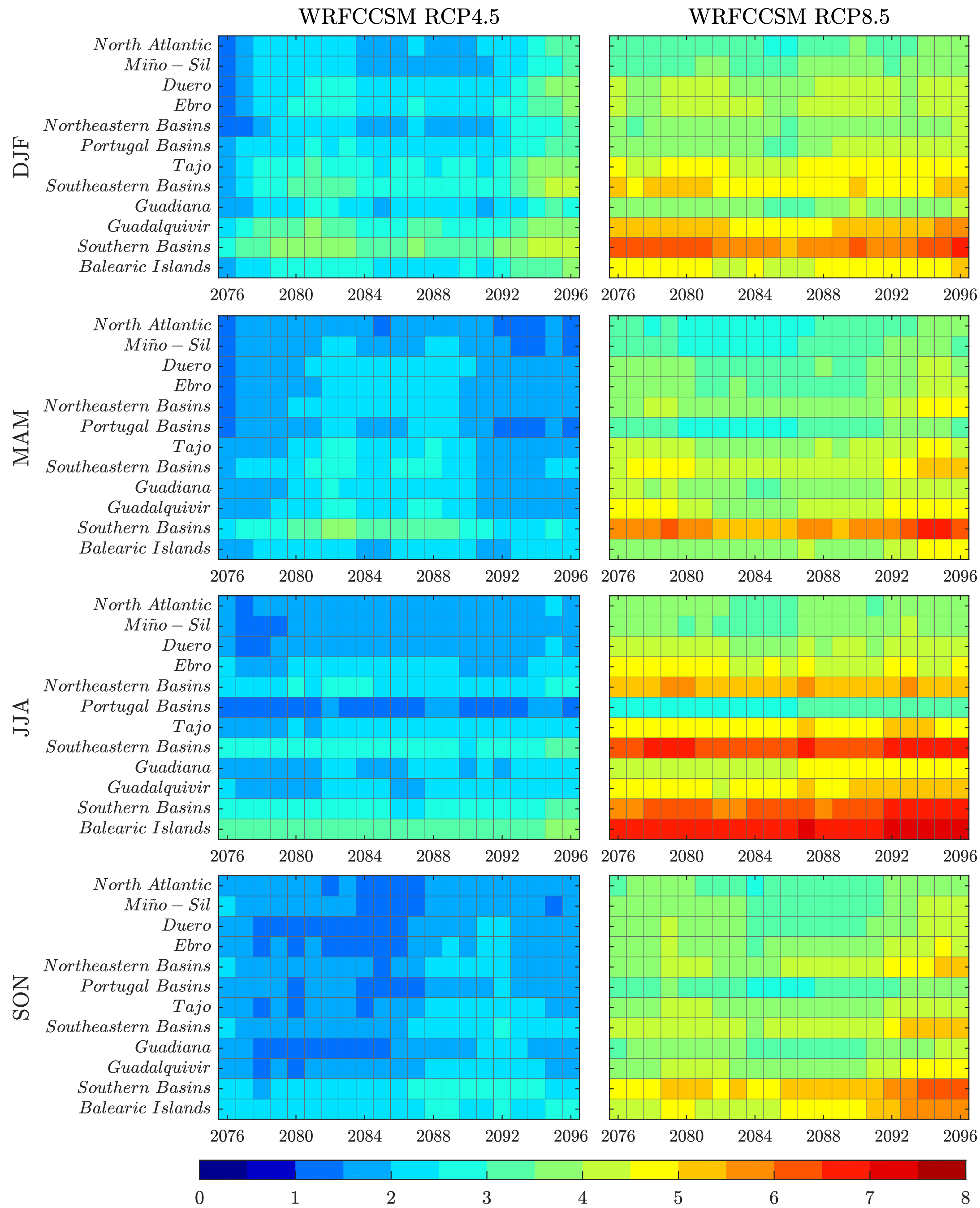

Figure 6.47: *Portrait diagrams of the seasonal S/N ratios of* T_{min} *for each river basin within the IP. Here, the evolution of the far future (2071-2100) in relation to the present (1980-2014) using the WRFCCSM outputs is illustrated. In rows, the different seasons are displayed and in columns the simulations driven for the different RCPs (RCP4.5 and RCP8.5).*

ESM-LR (Figure ***6.48***) portrayed substantial rising trends of T_{min}, which were more notorious than the values showed in T_{max} for winter, spring and summer, and higher for the RCP8.5. These results, remaining along the period, indicated a possible emergence of the signal in many watersheds. Here, the values by the end of the century were quite strong, especially for summer and autumn for all the IP except in the Portugal Basins in summer. For winter (Figure ***6.48***, DJF), both emission scenarios revealed increasing trends from around 2084, and the Northeastern and Balearic Islands Basins suffered the most severe climate signals, with S/N values up to 7.5 in some years for the RCP8.5.

The S/N ratios in spring (Figure ***6.48***, MAM) were more moderate than in winter. Under the RCP4.5, rising trends of the minimum temperature appeared in general. The Southern and Balearic Islands Basins suffered greater differences between the future and present values of T_{min} for nearly all the period.For the RCP8.5, increases in S/N ratios until the end of the period were shown in some cases, reaching values close to 6 in the Balearic Islands between 2089 and 2093. Summer (Figure ***6.48***, JJA) presented the highest climate change signals over all the IP, less marked in Portugal Basins. Note the evolution in the Balearic Islands where values up to 8 were reached at the end of the century under the RCP8.5. The behavior under the intermediate emissions pathway was similar in its evolution but with lower magnitudes in many cases. Lastly, autumn presented rising trends (Figure ***6.48***, SON), showing S/N values lower than the T_{max}, in general. Increasing evolution was shown particularly over the Southern Basins, where values above 6 appeared by the end of the century under the high emissions scenario. For the RCP4.5, increasing trends were also shown but lower in magnitude. For this season, the results indicated the possible emergence of the signal again.

6.3.3. Changes in Extreme Values

As for precipitation, changes in the temperature were examined by using the different ETCCDI extreme described in the section ***4.3.4***. In this context, because the temperature is affected by systematic errors, the daily T_{max} and T_{min} were previously bias-corrected[6] in order to avoid inadequate values of those

[6]The procedure applied here is the same that was applied in the model evaluation.

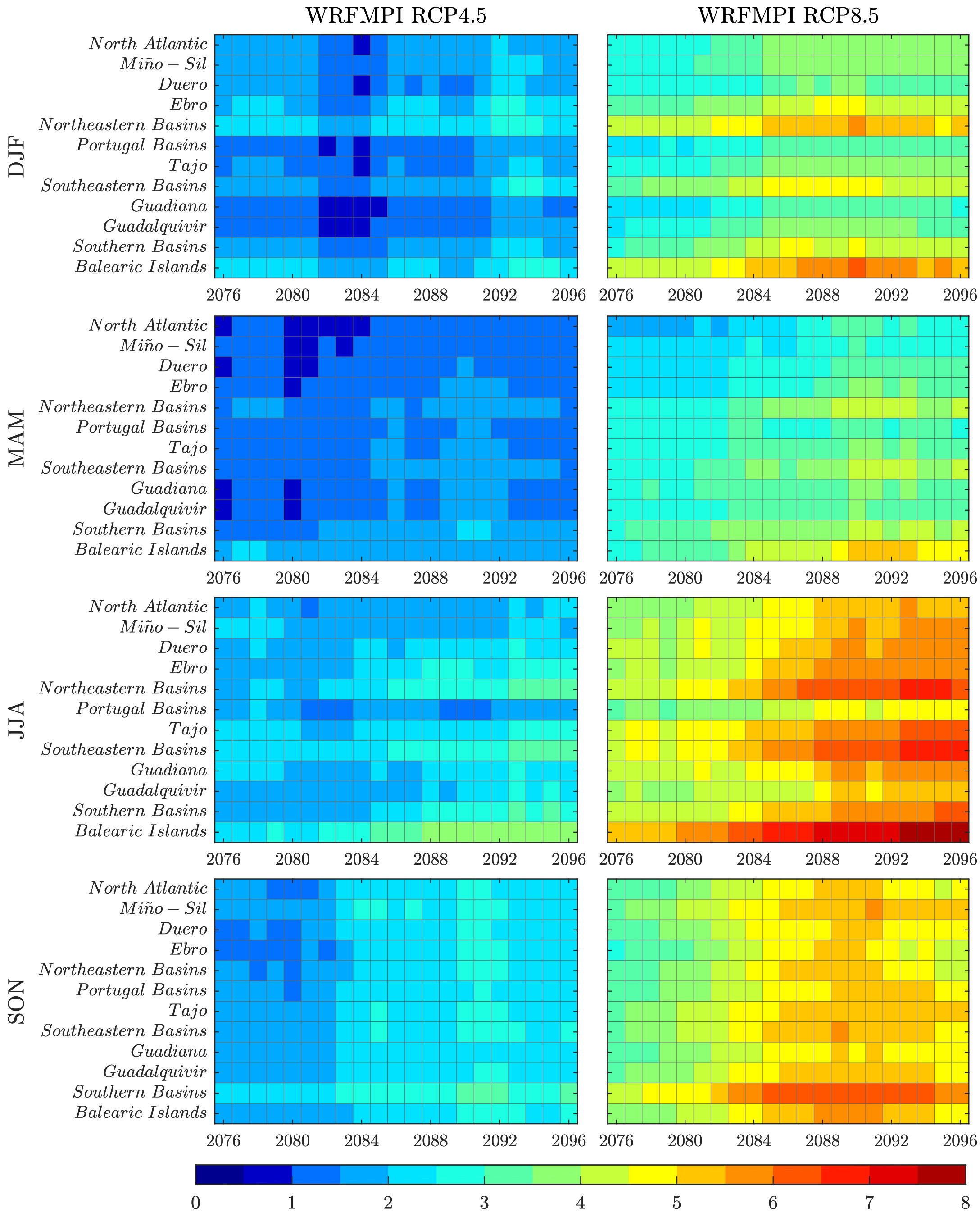

Figure 6.48: *As Figure **6.47** but for the WRFMPI simulations.*

indices that are based on a given threshold. Thus, temperature values were corrected by adding the present annual biases of the WRF outputs respect to the observations from E-OBS. For that purpose, future data were previously re-gridded onto the observational grid using bilinear interpolation.

Additionally, in order to facilitate the evaluation, the analysis of these indices was based on the comparison of their absolute values (Argüeso et al., 2012b), which can be directly compared due to the errors have been previously corrected. The indices examined are the frost days (FD), icing days (ID), summer days (SU), hot days (HD) and the tropical nights (TN). To this end, all indices were computed for each year, and then, the annual mean for the entire period were computed. The significance of the changes is also evaluated by using the two-tailed Mann-Whitney-Wilcoxon U test at the 95% confidence level over the temporal series of future values with respect to the present ones. In general, both T_{max} and T_{min} are affected by an increase in reference to the present values over the entire IP, generating more extremes. This behavior is common for all the indices analyzed, and then, only the more relevant results are shown.

Figure ***6.49*** depicts the number of days with T_{min} below 0°C (FD), for the present and the future using the two models and the two scenarios. For the near future (Figure ***6.49a***), the FD was projected similarly for all WRF simulations. In comparison to present values, the diminutions are mainly located in mountainous regions such as the Cantabrian Range and the Iberian System (differences of around 20 days/year) For the far future, the FD was drastically reduced, especially under the RCP8.5, where FD values above 40 day/year only appeared over the northern mountain ranges as well as in Sierra Nevada (Baetic System). In reference to the statistical significance of such changes, the near future depicted more non-significant significant changes under the RCP8.5 for both models, these being located in coastal areas as well as valley regions. For the far future (Figure ***6.49b***) most of the grid points showed significant changes in terms of this index. In reference to changes in the number of days with T_{max} below 0°C (ID), results (not shown) were very similar to the FD. Here, the main changes in this index were limited to mountainous regions such as the Pyrenees and the Cantabrian Range.

(a)

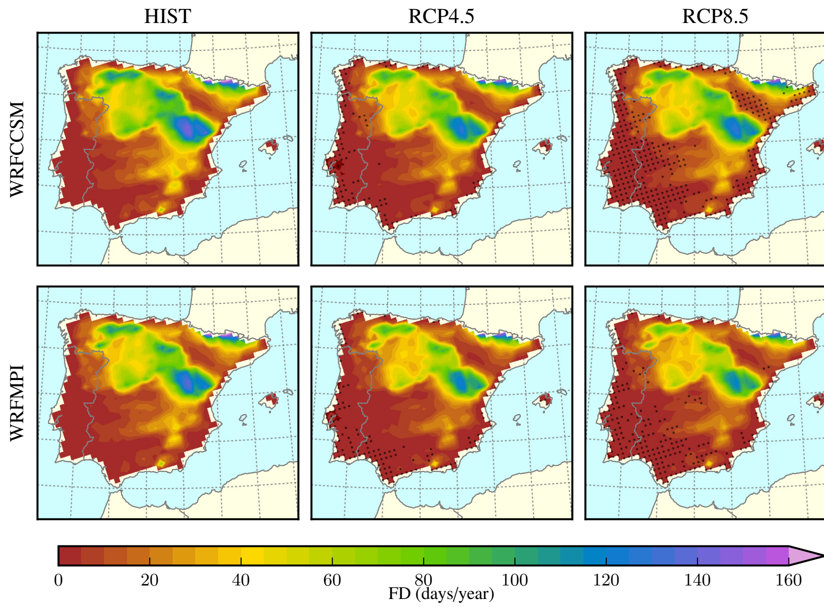

(b)

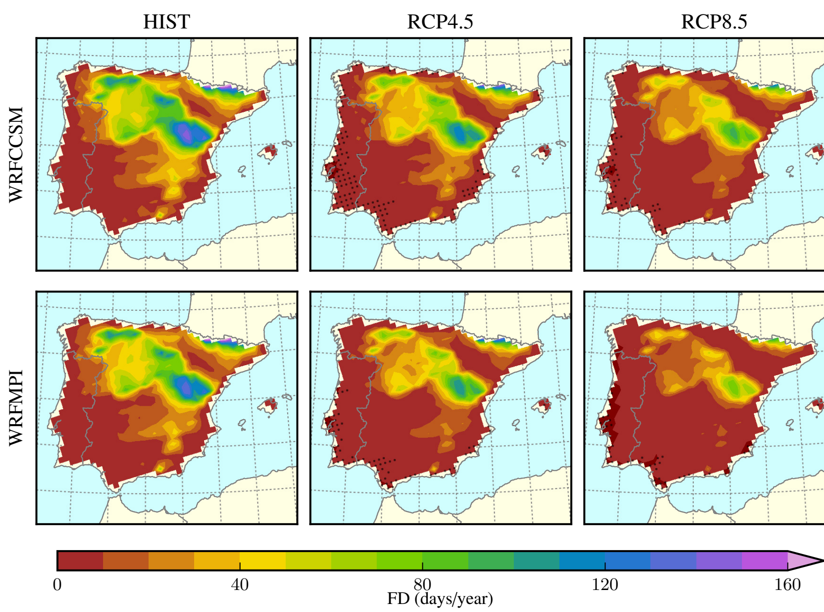

Figure 6.49: *Current (HIST) mean of the annual frost days (FD, days with $T_{min} < 0°C$) and its (a) near and (b) far future projected simulations for both the RCP4.5 and the RCP8.5. In rows, the simulations driven by CCSM4 and MPI-ESM-LR are represented. Black dots indicate non-significant changes according to a two-tailed Mann-Whitney-Wilcoxon U test at the 95% of confidence level projected changes.*

A significant increase of the number of days in which the T_{max} is above 25°C (SU) was found across the IP for all runs analyzed (Figure ***6.50***), and more marked in the RCP8.5. In the present, the highest values of SU were located in the Guadalquivir Valley and in the southeastern peninsular, which also appeared in the future, but more extended and with larger magnitude (increases up to 50 days/year in the far future under the RCP8.5). Only non-significant changes according to the Mann-Whitney-Wilkoxon test were projected in the near future (Figure ***6.50a***) and under the RCP4.5, particularly for the WRFMPI in some regions of the Atlantic and Cantabrian Coasts and Guadalquivir Valley. For the far future (Figure ***6.50b***), the differences between scenarios were clearly displayed throughout the IP, appearing highlighted differences over the Guadalquivir and Guadiana Valleys. Note that for this period, the projections from both GCMs present very similar values of SU, appearing only differences over the Cantabrian Range under both RCPs. Very similar conclusions can be drawn for the numbers of days with T_{max} that exceeds 35°C, and then the results for this latter index are not shown.

In reference to the projected changes in the number of days with T_{min} exceeding 20°C (TR), in the near future (Figure ***6.51a***), a substantial increase was revealed at least in the southern half of the Peninsula. Such enhancements appeared in certain regions over the Guadalquivir and Tajo Valley and over southeastern coast, with values of change up to 20 days/year. This behavior was displayed for both the WRFCCSM and WRFMPI and under the two scenarios. For northern areas and over the central coasts of Portugal there were still some points with non-significant changes, which were more numerous for the WRFMPI under the RCP4.5. For the far future (Figure ***6.51b***), the significant changes became more extended, and more marked for the RCP8.5. Under this scenario, TR values of more than 90 days/year are reached in the Guadalquivir Basin, and southern and southeastern Mediterranean Coast.

In the near future (Figure ***6.52a***), the projections in terms of diurnal temperature range (DTR) revealed more modest changes. Here, the WRFCCSM appeared to indicate non-significant changes practically over the entire IP, except for the Northern Plateau and the southeast of the Peninsula, which was clearly shown under the RCP4.5. The WRFMPI, however, located the most sig-

(a)

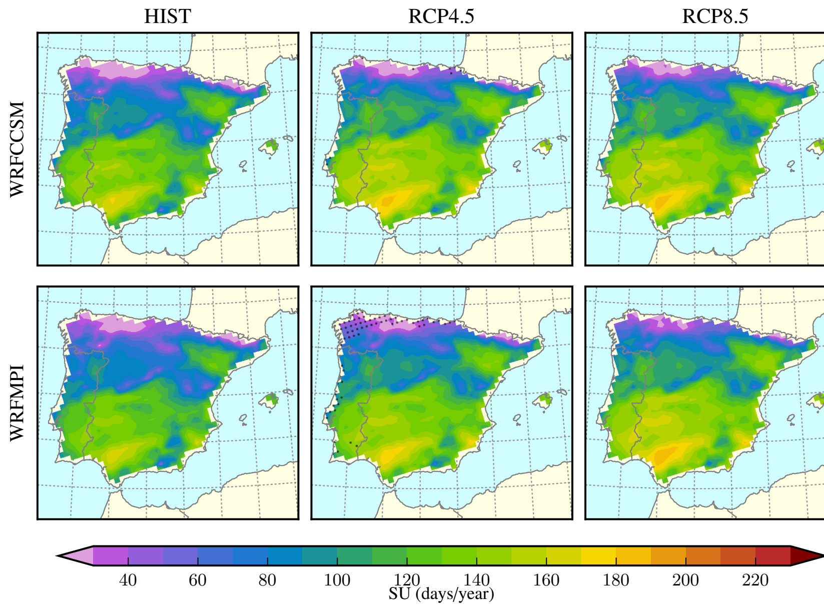

(b)

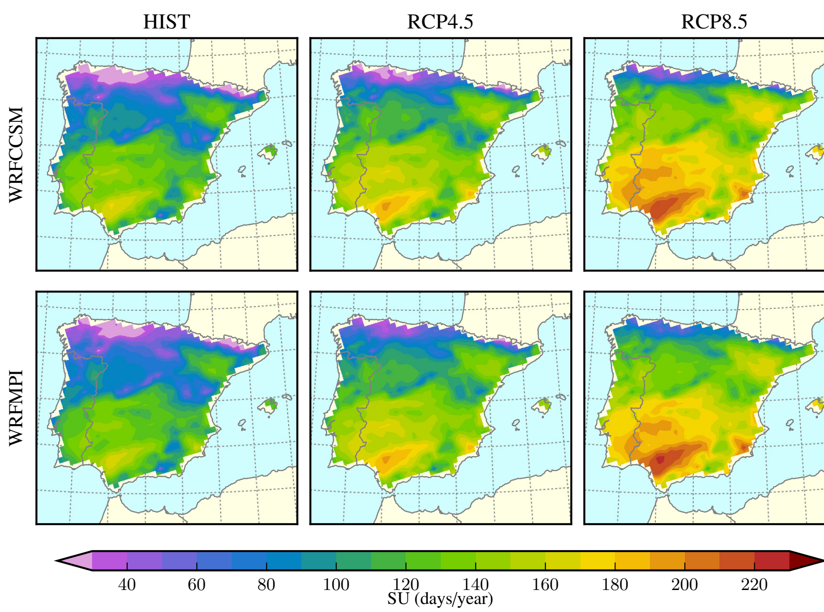

Figure 6.50: *The same as Figure **6.49** but for summer days (SU, days with $T_{max} >$ 25°C).*

(a)

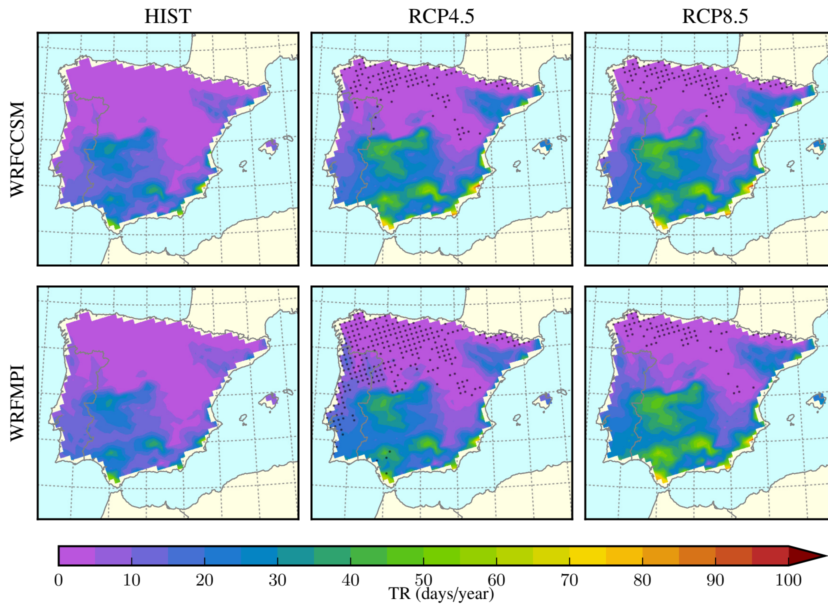

(b)

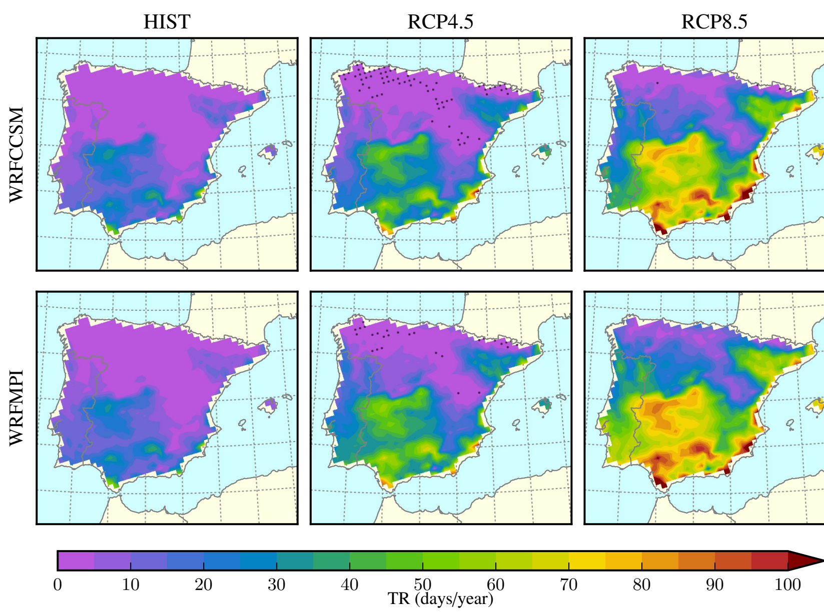

Figure 6.51: *The same as Figure **6.49** but for tropical nights (TR, days with T_{min} > 20°C).*

nificant increases in the eastern peninsular façade under the RCP4.5, whereas non-significant changes in DTR were reduced to coastal regions and the Ebro Valley under the RCP8.5. Additionally, in the far future (Figure ***6.52b***), more dramatic changes appeared, particularly under the RCP8.5. In this period, the results from simulations driven by both GCMs showed very similar spatial patterns. In general, results suggest that the daily maximum temperature is likely to suffer larger increases than the minima.

Finally, changes in the summer length were also examined as another extreme index. To this end, the approach developed by Peña-Ortiz et al. (2015) was applied using the mean values between the daily T_{max} and T_{min} calculated at the original WRF spatial resolution (0.088°). Such approach is based on defining the summer length through the definition of two thresholds, the onset (T_{on}) and the end (T_{end}) of the summer[7]. Thus, the summer length was computed and used to analyze the projected changes as the difference between the future and current values. Additionally, the significance of the changes was also tested according to a two-tailed Mann-Whitney-Wilcoxon U test at the 95% confidence level.

In general, results showed that the length of summer (Figure ***6.53***) increase for both, the near and far future, being such enhancements higher under the RCP8.5, except for the WRFCCSM in the near future. Non-significant changes were only found in the near future (Figure ***6.53a***) and mostly under the RCP4.5 over the north and west of the Peninsula. Regarding the spatial distribution of the changes, the WRFCCSM showed the largest increases under the RCP4.5 in the northwestern peninsular (Galician Massif and north of Portugal) as well as over certain regions in the center of the Peninsula. However, the RCP8.5 displayed the maximum values of increases across the entire Atlantic and Cantabrian Coast. By contrast, the WRFMPI simulations located the highest rising values over the southeast for the intermediate emissions pathway whereas under the RCP8.5 the WRFMPI appeared to project changes in more extended areas with increments of more 20 days/year.

For the far future (Figure ***6.53b***), large differences were shown between RCPs. While the intermediate emission scenario projected mean changes rang-

[7]The detailed procedure to compute summer length can be found in Peña-Ortiz et al. (2015).

(a)

(b)

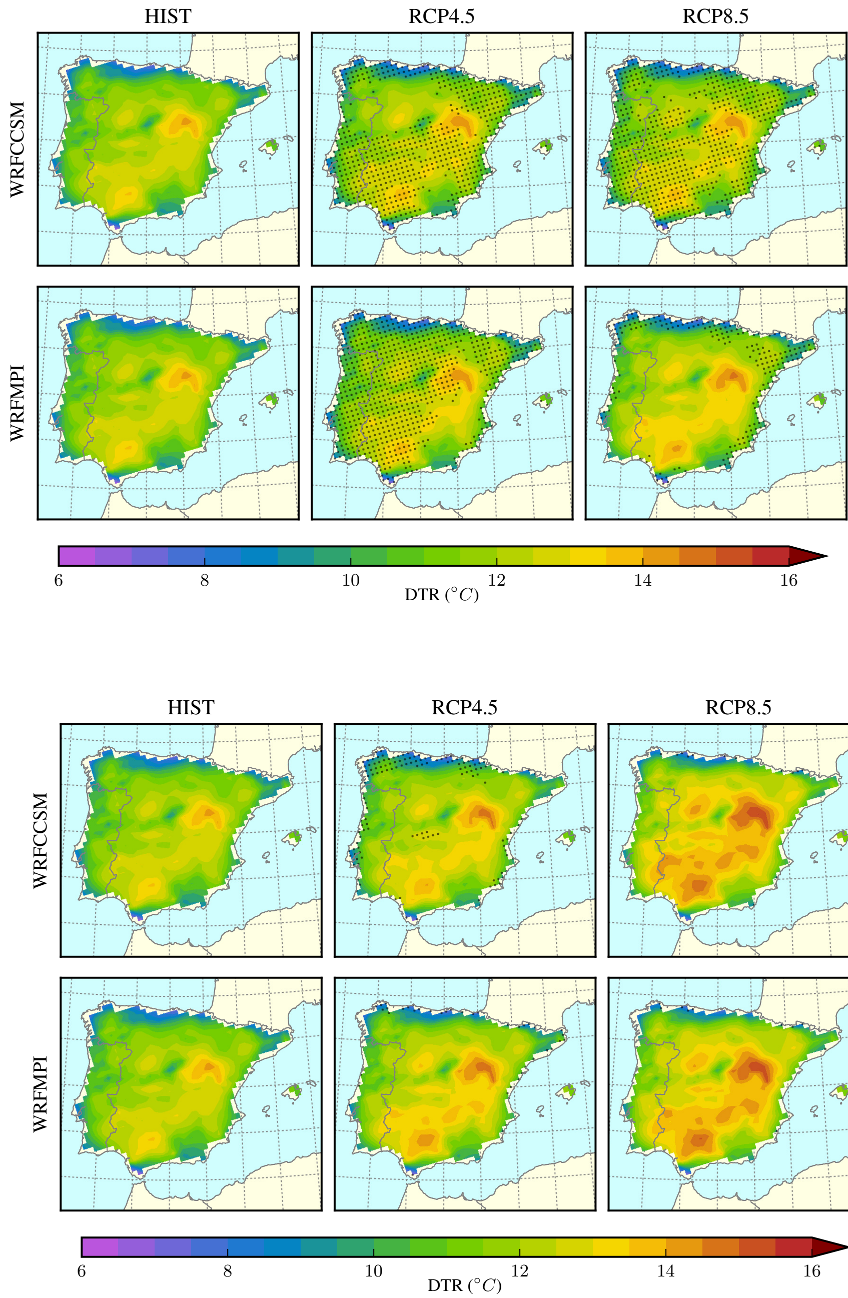

Figure 6.52: *Current (HIST) annual mean of the diurnal temperature range (DTR) and its (a) near and (b) far future projected simulations for both the RCP4.5 and the RCP8.5. In rows, the simulations driven by CCSM4 and MPI-ESM-LR are represented. Black dots indicate non-significant changes according to a two-tailed Mann-Whitney-Wilcoxon U test at the 95% confidence level projected changes.*

(a)

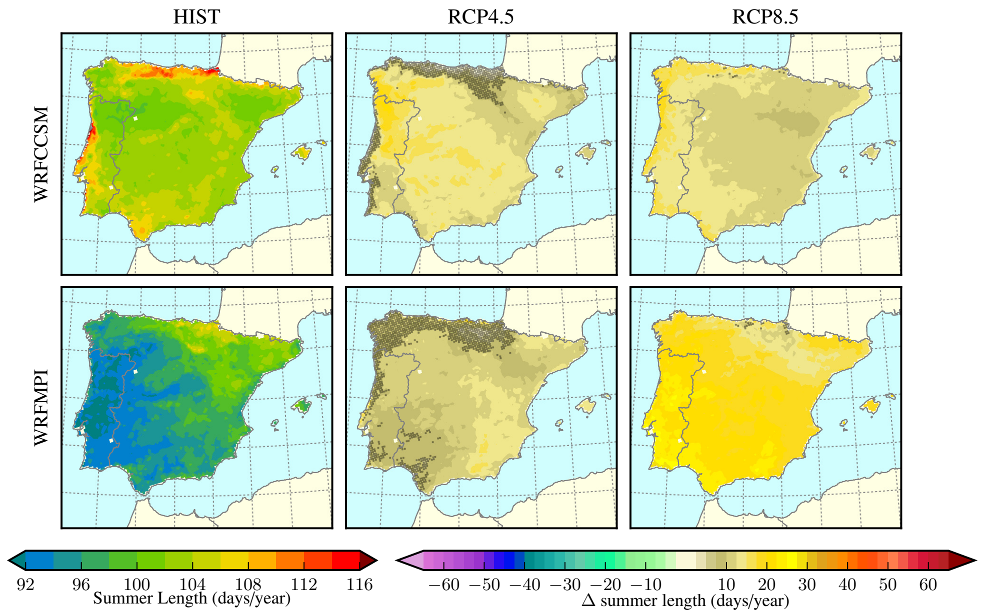

(b)

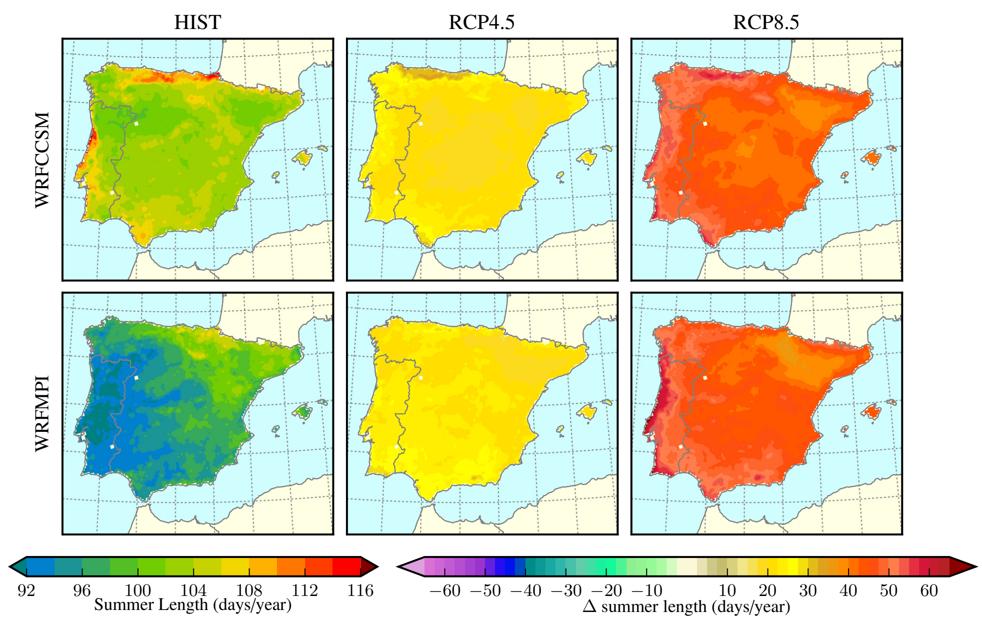

Figure 6.53: *Current (HIST) annual mean of summer lenght and its (a) near and (b) far future projected simulations for both the RCP4.5 and the RCP8.5. In rows, the simulations driven by CCSM4 and MPI-ESM-LR are represented. Black dots indicate non- significant changes according to a two-tailed Mann-Whitney-Wilcoxon U test at the 95% confidence level projected changes.*

ing from 20 to 30 days/year, the high emissions pathway indicated values above 45 days/year in many regions. Both, WRFCCSM and WRFMPI simulations appeared to show the largest increases over the Cantabrian Coast, along Coasts of Portugal and in the Atlantic Coast of Andalusia. The WRFMPI also projected important increases over the Baetic Systems.

6.4. Discussion and Conclusions from Primary Climate Variables Projections

Throughout this chapter, the results have revealed important projected changes in terms of precipitation and temperatures. These results provide valuable information to elucidate the evolution of these primary climate variables over the IP in a context of changing climate, which are strongly associated with changes in extreme phenomena such as drought. In fact, changes in drought events are likely associated with changes in mean values of precipitation and temperature, but also with changes in the extreme values. Thus, the main findings in this analysis are outlined below:

- In general, the high-resolution regional simulations have evidenced a reduction in the mean amount of the precipitation practically over the whole IP, which is influenced by the atmospheric concentration of GHGs showing more severe changes under the high emission scenario (RCP8.5) in general. However, such decreases are likely still moderate for the near future (2021-2050). Thus, for this period, the overall annual diminution in precipitation is of around 18% and a great number of grid points show non-significant changes in most of the simulations. The drier climate conditions seems to be stronger in the south and east of the peninsula, where important precipitation decreases up to 24% are projected. Our findings agree with those reported by Turco et al. (2015), who suggested reductions of the precipitation between 5 and 25% over the entire Spanish region. Furthermore, marked discrepancies appear between models and RCPs for this period, so these could be suggesting a great internal variability which is higher than the possible climate change signal. In fact, different studies point out that the main source of uncertainty in projections for a near future is due to the natural internal variability (Hawkins and Sutton, 2009).

- The most marked decreases in precipitation are found in warm seasons as has been suggested by Giorgi and Lionello (2008). Thus, for the period 2021-2050, the reductions in spring reach the maximum values related to the current period, with values of around 30%. Such results present similar magnitude of changes than those pointed out in Fernández et al. (2017) over the same period for Spain. For the period 2071-2100, however, the most substantial decrements in precipitation occur in summer when these are of around 50% for the entire IP. By contrast, the most moderate changes appear in winter for both near and far future, when an important extension is covered by non-significant changes with respect to the present, or even increments in the precipitation are found. In general, these results are in accordance with other studies performed at regional scale over the same area of study (Argüeso et al., 2012b, Jacob et al., 2014).

- Changes in variability of the seasonal precipitation present similar spatial behaviors to the changes in mean values, i.e. a diminution in the mean precipitation is associated with a reduction in the precipitation variability as well. However, such changes seem to be higher in magnitude in terms of interannual variability in many cases, as showed most of the regional simulations. In this context, the internal variability seems to be larger for the near future, reaching increases up to 150% in the eastern half of the peninsula for winter. However, results from both simulations present an important uncertainty because important different are found between them. The results agree with Pendergrass et al. (2017) who perfomed a study of the precipitation variability at global scale. There, these authors found that the precipitation variability seems to decreases (or increase) by at least as much as mean precipitations in the future.

- Changes in the S/N ratios reveal a great internal variability for the near future, as is suggested by the analysis of the seasonal precipitation changes in mean and interannual variability. However, clear decreasing trends appear in the mean amount of precipitation along the periods, more marked in the far future under the RCP8.5. In this latter period, the natural variability is still important, particularly in winter and for some watersheds. The induce signal of climate change is clearer in summer and especially over river basins located in the north of the Peninsula in a context of high emissions of GHGs. Here, simulations driven by CCSM4 reveal GHG-forced signal for spring and autumn, which is not so clear in the results from the WRFMPI simulations. These results partially agree with Giorgi et al. (2009) who found strong detriments of the precipitation in European Mediterranean region throughout the 21^{th} century, and that the emergence of the signal could occur before 2100.

- The decreases in extreme values of precipitation are less clear than in mean values. Indeed, although the projections reveal reductions in the most intense precipitation, stronger for the far future, there are important areas with increases or non-significant changes. These results suggest that the diminution in precipitation is mainly caused by reduction in the moderate rainfall events. Moreover, in general, results also show that the spatial patterns for most of the indices are very heterogeneous as was indicated by Argüeso et al. (2012b). However, substantial decreases (increases) in wet (dry) conditions are revealed, suggesting an increase in the duration of drought events.

- The mean values of temperature are likely to rise independently of the RCP considered, and more markedly for T_{max}. These results agree with Jerez et al. (2012), who found significant changes in temperature in a study about the effects of land-surface processes over the IP. As for precipitation, the results show certain uncertainties for the near future when higher discrepancies between simulations are shown. In this period, it is expected an overall annual change of around 1.2°C and 0.8°C respect to the present for T_{max} and T_{min}, respectively. Small differences are shown between RCPs, being even in some cases the changes greater in magnitude under the RCP4.5 for the WRFCCSM simulation. By contrast, the WRFMPI displays changes with similar spatial patterns but with greater magnitude for the RCP8.5. For the far future, the influence of GHG concentrations in the warming is more notorious. While for the RCP4.5 annual values of change remain with similar magnitude to the near future, the RCP8.5 presents more severe annual changes which are of around 3.5-5°C for all the IP, and more marked for T_{max}. For this period, results also present. Similar magnitude of the changes are found in (Jacob et al., 2014), where projected changes in temperature and precipitation were examined by using an ensemble of high-resolution climate change projections within the EURO-CORDEX project. Here, mean changes for the period 2071-2100 up to 2°C were found under the RCP4.5 as well as increases above 5°C for the RCP8.5, which are strongest over the southeast of the Peninsula.

- As for precipitation, the most substantial changes in temperature are projected in general over the south and east of the Peninsula. However, in terms of temperature, severe increases also were revealed in high mountain regions as well as coastal regions seem to suffer more moderate changes. This latter is clearly shown along the Atlantic and Cantabrian Coasts, where non-significant changes appear in most of the regional simulations for the near future. Regarding the distributions of the changes along the year, the projection from simulations driven by the two GCMs indicate changes in seasonal temperatures of about 0.2-2°C for both the T_{max} and T_{min} in the near future, appearing the greater increments in warm seasons. Our findings agree with the results founds in Fernández et al. (2018), who found changes in temperature similar in magnitude for the near future by using an ensemble of 196 future climate projections arising from different RCMs and GCMs. In the far future, summer seems to show the most substantial changes (values above 6°C), and winter the most moderate as occurs in the previous period (values of around 1°C and 3°C for the near and far future, respectively) for both extreme temperatures.

- In relation to projected changes in temperature variability results show both increases and decreases, which are not significant in many cases regarding to a two-tailed F Snedecor test at the 95% confidence level. The most relevant results are shown for T_{max}, where changes in the standard deviation broadly suggest positive differences in winter, as was indicated by all simulations in the near future. In the far future, however, the results show more discrepancies. The WRFCCSM projects increases for winter and decreases for summer, and only for the RCP4.5 WRFMPI projects higher increases for all seasons except for summer.

- The evolution of S/N ratios revealed a GHG-forced signal with more robustness than for the precipitation in both periods, being the rising temperatures more marked in general in the southern peninsular river basins. In this sense, Deser et al. (2012) pointed out that forced changes in temperature can be detected earlier than for precipitation. The evolution of S/N values also shows that the climate changes is likely to emerge against the background of natural climate variability early in summer, as pointed out other authors such as de Elía et al. (2013).

- Rising extreme temperatures are also projected with significant changes for all ITCCDI indices, as well as for the projection of summer length. These changes are more marked under a high emission scenario, especially for the far future. These results are in accordance with Barrera-Escoda et al. (2014), who found an increase in extreme temperatures over the northwestern Mediterranean Basin.

Chapter 7

Characterization on Future Drought Episodes

This chapter provides an analysis of changes in land-surface variables, i.e. soil moisture and evapotranspiration, which are strongly related to drought phenomena, by examining the projections from the different WRF simulations. Moreover, an analysis of drought projections has been performed through the application of drought indices, in order to examine the magnitude and extent of warming-induced drying over the IP. The drought indices analyzed here are the SPI and the SPEI that use primary climate variables (i.e. precipitation and maximum and minimum temperature), which have revealed vulnerable to suffer substantial changes in the future, as shown in Chapter ***6***.

7.1. Description of the Analysis

For a further examination of the effects of climate changes on the hydrological cycle for the IP, we used different outputs from the WRF simulations driven by the two GCMs (CCSM4 and MPI-ESM-LR), which were detailed in section ***6.1.1***. Thus, projected changes in mean values of surface evapotranspiration and soil moisture in the near (2021-2050) and far (2071-2100) future, and under the two RCPs (RCP4.5 and RCP8.5) were examined through the Delta-change approach, at annual and seasonal time scales through a directly grid-point analysis. In this context, only the root-zone soil moisture (the upper 1 m of the soil) was taken into account in order to elucidate the influence of the soil-water availability in the evapotranspiration. The significance of the changes was tested by using a two-tailed Kolmogorov-Smirnov test at the 95% confidence level, enabling us to evaluate whether the data of two samples come from the same continuous distribution.

Changes in these variables and the subsequent effects in the distribution of turbulent heat fluxes (latent and sensible heat fluxes) are expected to increase climate extremes such as drought (Miralles et al., 2014), so that an additional analysis concerning the projections of drought events was also performed. For this, precipitation and extreme temperatures (T_{max} and T_{min}) from the WRF simulations were aggregated at monthly time scale, and then, used to compute the SPI and the SPEI. These indices have been computed at 3- and at 12-month time scales, following the methodology detailed in section ***5.2***.

However, such drought indices are based on standardized values in relation to the average conditions in a given period and in a given place, which is a limitation to compare drought conditions between different time periods. To solve this issue a widely used procedure is to compute the indices relative to a current period (Dubrovsky et al., 2009, Leng et al., 2015). That is, the indices were firstly computed for the current period (1980-2014), and then, the distribution parameters in that fitting were applied to compute the indices in the future. Therefore, we assumed that the parameters of the log-logistic distribution would be unchanged over time, and thus, they could be extended to future projections. Projected changes of drought were analyzed through the Delta-Change approach in terms of duration, frequency, magnitude, and severity of drought events, using a direct grid-point comparison between indices, time scales, RCP, and periods. Also, the results found here were used to prepare a hybrid classification of the projected changes in droughts, in terms of such characteristics for each river basin in the IP, similar to the procedure of PaiMazumder and Done (2014), which could provide valuable information for policy makers.

7.2. Changes in Surface Evapotranspiration

7.2.1. Projections in Mean Annual Values

Concerning annual changes in surface evapotranspiration, Figure ***7.1*** and Figure ***7.2*** depict the relative projected changes for the near (2021-2050) and far (2071-2100) future related to the current (1980-2014) period, respectively. The non-significant changes according to a two-tailed Kolmogorov-Smirnov test, evaluated at the 95% confidence level, are marked with black dots. As in previous analyses in chapter ***6***, Figures also depict the historical mean values for each GCM-driven simulation in order to determine the magnitude of the changes.

All WRF simulations projected both increases and decreases, although the significant changes were predominantly negative. The most noticeable decreases appeared in the far future when reductions of almost 40% were reached, whereas for the near future the major changes were about -20%. The changes in this variable were similar to those found in precipitation in both periods (see Figures ***6.2*** and ***6.3*** for the near and far future, respectively) especially in southern regions. Thus, the results suggest that changes in evapotranspiration were associated mainly with the reduction in the water supply, at least, for the south of the Peninsula. In fact, in semi-arid regions such as a great part of the Peninsula, the evapotranspiration rate is primarily constrained by soil-moisture availability and, subsequently, by the precipitation. By contrast, certain areas located in mountainous regions in the north of the Peninsula (e.g. Cantabrian Range) presented increases in the annual evapotranspiration in both periods. This latter is likely associated with the increased demand of moisture by the atmosphere (i.e., potential evapotranspiration (PET) rises) in an area where the soil moisture is not limiting.

In the comparison between models, the WRFCCSM and the WRFMPI revealed certain differences. The changes in the near future (Figure ***7.1***) were more pronounced in the projections from the simulations driven by the MPI-ESM-LR, locating the greatest decline over the southeast of the IP under the RCP4.5. Such reductions, however, covered nearly the entire IP under the RCP8.5. By contrast, the WRFCCSM presented few significant changes in both scenarios, the two being similar. For the RCP8.5, a common reduction area

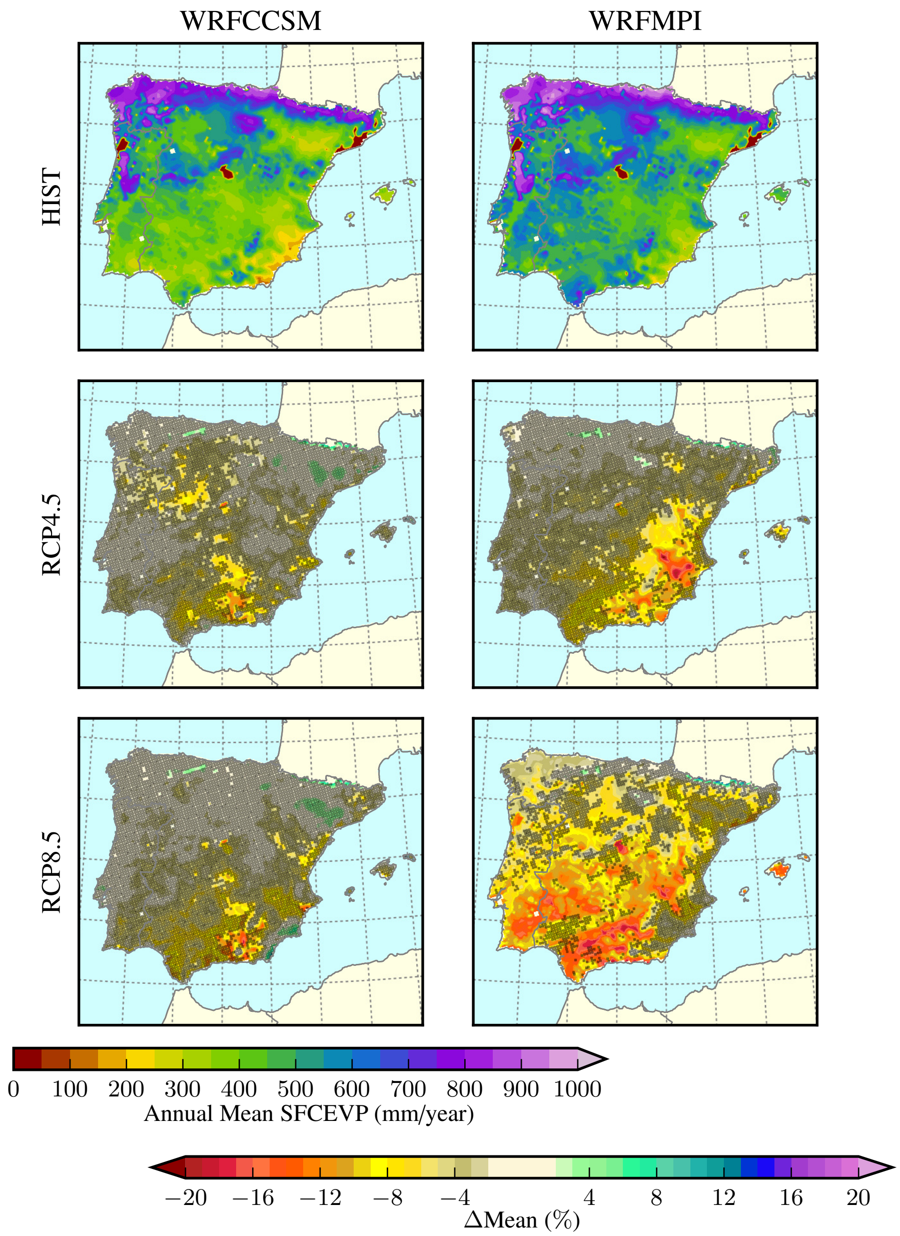

Figure 7.1: *Current annual mean of the amount of surface evapotranspiration (1980-2014) and its near future (2021-2050) projections. In columns, the WRF simulations conducted by the two GCMs (WRFCCSM and WRFMPI). In rows, the historical (HIST) and the two RCPs (RCP4.5 and RCP8.5) are displayed. Black dots indicate non-significant changes according to a Kolmogorov-Smirnov test at the 95% confidence level.*

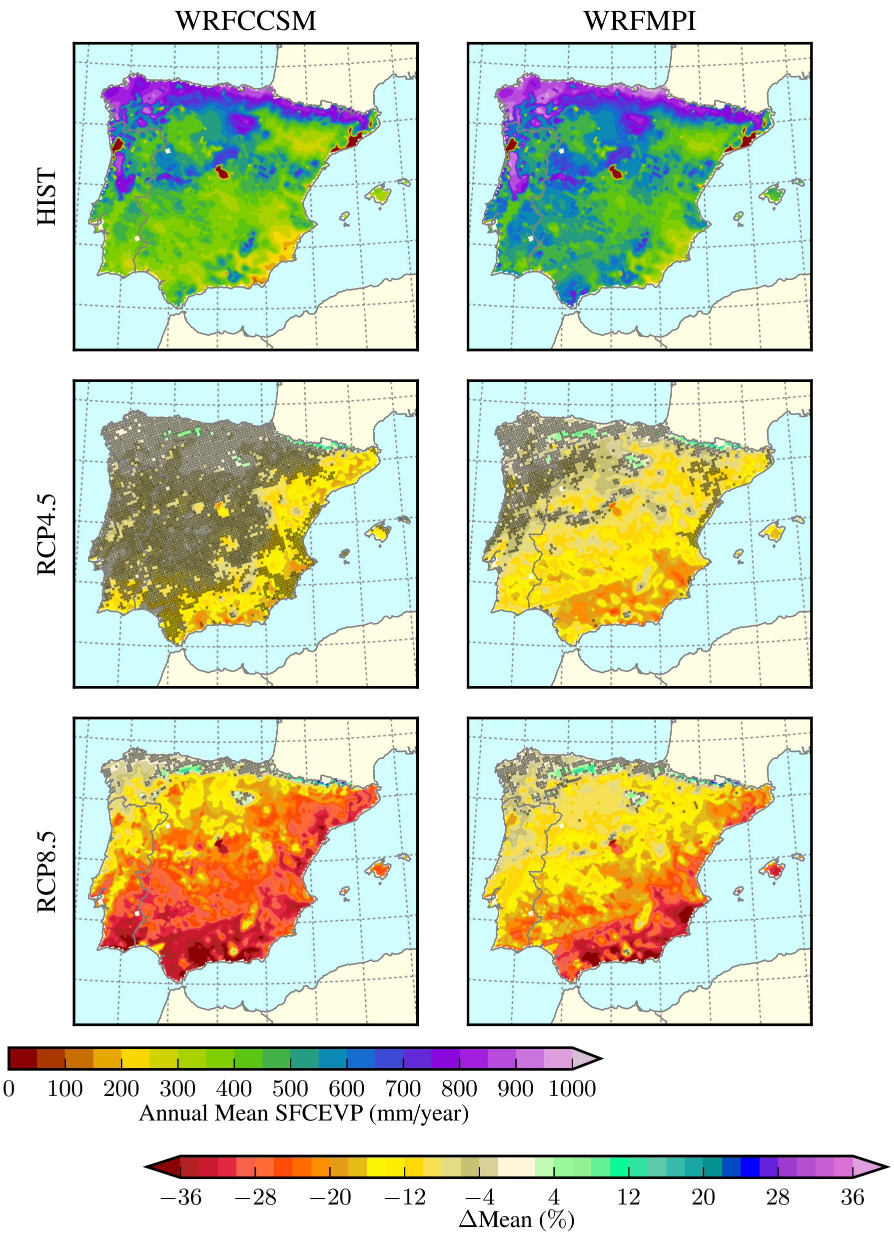

Figure 7.2: *The same as Figure **7.1** but for the far future (2071-2100).*

arose in the southern part of the peninsula, with values of about -16%.

For the far future (Figure ***7.2***), the reductions of surface evapotranspiration were projected to be already more extended, reaching values of up to 36% for the

RCP8.5. For this period, the simulations conducted using the CCSM4 proved broadly similar to resulting from the WRFMPI, with the difference between scenarios in any case being more pronounced. In a context of intermediate GHG emissions, changes in this variable appear to stabilize in certain areas in the southern IP, although the reduction was generally more widely extended than in the near future. In the north, the surface evapotranspiration appeared to rise slightly, suggesting an increasing trend throughout the 21^{th} century probably due to the greater evaporative demand in an area where the soil moisture is not constrained. On the other hand, for the higher radiative forcing, notable reductions were found, the most pronounced changes being shown by the WRFCCSM simulation. In this case, the decrease exceeded 28% in practically the entire southern half of the IP as well as throughout the eastern regions.

Annual values showed notable changes in surface evapotranspiration, more marked for the far future and in the RCP8.5. However, such annual changes may have different distributions. For this reason, seasonal projected changes are also examined.

7.2.2. Projections in Mean Seasonal Values

Analogous to the study of the projected changes in precipitation and extreme temperatures, changes for the accumulated seasonal values of surface evapotranspiration were also analyzed in order to elucidate the distribution of the projected changes over the year.

The WRFCCSM and the WRFMPI showed a broad common behavior for the evapotranspiration changes throughout the year, which were greater in magnitude in the far future, and especially under the RCP8.5. Changes in surface evapotranspiration depended on the water availability at each time, but also on the effect of the warming temperature. Thus, for the near future, all simulations showed generally non-significant changes throughout most of the IP during winter (Figures ***7.3*** and ***7.4***, DJF), being both positive and negative.

Spatial patterns similar to those of winter were shown in spring for the near future, but with more marked changes (values of changes ranging from -15% to 15%). Significant changes were forecast to cover larger areas, these being positive in the north and negative in the south. The greatest increases were

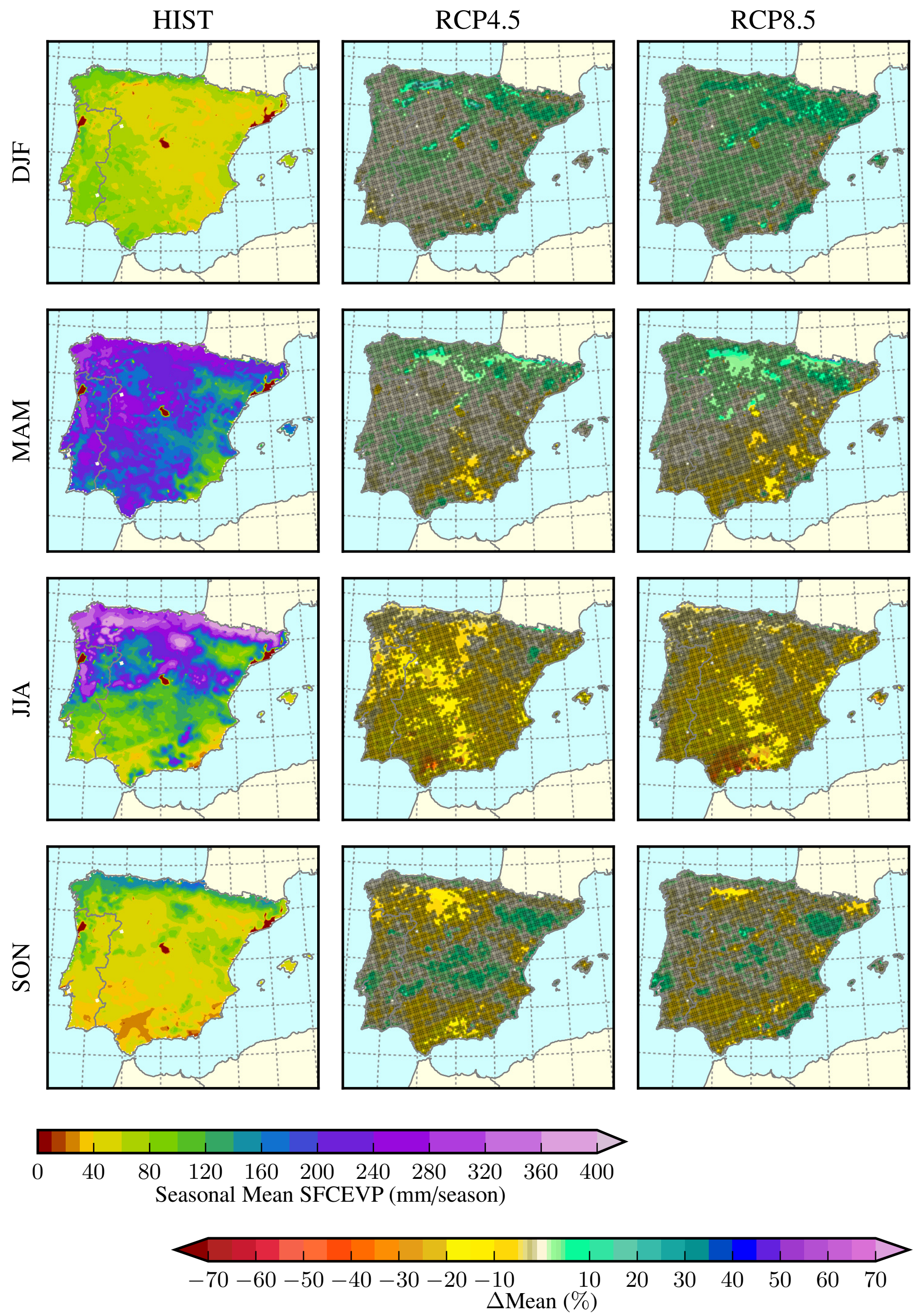

Figure 7.3: *Current (1980-2014) seasonal accumulated surface evapotranspiration (first column) and the projected changes in the near future (2021-2050) from the CCSM4-driven simulations . In second and third columns the results from the RCP4.5 and RCP8.5 are shown, respectively. Black dots indicate non-significant changes according to a two-sided Kolmogorov-Smirnov test at the 95% confidence level.*

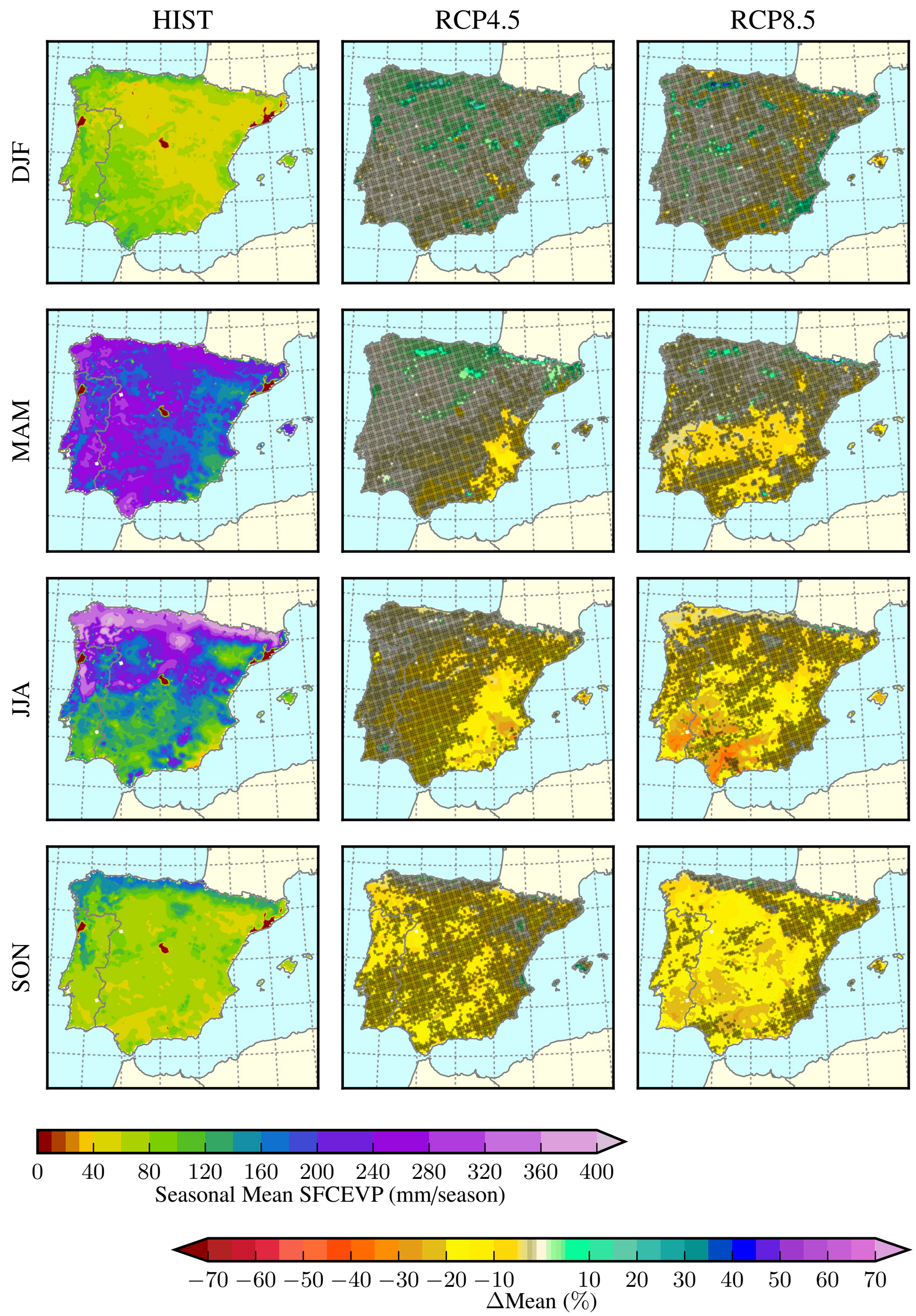

Figure 7.4: *The same as Figure **7.3** but from MPI-ESM-LR-driven simulations.*

projected by the WRFCCSM in the north (Figure ***7.3***, MAM), and the strongest decreases by the WRFMPI (Figure ***7.4***, MAM). The IP will likely undergo the most substantial reductions of evapotranspiration in summer, which was already notable in the near future when the WRFMPI (Figure ***7.4***, JJA) projected significant decreases for high emissions of GHGs (values of about -45% in southern IP). These changes were broadly similar to those found for precipitation (see Figures ***6.4*** and ***6.5***), indicating that the surface evapotranspiration depends strongly on the precipitation.

The most notable differences between the simulations from the two GCMs appeared in autumn. In the period 2021-2050, the WRFCCSM presented change pattern similar in both RCPs, showing both positive and negative changes. However, such changes proved non-significant over practically the entire IP, and in any case the significant points were only negative and located over certain regions across the IP (changes up to -20%, Figure ***7.3***, SON). However, the WRFMPI projected substantial decreases for nearly the entire IP, with the highest values under the RCP8.5, particularly over the southern IP (maximum reductions of about 25%, Figure ***7.4***, SON).

In the far future, the changes were nevertheless projected to be more marked (Figures ***7.5*** and ***7.6***). High-mountain regions over the northwest of the IP presented noteworthy increases in their accumulated winter means in relation to the present (values up to 70%), while coastal areas in the southern and eastern IP projected decreases of up to 25%. In this way, the WRFCCSM appeared to present the most widespread decreases in the southeastern IP whereas the WRFMPI showed greater increases in the Cantabrian Range. This behavior suggests that soil drying in the south, where the demand for soil moisture by the atmosphere cannot be satisfied, is due to the decreased precipitation. Nevertheless, in the north the evapotranspiration in winter (Figures ***7.5*** and ***7.6***, DJF) is probably not constrained by the soil moisture, and thus the rising temperature will likely lead to greater evapotranspiration.

For spring (Figures ***7.5*** and ***7.6***, MAM), wetting and drying conditions will remain steady (changes ranged between -45 and 45%), being predicted to intensify especially for the RCP8.5, where the changes were greater in magnitude. In this period, the WRFCCSM showed more marked changes, both positive and

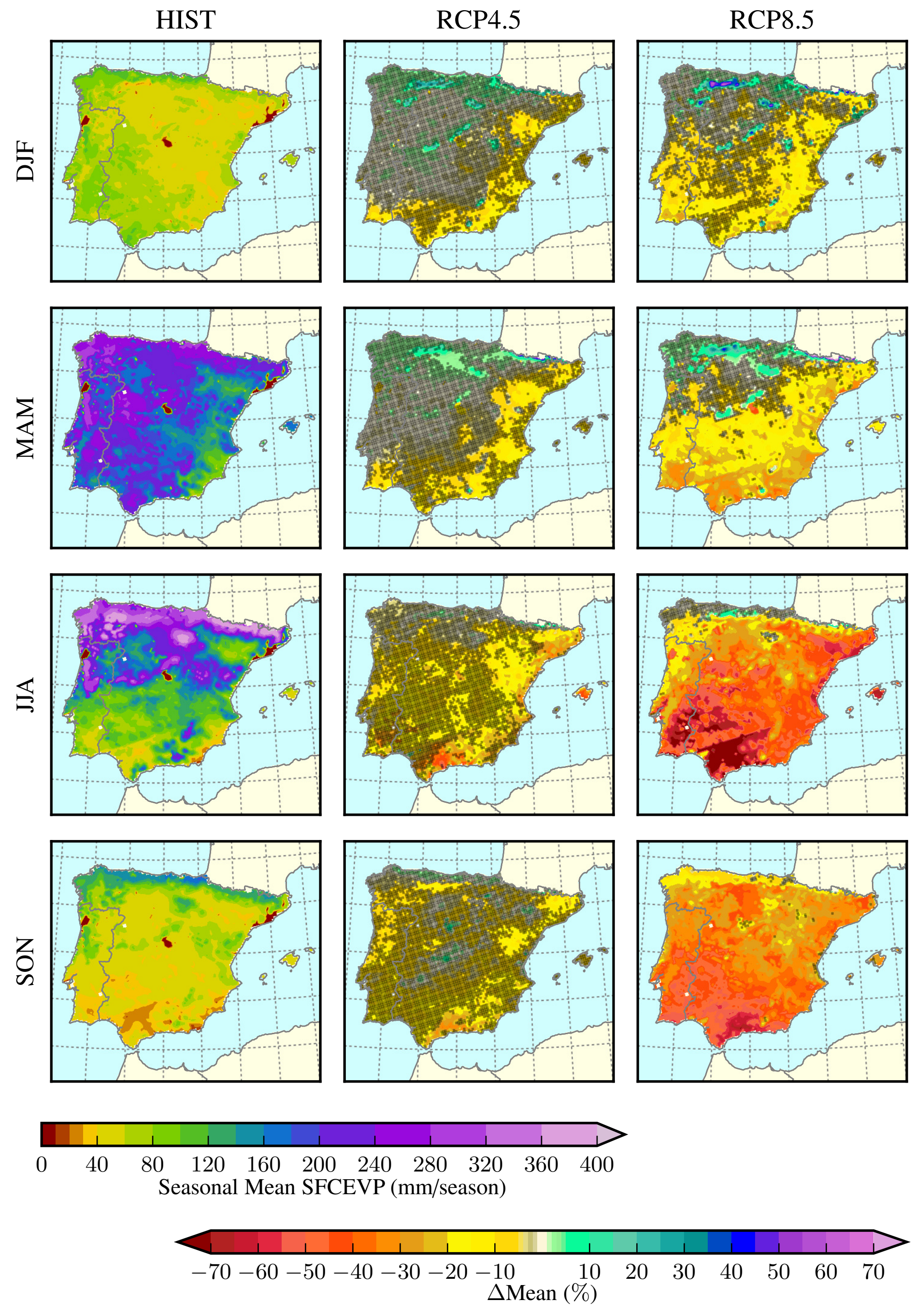

Figure 7.5: *Current (1980-2014) seasonal accumulated surface evapotranspiration (first column) and the projected changes in the far future (2071-2100) from the WRFCCSM simulations. In the second and third columns the results from the RCP4.5 and RCP8.5 are shown, respectively. Black dots indicate non-significant changes according to a two-sided Kolmogorov-Smirnov test at the 95% confidence level.*

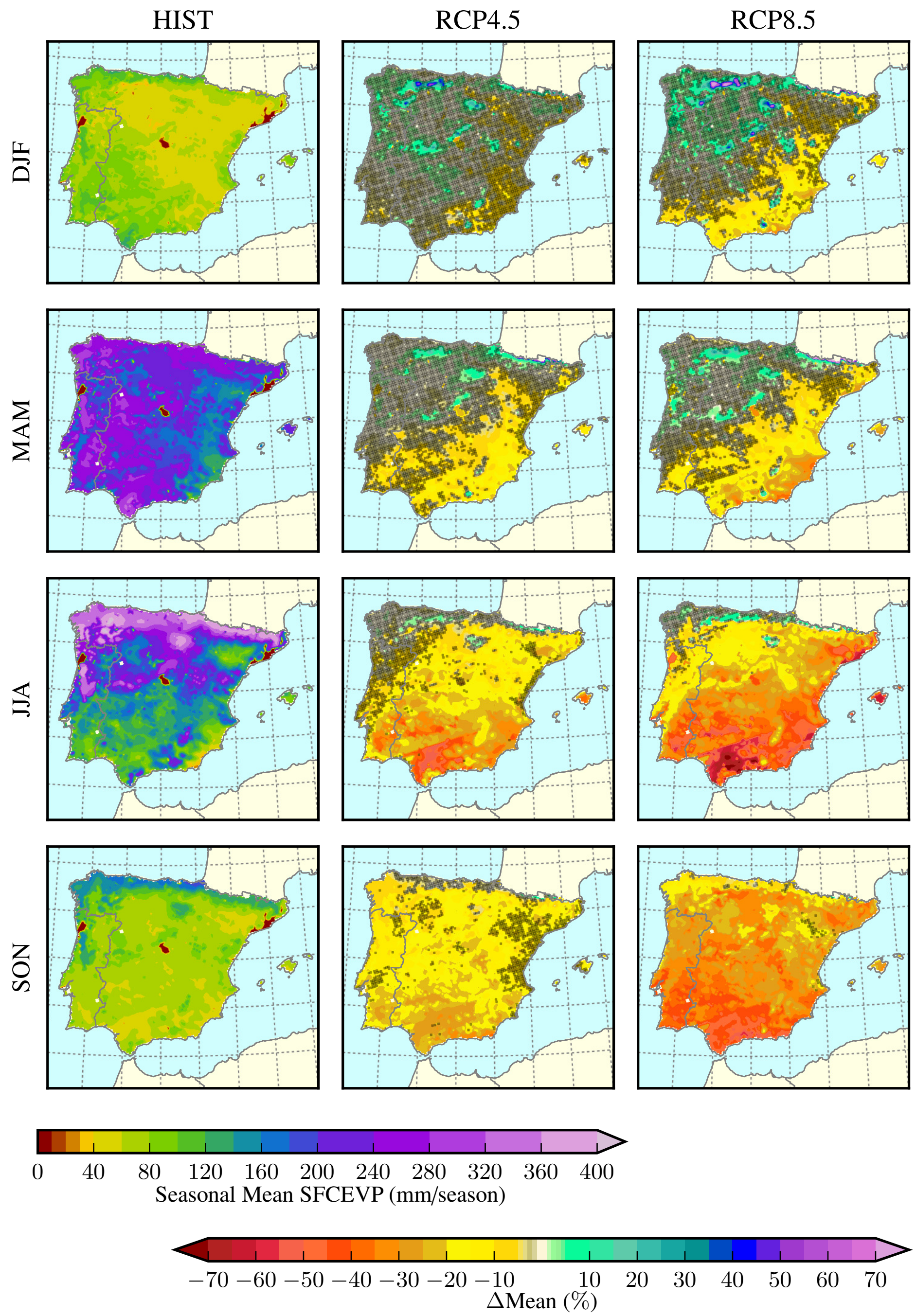

Figure 7.6: *The same as Figure* ***7.5*** *but from MPI-ESM-LR-driven simulations.*

negative. This finding is likely associated with the projected changes in temperature and precipitation since both are substantial in this season, which, indeed, intensifies the evaporative demand in the north (e.g. along the Cantabrian Range) but also the coupling soil moisture-evapotranspiration (e.g. in southeastern IP).

As for the near future, summer is the season with the most marked changes in surface evaporanspiration (Figure ***7.5*** and ***7.6***, JJA), appearing values stronger in magnitude and covering larger areas for the RCP8.5 (values of reduction above 70% over the Guadalquivir Valley). By contrast, certain regions over the Cantabrian Range will still show increasing values, but these are substantially reduced in surface area. For this period, and as occurs in other seasons, the intermediate emission scenario appeared to show a slight stabilization for the WRFCCSM, with values of change similar to the previous period, although more widespread. However, for this model, the projection from the simulation using the high GHG emissions scenario showed the most remarkable changes. Moreover, the substantial rise in the temperature projected for this period (see, for example, Figure ***6.27*** and ***6.28***, JJA) could be the consequence of a stronger land-atmosphere coupling. Namely, low water availability in the soil is probably driving the alterations in the flux partitioning between latent and sensible heat, with the subsequent intensification of the rising temperature.

In autumn, a more similar behavior was shown between the simulations driven by the two GCMs in this period, especially for the RCP8.5. For the RCP4.5, the WRFCCSM presented significant changes that were in general negative, with values reaching -45% in coastal areas in the southern IP, although there was also a large area with no significant changes (Figure ***7.5***, SON). Nonetheless, for the RCP8.5 the changes were noticeable for the entire IP, where the maximum values were located in the same areas as for the RCP4.5, but with large magnitudes (reductions > 60%). The WRFMPI showed significant reductions of evapotranspiration in relation to the present in most of IP, which were larger in southern regions (Figure ***7.5***, SON). This latter simulation revealed more substantial changes than the WRFCCSM under the RCP4.5, but the changes were slightly more moderate for the RCP8.5 (the highest values of changes were close to -50%).

In summary, annual and seasonal values of surface evapotranspiration revealed notable changes, more marked in the far future for the RCP8.5. Such changes proved be associated with different factors. On the one hand, the water evaporative demand (i.e. PET) was projected to increase almost everywhere in the future. This is because the trend towards global warming will increase the vapour-pressure deficit (in a warm atmosphere the water-holding capacity increases but would not be expected to markedly increase in humidity as well) as pointed out by some authors (Held and Soden, 2006, Cook et al., 2014, Sherwood and Fu, 2014, Prudhomme et al., 2014). On the other hand, changes in the wind also could have an effect, and changes in CO_2 concentrations also imply changes in the transpiration (Jung et al., 2010).

Nevertheless, in semi-arid regions such as most of the IP, the surface evapotranspiration is very likely to be constrained by the soil water available, and thus changes in evapotranspiration will largely follow the trend of the soil moisture. Indeed, soil moisture-evaporation coupling is expected to be stronger by the end of the century in semi-arid regions (Miralles et al., 2012, Greve et al., 2014, Seneviratne et al., 2006b, 2010). Also wet regions in the IP would become semi-arid (Jerez et al., 2012, Gao and Giorgi, 2008). This trend will likely lead to more frequent drought events in the future.

7.3. Changes in Soil Moisture

7.3.1. Projections in Mean Annual Values

For the near future (Figures **7.7**), all WRF simulations in general showed significant declines in the annual mean of soil-moisture content in relation to present values (reductions of about 2-16% in many cases). For the CCSM4-driven simulation, significant reductions were shown under the RCP4.5, these being located mainly in the northwest and especially in the southeast of the IP. By contrast, for the RCP8.5, widespread significant values were located only over certain regions across the entire IP, although the southeastern area remained steady. The results were similar to those found for evapotranspiration in most regions throughout the IP, suggesting future drying conditions. However, this relationship did not appear in some northern regions (e.g. the Cantabrian Range) where the simulations indicated an increase in surface evap-

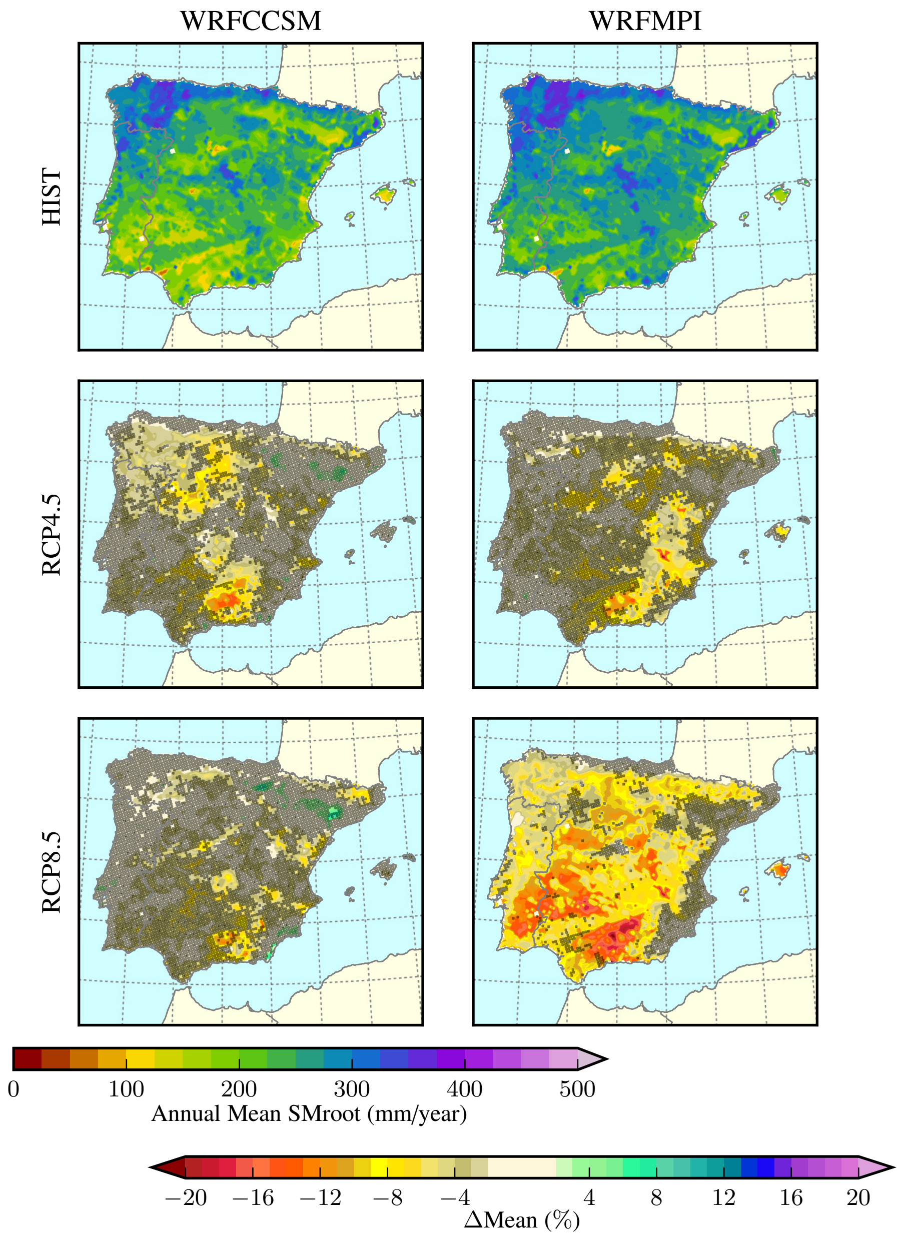

Figure 7.7: *Current (1980-2014) and near future (2021-2050) projections in annual mean root-zone soil moisture. In columns appear the WRF simulations conducted by the two GCMs (WRFCCSM and WRFMPI). In rows the historical (HIST) and the two pathways (RCP4.5 and RCP8.5) are shown. Black dots indicate non-significant changes according to a Kolmogorov-Smirnov test at the 95% confidence level.*

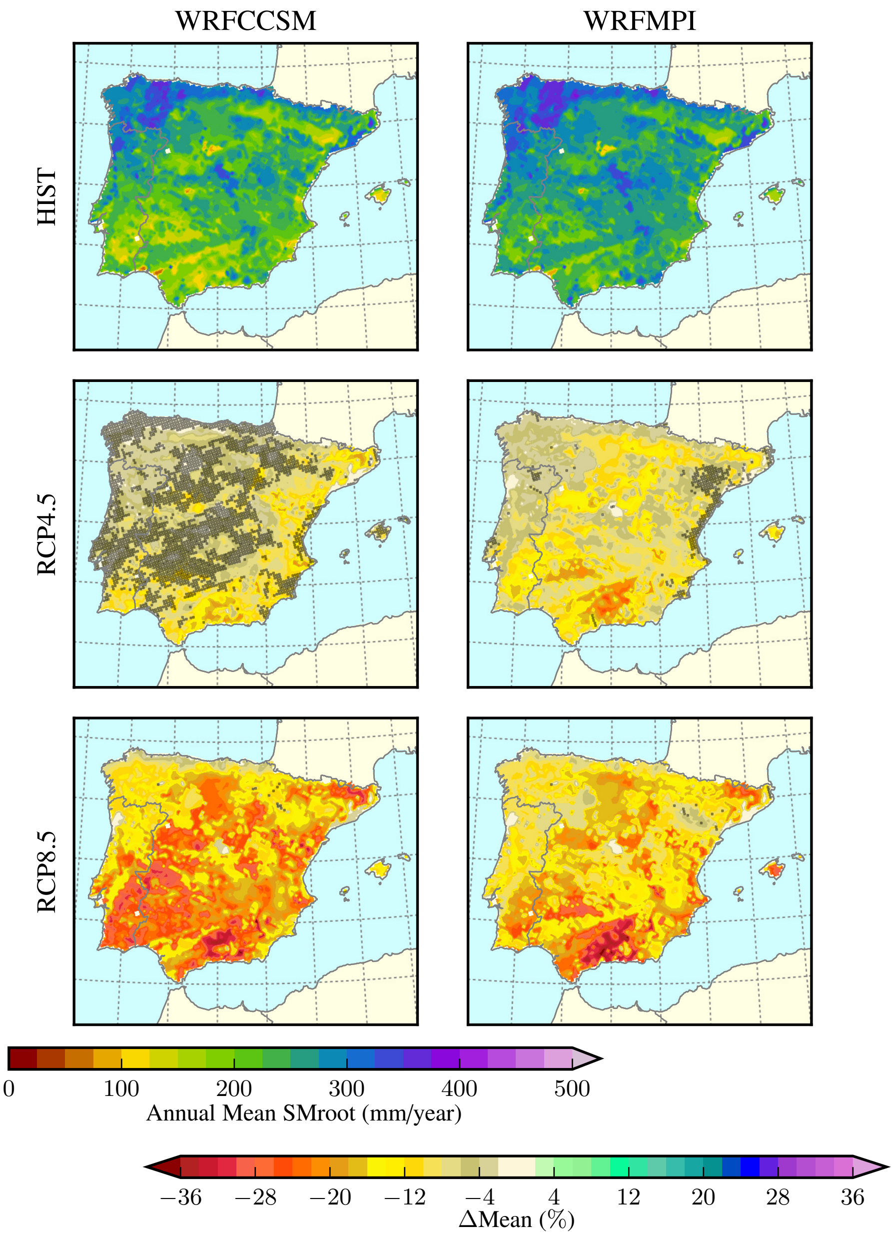

Figure 7.8: *As Figure* ***7.7*** *but for the MPI-ESM-LR-driven simulations.*

otranspiration whereas the soil moisture was likely to decrease. Such results suggest that although the trend is towards drying, the soil still registered enough moisture, and thus the evapotranspiration was not yet limited. On the other hand, the WRFMPI simulations presented more extended and severe decreases for the RCP8.5, especially in many regions located in the central and southern IP.

For the far future (Figure ***7.8***) the soil moisture will probably decrease with even more marked reductions (of between -2% and -36%). All simulations located the greatest changes over the Guadalquivir Valley (values below -14% and -36% for the RCP4.5 and the RCP8.5, respectively). In this period, changes between RCPs were more notable, especially for the WRFCCSM. This latter simulation, under the RCP8.5, projected larger areas affected by diminutions of more than 20% over the Northern Plateau and southern IP. In the RCP4.5, however, the declines ranged from 2% and 26%, so a certain stabilization was detected under this scenario, especially for the WRFCCSM, although significant decreases still covered a large area of the IP.

Changes in annual values have revealed a generalized reduction in soil-moisture content, more marked in the far future and for the RCP8.5. The increase in dryness conditions may alter the soil thermal inertia through changes in the interchange of latent and sensible heat fluxes. The results also corroborate that changes in soil-moisture content are tightly coupled with changes in water supply, i.e. precipitation (Sherwood and Fu, 2014) but also in changes in the moisture demand (i.e. potential evapotranspiration). In this context, further study in the distribution of the changes over the year is desirable, and therefore a seasonal analysis of the changes root zone soil moisture was also performed.

7.3.2. Projections in Mean Seasonal Values

Figure ***7.9*** and ***7.10*** display the projected changes in root-zone soil moisture for the WRFCCSM and WRFMPI simulations, respectively, for the near future. In general, the changes were predominantly negative, indicating drier conditions regarding to the present (values range between -30% and 15%).

Concerning mean winter values, the WRFCCSM projected moderate changes (Figure ***7.9***, DJF), which were both positive and negative. However, these were non-significant in nearly the entire IP. Similar results were found for the WRFMPI (Figure ***7.10***, DJF) under the RCP4.5, while for the RCP8.5, signifi-

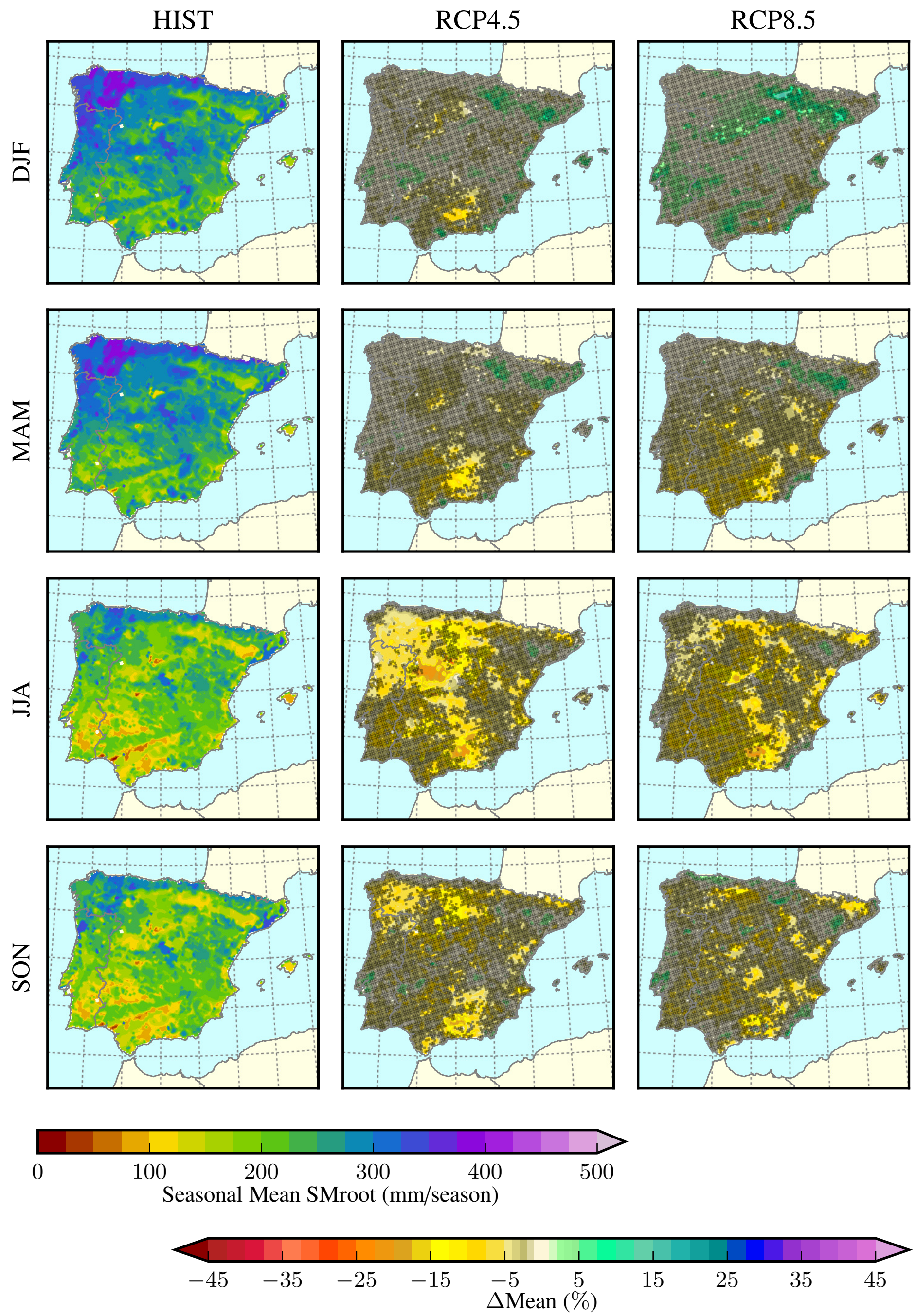

Figure 7.9: *Current (1980-2014) seasonal mean soil moisture at the upper 1 m of the soil (root zone) and projected changes in the near future (2021-2050) from simulations driven by CCSM4 under the two RCPs (RCP4.5 and RCP8.5). Black dots indicate non-significant changes according to a two-sided Kolmogorov-Smirnov test at the 95% confidence level.*

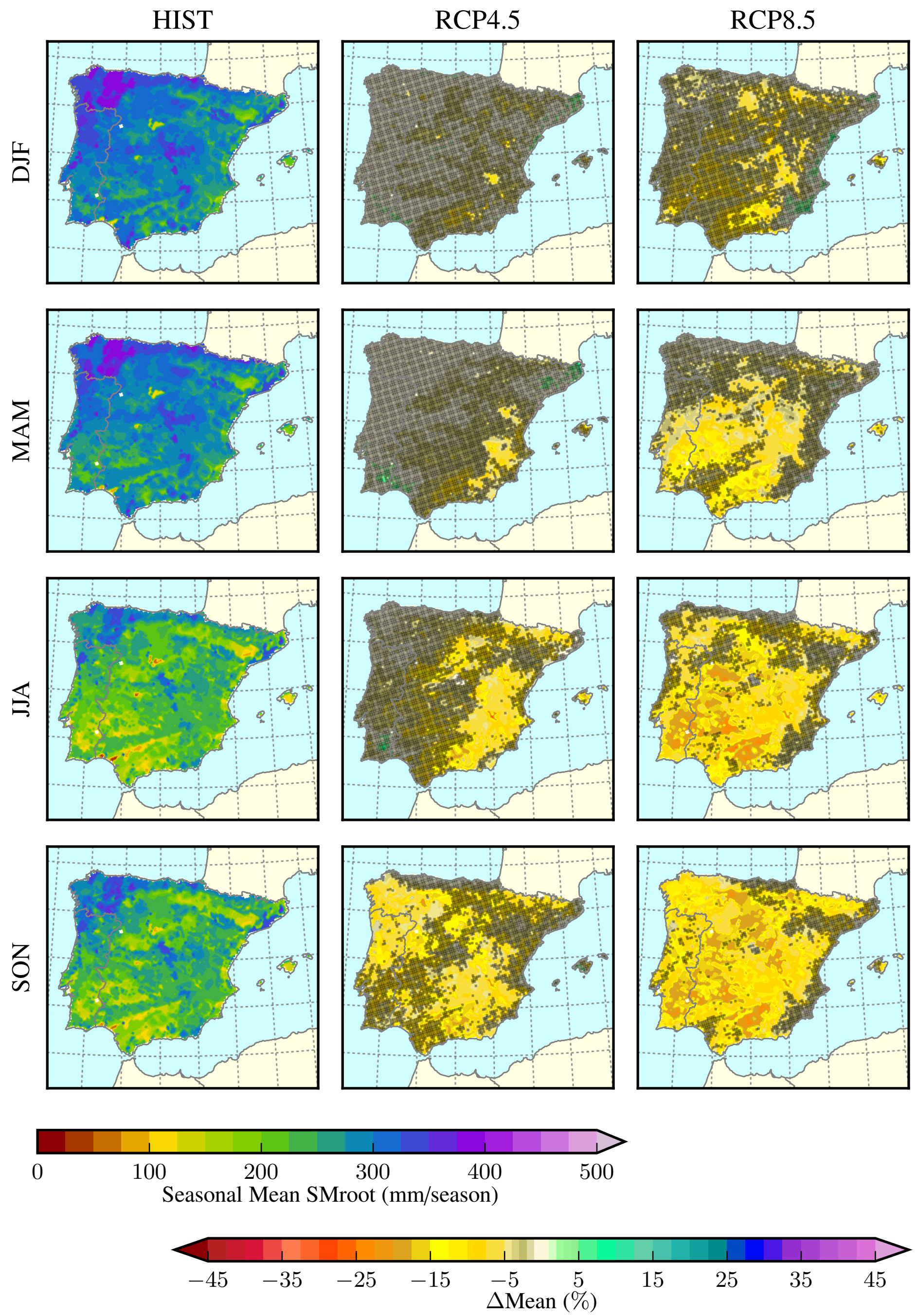

Figure 7.10: *As Figure **7.9** but from MPI-ESM-LR-driven simulations.*

cant decreases appeared over several areas in the east, where values up to 15% were reached. However, these changes in water availability did not translate as significant changes in evapotranspiration (Figure ***7.4***, DJF). Similar to the situation in winter, few significant changes were shown in spring except for the WRFMPI in the RCP8.5, these being predominantly negative (reductions up to 17.5%). Thus, the WRFMPI simulation (Figure ***7.10***, MAM) presented detriments of about 15% over the southeastern IP under the RCP4.5 and even greater over the southern half of the IP, part of the Northern Plateau as well as most of the Iberian System for the RCP8.5 while the WRFCCSM (Figure ***7.9***, MAM) showed significant reductions only in certain regions over the south and southeastern IP for both RCPs.

The most substantial reductions of root-zone soil moisture were projected for summer, and such changes were consistent with the changes found in surface evapotranspiration. However, certain areas in the north still presented independent performance between soil moisture and evapotranspiration, corroborating the results found for evapotranspiration in this season (Figure ***7.3*** and ***7.9***, JJA). On the other hand, the WRFMPI (Figure ***7.10***, JJA) revealed more affected areas (mainly the eastern part under the RCP4.5 and a most extended area for the RCP8.5) than those found in the simulations conducted using the CCSM4 model (Figure ***7.9***, JJA), but with similar magnitude (maximum reductions were about -25%). In autumn, different behaviors were found. In fact, while the WRFCCSM presented moderate changes in soil moisture, significant and negative over limited areas (Figure ***7.9***, SON), the WRFMPI simulation revealed values similar to those in summer and even more widespread and stronger in certain regions such as the Northern Plateau (Figure ***7.10***, SON).

For the far future (Figures ***7.11*** and ***7.12*** for WRFCCSM and WRFMPI simulations, respectively), broad characteristics were projected to be common for winter simulations driven by the two GCMs. In this way, the soil-moisture content will likely decrease by the end of the century, the greatest changes being located mainly in the southeastern IP, where the greatest reduction in evapotranspiration were also found (Figures ***7.5*** and ***7.6***, DJF). For the RCP8.5, larger areas were affected by substantial reductions in soil moisture, the magnitude of such values however being similar for both scenarios (changes in a

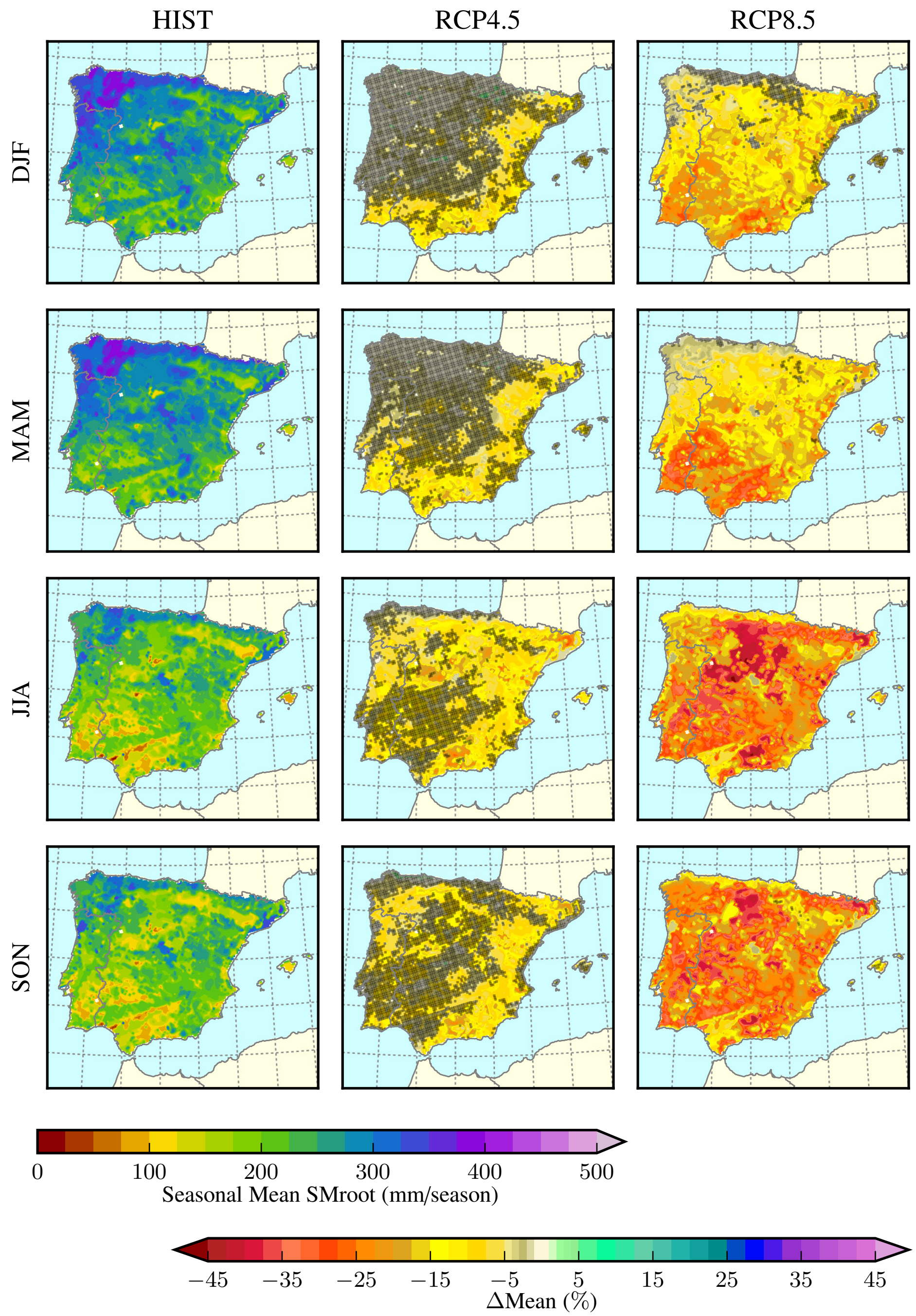

Figure 7.11: *Current (1980-2014) seasonal mean soil moisture at the upper 1 m of the soil (root zone) and projected changes in the far future (2071-2100) from simulations driven by CCSM4 under the two RCPs (RCP4.5 and RCP8.5). Black dots indicate non-significant changes according to a two-sided Kolmogorov-Smirnov test at the 95% confidence level.*

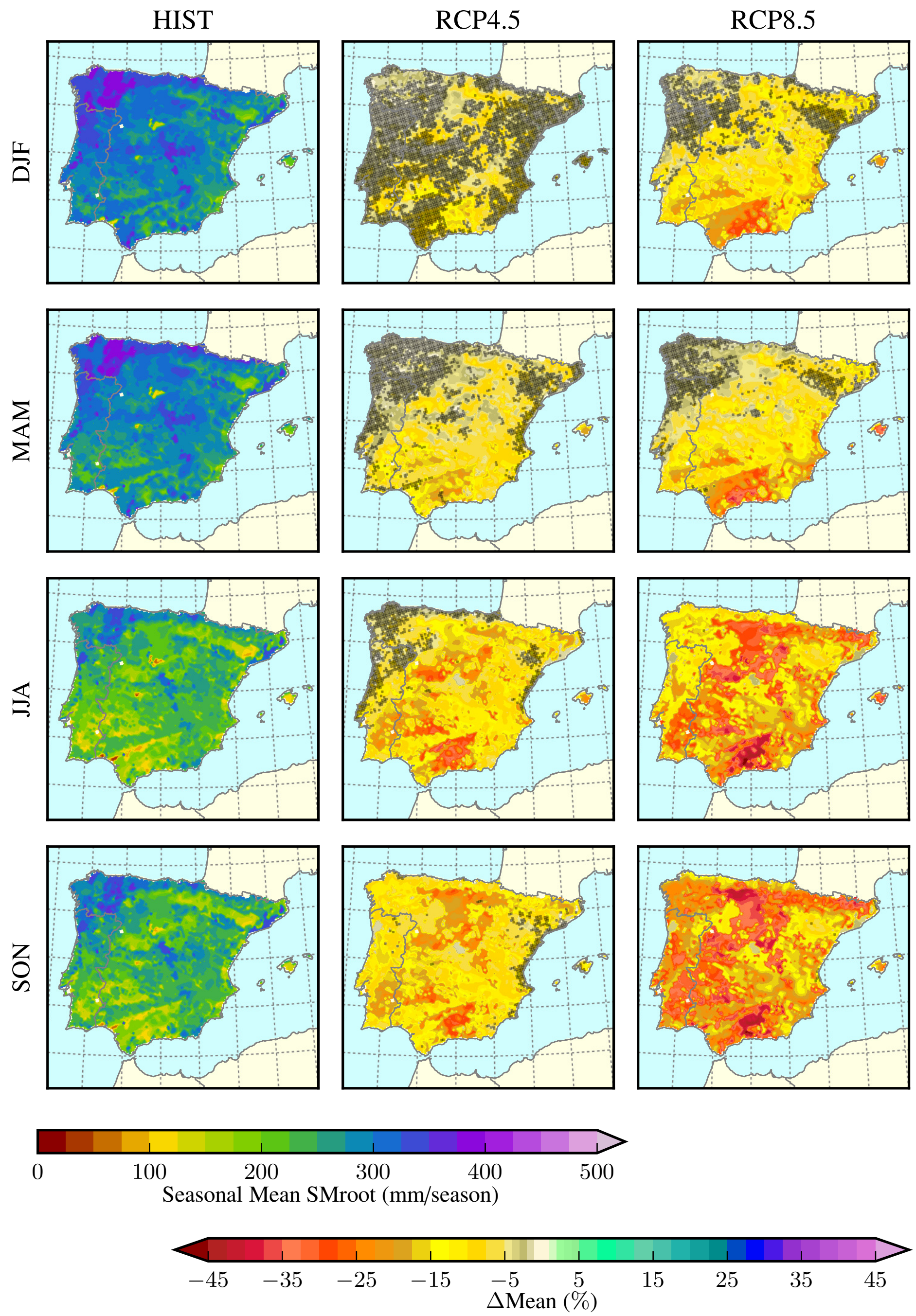

Figure 7.12: *The same as Figure **7.11** but from MPI-ESM-LR-driven simulations.*

range between -3% and -30%). In spring (Figure ***7.11*** and ***7.12***, MAM), more substantial decreases were found, the differences with respect to the present being up to 30% for the RCP8.5. The highest reductions were located mainly in southern regions such as the Guadalquivir Basin for both GCMs, values being higher in magnitude for the WRFMPI. The WRFCCSM presented significant changes throughout the IP under the RCP8.5, while non-significant changes were found in the northwestern for the WRFMPI simulations.

As for near future, the most remarkable changes were found in summer, and with broadly similar results in the simulations driven by the two GCMs (values of changes of about -5% and -45%). The greatest decreases appeared for simulations under the RCP8.5 in most of the IP, with the highest common values being located in regions over the Northern Plateau and Guadalquivir Valley, where values below -45% were found (Figure ***7.11*** and ***7.12***, JJA). Under the RCP4.5 the changes were also substantial, especially for the WRFMPI simulation, where a large area presented remarkable reductions, particularly, in the Guadalquivir Basin and in the Baetic System. Meanwhile, the WRFCCSM under the RCP4.5 showed fewer areas with significant changes. Similar features were shown for both GCM-driven simulations in autumn (Figure ***7.11*** and ***7.12***, SON). Thus, general and strong reductions in soil moisture were projected under the RCP8.5, where areas such as Cantabrian Range and Northern Plateau reached reduction values of up to 45%. This pattern likely suggests the intensification in the land surface-atmosphere coupling in this season.

As a summary of the projected changes found, we conclude that soil-moisture reductions tend to be more extended and stronger in summer and autumn for both GCMs and for both emission scenarios in the period 2071-2100, the changes being more marked under the RCP8.5. For winter and spring, reductions were also projected by the end of the century over broad areas. Minor changes were found for winter in the near future for both scenarios and GCMs. WRFCCSM simulations presented very few areas with significant changes for all the seasons in the period 2021-2050, meanwhile WRFMPI showed significant soil-moisture decreases in this period across many regions under both RCPs, covering almost the entire IP for RCP8.5 from spring to autumn. Such changes will probably lead to increased drying conditions and therefore to a possible exacerbation of drought events. In fact, several author have pointed out that the important reductions in these variables could be generating notable changes in the climate system, especially in warm seasons, leading the intensification in drought phenomena and heat waves (Berg et al., 2016, Seneviratne et al., 2012, Miralles et al., 2014, Lin et al., 2015). Thus, in the next section, regarding the projected changes in drought events, we analyze their frequency, duration, and severity of the changes projected.

7.4. Projected Changes in Drought Conditions

In assessing droughts using standardized indices in a changing climate, through the parameters fitting in current conditions, lies the possibility of projecting future climate values that sharply differ from the present ones. That is, future accumulated values of a given climate field could be occasionally anomalous, and therefore the probability of occurrence could be very low regarding present conditions. In such cases, the drought indices are equal to infinity for anomalously high values and minus infinity for anomalously lower values. This is particularly true in regions such as the IP, where, as previously mentioned, changes in both temperature and precipitation result are expected to be especially low in the accumulated values of precipitation (SPI) or water balance (SPEI).

Table ***7.1*** shows the percentage of area affected for more than 12 months with minus infinity values in the IP for the SPEI and the SPI, computed at 3- and 12-month time scales, using the outputs from all WRF simulations. Through this analysis, we conclude that the number of minus infinity values for the indices was higher for the far future, and especially under the RCP8.5, which is consistent with the projections of both temperatures and precipitation. Furthermore, a large area was affected for the SPEI due to the combined effect of the two variables. Hence, such minus infinity values, provide valuable information about the variables that drive drought indices since they result from exceptional low water availability. This makes it necessary to take into account such values in the analysis of projected drought changes.

However, minus infinity values cannot be used to quantify changes in terms of drought events, and therefore the analysis was performed by categorizing

Table 7.1: *Affected area for more than 12 months with minus infinity values expressed in percentage for drought indices computed at 3- (3-mo) and 12-month (12-mo) time scales)*

	CCSM4				**MPI-ESM-LR**			
	SPI		**SPEI**		**SPI**		**SPEI**	
	3-mo	12-mo	3-mo	12-mo	3-mo	12-mo	3-mo	12-mo
Historical	0	0	0	0	0	0	0	0
RCP 4.5 2021-2050	0.45	0.16	0.55	0.73	0.24	4.11	0.71	2.98
RCP 8.5 2021-2050	0.37	0.15	0.58	2.10	0.36	22.07	3.17	23.75
RCP 4.5 2071-2100	0.63	1.64	1.55	2.10	0.79	10.54	6.65	17.47
RCP 8.5 2071-2100	24.46	7.45	65.97	13.28	26.45	34.58	63.87	48.36

drought indices (Table ***7.2***), following a procedure similar to Spinoni et al. (2018). Namely, the well-known SPI categories (see Table ***7.2***) were used to set a new classification values for the drought indices. Thus, all index values below -2 were considered to be extreme drought and assigned the value of -2; severe drought (-1.5) was assigned to those SPEI/SPI values of between -2 and -1.5; drought (-1) was assigned to values below -1 but above -1.5; normal/wet conditions (1) were values above 0; and finally -0.5 was used for all other cases, identifying just dry conditions.

Thus, for the time series of these new categorical indices at both time scales, the onset of a drought event was established when wet/normal or dry conditions were followed by drought conditions (drought, severe drought or extreme drought), namely the values of the index below -1 at least for two con-

Table 7.2: *Drought Categories for the study of drought events.*

Drought index value	**Drought Category**	**Conditions**
$-\infty > \text{Index} \geq -2$	-2	Extremely Drougth
$-2 > \text{Index} \geq -1.5$	-1.5	Severely Drougth
$-1.5 > \text{Index} \geq -1$	-1	Drougth
$-1 > \text{Index} \geq 0$	-0.5	Dry
$0 > \text{Index} > \infty$	1	Normal/wet

secutive months. Similarly, the event was considered to end when the index recovered values corresponding to normal/wet conditions (index values equal to 1)[1]. Therefore, normal or wet conditions were taken into account only to define the onset and the end of drought events. These same thresholds have been used to determine drought events in other studies (Spinoni et al., 2014, 2015, Mishra et al., 2009, McKee et al., 1993). The drought events thus computed were used here to determine the time series of the different characteristics of droughts (i.e. duration, magnitude, frequency, and severity) which were computed in the same way as in Chapter ***5***[2]. Nonetheless, to examine changes in droughts, here we show the frequency instead of the magnitude. This is because magnitude is similar to the duration so that it does not provide additional information in terms of changes in drought events. The frequency, however, can be useful to further elucidate aspects related to the distribution of drought events, since, together with duration, this allows us to analyze the general trend in dry/wet conditions.

Frequency and duration for a given time period tend to be inversely correlated. Thus, longer events became less frequent, so that the increase in either duration or frequency could indicate an increase in drought events. However, increasing frequencies and decreasing durations or vice versa may suggest changes in the distribution of the events, but not drier conditions, so that the combination of the two characteristics should be interpreted with caution. On the other hand, changes in the severity of drought events must be interpreted taking into account that, by definition, for a mild drought event the category value is -1, whereas for an extreme drought the value is -2. Hence, if all the events that occurred during the entire period had a severity corresponding to extreme droughts, the average severity would be 2, while if all the drought events were mild, the average severity value would be 1. Therefore, differences between present and future values will be in a range between -1 and 1, this being a difference of 1 equivalent to stating that the trend of drought events is

[1]Here the definition of drought events differs from that used in Chapter **5** to set a stricter criterion for detecting drought events.

[2]The duration is defined as the number of months in each drought event, magnitude and severity as the sum of the absolute values of the index and the absolute value of the minimum index reached in such event, respectively. Frequency is defined as the number of events for the entire period.

changing from normal drought to extreme drought, on average.

7.4.1. Drought Characteristics for Current Simulations

Current simulations show a number of events between 17 and 35 for the entire study period (1980-2014), for indices computed at a 3-month time scale (Figure ***7.13***). Drought events were more frequent according the SPI in both the WRFCCSM and WRFMPI simulations, and therefore, the duration of such events (mean durations between 4 and 8 months) was longer for the SPEI. In any case, the results from both simulations and for both indices showed a broad common behavior in terms of drought conditions with changes in location and surface area. With regard to the severity, the values in the present ranged from 1.5 to 1.7 throughout most of the IP for both simulations and for both indices, indicating that, on average, the drought events were severe in general.

For events computed at the 12-month time scale (Figure ***7.14***), the current simulations generally displayed fewer events which were longer than at the 3-month time scale (values of between 6 and 16 events and between 9 and 25 months for frequency and duration, respectively). Again, the SPI showed more events, which were shorter for both simulations. In reference to the severity, the events were more moderate, with a greater number of grid points reaching lower values than at shorter time scale, at least for the WRFCCSM. Nevertheless, the magnitude of such values was within the same range of values. Concerning the comparison of such results with those shown for observed values from mprmt observational data (Fig ***5.8***), the drought events were longer for both SPEI and SPI from GCMs driven WRF simulations. Subsequently, these latter must be less frequent as well.

7.4.2. Projected Changes in Drought Parameters

At the 3-month time scale, all WRF simulations driven for the intermediate GHG emissions scenario projected both increases and decreases in the number of events, for the entire near future, in a range between -20 and 15 events (Figure ***7.15***). The SPEI in the WRFCCSM indicated large areas with greater frequency (first column) over the North Atlantic Basins as well as in the Miño-Sil and Guadiana, but also in certain areas located in the Duero, Tajo, Ebro,

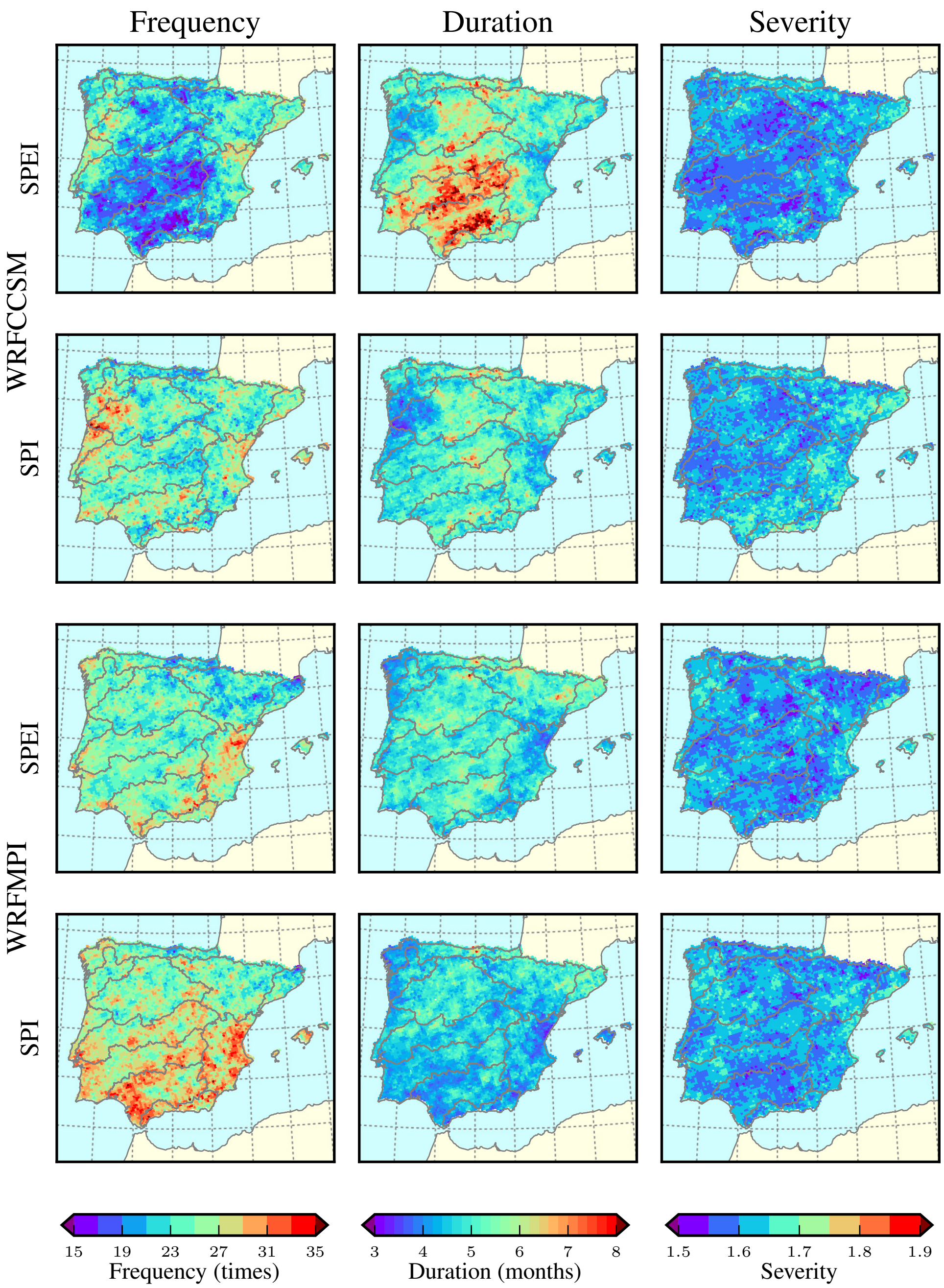

Figure 7.13: *Drought frequency (left), duration (middle) and severity (right) for the current period (1980-2014) for the SPEI and the SPI indices computed at the 3-month time scale. Duration and severity were calculated from values averaged for the entire period whereas the frequency is the number of events for the entire period.*

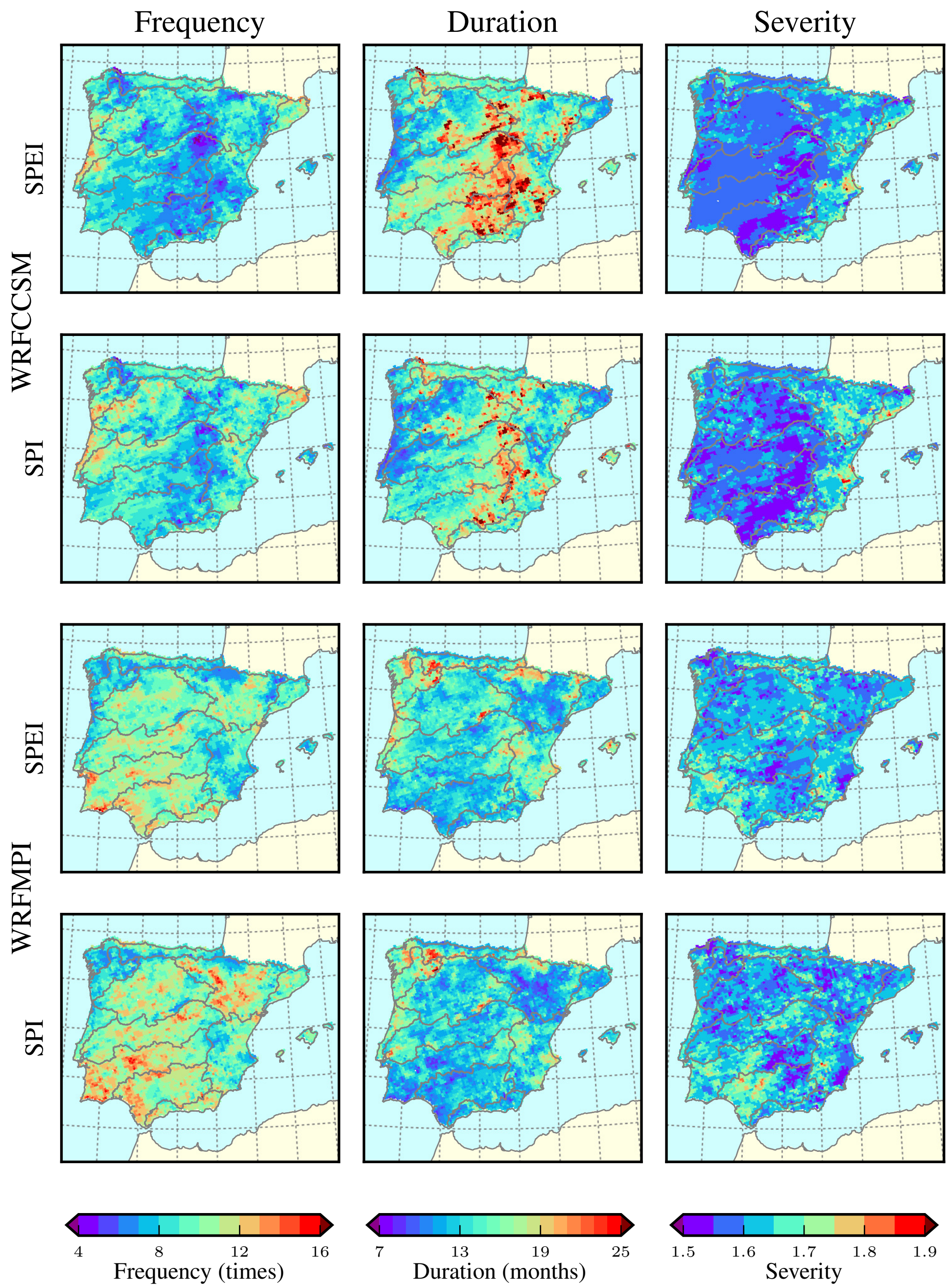

Figure 7.14: *As Figure **7.13** but for indices computed at 12-month time scale.*

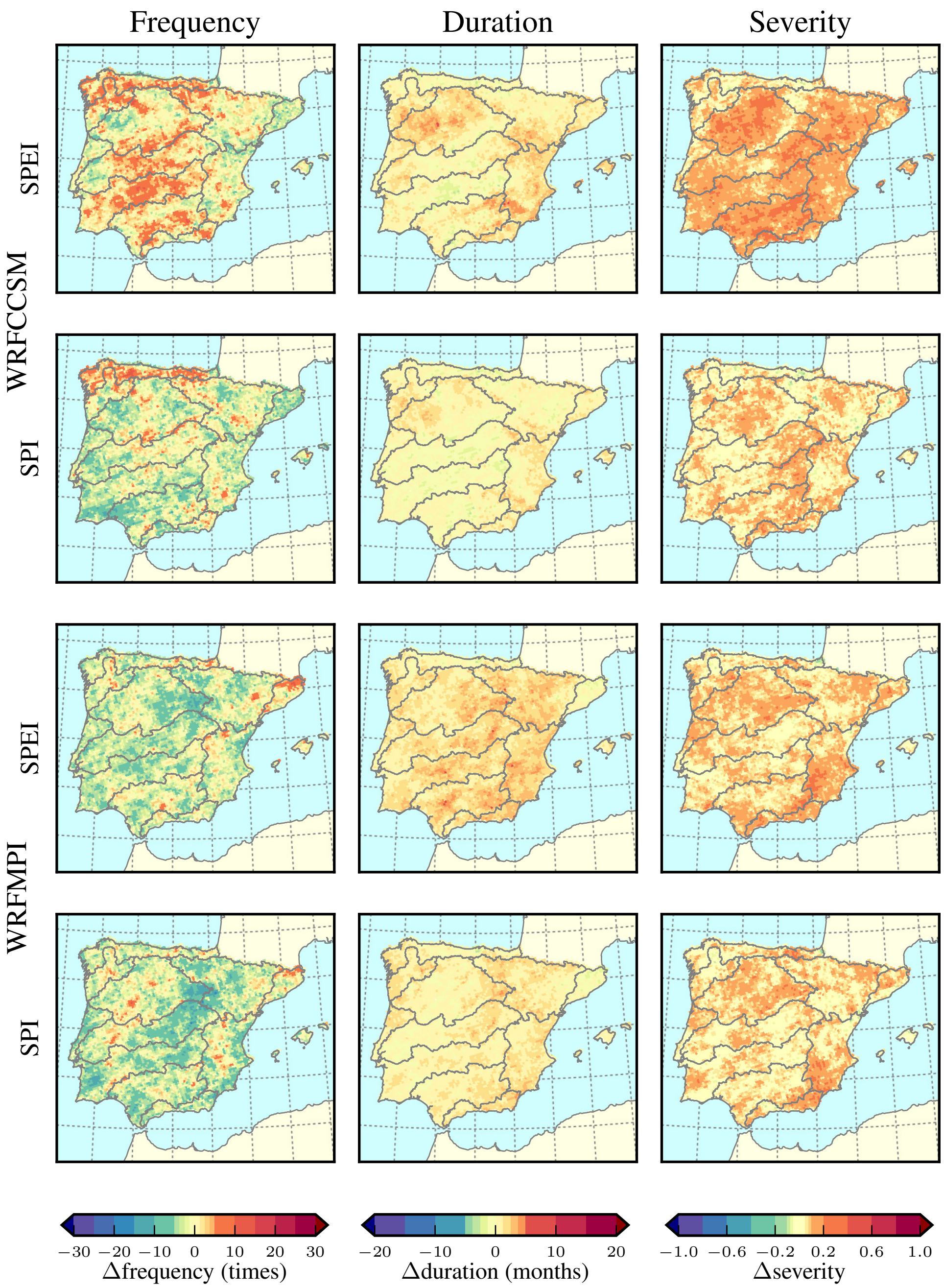

Figure 7.15: *Changes in the frequency (left), duration (middle) and severity (right) of drought events for the near future (2021-2050) relative to the current period (1980-2014) and under the RCP4.5. Drought events are based on indices computed at the 3-month time scale. Duration and severity are expressed through differences of average values for the entire period and frequency by changes in the number of events for the entire period.*

Guadalquivir, and Southern Basins. This same simulation, but using the SPI, indicated a widespread decrease in the frequency except for the North Atlantic Basins and over certain scattered regions across the entire IP. In the same way, the WRFMPI simulation projected an overall reduction in the number of events by using both the SPEI and the SPI for most of the IP.

Changes in mean duration of such events (second column) showed moderate increases, in general, in all WRF simulations (values ranging from -5 to 10 months). The lengthening of the average duration of the drought events proved slightly greater for the SPEI for both the WRFCCSM and the WRFMPI. In general, the changes in severity (third column) were positive in all simulations (values up to 0.4) although many areas presented almost an absence of changes with respect to this parameter. The most notable changes again appeared in the SPEI for the WRFCCSM, with values of about 0.1-0.4, practically throughout the entire IP, the highest values being located mainly in the Duero, Tajo, Ebro, Guadalquivir, and Southern Basins. Such increases in values indicate that the drought events in many regions of the IP will become extreme on average, since in general, the severity values in the present were about 1.6 on average (see Figure ***7.13***), so an increase in 0.6 signifies values above 2 on average.

Results from simulations under the RCP8.5 in the near future (Figure ***7.16***), revealed spatial patterns similar to those shown under the RCP4.5. With regard to the magnitude of the changes, however, the WRFCCSM simulation presented slightly moderate changes, and the WRFMPI, by contrast, revealed more substantial changes. For the latter, using the SPEI, we found striking increases in terms of duration (changes > 10 months) over the southwest of the Guadiana Basin and in a large part of the Guadalquivir Basin. Here, the increased severity was also substantial with respect to the RCP4.5, reaching values up to 0.4 relative to the present period. Again, the SPI, for the two simulations, presented more moderate values of change than did the SPEI. These results agree with the projections for precipitation and temperature (see Figure ***6.2*** for precipitation, and Figure ***6.21*** and ***6.23*** for maximum and minimum temperature, respectively), since for such variables the WRFCCSM revealed similar spatial changes between RCPs and even slightly more severe for the intermediate RCP forcing; meanwhile the WRFMPI indicated moderate changes

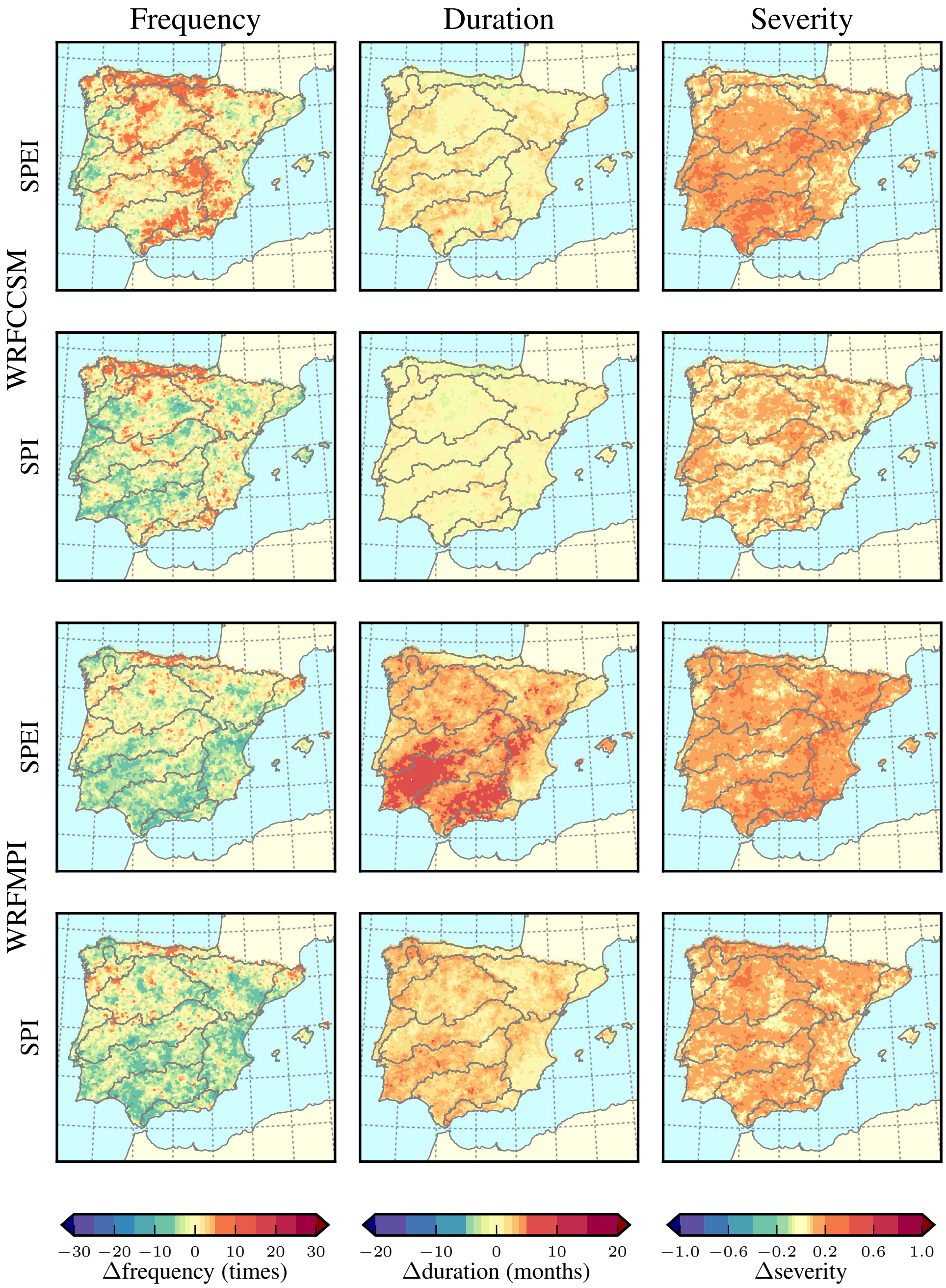

Figure 7.16: *The same as Figure **7.15** but for simulations driven by the GCMs under the RCP8.5.*

in the RCP4.5, which became substantial for the RCP8.5.

At the 12-month time scale (Figures ***7.17*** and ***7.18*** for the RCP4.5 and RCP8.5, respectively), changes in near future presented by the two indices showed a broader common spatial behavior than did those shown at the 3-month time scale, but with a greater magnitude for the SPEI. In fact, the drought indices evaluated at the 12-month time scale provided additional information on the general trend over time, since the accumulated values of either precipitation or water availability for each new month had less impact on the total amount, the response of the index being slower McKee et al. (1993). Therefore, the longer duration here means the stabilization in drier conditions.

Thus, under the RCP4.5, the WRFCCSM showed drought events to be more frequent in relation to the present in many parts of the IP (increases of up to 7 events/30 years in all watersheds). The Tajo Basin appeared to be the most affected by the increase in frequency of drought events, reflected especially by the SPEI (Figure ***7.17***). By contrast, the WRFMPI simulation presented a general decline in frequency to around 5 events for a large part of the IP. Exceptions of such behavior appeared in the Southeastern Basins and in part of the North Atlantic, Miño-Sil, and Portugal Basins where increases of about 7 events were reached. On average, the events will likely be longer in many parts of the IP (values ranging from -20 to 50 months), this being particularly marked for the SPEI. In this way, both indices presented major increases in the mean duration over the Duero, Guadalquivir, and Southern Basins. In terms of severity, changes for SPEI were again generally stronger than those found for SPI. Here, the WRFCCSM projected decreases as well as increases (values of about -0.4 and 0.6), the growing severity occurring mainly in the east areas and northern Portugal Duero Basin. By contrast, the WRFMPI under this scenario appeared to show more extended increases, covering a large area of IP. As an exception here, a part of North Atlantic watersheds showed less severity.

In terms of frequency, the patterns of change for the RCP8.5 in the near future (Figure ***7.18***) were similar to those found in the intermediate emission pathway forcing, although the number of events appeared to be slightly moderate. For duration and severity, however, and as occurred at 3-month time scale, the changes were also more moderate for the WRFCCSM, and substan-

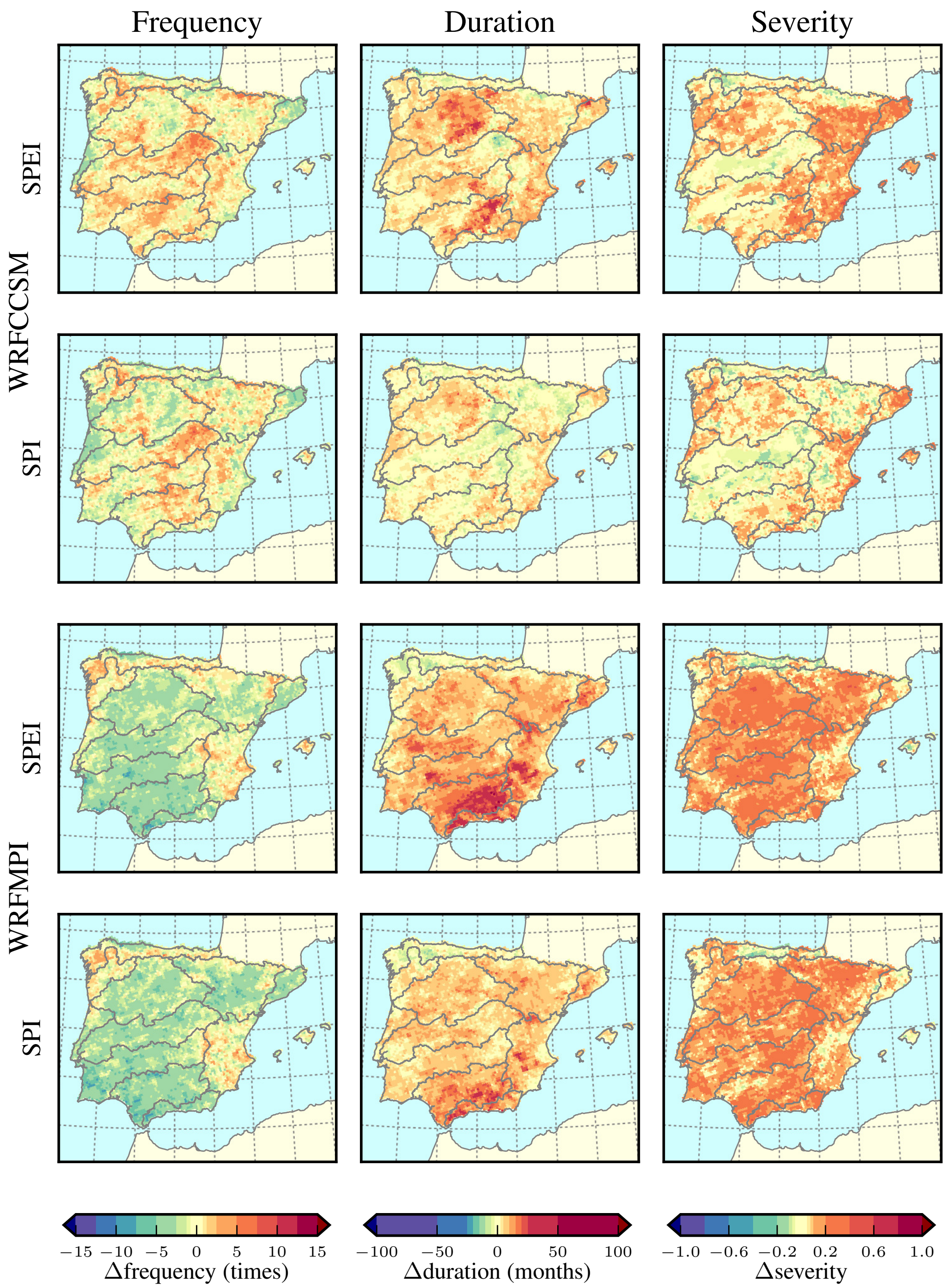

Figure 7.17: *Changes projected for the near future in drought frequency (left), duration (middle), and severity (right) for the indices computed at the 12-month time scale under the RCP4.5. Duration and severity are expressed in mean values, and frequency as number of events.*

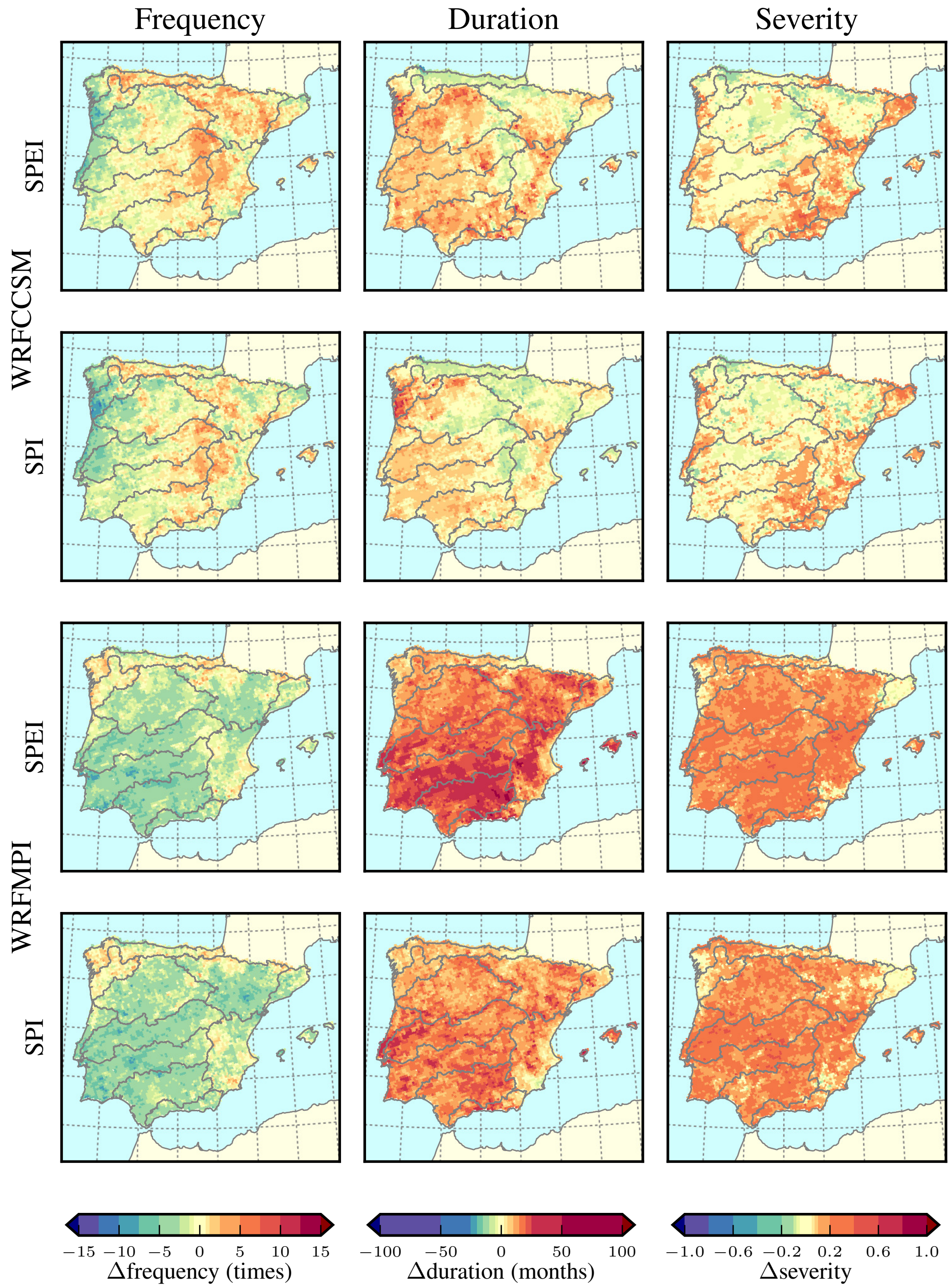

Figure 7.18: *As Figure **7.17** but for simulations driven by the two GCMs using the RCP8.5 forcing.*

tially more marked for the WRFMPI simulation. In the latter, a large area over the Guadiana, Guadalquivir, and Southern Basins presented quite long events, lasting over 50 months on average. These long values also appeared in certain areas over the Southeastern Basin as well as the watersheds of the Ebro, Tajo, Northeastern, and Balearic Islands. According to the WRFMPI simulation, the severity is likely to intensify throughout nearly the entire IP (values up to 0.6) except in certain regions over the Northeastern Basins as well as in some part in Miño-Sil and Southeastern Basins, for both the SPEI and SPI indices.

Therefore, in general, although increases in drought events were shown, these remained moderate for the near future for both RCPs, indices, and time scales. In general, the results revealed uncertainty between the WRFCCSM and the WRFMPI for some areas, while the difference between RCPs was less marked. These findings suggest that moderate GHG concentrations induced the climate-change effect for this period.

For the far future, changes projected for the indices at 3 months in the RCP4.5 presented spatial patterns similar to those found in the near future, albeit for this period drought conditions appeared to show greater magnitude (Figure ***7.19***). The CCSM4-driven simulation showed greater frequency, reaching values of 20 events per period throughout the Guadalquivir, Guadiana, and Tajo watersheds. The Duero Basin also appeared to be more affected by drier conditions than in the near future. However, other watersheds such as the North Atlantic, Southeastern, Ebro, Portugal, Northeastern, and Balearic Islands Basins presented a great surface area that undergoes changes as great as in the near future. Here, for the SPI, again, less pronounced changes were found than for the SPEI, showing more frequency for the North Atlantic and Southern Basins, as well as in certain areas across the rest of watersheds. For the WRFMPI, nevertheless, an increase in the number of drought events appeared in watersheds in the north (changes about 10 events/period) and a decline in the number of events was found in southern and southeastern IP watersheds (reduction by about 10 events/period) in general.

The mean duration also increases, showing more affected areas with longer events for the SPEI, and especially for the simulation driven by the MPI-ESM-LR (values above 15 months in some regions). For this parameter, the WR-

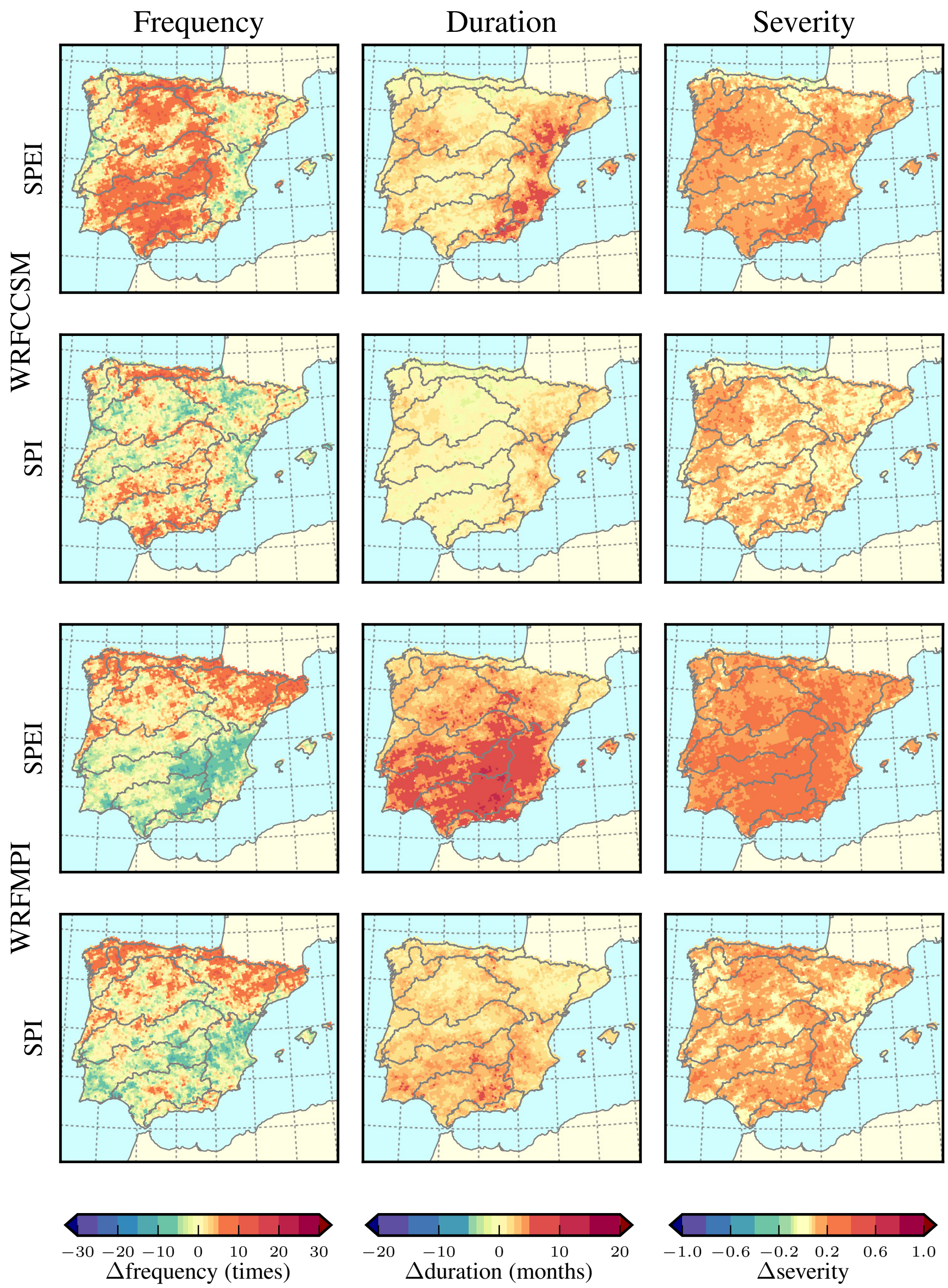

Figure 7.19: *Changes in the drought frequency (left), duration (middle), and severity (right) for indices computed at 3-month time scale for the far future (2071-2100) related to the present period (1980-2014) and under the RCP4.5. Changes in duration and severity are indicated in mean values while frequency is the difference in the number for the entire period.*

FCCSM projected the longest events in eastern watersheds (i.e. Ebro, Southeastern, Southern, Balearic Islands Basins and at certain points in the Guadalquivir), whereas the WRFMPI indicated particularly marked increases in the basins of the southern half of the IP, such as the Guadalquivir, Guadiana, and Southeastern Basins. The severity is also projected to increase, reaching values up to 0.6 in practically over the entire IP for the SPEI in both the WRFCCSM and the WRFMPI.

Under the RCP8.5, the results at 3 months in the far future (Figure ***7.20***) revealed a lower number of events in several regions of the IP from an analysis of the SPEI for the WRFCCSM simulation, while a prevalence of large areas with increases were found for the SPI (values of change between -20 and 15 events/period) from this same simulation. By contrast, the WRFMPI projected changes similar to the RCP4.5 for both indices, and with the same range of values as well. However, in terms of duration, marked changes were found, particularly for the SPEI. In the latter, the southern half of the IP underwent marked increases with values of more than 20 months on average. Although the increase in severity was also quite pronounced throughout the IP for both simulations and for the two indices, the strongest severities appear to be projected by the SPEI from the WRFCCSM simulation.

As occurred at 3 months, drought events at the 12-month time scale in the far future for the RCP4.5 (Figure ***7.21***) presented change patterns similar to those projected for the near future. In terms of changes in frequency, the values remained similar to those forecast for the near future in the WRFCCSM (values around -10 and 7 events per period) for both indices, although here the number of events for the entire period was slightly lower, particularly in the Ebro Basin. For the MPI-ESM-LR-driven simulation (with changes in the same range) the increase in the number of drought events is limited fundamentally to certain regions over the North Atlantic, Miño-Sil, and Portugal Basins for the SPEI and also in certain areas along the Duero watershed for the SPI. By contrast, the rest of the IP showed a lower number of drought events than in the present period.

On the other hand, substantial increases in the duration were shown in this period (values ranging from -20 to 100 months or higher). The longest events

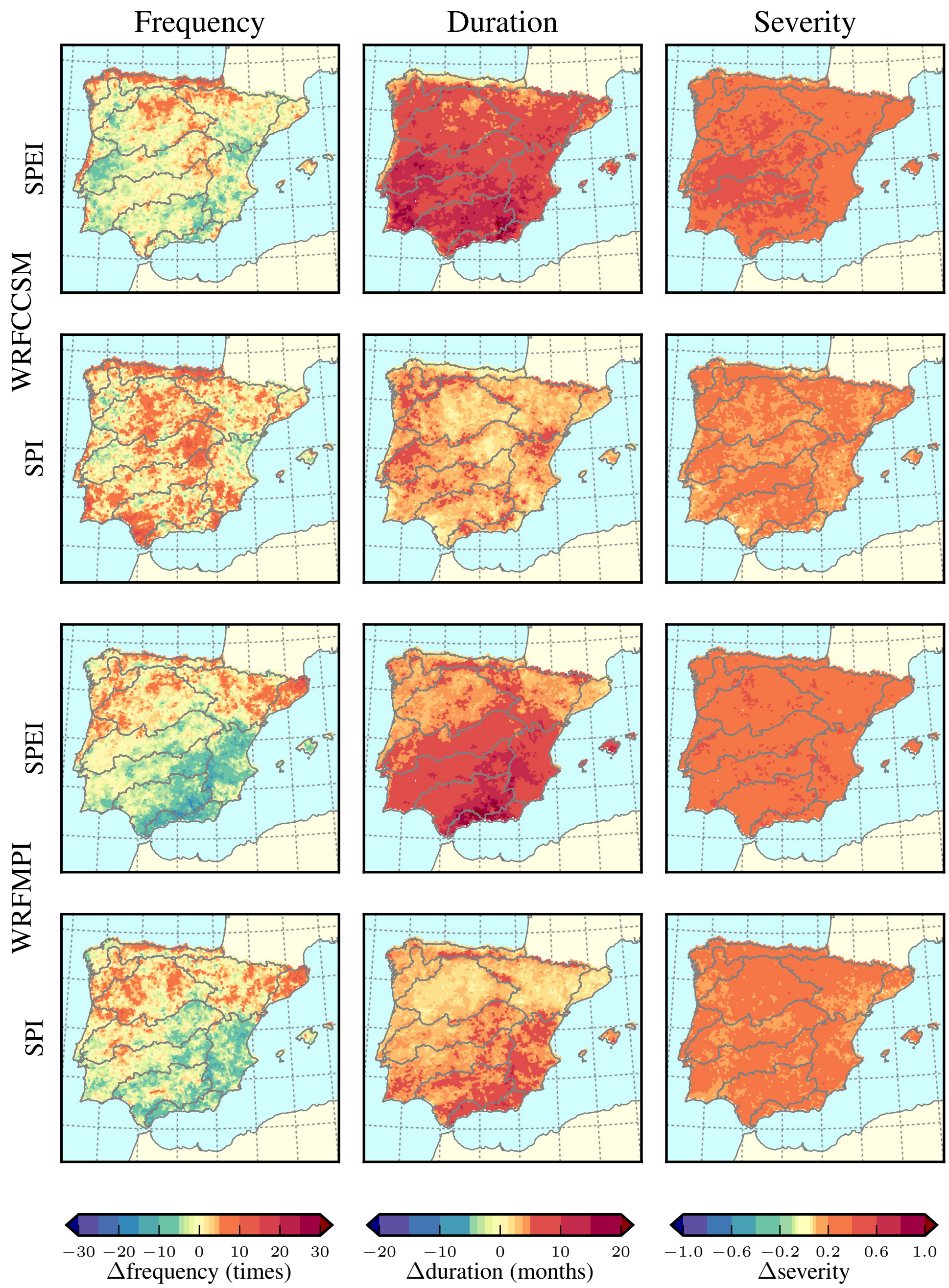

Figure 7.20: *As Figure **7.19** but for the simulations driven under the RCP8.5.*

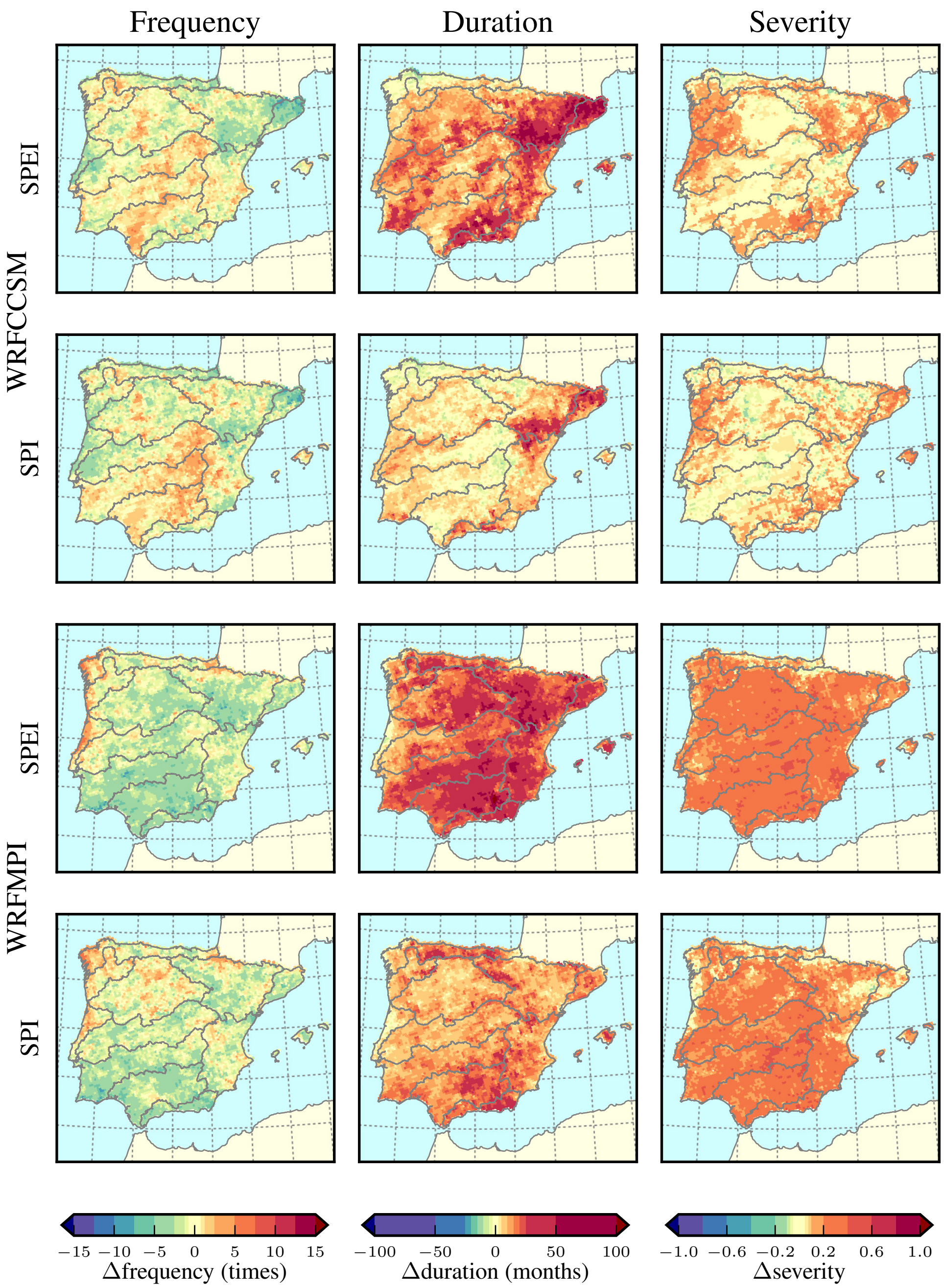

Figure 7.21: *Projected changes in drought frequency (left), duration (middle) and severity (right) from indices computed at the 12-month time scale in the far future (2071-2100) and for the RCP4.5. Changes in duration and severity correspond to differences in mean value in relation to the present, and frequency is the difference in the number of events for the entire period.*

were located mainly in the Ebro and Northeastern Basins for the WRFCCSM and for both indices. Additionally, for the SPEI, other regions also suffered these long events throughout the IP (Balearic Islands, Guadiana, Guadalquivir, Tajo, Duero, Southern and Southeastern Basins). WRFMPI showed similar spatial patterns, but with more pronounced increases over the entire IP. Thus, for the SPEI most of the IP presented drought increases of more of 50 months from both of the GCM-driven simulations.

Therefore, these results demonstrate the marked difference of using either the SPEI or the SPI to examine projected changes in drought events. In fact, although precipitation changes tended towards increased drought conditions in this region, the greater demand of water by the atmosphere due to the temperature rises may result in a further reduction in the water availability and consequently an intensification of the drought conditions (Cook et al., 2014). In terms of severity changes, the simulations driven by either the CCSM4 or the MPI-ESM-LR under the RCP4.5 (Figure ***7.21***) projected different drought patterns. The WRFCCSM indicated more moderate increases, which di not affect the entire IP, showing values of up to 0.4 with the most affected areas being Miño-Sil, Portugal Basins, Ebro, Balearic Islands and Northeastern Basins as well as parts of the Guadalquivir, Southern, and Southeastern Basins. Meanwhile, for WRFMPI the greater severity will spread over practically the entire IP, with values of up to 0.6.

For the RCP8.5 in the far future, the changes at the 12-month time scale (Figure ***7.22***) were extremely strong. The frequency was substantially reduced (values between -12 and 5 events for the overall period), which was likely associated with the extraordinary increase in the mean duration. Thus, for the WRFCCSM simulation, results from the SPEI showed a generalized decrease of as many as 12 events in most of the IP, the total number of event therefore being reduced to 1 or 2 events over the entire period in many cases (see Figure ***7.14***). For the SPI, decreases were also shown in general except for scattered regions (e.g. increases of about 5 events/30 year related to the present period in the northwest of the Ebro Basin). In the simulations driven by MPI-ESM-LR, although the overall trend was also to reduce the number of events, this was less marked, showing more broad areas with increases as well in the north-

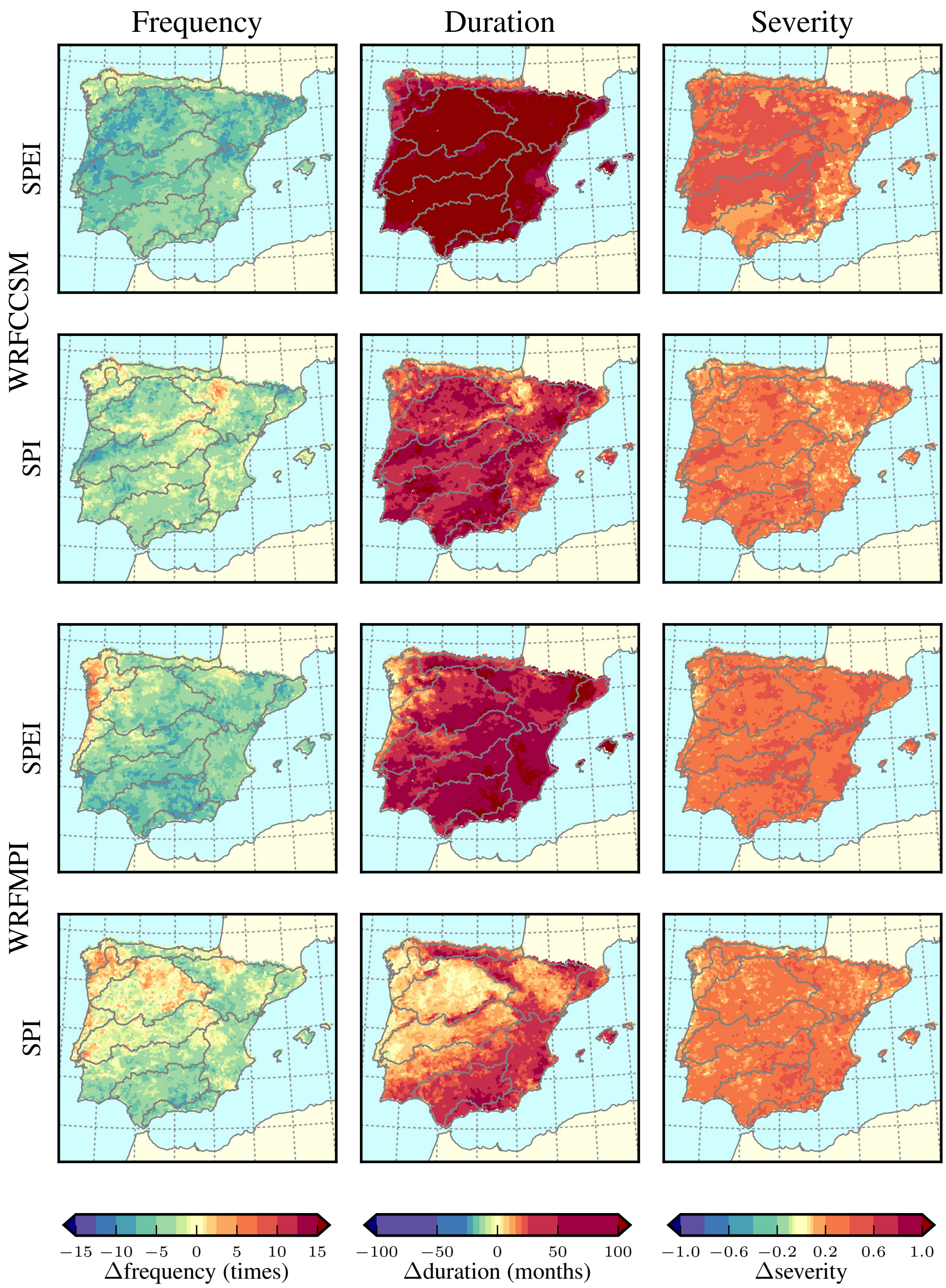

Figure 7.22: *As Figure **7.21** but for the simulations driven under the RCP8.5 scenario.*

western IP for both the SPI and SPEI.

Substantial changes in terms of duration were found (increases of more of 100 months in many cases), particularly for the SPEI and from the WRFCCSM simulation. These results suggest that by the end of the century and under a scenario where the emission of GHGs are especially high, the potential risk of megadroughts[3] will be very high, or the dramatic changes in precipitation and temperature could lead greater aridity in the IP[4]. Again, this evidences the importance of taking into account the temperature to predict changes in the aridity conditions. Although the SPI revealed great changes, these were more moderate than those of the SPEI. In terms of severity, all simulations showed a generalized increase throughout the IP, with values of up to 0.8, which rose for the SPEI WRFCCSM simulation.

Therefore, the results for the far future indicate a pronounced response to the GHGs on the climate signal, the difference between RCPs being highlighted especially for indices computed at the 12-month time scale. As a summary, both for the near future and the far future, and under both emission scenarios, a generalized increase in drought conditions is expected, more marked in the long term for RCP8.5.

7.4.3. Hybrid Classification in Drought Event Characteristics

Finally, to summarize projected changes in drought events, we performed a hybrid classification for the three parameters of drought events (Figures ***7.24*** and ***7.24***). To this end, the frequency, duration, and severity previously detailed, were spatially averaged for each river basin within the IP (see Figure ***6.1***) and thus, different categories have been established based on whether such characteristics increase or decrease in relation to the present values.

Some uncertainties appear in the sign of the change in drought characteristics for the near future (Figure ***7.23***) as indicated by the results found through the use of different driving data. In this context, the results from the WRFMPI appear to be more robust, showing similar patterns of change for both time

[3]According to the IPCC AR5 Report (IPCC, 2014), a megadrought is defined as an unusually lengthy and pervasive drought, usually persisting a decade or more.

[4]Whereas drought is referred to a temporary anomaly, aridity signifies a permanent characteristic of the climate in a given region.

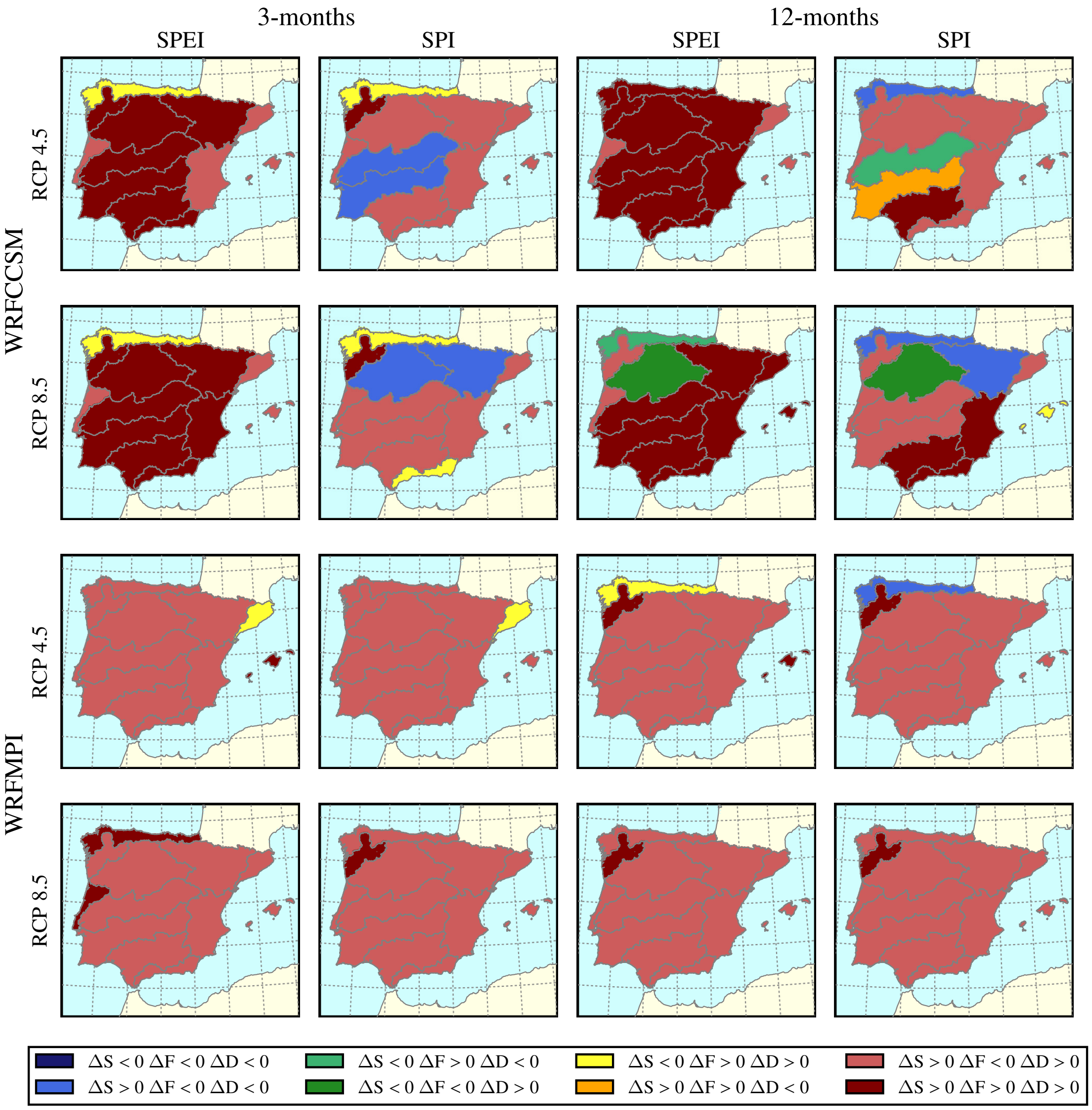

Figure 7.23: *Hybrid classification based on projected changes in severity, frequency and duration (ΔS,ΔF and ΔD, respectively) of droughts according to the SPEI and the SPI at 3- and 12-month time scales for the near future.*

scales in most of the watersheds of the IP. By contrast, the WRFCCSM simulations suggested a more different trend depending on the RCP, drought index, and time scale, although the results from the SPEI predicted drier conditions in general, as was previously explained at both time scales. In any case, all the results showed an increase of at least one drought characteristic, the duration increase being the most prevalent.

For the far future (Figure **7.24**), the sign of the change is clearer and more robust, as reflected by the results from the different simulations, indices, and time scales, the North Atlantic basins in any case being the least affected (and

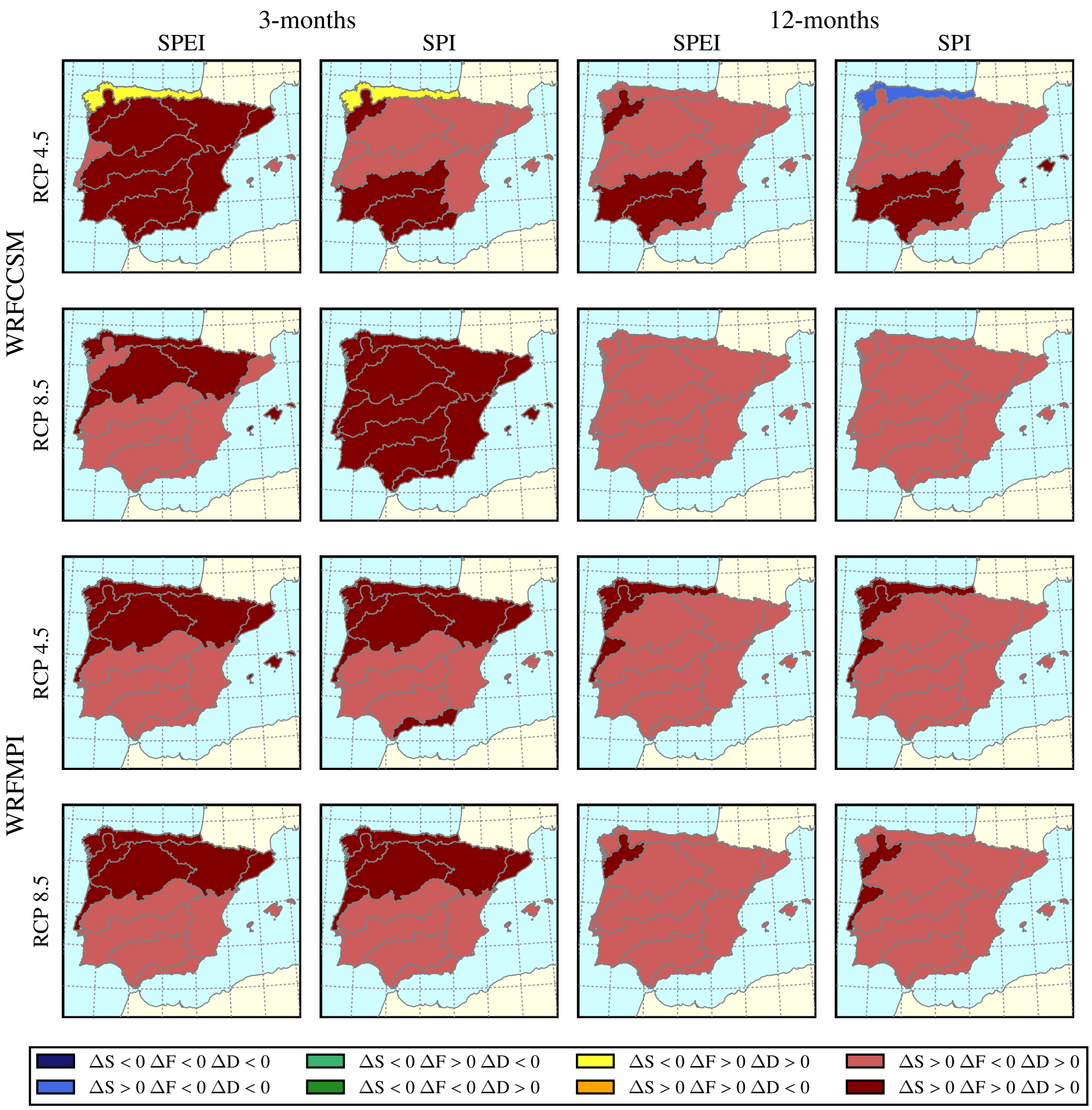

Figure 7.24: *As Figure **7.23** but for the far future.*

only for the WRFCCSM simulation). However, although the changes are different in magnitude between scenarios, the sign of the change is similar for both RCPs in most of the watersheds. The most prevalent characteristics are the increase in the duration and severity.

7.4.4. Trends in Drying Conditions

Finally, to elucidate the influence of GHG-forced signal of climate change, we also computed the S/N ratios in terms of drought indices. To do so, we grouped the temporal series of drought events, previously computed at each grid point, using the main watersheds of the IP (see Figure ***6.1***). Thereby, we were able to identify the area presenting drought conditions for each river basin in each month, thereby formulating a time series of the percentage of area affected by drought conditions. The extent of the area has been considered in many studies as a measure of drought severity (Burke et al., 2006, Wang and Zeng, 2018, Spinoni et al., 2015). These series of surface area affected by droughts were used to compute the S/N ratios from the different WRF simulations, following the same procedure used in sections ***6.2.2*** and ***6.3.2*** for precipitation and temperatures, respectively. This procedure was carried out for drought events from both the SPEI and SPI series, but taking into account that the spatial patterns for the SPI are almost identical to those for SPEI, but with lower magnitude, only the results for SPEI drought events are shown here. Moreover, previous analyses demonstrated (see Figures ***7.21*** and ***7.22***) that the results from SPEI are more adequate to characterize droughts in a warmer world.

In this context, the indices computed at the 3-month time scale have been used to study the trend in drought at the seasonal scale, and those computed at 12-months to examine annual climate-change signal. Namely, indices at 3 months in February correspond to the accumulated values of winter (DJF), as well as May, August and November to spring (MAM), summer (JJA), and autumn (SON), respectively. In the same way, the accumulated values for December for 12-month indices correspond to the entire year.

Figure ***7.25*** displays "portrait" diagrams of seasonal S/N ratios for the near future, for each river basin, using the data from CCSM4-driven simulations.

Here, the result of computing the S/N ratio in each 10-yr running mean is shown in its central year value.

In winter (Figure ***7.25***, DJF), the simulations projected both increases and decreases of mean values of the extent of the droughts in relation to the present period. Thus, for the RCP4.5 many watersheds began the period with negative S/N values (e.g. Northeastern Basin). Others, such as the North Atlantic and Miño-Sil watersheds, however, showed positive S/N values over the entire period. In any case, most of the watersheds presented a broad drying trend throughout the period. In general, the results also suggest that the internal variability was still notable because S/N values above 1 did not appear in in many cases. For the RCP8.5, a different trend was shown. Most of the watersheds presented declining trends at least until the middle of the period, although by the end of this time, the surface area under drought tended to rise in general, except for Northeastern Basins.

For spring (Figure ***7.25***, MAM), the GHG-forced climate change signal was more evident, with a broad trend towards dryness conditions throughout the watersheds. In this season, S/N values were influenced by the emission scenario used, being stronger for the RCP8.5. In this way, the S/N values above 1 were reached in the Duero Basin (decennia centered 2041-2043 and 2045) as well as in the Southeastern Basins (decennia centered 2034, 2036-2037, 2039-2040) for the RCP4.5, whereas in the RCP8.5 all watersheds except the North Atlantic ones reached values of more than 1 at some point in the second half of the period. Here, the Duero watershed appeared to be the most affected by drying conditions, reaching values above 1.5 for the decennia centered 2041 and 2042. The results also showed drier conditions by the end of the period, in all watersheds and for the two RCPs.

The summer results (Figure ***7.25***, JJA) also projected a pronounced trend towards drying, more marked for the RCP4.5. The results also showed that the size of area under drought conditions was larger in relation to the present period in many cases. For intermediate GHG emissions, S/N values of greater than 1 appeared in some watersheds, the most affected being those located in the north of the IP (i.e. Miño-Sil, Duero and Northeastern Basins). For higher emissions of GHGs, the drought surface-area trends were less marked, but

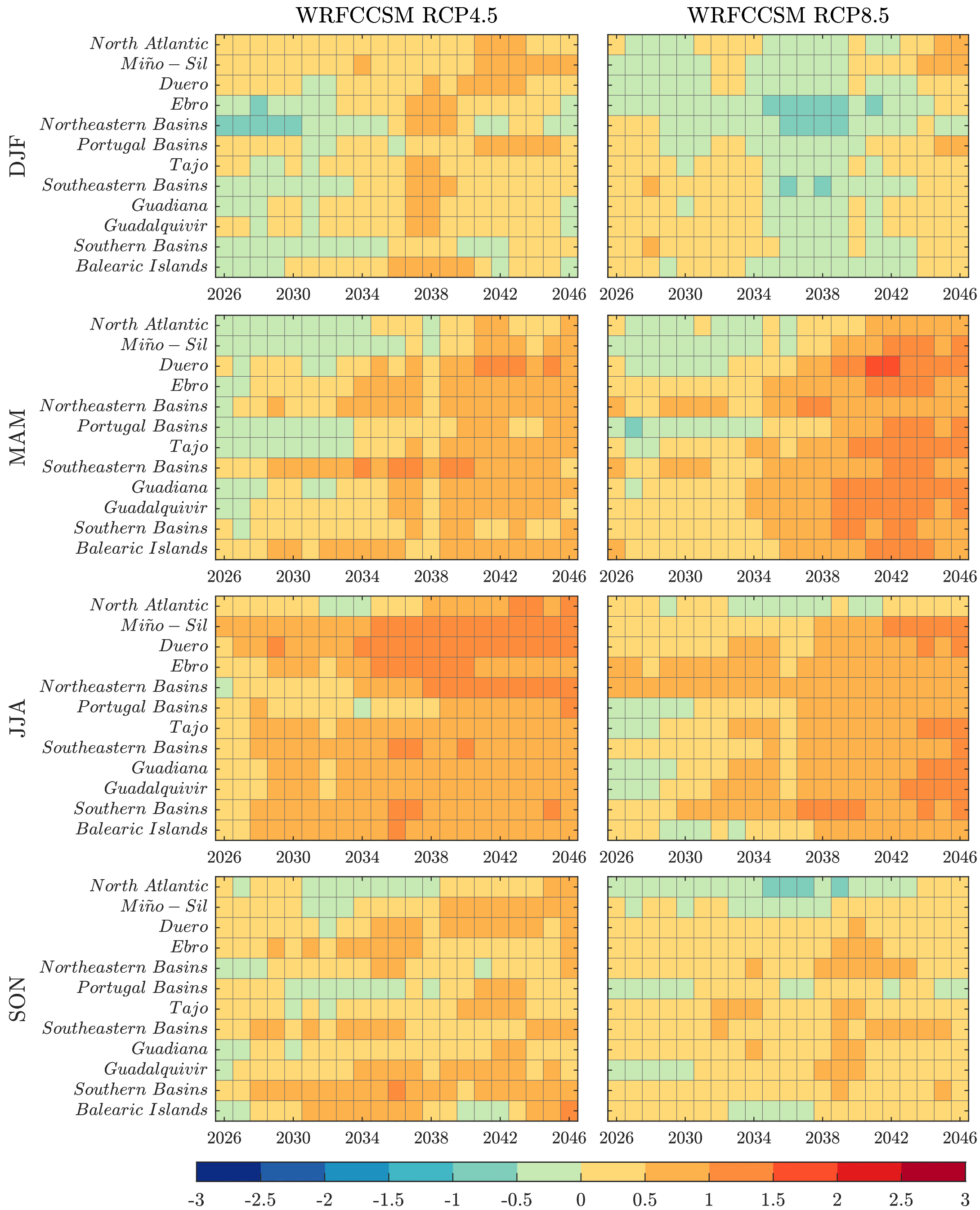

Figure 7.25: *Signal to noise (S/N) ratios of seasonal surface area under drought conditions for each river basin within the IP. The S/N values were computed by using the seasonal mean values from the SPEI for the near future (2021-2050) in relation to the present (1980-2014), for the WRFCCSM simulations.*

many watersheds also ended the period with S/N values of more than 1 (Miño-Sil, Duero, Tajo, Southeastern Basins, Guadiana, Guadalquivir, and Southern Basins).

In autumn (Figure ***7.25***, SON) the drying appeared to be moderate, indicating a large internal variability. Values above 1 were registered only in the Southern Basin (around 2036) and Balearic Islands (around 2046) in the RCP4.5. Again, the RCP4.5 presented more extended drought conditions than did the RCP8.5. In this season, the results also showed values below the present conditions in some cases for both RCPs,suggesting a diminution of the drought conditions in relation to the present. However, by the end of the period, the RCP4.5 revealed a more marked climate change signal, in general.

Concerning the results for the simulations driven by MPI-ESM-LR in near future (Figure ***7.26***), S/N ratios revealed a stronger GHG-forced climate signal than did those from the WRFCCSM. In winter (Figure ***7.26***, DJF) the S/N values that indicate wetter conditions in relation to the present were shown in both RCPs, the generalized trend differing between scenarios. Under the RCP4.5, the internal variability was notable (only the Balearic Islands Basins Basins showed a S/N value >1 for the around 2040), and in general all of the watersheds tended towards drying at least until 2040. Here, the watersheds farther south appeared to be the most affected by more extended drought conditions. For the RCP8.5, a rising trend appeared at the beginning of the period with a subsequent stabilization of the signal, or even showing a decreasing trend by the end of the period. For this scenario, the Balearic Islands Basins appeared to undergo drier conditions due to global warming.

Conditions similar to winter were shown in spring (Figure ***7.26***, MAM), but here the magnitudes of the S/N values were greater. Thus, for the RCP4.5, increased trends were projected at least until around 2042 in many watersheds, reaching values of more than 1 in the Ebro, Tajo, Southeastern Basins, Guadiana, Guadalquivir, and Southern Basins. For the RCP8.5, although all of the watersheds appeared to be affected by rising GHG emissions (values > 1 in many cases), the watersheds located in the south of the IP, and especially the Balearic Islands Basins, were more affected by dryness. However, the S/N values appeared to show a declining trend by the end of the period, and thus

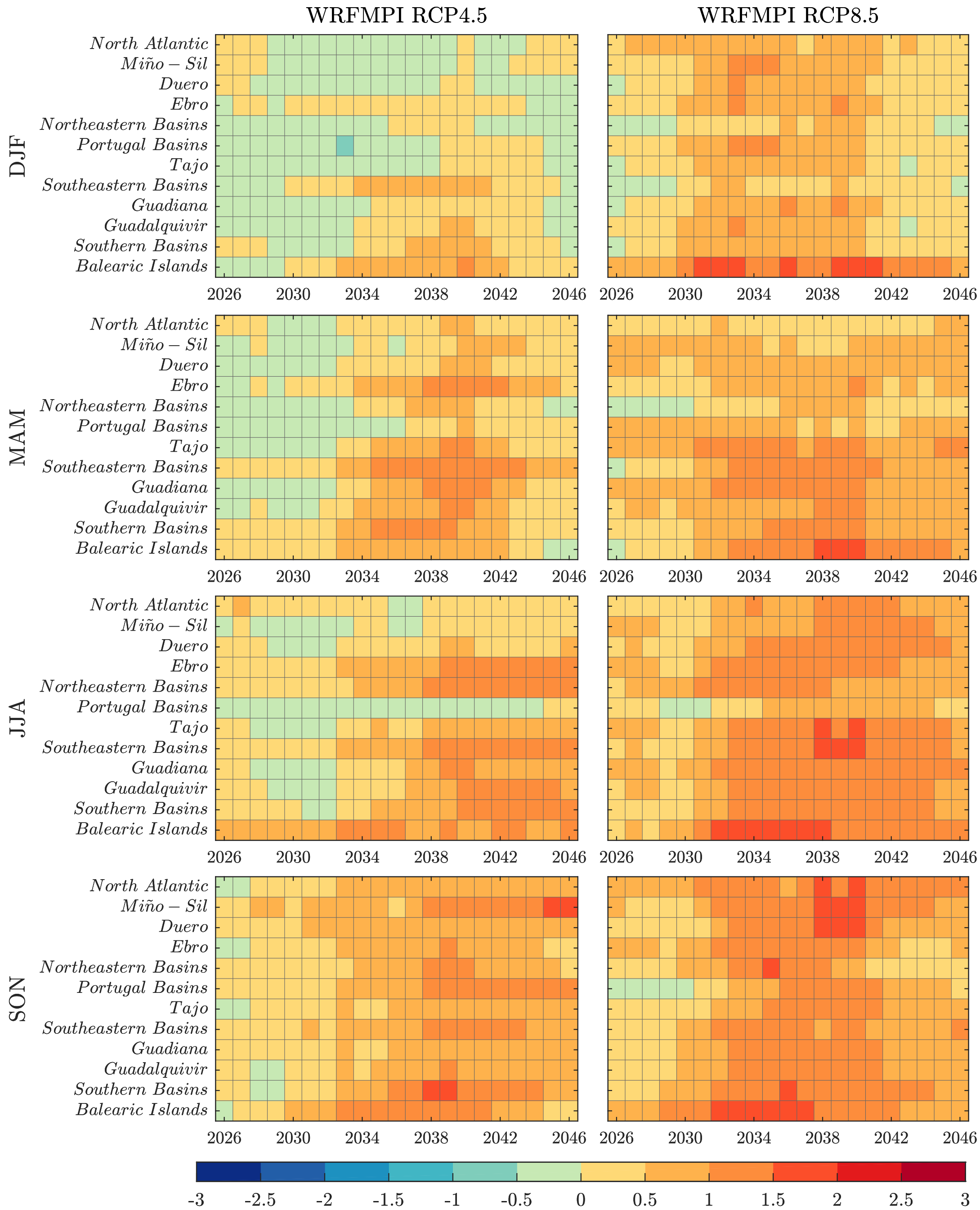

Figure 7.26: *As Figure* ***7.25*** *but for the WRFMPI simulations.*

the ToE appeared not be reached for this period.

Summer S/N values (Figure ***7.26***, JJA) presented the most noteworthy signal of change due to GHGs with rising values for simulations driven by MPI-ESM-LR in this period. For both scenarios, increased trends were shown, such trends being more marked by the RCP8.5. For the RCP4.5, Ebro, Northeastern, Southeastern, Southern Basins and the Balearic Islands appeared to undergo drying where values of greater than 1 were reached by the end of the period. By contrast, the Portugal Basins appeared to be less affected, showing S/N values lesser than the current ones over most of the entire period. Furthermore, in other watersheds located in the south of the IP registered S/N values of greater than 1 (e.g. Southeastern Basins). For the RCP8.5, drying was more generalized with most of the watershed affected by values above 1 for nearly the entire near future.

Drying conditions appeared to remain in autumn (Figure ***7.26***, SON), and even more marked than in summer for the RCP4.5. In this latter scenario, the Miño-Sil and Portugal Basins appeared to show the more marked drying trends with values above 1 from 2038 to the end. For the RCP8.5, all of the watersheds began with rising trends, though by the end of the near future the signal turned downward for many watersheds. These results suggest that the signal of climate change did not probably emerge in this period, at least in autumn.

As for the near future, the S/N ratios for the far future were also computed for simulations driven by the CCSM4 (Figure ***7.27***) and by the MPI-ESM-LR (Figure ***7.28***). In this period, the results presented a broad common trend, showing drying patterns much more marked than for the near future. This suggests lower uncertainties by the end of the 21^{th} century. The results also show differences between RCPs. In fact, while the RCP4.5 presented slight declines in the time course of areas covered by drought by the end in some cases, the trend towards drying conditions appeared to be generalized for the RCP8.5.

For the WRFCCSM, winter S/N values were still moderate (Figure ***7.27***, DJF), showing even wetter conditions than at present in some cases. For the RCP4.5, the watersheds that appeared to undergo drier conditions were those

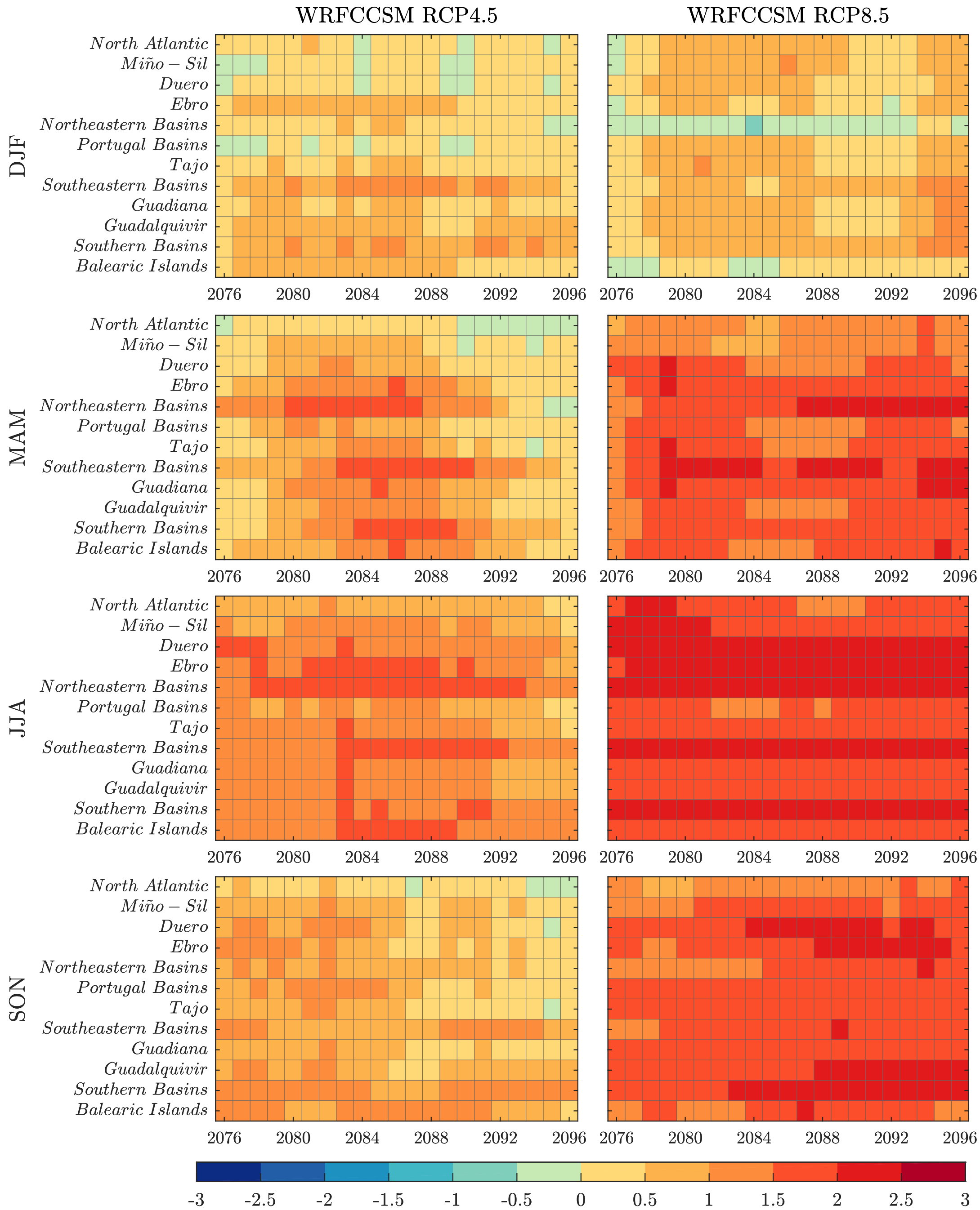

Figure 7.27: *Signal to noise (S/N) ratios of seasonal surface area under drought conditions for each river basin within the IP. The S/N values were computed using the seasonal mean values from the SPEI for the far future (2071-2100) in relation to the present (1980-2014) for the WRFCCSM simulations.*

located in the south of the IP, especially the Southeastern and Southern Basins (values > 1 for many of the decennia). For the RCP8.5, however, a widespread drying pattern emerged except for Portugal Basins, where the surface area under drought was even smaller than at present in nearly the entire period.

In spring (Figure ***7.27***, MAM), more marked drying trends were found, especially for the RCP8.5. In this latter scenario, the results showed S/N values of more than 1.5 for long periods in most watersheds, indicating that the climate change signal was at least 1.5 times higher than the internal variability. Moreover, these values remained at least until the end of the century. For the RCP4.5, although the drying was also severe in many cases, it appeared to decline by the end of the period. For both scenarios, the North Atlantic and Miño-Sil watersheds appeared to show a smaller surface area involved under drought.

The most marked drying conditions were shown for summer again (Figure ***7.27***, JJA) with values above 1 for the entire period in the Northeastern, Southeastern, Southern, and Balearic Islands watersheds in the RCP4.5. In this latter scenario, the North Atlantic Basins presented a weaker GHG-induced climate signal, showing values greater than 1 only around 2082. For the RCP8.5, all of the watersheds except for the North Atlantic and Portugal Basins presented values of close to 2 or even higher over the entire period, suggesting a possible emergence of the GHG-forced signal. In this regard, we cannot ensure that the S/N values remain after 2100.

For autumn (Figure ***7.27***, SON), drying conditions were also substantial and more marked for the RCP8.5. The lower concentrations of GHGs expected in this period for the RCP4.5 appeared to have an effect in the drying trends, showing a slowdown in some watersheds by the end of the period (e.g. North Atlantic Basins). Such trends, nonetheless, do not emerge in the Southern, Southeastern, and Guadalquivir watersheds. By contrast, the RCP8.5 presents increased drought-extension trends, with values above 2 until the end of the 21^{th} century in many watersheds. The watersheds projected to undergo drier conditions are the Duero, Ebro, Guadalquivir, and Southern Basins, where values above 2 are expected to be reached for long periods.

For the WRFMPI simulations in the far future (Figure ***7.28***), substantial

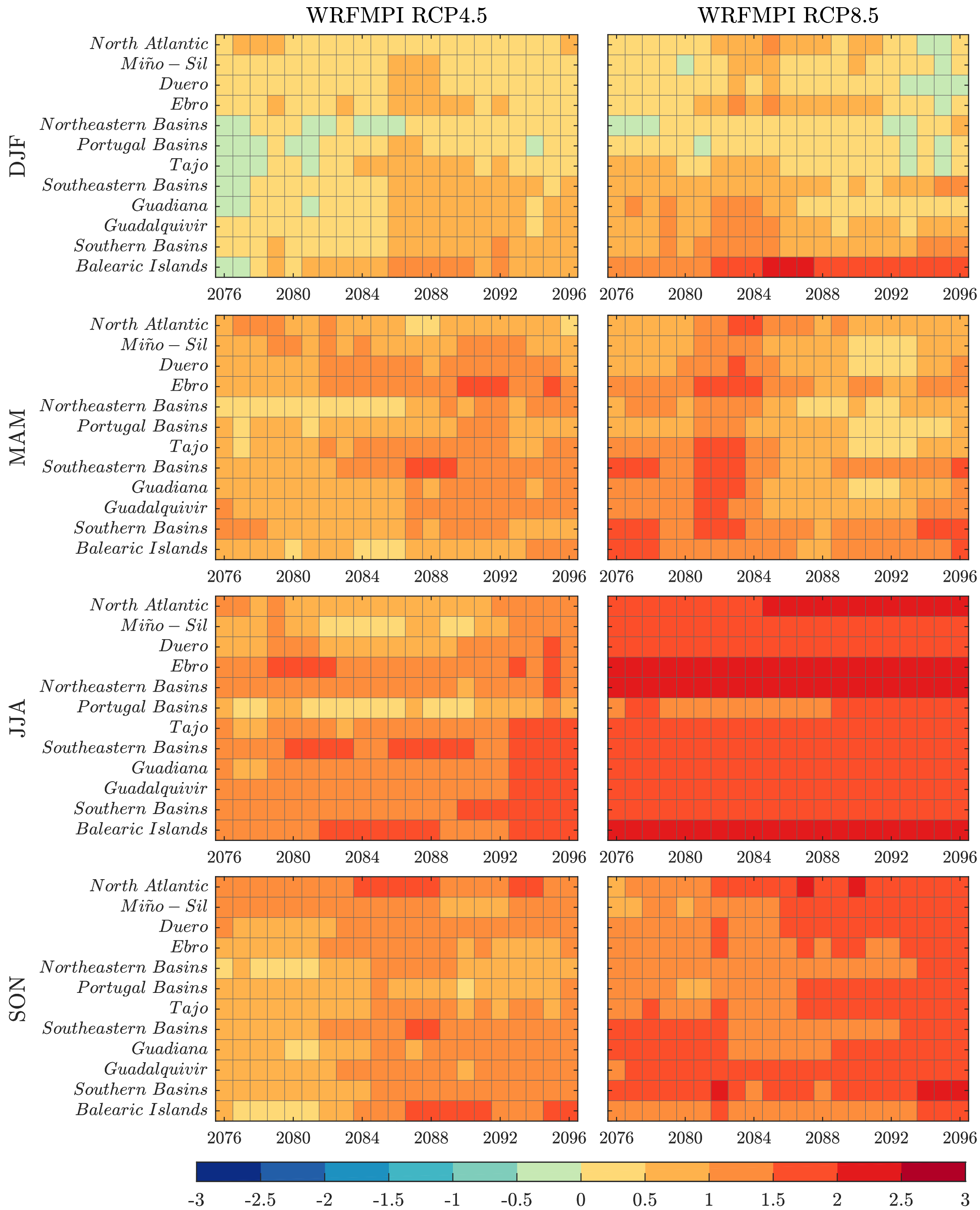

Figure 7.28: *As Figure **7.27** but for the WRFMPI simulations.*

changes in drought conditions also appeared, showing drier conditions than those in the present periods in all seasons except in winter. In this latter season (Figure ***7.28***, DJF), increased trends in the extension of droughts were clearly shown in the Southeastern Basins, Guadiana, Guadalquivir, Southern, and Balearic Islands Basins. This latter, appeared to be the watershed most affected by drying with values above 1 from 2086 to 2090 and for 2092. For the RCP8.5, most watersheds began the period under dryness conditions but these tended to be weaker in many cases by the end. However, the Southeastern, Guadalquivir, Southern, and especially the Balearic Islands Basins remained with high S/N values until the end of the 21^{th} century.

For spring (Figure ***7.28***, MAM), the S/N values showed more substantial changes, registering values above 1 at times in all of the watersheds. Under the RCP4.5, trends of an expanding drought surface area appeared from the second half of the period until the end in many watersheds. For the RCP8.5, most of the watersheds presented an increasing trend from the beginning of the period until 2084. However, the trends changed, again falling to below 1 in many cases (e.g. North Atlantic Basins).

In summer (Figure ***7.28***, JJA), again the most severe changes in terms of drought severity were registered, these being especially notable for the RCP8.5 in all watersheds. These results suggest the possible emergence of the GHG-induced signal, at least in the RCP8.5. However, it is not possible to ensure such trends because we cannot predict the change in drought surface area from 2100 onwards. In this latter scenario, the Portugal Basins appear to be less affected, with S/N values below 1.5 in most of the period 2076-2088. For the RCP4.5, the increase in the surface area affected by drought was more moderate although values above 1 were found for the entire period in most of the watersheds. In autumn (Figure ***7.28***, SON), the drought surface area tended to be more moderate than in summer, but generalized increasing trends were also shown until the end of the century for both scenarios. This suggests also the possible emergence of the signal, at least under the RCP8.5.

Similarly, trends through the near and far future were examined for annual drought conditions through the use of the SPEI values at the 12-month time scale (Figure ***7.29***). In general, higher S/N ratios appeared for all WRFMPI simulations, except for the RCP8.5 in the far future, revealing the possible drought signal emergence for many watersheds, at least under the RCP8.5 since 2040, although the increased trends weakened for the end of the period 2021-2050. For the far future, the stronger climate-change signal is clearer for the entire IP at least under the RCP8.5, showing under the RCP4.5 a possible stabilization of drought surface-area trends except in Southeastern, Southern, Guadalquivir, and Balearic Islands watersheds for the WRFCCSM. For the period 2071-2100, the S/N ratios increased, being very high for the RCP8.5 in all basins, particularly for the WRFCCSM, where the trends were projected to be high until the end of the 21^{th} century in general.

7.5. Discussion and Conclusions from Hydrological Conditions Projections

At the global scale, it is well known that both precipitation and evapotranspiration increase as a consequence of an intensified hydrological cycle in a warmer world (Allen and Ingram, 2002, Huntington, 2006). However, changes at the regional scale proved more uncertain although these are critical for predicting potential changes in aridity. For this reason, in this chapter the projected changes at the regional scale in terms of drought and related variables were analyzed in a hotspot region such as the IP. The results shown here project remarkable changes, particularly notable by the end of the century. Such changes depend strongly on the scenario analyzed. The main conclusions of this chapter are the following:

- Changes in terms surface evapotranspiration and soil moisture content in the root zone reveal that the IP will very likely undergo drier conditions by the end of this century, in relation to the present, especially under a scenario of higher GHG emissions. The annual reductions found here are around 16% and 12% for surface evapotranspiration and root-zone soil moisture in the near future, whereas by the end of the century decreases are projected to be more marked, reaching values of around 30% in surface evapotranspiration and 25% in soil moisture. Such a magnitude of the change suggests a serious climate-change impact on the water availability in this region due to the rising GHG emissions.

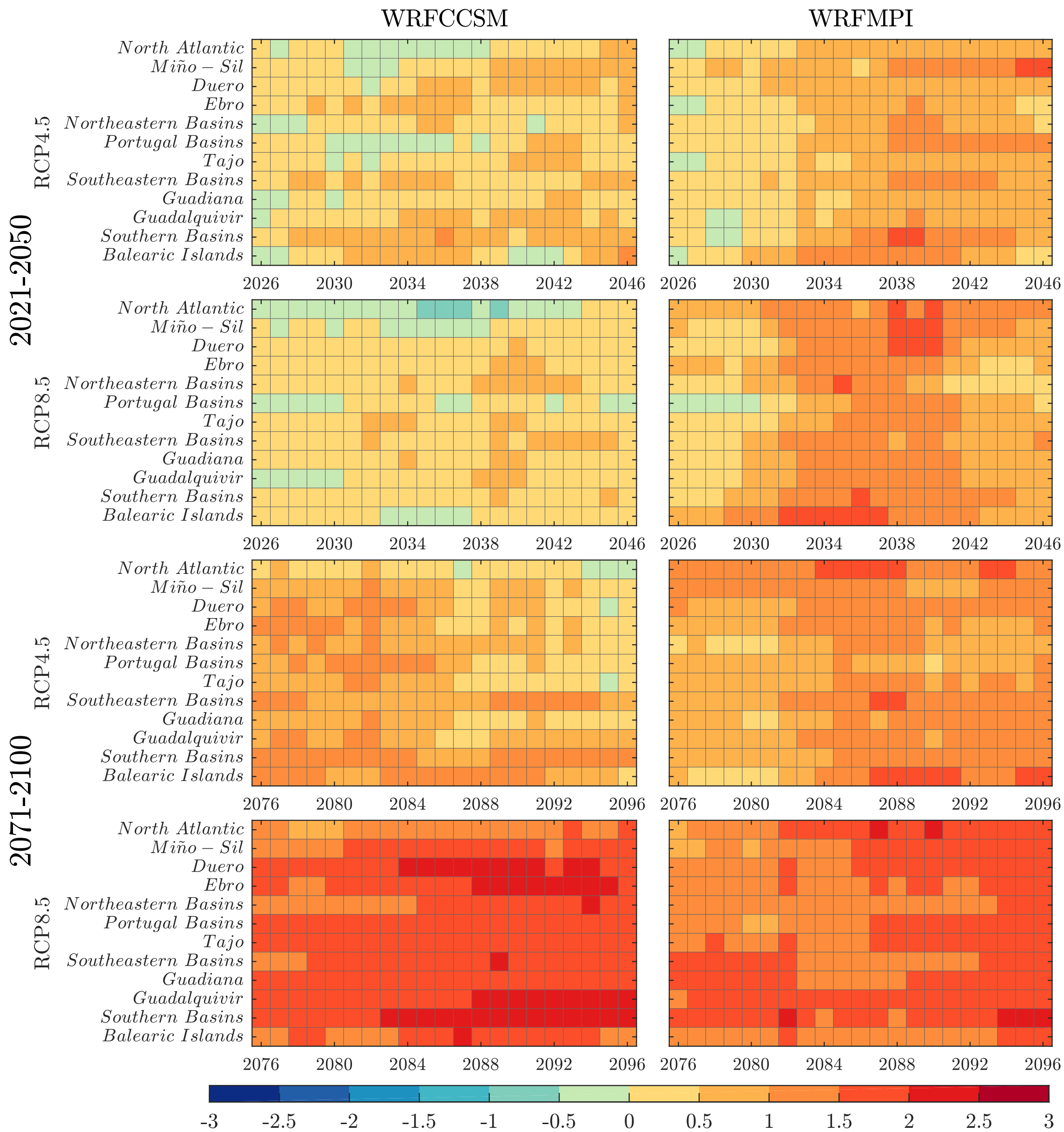

Figure 7.29: *Signal to noise (S/N) ratios of the surface area under drought for the main river basin of the IP. The S/N values were computed through the time series of the area effected by drought, which are taken from the SPEI computed at the 12-month time scale, for near future (2021-2050,up) and far future (2071-2100, bottom) in relation to the present (1980-2014), for both GCM-driven simulations.*

- All WRF simulations also present the most highlighted changes in warm seasons for both variables arising values of changes of about -50% and -25% for surface evapotranspiration and root-zone soil moisture, respectively, by the end of the 21^{th} century. In these seasons, the southern half of the IP is likely to suffer the largest changes, where the simulations driven by the two GCMs indicate reductions of similar magnitude for both variables.

- Changes are expected to be especially strong over the Guadalquivir Valley, where the reductions are projected to be around 60% and 35% for surface evapotranspiration and root-zone soil moisture, respectively, under the RCP8.5. In general, the IP shows that the changes in terms of such variables are closely related to changes in water supply, although such conditions seem to be intensifying for a higher water demand by the atmosphere as consequence of the rise of the temperature in areas classified as semi-arid. For the near future, the WRFMPI projects shifts of greater magnitude than does the WRFCCSM, showing more similar spatial patterns than those found for precipitation. However, some differences still appear between the simulations driven by the two GCMs, particularly in autumn, suggesting a certain degree of uncertainty. For the far future, the major uncertainty is due to the different pathway forcing, and more severe for simulations driven by the MPI-ESM-LR in the RCP4.5, while for the RCP8.5 WRFCCSM appears to project the strongest drying conditions in general.

- The results reported here in terms of changes in soil moisture agree with other works (Zhao and Dai, 2015, Seneviratne et al., 2013, Dai, 2013), which forecast significant decreases in soil moisture for the IP. These results also suggest that the potential increases of surface evapotranspiration due to warming could be limited by soil moisture, particularly by the end of the century, at least in the southern half of the IP. In this sense, there is a general consensus that the drying trends are closely associated with the increasing loss of soil moisture (Berg et al., 2016, Seneviratne et al., 2013), which is especially true in semi-arid regions such as almost the entire IP. Indeed, the amount of water-soil content is expected to be unable to satisfy the increases in atmospheric demand due to global warming. Therefore, the projected changes in surface evapotranspiration are robust in relation to changes in moisture content. Declining trends in current global evapotranspiration have already been documented over the last two decades (Jung et al., 2010), and are expected to intensify even more in the future. In fact, for the IP, where the coupling of land-surface-atmosphere is already strong, authors such as (Greve et al., 2014) predict an increase in the dryness, causing dry regions to become drier, as argued in Held and Soden (2006). In this context, wet regions (the northwestern IP) are likely to become semi-arid by the end of the century, as suggested in Gao and Giorgi (2008). Changes are expected to be more extreme for both variables, evapotranspiration and soil moisture, in the summer season and more moderate for winter, this being consistent with the results from the projections of primary climate variables.

- Current simulations of both the SPEI and SPI from the GCM-driven WRF reveal longer drought events than those observed, suggesting thus, less frequency as well. This feature has previously been noted in other works (Burke et al., 2006, Guerreiro et al., 2017).
- Using standardized drought indices to assess changes in drought phenomena in a future with pronounced changes in dryness conditions could be inaccurate to suitably quantify the projected changes, as pointed out Guerreiro et al. (2017). Actually, all WRF simulations project substantial changes in primary climate variables by the end of the century, particularly under the RCP8.5, so that marked differences in relation to the present are shown. This feature leads to a high number of minus infinite drought indices values, which must not be rejected because they provide valuable information. Therefore, to solve the quantification of minus infinity values, we adopted a categorized new classification, finding results similar to those reported by Guerreiro et al. (2017), in general terms. These authors, using the DSI drought index at a 12-month time scale, found a marked increase in the length of drought, corresponding to multi-year drought events, for the Duero, Tajo, and Guadiana watersheds.
- For the near future, moderate changes in drought events were found, par-

ticularly in terms of duration, with minor differences between scenarios. By contrast, by the end of the 21^{th} century, drier conditions are expected, with noteworthy differences in relation to the present. In this period, the differences between RCPs are also evident. In fact, while the results from the RCP4.5 suggest a downturn in the upward trends, notable increases are found for the RCP8.5, indicating that drought conditions are likely to become more common by the end of the century. In relation to the spatial patterns of the changes, similar results are found in the simulations driven by both GCMs for the two periods and scenarios, suggesting a relatively robust response in terms of drought events. In this context, the magnitude of such changes is determined by the period and emission scenario. For the far future, these results partially agree with those of Stagge et al. (2015), who found an increase in the drying conditions by the end of the century over the IP by computing the SPI from an ensemble of EURO-CORDEX projections for different future periods. In that study, the authors pointed out a progression in dry conditions under the RCP8.5, while for the RCP4.5 the drought indices reached maximum values for the period 2041-2070.

- Concerning the comparison between indices, the results clearly corroborate the importance of taking into account the effect of the temperature to perform impact of climate change on drought assessments for the future. Thus, projections in drought events using the SPI show more moderate changes than those from the SPEI, especially for the far future. This is because an index based solely on precipitation cannot explain the full magnitude or spatial extent of drying reflected by the SPEI (Cook et al., 2014). In fact, the expected rises in temperature lead to greater moisture demand by the atmosphere and, consequently, increased evapotranspiration, which could result in even more severe impacts than precipitation deficits in a warmer world (Ault et al., 2017). In the far future, for the higher emission scenario, simulations show a substantial rise in temperatures as well as a reduction in precipitation, indicating a strong joint effect. This has been pointed out by many authors (Burke et al., 2006, Dai, 2013, Ault et al., 2016, Marcos-Garcia et al., 2017).

- The results from drought indices computed for the end of the century, and especially for the longest time scale (12-months) and for the SPEI, suggest a serious risk of megadrought events. In fact, in the far future, drought events from the SPEI at 12-month are extremely long (more than 15 years in many cases), suggesting that the IP could likely undergo a megadrought, in accordance with the definition provided by Ault et al. (2016). That study defined a megadrought as an event in which PDSI values fall below -0.5 standard deviations for a period of at least 35 years. Although our study period is somewhat shorter than 35 years, the results found here from the 12-month SPEI, which is and drought index analogous to the PDSI (Vicente-Serrano et al., 2010), could suggest that the IP will follow trends towards this kind of drought.

- The results could also indicate a change in the aridity conditions, namely, the values that are below normal conditions in the present (rare events or extremes) could become normal in the future. This agrees in general terms with the study of Gao and Giorgi (2008), who examined projected changes in arid climate regimes by computing three different measures of aridity using high-resolution projections over the Mediterranean region. They found that this region will likely undergo a notable increase in dry and arid land under increased GHG concentrations, particularly in regions such as the IP. In this context, our results could also indicate that PET effects could intensify and expand the drying northwards from the Mediterranean.

- The analysis of trends within the period through the S/N values imply that for the near future the GHG-induced climate signal is still low, the internal variability being higher in general. Such results suggest that the possible emergence of the signal will not appear in the near future. With regard to the comparison between simulations driven by the two GCMs, different results are found, suggesting some degree of uncertainty for this near-future period. In this context, the WRFMPI simulations present more marked drought-extension trends, especially for the RCP8.5. By contrast, the WRFCCSM simulations present larger drying trends for winter, summer, and autumn for the RCP4.5. For the simulations driven by both

GCMs, summer and springs show clearer signals of climate change but winter not so clear. By contrast, by the end of the century, a possible emergence of the GHG-induced signal is shown in spring, summer, and autumn at least under the RCP8.5, this being more distinct for the WRFCCSM simulation.

- In general, the results of S/N values in terms of surface area under drought conditions are closely associated with the precipitation values, but the results here show a broader common trend than S/N values of precipitation (see Figures ***6.12***, ***6.13***, ***6.14*** and ***6.15***). These indicate that, with precipitation (water supply) being the key variable that drives the drought conditions in the IP, rising temperatures exacerbate the situation due to the higher water demand of the atmosphere.

Chapter 8

Conclusions

In this study, different WRF simulations were performed to examine the effects of the anthropogenic climate change in hydrological variables over the IP. For this, projected changes in primary climate variables, i.e. precipitation and maximum and minimum temperature have been analyzed, but also changes in variables closely associated with water availability, i.e. surface evapotranspiration and soil-moisture content. The evaluation of the future changes of all these variables constitutes the framework to attempt to discern whether the hydrological cycle will be altered, and consequently whether an increase in duration, severity, and frequency of drought events will occur.

Therefore, the motivation of this work lies in the necessity of gathering climate future information at an adequate spatio-temporal scale (~10 km) to evaluate the potential impact of the warming in the hydrological cycle for an especially vulnerable region such as the IP.

The selection of suitable driving data to conduct the WRF simulations is essential for the projection of the characteristics of the climate in the future. Unfortunately, the GCMs are usually affected by systematic biases. However, they can be reduced through different approaches. In this sense, a prior step in this work was to perform a bias correction over the outputs from the MPI-ESM-LR following the same methodology applied over the other model used in this study to drive WRF, the NCAR CESM Bias-corrected CMIP5 outputs, which are performed over the output from the CCSM4. The results of using such an approach were analyzed in terms of seasonal long-term mean of the SLP for the period 1980-2014, and showed that the correction applied provides a noteworthy change in the driving data that could improve the results of mean precipitation simulated by WRF, at least for winter.

For an appropriate simulation of the climate characteristics of the IP, the model should be correctly configured. In this context, a critical step is to select a combination of parameterizations to ensure that the model captures the main spatio-temporal patterns in the region of interest. For that purpose, a set of 7 runs were completed by combining different physics schemes, which were compared with observational gridded products in terms of precipitation and extreme temperatures (T_{max} and T_{min}). The main conclusions of this preliminary study (Chapter ***3***) regarding the selection of an adequate set of parameterizations are detailed below:

- **The precipitation is the key variable in order to select a suitable combination of parameterizations.** Among the different combinations of parameterization used, most of the changes between configurations were related to the ability of the model to capture precipitation values, especially for wetter conditions. Therefore, the results for this variable prevailed in order to determine the final configuration of physics schemes.
- **No configuration performs better than others for all variables, and over the entire IP**. The same configuration might perform unevenly over different regions and variables, so that here the configuration that presented the best broad agreement with respect to observations was selected. In this context, the **BA3** was finally chosen due to its statistical robustness throughout all the analyses at different time scales and for all variables.

In addition, this work addresses model evaluation. In fact, for an adequate study of the impact of climate changes on hydrological variables in the future, it is important to ascertain the model's capability to represent the current climate characteristics in the study region. For this, a model evaluation was performed by simulating current climate through different WRF simulations. Thus, three different simulations, one driven by ERA-Interim reanalysis, and two by the outputs from the aforementioned bias-corrected data from CCSM4 and the MPI-ESM-LR, were undertaken for the period 1980-2014. The model's ability was analyzed in terms of the different hydrological variables of interest, namely precipitation, T_{max}, T_{min}, surface evapotranspiration, and soil-moisture content (Chapter ***4***). The main conclusions of the model evaluation are:

- **The WRF model proved to be a noteworthy tool to represent current regional climate characteristics, providing valuable results for a topographically complex region such as the IP**. The WRF satisfactory simulates broad climate characteristics at a scale that the GCMs are not able to achieve, but also adds topographical details that increase the added value regarding driving data.

- **The WRF model accurately represents current precipitation and temperature characteristics**. The climate characteristics over the IP were well captured by the WRF in terms of long-term mean values, but also in high-order statistics, as shown by the analysis performed in term of PSS and the analysis in different ETCCDI indices. These results evidence the added value provided by the WRF model, especially important in terms of extreme events.

- **The capability of adequately representing the precipitation patterns is strongly associated with the LBCs used**. The results from using different LBCs to conduct the WRF model showed a different capability throughout the year. The results from simulations driven with different data, particularly in winter, revealed that the ability to reproduce seasonal precipitation patterns is strongly associated with the LBCs. Indeed, winter was the season most influenced by the large-scale circulation patterns.

- **The WRF model presents a remarkable ability to represent spatial patterns of temperature, but the results are systematically underestimated in general.** Throughout all analyses performed in terms of both T_{max} and T_{min}, the results have broadly underestimated the entire

IP. However, this shortcoming could be easily resolved by using a bias-correction approach, as achieved in the analysis of extreme temperatures, offering suitable results. Moreover, systematic errors are probably offset in the analysis of the future projections by using a Delta-Change approach.

- **Land-surface processes have a strong effect in the simulations of precipitation and temperatures, especially in warm seasons.** Such effects are especially evidenced by the comparison between results from the different GCM-driven simulations, which differ in the initialization of soil-moisture characteristics. In summer, when the large-scale forcings are weaker, the results showed different magnitudes in the underestimation of temperature and overestimation of precipitation. In this context, land-surface processes had a notable influence due the strong land surface-atmosphere coupling that occurs in transitional regions such as the IP. This situation was corroborated by the overestimation of the surface evapotranspiration. Indeed, the simulations that generate large overestimations of surface evapotranspiration in summer also produced larger overestimations of precipitation and underestimations in temperature.

- **The WRF model can acceptably represent land-surface-related variables.** In terms of surface evapotranspiration and soil-moisture content, the model showed certain weaknesses, but these were still quite acceptable, especially for cold seasons. The results also evidenced the effect of land-surface processes in the ability to simulate precipitation and temperature.

Next (Chapter ***5***), the ability of the WRF model to characterize drought events in Spain was analyzed using two well-known drought indices, i.e. the Standardized Precipitation Index (SPI) and the Standardized Precipitation Evapotranspiration Index (SPEI). Two different comparison analyses were used: first, a region-by-region analysis was performed by aggregating drought indices for the different regions established in a regionalization procedure; and second, an analysis directly comparing grid points was performed (local scale analysis). For this purpose, the precipitation and extreme temperatures from the simulation conducted by ERA-Interim for the period 1980-2010 were used. Moreover, this analysis was also focused on determining the added value by using downscaled climate data to detect drought events, so that the drought indices computed from WRF data were also compared with those from ERA-Interim fields. The main conclusions in this regard are summarized below:

- **WRF characterizes reasonably well the spatio-temporal drought variability in Spain.** The results from drought indices by using WRF downscaled fields agreed well with those computed from observational gridded products, showing reliable temporal correlations and a good agreement in terms of different capability scores.
- **The WRF model gained added value regarding its driving data in order to detect drought events.** In the comparison between drought indices derived from WRF climate fields and those from its driving data, the different analyses showed that downscaled fields usually outperformed the ERA-Interim in detecting drought events in topographically complex regions such as Spain.
- **The added value provided by the WRF model is strongly influenced by the time scale used.** The results from the comparison of drought indices computed at 3- and 12-month time scales suggest that the added value was greater for longer time scales, showing greater differences between temporal correlations of drought indices computed with WRF and those from driving data with respect to observations in all the regions analyzed except for the southern IP. Such results were corroborated at the local scale by greater differences in terms of CSI at 12-month time scale, especially in the north of the Peninsula and for a higher increase of the PSS values of severity, duration and magnitude around the entire IP. These findings evidence the benefit of using the WRF downscaled fields to monitor, analyze, and detect drought events, this being a valuable source of knowledge for decision making, especially for water-resource management.
- **There are no substantial differences between the SPEI and the SPI when the ability of the WRF model to simulate droughts in**

Spain is evaluated. Although the improvement provided by the WRF with respect to the ERA data was higher for the SPI than for the SPEI simulations, the SPEI generally provided slightly better results in detecting wet and dry periods. For example, the RMSE local analysis showed that the improvement found for SPI was greater than for SPEI over the entire IP when the WRF field was compared with the driving data, but this was due mainly to the driving data field already resolved well in terms of SPEI in many areas.

In the next part (Chapter ***6***), future climate projections in terms of precipitation and temperatures were examined. For this purpose, 8 different runs were generated by using the bias-corrected outputs from the two GCMs used, the CCSM4 and the MPI-ESM-LR. To analyze the effects of different GHG concentrations, the model was driven under two different RCPs, an intermediate emission scenario, the RCP4.5 and the highest emissions scenario, the RCP8.5, and for two different periods, the so-called near (2021-2050) future period and the far (2071-2100) future. The main findings in this analysis are:

- **Changes in precipitation and extreme temperatures (T_{max} and T_{min}) present a number of uncertainties for the projections over the near future.** Some differences arose from the simulations driven by the two GCMs in terms of both precipitation and extreme temperatures, especially for precipitation, suggesting great uncertainty in this period.
- **Severe changes in precipitation and temperature are likely to occur under high GHG concentrations by the end of the century.** Projections under the RCP8.5 present substantial changes over the entire IP, particularly over the period 2071-2100. This finding evidenced the strong effect of the increasing trend of GHG concentrations.
- **It is virtually certain that the annual precipitation will substantially decrease by the end of the 21^{th} century over practically the entire IP.** Although the changes will be non-significant in many areas in the near future, average values will fall by as much as 18% over the entire IP, with greater reductions by the end of the century, reaching 45%, mainly in the southeastern IP.

- **Changes in mean precipitation differ between seasons.** The most marked changes are likely to occur during warm seasons. That is, for the near future most of the IP will undergo the largest reductions in spring, averaging around 30% for the entire period. For the far future, summer will register the most severe declines, with values of up to 70% in the southern IP. Less marked changes will appear in winter for both future periods, in most cases non-significant for the near future.

- **There is no evidence of substantial changes in the long-term mean precipitation for the near future.** Changes in precipitation will likely not be severe for the period 2021-2050, at least under the RCP4.5, showing non-significant changes throughout most of the IP. Under the RCP8.5, changes will be more pronounced over the eastern peninsular façade, showing reductions of around 17.5%. For seasonal values, the changes in many cases will also be non-significant except for spring.

- **Changes in interannual variability of precipitation are greater than those in mean values.** Changes in variability of the seasonal precipitation presented similar spatial patterns to the changes in mean values, i.e. a decline in the mean precipitation was associated with lower precipitation variability as well. However, such changes appeared to be higher in magnitude.

- **There is certain evidence that the anthropogenic climate-change signal will have emerged by the end of this century in most of the IP.** Nearly all the river basins will register deviations in their mean precipitations in relation to present, at least as large as the internal variability, more marked in warm seasons and under the RCP8.5.

- **There is no evidence of marked changes in terms of extreme values of precipitation.** Although reductions are projected for the most intense precipitation events, stronger for the far future, there are broad areas with increases or non-significant changes. These results suggest that the decline in precipitation will be mainly caused by reductions in moderate rainfall events.

- **In most of the IP the number of consecutive dry days may sharply rise by the end of the century.** Projected changes showed increases of some 20-40% throughout the IP. However, although such values will begin to be noted in the near future, they will be non-significant in many regions.

- **The IP could likely undergo a pronounced warming.** Substantial changes were projected in terms of T_{max} and T_{min} by the end of the century, with increases averaging some 2.5-4°C and 1.5-3°C, respectively (indicating that fluctuations will be greater for T_{max}). For the near future, although more moderate, projected changes will also occur (increases of c. 1.2°C and 0.8°C for T_{max} and T_{min}, respectively).

- **High-altitude regions may register the sharpest temperature increases.** The largest changes will likely occur in high-altitude regions and in the southeastern part of the IP, while the lowest are expected in coastal regions.

- **The largest temperature increases will probably occur during summer an the lowest ones in winter.** For the IP, on average, changes are projected to be approximately 3-5.5°C and 2-4°C for T_{max} and T_{min}, respectively, by the end of the century during summer. By contrast, winter values are of around 1-3.5°C and between below 1 and 2.5°C for T_{max} and T_{min}, respectively.

- **No evidence is found for significant changes in interannual variability of temperatures.** Changes in interannual variability of temperature showed non-significant changes in many areas, and the results were sometimes contradictory, at least for spring, summer, and autumn. For winter, the results appeared to show greater variability.

- **GHG-induced climate signal over temperature is very likely to occur before the end of this century.** This is more pronounced than for precipitation. The time course of the S/N ratios indicates extremely high increases in both T_{max} and T_{min} until the end of the century, reaching 8-fold the internal variability in summer in certain regions of the IP. This induced climate signal may be more pronounced in terms of T_{min}.

- **It is virtually certain that strong increases in extreme temperatures will occur by the end of the 21th century over the entire IP**. Significant changes of extreme temperatures are projected, these being more marked for the far future. For instance, over the period 2071-2100 mean annual changes in the number of tropical nights of about 50 days are projected over southern regions, as well as an increase of summer days of about 40 days/year over the Guadalquivir Valley. Moreover, sharp reductions are expected in areas with around 40 frost days/year at present.

- **A notable increase is expected in the length of summer.** This increase is expected to reach around 20 days/year throughout the IP under the RCP4.5, and could even reach values higher than 45 days/year for most of the IP.

In the next part (Chapter **7**), projected changes in land-surface variables as well as changes in frequency, duration, and severity of drought events were examined. The main findings are the following:

- **The water balance is influenced by a higher GHG concentration.** In general, the changes are more marked in the scenarios that involve higher emissions. This fact suggests that the water cycle is affected by the increase in the concentration of GHGs.

- **Nearly the entire IP is very likely to undergo a severe reduction in the water availability by the end of the 21th century.** The reduction in total surface evapotranspiration is likely to exceed 8% and 20% in the near and far future, respectively, at least in the southern half of the IP, as shown by the results from both RCPs. Similar trends are expected for the soil-moisture content, which is strongly associated with the surface evapotranspiration in semi-arid regions. Thus, reductions in root-zone soil moisture are expected to exceed 4% and 10%, on average, for the near and far future, respectively. Such changes are also shown, by the end of the century, in currently wet regions, indicating a possible shift of the now wet regions into semi-arid regions.

- **The driest conditions are projected to occur in summer.** Substantial changes in surface evapotranspiration are projected in this season with reductions likely to exceed 20% in nearly the entire IP in the near future, and reaching some 20-45% for the far future. This trend results from a sharp decrease in root-zone soil moisture (values of up to 15% and c. 15-25% for the near and far future, respectively) in this season, when a strong coupling land-surface atmosphere occurs.

- **Southern areas of the IP will likely suffer the strongest reductions in surface evapotranspiration and soil-moisture content.** This is projected for both periods and scenarios throughout the year, thus corroborating that dry regions will become drier.

- **The IP is very likely to undergo longer and more severe drought events.** Substantial increases in drought parameters are projected by both indices and at both time scales analyzed (3 and 12 months) in most of the IP by the end of the century, with a greater duration and severity of drought events, which will be especially strong by the end of the century and for the RCP8.5. However, intensification of drought conditions is expected to be more moderate for the near future.

- **There are key differences when evaluating drought events using an index based solely in precipitation and another that takes into account the effect of the rising temperature.** Projected drought conditions by using the SPEI show more severe increases in drought events than those from SPI by the end of the century and, especially, for the high-emission scenario. The more extreme conditions are projected particularly in terms of the duration of the events.

- **Drier conditions projected by the end of the century are likely to magnify the risk of megadrought events.** Longer drought events (15 years or more) are projected for nearly the entire IP over the period 2071-2100 under the RCP8.5.

- **The IP is likely to undergo more arid conditions.** That is, the drought indices values that are below normal conditions in the present (rare events or extremes) could become normal in the future, and for this reason extremely long droughts (megadroughts) are projected.

- **A clear induced climate change signal will occur before the end of the 21th century in terms of drought extent.** The expansion of areas affected by drought, especially in warm seasons, indicates the high probability of the emergence of the climate-change signal in terms of drought conditions.

- **Dryness conditions in the IP are driven mainly by reductions in precipitation, but the consequences are seriously intensified by higher temperatures.** The spatial patterns of changes of surface evapotranspiration and root-zone soil moisture projected, as well as the similarity between the time course of drought expansion and precipitation reduction, indicate that drying in this region is closely associated with changes in the water supply. The results from changes in drought parameters by using drought indices evidence the strong intensification of such behavior due to warmer temperatures.

- **The use of standardized drought indices to assess potential changes in drought phenomena, in a future with marked changes in dryness conditions, could be inaccurate to suitably quantify the projected changes.** Due to the substantial shifts projected for primary climate variables, the fitting of the SPI and SPEI to the current distribution leads occasionally to values of minus infinity for the indices. Such values, while providing information on the characteristics of drought conditions, cannot be quantified. In this work, a reclassification using different intervals based on the well-known SPI categories was used in order to solve this issue.

Potential Future Works

This work has evidenced that the dynamical downscaling approach, through the regional model WRF, is an extraordinary tool to study future changes of processes that require of a finer spatial resolution. This aspect is particularly relevant in regions such as the IP where the orography has a decisive role in the climate. One of the main advantages of the dynamical downscaling approach by using a RCM is the significant number of variables that the model provides, enabling us to study the potential effects of the global warming. In this way, we can compile long-term data of variables such as the surface evapotranspiration or the snow cover, which follow a more unknown trend due to the difficulty of recording them in situ. In this sense, it would be informative to further explore the climate fluctuations in land-surface variables such as soil moisture and runoff in order to prepare suitable validated daily gridded products that can be used for other applications, including risk management or hydrological studies.

On the other hand, for a fuller understanding of the implication of the Earth-surface processes in climate change, the study of the effect of different initial land-surface conditions as well as changes in land use offer a new framework. In this context, improved meteorological inputs could be used for hydrological impact assessments through hydrological models such as the Variable Infiltration Capacity (VIC) model. Moreover, in a context of drying conditions, some ecosystems may not be able to recover their prior conditions before a new drought event occurs, so that it would also be useful to study the recovery time of the different semi-arid ecosystems over the IP for the current climate by using high-resolution climate information (e.g. soil moisture) together with vegetal indicators such as the satellite-derived NDVI.

Additionally, an analysis of high-resolution projections of hydrological variables by using longer time series is also promising. In fact, this work has revealed that the IP will likely suffer major changes in water availability by the end of this century, which could lead to the occurrence of megadrought event or even shifts in the aridity conditions in this area. Thus, further analysis of such aspects through the use of study periods of 100 years or longer could provide additional information which could be valuable for suitable decision making. Longer time series would also allow a more exact determination of the time of emergence of the anthropogenic climate signal in the different variables analyzed here.

Conclusiones

En este estudio, se realizaron diferentes simulaciones con el modelo WRF para examinar los efectos del cambio climático antropogénico en las variables hidrológicas sobre Península Ibérica, IP. Para ello, se analizaron los cambios proyectados en las variables climáticas primarias, es decir, la precipitación y la temperatura máxima y mínima, pero también los cambios en variables estrechamente asociadas con la disponibilidad de agua, como son la evapotranspiración superficial y el contenido de humedad del suelo. La evaluación de los cambios futuros de todas estas variables constituye el marco en el que se trata de discernir si el ciclo hidrológico se verá alterado y, en consecuencia, si se produce un aumento en la duración, gravedad y frecuencia de los eventos de sequía.

Por lo tanto, la motivación de este trabajo radica en la necesidad de obtener información climática sobre el futuro a una escala espacial (~10 km) y temporal adecuada para evaluar el impacto potencial del calentamiento en el ciclo hidrológico para una región especialmente vulnerable como la IP. La selección de datos de entrada apropiados para realizar las simulaciones de WRF es esencial para una proyección adecuada de las características del clima en el futuro. Desafortunadamente, los GCMs generalmente se ven afectados por sesgos sistemáticos. Sin embargo, estos se pueden reducir a través de diferentes enfoques. En este sentido, como paso previo en este trabajo, se realizó una corrección de sesgos sobre los salidas del MPI-ESM-LR siguiendo la misma metodología aplicada sobre el otro modelo utilizado en este estudio como condiciones de contorno del WRF, el NCAR CESM Bias-correction, obtenido a partir de las salidas del CCSM4 incluidas en el CMIP5. Los resultados del uso de dicho enfoque se analizaron en términos de la media estacional a largo plazo de la SLP para el período 1980-2014, y mostraron que esta corrección proporciona un cambio notable en los datos de entrada del WRF, que podrían mejorar los resultados de la precipitación media simulada por este, al menos para el invierno.

Para simular de forma adecuada las características climáticas de la IP, el modelo debe estar configurado correctamente. Para ello, es importante seleccionar una combinación de parametrizaciones para garantizar que el modelo capture los principales patrones espacio-temporales en la región de interés. Con tal fin, se completó un conjunto de 7 simulaciones combinando diferentes esquemas de física, que se compararon con los datos observacionales en rejilla de precipitación y temperaturas extremas (T_{max} y T_{min}). Las principales conclusiones de este estudio preliminar con respecto a la selección de un conjunto adecuado de parametrizaciones se detallan a continuación:

- **La precipitación es la variable fundamental para seleccionar una combinación adecuada de parametrizaciones.** Entre las diferentes combinaciones de parametrización utilizadas, la mayoría de las variaciones se relacionaron con la capacidad del modelo para reproducir los valores de precipitación, especialmente, para las condiciones más húmedas. Por lo tanto, los resultados asociados a dicha variable prevalecieron para determinar la configuración final de los esquemas de física.

- **Ninguna configuración funciona mejor que otras para todas las variables y en toda la IP.** La misma configuración podría funcionar de manera diferente en diferentes regiones y variables, por lo que aquí se seleccionó la configuración que presentaba un mejor y amplio acuerdo respecto a las observaciones. En este contexto, la BA3 fue finalmente elegida debido a su robustez estadística a lo largo de todos los análisis en diferentes escalas de tiempo y para todas las variables.

La segunda parte de esta Tesis aborda la evaluación del modelo. De hecho, para realizar adecuadamente el estudio de los impactos del cambio climático en las variables hidrológicas en el futuro, es importante determinar la capacidad del modelo para representar las características climáticas del presente en la región de estudio. Para ello, se realizó una evaluación de modelo simulando el clima actual a través de diferentes simulaciones de WRF. Por lo tanto, se llevaron a cabo tres simulaciones diferentes, una conducida por el reanálisis ERA-Interim, y las otras dos por los resultados de los datos previamente corregidos de las salidas de los modelos CCSM4 y MPI-LSM-LR, respectivamente, para el período 1980-2014. La capacidad del modelo se analizó para las diferentes variables hidrológicas de interés, a saber, precipitación, T_{max}, T_{min}, evapotranspiración superficial y contenido de humedad del suelo (Capítulo ***4***). Las principales conclusiones de la evaluación del modelo son:

- **El modelo WRF representa adecuadamente las características climáticas regionales actuales, proporcionando resultados valiosos en una región topográficamente compleja como la IP.** El WRF simula satisfactoriamente características climáticas amplias a una escala que los GCMs no pueden lograr, agregando detalles topográficos que aumentan el valor añadido con respecto a los datos de entrada del modelo.

- **WRF ha mostrado su capacidad de representar con precisión las características actuales de precipitación y temperatura.** Las características climáticas sobre la IP han sido bien captadas por el WRF en términos de valores medios a largo plazo, pero también en estadísticas de alto orden, como muestra el análisis realizado en términos del Perkins Skill Score y el análisis en diferentes índices de extremos del ETCCDI. Estos resultados evidencian el valor añadido proporcionado por el modelo WRF, especialmente importante en términos de eventos extremos.

- **La capacidad de representar adecuadamente los patrones de precipitación está fuertemente asociada con las condiciones de contorno (LBC) utilizadas.** Los resultados mediante el uso de diferentes LBC para llevar a cabo las simulaciones del WRF han mostrado una capacidad diferente de reproducir el clima presente en distintas estaciones del año. Así, los resultados obtenidos de simulaciones realizadas con diferentes datos, revelaron que la capacidad de reproducir los patrones de precipitación estacional está fuertemente asociada con las LBC, particularmente en invierno. De hecho, el invierno es la estación más influenciada por los patrones de circulación a gran escala.

- **El modelo WRF presenta una notable capacidad para representar los patrones espaciales de temperatura, pero los resultados en general subestiman sistemáticamente esta variable.** A lo largo de todos los análisis realizados en términos de T_{max} y T_{min}, los resultados han presentado una considerable subestimación en toda la IP. Sin embargo, tal característica podría resolverse fácilmente mediante una corrección de sesgos, como se ha realizado en el análisis de las temperaturas extremas, con resultados adecuados. Además, los errores sistemáticos probablemente se compensen en el análisis de las proyecciones futuras mediante el uso de la aproximación Delta-Change.

- **Los procesos en la superficie terrestre tienen un fuerte efecto en las simulaciones de precipitación y temperaturas, especialmente en estaciones del año cálidas.** Tales efectos se evidencian especialmente por la comparación entre los resultados de las diferentes simulaciones basadas en los dos GCMs, que difieren en la inicialización de las características de humedad del suelo. En verano, cuando los forzamientos a gran escala son más débiles, los resultados muestran una magnitud diferente en la subestimación de la temperatura y en la sobreestimación de la precipitación. En este contexto, los procesos de la superficie terrestre tienen una gran influencia debido al fuerte acoplamiento superficie-atmósfera que ocurre en las regiones de transición climática, como la IP. Este hecho es corroborado por la sobreestimación de la evapotranspiración superficial. De hecho, las simulaciones que generaron mayores sobreestimaciones de la evapotranspiración de la superficie en verano también presentaron una mayor sobreestimación de la precipitación y una subestimación de la temperatura.

- **El modelo WRF puede representar aceptablemente variables relacionadas con la superficie terrestre.** Para la evapotranspiración superficial y contenido de humedad del suelo, el modelo mostró ciertas limitaciones en su reproducción, pero aún si, son bastante aceptables, especialmente en estaciones frías. Los resultados también ponen de manifiesto el efecto que los procesos en la superficie terrestre tienen en la habilidad del modelo para simular la precipitación y la temperatura.

La siguiente parte (Capítulo ***5***) se dedicó a analizar la capacidad del modelo WRF para caracterizar los eventos de sequía en España mediante dos índices de sequía, el SPI y el SPEI, a través de dos análisis de comparación diferentes. Por un lado, se realizó un análisis región por región agregando los índices de sequía para las diferentes regiones obtenidas en un procedimiento de regionalización. Por otra parte, se realizó un análisis de escala local comparando directamente resultados en puntos de rejilla. Para este propósito, se utilizaron la precipitación y las temperaturas extremas obtenidas de la simulación llevada a cabo usando ERA-Interim. Este análisis también se centró en determinar el valor añadido que el uso de datos climáticos a escala local proporciona para detectar eventos de sequía, por lo que los índices de sequía calculados a partir de los datos del WRF también se compararon con los de los campos ERA-Interim. Las principales conclusiones al respecto se resumen a continuación:

- **WRF caracteriza razonablemente bien la variabilidad espacio-temporal de la sequía en España.** Los índices de sequía calculados mediante el uso de campos de temperaturas y precipitación obtenidos por WRF presentan un buen acuerdo con los calculados a partir de datos observacionales en rejilla, con correlaciones temporales altas y buen acuerdo en términos de otras medidas de similitud.

- **WRF caracteriza razonablemente bien la variabilidad espacio-temporal de la sequía en España.** Los índices de sequía calculados mediante el uso de campos de temperaturas y precipitación obtenidos por WRF presentan un buen acuerdo con los calculados a partir de datos observacionales en rejilla, con correlaciones temporales altas y buen acuerdo en términos de otras medidas de similitud.

- **El modelo WRF presenta un valor añadido con respecto a sus datos de entrada para detectar eventos de sequía.** En la comparación entre los índices de sequía obtenidos de los campos climáticos del WRF y los obtenidos de los datos usados como entrada, los diferentes análisis mostraron que los primeros superan a los obtenidos directamente a partir de ERA-Interim para detectar eventos de sequía en regiones topográficamente complejas como España.

- **El valor añadido proporcionado por el modelo WRF está fuertemente influenciado por la escala de tiempo utilizada.** La comparación de los resultados asociados a los índices de sequía calculados en escalas de 3 y 12 meses sugieren que el valor añadido destaca para escalas de tiempo más largas, mostrando mayores diferencias entre las correlaciones temporales de los índices de sequía calculados con WRF y los de los datos de entrada con respecto a las observaciones en todas las regiones analizadas a excepción del sur de la IP. Dichos resultados se corroboran a escala local por mayores diferencias en términos de CSI en escala de tiempo de 12 meses, especialmente en el norte de la IP y por un mayor aumento de los valores del PSS para los parámetros severidad, duración y magnitud en toda la IP. Estos hallazgos evidencian el beneficio de utilizar campos con mayor resolución obtenidos por WRF para el seguimiento, análisis y detección de eventos de sequía, siendo una valiosa fuente de conocimiento para una adecuada toma de decisiones, especialmente para la gestión de los recursos hídricos.

- **No hay diferencias sustanciales entre el SPEI y el SPI cuando se evalúa la capacidad del modelo WRF para simular sequías en España.** Aunque la mejora proporcionada por el WRF con respecto a los datos de ERA-Interim es más alta para el SPI que para las simulaciones SPEI, el SPEI generalmente proporciona resultados ligeramente mejores en la detección de períodos húmedos y secos. Por ejemplo, el análisis local del RMSE mostró que la mejora obtenida por el SPI fue mayor que por el SPEI en toda la IP cuando se compara el campo obtenido por WRF con los datos de entrada, pero esto se debe principalmente a que el SPEI obtenido a partir los datos de ERA-Interim ya reproduce bien las características observacionales en muchas áreas.

En la cuarta parte (Capítulo ***6***), se examinaron las proyecciones climáticas futuras en términos de precipitación y temperaturas. Para este propósito, se generaron 8 simulaciones diferentes mediante el uso de las salidas corregidas por sesgo de los dos GCM utilizados, el CCSM4 y el MPI-ESM-LR. Para analizar los efectos de las diferentes concentraciones de GHGs, el modelo se condujo bajo dos trayectorias de forzamiento diferentes, un escenario de emisiones intermedias, el RCP4.5 y el escenario de emisiones más altas, el RCP8.5, y para dos períodos diferentes, llamados futuro cercano (2021-2050) y el futuro lejano (2071-2100). Los principales hallazgos en este análisis se detallan a continuación:

- **Los cambios en la precipitación y las temperaturas extremas (**T_{max} **y** T_{min}**) presentan ciertas incertidumbres para las proyecciones en el futuro cercano.** Se han obtenido diferencias de las simulaciones impulsadas por los dos GCMs en términos de precipitación y temperaturas extremas, especialmente destacables para la precipitación, lo que sugiere una elevada incertidumbre en este período.

- **Es probable que ocurran cambios severos en las precipitaciones y la temperatura bajo altas concentraciones de GHGs para fines de siglo.** Las proyecciones para el RCP8.5 presentan cambios sustanciales durante todo el período de estudio, particularmente durante el período 2071-2100. Este hallazgo evidencia el fuerte efecto de la tendencia creciente de las concentraciones de GHGs.

- **Es prácticamente seguro que la cantidad anual de precipitación disminuirá sustancialmente a fines del siglo XXI prácticamente en toda la IP.** Aunque los cambios no son significativos en muchas áreas en el futuro cercano, alcanzando, en promedio, disminuciones de alrededor del 18 % durante todo este período de estudio, se encontraron reducciones muy marcadas para fines de siglo en casi toda la IP, de hasta 45 %, principalmente en regiones ubicadas en el sureste de la Península.

- **Los cambios en la precipitación media difieren según la estación del año.** Es probable que los cambios más marcados se produzcan durante las estaciones cálidas. Es decir, para el futuro cercano, la mayor parte de la IP presenta las mayores reducciones en la primavera, siendo en promedio, de alrededor del 30 % para este período. Para el futuro lejano, el verano es la estación con disminuciones más severas, de hasta 70 % en el sur de la IP. Por el contrario, los cambios menos marcados aparecen en invierno para ambos períodos, y en la mayoría de los casos no son significativos para el futuro cercano.

- **No hay evidencia de cambios sustanciales en la precipitación media a largo plazo para el futuro cercano.** Es probable que los cambios en la precipitación no sean severos para el período 2021-2050, al menos bajo el RCP4.5, mostrando cambios no significativos en prácticamente toda la IP. Bajo el escenario RCP8.5, los cambios son más importantes en la fachada este de la IP, mostrando una disminución de alrededor del 17.5 %. Para los valores estacionales, los cambios también son en muchos casos no significativos, excepto para primavera.
- **Los cambios en la variabilidad interanual de la precipitación son mayores que en los valores medios.** Los cambios en la variabilidad de la precipitación estacional presentan patrones espaciales similares a los cambios en los valores medios, es decir, una disminución en la precipitación media se asocia con una reducción en la variabilidad de la precipitación. Sin embargo, tales cambios parecen ser de mayor magnitud.
- **Existe cierta evidencia de que la señal antropogénica de cambio climático habrá emergido a fines de este siglo en la mayoría de la IP.** Casi todas las cuencas sufrirán desviaciones en sus precipitaciones medias respecto al presente, al menos tan acusadas como la variabilidad interna, más marcadas en las estaciones cálidas y bajo el escenario RCP8.5.
- **No hay evidencia de cambios marcados en términos de valores extremos.** Aunque se proyectan reducciones para los eventos de precipitación más intensas, más marcadas para el futuro lejano, aparecen amplias áreas con aumentos o cambios no significativos. Estos resultados sugieren que la disminución en la precipitación será causada principalmente por la reducción en los eventos de lluvia moderada.
- **La mayor parte de la IP podría sufrir un aumento importante en el número de días secos consecutivos para fines de siglo.** Los cambios proyectados muestran aumentos de alrededor del 20-40 % en toda la IP.

Sin embargo, aunque dichos valores comienzan a ser importantes en el futuro cercano, estos no son significativos en muchas regiones.

- **La IP podría sufrir un notorio calentamiento.** Cambios sustanciales se proyectan en las T_{max} y T_{min} para el final del siglo, siendo mayores para la T_{max}, (aumentos en promedio de alrededor de 2.5-4°C y 1.5-3°C para T_{max} y T_{min}, respectivamente). Para el futuro cercano, se proyectan cambios más moderados (aumentos de alrededor de 1.2°C y 0.8°C para T_{max} y T_{min}, respectivamente).

- **Las regiones a mayor altitud podrían sufrir los mayores aumentos de temperatura.** Los mayores cambios probablemente ocurran en regiones altas y en el sureste de la IP, mientras que los cambios más pequeños se esperan en las regiones costeras.

- **Los mayores aumentos de temperatura probablemente ocurrirán durante el verano y los menores en invierno.** Para toda la IP, en promedio, los cambios proyectados son de alrededor de 3-5.5°C y 2-4°C para T_{max} y T_{min}, respectivamente, para finales de siglo durante rel verano. Para invierno, sin embargo, los cambios serán de alrededor de 1-3.5°C y por debajo de 1 hasta 2.5°C para T_{max} y T_{min}, respectivamente.

- **No hay evidencia de cambios significativos en la variabilidad interanual de las temperaturas.** La variabilidad interanual de la temperatura muestra cambios no significativos en muchas áreas, y los resultados a veces son contradictorios, al menos para la primavera, el verano y el otoño. Para el invierno, los resultados parecen mostrar una mayor variabilidad.

- **La señal climática inducida por los GHGs sobre la temperatura es muy probable que ocurra antes de finales de este siglo, siendo más notoria que para la precipitación.** La evolución de la ratio S/N indica valores de aumento muy elevados tanto en T_{max} como en T_{min} hasta finales de siglo, alcanzando incrementos de hasta 8 veces la variabilidad interna en verano en determinadas regiones de la IP. Tal señal climática inducida parece ser más pronunciada para la T_{min}.

- **Es prácticamente seguro que habrá aumentos importantes en las temperaturas extremas para finales del siglo XXI en todo la IP.** Se proyectan cambios significativos de temperaturas extremas, más marcados para el futuro lejano. Por ejemplo, durante el período 2071-2100 se proyectan cambios anuales medios en el número de noches tropicales de unos 50 días en las regiones del sur, así como un aumento de los días de verano de aproximadamente 40 días/año en el valle del Guadalquivir. Además, se espera una reducción importante en las áreas donde los días de helada son de alrededor de 40 días/año en el presente.
- **Se espera un aumento notable en la duración del verano.** En promedio, se espera un aumento en la duración del verano de alrededor de 20 días/año en toda la IP bajo el escenario RCP4.5, e incluso podrían alcanzarse valores superiores a 45 días/año para la mayor parte de la IP.

En la última parte (Capítulo **7**), se examinaron los cambios proyectados en las variables hidrológicas asociadas a la superficie terrestre, así como los cambios en la frecuencia, duración y severidad de los eventos de sequía tanto para el futuro cercano como lejano. Los principales hallazgos son los siguientes:

- **El balance hídrico está influenciado por un aumento en la concentración de GHGs.** En general, los cambios son más marcados en los escenarios que contemplan mayores emisiones. Este hecho sugiere que el ciclo del agua se ve afectado por el aumento en la concentración de GHGs.
- **Casi toda la IP probablemente sufrirá una reducción severa en la disponibilidad de agua a finales del siglo XXI.** Es probable que la reducción en la evapotranspiración superficial total exceda el 8 % y el 20 % en el futuro cercano y lejano, respectivamente, al menos en la mitad sur de la IP, como muestran las proyecciones para ambos RCPs. Una evolución similar muestra el contenido de humedad del suelo, fuertemente asociado con la evapotranspiración superficial en regiones semiáridas. Por tanto, se esperan reducciones en la humedad del suelo en la zona de la raíz que excederán el 4 % y 10 %, en promedio, para el futuro cercano y lejano, respectivamente. Dichos cambios también se muestran, hacia el fi-

nal del siglo, en regiones actualmente húmedas, lo que indica una posible transición de las regiones ahora húmedas a regiones semiáridas.

- **Se proyecta que las mayores condiciones de sequedad ocurran en verano.** Se proyectan cambios sustanciales en la evapotranspiración superficial en esta estación con reducciones que probablemente excederán el 20 % en casi toda la IP en el futuro cercano, y que alcanzarán disminuciones de alrededor del 20-45 % en el futuro lejano. Tal comportamiento vendrá acompañado de reducciones importantes en la humedad de la suelo de la zona radicular (valores de hasta 15 % y alrededor del 15-25 % para el futuro cercano y lejano, respectivamente) en esta estación del año, cuando se produce un fuerte acoplamiento entre la atmósfera y la superficie terrestre.

- **Las áreas del sur de la IP probablemente sufrirán las mayores reducciones en la evapotranspiración de la superficie y en el contenido de humedad del suelo.** Estas reducciones se proyectan para ambos períodos y escenarios a lo largo del año, lo que corrobora que las regiones secas se volverán más secas.

- **Es muy probable que la IP sufra eventos de sequía más largos y más severos.** Se proyectan aumentos sustanciales en los parámetros de sequía en ambos índices (SPI y SPEI) así como en las dos escalas de tiempo analizadas (3 y 12 meses) en la mayor parte de la IP hacia finales de siglo, con una mayor duración y severidad de los eventos de sequía, que serán especialmente fuertes a finales de siglo y para el RCP8.5. Sin embargo, se espera que la intensificación de las condiciones de sequía sea más moderada para el futuro cercano.

- **Existen diferencias substanciales al evaluar los eventos de sequía utilizando un índice basado únicamente en la precipitación y otro que tiene en cuenta el efecto del aumento de la temperatura.** Las condiciones de sequía proyectadas mediante el uso del SPEI muestran aumentos más severos en los eventos de sequía que los proyectados usando el SPI, antes de fin de siglo y, especialmente, para el escenario de altas emisiones. Las condiciones más extremas se proyectan particularmente en términos de la duración de los eventos.

- **Las condiciones más secas proyectadas para el final del siglo probablemente aumentarán el riesgo de ocurrencia de eventos de megasequías.** Eventos más largos de sequía (15 años o más) se proyectan para casi toda la IP durante el período 2071-2100 bajo el RCP8.5.

- **Es probable que la IP experimente condiciones más áridas.** Esto es, los valores de los índices de sequía que están por debajo de las condiciones normales en el presente (eventos raros o extremos) podrían volverse normales en el futuro, y por esta razón se proyectan sequías extremadamente largas (megasequías).

- **Se producirá una clara señal de cambio climático inducido antes de que finalice el siglo XXI en términos de extensión de la sequía.** La expansión de las áreas afectadas por la sequía, especialmente en estaciones cálidas del año, indica una alta probabilidad de que emerja la señal del cambio climático en términos de condiciones de sequía.

- **Las condiciones de sequedad en el período de estudio se deben principalmente a la reducción de las precipitaciones, pero las consecuencias se ven seriamente intensificadas por las altas temperaturas.** Los patrones espaciales de los cambios proyectados para la evapotranspiración superficial y la humedad del suelo de la zona radicular, así como la similitud entre el evolución temporal de la expansión de la sequía y la reducción de la precipitación, indican que el aumento de las condiciones secas en esta región está estrechamente relacionado con cambios en el aporte de agua. Los resultados relativos a los cambios en los parámetros de sequía mediante el uso de índices de sequía evidencian la fuerte intensificación de tales tendencias debido a las temperaturas más cálidas.

- **El uso de índices de sequía estandarizados para evaluar los cambios potenciales en los fenómenos de sequía en un futuro con cambios marcados en las condiciones de sequedad, podría ser inadecuado para cuantificar adecuadamente las tendencias proyectadas.** Debido a los cambios sustanciales proyectados para las variables climáticas primarias, el ajuste de los índices SPI y SPEI a la distribución actual conduce ocasionalmente a valores de menos infinito para los índices. Dichos valores, al tiempo que proporcionan información sobre las condiciones de sequía, no se pueden cuantificar. En este trabajo, se utilizó una reclasificación con diferentes intervalos basados en las categorías de SPI usadas tradicionalmente para clasificar periodos con distintas condiciones de humedad y sequía para intentar resolver este problema.

Trabajos Futuros

Este trabajo ha puesto de manifiesto que el downscaling dinámico, a través del modelo regional WRF, proporciona una herramienta extraordinaria para estudiar cambios futuros de procesos que requieren una resolución espacial más fina. Este aspecto es particularmente relevante en regiones como la IP, donde la orografía tiene un importante y decisivo papel en el clima. Una de las ventajas más importantes de la reducción de escala dinámica mediante el uso de un RCM es la cantidad de variables de interés que proporciona el modelo, que nos permite estudiar los efectos potenciales del calentamiento global. De esta forma, podemos obtener datos que proporcionen estimaciones a largo plazo de variables como la evapotranspiración superficial o la capa de nieve, que tienen una tendencia de comportamiento más incierta debido a la dificultad de obtener registros in situ. En este sentido, sería muy interesante conocer las fluctuaciones climáticas de las variables de la superficie terrestre, como la humedad del suelo y la escorrentía, para elaborar bases de datos en base diaria en rejilla, adecuados para poder utilizarse en otras aplicaciones, incluyendo, por ejemplo, la gestión de riesgos u otros estudios hidrológicos.

Por otro lado, para una comprensión más completa de la implicación de los procesos de la superficie de la Tierra en el cambio climático, el estudio del efecto de las diferentes condiciones iniciales de la superficie terrestre y los cambios en el uso de la tierra ofrecen un nuevo marco. En este contexto, se podrían utilizar estimaciones de datos meteorológicos mejoradas para las evaluaciones del impacto hidrológico a través de modelos hidrológicos como el modelo de Variable Infiltration Capacity (VIC). Además, en un contexto de condiciones de sequía, algunos ecosistemas pueden no ser capaces de recuperar sus condiciones previas antes de que ocurra un nuevo evento de sequía, por lo que también sería útil estudiar el tiempo de recuperación de los diferentes ecosistemas semiáridos en la IP para clima presente utilizando información climática de alta resolución (por ejemplo, humedad del suelo) junto con indicadores vegetales como el NDVI derivado de datos de satélite.

Además, un análisis de proyecciones de alta resolución de variables hidrológicas mediante el uso de series temporales más largas también es prometedor. De hecho, este trabajo ha revelado que es probable que la IP sufra cambios importantes en la disponibilidad de agua para fines de este siglo, lo que podría llevar a la ocurrencia de un evento de megasequía o incluso cambios en las condiciones de aridez en esta área. Por lo tanto, un análisis de tales aspectos mediante el uso de períodos de 100 años o más podría proporcionar información adicional que podría ser valiosa para una adecuada toma de decisiones. Las series temporales más largas también permitirían una determinación más exacta del momento de aparición de la señal climática antropogénica en las diferentes variables analizadas aquí.

Appendix A

Statistical Parameters for the Model Evaluation

A.1. Statistical Parameters for the Model Evaluation in terms of Mean Fields

For every time accumulation period and time series with N observations, the following errors statistics parameters have been used to evaluated the model performance: average (A.1 and A.2), standard deviation (A.3 and A.4), normalized standard deviation (A.5), bias (for temperature; A.7) and relative bias (for precipitation and real evapotranspiration data; A.8). For all equations, S and O denote simulations and observations data respectively.

Average: The average of temporal series is a measurement that characterize the distribution of climate variables using a representative value.

$$\overline{S} = \frac{1}{N}\sum_{k=1}^{N} S_k \tag{A.1}$$

$$\overline{O} = \frac{1}{N}\sum_{k=1}^{N} O_k \tag{A.2}$$

Standard deviation: The standard deviation allows to evaluate the variations with respect to the mean values for different accumulated periods distributions. For example, for annual values, the standard deviation means the variability within the annual time series. The corresponded standard deviation equation for modeled (A.3) and observed (A.4) are:

$$\sigma_S = \sqrt{\frac{1}{N}\sum_{k=1}^{N}(S_k - \overline{S})^2} \tag{A.3}$$

$$\sigma_O = \sqrt{\frac{1}{N}\sum_{k=1}^{N}(O_k - \overline{O})^2} \tag{A.4}$$

Normalized standard deviation: The normalized standard deviation expressed in percentage is a error measurement that is used to identify the standard deviation for every simulations in relative terms. The equation is:

$$\sigma_{norm} = \frac{\sqrt{\frac{1}{N}\sum_{k=1}^{N}(S_k - \overline{S})^2}}{\sqrt{\frac{1}{N}\sum_{k=1}^{N}(O_k - \overline{O})^2}} \tag{A.5}$$

Pattern correlation (r): (or Pearson correlation coefficients over the space). The simple correlation coefficients allows to compare the similarity between two spatial fields using for that a linear assumption. It has a value in a range between 1 (total positive linear correlation) and -1 (total negative correlation). A value of 0 indicates the absence of correlation. The correlation patterns is expressed as:

$$r = \frac{Cov(S,O)}{\sigma_S \sigma_O} \tag{A.6}$$

where $Cov(S,O)$ is the covariance between modeled and observed data and σ_S and σ_O the standard deviation of modeled and observed data respectively.

Bias: Mean difference between the simulated and the observed data.

$$Bias = \frac{1}{N}\sum_{k=1}^{N}(S_k - O_k) = \overline{S} - \overline{O} \tag{A.7}$$

Relative Bias: Bias regarding to the observed mean.

$$Bias(\%) = \frac{1}{N}\frac{\sum_{k=1}^{N}(S_k - O_k)}{\sum_{k=1}^{N}(O_k)} = \frac{\overline{S} - \overline{O}}{\overline{O}} \tag{A.8}$$

A.2. Statistical Parameters for the Model Evaluation in terms of Statistical Distributions

The PSS measures the similarity between observed and simulated distributions, using for that the common area between the PDF. The formal expression of this skill score is:

$$PSS_{score} = \sum_{i=1}^{n} min(Z_{sim}, Z_{obs.}) \tag{A.9}$$

where n is the number of interval used to calculated the PDFs, Z_{sim} is the frequency of values for every interval by using the model data, and $Z_{obs.}$ is the frequency from the observed ones.

A.3. Statistical Parameters for Assessing the Added Value of Downscaled Fields in terms of Drought Indices and Sensitivity Test

RMSE: The root-mean-squared error is considered as a measure of the magnitude of the error.

$$RMSE = \sqrt{\frac{\sum_{i=1}^{N}(S_i - O_i)^2}{N}} \tag{A.10}$$

Mean Absolute Error: Average of the absolute error.

$$MAE = \frac{1}{N} \sum_{k=1}^{N} \mid S_k - O_k \mid \tag{A.11}$$

Spatial Correlation: Based on the Pearson correlation coefficient calculating at different spatial intervals along longitude and latitude.

$$r_{L,I,s_1,s_2} = \frac{\sum_{i=1}^{N}(x_{i,L,I} - \bar{x}_{L,I})(x_{i,L+s_1,I+s_2} - \bar{x}_{L+s_1,I+s_2})}{\sqrt{\sum_{i=1}^{N}(x_{i,L,I} - \bar{x}_{L,I})^2}\sqrt{\sum_{i=1}^{N}(x_{i,L+s_1,I+s_2} - \bar{x}_{L+s_1,I+s_2})^2}} \tag{A.12}$$

where x is the drought index value for every i month with coordinates (L, I) in latitude and longitude, respectively. s_1 is the south-to-north interval and s_2 is the west-to-east interval.

CSI: The Critical Success Index is a categorical parameter that measures the ability to detect episodes above or below a certain threshold.

$$CSI = \frac{TP}{TP + FP + FN} \tag{A.13}$$

where TP are the excedeences given by the modeled data which are corroborated by observations, i.e. the true positive, FP are the ones found by the models that are not corroborated by the observed data (false positive) and FN are the noncaptured models excedeences that actually occurred (false Positive).

Appendix B

The Regionalization of the Observational Data sets

B.1. Multi-step Regionalization

In order to analyze drought events at regional scale, a climate classification (also known as regionalization) was used. For this, the SPEI and SPI temporal series computed at 3- and 12- month time scales were computed through the precipitation and temperature data from the observed mprmt data, which cover a period between 1950 and 2010.

To this end, the multi-step approach proposed by Argüeso et al. (2011) was used here, which is based on the application of three statistical techniques: a principal component analysis (PCA), an agglomerative hierarchical clustering (AHC) and, a final k-means clustering analysis (CA). The suitability of using a hybrid climate classification lies in that the application of successive techniques reduces errors associated to subjective decisions used in every technique.

The regionalization was performed on the different indices and time scales, but due to the similarity between the regions for the different indices and time scales only the results from the 3-month Standardized Precipitation Evapotranspiration Index (SPEI) was used to define the homogeneous climate regions for comparative purposes.

B.1.1. Principal Components Analysis (PCA)

The PCA is a widespread technique used in climatology to reduce the size of the data. Indeed, because of the climate information is commonly very large, the PCA facilitates the analysis and understanding of the behavior of the climate variables, reducing the dimension of the original data without loss of information (Fovell, 1997). In this sense, a S-mode PCA (Wilks, 2006) was applied to the 3-month SPEI anomalies by using the covariance matrix.

In order to facilitate the physical interpretation of the results computed, the principal components computed were rotated redistributing thus the explained variance and increasing the spatial coherence using the Varimax Wilks (2006) method. For this, the number of components that explained a minimum of about 80% of the temporal variability (Russo et al., 2015) of the drought index was selected. Using this criteria, three principal components were retained, explaining 81.06% of the total variance of the data.

However, this technique does not provide results to establish specific regions with the same climate patterns, so the rotated factor loadings here were used to apply a cluster analysis (CA).

B.1.2. Agglomerative Hierarchical Clustering (AHC)

Through the AHC, we group hierarchically data with similar climate behavior. Such groups are the result of joining pairs of points successively by using a measurement of similarity. To do this, the method needs to define the cluster by two parameters: the measurement of similarity and a distance between clusters (linkage method). Here, the square Euclidean distance was selected as a measurement of similarity and the average linkage algorithm as a method to group each object into a cluster. Additionally, to determine the optimal number of clusters the pseudo F test (Calinski and Harabasz, 1974) was used, which showed a local maximum for a six-cluster configuration.

Thereby, the rotated factor loadings were used to feed the AHC and a six-cluster configuration was drawn. However, one characteristic of this method is that once a group is assigned within a cluster, it is not removed, so, this procedure does not allow a clustering recombination. For this reason, it is desirable to use an additional non hierarchical k-means CA technique in order to identify the most suitable regions.

B.1.3. K-means Clustering Analysis

The K-means (CA) method checks each of the cluster members in order to reallocate them according to their spatial coherence. However, the results drawn in this application rely strongly on the initial cluster configuration (initial seeds) and the number of groups (K), here the average of the initial 3-month SPEI for each cluster was used as seeds, the K groups being thus determined by the Pesudo-F test applied to the AHC.

The regionalization thus resulted in a final configuration of six homogeneous climate regions in terms of 3-month SPEI, which are: the northwestern (NW) region, the Cantabrian (CA) region, the northeastern (NE) region, the interior (IN) region, the southern (S) region, and the southeastern (SE) region. These regions agree with the results reported by Vicente-Serrano (2006), where a regionalization technique was performed over the Iberian Peninsula in terms of 3-month SPEI.

References

Alexandru, A., R. de Elia, R. Laprise, L. Separovic, and S. Biner (2009). Sensitivity Study of Regional Climate Model Simulations to Large-Scale Nudging Parameters. *Monthly Weather Review*, 137(5):1666–1686, doi:10.1175/2008MWR2620.1.

Allen, M. R. and W. J. Ingram (2002). Constraints on future changes in climate and the hydrologic cycle. *Nature*, 419:224–232, doi:10.1038/nature01092.

Allen, R. G., L. S. Pereira, D. Raes, and M. Smith (1998). Crop evapotranspiration-Guidelines for computing crop water requirements-FAO Irrigation and drainage paper 56. *FAO, Rome*, 300(9):D05109.

Arakawa, A. (2004). The Cumulus Parameterization Problem: Past, Present, and Future. *Journal of Climate*, 17(13):2493–2525, doi:10.1175/1520-0442(2004)017<2493:RATCPP>2.0.CO;2.

Argüeso, D. (2011). *High-resolution projections of climate change over the Iberian Peninsula using a mesoscale model*. PhD dissertation, Departamento de Física Aplicada, Universidad de Granada.

Argüeso, D., J. M. Hidalgo-Muñoz, S. R. Gámiz-Fortis, M. J. Esteban-Parra, and Y. Castro-Díez (2012a). Evaluation of WRF Mean and Extreme Precipitation over Spain: Present Climate (1970–99). *Journal of Climate*, 25(14):4883–4897, doi:10.1175/JCLI-D-11-00276.1.

Argüeso, D., J. M. Hidalgo-Muñoz, S. R. Gámiz-Fortis, M. J. Esteban-Parra, and Y. Castro-Díez (2012b). High-resolution projections of mean and extreme precipitation over Spain using the WRF model (2070–2099 versus

1970–1999). *Journal of Geophysical Research: Atmospheres*, 117(D12), doi:10.1029/2011JD017399. D12108.

Argüeso, D., J. M. Hidalgo-Muñoz, S. R. Gámiz-Fortis, M. J. Esteban-Parra, J. Dudhia, and Y. Castro-Díez (2011). Evaluation of WRF Parameterizations for Climate Studies over Southern Spain Using a Multistep Regionalization. *Journal of Climate*, 24(21):5633–5651, doi:10.1175/JCLI-D-11-00073.1.

Ault, T. R., J. S. Mankin, B. I. Cook, and J. E. Smerdon (2016). Relative impacts of mitigation, temperature, and precipitation on 21st-century megadrought risk in the American Southwest. *Science Advances*, 2(10), doi:10.1126/sciadv.1600873.

Bador, M., L. Terray, and J. Boé (2016a). Detection of anthropogenic influence on the evolution of record-breaking temperatures over Europe. *Climate Dynamics*, 46(9):2717–2735, doi:10.1007/s00382-015-2725-8.

Bador, M., L. Terray, and J. Boé (2016b). Emergence of human influence on summer record-breaking temperatures over Europe. *Geophysical Research Letters*, 43(1):404–412, doi:10.1002/2015GL066560.

Barrera-Escoda, A., M. Gonçalves, D. Guerreiro, J. Cunillera, and J. M. Baldasano (2014). Projections of temperature and precipitation extremes in the North Western Mediterranean Basin by dynamical downscaling of climate scenarios at high resolution (1971–2050). *Climatic Change*, 122(4):567–582, doi:10.1007/s10584-013-1027-6.

Beguería, S. and S. M. Vicente-Serrano (2013). *SPEI: Calculation of Standardized Precipitation-Evapotranspiration Index*. R package version 1.6.

Beguería, S., S. M. Vicente-Serrano, F. Reig, and B. Latorre (2014). Standardized precipitation evapotranspiration index (SPEI) revisited: parameter fitting, evapotranspiration models, tools, datasets and drought monitoring. *International Journal of Climatology*, 34(10):3001–3023, doi:10.1002/joc.3887.

Belo-Pereira, M., E. Dutra, and P. Viterbo (2011). Evaluation of global precipitation data sets over the Iberian Peninsula. *Journal of Geophysical Research: Atmospheres*, 116(D20), doi:10.1029/2010JD015481. D20101.

Berg, A., K. Findell, B. Lintner, A. Giannini, S. I. Seneviratne, B. van den Hurk, R. Lorenz, A. Pitman, S. Hagemann, A. Meier, F. Cheruy, A. Ducharne, S. Malyshev, and P. C. D. Milly (2016). Land–atmosphere feedbacks amplify aridity increase over land under global warming. *Nature Climate Change*, 6:869–874, doi:10.1038/nclimate3029.

Berrisford, P., D. P. Dee, P. Poli, R. Brugge, K. Fielding, M. Fuentes, P. W. Kållberg, S. Kobayashi, S. Uppala, and A. Simmons (2011). The ERA-Interim archive Version 2.0. Shinfield Park, Reading.

Betts, A. K. (1986). A new convective adjustment scheme. Part I: Observational and theoretical basis. *Quarterly Journal of the Royal Meteorological Society*, 112(473):677–691, doi:10.1002/qj.49711247307.

Betts, A. K. and M. J. Miller (1986). A new convective adjustment scheme. Part II: Single column tests using GATE wave, BOMEX, ATEX and arctic air-mass data sets. *Quarterly Journal of the Royal Meteorological Society*, 112(473):693–709, doi:10.1002/qj.49711247308.

Boberg, F., P. Berg, P. Thejll, W. J. Gutowski, and J. H. Christensen (2010). Improved confidence in climate change projections of precipitation further evaluated using daily statistics from ENSEMBLES models. *Climate Dynamics*, 35(7):1509–1520, doi:10.1007/s00382-009-0683-8.

Bowden, J. H., K. D. Talgo, T. L. Spero, and C. G. Nolte (2016). Assessing the added value of dynamical downscaling using the Standardized Precipitation Index. *Advances in Meteorology*, 2016:14, doi:10.1155/2016/8432064. 8432064.

Brands, S., J. M. Gutiérrez, S. Herrera, and A. S. Cofiño (2012). On the Use of Reanalysis Data for Downscaling. *Journal of Climate*, 25(7):2517–2526, doi:10.1175/JCLI-D-11-00251.1.

Brands, S., S. Herrera, J. Fernández, and J. M. Gutiérrez (2013). How well do CMIP5 Earth System Models simulate present climate conditions in Europe and Africa? *Climate Dynamics*, 41(3):803–817, doi:10.1007/s00382-013-1742-8.

Bretherton, C. S. and S. Park (2009). A New Moist Turbulence Parameterization in the Community Atmosphere Model. *Journal of Climate*, 22(12):3422–3448, doi:10.1175/2008JCLI2556.1.

Bruyère, C. L., J. M. Done, G. J. Holland, and S. Fredrick (2014). Bias corrections of global models for regional climate simulations of high-impact weather. *Climate Dynamics*, 43(7):1847–1856, doi:10.1007/s00382-013-2011-6.

Bruyère, C. L., A. J. Monaghan, D. F. Steinhoff, and D. Yates (2015). Bias-Corrected CMIP5 CESM Data in WRF/MPAS Intermediate File Format. *NCAR Technical Note*, NCAR/TN-515+STR(7):27, doi:10.5065/D6445JJ7.

Burke, E. J. and S. J. Brown (2008). Evaluating Uncertainties in the Projection of Future Drought. *Journal of Hydrometeorology*, 9(2):292–299, doi:10.1175/2007JHM929.1.

Burke, E. J., S. J. Brown, and N. Christidis (2006). Modeling the Recent Evolution of Global Drought and Projections for the Twenty-First Century with the Hadley Centre Climate Model. *Journal of Hydrometeorology*, 7(5):1113–1125, doi:10.1175/JHM544.1.

Caesar, J., L. Alexander, and R. Vose (2006). Large-scale changes in observed daily maximum and minimum temperatures: Creation and analysis of a new gridded data set. *Journal of Geophysical Research: Atmospheres*, 111(D5), doi:10.1029/2005JD006280. D05101.

Caldwell, P., H.-N. S. Chin, D. C. Bader, and G. Bala (2009). Evaluation of a WRF dynamical downscaling simulation over California. *Climatic Change*, 95(3):499–521, doi:10.1007/s10584-009-9583-5.

Calinski, T. and J. Harabasz (1974). A dendrite method for cluster analysis. *Communications in Statistics*, 3(1):1–27, doi:10.1080/03610927408827101.

Cardoso, R. M., P. M. M. Soares, P. M. A. Miranda, and M. Belo-Pereira (2013). WRF high resolution simulation of Iberian mean and extreme precipitation climate. *International Journal of Climatology*, 33(11):2591–2608, doi:10.1002/joc.3616.

Chen, F. and J. Dudhia (2001). Coupling an Advanced Land Surface–Hydrology Model with the Penn State–NCAR MM5 Modeling System. Part I: Model Implementation and Sensitivity. *Monthly Weather Review*, 129(4):569–585, doi:10.1175/1520-0493(2001)129<0569:CAALSH>2.0.CO;2.

Christensen, J. H., T. R. Carter, M. Rummukainen, and G. Amanatidis (2007a). Evaluating the performance and utility of regional climate models: the PRUDENCE project. *Climatic Change*, 81(1):1–6, doi:10.1007/s10584-006-9211-6.

Christensen, J. H., B. Hewitson, A. Busuioc, A. Chen, X. Gao, R. Held, R. Jones, R. K. Kolli, W. K. Kwon, R. Laprise, V. M. Rueda, L. Mearns, C. G. Menendez, J. Räisänen, A., Rinke, A. Sarr, P. Whetton, R. Arritt, R. Benestad, M. Beniston, D. Bromwich, D. Caya, J. Comiso, R. de Elia, and K. Dethloff (2007b). Regional Climate Projections. In *Regional climate projections , Climate Change, 2007: The Physical Science Basis. Contribution of Working group I to the Fourth Assessment Report of the Intergovernmental Panel on Climate Change*. Cambridge University Press, Cambridge, United Kingdom and New York, NY, USA. Cambridge, United Kingdom and New York, NY, USA.

Colette, A., R. Vautard, and M. Vrac (2012). Regional climate downscaling with prior statistical correction of the global climate forcing. *Geophysical Research Letters*, 39(13), doi:10.1029/2012GL052258. L13707.

Collins, W. D., P. J. Rash, B. A. Boville, J. J. Hack, J. R. Mccaa, J. T. K. D. L. Williamsom, B. Briegleb, C. Bitz, S.-J. Lin, M. Zhang, and Y. Dai (2004). Description of the NCAR Community Atmosphere Model (CAM 3.0). doi:10.5065/D63N21CH. NCAR Technical Note NCAR/TN-464+STR.

Cook, B. I., J. E. Smerdon, R. Seager, and S. Coats (2014). Global warming and 21st century drying. *Climate Dynamics*, 43(9):2607–2627, doi:10.1007/s00382-014-2075-y.

Cook, K. H. and E. K. Vizy (2008). Effects of Twenty-First-Century Climate Change on the Amazon Rain Forest. *Journal of Climate*, 21(3):542–560, doi:10.1175/2007JCLI1838.1.

Dai, A. (2011). Drought under global warming: a review. *Wiley Interdisciplinary Reviews: Climate Change*, 2(1):45–65, doi:10.1002/wcc.81.

Dai, A. (2013). Increasing drought under global warming in observations and models. *Nature Climate Change*, 3:52–58, doi:10.1038/nclimate1633.

Davies, H. C. (1976). A lateral boundary formulation for multi-level prediction models. *Quarterly Journal of the Royal Meteorological Society*, 102(432):405–418, doi:10.1002/qj.49710243210.

de Elía, R., S. Biner, and A. Frigon (2013). Interannual variability and expected regional climate change over North America. *Climate Dynamics*, 41(5):1245–1267, doi:10.1007/s00382-013-1717-9.

Dee, D. P., S. M. Uppala, A. J. Simmons, P. Berrisford, P. Poli, S. Kobayashi, U. Andrae, M. A. Balmaseda, G. Balsamo, P. Bauer, P. Bechtold, A. C. M. Beljaars, L. van de Berg, J. Bidlot, N. Bormann, C. Delsol, R. Dragani, M. Fuentes, A. J. Geer, L. Haimberger, S. B. Healy, H. Hersbach, E. V. Hólm, L. Isaksen, P. Kållberg, M. Köhler, M. Matricardi, A. P. McNally, B. M. Monge-Sanz, J.-J. Morcrette, B.-K. Park, C. Peubey, P. de Rosnay, C. Tavolato, J.-N. Thépaut, and F. Vitart (2011). The ERA-Interim reanalysis: configuration and performance of the data assimilation system. *Quarterly Journal of the Royal Meteorological Society*, 137(656):553–597, doi:10.1002/qj.828.

Denis, B., R. Laprise, D. Caya, and J. Côte (2002). Downscaling ability of one-way nested regional climate models: the Big-Brother Experiment. *Climate Dynamics*, 18:627–646, doi:10.1007/s00382-001-0201-0.

Deser, C., A. Phillips, V. Bourdette, and H. Teng (2012). Uncertainty in climate change projections: the role of internal variability. *Climate Dynamics*, 38(3):527–546, doi:10.1007/s00382-010-0977-x.

Di Luca, A., D. Argüeso, J. P. Evans, R. Elía, and R. Laprise (2016a). Quantifying the overall added value of dynamical downscaling and the contribution from different spatial scales. *Journal of Geophysical Research: Atmospheres*, 121(4):1575–1590, doi:10.1002/2015JD024009.

Di Luca, A., R. de Elía, and R. Laprise (2015). Challenges in the Quest for Added Value of Regional Climate Dynamical Downscaling. *Current Climate Change Reports*, 1(1):10–21.

Di Luca, A., J. P. Evans, A. S. Pepler, L. V. Alexander, and D. Argüeso (2016b). Evaluating the representation of Australian East Coast Lows in a regional climate model ensemble. *Journal of Southern Hemisphere Earth Systems Science*, 66:108–124.

Diffenbaugh, N. S. and F. Giorgi (2012). Climate change hotspots in the CMIP5 global climate model ensemble. *Climatic Change*, 114(3):813–822, doi:10.1007/s10584-012-0570-x.

Dolman, A. J. and R. A. M. de Jeu (2010). Evaporation in focus. *Nature Geoscience*, 3:296, doi:dx.doi.org/10.1038/ngeo849.

Domínguez, M., R. Romera, E. Sánchez, L. Fita, J. Fernández, P. Jiménez-Guerrero, J. P. Montávez, W. D. Cabos, D, G. Liguori, and M. A. Gaertner (2013). Present-climate precipitation and temperature extremes over Spain from a set of high resolution RCMs. *Climate research*, 58(2):149–164, doi:10.3354/cr01186.

Done, J. M., G. J. Holland, C. L. Bruyère, L. R. Leung, and A. Suzuki-Parker (2015). Modeling high-impact weather and climate: lessons from a tropical cyclone perspective. *Climatic Change*, 129(3):81–395, doi:10.1007/s10584-013-0954-6.

Droogers, P. and R. G. Allen (2002). Estimating Reference Evapotranspiration Under Inaccurate Data Conditions. *Irrigation and Drainage Systems*, 16(1):33–45, doi:10.1023/A:1015508322413.

Dubrovsky, M., M. D. Svoboda, M. Trnka, M. J. Hayes, D. A. Wilhite, Z. Zalud, and P. Hlavinka (2009). Application of relative drought indices in assessing climate-change impacts on drought conditions in Czechia. *Theoretical and Applied Climatology*, 96(1):155–171, doi:10.1007/s00704-008-0020-x.

Easterling, D., G. A. Meehl, C. Parmesan, S. A. Changnon, T. R. Karl, and L. O. Mearns (2000). Climate extremes: observations, modeling, and impacts. *Science*, 289(5487):2068–2074.

Edwards, D. and T. McKee (1997). Characteristics of 20th century drought in the United States at multiple time scales. Climatology Report 97-2, Colorado State University, Fort Collins, Colorado.

Esteban-Parra, M. J., F. S. Rodrigo, and Y. Castro-Díez (1998). Spatial and temporal patterns of precipitation in Spain for the period 1880–1992. *International Journal of Climatology*, 18(14):1557–1574, doi:10.1002/(SICI)1097-0088(19981130)18:14<1557::AID-JOC328>3.0.CO;2-J.

Evans, J. P., F. Ji, C. Lee, P. Smith, D. Argüeso, and L. Fita (2014). Design of a regional climate modelling projection ensemble experiment – NARCliM. *Geoscientific Model Development*, 7(2):621–629, doi:10.5194/gmd-7-621-2014.

Evans, J. P. and M. F. McCabe (2010). Regional climate simulation over Australia's Murray-Darling basin: A multitemporal assessment. *Journal of Geophysical Research: Atmospheres*, 115(D14), doi:doi.org/10.1029/2010JD013816.

Feng, S. and Q. Fu (2013). Expansion of global drylands under a warming climate. *Atmospheric Chemistry and Physics*, 13:10081–10094, doi:10.5194/acp-13-10081-2013.

Fernández, J., A. Casanueva, J. P. Montávez, M. A. Gaertner, M. J. Casado, R. Manzanas, and J. M. Gutiérrez (2017). *Regional Climate Projections over Spain: Atmosphere. Future Climate Projections*, pages 45–52. International CLIVAR Project Office.

Fernández, J., M. D. Frías, W. D. Cabos, A. S. Cofiño, M. Domínguez, L. Fita, M. A. Gaertner, M. García-Díez, J. M. Gutiérrez, P. Jiménez-Guerrero., G. Liguori, J. P. Montávez, R. Romera, and E. Sánchez (2018). Consistency of climate change projections from multiple global and regional model intercomparison projects. *Climate Dynamics*, doi:10.1007/s00382-018-4181-8.

Fernández, J., J. P. Montávez, J. Sáez, J. F. G. Rouco, and E. Zorita (2007). Sensitivity of the MM5 mesoscale model to physical parameterizations for regional climate studies: Annual cycle. *Journal of Geophysical Research: Atmospheres*, 112(D4), doi:10.1029/2005JD006649.

Fita, L., J. Fernández, and M. García-Díez (2010). CLWRF: WRF modifications for regional climate simulation under future scenarios. In *11th WRF Users' Workshop*, Boulder, Colo. NCAR.

Fovell, R. G. (1997). Consensus Clustering of U.S. Temperature and Precipitation Data. *Journal of Climate*, 10(6):1405–1427, doi:10.1175/1520-0442(1997)010<1405:CCOUST>2.0.CO;2.

Gao, X. and F. Giorgi (2008). Increased aridity in the Mediterranean region under greenhouse gas forcing estimated from high resolution simulations with a regional climate model. *Global and Planetary Change*, 62(3):195 – 209, doi:10.1016/j.gloplacha.2008.02.002.

García-Herrera, R., E. Hernández, D. Barriopedro, D. Paredes, R. M. Trigo, I. F. Trigo, and M. A. Mendes (2007). The Outstanding 2004/05 Drought in the Iberian Peninsula: Associated Atmospheric Circulation. *Journal of Hydrometeorology*, 8(3):483–498, doi:10.1175/JHM578.1.

García-Valdecasas Ojeda, M., S. R. Gámiz-Fortis, Y. Castro-Díez, and M. J. Esteban-Parra (2017). Evaluation of WRF capability to detect dry and wet periods in Spain using dought indices. *Journal of Geophysical Research:Atmospheres*, 122:1569–1594, doi:10.1002/2016JD025683.

Gent, P. R., G. Danabasoglu, L. J. Donner, M. M. Holland, E. C. Hunke, S. R. Jayne, D. M. Lawrence, R. B. Neale, P. J. Rasch, M. Vertenstein, P. H. Worley, Z.-L. Yang, and M. Zhang (2011). The Community Climate System Model Version 4. *Journal of Climate*, 24(19):4973–4991, doi:10.1175/2011JCLI4083.1.

Giorgeta, M. A., J. Jungclaus, C. H. Reick, S. Legutcke, J. Bader, M. Böttiger, V. Brovkin, T. Crueger, M. Esch, K. Fieg, K. Glushak, V. Gayler, H. Haak, H.-D. Hollweg, T. Ilyina, S. Kinne, L. Kornblueh, D. Matei, T. Mauritsen, U. Mikolajewicz, W. Mueller, D. Notz, F. Pithan, T. Raddatz, S. Rast, R. Redler, E. Roeckner, H. Schmidt, R. Schnur, J. Segschneider, K. D. Six, M. Stockhause, C. Timmreck, J. Wegner, H. Widmann, K.-H. Wieners, M. Claussen, J. Marotzke, and B. Stevens (2013). Climate and carbon cycle changes from 1850 to 2100 in MPI-ESM simulations for the Coupled Model Intercomparison Project phase 5. *Journal of Advances in Modeling Earth Systems*, 5(3):572–597, doi:10.1002/jame.20038.

Giorgi, F. (2006). Regional climate modeling: Status and perspectives. *Journal de Physique IV*, 139:101–118, doi:10.1051/jp4:2006139008.

Giorgi, F., E.-S. Im, E. Coppola, N. S. Diffenbaugh, X. J. Gao, L. Mariotti, and Y. Shi (2011). Higher Hydroclimatic Intensity with Global Warming. *Journal of Climate*, 24(20):5309–5324, doi:10.1175/2011JCLI3979.1.

Giorgi, F., C. Jones, G. R. Asrar, et al. (2009). Addressing climate information needs at the regional level: the CORDEX framework. *World Meteorological Organization (WMO) Bulletin*, 58(3):175.

Giorgi, F. and P. Lionello (2008). Climate change projections for the Mediterranean region. *Global and Planetary Change*, 63(2):90–104, doi:10.1016/j.gloplacha.2007.09.005.

Gonzalez-Hidalgo, J. C., D. Peña-Angulo, M. Brunetti, and N. Cortesi (2015). MOTEDAS: a new monthly temperature database for mainland Spain and the trend in temperature (1951–2010). *International Journal of Climatology*, 35(15):4444–4463, doi:10.1002/joc.4298.

González-Hidalgo, J. C., M. Brunetti, and M. de Luis (2011). A new tool for monthly precipitation analysis in Spain: MOPREDAS database (monthly precipitation trends December 1945–November 2005). *International Journal of Climatology*, 31(5):715–731, doi:10.1002/joc.2115.

González-Rojí, S. J., J. Sáenz, G. Ibarra-Berastegi, and J. D. Argandoña (2018). Moisture Balance Over the Iberian Peninsula According to a Regional Climate Model: The Impact of 3DVAR Data Assimilation. *Journal of Geophysical Research: Atmospheres*, 123(2):708–729, doi:10.1002/2017JD027511.

Granier, C., B. Bessagnet, T. T. Bond, A. D'Angiola, H. D. van der Gon, G. J. Frost, A. Heil, J. W. Kaiser, S. Kinne, Z. Klimont, S. Kloster, J. F. Lamarque, C. Liousse, T. Masui, F. Meleux, A. Mieville, T. Ohara, J. C. Raut, K. Riahi, M. G. Schultz, S. J. Smith, A. Thompson, J. van Aardenne, G. R. van der Werf, and D. P. van Vuuren (2011). Evolution of anthropogenic and biomass burning emissions of air pollutants at global and regional scales during the 1980–2010 period. *Climatic Change*, 109(1):163, doi:10.1007/s10584-011-0154-1.

Grell, G. A. and D. Dévényi (2002). A generalized approach to parameterizing convection combining ensemble and data assimilation techniques. *Geophysical Research Letters*, 29(14):38–1–38–4, doi:10.1029/2002GL015311.

Grell, G. A. and S. R. Freitas (2014). A scale and aerosol aware stochastic convective parameterization for weather and air quality modeling. *Atmospheric Chemistry and Physics*, 14(10):5233–5250, doi:10.5194/acp-14-5233-2014.

Grenier, H. and C. S. Bretherton (2001). A Moist PBL Parameterization for Large-Scale Models and Its Application to Subtropical Cloud-Topped Marine Boundary Layers. *Monthly Weather Review*, 129(3):357–377, doi:10.1175/1520-0493(2001)129<0357:AMPPFL>2.0.CO;2.

Greve, P., B. Orlowsky, B. Mueller, J. Sheffield, M. Reichstein, and S. I. Seneviratne (2014). Global assessment of trends in wetting and drying over land. *Nature Geoscience*, 7:716–721, doi:10.1038/ngeo2247.

Greve, P., K. Warrach-Sagi, and V. Wulfmeyer (2013). Evaluating Soil Water Content in a WRF-Noah Downscaling Experiment. *Journal of Applied Meteorology and Climatology*, 52(10):2312–2327, doi:10.1175/JAMC-D-12-0239.1.

Guerreiro, S. B., C. Kilsby, and H. J. Fowler (2017). Assessing the threat of future megadrought in Iberia. *International Journal of Climatology*, 37:5024–5034, doi:10.1002/joc.5140.

Guttman, N. B. (1998). Comparing the Palmer Drought Index and the Standardized Precipitation Index. *JAWRA Journal of the American Water Resources Association*, 34(1):113–121, doi:10.1111/j.1752-1688.1998.tb05964.x.

Gómez, G., W. D. Cabos, G. Liguori, D. Sein, S. Lozano-Galeana, L. Fita, J. Fernández, M. E. Magariño, P. Jiménez-Guerreo, J. P. Montávez, M. Domínguez, R. Romera, and M. A. Gaertner (2016). Characterization of the wind speed variability and future change in the Iberian Peninsula and the Balearic Islands. *Wind Energy*, 19(7):1223–1237, doi:10.1002/we.1893.

Gómez-Navarro, J., J. P. Montávez, P. Jimenez-Guerrero, S. Jerez, J. A. García-Valero, and J. F. González-Rouco (2010). Warming patterns in regional climate change projections over the Iberian Peninsula. *Meteorologische Zeitschrift*, 19(3):275–285, doi:10.1127/0941-2948/2010/0351.

Gómez-Navarro, J. J., J. P. Montávez, S. Jerez, P. Jimenez-Guerrero, and E. Zorita (2012). What is the role of the observational dataset in the evaluation and scoring of climate models? *Geophysical Research Letters*, 39(24), doi:10.1029/2012GL054206. L24701.

Gómez-Navarro, J. J., J. P. Montávez, S. Wagner, and E. Zorita (2013). A regional climate palaeosimulation for Europe in the period 1500–1990 – Part 1: Model validation. *Climate of the Past*, 9(4):1667–1682, doi:10.5194/cp-9-1667-2013.

Hawkins, E. and R. Sutton (2009). The Potential to Narrow Uncertainty in Regional Climate Predictions. *Bulletin of the American Meteorological Society*, 90(8):1095–1108, doi:10.1175/2009BAMS2607.1.

Hawkins, E. and R. Sutton (2011). The potential to narrow uncertainty in projections of regional precipitation change. *Climate Dynamics*, 37(1):407–418, doi:10.1007/s00382-010-0810-6.

Hawkins, E. and R. Sutton (2012). Time of emergence of climate signal. *Geophysical Research Letters*, 39(1), doi:10.1029/2011GL050087.

Hay, L. E., R. L. Wilby, and G. H. Leavesley (2000). A Comparison of Delta Change and Downscaled GCM Scenarios For Three Mountainous Basins in the United States. *JAWRA Journal of the American Water Resources Association*, 36(2):387–397, doi:10.1111/j.1752-1688.2000.tb04276.x.

Haylock, M. R., N. Hofstra, A. M. G. Klein Tank, E. J. Klok, P. D. Jones, and M. New (2008). A European daily high-resolution gridded data set of surface temperature and precipitation for 1950–2006. *Journal of Geophysical Research: Atmospheres*, 113(D20), doi:10.1029/2008JD010201. D20119.

Heathcote, R. L. (1983). *The Arid Lands: Their Use and Abuse*. Longman.

Hegerl, G. C., F. W. Zwiers, P. Braconnot, N. P. Gillett, Y. Luo, J. A. M. Orsini, N. Nicholls, J. E. Penner, and P. A. Stott (2007). Understanding and attributing climate change In *The Physical Science Basis, Contribution of Working Group I to the Fourth Assessment Report of the Intergovernmental Panel on Climate Change*. [Solomon, S., D. Qin, M. Manning, Z. Chen, M. Marquis, K. B. Averyt, M. Tignor, and H. L. Miller, (eds.)], pages 663–745. Cambridge University Press, Cambridge, United Kingdom and New York, NY, USA. Cambridge, United Kingdom and New York, NY, USA.

Hegerl, G. C., F. W. Zwiers, P. A. Stott, and V. V. Kharin (2004). Detectability of Anthropogenic Changes in Annual Temperature and Precipitation Extremes. *Journal of Climate*, 17(19):3683–3700, doi:10.1175/1520-0442(2004)017<3683:DOACIA>2.0.CO;2.

Heikkilä, U., A. Sandvik, and A. Sorteberg (2011). Dynamical downscaling of ERA-40 in complex terrain using the WRF regional climate model. *Climate Dynamics*, 37(7):1551–1564, doi:10.1007/s00382-010-0928-6.

Held, I. M. and B. J. Soden (2006). Robust Responses of the Hydrological Cycle to Global Warming. *Journal of Climate*, 19(21):5686–5699, doi:10.1175/JCLI3990.1.

Herrera, S. (2011). *Desarrollo, validación y aplicaciones de Spain02: Una rejilla de alta resolución de observaciones interpoladas para precipitación y temperatura en España*. PhD dissertation, Departamento de Matemática Aplicada y Ciencias de la Computación, Universidad de Cantabria.

Herrera, S., J. Fernández, and J. M. Gutiérrez (2016). Update of the Spain02 gridded observational dataset for EURO-CORDEX evaluation: assessing the effect of the interpolation methodology. *International Journal of Climatology*, 36(2):900–908, doi:10.1002/joc.4391.

Herrera, S., L. Fita, J. Fernández, and J. M. Gutiérrez (2010). Evaluation of the mean and extreme precipitation regimes from the ENSEMBLES regional climate multimodel simulations over Spain. *Journal of Geophysical Research: Atmospheres*, 115(D21), doi:10.1029/2010JD013936. D21117.

Herrera, S., J. M. Gutiérrez, R. Ancell, M. R. Pons, M. D. Frías, and J. Fernández (2012). Development and analysis of a 50-year high-resolution daily gridded precipitation dataset over Spain (Spain02). *International Journal of Climatology*, 32(1):74–85, doi:10.1002/joc.2256.

Holland, G. J., J. Done, C. Bruyère, C. Cooper, and A. Suzuki (2010). Model investigations of the effects of climate variability and change on future Gulf of Mexico tropical cyclone activity. In *Offshore Technology Conference*.

Hong, S.-. Y., J. Dudhia, and S.-H. Chen (2004). A Revised Approach to Ice Microphysical Processes for the Bulk Parameterization of Clouds and Precipitation. *Monthly Weather Review*, 132(1):103–120, doi:10.1175/1520-0493(2004)132<0103:ARATIM>2.0.CO;2.

Hong, S.-Y., Y. Noh, and J. Dudhia (2006). A New Vertical Diffusion Package with an Explicit Treatment of Entrainment Processes. *Monthly Weather Review*, 134(9):2318–2341, doi:10.1175/MWR3199.1.

Hsu, S. A., E. A. Meindl, and D. B. Gilhousen (1994). Determining the Power-Law Wind-Profile Exponent under Near-Neutral Stability Conditions at Sea. *Journal of Applied Meteorology*, 33(6):757–765, doi:10.1175/1520-0450(1994)033<0757:DTPLWP>2.0.CO;2.

Huntington, T. G. (2006). Evidence for intensification of the global water cycle: Review and synthesis. *Journal of Hydrology*, 319(1):83 – 95, doi:10.1016/j.jhydrol.2005.07.003.

Hurrell, J. W., M. M. Holland, P. R. Gent, S. Ghan, J. E. Kay, P. J. Kushner, J.-F. Lamarque, W. G. Large, D. Lawrence, K. Lindsay, W. H. Lipscomb, M. C. Long, N. Mahowald, D. R. Marsh, R. B. Neale, P. Rasch, S. Vavrus, M. Vertenstein, D. Bader, W. D. Collins, J. J. Hack, J. Kiehl, and S. Marshall (2013). The Community Earth System Model: A Framework for Collaborative Research. *Bulletin of the American Meteorological Society*, 94(9):1339–1360, doi:10.1175/BAMS-D-12-00121.1.

IPCC (2007). Climate Models and their Evaluation In *The Physical Science Basis. Contribution of Working Group I to the Fourth Assessment Report of the Intergovernmental Panel on Climate Change*. [Solomon, S., D. Qin, M. Manning,

Z. Chen, M. Marquis, K. Averyt, M. Tignor, and H. Miller, (eds.)], page 996. Cambridge University Press, Cambridge, United Kingdom and New York, NY, USA. Cambridge, United Kingdom and New York, NY, USA.

IPCC (2014). Climate Change 2014: Synthesis Report, Meyer, L. A. and S. Brinkman and L. van Kesteren and N. Leprince-Ringuet and F. van Boxmeer. Contribution of Working Groups I, II and III to the fifth assessment report of the Intergovernmental Panel on Climate Change. page 151pp. Geneva, Switzerland. Geneva, Switzerland.

Jacob, D., J. Petersen, B. Eggert, A. Alias, C. O. B, L. M. Bouwer, A. Braun, A. B. A. Colette, M. Déqué, G. Georgievski, E. Georgopoulou, A. Gobiet, L. Menut, G. Nikulin, A. Haensler, N. Hempelmann, C. Jones, K. Keuler, S. Kovats, N. Kröner, S. Kotlarski, A. Kriegsmann, E. Martin, E. van Meijgaard, C. Moseley, S. Pfeifer, S. Preuschmann, C. Radermacher, K. Radtke, D. Rechid, M. Rounsevell, P. Samuelsson, S. Somot, J.-. F. Soussana, C. Teichmann, R. Valentini, R. Vautard, B. Weber, and P. Yiou (2014). EURO-CORDEX: new high-resolution climate change projections for European impact research. *Regional Environmental Change*, 14(2):563–578, doi:10.1007/s10113-013-0499-2.

Jacob, D. and R. Podzun (1997). Sensitivity studies with the regional climate model REMO. *Meteorology and Atmospheric Physics*, 63(1):119–129.

Jaeger, E. B. and S. I. Seneviratne (2011). Impact of soil moisture–atmosphere coupling on European climate extremes and trends in a regional climate model. *Climate Dynamics*, 36(9):1919–1939, doi:10.1007/s00382-010-0780-8.

Janjić, Z. I. (1994). The Step-Mountain Eta Coordinate Model: Further Developments of the Convection, Viscous Sublayer, and Turbulence Closure Schemes. *Monthly Weather Review*, 122(5):927–945, doi:10.1175/1520-0493(1994)122<0927:TSMECM>2.0.CO;2.

Jerez, S., J. M. López-Romero, M. Turco, P. Jiménez-Guerrero, R. Vautard, and J. P. Montávez (2018). Impact of evolving greenhouse gas forcing on the warming signal in regional climate model experiments. *Nature Communications*, 9(1), doi:10.1038/s41467-018-03527-y.

Jerez, S., J. P. Montavez, J. J. Gomez-Navarro, P. A. Jimenez, P. Jimenez-Guerrero, R. Lorente, and J. F. Gonzalez-Rouco (2012). The role of the land-surface model for climate change projections over the Iberian Peninsula. *Journal of Geophysical Research: Atmospheres*, 117(D1), doi:10.1029/2011JD016576. D01109.

Jerez, S., J. P. Montavez, J. J. Gomez-Navarro, P. Jimenez-Guerrero, and J. J. J. F. Gonzalez-Rouco (2010). Temperature sensitivity to the land-surface model in MM5 climate simulations over the Iberian Peninsula. *Meteorologische Zeitschrift*, 19(4):363–374, doi:10.1127/0941-2948/2010/0473.

Jerez, S., J. P. Montavez, P. Jimenez-Guerrero, J. J. Gomez-Navarro, R. Lorente-Plazas, and E. Zorita (2013). A multi-physics ensemble of present-day climate regional simulations over the Iberian Peninsula. *Climate Dynamics*, 40(11):3023–3046, doi:10.1007/s00382-012-1539-1.

Ji, F., J. P. Evans, J. Teng, Y. Scorgie, D. Argüeso, and A. D. Luca (2016). Evaluation of long-term precipitation and temperature Weather Research and Forecasting simulations for southeast Australia. *Climate Research*, 67(2):99–115, doi:10.3354/cr01366.

Jiménez, P. A., J. F. González-Rouco, E. García-Bustamante, J. Navarro, J. P. Montávez, J. Vilà-Guerau, J. Dudhia, and A. Muñoz-Roldan (2010). Surface Wind Regionalization over Complex Terrain: Evaluation and Analysis of a High-Resolution WRF Simulation. *Journal of Applied Meteorology and Climatology*, 49(2):268–287, doi:10.1175/2009JAMC2175.1.

Jones, R. G., J. M. Murphy, and M. Noguer (1995). Simulation of climate change over europe using a nested regional-climate model. I: Assessment of control climate, including sensitivity to location of lateral boundaries. *Quarterly Journal of the Royal Meteorological Society*, 121(526):1413–1449, doi:10.1002/qj.49712152610.

Jung, M., M. Reichstein, P. Ciais, S. I. Seneviratne, J. Sheffield, M. L. Goulden, G. Bonan, A. Cescatti, J. Chen, R. de Jeu, A. J. Dolman, W. Eugster, D. G. andD. Gianelle, N. Gobron, J. Heinke, J. Kimball, B. E. Law, L. Montagnani, Q. Mu, B. Mueller, K. Oleson, D. Papale, A. D. Richardson, O. Roupsard, S. Running, E. Tomelleri, N. Viovy, U. Weber, C. Williams, E. Wood, S. Zaehle, and K. Zhang (2010). Recent decline in the global land evapotranspiration trend due to limited moisture supply. *Nature*, 467:951–954, doi:10.1038/nature09396.

Kain, J. S. and J. M. Fritsch (1990). A one-dimensional entraining/detraining plume model and its application in convective parameterization. *Journal of the Atmospheric Sciences*, 47(23):2784–2802, doi:10.1175/1520-0469(1990)047<2784:AODEPM>2.0.CO;2.

Kain, J. S. and J. M. Fritsch (1993). *Convective parameterization for mesoscale models: The Kain–Fritsch scheme*, pages 165–170. American Meteorological Society, Boston, MA.

Kain, K. F. (2004). The Kain–Fritsch Convective Parameterization: An Update. *Journal of Applied Meteorology*, 43(1):170–181, doi:10.1175/1520-0450(2004)043<0170:TKCPAU>2.0.CO;2.

Kanamitsu, M., W. Ebisuzaki, J. Woollen, S.-K. Yang, J. J. Hnilo, M. Fiorino, and G. L. Potter (2002). NCEP–DOE AMIP-II Reanalysis (R-2). *Bulletin of the American Meteorological Society*, 83(11):1631–1643, doi:10.1175/BAMS-83-11-1631.

Kang, D., B. K. Eder, A. F. Stein, G. A. Grell, S. E. Peckman, and J. McHenry (2005). The New England air quality forecasting pilot program: Development of an evaluation protocol and performance benchmark. *Journal of the Air & Waste Management Association*, 55(12):1782–1796, doi:10.1080/10473289.2005.10464775.

Keellings, D. (2016). Evaluation of downscaled CMIP5 model skill in simulating daily maximum temperature over the southeastern United States. *International Journal of Climatology*, 36(12):4172–4180, doi:10.1002/joc.4612.

Kim, B. S., I. G. Chang, J. H. Sung, and H. J. Han (2016). Projection in Future Drought Hazard of South Korea Based on RCP Climate Change Scenario 8.5 Using SPEI. *Advances in Meteorology*, 2016:23, doi:10.1155/2016/4148710. 4148710.

King, A. D., M. T. Black, S. Min, E. M. Fischer, D. M. Mitchell, L. J. Harrington, and S. E. Perkins-Kirkpatrick (2016). Emergence of heat extremes attributable to anthropogenic influences. *Geophysical Research Letters*, 43(7):3438–3443, doi:10.1002/2015GL067448.

Kirtman, B., S. B. Power, J. A. Adedoyin, G. J. Boer, R. Bojariu, I. Camilloni, F. J. Doblas-Reyes, A. M. Fiore, M. Kimoto, G. A. Meehl, M. Prather, A. Sarr, C. Schär, R. Sutton, G. J. van Oldenborgh, G. Vecchi, and H. J. Wang (2013). Near-term Climate Change: Projections and Predictability In *The Physical Science Basis. Contribution of Working Group I to the Fifth Assessment Report of the Intergovernmental Panel on Climate Change*. [Stocker, T. F., D. Qin, G. K. Plattner, M. Tignor, S. K. Allen, J. Boschung, A. Nauels, Y. Xia, V. Bex, and P. Midgley, (eds.)]. Cambridge University Press, Cambridge, United Kingdom and New York, NY, USA. Cambridge, United Kingdom and New York, NY, USA.

Kjellström, E., F. Boberg, M. Castro, J. H. Christensen, G. Nikulin, and E. Sánchez (2010). Daily and monthly temperature and precipitation statistics as performance indicators for regional climate models. *Climate Research*, 44:135–150, doi:10.3354/cr00932.

Knist, S., K. Goergen, E. Buonomo, O. B. Christensen, A. Colette, R. M. Cardoso, F. R, J. Fernández, M. García-Díez, D. Jacob, S. Kartsios, E. Katragkou, K. Keuler, S. Mayer, E. van Meijgaard, G. Nikulin, P. M. M., Soares, S. Sobolowski, G. Szepszo, C. Teichmann, R. Vautard, K. Warrach-Sagi, V. Wulfmeyer, and C. Simmer (2017). Land-atmosphere coupling in EURO-CORDEX evaluation experiments. *Journal of Geophysical Research: Atmospheres*, 122(1):79–103, doi:10.1002/2016JD025476. 2016JD025476.

Kobayashi, S., Y. Ota, Y. Harada, A. Ebita, M. Moriya, H. Onoda, K. Onogi, H. Kamahori, C. Kobayashi, H. Endo, K. Miyaoka, and K. Takahashi (2015). The JRA-55 reanalysis: General specifications and basic characteristics. *Journal of the Meteorological Society of Japan. Ser. II*, 93(1):5–48, doi:10.2151/jmsj.2015-001.

Koster, R. D. and M. J. Suarez (2004). Suggestions in the Observational Record of Land–Atmosphere Feedback Operating at Seasonal Time

Scales. *Journal of Hydrometeorology*, 5(3):567–572, doi:10.1175/1525-7541(2004)005<0567:SITORO>2.0.CO;2.

Leduc, M. and R. Laprise (2009). Regional climate model sensitivity to domain size. *Climate Dynamics*, 32:833–854, doi:10.1007/s00382-008-0400-z.

Lee, D., S.-K. Min, C. Park, M.-S. Suh, J.-B. Ahn, D.-H. Cha, D.-K. Lee, , S.-Y. Hong, S.-C. Park, and H.-S. Kang (2016). Time of emergence of anthropogenic warming signals in the Northeast Asia assessed from multi-regional climate models. *Asia-Pacific Journal of Atmospheric Sciences*, 52(2):129–137, doi:10.1007/s13143-016-0014-z.

Lehner, F., C. Deser, and L. Terray (2017). Toward a New Estimate of "Time of Emergence" of Anthropogenic Warming: Insights from Dynamical Adjustment and a Large Initial-Condition Model Ensemble. *Journal of Climate*, 30(19):7739–7756, doi:10.1175/JCLI-D-16-0792.1.

Leng, G., Q. Tang, and S. Rayburg (2015). Climate change impacts on meteorological, agricultural and hydrological droughts in China. *Global and Planetary Change*, 126:23 – 34, doi:10.1016/j.gloplacha.2015.01.003.

Leung, L. R., L. O. Mearns, F. Giorgi, and R. L. Wilby (2003). Regional Climate Research. *Bulletin of the American Meteorological Society*, 84(1):89–95, doi:10.1175/BAMS-84-1-89.

Lin, L., A. Gettelman, S. Feng, and Q. Fu (2015). Simulated climatology and evolution of aridity in the 21st century. *Journal of Geophysical Research: Atmospheres*, 120(12):5795–5815, doi:10.1002/2014JD022912.

Lin, T. and F. Cheng (2016). Impact of Soil Moisture Initialization and Soil Texture on Simulated Land–Atmosphere Interaction in Taiwan. *Journal of Hydrometeorology*, 17(5):1337–1355, doi:10.1175/JHM-D-15-0024.1.

Lorente-Plazas, R., J. P. Montávez, S. Jeréz, J. J. Gómez-Navarro, P. Jiménez-Guerrero, and P. A. Jiménez (2015a). A 49 year hindcast of surface winds over the Iberian Peninsula. *International Journal of Climatology*, 35(10):3007–3023, doi:10.1002/joc.4189.

Lorente-Plazas, R., J. P. Montávez, P. A. Jimenez, S. J. J. J. Gómez-Navarro, and J. A. G.-V. P. Jimenez-Guerrero (2015b). Characterization of surface winds over the Iberian Peninsula. *International Journal of Climatology*, 35(6):1007–1026, doi:10.1002/joc.4034.

López-Franca, N., E. Sánchez, and M. Domínguez (2013). Changes in the onset and length of seasons from an ensemble of regional climate models over Spain for future climate conditions. *Theoretical and Applied Climatology*, 114(3):635–642, doi:10.1007/s00704-013-0868-2.

López-Franca, N., E. Sánchez, T. Losada, M. Domínguez, R. Romera, and M. A. Gaertner (2015). Markovian characteristics of dry spells over the Iberian Peninsula under present and future conditions using ESCENA ensemble of regional climate models. *Climate Dynamics*, 45(3):661–677, doi:10.1007/s00382-014-2280-8.

Mahlstein, I., R. Knutti, S. Solomon, and R. Portmann (2011). Early onset of significant local warming in low latitude countries. *Environmental Research Letters*, 6(3), doi:10.1088/17489326/6/3/034009.

Mallard, M. S., C. G. Nolte, T. L. Spero, O. R. Bullock, K. Alapaty, J. A. Herwehe, J. Gula, and J. H. Bowden (2015). Technical challenges and solutions in representing lakes when using WRF in downscaling applications. *Geoscientific Model Development*, 8(4):1085–1096, doi:10.5194/gmd-8-1085-2015.

Maraun, D. (2013). When will trends in European mean and heavy daily precipitation emerge? *Environmental Research Letters*, 8(1):014004, doi:10.1088/1748-9326/8/1/014004.

Marcos-Garcia, P., A. Lopez-Nicolas, and M. Pulido-Velazquez (2017). Combined use of relative drought indices to analyze climate change impact on meteorological and hydrological droughts in a Mediterranean basin. *Journal of Hydrology*, 554:292 – 305, doi:10.1016/j.jhydrol.2017.09.028.

Martens, B., D. G. Miralles, H. Lievens, R. van der Schalie, R. A. M. de Jeu, D. Fernádez-Prieto, H. E. Beck, W. A. Dorigo, and N. E. C. Verhoest

(2017). GLEAM v3: satellite-based land evaporation and root-zone soil moisture. *Geoscientific Model Development*, 10(5):1903–1925, doi:10.5194/gmd-10-1903-2017.

Maule, C. F., P. Thejll, J. H. Christensen, S. H. Svendsen, and J. Hannaford (2013). Improved confidence in regional climate model simulations of precipitation evaluated using drought statistics from the ENSEMBLES models. *Climate Dynamics*, 40(1):155–173, doi:10.1007/s00382-012-1355-7.

McKee, T. B., N. Doesken, and J. Kleist (1993). The Relationship of Drought Frequency and Duration to Time Scales. American Meteorological Society, Anaheim, California, 17-22 Jan.

McSweeney, C. F., R. G. Jones, R. W. Lee, and D. P. Rowell (2015). Selecting CMIP5 GCMs for downscaling over multiple regions. *Climate Dynamics*, 44(11):3237–3260, doi:10.1007/s00382-014-2418-8.

Mearns, L. O., R. Arritt, S. Biner, M. S. Bukovsky, S. McGinnis, S. Sain, D. Caya, J. C. Jr., D. Flory, W. Gutowski, E. S. Takle, R. Jones, R. Leung, W. Moufouma-Okia, L. McDaniel, A. M. B. Nunes, Y. Qian, J. Roads, L. Sloan, and M. Snyder (2012). The North American Regional Climate Change Assessment Program: Overview of Phase I Results. *Bulletin of the American Meteorological Society*, 93(9):1337–1362, doi:10.1175/BAMS-D-11-00223.1.

Meinshausen, M., S. J. Smith, , K. Calvin, J. S. Daniel, M. L. T. Kainuma, J.-F. Lamarque, K. Matsumoto, S. A. Montzka, S. C. B. Raper, K. Riahi, A. Thomson, G. J. M. Velders, and D. P. P. van Vuuren (2011). The RCP greenhouse gas concentrations and their extensions from 1765 to 2300. *Climatic Change*, 109(1):213, doi:10.1007/s10584-011-0156-z.

Meque, A. and B. J. Abiodun (2015). Simulating the link between ENSO and summer drought in Southern Africa using regional climate models. *Climate Dynamics*, 44(7):1881–1900, doi:10.1007/s00382-014-2143-3.

Messmer, M., C. C. J. J. Gómez-Navarro, and Raible (2017). Sensitivity experiments on the response of Vb cyclones to sea surface temperature and soil moisture changes. *Earth System Dynamics*, 8(3):477–493, doi:10.5194/esd-8-477-2017.

Miguez-Macho, G., G. L. Stenchikov, and A. Robock (2004). Spectral nudging to eliminate the effects of domain position and geometry in regional climate model simulations. *Journal of Geophysical Research: Atmospheres*, 109(D13), doi:10.1029/2003JD004495. D13104.

Milly, P. C. D., R. T. Wetherald, K. A. Dunne, and T. L. Delworth (2002). Increasing risk of great floods in a changing climate. *Nature*, 415:514–517, doi:10.1038/415514a.

Min, S.-K., Y.-H. Kim, M.-K. Kim, and C. Park (2014). Assessing human contribution to the summer 2013 Korean heat wave. *Bulletin of the American Meteorological Society*, 95(9):S48.

Miralles, D. G., M. J. den Berg, A. J. Teuling, and R. A. M. Jeu (2012). Soil moisture-temperature coupling: A multiscale observational analysis. *Geophysical Research Letters*, 39(21), doi:10.1029/2012GL053703.

Miralles, D. G., T. R. H. Holmes, R. A. M. D. Jeu, J. H. Gash, A. G. C. A. Meesters, and A. J. Dolman (2011). Global land-surface evaporation estimated from satellite-based observations. *Hydrology and Earth System Sciences*, 15(2):453–469, doi:10.5194/hess-15-453-2011.

Miralles, D. G., A. J. Teuling, C. C. van Heerwaarden, and J. V.-G. de Arellano (2014). Mega-heatwave temperatures due to combined soil desiccation and atmospheric heat accumulation. *Nature Geoscience*, 7:345–349, doi:10.1038/ngeo2141.

Mishra, A. K., V. P. Singh, , and V. R. Desai (2009). Drought characterization: a probabilistic approach. *Stochastic Environmental Research and Risk Assessment*, 23(1):41–55, doi:10.1007/s00477-007-0194-2.

Mishra, A. K. and V. P. Singh (2010). A review of drought concepts. *Journal of Hydrology*, 391(1):202–216, doi:10.1016/j.jhydrol.2010.07.012.

Montávez, J. P., J. Fernández, A. Casanueva, J. M. Gutiérrez, and E. Sánchez (2017). *Regional climate projections over Spain: Atmosphere. Present climate evaluation*, pages 39–44. International CLIVAR Project Office.

Mora, C., A. G. Frazier, R. J. Longman, R. S. Dacks, M. M. Walton, E. J. Tong, J. J. Sanchez, L. R. Kaiser, Y. O. Stender, J. M. Anderson, C. M. Ambrosino, I. Fernandez-Silva, L. M. Giuseffi, and T. W. Giambelluca (2013). The projected timing of climate departure from recent variability. *Nature*, 502:183–187, doi:10.1038/nature12540.

Moss, R. H., J. A. Edmonds, K. A. Hibbard, M. R. Manning, S. K. Rose, D. P. van Vuuren, T. R. Carter, S. Emori, M. Kainuma, T. Kram, G. A. Meehl, J. F. B. Mitchell, N. Nakicenovic, K. Riahi, S. J. Smith, R. J. Stouffer, A. M. Thomson, J. P. Weyant, and T. J. Wilbanks (2010). The next generation of scenarios for climate change research and assessment. *Nature*, 463(7282):747–756, doi:10.1038/nature088.

Neale, R. B., C.-C. Chen, A. Gettelman, P. H. Lauritzen, S. Park, D. L. Williamson, A. J. Conley, R. Garcia, D. Kinnison, J.-F. Lamarque, D. Marsh, M. Mills, A. K. Smith, S. Tilmes, F. Vitt, H. Morrison, P. Cameron-Smith, W. D. C. M. J. Iacono, R. C. Easter, S. J. Ghan, X. Liu, and P. J. R. M. A. Taylor (2012). Description of the NCAR Community Atmosphere Model (CAM 5.0). page 289 pp. NCAR Technical Note NCAR/TN-486+STR.

New, M., M. Hulme, and P. Jones (2000). Representing Twentieth-Century Space–Time Climate Variability. Part II: Development of 1901–96 Monthly Grids of Terrestrial Surface Climate. *Journal of Climate*, 13(13):2217–2238, doi:10.1175/1520-0442(2000)013<2217:RTCSTC>2.0.CO;2.

New, M., D. Lister, M. Hulme, and I. Makin (2002). A high resolution data set of surface climate over global land areas. *Climate Research*, 21:1–25, doi:10.3354/cr021001.

Nguyen, T.-H., S.-K. Min, S. Paik, and D. Lee (2018). Time of emergence in regional precipitation changes: an updated assessment using the CMIP5 multimodel ensemble. *Climate Dynamics*, doi:10.1007/s00382-018-4073-y.

Orlowsky, B. and S. I. Seneviratne (2013). Elusive drought: uncertainty in observed trends and short- and long-term CMIP5 projections. *Hydrology and Earth System Sciences*, 17(5):1765–1781, doi:10.5194/hess-17-1765-2013.

Osborn, T. J. and M. Hulme (1997). Development of a Relationship between Station and Grid-Box Rainday Frequencies for Climate Model Evaluation. *Journal of Climate*, 10(8):1885–1908, doi:10.1175/1520-0442(1997)010<1885:DOARBS>2.0.CO;2.

PaiMazumder, D. and J. M. Done (2014). Uncertainties in long-term drought characteristics over the Canadian Prairie provinces, as simulated by the Canadian RCM. *Climate Research*, 58(3):209–220, doi:10.3354/cr01196.

PaiMazumder, D., L. Sushama, R. Laprise, M. N. Khaliq, and D. Sauchyn (2013). Canadian RCM projected changes to short- and long-term drought characteristics over the Canadian Prairies. *International Journal of Climatology*, 33:1409–1423, doi:10.1002/joc.3521.

Palmer, W. C. (1965). *Meteorological drought*, volume 30. US Department of Commerce, Weather Bureau Washington, DC.

Panu, U. S. and T. C. Sharma (2002). Challenges in drought research: some perspectives and future directions. *Hydrological Sciences Journal*, 47(sup1):S19–S30, doi:10.1080/02626660209493019.

Pendergrass, A. G., R. Knutti, F. Lehner, C. Deser, and B. M. Sanderson (2017). Precipitation variability increases in a warmer climate. *Scientific Reports*, 7(17966), doi:10.1038/s41598-017-17966-y.

Perkins, S. E., L. V. Alexander, and J. R. Nairn (2012). Increasing frequency, intensity and duration of observed global heatwaves and warm spells. *Geophysical Research Letters*, 39(20).

Perkins, S. E., A. J. Pitman, N. J. Holbrook, and J. McAneney (2007). Evaluation of the AR4 Climate Models' Simulated Daily Maximum Temperature, Minimum Temperature, and Precipitation over Australia Using Probability Density Functions. *Journal of Climate*, 20(17):4356–4376, doi:10.1175/JCLI4253.1.

Peña-Ortiz, C., D. Barriopedro, and R. García-Herrera (2015). Multidecadal variability of the summer length in Europe. *Journal of Climate*, 28(13):5375–5388, doi:10.1175/JCLI-D-14-00429.1.

Pleim, J. E. (2007). A Combined Local and Nonlocal Closure Model for the Atmospheric Boundary Layer. Part I: Model Description and Testing. *Journal of Applied Meteorology and Climatology*, 46(9):1383–1395, doi:10.1175/JAM2539.1.

Pons, M., S. Herrera, and J. M. Gutiérrez (2016). Future Trends of Snowfall Days in Northern Spain from ENSEMBLES Regional Climate Projections. *Climate Dynamics*, 46:3645–3655, doi:10.1007/s00382-015-2793-9.

Prein, A. F. and A. Gobiet (2017). Impacts of uncertainties in European gridded precipitation observations on regional climate analysis. *International Journal of Climatology*, 37(1):305–327, doi:10.1002/joc.4706.

Prein, A. F., A. Gobiet, H. Truhetz, K. Keuler, K. Goergen, C. Teichmann, C. F. Maule, E. van Meijgaard, M. Déqué, G. Nikulin, R. Vautard, A. Colette, E. Kjellström, and D. Jacob (2016). Precipitation in the EURO-CORDEX 0.11º and 0.44º simulations: high resolution, high benefits? *Climate Dynamics*, 46(1):383–412, doi:10.1007/s00382-015-2589-y.

Prudhomme, C., I. Giuntoli, E. L. Robinson, D. B. Clark, N. W. Arnell, R. Dankers, B. M. Fekete, W. Franssen, D. Gerten, S. N. Gosling, S. Hagemann, D. M. Hannah, H. Kim, Y. Masaki, Y. Satoh, T. Stacke, Y. Wada, and D. Wisser (2014). Hydrological droughts in the 21st century, hotspots and uncertainties from a global multimodel ensemble experiment. *Proceedings of the National Academy of Sciences*, 111(9):3262–3267, doi:10.1073/pnas.1222473110.

Pérez, J. C., J. P. Díaz, A. González, J. Expósito, F. Rivera-López, and D. Taima (2014). Evaluation of WRF Parameterizations for Dynamical Downscaling in the Canary Islands. *Journal of Climate*, 27(14):5611–5631, doi:10.1175/JCLI-D-13-00458.1.

Quintana-Seguí, P., M. Turco, S. Herrera, and G. Miguez-Macho (2017). Validation of a new SAFRAN-based gridded precipitation product for Spain and comparisons to Spain02 and ERA-Interim. *Hydrology and Earth System Sciences*, 21(4):2187–2201, doi:10.5194/hess-21-2187-2017.

Rodriguez-Puebla, C., A. H. Encinas, S. Nieto, and J. Garmendia (1998). Spatial and temporal patterns of annual precipitation variability over the Iberian Peninsula. *International Journal of Climatology*, 18(3):299–316, doi:10.1002/(SICI)1097-0088(19980315)18:3<299::AID-JOC247>3.0.CO;2-L.

Ruiz-Arias, J. A., J. Dudhia, F. J. Santos-Alamillos, and D. Pozo-Vázquez (2013). Surface clear-sky shortwave radiative closure intercomparison in the Wetaher Research and Forecasting model. *Journal of Geophysical Research: Atmospheres*, 118(17):9901–9913, doi:10.1002/jgrd.50778.

Russo, A., C. M. Gouveia, P. Páscoa, C. C. DaCamara, M. Sousa, and R. M. Trigo (2017). Assessing the role of drought events on wildfires in the Iberian Peninsula. *Agricultural and Forest Meteorology*, 237-238:50–59, doi:10.1016/j.agrformet.2017.01.021.

Russo, A. C., C. M., Gouveia, R. M. Trigo, M. L. R. Liberat, and C. C.DaCamara (2015). The influence of circulation weather patterns at different spatial scales on drought variability in the Iberian Peninsula. *Frontiers in Environmental Science*, 3:1–15, doi:10.3389/fenvs.2015.00001.

Ruti, P. M., S. Somot, F. Giorgi, C. Dubois, E. Flaounas, A. Obermann, A. Dell'Aquila, G. Pisacane, A. Harzallah, E. Lombardi, B. Ahrens, N. Akhtar, A. Alias, T. Arsouze, R. Aznar, S. Bastin, J. Bartholy, K. Béranger, J. Beuvier, S. Bouffies-Cloché, J. Brauch, W. Cabos, S. Calmanti, J.-C. Calvet, A. Carillo, D. Conte, E. Coppola, V. Djurdjevic, P. Drobinski, A. Elizalde-Arellano, M. Gaertner, P. Galàn, C. Gallardo, S. Gualdi, M. Goncalves, O. Jorba, G. Jordà, B. L'Heveder, C. Lebeaupin-Brossier, L. Li, G. Liguori, P. Lionello, D. Maciàs, P. Nabat, B. Önol, B. Raikovic, K. Ramage, F. Sevault, G. Sannino, M. V. Struglia, A. Sanna, C. Torma, and V. Vervatis (2016). Med-CORDEX Initiative for Mediterranean Climate Studies. *Bulletin of the American Meteorological Society*, 97(7):1187–1208, doi:10.1175/BAMS-D-14-00176.1.

Rökstrom, J., W. Steffen, K. Noone, A. Peerson, F. S. C. III, E. F. Lambin, T. M. Lenton, M. Scheffer, C. Folke, H. J. Schellnhuber, B. Nykvist, C. A. de Wit, T. Hughes, S. van der Leeuw, H. Rodhe, S. Sörlin, P. K. Snyder, R. Costanza, U. Svedin, M. Falkenmark, L. Karlberg, R. W. Corell, V. J. Fabry, J. Hansen, B. Walker, D. Liverman, K. Richardson, P. Crutzen, and J. A.

Foley (2009). A safe operating space for humanity. *Nature*, 461:472–475, doi:10.1038/461472a.

San-Martín, D., R. Manzanas, S. Brands, S. Herrera, and J. M. Gutiérrez (2017). Reassessing Model Uncertainty for Regional Projections of Precipitation with an Ensemble of Statistical Downscaling Methods. *Journal of Climate*, 30(1):203–223, doi:10.1175/JCLI-D-16-0366.1.

Santer, B. D., C. Mears, C. Doutriaux, P. Caldwell, P. J. Gleckler, T. M. L. Wigley, S. Solomon, N. P. Gillett, D. Ivanova, T. R. Karl, J. R. Lanzante, G. A. Meehl, P. A. Stott, K. E. Taylor, P. W. Thorne, M. F. Wehner, and F. J. Wentz (2011). Separating signal and noise in atmospheric temperature changes: The importance of timescale. *Journal of Geophysical Research: Atmospheres*, 116(D22).

Santos, J. F., I. Pulido-Calvo, and M. M. Portela (2010). Spatial and temporal variability of droughts in Portugal. *Water Resources Research*, 46(3), doi:10.1029/2009WR008071. W03503.

Sato, T., F. Kimura, and A. Kitoh (2007). Projection of global warming onto regional precipitation over Mongolia using a regional climate model. *Journal of Hydrology*, 333(1):144 – 154, doi:10.1016/j.jhydrol.2006.07.023.

Seneviratne, S. I., T. Corti, E. L. Davin, M. Hirschi, E. B. Jaeger, I. Lehner, B. Orlowsky, and A. J. Teuling (2010). Investigating soil moisture–climate interactions in a changing climate: A review. *Earth-Science Reviews*, 99(3):125 – 161, doi:10.1016/j.earscirev.2010.02.004.

Seneviratne, S. I., R. D. Koster, Z. Guo, P. A. Dirmeyer, E. Kowalczyk, D. Lawrence, P. Liu, D. Mocko, C.-H. Lu, K. W. Oleson, and D. Verseghy (2006a). Soil Moisture Memory in AGCM Simulations: Analysis of Global Land–Atmosphere Coupling Experiment (GLACE) Data. *Journal of Hydrometeorology*, 7(5):1090–1112, doi:10.1175/JHM533.1.

Seneviratne, S. I., D. Luthi, M. Litschi, and C. Scha (2006b). Land–atmosphere coupling and climate change in Europe. *Nature*, 443(7108):205, doi:10.1038/nature05095.

Seneviratne, S. I., N. Nicholls, D. Easterling, C. Goodess, S. Kanae, J. Kossin, Y. Luo, J. Marengo, K. McInnes, M. Rahimi, M. Reichstein, A. Sorteberg, C. Vera, and X. Zhang (2012). Changes in climate extremes and their impacts on the natural physical environment In *Managing the Risks of Extreme Events and Disasters to Advance Climate Change Adaptation. A Special Report of Working Groups I and II of the Intergovernmental Panel on Climate Change (IPCC)*. [Field, C., V. Barros, T. Stocker, D. Qin, D. Dokken, K. Ebi, M. Mastrandrea, K. Mach, G.-K. Plattner, S. Allen, M. Tignor, and P. Midgley, (eds.)]. Cambridge University Press, Cambridge, United Kingdom and New York, NY, USA. Cambridge, United Kingdom and New York, NY, USA.

Seneviratne, S. I., M. Wilhelm, T. Stanelle, B. Hurk, S. Hagemann, A. Berg, F. Cheruy, M. E. Higgins, A. Meier, V. Brovkin, M. Claussen, A. Ducharne, J. L. Dufresne, K. L. Findell, J. Ghattas, D. M. Lawrence, S. Malyshev, M. Rummukainen, and B. Smith (2013). Impact of soil moisture-climate feedbacks on CMIP5 projections: First results from the GLACE-CMIP5 experiment. *Geophysical Research Letters*, 40(19):5212–5217, doi:10.1002/grl.50956.

Seth, A. and F. Giorgi (1998). The effects of domain choice on summer precipitation simulation and sensitivity in a regional climate model. *Journal of Climate*, 11(10):2698–2712, doi:10.1175/1520-0442(1998)011<2698:TEODCO>2.0.CO;2.

Sheffield, J. and E. F. Wood (2008). Projected changes in drought occurrence under future global warming from multi-model, multi-scenario, IPCC AR4 simulations. *Climate Dynamics*, 31(1):79–105, doi:10.1007/s00382-007-0340-z.

Sheffield, J., E. F. Wood, and M. L. Roderick (2012). Little change in global drought over the past 60 years. *Nature*, 491:435–438, doi:10.1038/nature11575.

Sherwood, S. and Q. Fu (2014). A Drier Future? *Science*, 343(6172):737–739, doi:10.1126/science.1247620.

Sillmann, J., V. V. Kharin, X. Zhang, F. W. Zwiers, and D. Bronaugh (2013).

Climate extremes indices in the CMIP5 multimodel ensemble: Part 1. Model evaluation in the present climate. *Journal of Geophysical Research: Atmospheres*, 118(4):1716–1733, doi:10.1002/jgrd.50203.

Sims, A. P., D. S. Niyogi, and S. Raman (2002). Adopting drought indices for estimating soil moisture: A North Carolina case study. *Geophysical Research Letters*, 29(8):24–1–24–4, doi:10.1029/2001GL013343.

Skamarock, W. C., J. B. Klemp, J. Dudhia, D. O. Gill, D. M. Barker, M. G. Duda, X.-Y. Huang, W. Wang, and J. G. Powers (2008). A Description of the Advanced Research WRF Version 3. Technical report. NCAR Technical Note NCAR/TN-475+STR.

Soares, P. M. M., R. M. Cardoso, D. C. A. Lima, and P. M. A. Miranda (2016). Future precipitation in Portugal: high-resolution projections using WRF model and EURO-CORDEX multi-model ensembles. *Climate Dynamics*, pages 1–28, doi:10.1007/s00382-016-3455-2.

Soares, P. M. M., R. M. Cardoso, P. M. A. Miranda, J. de Madeiros, M. Belo-Pereira, and F. Espirito-Santo (2012a). WRF high resolution dynamical downscaling of ERA-Interim for Portugal. *Climate Dynamics*, 39:2497–2522, doi:10.1007/s00382-012-1315-2.

Soares, P. M. M., R. M. Cardoso, P. M. A. Miranda, P. Viterbo, and M. Belo-Pereira (2012b). Assessment of the ENSEMBLES regional climate models in the representation of precipitation variability and extremes over Portugal. *Journal of Geophysical Research: Atmospheres*, 117(D7), doi:10.1029/2011JD016768. D07114.

Spinoni, J., G. Naumann, H. Carrao, P. Barbosa, and J. Vogt (2014). World drought frequency, duration, and severity for 1951–2010. *International Journal of Climatology*, 34(8):2792–2804, doi:10.1002/joc.3875.

Spinoni, J., G. Naumann, J. V. Vogt, and P. Barbosa (2015). The biggest drought events in Europe from 1950 to 2012. *Journal of Hydrology: Regional Studies*, 3:509 – 524, doi:10.1016/j.ejrh.2015.01.001.

Spinoni, J., J. V. Vogt, G. Naumann, P. Barbosa, and A. Dosio (2018). Will drought events become more frequent and severe in Europe? *International Journal of Climatology*, 38(4):1718–1736, doi:10.1002/joc.5291.

Stagge, J., L. Tallaksen, and J. Rizzi (2015). Future meteorological drought: projections of regional climate models for Europe. In *EGU General Assembly Conference Abstracts*, volume 17.

Staniforth, A. (1997). Regional modeling: A theoretical discussion. *Meteorology and Atmospheric Physics*, 63(1):15–29, doi:10.1007/BF01025361.

Stensrud, D. J. (2007). *Parameterization Schemes: Keys to Understanding Numerical Weather Prediction Models*. Cambridge University Press.

Stevens, B., M. Giorgetta, M. Esch, T. Mauritsen, T. Crueger, S. Rast, M. Salzmann, H. Schmidt, J. Bader, K. Block, R. Brokopf, I. Fast, S. Kinne, L. Kornblueh, U. Lohmann, R. Pincus, T. Reichler, and E. Roeckner (2013). Atmospheric component of the MPI-M Earth System Model: ECHAM6. *Journal of Advances in Modeling Earth Systems*, 5(2):146–172, doi:10.1002/jame.20015.

Stull, R. B. (1988). *An introduction to boundary layer meteorology*. Kluwer Academic Publishers, Dordrecht: Kluwer.

Sui, Y., X. Lang, and D. Jiang (2014). Time of emergence of climate signals over China under the RCP4.5 scenario. *Climatic Change*, 125(2):265–276, doi:10.1007/s10584-014-1151-y.

Tank, A. M. G. K., F. W. Zwiers, and X. Zhang (2009). *Guidelines on analysis of extremes in a changing climate in support of informed decisions for adaptation*. World Meteorological Organization.

Taylor, K. E., R. J. Stouffer, and G. A. Meehl (2012). An Overview of CMIP5 and the Experiment Design. *Bulletin of the American Meteorological Society*, 93(4):485–498, doi:10.1175/BAMS-D-11-00094.1.

Touma, D., M. Ashfaq, M. A. Nayak, S.-C. Kao, and N. S. Diffenbaugh (2015). A multi-model and multi-index evaluation of drought characteristics in the 21st century. *Journal of Hydrology*, 526:196 – 207, doi:10.1016/j.jhydrol.2014.12.011.

Trenberth, K. E. (2010). Changes in precipitation with climate change. *Climate Research*, 47(1-2):123–138, doi:doi.org/10.3354/cr00953.

Turco, M., , A. Sanna, H. Sixto, M.-C. Llasat, and J. M. Guitiérrez (2015). Evaluation of the ENSEMBLES Transient RCM Simulations Over Spain: Present Climate Performance and Future Projections In *Engineering Geology for Society and Territory - Volume 1*. [Lollino, G., A. Manconi, J. Clague, W. Shan, and M. Chiarle, (eds.)], pages 199–203, Cham. Springer International Publishing.

Turco, M., M. C. Llasat, S. Herrera, and J. M. Gutiérrez (2017). Bias correction and downscaling of future RCM precipitation projections using a MOS-Analog technique. *Journal of Geophysical Research: Atmospheres*, 122(5):2631–2648, doi:10.1002/2016JD025724. 2016JD025724.

Ulazia, A., J. Saenz, and G. Ibarra-Berastegui (2016). Sensitivity to the use of 3DVAR data assimilation in a mesoscale model for estimating offshore wind energy potential. A case study of the Iberian northern coastline. *Applied Energy*, 180:617 – 627, doi:10.1016/j.apenergy.2016.08.033.

Uppala, S. M., P. W. Kållberg, A. J. Simmons, U. Andrae, V. D. C. Bechtold, M. Fiorinoa, M., and X. Li (2005). The ERA-40 re-analysis. *Quarterly Journal of the Royal Meteorological Society*, 131:2961–3012.

van der Linden, P. and J. F. B. Mitchell (2009). ENSEMBLES: Climate Change and its impacts: Summary of research and results from the ENSEMBLES projects. Technical report, Met Office Hadley Centre, Exeter, UK. Technical report.

van Vuuren, D. P. P., J. Edmonds, M. Kainuma, K. Riahi, A. Thomsom, K. Hibbard, G. C. Hurtt, T. Kram, V. Krey, J.-F. Lamarque, T. Masui, M. Meinshausen, N. Nakicenovic, S. J. Smith, and S. K. Rose (2011). The representative concentration pathways: an overview. *Climatic Change*, 109(1):5, doi:10.1007/s10584-011-0148-z.

Vicente-Serrano, S. M. (2006). Differences in Spatial Patterns of Drought on Different Time Scales: An Analysis of the Iberian Peninsula. *Water Resources Management*, 20(1):37–60, doi:10.1007/s11269-006-2974-8.

Vicente-Serrano, S. M., C. Azorin-Molina, A. Sanchez-Lorenzo, J. Revuelto, E. Morán-Tejeda, J. I. López-Moreno, and F. Espejo (2014a). Sensitivity of reference evapotranspiration to changes in meteorological parameters in Spain (1961–2011). *Water Resources Research*, 50(11):8458–8480, doi:10.1002/2014WR015427.

Vicente-Serrano, S. M., S. Beguería, and J. I. López-Moreno (2010). A Multiscalar Drought Index Sensitive to Global Warming: The Standardized Precipitation Evapotranspiration Index. *Journal of Climate*, 23(7):1696–1718, doi:10.1175/2009JCLI2909.1.

Vicente-Serrano, S. M., J. I. Lopez-Moreno, S. Beguería, J. Lorenzo-Lacruz, A. Sanchez-Lorenzo, J. M. García-Ruiz, C. Azorin-Molina, E. Morán-Tejeda, J. Revuelto, R. Trigo, F. Coelho, and F. Espejo (2014b). Evidence of increasing drought severity caused by temperature rise in southern Europe. *Environmental Research Letters*, 9(4), doi:10.1002/2014WRO15427.

Vicente-Serrano, S. M., J. I. López-Moreno, A. Drumond, L. Gimeno, R. Nieto, E. Morán-Tejeda, S. B. J. Lorenzo-Laruz, and J. Zabalba (2011a). Effects of warming processes on droughts and water resources in the NW Iberian Peninsula (1930-2006). *Climate Research*, 48:203–212, doi:10.3354/cr01002.

Vicente-Serrano, S. M., R. M.Trigo, J. I. López-Moreno, M. L. R. Liberato, J. Lorenzo-Lacruz, S. Beguería, E. Morán-Tejeda, and A. M. E. Kenawy (2011b). Extreme winter precipitation in the Iberian Peninsula in 2010: anomalies, driving mechanisms and future projections. *Climate Research*, 46:51–65, doi:10.3354/cr00977.

von Storch, H., H. Langenberg, and F. Feser (2000). A Spectral Nudging Technique for Dynamical Downscaling Purposes. *Monthly Weather Review*, 128(10):3664–3673, doi:10.1175/1520-0493(2000)128<3664:ASNTFD>2.0.CO;2.

Waldron, K. M., J. Paegle, and J. D. Horel (1996). Sensitivity of a Spectrally Filtered and Nudged Limited-Area Model to Outer Model Options. *Monthly Weather Review*, 124(3):529–547, doi:10.1175/1520-0493(1996)124<0529:SOASFA>2.0.CO;2.

Wang, H. and X. Zeng (2018). Impacts of internal climate variability on meteorological drought changes in China. *Atmospheric and Oceanic Science Letters*, 11(1):78–85, doi:10.1080/16742834.2017.1379865.

Wang, J., F. N. U. Swati, M. L. Stein, and V. R. Kotamarthi (2015). Model performance in spatiotemporal patterns of precipitation: New methods for identifying value added by a regional climate model. *Journal of Geophysical Research: Atmospheres*, 120(4):1239–1259, doi:10.1002/2014JD022434. 2014JD022434.

Warrach-Sagi, K., T. Schwitalla, V. Wulfmeyer, and H.-S. Bauer (2013). Evaluation of a climate simulation in Europe based on the WRF–NOAH model system: precipitation in Germany. *Climate Dynamics*, 41(3):755–774, doi:10.1007/s00382-013-1727-7.

Wilhite, D. A. (2000). Drought as a natural hazard: concepts and definitions. In *Drought: A Global Assessment*, pages 3–18. Routledge, London. London.

Wilks, D. S. (2006). *Statistical Methods in the Atmospheric Sciences, International Geophysics Series*, volume 91. Academic Press, Burlington, Mass, 2 edition.

Wu, W. and A. H. Lynch (2000). Response of the seasonal carbon cycle in high latitudes to climate anomalies. *Journal of Geophysical Research: Atmospheres*, 105(D18):22897–22908, doi:10.1029/2000JD900340.

Xu, Z. and Z. L. Yang (2012). An Improved Dynamical Downscaling Method with GCM Bias Corrections and Its Validation with 30 Years of Climate Simulations. *Journal of Climate*, 25(18):6271–6286, doi:10.1175/JCLI-D-12-00005.1.

Yang, H., B. Wang, and B. Wang (2012). Reduction of systematic biases in regional climate downscaling through ensemble forcing. *Climate Dynamics*, 38(3):655–665, doi:10.1007/s00382-011-1006-4.

Yang, Y., H. Kuo, E. A. Hendriks, Y. Liu, and M. S. Peng (2015). Relationship between typhoons with concentrics eyewalls and ENSO in the western North

Pacific Basins. *Journal of Climate*, 28:3612–3623, doi:10.1175/JCLI-D-14-00541.1.

Yang, Y., M. Uddstrom, and D. Maurice (2011). Effects of short spin-up periods on soil moisture simulation and the causes over New Zealand. *Journal of Geophysical Research: Atmospheres*, 116(D24), doi:10.1029/2011JD016121. D24108.

Yu, M., Q. Li, M. J. Hayes, M. D. Svoboda, and R. R. Heim (2014). Are droughts becoming more frequent or severe in China based on the Standardized Precipitation Evapotranspiration Index: 1951–2010. *International Journal of Climatology*, 34(3):545–558, doi:10.1002/joc.3701.

Zhao, T. and A. Dai (2015). The Magnitude and Causes of Global Drought Changes in the Twenty-First Century under a Low–Moderate Emissions Scenario. *Journal of Climate*, 28(11):4490–4512, doi:10.1175/JCLI-D-14-00363.1.